

Microstructurally-based Constitutive Models of Cytoskeletal Networks for Simulation of the Biomechanical Response of Biological Cells

by

Jeffrey Shane Palmer

Bachelor of Science in Mechanical Engineering
New Mexico State University, 1994

Master of Science in Mechanical Engineering
Rensselaer Polytechnic Institute, 1997

Submitted to the Department of Mechanical Engineering
in partial fulfillment of the requirements for the degree of

Doctor of Philosophy in Mechanical Engineering

at the

MASSACHUSETTS INSTITUTE OF TECHNOLOGY

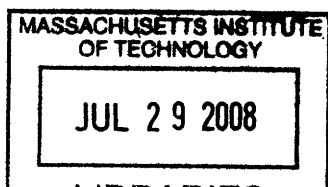
June 2008

© Massachusetts Institute of Technology 2008. All rights reserved.

Author.....
Department of Mechanical Engineering
May 9, 2008

Certified by.....
Mary C. Boyce
Gail E. Kendall Professor of Mechanical Engineering
Thesis Supervisor

Accepted by.....
Lallit Anand
Chairman, Department Committee on Graduate Students



ARCHIVES

Microstructurally-based Constitutive Models of Cytoskeletal Networks for Simulation of the Biomechanical Response of Biological Cells

by

Jeffrey Shane Palmer

Submitted to the Department of Mechanical Engineering
on May 9, 2008 in partial fulfillment of the
requirements for the degree of
Doctor of Philosophy in Mechanical Engineering

Abstract

The elastic and viscoelastic stress-strain behavior of cytoskeletal networks, important to many cellular functions, is modeled via a microstructurally-informed continuum mechanics approach. The force-extension behavior of the individual filaments is captured with a new analytical expression of the MacKintosh worm-like chain relationship for semiflexible filaments. The filament expression is used in the Arruda-Boyce eight-chain network model to capture the 3D stress-strain behavior, quantifying the effects of isotropic network prestress and tracking microstructural stretch and orientation states during large deformations. The network model captures the initial stiffness of the network as well as the nonlinear strain stiffening observed at large stresses in shear rheological data of bundled/unbundled *in vitro* F-actin networks.

The cytoskeletal network model has also been extended to include the internal energy-based mechanical contributions at the filament and network levels from torsional cross-link deformations as well as from direct axial stretching of filaments. This enhanced model effectively captures the stress-strain behavior of F-actin networks cross-linked with two different types of actin binding proteins (filamin and streptavidin). The enhanced model is also used to evaluate the influence of the cross-links' torsional stiffness on the entropic bending configuration space of the cytoskeletal filaments.

The 3D constitutive network model provides a framework for capturing time-dependent spatial diffusion of cytosol within a porous, viscohyperelastic filament network. The poroelastic behavior is coupled with the hyperelastic network behavior through a 3D biphasic theory that includes network swelling effects for finite deformations. The mechanical response of the cytoskeletal network due to the localized swelling is captured by employing multiplicative decomposition of mechanical and swelling stretches. Nonlinear shear viscoelasticity is also included to create a 3D poroviscohyperelastic network model capable of capturing the time-dependent response of cytoskeletal networks on short and long time scales. The model captures the nonlinear time-dependent behavior of *in vitro* actin-filamin and actin-avidin networks observed in shear rheological experiments. The constitutive models are evaluated in a finite element model with a cellular geometry (including membrane and nucleus submodels) and the ability to spatially vary network properties throughout the cell.

Thesis Supervisor: Mary C. Boyce

Title: Gail E. Kendall Professor of Mechanical Engineering

Acknowledgements

I will praise You, for I am fearfully and wonderfully made. - Psalm 139:14

A sense of awe and fascination for complex structures, systems, and machines inspired me to switch from investigating human engineered microsystems to these hierarchical biological architectures that span length scales from nano to micro (and eventually macro). This change was prompted by an impromptu discussion in a hallway with my advisor, Prof. Mary Boyce, to whom I am forever indebted for her vision, investment, and patience with my development. She was committed to the rigor and accuracy of my primary work as well as the finer points in my development such as the ongoing transformation from an analyst who does “trade studies” to a scholar who can critically, and creatively, evaluate the parametric space that defines the mechanical behavior of a complex material. Through her generosity and encouragement, I have had wonderful opportunities to present our work on three continents and interact with the top minds in the field of mechanics. And in retrospect, I am thankful for the chance to have worked with a mechanic whose talents and capabilities I consider second to none.

I was also very fortunate to have a fantastic thesis committee. Professor Roger Kamm influenced my education in many ways: as my teacher in one of my favorite classes at MIT (*Molecular, Cellular, and Tissue Biomechanics*), as an engaged member of my thesis committee, as a pro bono collaborator for rheological experiments to support my thesis, and finally for taking extra time to advise me on different applications and issues within cytoskeletal mechanics. Professor Matt Lang was very supportive of my work in its evolving stages, and I truly appreciated his friendliness and willingness to take extra time for discussions in his office about life as a junior faculty member, strategy sessions for proposals, and advice on cross-linking protein and filament mechanics. I also thank Dean Subra Suresh for his encouragement and help obtaining extra resources/references despite his incredibly busy schedule.

There have been so many labmates to thank for their help, encouragement, and laughter: H. Jerry Qi, Raj Sharma, Franco Capaldi, Adam Mulliken, Nuo Sheng, Ethan Parsons, Ben Bruet, Cathal Kearney, Melis Arslan, Mohit Garg, Carlos Castro, Katia Bertoldi, Meri Silberstein, Juha Song, and Hyungsuk Lee. A special thanks to Una too! I owe a special thanks and debt to my study partners for the MechE quals: Josh Alper, Erin Swan,

Dave Quinn, and Brandon Epps. It was an ordeal that we endured together, but also a great environment to ask the “dumb” questions we never could in classes, dispel fundamental misconceptions, and spur each other to replace hand-waving with solutions we could prove, step-by-step, on a blackboard. We got to see sides of each other that not many people get to see, and I was proud to go through that adventure with you and come out the other side to find out that the light at the end of the tunnel wasn’t a train after all!

This journey would not have been possible without the support of my family and friends. Thanks to friends at GCC such as John Feehrer, and the men’s group at Immanuel Church in Chelmsford for praying for me and helping to keep me grounded and growing in His word while also learning at MIT. Thank you Mom, Pop, Sara, and Katie, for your relentless love and support via phone, e-mail, and “storming the gates.” And thanks to all of my Lancaster family (Dad, Jane, Grandpa & Grandma Jacobs, Zel, Sara, Marie, and others) for your support, prayers and love.

I also want to thank my kiddos, Emily (8) and Eric (1½), for their patience and enthusiastic love and affection. You two put a smile on my face and joy in my heart, whether it’s your big waves to me when I’m driving off in the mornings or your running hugs that knock me over when I return at night. Of course, the person who has sacrificed just as much, if not more, than I have during the last four years is my wonderful wife, Heather. She has at various times played the role of wife, friend, comforter, no-nonsense encourager, and (essentially) single mother. She deserves much more recognition for her hard work and share in my completion of this doctorate that I am able to give her in these pages. Heather, I love you and could not have done this without you!

I would also like to acknowledge the generous support from my supervisors (Dr. Bob Davis, Dr. Steve Forman) and colleagues (Dr. Dennis Burianek, Carol Mullinax, and others) from Lincoln Laboratory. The funding for this academic journey came from Lincoln Laboratory through its Lincoln Doctoral Scholars Program. This work is sponsored by the Department of the Air Force under Air Force contract number FA8721-05-C-0002. The opinions, interpretations, recommendations, and conclusions are those of the author and are not necessarily endorsed by the United States Government.

Soli Deo Gloria

Contents

LIST OF FIGURES AND TABLES.....	12
CHAPTER 1 INTRODUCTION	32
1.1 Cell mechanics and role of cytoskeleton	32
1.2 Cytoskeletal filament networks.....	36
1.2.1 Morphology & filament properties	36
1.2.1.1 Actin filaments.....	36
1.2.1.2 Intermediate filaments	42
1.2.1.3 Microtubules	44
1.2.2 Cross-linked network behavior	48
1.2.2.1 Actin filaments.....	48
1.2.2.2 Intermediate filaments	53
1.2.2.3 Microtubules	55
CHAPTER 2 FILAMENT MODEL	58
2.1 Filament energy and stiffness regimes.....	58
2.2 Inextensible Entropic Models	63
2.2.1 Freely jointed chain model.....	63
2.2.2 Worm-like chain model	66
2.3 Internal energy axial stretching model.....	81
2.4 Extensible model.....	83
2.4.1 Kinematics: multiplicative decomposition	84
2.4.2 Kinematics: additive decomposition.....	90

2.4.3	Comparison with F-actin stretching experiments	92
CHAPTER 3	NETWORK MODEL	96
3.1	Previous cell models and experimental techniques	96
3.2	8-chain Network Model	111
3.2.1	Stress-strain behavior.....	117
3.2.2	Implementation in finite element analysis	120
3.3	Isotropically prestressed Networks	123
3.4	Rheological experimental techniques	124
3.5	8-chain/MacKintosh Network Model Results	129
3.5.1	Experimental data used for comparison.....	129
3.5.2	Representative low concentration case	130
3.5.3	Effects of increasing actin concentration.....	134
3.5.4	Parametric evaluation of bundling effects	136
3.5.5	Network stress-strain with linear filament force-extension.....	139
3.5.5.1	Comparison with representative low concentration case.....	141
3.5.6	Network model performance with varying persistence length	143
3.6	Extensible 8-chain Network Model	145
3.6.1	Implementation in finite element analysis	146
3.6.2	Evaluation of extensible network model behavior.....	146
3.7	Equilibrium swelling of cytoskeletal networks.....	150
3.7.1	Kinematics of equilibrium swelling.....	151
3.7.2	Thermodynamics, constitutive equations for equilibrium swelling	153
3.7.3	Implementation in finite element analysis	156

3.7.4	Swelling of actin networks in a spherical geometry	158
CHAPTER 4	INFLUENCE OF NETWORK CROSS-LINKS	164
4.1	Cross-link types, roles, and geometries	164
4.2	Cross-link stiffness and torsion properties.....	170
4.3	Cross-link torsional potential model.....	172
4.3.1	Implementation in finite element analysis	176
4.3.2	Parametric evaluation of cross-link torsion model	178
4.3.3	Comparison with experimental data of actin-FLNa networks	180
4.3.4	Comparison with experimental data of actin-avidin networks	184
4.4	Evaluation of cross-link coupling with entropic configuration space	187
CHAPTER 5	VISCOELASTIC NETWORK MODEL	195
5.1	Previous viscoelastic modeling work.....	195
5.1.1	Maxwell model	195
5.1.2	Kelvin-voigt model	197
5.1.3	Standard linear solid model	198
5.1.4	Quasilinear viscoelastic model	205
5.1.5	Power law model.....	213
5.2	Linear rheological model	214
5.2.1	Continuum mechanics derivation	216
5.2.2	Comparison with actin-FLNa experimental data.....	219
5.3	Nonlinear rheological model.....	224
5.3.1	Actin-avidin networks.....	236
5.4	Stress relaxation of actin networks in a cell geometry	246

5.4.1	Mechanical properties of the nucleus and membrane.....	247
5.4.2	Axisymmetric cell model.....	251
5.4.3	Axisymmetric cell model with varying actin concentration	255
CHAPTER 6 POROELASTIC NETWORK MODELS.....		261
6.1	Background.....	261
6.1.1	Biphasic, poroelastic models: Terzaghi model	262
6.1.2	Biphasic, poroelastic models: Biot model	267
6.1.3	Biphasic, poroelastic models: Mow model.....	269
6.1.4	Poroelastic testing procedures.....	271
6.1.5	Biphasic poroviscoelastic theory	273
6.2	Poroelastic governing equations	278
6.3	Actin permeability	281
6.4	Confined and unconfined compression simulations	284
6.5	Compressed cell simulation	294
6.5.1	Poroelastic cell compression.....	294
6.5.2	Axisymmetric poroelastic cell model and results	295
6.5.3	Poroviscoelastic cell compression	308
CHAPTER 7 SUMMARY AND FUTURE APPLICATIONS		314
7.1	Summary discussion	314
7.1.1	Inextensible filament and network models	314
7.1.2	Extensible filament and network models.....	316
7.1.3	Equilibrium network swelling model.....	317
7.1.4	Cross-link effects	317

7.1.5	Viscoelastic network models	319
7.1.6	Poroviscoelastic network models.....	320
7.2	Future applications in cell motility	324
7.2.1	Dynamic nature of cytoskeleton for cell motility	324
7.2.2	Cell motility modalities and modeling needs.....	329
7.2.3	Modeling of anisotropic migrational cellular structures.....	331
7.2.4	Membrane-substrate interactions	333
7.2.5	Model validation	334
REFERENCES		335

List of Figures and Tables

Figure 1–1. Cellular structures: plasma membrane, nucleus, and cytoskeletal filaments (adapted from (Cummings, 2001)).	32
Figure 1–2. Actin network morphologies throughout the cell (Alberts, 1996).	37
Figure 1–3. The endothelial cytoskeleton in increasing magnification, clockwise. A, Fluorescently labeled endothelial cell cytoskeletons with nuclei stained blue, F-actin stained red, and microtubules stained green. The “striped” actin appearance throughout the cells is due to the bundling of F-actin into stress fibers which are differentiable at optical resolution, panel width 200 μm . B, Higher magnification reveals that the cells actually contain a pervasive network of actin filaments that fills the space between stress fibers (arrowheads), staining a diffuse red in fluorescent imaging, panel width 20 μm . C, D, Increasing magnification of the network showing it to be a dense, porous, evenly-distributed web of individual filaments. The pore size of the network is approximately 100 nm, (A, image courtesy of Molecular Probes. B-D, images courtesy of John Hartwig. All four panels are taken from different cells; inset boxes are placed solely for scale). Hartemink, C.A., Ph.D. Thesis, MIT (2005).	38
Figure 1–4. F-actin polymerization and polarity, bar=10nm (Lodish et al., 2004)	38
Figure 1–5. (A) Crystal structure of monomeric G-actin and (B) structural surface representation F-actin with 13 monomers (Images courtesy of Thomas Splettstoesser with the open source molecular visualization tool PyMol, based on the atomic models of (A) Kabsch, et al. (Kabsch et al., 1990) and (B) Holmes, et al. (Holmes et al., 1990)).	40
Figure 1–6. Electron micrograph of the actin cortex of a macrophage cytoskeleton, labeled with myosin subfragment 1. Bar, 0.1 μm (top right corner). (Hartwig and Shevlin, 1986).	41
Figure 1–7. Intermediate filament substructures (Campbell et al., 1999)	43
Figure 1–8. Electron micrograph of in vitro vimentin IF. Bar = 100nm. (Mucke et al., 2004).	43

Figure 1–9. Microtubule composition (Alberts, 2002).....	45
Figure 1–10. Microtubules with sinusoidal shapes (arrowheads) at their ends (white line indicates cell periphery). Bar = 5 μ m. (Brangwynne et al., 2006).....	45
Figure 1–11. Primary experimental methods to measure mechanical properties of individual microtubules. P is the loading force, F is the response from the microtubule. (Kikumoto et al., 2006).....	46
Figure 1–12. The persistence lengths of MT as a function of their contour lengths (Pampaloni et al., 2006).....	47
Figure 1–13. (a) Storage modulus $G'(\omega)$ and (b) Loss modulus $G''(\omega)$ of F-actin filaments. Solid lines: theory with $G''(\omega) \sim \omega^{3/4}$ [adapted from (Koenderink et al., 2006)].....	50
Figure 1–14. Dynamic shear storage moduli as a function of shear strain (Storm et al., 2005).....	51
Figure 1–15. Elastic shear modulus of actin-scurin networks as a function of (A) ratio of c_{CL} / c_A and (B) actin concentration; $R = 0.03(\blacksquare)$, $0.13(\Delta)$, and $0.3(\bullet)$. (adapted from (Gardel et al., 2004a)).....	51
Figure 1–16. Differential elastic modulus, K' , as a function of applied shear prestress, σ_0 , for actin-scurin networks: $R=0.03$ and $c_A = 29.4 \mu\text{M}(\blacktriangle)$, $21.4 \mu\text{M}(\bullet)$, $11.9 \mu\text{M}(\blacksquare)$, $8.33 \mu\text{M}(\blacklozenge)$ (Gardel et al., 2004a). Inset: schematic showing implications of the nonlinear stress-strain relationship for networks in which $G'' \ll G'$ (Gardel et al., 2006b).....	52
Figure 1–17. Dynamic shear storage modulus of vimentin IF as a function of shear strain γ ($c = 2\text{mg/ml}$), and as a function of vimentin concentration (low initial strain) [adapted from (Janmey et al., 1991)].....	54
Figure 1–18. Shear stress-strain response of vimentin (2 mg/ml) [adapted from (Janmey et al., 1991)].....	54
Figure 1–19. Electron micrograph of a fibroblast after dissolution of actin filaments revealing microtubules (orange), IFs assembled from vimentin (green), plectin (red), and gold particles marking plectin (yellow). Gold particles are 10 nm in diameter. [(Fuchs and Cleveland, 1998) adapted from (Svitkina et al., 1996)].....	55

Figure 1–20. Dynamic shear storage modulus of microtubules as a function of shear strain γ ($c = 2\text{mg/ml}$), and as a function of microtubule concentration (low initial strain) [adapted from (Janmey et al., 1991)].....	56
Figure 1–21. Shear stress-strain response of microtubules (2 mg/ml) [adapted from (Janmey et al., 1991)]	57
Figure 2–1. Geometric quantities for biopolymer filaments.....	61
Figure 2–2. Freely Jointed Chain	64
Figure 2–3. WLC filament schematic [adapted from (MacKintosh, 2006)].....	66
Figure 2–4. Comparison of WLC, FJC, and linear models for dsDNA data (Bustamante et al., 2000).....	70
Figure 2–5. Normalized force-extension plot of WLC approximation for increasing persistence length, l_p	71
Figure 2–6. (a) The effect of persistence length on filament force-extension behavior as computed using MacKintosh model (fixing contour length to $L_c=1.02\mu\text{m}$); (b) the effect of pretension on filament force-stretch behavior as computed using MacKintosh model (for case of $L_c=1.02\mu\text{m}$; $l_p=3\mu\text{m}$). Both figures show exact results as well as results using the proposed approximation, Equation (2.53), illustrating the accuracy of the approximation.	76
Figure 2–7. Force-extension behavior of WLC filaments subject to pinned-pinned or clamped-clamped boundary conditions ($L_c=1\mu\text{m}$; $l_p=3\mu\text{m}$)	79
Table 2–1 Single filament force-extension models	83
Figure 2–8. Extensible filament schematic including entropic unbending and internal energy stretching	84
Figure 2–9. Multiplicative decomposition of λ_f into entropic unbending and internal energy stretching components. Adapted from (Bertoldi and Boyce, 2007b).....	85
Figure 2–10. Stretch contributions from entropic unbending and internal energy stretching	85

Figure 2–11. Force comparison of inextensible entropic unbending model and extensible model with stretch decomposition of entropic unbending and internal energy axial stretching	87
Figure 2–12. Strain energy contributions from entropic unbending and internal energy axial stretching	88
Figure 2–13. Force comparison of inextensible entropic unbending model and extensible model with varying persistence lengths	89
Figure 2–14. Tensile strength of actin filament as a function of rotational angle. (a) Schematic of experimental procedure using microneedles. θ_B is the rotational angle of the actin filament undergoing the rotation under no tension, and θ_N is the angle of the filament rotated by the needle. (b) Average tensile strengths of single actin filaments ($L_c=10\pm 2\mu\text{m}$). Temperature = $25\pm 2^\circ\text{C}$. Bars = SD for 20-150 filaments. (c) Distribution of thermal rotational angles ($\theta_N=0^\circ$). (d-h) Histograms of tensile strength of single actin filaments twisted by 0° (d), 45° (e), 90° (f), 180° (g), and 360° (h). Figures and experimental data from (Tsuda et al., 1996).....	90
Figure 2–15. Comparison of kinematics methods in extensible model: additive and multiplicative decompositions	92
Figure 2–16. Experimental setup for F-actin stretching with micro-scale SiN_3 cantilevers. Inset fluorescence image shows a captured actin filament between two cantilevers (cantilever width $\sim 4\mu\text{m}$). Adapted from (Liu and Pollack, 2002).	93
Figure 2–17. Experimental data using micro-scale cantilevers to stretch actin filaments ($L_c=19.128\mu\text{m}$). Best fits with extensible WLC models.(Liu and Pollack, 2002).....	93
Figure 2–18. Force–extension plot of Odijk’s extensible WLC approximation for increasing persistence length, l_p ($L_c=19.1\mu\text{m}$, $K_s=34.5\text{nN}$)	95
Figure 3–1. Biomechanical continuum models for whole cell deformation in common experimental techniques (adapted from (Vaziri et al., 2007)).	97
Figure 3–2. (a) Force scale and (b) deformation length scale associated with different biomechanical assays (Suresh, 2007).....	98

Figure 3–3. Single filament subjected to a shearing force [adapted from (Mackintosh, 2006)].....	105
Figure 3–4. Experimental data for fibrin protofilaments (dots) at various concentrations, and corresponding theoretical curves (solid lines). Best-fit values were determined for A–D as follows: A, $c = 0.5$ mg/ml ($l_p = 0.39$ mm), $K_s = 67$ pN; B, $c = 1.0$ mg/ml ($l_p = 0.27$ mm), $K_s = 58$ pN; C, $c = 2.0$ mg/ml ($l_p = 0.19$ mm), $K_s = 73$ pN; D, $c = 4.5$ mg/ml ($l_p = 0.12$ mm), $K_s = 110$ pN (Storm et al., 2005).....	106
Figure 3–5. Chain stretch and rotation for 1D-based models in (A) volume averaged single chain network and (B) multiple chain networks	106
Figure 3–6. Geometry for 3-chain network model.....	107
Figure 3–7. Geometry for 4-chain (tetrahedral) network model (adapted from (Treloar, 1958)).....	109
Figure 3–8. Random F-actin network and corresponding idealized eight-chain network model. The stereo micrograph of actin cortex reproduced from The Journal of Cell Biology, 1983, 96:1400-1413. Copyright 1983 The Rockefeller University Press (Niederman et al., 1983; Hartwig, 2004); bar in (a-b), 100 nm)	112
Figure 3–9. Eight-chain network model geometry and deformation (adapted from (Arruda and Boyce, 1993b)).....	114
Figure 3–10. Simple shear deformation of eight-chain network model	115
Figure 3–11. 2D illustration of affine and non-affine simple shear deformation	116
Figure 3–12. Effect of network isotropic prestress on the network shear stress-shear strain behavior (a) and the network tangent modulus-shear stress behavior (b), with the initial isotropic prestress (σ_0) based on $r_0 = r_{F=0} (1 + \alpha)$	124
Figure 3–13. Phase contrast (top) and immunofluorescence (bottom) micrographs of 100nm fluorescent nanoparticles in Swiss 3T3 fibroblasts before (left) and after (right) shear flow. The inset is a magnified view of focal adhesions at the ends of actin stress fibers. Bar, 20 μ m. Adapted from (Lee et al., 2006).....	125

Figure 3–14. Sketch of 1-particle and 2-particle microrheology using lasers for trapping, displacing, detecting. (Janmey and Schmidt, 2006)	126
Figure 3–15. Torsional rheometer geometries	127
Figure 3–16. Linear and nonlinear rheology with stress stiffening from cross-linked gels (adapted from (Kasza et al., 2007)).....	128
Figure 3–17. Storage modulus (G') and loss modulus (G'') over a range of frequencies for reconstituted actin-scrutin networks (adapted from (Gardel et al., 2004a)).....	129
Figure 3–18. (a) Shear stress and normal stress difference (N_1-N_2) vs. shear strain and (b) Tangent shear modulus vs. shear stress for <i>in vitro</i> F-actin networks ($c_{AF} = 8\mu\text{M}$, $R=0.03$). (experimental data adapted from (Gardel et al., 2004a)).....	131
Figure 3–19. (a) Shear stress vs. shear strain and (b) Tangent shear modulus vs. shear stress for <i>in vitro</i> F-actin networks ($c_{AF} = 8\mu\text{M}$, $R=0.03$) using WLC filament model with pinned-pinned or clamped-clamped boundary conditions. Experimental data adapted from (Gardel et al., 2004a).....	132
Figure 3–20. F-actin filament molecular orientation evolution.....	133
Figure 3–21. (a) Tangent shear modulus-shear stress theory and experimental data, (b) shear stress-shear strain theory and experimental curve fit data of actin networks with varying actin concentration ($c_{AF}=8, 12, 21, 29\mu\text{M}$, $R=0.03$), (experimental data adapted from (Gardel et al., 2004a)).....	135
Table 3–1. Network parameters for different actin concentrations.....	135
Figure 3–22. Filament bundling geometry with (a) bonded bundles and (b) unbonded bundles	137
Figure 3–23. (a) Shear stress-shear strain response and (b) tangent shear modulus-shear stress response of bundled F-actin networks with varying persistence length ($R=0.5$, $c_{AF}=7\mu\text{M}$) (experimental data from (Gardel et al., 2004a)).....	138
Table 3–2. Network parameters for different amounts of filament bundling.....	138

Figure 3–24. (a) Force vs. end-to-end distance and (b) force vs. chain stretch behavior of F-actin filaments using the linear and MacKintosh models.....	140
Table 3–3. Network parameters and material properties MacKintosh, Linear models.....	141
Figure 3–25. (a) Shear stress-strain and (b) tangent shear modulus-shear stress for <i>in vitro</i> F-actin networks ($c_{AF} = 8\mu\text{M}$, $R=0.03$). Experimental data from (Gardel et al., 2004a).....	142
Figure 3–26. (a) Shear stress-shear strain and (b) tangent shear modulus-shear stress for <i>in vitro</i> F-actin networks over the range of published persistence lengths $l_p=3, 10, 17\mu\text{m}$ ($c_{AF} = 8\mu\text{M}$, $R=0.03$), vary L_c for best fit. Experimental data from (Gardel et al., 2004a).....	143
Figure 3–27. (a) Shear stress-shear strain and (b) tangent shear modulus-shear stress for <i>in vitro</i> F-actin networks over the range of published persistence lengths $l_p=3, 10, 17\mu\text{m}$ ($c_{AF} = 8\mu\text{M}$, $R=0.03$), vary L_c and α for best fit. Experimental data from (Gardel et al., 2004a).....	144
Figure 3–28. Stretch contributions from entropic unbending and enthalpic stretching in a network subjected to simple shear deformation.....	147
Figure 3–29. (a) Shear stress-strain and (b) shear stress-filament extension comparison of inextensible model and extensible model.....	148
Figure 3–30. (a) Shear stress-shear strain and (b) Normal stress-shear strain comparison of inextensible model and extensible model with varying persistence lengths.....	149
Figure 3–31. Swelling decomposition [adapted from (Therkelsen, 2005)].....	151
Figure 3–32. (a) Undeformed axisymmetric mesh and (b) Radial expansion in a swelled sphere ($\lambda_{SW} = 1.1$) held fixed at its center. $6\mu\text{m}$ diameter sphere consists of an actin network ($c_{AF}=170\mu\text{M}$, $L_c=0.9\mu\text{m}$, $l_p=3\mu\text{m}$, $\alpha=1.1\%$).	159
Figure 3–33. (a) Reaction forces on plates compressing a swelled sphere ($\lambda_{SW} = 1.02, 1.03, 1.04, 1.05$). The $6\mu\text{m}$ diameter sphere consists of an actin network ($c_{AF}=170\mu\text{M}$, $L_c=0.9\mu\text{m}$, $l_p=3\mu\text{m}$, $\alpha=1.1\%$). (b) Contour plot of normal strain in 2-direction.....	160

Figure 3–34. Contour plots of normal stress in 2-direction from plates compressing a swelled sphere: (a) $\lambda_{SW}=1.02$, (b) $\lambda_{SW}=1.03$, (c) $\lambda_{SW}=1.04$, (d) $\lambda_{SW}=1.05$. The 6 μm diameter sphere consists of an actin network ($c_{AF}=170\mu\text{M}$, $L_c=0.9\mu\text{m}$, $l_p=3\mu\text{m}$, $\alpha=1.1\%$). Stress units are Pascals.	160
Figure 3–35. (a) Reaction forces on plates compressing a swelled sphere ($\lambda_{SW}= 1.02, 1.03, 1.04, 1.05$). The 6 μm diameter sphere consists of a nearly incompressible neo-Hookean solid ($G=13.5\text{Pa}$). (b) Contour plot of normal strain in 2-direction.....	162
Figure 3–36. Contour plots of normal stress in 2-direction from plates compressing a swelled sphere: (a) $\lambda_{SW}=1.02$, (b) $\lambda_{SW}=1.03$, (c) $\lambda_{SW}=1.04$, (d) $\lambda_{SW}=1.05$. The 6 μm diameter sphere consists of a nearly incompressible neo-Hookean solid ($G=13.5\text{Pa}$). Stress units are Pascals.....	162
Table 4–1. Structural binding proteins of actin and their properties (Hartemink, 2005).....	165
Figure 4–1. (A) Orthogonal actin network polymerized in presence of FLNa (B) Identically prepared actin network/bundles except polymerized with α -actinin. Bars, 100 nm. (Stossel et al., 2001)	166
Figure 4–2. Schematics of (a) actin network with FLNa cross-links (adapted from (Lodish, 2000)), (b) FLNa structure (adapted from (Gardel et al., 2006b)). ...	166
Figure 4–3. Schematics of avidin-biotin cross-link structure (Theoretical Biophysics Group, 2007).....	167
Figure 4–4. Storage (G' , closed symbols) and loss (G'' , open symbols) moduli of 12 μM actin-FLNa. R is varied from 1/2000 (squares), 1/1000 (triangles), 1/500 (diamonds), and 1/100 (circles). Inset: G' at 0.01 Hz as a function of R (Gardel et al., 2006a).	168
Figure 4–5. Frequency dependence of the complex modulus and phase shift for 15 μM actin-avidin networks with 2% biotinylated actin alone (\square), 0.03 μM avidin (\blacksquare), 0.1 μM avidin (\circ), or 0.3 μM avidin (\bullet) (Wachsstock et al., 1994).....	168
Figure 4–6. (a) A force–extension curve of Filamin A molecule in aqueous solution measured by AFM at room temperature. Filamin A was stretched at a pulling speed of 0.37 $\mu\text{m/s}$. (b) The fit between the WLC model and the	

sawtooth pattern of the force-extension curve where the force gradually increased after the abrupt decrease in force. Filamin A was stretched at a pulling speed of 0.37 $\mu\text{m/s}$ (Furuike et al., 2001).....	170
Figure 4–7. Thermal fluctuations of branched actin filaments formed from 4 μM muscle actin and 15nM Arp2/3 complex. Every frame illustrates the stiffness of the branch point relative to the flexibility of the filament. Branch length=2 μm . (Blanchoin et al., 2000).....	171
Figure 4–8. Schematics of torsion potential to simulate cross-link stiffness in 8-chain unit cell.....	173
Figure 4–9. Shear stress and normal stress contributions from cross-link torsion.....	178
Figure 4–10. Cross-link torsion contribution to network elasticity: (a) Shear stress and (b) normal stress difference	179
Figure 4–11. Experimental storage modulus (G') and loss modulus (G'') of actin-FLNa networks ($c_{AF} = 20\mu\text{M}$, $R=0.02$, and $\omega=0.05\text{Hz}$) (Lee and Kamm, 2008).....	181
Figure 4–12. Shear stress-shear strain comparison of extensible network model with cross-link torsion with experimental data of actin-FLNa networks ($c_{AF} = 20\mu\text{M}$, $R=0.02$, and $\omega=0.05\text{Hz}$) (Lee and Kamm, 2008)	182
Table 4–2. Network parameters for actin-FLNa model	182
Figure 4–13. Tangent shear modulus-shear stress comparison of extensible network model with cross-link torsion with experimental data of actin-FLNa networks ($c_{AF} = 20\mu\text{M}$, $R=0.02$, and $\omega=0.05\text{Hz}$) (Lee and Kamm, 2008).....	183
Figure 4–14. Experimental storage modulus (G') and loss modulus (G'') as a function of of shear stress (τ) for actin-avidin networks ($c_{AF} = 20\mu\text{M}$, $R=0.01$, and $\omega=0.05\text{Hz}$) (Lee and Kamm, 2008).....	184
Table 4–3. Network parameters for actin-avidin model.....	185
Figure 4–15. Shear stress-shear strain comparison of extensible network model with cross-link torsion with experimental data of actin-FLNa networks ($c_{AF} = 20\mu\text{M}$, $R=0.01$, and $\omega=0.05\text{Hz}$) (Lee and Kamm, 2008)	185

Figure 4–16. Tangent shear modulus-shear stress comparison of extensible network model with cross-link torsion with experimental data of actin-avidin networks ($c_{AF} = 20\mu\text{M}$, $R=0.01$, and $\omega=0.05\text{Hz}$) (Lee and Kamm, 2008).....	186
Figure 4–17. Schematic of finite element model of actin filament cross-linked by FLNa.....	187
Table 4–4. Network parameters for finite element actin-FLN model with varying filament stiffness	188
Figure 4–18. Force-extension response of actin-FLN finite element model.....	189
Figure 4–19. Curvature evolution with extension of actin-FLN finite element model for varying torsional stiffness.....	189
Figure 4–20. Chain angle evolution with extension of actin-FLN finite element model for varying torsional stiffness	190
Figure 4–21. Geometry for hybrid model with three sections: two ends and center	191
Figure 4–22. Force-extension of hybrid model with constant rigid end length	193
Figure 4–23. Force-extension of hybrid model with varying rigid end length	194
Figure 5–1. (a) Maxwell viscoelastic rheological model and (b) corresponding stress relaxation response from constant strain input (inset).	196
Figure 5–2. (a) Kelvin-Voigt viscoelastic rheological model and (b) corresponding creep response from constant stress input (inset).	197
Figure 5–3. Vertical displacement of magnetic bead center as a function of time for three cytoskeletal shear moduli ($G=0.4, 0.6, 1.0\text{kPa}$) using a Maxwell model. Experimental data performed on NIH 3T3 fibroblasts. (Karcher et al., 2003).....	198
Figure 5–4. Standard linear solid rheological model, and (b) corresponding stress relaxation response from constant strain input (inset).	199
Figure 5–5. (a) Rheological model consisting of a SLS model in series with an extra dashpot (D), (b) Creep response and relaxation curve for rheological model with three response regions (I-III), (c) Experimental force input and displacement response with corresponding response regions (I-III), (d) Curve fit for creep data for $F=1.1\text{nN}$ on a cell probed via magnetic bead microrheology. Adapted from (Bausch et al., 1998).....	200

Figure 5–6. (a) Closed-loop control during stress-relaxation tests of an articular chondrocyte using a spherical AFM probe tip, (b) corresponding AFM probe displacement input and stress relaxation response of chondrocytes, and (c) example data sets shown with elastic and viscoelastic curve fits. Adapted from (Darling et al., 2006).....	202
Figure 5–7. Normalized (a,b) and nonnormalized (c,d) stress relaxation of flexor tendon at different strains using the G-method (a,c) and Q_n -method (b,d). Adapted from (Sarver et al., 2003).....	207
Table 5–1 QLV viscoelastic (C , τ_1 , τ_2) and elastic (A , B) parameters used to fit stress relaxation data of flexor tendon at four strain increments using the G-method and the Q_n -method. Adapted from (Sarver et al., 2003).	208
Figure 5–8. (a) Fully preconditioned stress -stretch response for uniaxial tension of porcine skin and myocardium with varying stretch or load rates (cyclic deformation periods of $t=5, 50, 500$ sec), and (b) elastic tangent stiffness ($d\sigma_e/d\lambda$) at the start of each loading cycle as a function of cycle number with the same deformation periods. Adapted from (Giles et al., 2007).	210
Figure 5–9. (a) Storage modulus (G'), (b) loss modulus (G''), (c) dynamic viscosity (η), and (d) damping ratio ($\tan(\delta)$) for canine vocal fold mucosa based on the QLV model (o =mean value, $+$ =standard deviation). Adapted from(Chan, 2004).....	212
Figure 5–10. Viscoelastic rheological model for cytoskeletal network with intermolecular shear viscosity.....	215
Figure 5–11. Multiplicative decomposition of the deformation gradient into viscous and elastic components	217
Figure 5–12. Simulated time histories of shear strain and shear stress for actin-FLNa networks ($c_{AF} = 20\mu\text{M}$, $R=0.02$, and $\omega=0.05\text{Hz}$).....	221
Figure 5–13. Theoretical and experimental storage modulus (G') and loss modulus (G'') of actin-FLNa networks ($c_{AF} = 20\mu\text{M}$, $R=0.02$, and $\omega=0.05\text{Hz}$) (Lee and Kamm, 2008)	222
Figure 5–14. (a) Simulated time history of an oscillating shear strain ($\tan(\gamma)=\pm 0.4$) for the three components of the rheological model (8-chain network, linear	

elastic spring, viscous dashpot), with the strain in the 8-chain network equal to the total strain. (b) Time history for shear stress in linear elastic Maxwell leg, 8-chain network, and total stress.	223
Figure 5–15. Nonlinear viscoelastic rheological model for cytoskeletal network with the hyperelastic network response separated into fixed regions with volume fraction v_f and relaxing regions with volume fraction $v_r=1-v_f$; the nonlinear viscosity due to molecular relaxation is η_{mr}	225
Figure 5–16. Nonlinear viscosity ($C=0.15$, $\theta_r = 47^\circ$) and average network chain angle as a function of shear strain.....	227
Figure 5–17. (a) Nonlinear viscoelastic elements included in the simulated time history of an oscillating shear strain ($\tan(\gamma)=\pm 0.3$) for the three components of the rheological model (Fixed hyperelastic network spring, Relaxing hyperelastic network spring, nonlinear dashpot), with the strain in the 8-chain network equal to the total strain. (b) Time history for shear stress in relaxing 8-chain network, fixed 8-chain network, and total stress.....	228
Figure 5–18. Phase angle for linear viscoelastic model, nonlinear viscoelastic model, and experiments of actin-FLNa networks ($c_{AF} = 20\mu\text{M}$, $R=0.02$, and $\omega=0.05\text{Hz}$) (Lee and Kamm, 2008).....	229
Figure 5–19. Theoretical (with nonlinear viscoelasticity) and experimental storage modulus (G') and loss modulus (G'') of actin-FLNa networks ($c_{AF} = 20\mu\text{M}$, $R=0.02$, and $\omega=0.05\text{Hz}$) (Lee and Kamm, 2008)	229
Figure 5–20. Shear stress-strain response for nonlinear viscoelastic model of actin-FLN at multiple frequencies ($\omega=0.005, 0.05, 0.5, 5\text{ Hz}$) taking $\tau=G' \tan(\gamma)$	231
Figure 5–21. Shear storage modulus (G') and loss modulus (G'') for nonlinear viscoelastic model at multiple frequencies ($\omega=0.005\text{--}0.5\text{ Hz}$)	232
Figure 5–22. Wiechert rheological model with n Maxwell elements for cytoskeletal network to capture distribution of relaxation times for intermolecular shear viscosity.	233
Figure 5–23. Simulated stress relaxation of an actin-FLNa network ($c_{AF} = 20\mu\text{M}$, $R=0.02$) with constant shear strains of $\tan(\gamma)=0.05, 0.1, 0.15$ (inset).....	234

Figure 5–24. Simulated stress relaxation modulus of an actin-FLNa network ($c_{AF} = 20\mu\text{M}$, $R=0.02$) with constant shear strains of $\tan(\gamma)=0.05, 0.1, 0.15$ (inset).....	234
Figure 5–25. Simulated creep response of an actin-FLNa network ($c_{AF} = 20\mu\text{M}$, $R=0.02$) with a constant shear stress of $\tau=0.02, 0.04, 0.06$ Pa (inset).	235
Figure 5–26. Simulated creep function of an actin-FLNa network ($c_{AF} = 20\mu\text{M}$, $R=0.02$) with a constant shear stress of $\tau=0.02, 0.04, 0.06$ Pa (inset).	236
Figure 5–27. Simulated time histories of shear strain and shear stress for actin-avidin networks ($c_{AF} = 20\mu\text{M}$, $R=0.01$, and $\omega=0.05\text{Hz}$).....	237
Figure 5–28. Theoretical (with nonlinear viscoelasticity) and experimental storage modulus (G') and loss modulus (G'') of actin-avidin networks ($c_{AF} = 20\mu\text{M}$, $R=0.01$, and $\omega=0.05\text{Hz}$). Experimental data from (Lee and Kamm, 2008). ...	238
Figure 5–29. (a) Nonlinear scaling included in the simulated time history of an oscillating shear strain ($\tan(\gamma)=\pm 0.2$) for the three components of the rheological model (Fixed hyperelastic network spring, Relaxing hyperelastic network spring, nonlinear dashpot), with the strain in the 8-chain network equal to the total strain. (b) Time history for shear stress in relaxing 8-chain network, fixed 8-chain network, and total stress.....	239
Figure 5–30. Phase angle for nonlinear viscoelastic network model and experiments of actin-avidin networks ($c_{AF} = 20\mu\text{M}$, $R=0.01$, and $\omega=0.05\text{Hz}$) (Lee and Kamm, 2008)	240
Figure 5–31. Shear stress-strain response for nonlinear viscoelastic model of actin-avidin at multiple frequencies ($\omega=0.005, 0.05, 0.5, 5$ Hz) taking $\tau=(G')\tan(\gamma)$	241
Figure 5–32. Shear storage modulus (G') and loss modulus (G'') for nonlinear viscoelastic model as a function of frequency.....	242
Figure 5–33. Complex shear modulus, G^* , and phase shift, δ , as a function of frequency for theory (fit to $c_{AF}=20\mu\text{M}$, $R=0.01$) and experimental ($c_{AF}=15\mu\text{M}$, $R=0.02$) (Wachsstock et al., 1994) actin-avidin networks.....	243

Figure 5–34. Simulated stress relaxation of an actin-avidin network ($c_{AF} = 20\mu\text{M}$, $R=0.01$) with constant shear strains of $\tan(\gamma)=0.05, 0.1, 0.15$ (inset).....	244
Figure 5–35. Simulated stress relaxation modulus of an actin-avidin network ($c_{AF} = 20\mu\text{M}$, $R=0.01$) with constant shear strains of $\tan(\gamma)=0.05, 0.1, 0.15$ (inset).....	244
Figure 5–36. Simulated creep response of an actin-avidin network ($c_{AF} = 20\mu\text{M}$, $R=0.01$) with constant shear stresses of $\tau=0.02, 0.04, 0.06\text{Pa}$ (inset).....	245
Figure 5–37. Simulated creep function of an actin-avidin network ($c_{AF} = 20\mu\text{M}$, $R=0.01$) with constant shear stresses of $\tau=0.02, 0.04, 0.06\text{Pa}$ (inset).....	245
Figure 5–38. 3D whole cell geometry.....	246
Figure 5–39. Membrane deformation modes.....	248
Figure 5–40. (a) Axisymmetric mesh schematic with axial normal strain contours in deformed mesh, and (b) Input (total) strain time history for compression of a viscoelastic cell with loading ramp time of 0.01 second and a hold time of 20 seconds.....	251
Figure 5–41. Element strain in the 2-direction (ϵ_{22}) within actin networks in a compressed cell ($\epsilon_{2,\text{total}} = -15\%$) at two different times, (a) $t=0.01$ sec, immediately after compression and (b) $t=20$ sec, in the compressed but relaxed state.	252
Figure 5–42. Element stress in the 2-direction (σ_{22}) within actin networks in a compressed cell ($\epsilon_{2,\text{total}} = -15\%$) at two different times, (a) $t=0.01$ sec, immediately after compression and (b) $t=20$ sec, in the compressed but relaxed state. Units are Pa.....	253
Figure 5–43. Relaxation of reaction force on a solid plate compressing a cell ($\epsilon_{2,\text{total}} = -5\%$, -10% , and -15%). Cell consists of a neo-Hookean nucleus, orthotropic membrane, and a cytoplasm consisting of an actin network ($c_{AF}=20\mu\text{M}$, $L_c=0.9\mu\text{m}$, $l_p=3\mu\text{m}$, $\alpha=1.1\%$)	254
Figure 5–44. Relaxation of reaction force on a solid plate compressing a cell ($\epsilon_{2,\text{total}} = -5\%$, -10% , and -15%). Cell consists of a neo-Hookean nucleus,	

orthotropic membrane, and a cytoplasm consisting of an actin network ($c_{AF}=20\mu\text{M}$, $L_c=0.9\mu\text{m}$, $l_p=3\mu\text{m}$, $\alpha=1.1\%$)	254
Figure 5–45. (a) Axisymmetric mesh schematic with axial normal strain contours in deformed mesh, and (b) Input (total) strain time history for compression of a viscoelastic cell with loading ramp time of 0.01 second and a hold time of 20 seconds.....	256
Figure 5–46. Element strain in the 2-direction (ϵ_{22}) within actin networks in a compressed cell ($\epsilon_{2,\text{total}}= -15\%$) at two different times, (a) $t=0.01$ sec, immediately after compression and (b) $t=20$ sec, in the compressed but relaxed state.	257
Figure 5–47. Element stress in the 2-direction (σ_{22}) within actin networks in a compressed cell ($\epsilon_{2,\text{total}}= -15\%$) at two different times, (a) $t=0.01$ sec, immediately after compression and (b) $t=20$ sec, in the compressed but relaxed state. Units are Pa.....	258
Figure 5–48. Relaxation of reaction force on a solid plate compressing a cell ($\epsilon_{2,\text{total}}=-5\%$, -10% , and -15%). Cell consists of a neo-Hookean membrane and nucleus, and a cytoplasm consisting of three regions of actin networks ($c_{AF}=10-170\mu\text{M}$, $L_c=0.9\mu\text{m}$, $l_p=3\mu\text{m}$, $\alpha=1.1\%$)	259
Figure 5–49. Relaxation of reaction force on a solid plate compressing a cell ($\epsilon_{2,\text{total}}=-5\%$, -10% , and -15%). Cell consists of a neo-Hookean membrane and nucleus, and a cytoplasm consisting of three regions of actin networks ($c_{AF}=10-170\mu\text{M}$, $L_c=0.9\mu\text{m}$, $l_p=3\mu\text{m}$, $\alpha=1.1\%$)	259
Figure 6–1. Biphase porous media in soil mechanics from the superposition of two continuous media [adapted from (Mokdad et al., 2004)].....	263
Figure 6–2. Normalized vertical displacement evolution of a soil in confined compression with a porous platen boundary ($p=0$) and subject to a sudden vertical pressure load. Qualitative contour plot of vertical stress (σ_{22}) shown in inset at $t=0.01\text{min}$	266
Figure 6–3. Normalized pore pressure evolution of a soil in confined compression with a porous platen boundary ($p=0$) and subject to a sudden vertical pressure	

load. Qualitative contour plot of pore pressure shown in inset at $t=0.01\text{min}$ (0.9sec).....	266
Figure 6–4. Articular cartilage permeability for varying compressive strain and applied pressure (Lai and Mow, 1980).....	270
Figure 6–5. (a) Schematic for confined compression test, (b) Input displacement profile with ramp time (t_0), and (c) Stress relaxation time history and curve fit of bovine cartilage (adapted from (Ateshian et al., 1997)).....	271
Figure 6–6. (a) Schematic for unconfined compression test and (b) Stress relaxation time history for a ramped displacement with ramp time (t_0) and an internal material diffusion time (t_d) of bovine cartilage (adapted from (Cohen et al., 1998)).....	272
Figure 6–7. (a) Electrokinetic transduction in cartilage via confined compression setup with a streaming potential, and (b) Oscillatory input displacement with measured load and streaming potential response (adapted from (Frank and Grodzinsky, 1987)).....	275
Figure 6–8. (a) Schematic of isochoric blebbing based on poroelastic fluid flow. (b) Confocal micrograph of a GFP–actin-transfected cell during bleb expansion. Scale bar, 5 μm (adapted from (Charras et al., 2005)).....	277
Figure 6–9. Vertical strain magnitude of F-actin networks ($k_H=0.1\times 10^{-13}$, 2×10^{-13} $\text{m}^4/\text{N}\cdot\text{s}$) in confined compression with a porous platen boundary ($p=0$) and subject to a sudden vertical pressure load of $p=10\text{Pa}$. Inset: Time history of applied pressure load, and qualitative contour plot of vertical stress (σ_{22}) shown in inset at $t=10\text{min}$	285
Figure 6–10. Time evolution of fluid pore pressure of top nodes below solid platen, normalized by equilibrium pore pressure in confined compression with a porous platen boundary ($p=0$) and subject to a sudden vertical pressure load of $p=10\text{Pa}$. F-actin network ($k_H=0.1\times 10^{-13}$, 2×10^{-13} $\text{m}^4/\text{N}\cdot\text{s}$). Inset: Time history of applied pressure load, and qualitative contour plot of pore pressure shown in inset at $t=10\text{min}$	286
Figure 6–11. (a) Boundary conditions and (b) Input displacement time history for unconfined compression simulation.....	287

Figure 6–12. (a) Reaction force normalized by the peak reaction force, and (b) Lateral strain/vertical strain of F-actin networks ($k_H=0.1 \times 10^{-13}$, 2×10^{-13} m ⁴ /N-s) in unconfined compression with porous side boundaries ($p=0$) and $\varepsilon_2=-15\%$ compressive vertical strain with a peak lateral strain of $\varepsilon_1=-8.4\%$ for both cases.....	288
Figure 6–13. (a) Reaction force normalized by peak reaction forces and (b) Reaction force magnitudes of an F-actin network ($k_H = 2 \times 10^{-13}$ m ⁴ /N-s) in unconfined compression with porous side boundaries ($p=0$) and 5%, 10%, and 15% total compressive vertical strain.....	289
Figure 6–14. (a) Lateral strain normalized by peak lateral strain and (b) Lateral strain/vertical strain of an F-actin network ($k_H = 2 \times 10^{-13}$ m ⁴ /N-s) in unconfined compression with porous side boundaries ($p=0$) and 5%, 10%, and 15% total compressive vertical strain.....	290
Figure 6–15. Pore pressure time history for an F-actin network ($k_H=2 \times 10^{-13}$ m ⁴ /N-s) in unconfined compression with porous side boundaries ($p=0$) and 15% compressive strain with a ramp time of 0.1 second. Pore pressure data are from nodes equidistantly spaced from the specimen's center to just inside the outer boundary as shown in the pore pressure contour plot on the right.....	292
Figure 6–16. Pore pressure time history for an F-actin network ($k_H=2 \times 10^{-13}$ m ⁴ /N-s) in unconfined compression with porous side boundaries ($p=0$) and 15% compressive strain with a ramp time of 250 seconds. Pore pressure data are from nodes equidistantly spaced from the specimen's center to just inside the outer boundary as shown in the pore pressure contour plot on the right.....	293
Figure 6–17. Swelling stretch time history for an F-actin network ($k_H=2 \times 10^{-13}$ m ⁴ /N-s) in unconfined compression with porous side boundaries ($p=0$) and 15% compressive strain with a ramp time of 0.1 second. Swelling stretch data are from nodes equidistantly spaced from the specimen's center to just inside the outer boundary as shown in the swelling stretch contour plot on the right.....	294
Table 6–1. Summary of geometry and key mechanical properties for cellular model.....	295

Figure 6–18. (a) Axisymmetric mesh schematic with axial normal displacement contours in deformed mesh at $t=0.01\text{sec}$ for $\varepsilon_{2,\text{total}}=15\%$, and (b) Input (total) strain time history for compression of a poroelastic cell with loading ramp time of $t=0.01\text{sec}$ and a hold time of $t=1.0\text{sec}$.	296
Figure 6–19. Element strain in the 2-direction (ε_{22}) within actin networks in a compressed cell ($\varepsilon_{2,\text{total}}= -15\%$) at two different times, (a) $t=0.01$ sec, immediately after compression and (b) $t=1.0$ sec, in the compressed but relaxed state.	297
Figure 6–20. Element shear strain (ε_{12}) within actin networks in a compressed cell ($\varepsilon_{2,\text{total}}= -15\%$) at two different times, (a) $t=0.01$ sec, immediately after compression and (b) $t=1.0$ sec, in the compressed but relaxed state.	297
Figure 6–21. Element axial normal stress (σ_{22}) in a compressed cell ($\varepsilon_{2,\text{total}}= -15\%$) at four different times, (a) $t=0.01\text{sec}$, immediately after compression, (b) $t=0.02\text{sec}$, (c) $t=0.05\text{sec}$, (d) $t=1.0$ sec, in the compressed but relaxed state. Cell consists of a neo-Hookean nucleus, orthotropic membrane, and a poroelastic cytoplasm consisting of an actin network ($c_{AF}=20\mu\text{M}$, $L_c=0.9\mu\text{m}$, $l_p=3\mu\text{m}$, $\alpha=1.1\%$, $k_H= 2\times 10^{-13} \text{ m}^4/\text{N-s}$), Units in Pa.	298
Figure 6–22. Relaxation of reaction force normalized by peak reaction force on a solid plate compressing a cell ($\varepsilon_{2,\text{total}}=-5\%$, -10% , and -15%). Cell consists of a neo-Hookean nucleus, orthotropic membrane, and a poroelastic cytoplasm consisting of an actin network ($c_{AF}=20\mu\text{M}$, $L_c=0.9\mu\text{m}$, $l_p=3\mu\text{m}$, $\alpha=1.1\%$, $k_H= 2\times 10^{-13} \text{ m}^4/\text{N-s}$).	299
Figure 6–23. Reaction force/displacement relaxation for a solid plate compressing a cell ($\varepsilon_{2,\text{total}}=-5\%$, -10% , and -15%). Cell consists of a neo-Hookean nucleus, orthotropic membrane, and a poroelastic cytoplasm consisting of an actin network ($c_{AF}=20\mu\text{M}$, $L_c=0.9\mu\text{m}$, $l_p=3\mu\text{m}$, $\alpha=1.1\%$, $k_H= 2\times 10^{-13} \text{ m}^4/\text{N-s}$).	300
Figure 6–24. Relaxation of reaction force on a solid plate compressing a cell ($\varepsilon_{2,\text{total}}=-5\%$, -10% , and -15%). Cell consists of a neo-Hookean nucleus, orthotropic membrane, and a poroelastic cytoplasm consisting of an actin network ($c_{AF}=20\mu\text{M}$, $L_c=0.9\mu\text{m}$, $l_p=3\mu\text{m}$, $\alpha=1.1\%$, $k_H= 2\times 10^{-13} \text{ m}^4/\text{N-s}$).	301

Figure 6–25. Pore pressure in a compressed cell ($\epsilon_{2,\text{total}} = -15\%$) at four different times, (a) $t=0.01\text{sec}$, immediately after compression, (b) $t=0.02\text{sec}$, (c) $t=0.05\text{sec}$, (d) $t=1.0\text{ sec}$, in the compressed but relaxed state. Cell consists of a neo-Hookean nucleus, orthotropic membrane, and a poroelastic cytoplasm consisting of an actin network ($c_{AF}=20\mu\text{M}$, $L_c=0.9\mu\text{m}$, $l_p=3\mu\text{m}$, $\alpha=1.1\%$, $k_H = 2 \times 10^{-13} \text{ m}^4/\text{N}\cdot\text{s}$), pore pressure units in Pa..... 302

Figure 6–26. Swelling stretch within actin networks in a compressed cell ($\epsilon_{2,\text{total}} = -15\%$) at four different times, (a) $t=0.01\text{ sec}$, immediately after compression, (b) $t=0.02\text{sec}$, (c) $t=0.05\text{sec}$, (d) $t=1.0\text{ sec}$, in the compressed but relaxed state. 303

Figure 6–27. Filament stretch within actin networks in a compressed cell ($\epsilon_{2,\text{total}} = -15\%$) at four different times, (a) $t=0.01\text{ sec}$, immediately after compression, (b) $t=0.02\text{sec}$, (c) $t=0.05\text{sec}$, (d) $t=1.0\text{ sec}$, in the compressed but relaxed state. 304

Figure 6–28. Angle between filaments and the maximum principal stretch direction of the 8-chain network unit cell for actin networks in a compressed cell ($\epsilon_{2,\text{total}} = -15\%$) at four different times, (a) $t=0.01\text{ sec}$, immediately after compression, (b) $t=0.02\text{sec}$, (c) $t=0.05\text{sec}$, (d) $t=1.0\text{ sec}$, in the compressed but relaxed state. Angles shown in degrees..... 306

Figure 6–29. Angle between maximum principal stretch direction and horizontal, 2-direction for actin networks in a compressed cell ($\epsilon_{2,\text{total}} = -15\%$) at four different times, (a) $t=0.01\text{ sec}$, immediately after compression, (b) $t=0.02\text{sec}$, (c) $t=0.05\text{sec}$, (d) $t=1.0\text{ sec}$, in the compressed but relaxed state. Angles shown in degrees. 307

Figure 6–30. Relaxation of reaction force on a solid plate compressing a cell ($\epsilon_{2,\text{total}} = -10\%$). Cell consists of a neo-Hookean nucleus, orthotropic membrane and either a poroelastic, viscoelastic, or poroviscoelastic cytoplasm consisting of an actin network ($c_{AF}=20\mu\text{M}$, $L_c=0.9\mu\text{m}$, $l_p=3\mu\text{m}$, $\alpha=1.1\%$, $k_H = 2 \times 10^{-13} \text{ m}^4/\text{N}\cdot\text{s}$) 309

Figure 6–31. Relaxation of reaction force normalized by peak reaction force on a solid plate compressing a cell ($\epsilon_{2,\text{total}} = -10\%$). Cell consists of a neo-Hookean

nucleus, orthotropic membrane and either a poroelastic, viscoelastic, or poroviscoelastic cytoplasm consisting of an actin network ($c_{AF}=20\mu\text{M}$, $L_c=0.9\mu\text{m}$, $l_p=3\mu\text{m}$, $\alpha=1.1\%$, $k_H=2\times 10^{-13}\text{ m}^4/\text{N-s}$) .	310
Figure 6–32. Relaxation of reaction force on a solid plate compressing a cell ($\varepsilon_{2,\text{total}}=-10\%$). Cell consists of a neo-Hookean nucleus, orthotropic membrane, and either a poroelastic or poroviscoelastic cytoplasm consisting an actin network ($c_{AF}=20\mu\text{M}$, $L_c=0.9\mu\text{m}$, $l_p=3\mu\text{m}$, $\alpha=1.1\%$) with either $\phi_T=0.95$, $k_H=2\times 10^{-13}\text{ m}^4/\text{N-s}$ or $\phi_T=0.82$, $k_H=0.1\times 10^{-13}\text{ m}^4/\text{N-s}$.	311
Figure 6–33. Relaxation of reaction force normalized by peak reaction force on a solid plate compressing a cell ($\varepsilon_{2,\text{total}}=-10\%$). Cell consists of a neo-Hookean membrane and nucleus, and either a poroelastic or poroviscoelastic cytoplasm consisting of three regions of actin networks ($c_{AF}=10-170\mu\text{M}$, $L_c=0.9\mu\text{m}$, $l_p=3\mu\text{m}$, $\alpha=1.1\%$) with either $\phi_T=0.95$, $k_H=2\times 10^{-13}\text{ m}^4/\text{N-s}$ or $\phi_T=0.82$, $k_H=0.1\times 10^{-13}\text{ m}^4/\text{N-s}$.	312
Figure 7–1. Mesenchymal and amoeboid migration in ECM (Yamazaki et al., 2005)	328
Figure 7–2. Summary of cell motility and modeling needs [illustration from (Lodish, 2000)]	330

CHAPTER 1 INTRODUCTION

1.1 Cell mechanics and role of cytoskeleton

Many important biological cellular functions in multicellular organisms rely on the micromechanics of the cell and its cytoskeleton. Microstructural cellular features govern the cell's mechanical behavior primarily via three main components: the plasma membrane, nucleus, and internal cytoskeleton (see Figure 1–1) (Boal, 2002). The semipermeable plasma membrane, composed of a lipid bilayer and transmembrane and surface proteins, provides a protective barrier for the cell while simultaneously facilitating interactions with its external environment (Lodish et al., 2004). The cell nucleus is enclosed by a double membrane and filled with chromatin-rich nucleoplasm and a nucleolus. Nuclei can dominate the mechanical response for cells such as inactive B lymphocytes (B cells) in which their nuclear volume consumes a large fraction of the cell, and they are often modeled as a viscoelastic solid (Guilak et al., 2000).

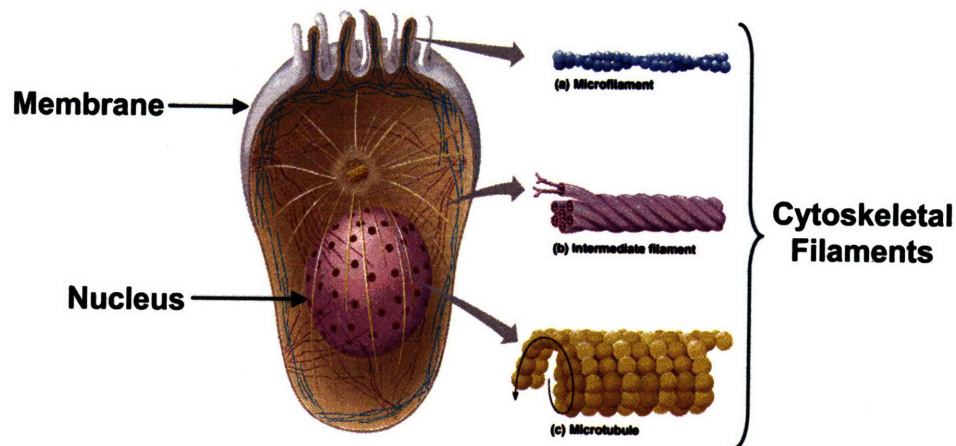


Figure 1–1. Cellular structures: plasma membrane, nucleus, and cytoskeletal filaments (adapted from (Cummings, 2001)).

The membrane works in concert with the dynamic cytoskeletal microstructure to perform a crucial role in many of the regulating cellular functions including cell division, adhesion, spreading, migration, contraction (Stamenovic and Wang, 2000; Boal, 2002; Lim et al., 2006), and other mechanotransductive effects which influence many biochemical processes such as gene expression (Maniotis et al., 1997; Guilak et al., 2000).

The membrane and cytoskeleton can play an equally important role in many abnormal cellular actions that lead to disease. Environmental influences and genetic mutations leading to disruption or dysfunction in cytoskeletal proteins have been linked to heart failure (Hein et al., 2000; Lemler et al., 2000) and neurodegenerative diseases such as Alzheimer's disease (Lee, 1995; McMurray, 2000; Nigel J Cairns, 2004). Chemomechanical pathways can lead to microstructural alterations in the cytoskeleton resulting in less cell deformability and a decrease in cell mobility for diseased states such as malaria and gastrointestinal cancer (Suresh et al., 2005). Increases in cell stiffness have also been linked to complications in diabetes mellitus (Perrault et al., 2004). Some therapeutic treatments can alter the cytoskeleton, thereby causing additional complications. For example, an increased stiffness is observed in leukemia cells after exposure to chemotherapy, leading to leukostasis; while a combination of chemotherapy and cytoskeletal inhibitors led to apoptosis (cell death) of leukemia cells without the complications of decreased deformability (Rosenbluth et al., 2006).

The cytoskeleton is composed of three protein filament networks: actin microfilaments (AF), intermediate filaments (IF), and microtubules (MT). Microrheological studies have been conducted on all three cytoskeletal filament

networks. These studies have quantified the detailed mechanical behaviors (e.g. force-deformation, shear moduli vs frequency, or shear moduli vs concentration) of the cytoskeletal filaments for both in vitro (Isambert and Maggs, 1996; Shin et al., 2004; Liu et al., 2006) and in vivo (Schliwa, 1986; Elson, 1988; Lyass et al., 1988; Portet et al., 2004; Daniels et al., 2006) environments. The rheology of in vitro single filament networks (Janmey et al., 1991; Tseng et al., 2002b; Gardel et al., 2006b) has also been examined, as well as the rheology of multiple filament networks (Schliwa et al., 1982; Leung et al., 1999; Karakesisoglou et al., 2000) with and without cross-linking proteins. The constitutive behavior of the cytoskeletal filaments can be integrated into structure-based micromechanical models of the entire cell to predict the mechanical response of the combined network in the cytoplasm. When combined with membrane and nucleus structural models, the composite cellular microstructure is amenable to detailed mechanical modeling.

Three-dimensional (3D) cytoskeletal network models, especially when integrated with cellular models containing membrane and nucleus components, have utility for a wide variety of applications. The integrated model can be used to understand mechanotransductive effects during cancer tumor growth (Paszek and Weaver, 2004; Thamilselvan et al., 2004), cardiac cell remodeling/heart failure (Hoshijima, 2006), angiogenesis (Li et al., 2005c), and stretch-activated ion channels (Itano et al., 2003). The model could be used for directing multiple types of tissue engineering experiments (e.g. controlling growth of budding/branching of embryonic lungs via cytoskeletal tension) (Ingber, 2005). Models of cellular manipulation are also useful for blood cell

separation processes (Li et al., 2005a) and for BioMEMS applications such as deformation on cell culture scaffolds (O'Brien et al., 2004).

The focus of this doctoral research has been the development of a microstructurally-motivated model of the 3D biomechanical response of cross-linked cytoskeletal networks during elastic and viscoelastic deformations, with a specific emphasis on actin networks. This thesis is composed of seven chapters. The remainder of the first chapter will give some background on the morphology, properties, and network behavior of the three cytoskeletal filaments (AF, IF, MT). The second chapter will focus on approaches for modeling the behavior of single cytoskeletal filaments including entropic unbending and internal energy-based axial stretching. These two behaviors are combined in an extensible model that employs a new analytical approximation for entropic unbending of semiflexible filaments. The third chapter addresses cytoskeletal network behavior through a brief review of other modeling approaches, and a detailed derivation and validation of a network model that incorporates the extensible filament model with the Arruda-Boyce eight-chain network model. The model also includes bundling, swelling and prestress effects. Chapter four examines the mechanical contribution of network cross-links (through torsional potentials) and the cross-links' influence on the entropic configuration space. The fifth chapter adds the effects of nonlinear interfilament shear viscoelasticity to the network model and compares the model with rheological experimental data of actin networks. The nonlinear viscoelastic cytoskeletal model is also incorporated within a larger finite element model of the cell that includes a neo-Hookean nucleus and an orthotropic, linear elastic membrane. Chapter six shows the mechanical effect of cytosolic fluid flowing through

the cytoskeletal network via a poroelastic network model demonstrated in confined compression, unconfined compression, and compression of a cell with a membrane and nucleus. Finally, the seventh chapter presents a summary and a number of future enhancements for the model and their applications.

1.2 Cytoskeletal filament networks

1.2.1 Morphology & filament properties

1.2.1.1 Actin filaments

Actin is one of the most abundant proteins in the human body and can reach concentrations over $100\mu\text{M}$ in eukaryotic cells (Higgs, 2001), with cortical actin concentrations in lamellae averaging $300\mu\text{M}$ (Hartwig and Shevlin, 1986). Actin plays a crucial role in many cellular processes including migration, contraction, cell division, and it has accordingly been of key interest since it was first observed by Straub in 1942 (Straub, 1942).

The morphology of in vivo actin networks varies depending on the location within the cell. Figure 1–2 shows three different locations within the cell for cross-linked and bundled actin networks. The different types of bundled and cross-linked network

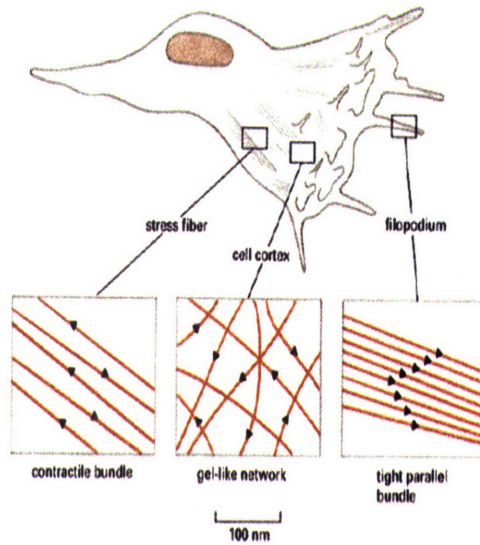


Figure 1–2. Actin network morphologies throughout the cell (Alberts, 1996)

morphologies are necessary for normal cellular functions (structural stability, motility, mechanotransduction, etc.). These different morphologies for F-actin are readily seen in the micrographs of Figure 1–3.

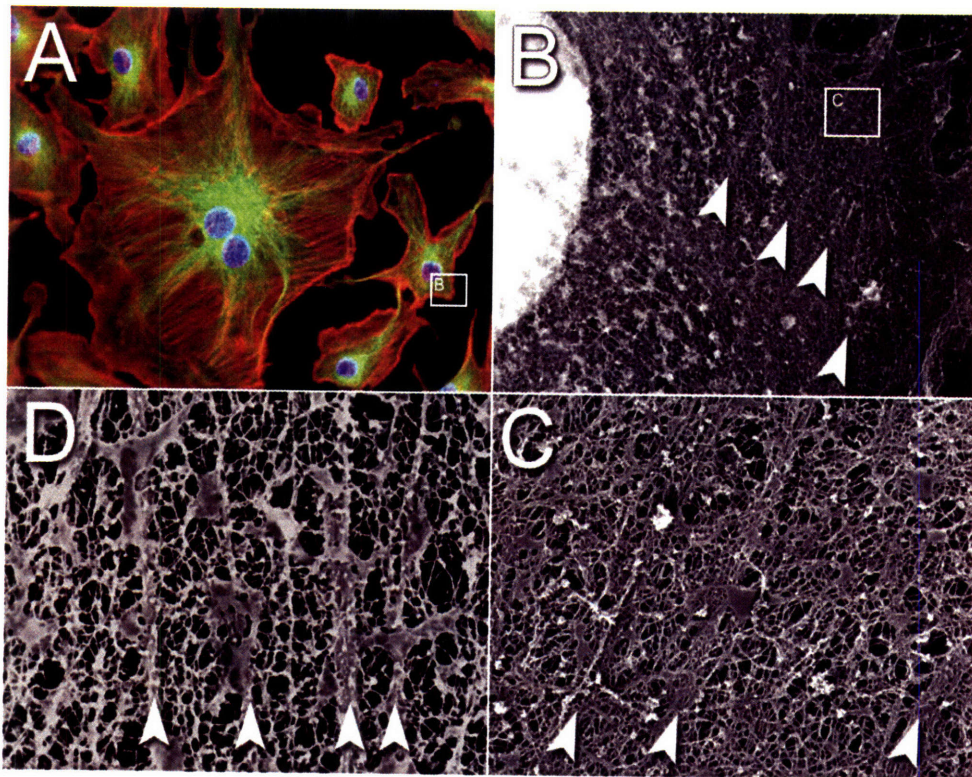


Figure 1–3. The endothelial cytoskeleton in increasing magnification, clockwise. A, Fluorescently labeled endothelial cell cytoskeletons with nuclei stained blue, F-actin stained red, and microtubules stained green. The “striped” actin appearance throughout the cells is due to the bundling of F-actin into stress fibers which are differentiable at optical resolution, panel width 200 μm . B, Higher magnification reveals that the cells actually contain a pervasive network of actin filaments that fills the space between stress fibers (arrowheads), staining a diffuse red in fluorescent imaging, panel width 20 μm . C, D, Increasing magnification of the network showing it to be a dense, porous, evenly-distributed web of individual filaments. The pore size of the network is approximately 100 nm, (A, image courtesy of Molecular Probes. B-D, images courtesy of John Hartwig. All four panels are taken from different cells; inset boxes are placed solely for scale). Hartemink, C.A., Ph.D. Thesis, MIT (2005).

The actin cytoskeleton employs its polymerization and structural capabilities in support of cell motility and migration. Actin cytoskeletal filaments actively rearrange their microstructure in response to mechanical as well as chemical stimuli. Globular actin

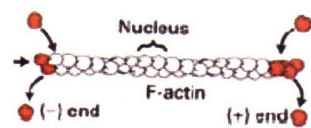


Fig 19-6

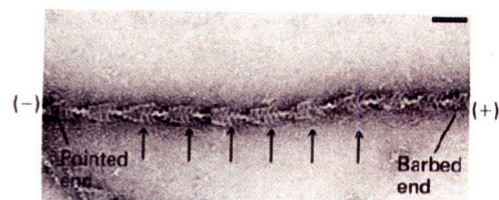


Fig 19-4

Figure 1–4. F-actin polymerization and polarity, bar=10nm (Lodish et al., 2004)

monomers (G-actin) polymerize into polar, helical strands of filamentous actin (F-actin) as seen in Figure 1–4. Aided by actin binding proteins (ABPs) to regulate filament length and geometries, *in vivo* actin polymerization can achieve incredible speed and flexibility, with polymerization of micrometer-thick layers of densely packed filaments in seconds (Higgs, 2001). During the creation of migratory protrusions, the actin cytoskeleton is dynamically remodeled via polymerization, and this reorganization leads to the force necessary for cell migration (Pollard and Borisy, 2003). The cylindrical-like protrusions, or pseudopods, extend into the 3D extracellular matrix (ECM) via a polymerization/depolymerization cycle, or “treadmilling,” at the inner surface of the membrane. These protrusions are generated from the dense, porous sections of the actin network (see Figure 1–3) in conjunction with localized cytosolic swelling and poroviscoelastic effects (Herant and Dembo, 2006). The importance of actin microstructures is emphasized through the fact that regulating or inhibiting actin polymerization decreases cell motility. Mechanical deformation of neutrophils flowing in pulmonary capillaries, for example, can cause cytoskeletal disruption, pseudopod projections, and a resulting decrease in overall cell shear modulus of more than 60% (Yap and Kamm, 2005). An increased understanding of the mechanics of the actin cytoskeleton during the cellular protrusions and contractions can therefore augment understanding of critical immunological responses (i.e. extravasation, migration) as well as actin polymerization regulation therapies for treating cancer (Zigmond, 2004; Quinlan et al., 2005; Walker and Olson, 2005).

The morphology of the actin filament is two long-pitch right handed helices as shown in Figure 1–5. The crystal structure of the globular actin monomer is also shown in Figure 1–5. The radius of gyration of the F-actin helix has been shown to be 10 nm (Egelman and Padron, 1984) or greater (depending on osmotic pressures, etc.)(Grazi, 1997; Oda et al., 1998), equivalent to a homogeneous rod with a diameter of 7.1 nm (Egelman and Padron, 1984).

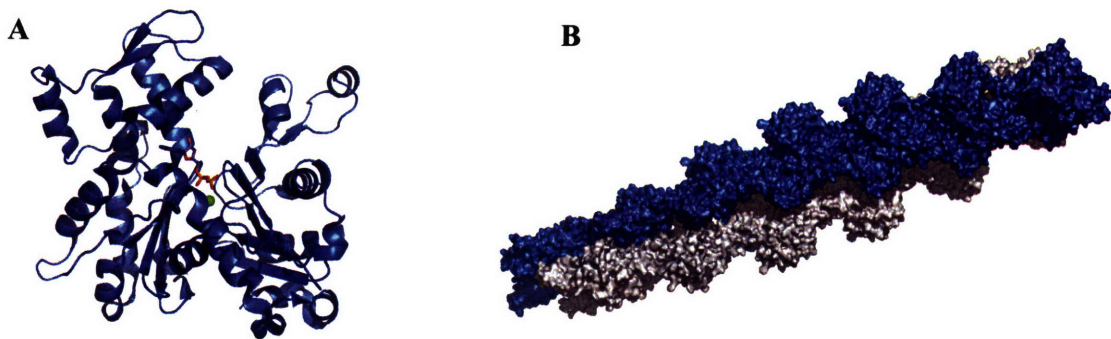


Figure 1–5. (A) Crystal structure of monomeric G-actin and (B) structural surface representation F-actin with 13 monomers (Images courtesy of Thomas Spletstoesser with the open source molecular visualization tool PyMol, based on the atomic models of (A) Kabsch, et al. (Kabsch et al., 1990) and (B) Holmes, et al. (Holmes et al., 1990))

F-actin can have in vitro contour lengths of up to 20 μm (Gittes et al., 1993). In vivo measurements of contour lengths of F-actin filaments, however, range from 0.1-1 μm in the actin cortex (Hartwig and Shevlin, 1986; Podolski and Steck, 1990; Medalia et al., 2002) as shown in Figure 1–6.

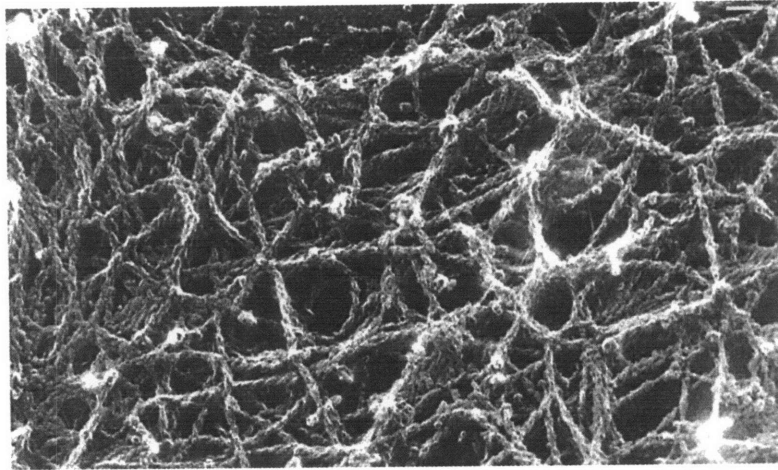


Figure 1–6. Electron micrograph of the actin cortex of a macrophage cytoskeleton, labeled with myosin subfragment 1. Bar, 0.1 μm (top right corner). (Hartwig and Shevlin, 1986)

The persistence length of a filament is a representative length beyond which the filament's curvature is uncorrelated due to thermal fluctuations, and will be defined in more detail in Chapter 2. The persistence length of F-actin has been obtained from many experimental techniques involving both native and fluorescently labeled actin filaments (Boal, 2002), generally within the range of 3-18 μm (Janmey, 2000; Wagner et al., 2007). The principle techniques include dynamic light scattering, microscopic observation of thermal fluctuations, and microscopic observation of driven oscillation of labeled actin filaments. Dynamic light scattering has a broad range of results with the most recent converging on $l_p \sim 16 \mu\text{m}$ (Janmey et al., 1994; Boal, 2002). Direct microscopic observation of the thermal fluctuations of fluorescently labeled actin filaments yield persistence length values of $18 \pm 1 \mu\text{m}$ when stabilized by phalloidin (Gittes et al., 1993; Isambert et al., 1995) and $9 \pm 0.5 \mu\text{m}$ when not stabilized (Isambert et al., 1995). Direct microscopic observation of hydrodynamically driven filaments have provided more flexible values at $7.4 \pm 0.2 \mu\text{m}$ (Riveline et al., 1997; Wiggins et al., 1998). Steinmetz, et

al. measured the persistence length of F-actin using conventional transmission electron microscopy (CTEM), while taking into account that the adsorption of the filaments onto the carbon support film would force the filament from a 3D configuration into a 2D environment and thereby leading to artificially stiff filaments (Steinmetz et al., 1997a). They found that the persistence lengths varied from $l_p \sim 3\mu\text{m}$ for native filaments to $l_p \sim 6\mu\text{m}$ for filaments fluorescently labeled with phalloidin (Steinmetz et al., 1997a; Steinmetz et al., 1997b). Kas, et al. (Kas et al., 1994) and Takebayashi, et al. (Takebayashi et al., 1977) also measured a persistence length of $l_p \sim 4\mu\text{m}$. And F-actin persistence lengths have been found as low as $l_p \sim 0.1\text{-}0.5\mu\text{m}$ by Piekenbrock and Sackmann (Piekenbrock and Sackmann, 1992), although the results were obtained with F-actin that wasn't purified as much as in other experiments. It should also be noted that eukaryotic cells express three classes of actin isoforms (α , β , γ), each with different functions and properties: α -actin (in muscle cells) is associated with contractile/muscle cells; γ -actin exists in nonmuscle stress fibers; and β -actin is present at the leading edge of filopodia and lamellipodia (Lodish et al., 2004). And while some isoforms are easier to extract (i.e. α -actin from skeletal muscle), other isoforms (i.e. β -actin) are much more plentiful in cells and are more flexible (Allen et al., 1996; Steinmetz et al., 2000).

1.2.1.2 Intermediate filaments

Intermediate filaments (IF), composed of a large heterogeneous family of proteins, extend across the cell and are important to the cell architecture as well as nuclear/ cellular stability (Portet et al., 2004). IF form a cage-like structure around the nucleus and can be modulated to meet the changing needs of cells such as mechanical support,

cytoarchitecture, cell migration, and signal modulation for cell growth/death through dynamic interactions with non-structural proteins (Coulombe and Wong, 2004).

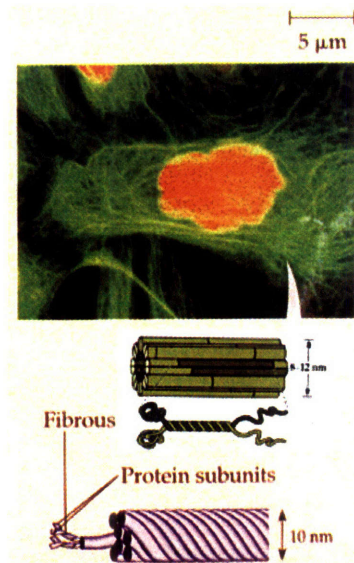


Figure 1-7. Intermediate filament substructures (Campbell et al., 1999)

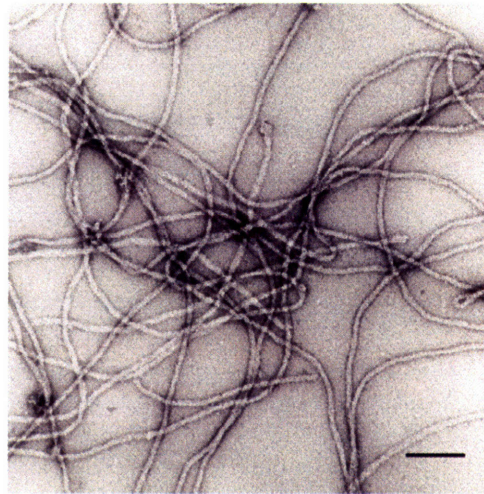


Figure 1-8. Electron micrograph of in vitro vimentin IF. Bar = 100nm. (Mucke et al., 2004)

They are assembled from a 45 nm long coiled-coil dimer as the elementary building block (i.e. in stranded-rope fashion shown in Figure 1-7 with an overall diameter of 10 nm) (Herrmann and Aebi, 2004). In vivo contour lengths of intermediate filaments have been observed to range from 10-20 μm (Fudge et al., 2003). In general, vimentin IF (Figure 1-8) contribute about 20% of cytoskeleton stiffness in endothelial cells and fibroblasts as measured with magnetic twisting cytometry (Wang and Stamenovic, 2000). Persistence lengths for intermediate filaments such as vimentin can vary from 0.3-3 μm depending on the measurement technique. Similar values are seen for desmin IF (0.1-1 μm) when measured by light scattering (Hohenadl et al., 1999). The higher value of l_p for vimentin, 3 μm (Inagaki et al., 1989), represents an upper bound since it was obtained via electron micrograph (EM) and the forces associated with adsorption to the EM grid

can cause significant nonthermal bending (Howard, 2001). Lower values, ranging from 0.3-1 μm (Mucke et al., 2004), were measured by adsorbing the IF to mica and glass, then measuring the contours with an AFM. Mucke, et al. note that the lowest values are likely due to the constraints of the adsorption process on the glass/mica substrates, thus yielding a persistence length of $\sim 1 \mu\text{m}$ for vimentin in a dilute solution. The lower persistence length of IF compared to that of F-actin filaments is caused by the presence of flexible linker regions within the coiled-coil dimer and also due to axial slipping between dimers within the filaments (Mucke et al., 2004). This structure, while still highly resistant to elongation, is much less resistant to bending and torsional stresses (Howard, 2001). The coiled-coil dimer structure enables the IF to have a Young's modulus on the order of $E \sim 6 \text{ MPa}$ (calculated from persistence length and diameter measurements) and a high tensile strength of approximately 180 MPa for keratin-like IF (Fudge et al., 2003).

1.2.1.3 Microtubules

Microtubules are polar, tube-like structures with an outer diameter of 25 nm, an inner diameter of $\sim 15 \text{ nm}$, and are typically composed of 13 protofilaments consisting of multiple heterodimer subunits (see Figure 1–9) (Amos and Baker, 1979; Bordas et al., 1983).

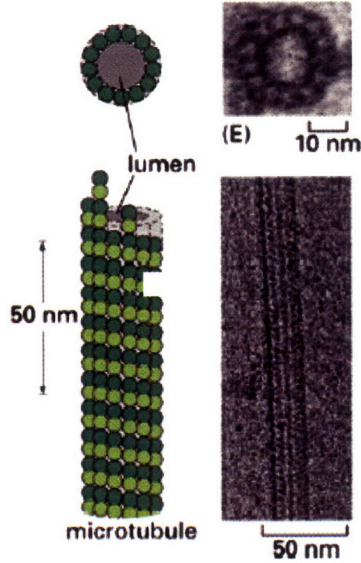


Figure 1-9. Microtubule composition (Alberts, 2002)

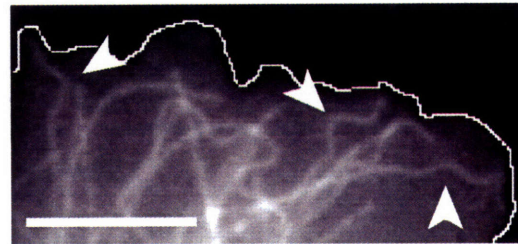


Figure 1-10. Microtubules with sinusoidal shapes (arrowheads) at their ends (white line indicates cell periphery). Bar = 5 μ m. (Brangwynne et al., 2006)

In vivo contour lengths for MT (see Figure 1-10) generally range from 1-10 μ m, while in axons their length can vary from 50-100 μ m (Bray, 2001). Microtubules provide the pathways for intracellular transport of vesicles and organelles in addition to helping to define the cellular structure in conjunction with other filaments. Microtubules are of primary structural importance during mitosis (i.e. composing the mitotic spindle) and for dynamic cellular structures such as cilia and flagella. Microtubules extend radially from the centrosome with higher concentration patterns near the nucleus (Alieva and Vorobev, 1992; Lodish et al., 2004). Microtubules also interact with other cytoskeletal filaments through cross-linking proteins such as plakins at cellular junctions (Karakesisoglou et al., 2000), and microtubule actin cross-linking factor (MACF) (Leung et al., 1999).

Mechanical properties (flexural rigidity, persistence length, etc.) are measured via a variety of empirical methods for bending and buckling of individual microtubules:

buckling force measurement using optical traps (Kurachi et al., 1995; Tran et al., 1995) or within vesicles (Kuchnir Fygenon et al., 1997), bending response via AFM (Vinckier et al., 1996; Kis et al., 2002), analysis of post-bending relaxation (Felgner et al., 1996; Felgner et al., 1997), image analysis of bending from hydrodynamic flow (Venier et al., 1994; Kurz and Williams, 1995), and thermally induced vibrations or shape fluctuations (Mizushima-Sugano et al., 1983; Gittes et al., 1993; Venier et al., 1994; Kurz and Williams, 1995; Mickey and Howard, 1995; Janson and Dogterom, 2004). These methods are illustrated in Figure 1–11.

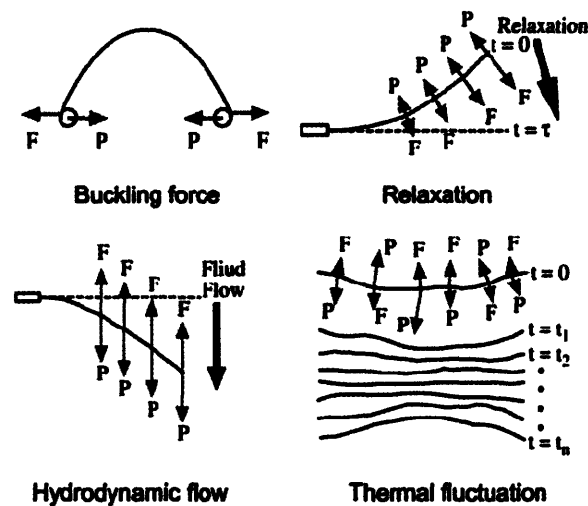


Figure 1–11. Primary experimental methods to measure mechanical properties of individual microtubules. P is the loading force, F is the response from the microtubule. (Kikumoto et al., 2006)

In vitro values for persistence length of MT composed from highly purified tubulin have ranged from 1 mm (Gittes et al., 1993; Venier et al., 1994) via thermal fluctuation imaging to 8 mm (Kurz and Williams, 1995) using the hydrodynamic flow method at physiologic temperatures and pH levels. Typical values for Young’s modulus range between 1 MPa, measured with an AFM and calculated via the Hertz formula (Vinckier

et al., 1996), and 7 GPa from buckling experiments with optical traps (Kurachi et al., 1995) assuming a tube-like MT cross-section. They are often modeled as homogeneous and isotropic, but experimental evidence suggests anisotropic behavior with stronger longitudinal bonds between heterodimers than the transverse, inter-protofilament bonds (Kis et al., 2002; Pampaloni et al., 2005). “Bending” occurs by sliding between filaments (governed by shear modulus) in addition to stretching of protofilaments (governed by Young’s modulus). When measured with the same method (e.g. AFM deflection), the shear modulus (upper limit of 1.4 MPa) is two orders of magnitude lower than the Young’s modulus (~100 MPa), giving rise to a length-dependent flexural rigidity of MT (Kis et al., 2002). Short MT are flexible due to a low value of the shear modulus while longer MT become more rigid as the Young’s modulus dominates the mechanical behavior (Kasas et al., 2004). The length-dependence can be seen in persistence length measurements for MT with increasing contour lengths (see Figure 1–12) measured through a single-particle tracking method combined with a fluctuation analysis (Pampaloni et al., 2006).

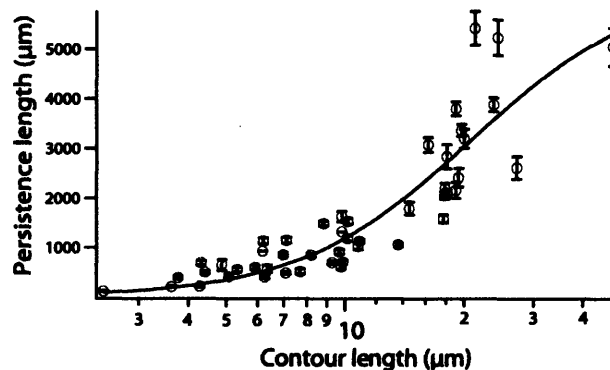


Figure 1–12. The persistence lengths of MT as a function of their contour lengths (Pampaloni et al., 2006)

Some recent work, however, has added to the debate by extending the isotropic, homogeneous models to include protofilament corrugations in order to explain the linear elastic response of microtubules (Schaap et al., 2006).

In vitro studies suggest that MT can only withstand small compressive loads ~ 1 pN (Deguchi et al., 2005; Dogterom et al., 2005). It has recently been shown, however, that highly curved in vivo MT influence cell shape by resisting large-scale compressive forces (~ 100 pN) exerted by the surrounding contractile cytoskeleton, and that their buckling wavelength is reduced significantly because of mechanical coupling to the surrounding elastic cytoskeleton (Brangwynne et al., 2006). Brangwynne, et al. compressively loaded initially straight MTs (that has polymerized out to the cell boundary) with a microneedle and then imaged over time to capture the sinusoidal shapes and compared them to thin plastic rods (0.1mm diameter) compressed in aqueous solutions (exhibiting classic long-wavelength Euler buckling) and in gelatin (exhibiting short-wavelength buckling with repeatable, local disruptions in the gelatin near the buckled region) (Brangwynne et al., 2006).

1.2.2 Cross-linked network behavior

1.2.2.1 Actin filaments

In vitro rheological experiments on reconstituted actin gel-like networks have been conducted with varying levels of actin and cross-link concentrations (Janmey et al., 1988; MacKintosh et al., 1995; Gisler and Weitz, 1999; Shin et al., 2004; Storm et al., 2005; Gardel et al., 2006b). Reconstituted actin gels under physiological conditions exhibit in

vitro shear moduli that are low, ~ 0.1 - 1 Pa (Hinner et al., 1998; Gardel et al., 2004a; Gardel et al., 2006b), compared to in vivo values, ~ 100 - 1000 s Pa (Fabry et al., 2001; Wang et al., 2002a; Alcaraz et al., 2003). Much of the variation, even for gels at the same concentration, can be attributed to differences in gel preparation, polymerization, and storage in addition to the measurement method chosen (Xu et al., 1998a). Many of the measurement techniques are indirect, either conducted from outside the cell or by physically altering the structure of the cytoskeleton to measure its properties. And local microrheological measurements have been found to yield different results for in vitro actin gels depending on the method chosen (e.g. the number of sampling points) (Shin et al., 2004). Variation is also seen for different cell types (Zahalak et al., 1990; Bausch et al., 1999; Sato et al., 2000). In vitro network prestress appears to increase the shear modulus to typical values found in the in vivo networks, which is a reasonable assumption for adherent cells and cells in a 3D extracellular matrix (Gardel et al., 2004a). While the empirically obtained dynamic modulus values vary considerably, a power-law description for modulus behavior is often used (Fabry et al., 2001; Koenderink et al., 2006). Microrheological test data exhibiting this power-law relationship are conventionally presented through plots showing the dynamic shear moduli as a function of frequency. Figure 1–13 demonstrates this behavior, for a 1 mg/ml solution of F-actin with and without cross-linking, obtained via an optical microrheology technique based on laser-interferometric detection of thermal fluctuations of embedded probe particles (Koenderink et al., 2006). Note the plateau region for the storage modulus (G')

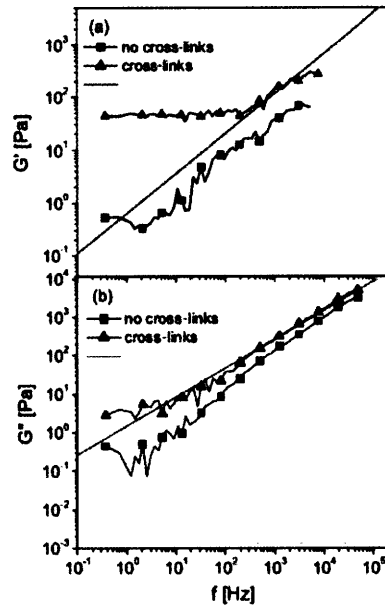


Figure 1–13. (a) Storage modulus $G'(\omega)$ and (b) Loss modulus $G''(\omega)$ of F-actin filaments. Solid lines: theory with $G^*(\omega) \sim \omega^{3/4}$ [adapted from (Koenderink et al., 2006)]

at low frequencies in Figure 1–13a. For semi-dilute solutions without cross-links, this plateau region can be attributed to polymer entanglements, with G' again decreasing at lower frequencies according to a power law relationship (not shown in Figure 1–13). For semi-dilute solutions with cross-links, however, the G' plateau modulus shown in Figure 1–13a extends indefinitely to low frequencies (Gittes and MacKintosh, 1998). Whether through entanglements behaving like a network of temporarily fixed cross-links or through a truly cross-linked network, the plateau region for G' at intermediate frequencies suitably corresponds to time scales of importance within the biological cells (Boal, 2002).

For low frequency, the shear modulus is often shown as a function of the shear strain. Figure 1–14 shows this relationship for F-actin/filamin-a (FLNa) (2 mg/ml), and a number of cross-linked biopolymer networks, at 10 rad/s measured in a strain-controlled rheometer which applies a sinusoidally varying strain with controllable maximal strain

amplitude and computes the elastic storage moduli from the amplitude and phase shift of the resulting stress (Storm et al., 2005).

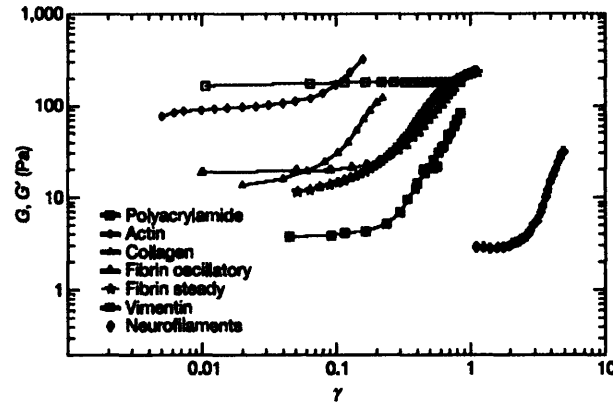


Figure 1-14. Dynamic shear storage moduli as a function of shear strain (Storm et al., 2005)

The influence of cross-links in actin networks is often examined by tuning the degree of filament cross-linking and bundling by varying the concentration of cross-links (c_{CL}) for a fixed actin concentration (c_A), or $R = c_{CL} / c_A$. Using the cross-linker scruin, Gardel, et al. determined that actin-scrutin gels exhibited elastic network behavior for values of $R > 0.03$, with a viscous, fluid-like response for $R < 0.03$ (Gardel et al., 2004a).

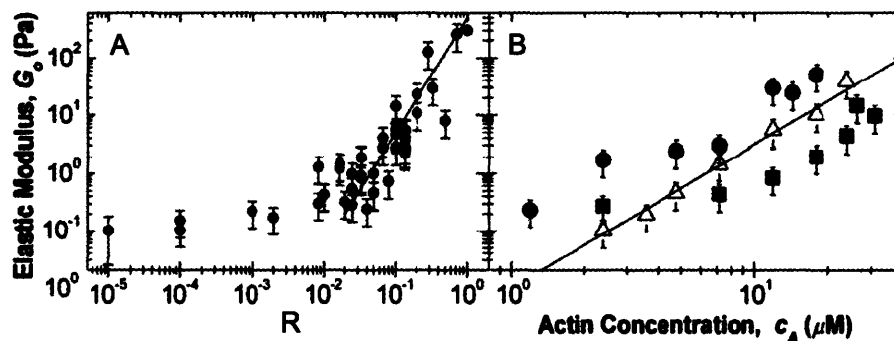


Figure 1-15. Elastic shear modulus of actin-scrutin networks as a function of (A) ratio of c_{CL} / c_A and (B) actin concentration; $R = 0.03$ (■), 0.13 (△), and 0.3 (●). (adapted from (Gardel et al., 2004a))

The results in Figure 1–15, obtained by polymerizing the cross-linked networks in situ within a stress-controlled rheometer, show G_0 decreasing weakly for $R < 0.03$ (Figure 1–15A). The elastic shear modulus increases with concentration according to the power-law relationship of $G_0 \sim c_A^{5/2}$ (Figure 1–15B), with a stiffer response for increasing values of R , possibly due to bundling of filaments (Gardel et al., 2004a).

At high strains (e.g. $\gamma > 0.4$ for FLNa–F-actin), however, nonlinear effects dominate the stress-strain response, and the (secant) shear modulus ($G = \sigma / \gamma$) used in the linear elastic regime is less useful than a differential (tangent) shear modulus ($K = d\sigma / d\gamma$) evaluated at a fixed stress (Gardel et al., 2006b). This concept is illustrated in Figure 1–16 (inset) for a network in which $G'' \ll G'$.

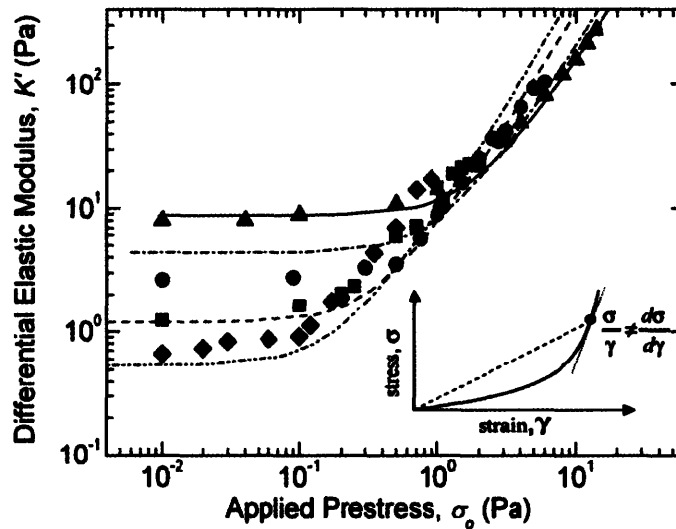


Figure 1–16. Differential elastic modulus, K' , as a function of applied shear prestress, σ_0 , for actin-scrutin networks: $R=0.03$ and $c_A = 29.4 \mu\text{M}$ (\blacktriangle), $21.4 \mu\text{M}$ (\bullet), $11.9 \mu\text{M}$ (\blacksquare), $8.33 \mu\text{M}$ (\blacklozenge) (Gardel et al., 2004a). Inset: schematic showing implications of the nonlinear stress-strain relationship for networks in which $G'' \ll G'$ (Gardel et al., 2006b)

To obtain linear measurements in the nonlinear elastic regime, rheological experiments employ a superposed oscillatory stress for a constant applied prestress (σ_o) to determine the dynamic differential elastic modulus $K'(\sigma_o) = (\partial\sigma/\partial\gamma)_{\sigma_o}$ as shown in Figure 1–16 for four different concentrations of actin (Gardel et al., 2004a). For small prestress, K' is nearly constant, corresponding to a linear network response while increasing prestress leads to elastic stiffening (from the nonlinear force-deflection behavior of individual filaments) which is consistent with an entropic model for the elasticity of actin networks (Gardel et al., 2004a; MacKintosh, 2006).

1.2.2.2 Intermediate filaments

The in vitro shear storage modulus of 2 mg/ml vimentin IF networks was found to be 3.2 Pa using a torsion pendulum viscoelastometer [corrected value from (Janmey et al., 1991)]. The storage modulus $G'(\omega, \gamma)$ (considered to be the differential modulus $G'(\omega, \gamma) = G(\gamma) + \gamma dG/d\gamma$ for short times (Janmey et al., 1983)) was also measured for the same 2 mg/ml vimentin networks as a function of shear strain and concentration (Figure 1–17).

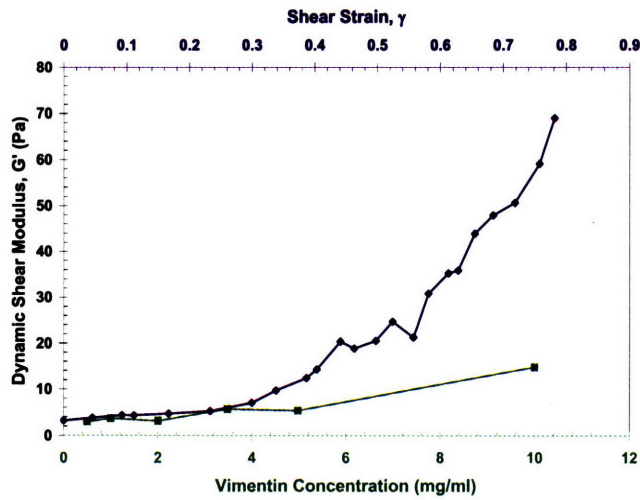


Figure 1-17. Dynamic shear storage modulus of vimentin IF as a function of shear strain γ ($c = 2\text{mg/ml}$), and as a function of vimentin concentration (low initial strain) [adapted from (Janmey et al., 1991)]

The vimentin IF networks exhibit strain hardening at larger strains, a feature predicted to be characteristic of polymer networks where the elastic response results from bending of the filaments (Doi and Kuzuu, 1980). The static stress-strain response of vimentin in a torsion rheometer also exhibits the strain hardening behavior (Figure 1-18).

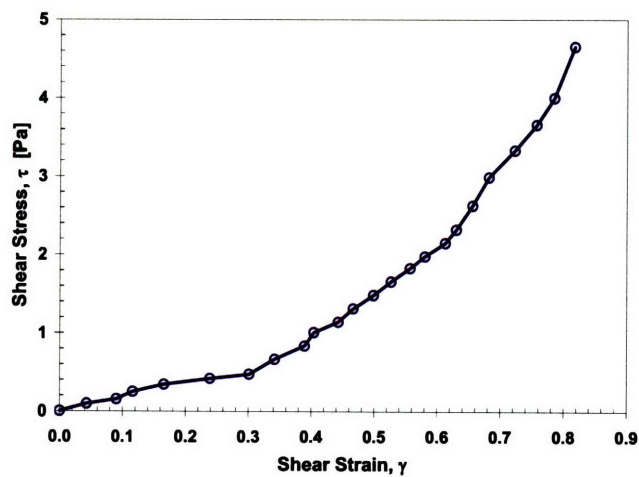


Figure 1-18. Shear stress-strain response of vimentin (2 mg/ml) [adapted from (Janmey et al., 1991)]

Vimentin also exhibits some unusual viscoelastic properties not shared by actin or tubulin. Vimentin is less rigid (lower shear moduli) at low strain but hardens at high strains and resists breakage, suggesting it maintains cell integrity (Janmey et al., 1991). The differences between F-actin and vimentin are optimal for the formation of a composite material with a range of properties that cannot be achieved by either polymer alone (Janmey et al., 1991). In addition to interacting with F-actin, vimentin can also interact with microtubules via plectin cross-linking protein bridges as shown in Figure 1–19.

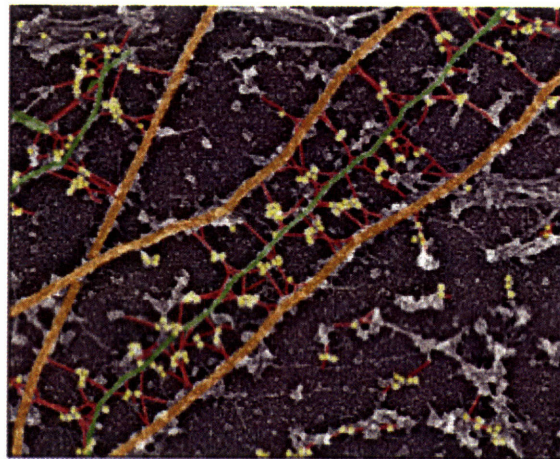


Figure 1–19. Electron micrograph of a fibroblast after dissolution of actin filaments revealing microtubules (orange), IFs assembled from vimentin (green), plectin (red), and gold particles marking plectin (yellow). Gold particles are 10 nm in diameter. [(Fuchs and Cleveland, 1998) adapted from (Svitkina et al., 1996)]

1.2.2.3 Microtubules

The in vitro shear storage modulus of 2 mg/ml MT networks, stabilized with 2 μ g/ml taxol, was found to be 3.4 Pa using a torsion pendulum viscoelastometer [corrected value

from (Janmey et al., 1991)]. The storage modulus $G'(\omega, \gamma)$ was also measured for the same 2 mg/ml MT networks as a function of shear strain and concentration (Figure 1–20).

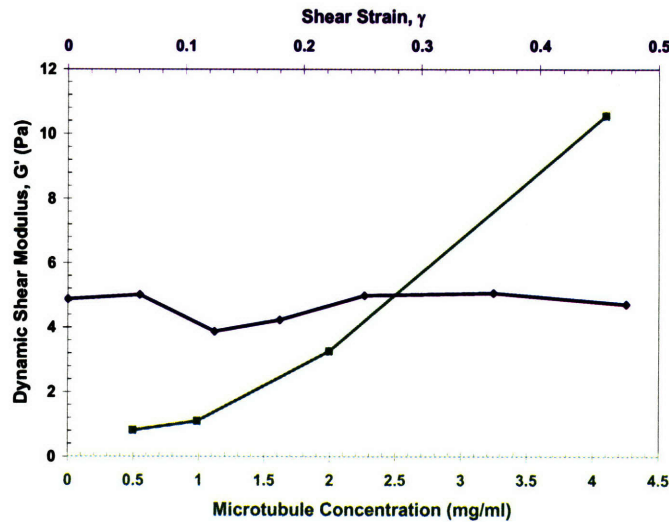


Figure 1–20. Dynamic shear storage modulus of microtubules as a function of shear strain γ ($c = 2\text{mg/ml}$), and as a function of microtubule concentration (low initial strain) [adapted from (Janmey et al., 1991)]

As would be expected from a very stiff, pipe-like structure, the MT do not exhibit strain hardening at larger strains, unlike F-actin and vimentin networks. The slope of the static stress-strain response (Figure 1–21) of a MT network (2 mg/ml) in a torsion rheometer also exhibits the relatively constant (secant) shear modulus of ~ 1 Pa, within a factor of 2-3 of storage modulus value at high frequency.

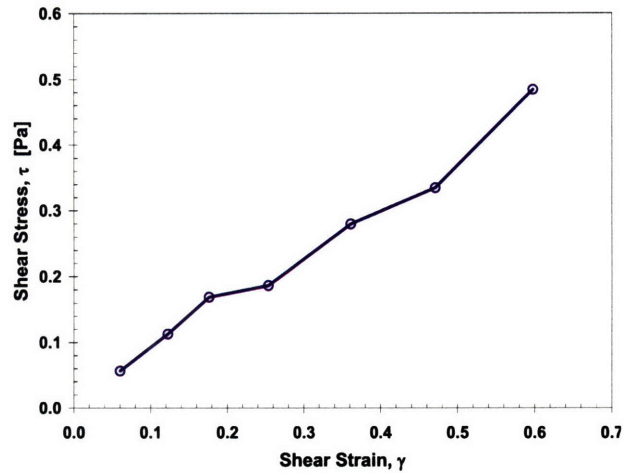


Figure 1–21. Shear stress-strain response of microtubules (2 mg/ml) [adapted from (Janmey et al., 1991)]

Although there has been considerable experimental evaluation of the cytoskeletal networks, microstructurally-based mechanical models of the networks are less plentiful. The next two chapters will review the previous modeling work in addition to detailing the framework for a new micromechanical model of an isotropic cytoskeletal network. The fundamental component of that framework, modeling the mechanical response of the filament, is addressed next in Chapter 2.

CHAPTER 2 FILAMENT MODEL

This chapter focuses on modeling approaches for single cytoskeletal filaments. The three filament stiffness regimes are delineated: flexible, stiff, and semiflexible. Next follows a description of entropic models and their applications while introducing a new analytical approximation for entropic unbending of semiflexible filaments. An internal energy stretching relationship is introduced and combined with the entropic unbending approximation to form an extensible filament model for semiflexible filaments. The chapter concludes with an examination of pretension in filaments.

2.1 Filament energy and stiffness regimes

According to the first law of thermodynamics, the net change in the internal energy ($d\mathcal{E}$) of a body is the sum of the heat absorbed (dQ) by the body and the work done ($d^r\mathcal{W}$) on the body, with negligible changes in kinetic energy.

$$d\mathcal{E} = dQ + d^r\mathcal{W} \quad (2.1)$$

The work done on the body is solely a function of the applied stresses (neglecting body forces), allowing Eq (2.1) to be given as

$$d\mathcal{E} = dQ + \frac{1}{\rho}(\mathbf{S} : d\mathbf{E}), \quad (2.2)$$

where \mathbf{S} is the symmetric 2nd Piola-Kirchoff stress tensor and \mathbf{E} is the Green-Lagrange strain tensor defined by

$$\mathbf{E} = \frac{1}{2}(\mathbf{C} - \mathbf{I}) = \frac{1}{2}(\mathbf{F}^T \mathbf{F} - \mathbf{I}), \quad (2.3)$$

where $\mathbf{C}=\mathbf{F}^T\mathbf{F}$ is the right Cauchy-Green strain tensor, \mathbf{I} is the identity tensor, and \mathbf{F} is the deformation gradient, $\mathbf{F}=\partial\mathbf{x}/\partial\mathbf{X}$ where \mathbf{x} is the position vector of a material point in the current configuration and \mathbf{X} is the original position. Additionally, the second law of thermodynamics relates the change in heat added to the body, for a reversible process, solely to the temperature (T) and change in entropy per unit mass (dS).

$$dQ = TdS \quad (2.4)$$

It is important to recognize that this equation applies to elastic deformations because they are reversible processes. Equations (2.2) and (2.4) can be combined to give,

$$d\mathfrak{E} = TdS + \frac{1}{\rho}(\mathbf{S} : d\mathbf{E}). \quad (2.5)$$

The Helmholtz free energy, A , for any system (and the incremental change in A) are defined as

$$A = \mathfrak{E} - TS, \quad (2.6)$$

$$dA = d\mathfrak{E} - TdS - SdT. \quad (2.7)$$

Assuming typical loading conditions and a constant temperature, Equation (2.7) becomes

$$(dA)_T = (d\mathfrak{E})_T - T(dS)_T. \quad (2.8)$$

This can now be combined with Equation (2.5) to give

$$\frac{1}{\rho}(\mathbf{S} : d\mathbf{E}) = (dA)_T = (d\mathfrak{E})_T - T(dS)_T, \quad (2.9)$$

or, given in terms of unit volume (i.e. ρS , ρA , $\rho\mathfrak{E}$), the work done on the body from applied stresses (in the absence of body forces), can be given as

$$[\mathbf{S} : d\mathbf{E}]_T = [d(\rho A)]_T = [d(\rho\mathfrak{E})]_T - T[d(\rho S)]_T. \quad (2.10)$$

The strain energy density per unit volume (W) is defined through the integral

$$W(\mathbf{E}) = \int_0^{\mathbf{E}} \mathbf{S} : d\mathbf{E} . \quad (2.11)$$

Using this definition of W for materials with negligible changes in internal energy (e.g. elastomers and other rubbery elastic materials), we assume that $d\rho\mathcal{E}=0$, and Equation (2.10) becomes

$$(W)_{T,\mathcal{E}} = -T[d(\rho S)]_T , \quad (2.12)$$

or solving for stress we have

$$\mathbf{S} = \left(\frac{\partial W}{\partial \mathbf{E}} \right)_{T,\mathcal{E}} = -\rho T \left(\frac{\partial S}{\partial \mathbf{E}} \right)_{T,\mathcal{E}} . \quad (2.13)$$

For the case of biopolymers, the entropy for each macromolecular filament can be given by

$$S = k_B \ln(\Omega) \quad (2.14)$$

where k_B is Boltzmann's constant and Ω is the number of available configurations. The number of configurations of a filament with total contour length, L_c , can be expressed in terms of a filament-specific probability density (per unit volume), $p(r)$, where r is the end-to-end distance of the chain. For the case of a freely jointed chain, to be discussed in Section 2.2, $\Omega = \int p(r) dV$ and $p(r)$ is the Gaussian distribution function.

However, if the entropy change during deformation of a material is infinitely small (e.g. metals, ceramics, or fully extended biopolymer filaments), then the isentropic assumption ($dS=0$) causes Equations (2.10) and (2.11) to become

$$(W)_T = [\mathbf{S} : d\mathbf{E}]_T = [d(\rho\mathcal{E})]_T . \quad (2.15)$$

Thus, in this case the isothermal work applied to deform these materials is converted to a change in internal energy ($d\mathcal{E}$) without affecting the conformation of the filament or

structure of material (e.g. stretching of interatomic bonds from bending, torsion, or axial extension).

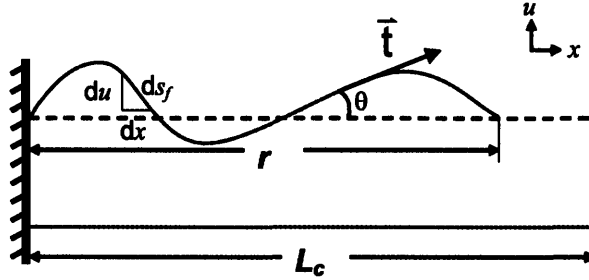


Figure 2–1. Geometric quantities for biopolymer filaments.

Entropic effects, enthalpic effects (based on changes in internal energy), or sometimes a combination of the two will control a filament's elastic behavior depending on its stiffness regime. The stiffness regimes are based on the relative magnitudes of the persistence length, l_p , and contour length of the filament. The persistence length, is defined in terms of the distance (ds_f) along the length of the filament (see Figure 2–1) beyond which the filament's curvature is uncorrelated due to thermal fluctuations. The tangent vector at any point along the filament's contour length is given by

$$\vec{t}(s_f) = \partial \vec{r}(s_f) / \partial s_f, \quad (2.16)$$

where $\vec{r}(s_f)$ is the radius vector to the point on the curve from the curve's end point (Yamakawa, 1976; Kroy and Frey, 1996). The average correlation between tangent vectors decays according the following relationship for three dimensions (Landau and Lifshitz, 1951),

$$\langle \vec{t}(s_f) \cdot \vec{t}(0) \rangle = \langle \cos[\theta(s_f) - \theta(0)] \rangle = e^{-|\Delta s_f| \frac{k_B T}{EI}} = e^{-|\Delta s_f| / l_p}. \quad (2.17)$$

where E = Young's modulus and I = area moment of inertia. The persistence length is therefore defined in its more familiar form as $l_p = \kappa/(k_B T)$, where $\kappa = EI$ = bending stiffness of the filament.

Biopolymer filaments are traditionally considered to be flexible if their persistence length is much less than their contour length ($l_p \ll L_c$) and stiff if the opposite is true ($l_p \gg L_c$). The intermediate regime of semiflexible filaments, in which $l_p \sim L_c$, describes the behavior of many biological macromolecules including F-actin (MacKintosh et al., 1995).

Due to a high bending stiffness, the number of filament configurations available (and entropy contribution) to stiff filaments is very small, and internal energy dominates their response. Internal energy-based filament deformations such as axial extension, torsion, and bending increase the internal energy of the stiff filament by straining interatomic bonds without causing a significant change in entropy. Bertoldi and Boyce modeled the behavior of mussel byssus using an internal energy-based filament model that captures the straightening out of bends in byssus molecular chains using an elastica-type solution followed by axial stretching of the chains and subsequent force-induced unfolding of the modular domains (Bertoldi and Boyce, 2007b). An internal energy-based elastica approximation has also been used to capture the elasticity of other soft tissue fibrils (Garikipati et al., 2008) and fibrous networks of collagen fascicles (Castro et al., 2008a). The mechanical response of flexible polymers, to be discussed in the next section, is entropic in origin, with an initial end-to-end distance $r=0$ to maximize the entropy difference and minimize its energy state. Semiflexible filaments, however, behave more like continuously flexible filaments, often called a worm-like chain (WLC),

rather than the traditional freely jointed chains of rigid rods (Boal, 2002). Except for large extensions ($r/L_c \sim 1$), the mechanical response of a semiflexible filament is based on entropic unbending. As a semiflexible filament is unbent, the change in entropy comes from sampling fewer configurations of bent filaments, which will be covered in the next section.

2.2 Inextensible Entropic Models

The force-extension response of biopolymers is usually characterized by a linear region followed by a nonlinear region of increasing tangent stiffness as the filament's extensional limit is reached (Fernandez et al., 2006; Kasza et al., 2007). Entropic models have been successful in capturing the majority of both regions of the force-extension response for many biopolymers.

2.2.1 Freely jointed chain model

Flexible polymers, with high molecular weight polymers with long contour lengths, often behave like freely jointed chains (FJC) (Kuhn and Gr \ddot{u} n, 1942; Treloar, 1958) made of many discrete rigid rods, and therefore many possible configurations. Figure 2-2 shows a schematic of a FJC which is subject to the assumptions that all bond angles, θ , and rotational angles, ϕ are equally probable, no restriction on bond rotations, and no

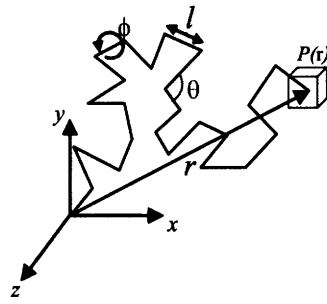


Figure 2–2. Freely Jointed Chain

excluded volume effects. The total contour length (L_c) consists of “ N ” statistical segment lengths (Kuhn length) “ l ”, or $L_c = Nl$. To develop a quantitative evaluation of the probability of chain configurations, we can employ an appropriate probability, $p(r)dV$, that the free end of the chain is found within a small volume element ($dV = dx dy dz$), with the fixed end at the origin as illustrated in Figure 2–2. The Gaussian error function provides a good model for this probability, for $r \ll L_c$,

$$p(x, y, z)dx dy dz = \frac{b^3}{\pi^{3/2}} \exp(-b^2(x^2 + y^2 + z^2))dx dy dz \quad (2.18)$$

where

$$b = \sqrt{\frac{3}{2Nl^2}} \quad (2.19)$$

The Gaussian distribution, often referred to as a random walk profile, can be given in terms of the radial distance from the origin of the “walk”,

$$p(r) = \left(\frac{3Nl^2}{2\pi}\right)^{3/2} \exp\left(-\frac{3r^2}{2Nl^2}\right), \quad (2.20)$$

which is valid for approximately $r < Nl/3$ (Boyce and Arruda, In preparation). Substituting the Gaussian probability function into Equation (2.14), we obtain the change in entropy per unit volume for the FJC,

$$S = k_B \ln(p(r)dV) = k_B \left\{ \ln \left(\frac{3Nl^2}{2\pi} \right)^{3/2} - \left(\frac{3r^2}{2Nl^2} \right) + \ln(dV) \right\}. \quad (2.21)$$

The entropy per unit volume for an undeformed single molecule is then given by

$$S = -k_B \frac{3r^2}{2Nl^2} + c, \quad (2.22)$$

where the arbitrary constant, c , will cancel out when the change in entropy (ΔS) is evaluated:

$$\Delta S = -k_B \frac{3r^2}{2Nl^2} = -k_B \frac{3}{2Nl^2} (x^2 + y^2 + z^2). \quad (2.23)$$

The isothermal work done to extend a single biopolymer filament can be found (in terms of the change in entropy per unit volume, ΔS) from Equation (2.12), still assuming no change in internal energy or polymer volume,

$$(W)_{T,s} = \int_{chain} dr = -T(\Delta S)_T, \quad (2.24)$$

or, rewritten using the Gaussian statistical distribution, we can calculate the force required to extend the FJC according to

$$f_{G,FJC} = -T \frac{\partial \Delta S}{\partial r} = -\frac{3k_B T}{Nl^2} r \quad (2.25)$$

At deformations where the macromolecular end-to-end length approaches the contour length, non-Gaussian effects must be addressed (typically for $r/L_c \geq 0.4$) (Boyce and Arruda, 2000). The non-Gaussian behavior is captured through the use of Langevin chain statistics which describe the limited extensibility of polymer chains during the

elastic extension as derived by Kuhn and Gr \ddot{u} n (Kuhn and Gr \ddot{u} n, 1942). The corresponding non-Gaussian extensional force is given by

$$f_{NG,FJC} = -\frac{k_B T}{l} \beta \quad (2.26)$$

where $\beta = \mathcal{L}^{-1}(r/Nl)$ is the inverse Langevin function and $\mathcal{L}(\beta)$ is the Langevin function defined by $\mathcal{L}(\beta) = \coth(\beta) - 1/\beta$.

2.2.2 Worm-like chain model

The worm-like chain (WLC) model, a more appropriate representation of the axial extension of semiflexible filaments, is derived from the Kratky-Porod expression (Kratky and Porod, 1949) for total energy of bending deformation due to thermal fluctuations:

$$E_{K-P} = \frac{\kappa}{2} \int_0^{L_c} (\partial \bar{t}(s_f) / \partial s_f)^2 ds_f \quad (2.27)$$

where the tangent vector, \bar{t} , arc length, s_f , and contour length are shown in Figure 2–3 for a WLC. The WLC is a continuous chain that can be interpolated to any amount of

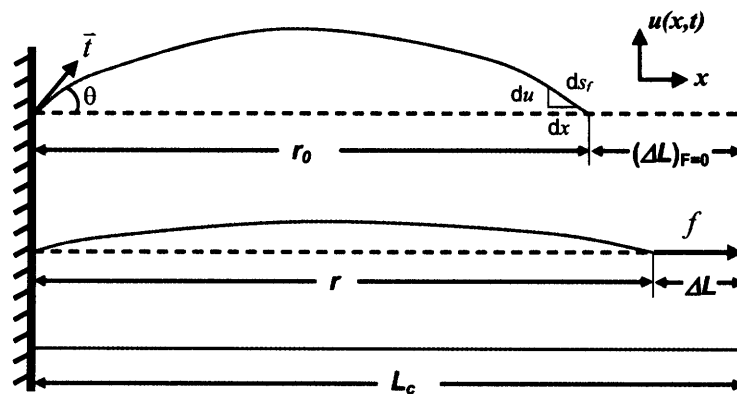


Figure 2–3. WLC filament schematic [adapted from (MacKintosh, 2006)]

stiffness or flexibility between the two extremes of a FJC and a rigid rod (Yamakawa, 1976). With a force (f) applied along the x-axis (Figure 2–3), the total energy of a stretched WLC becomes (Fixman and Kovac, 1973; Yamakawa, 1976)

$$E_{WLC} = k_B T \int_0^{L_c} \left[\frac{l_p}{2} \left(\frac{\partial \bar{t}(s_f)}{\partial s_f} \right)^2 - f \cos \theta(s_f) \right] ds_f \quad (2.28)$$

with $L_c \gg l_p$ assumed. Using the rigid constraint of $|\bar{t}(s_f)| = 1$ (Yamakawa, 1976; Kroy and Frey, 1996; Spakowitz and Wang, 2005), we can express the tangent vector fluctuations in the x-direction are quadratic in terms of the lateral tangent vectors, $\bar{t}_L = [t_y, t_z]$, or $t_x = 1 - \bar{t}_L^2/2 + O(\bar{t}_L^4)$; and to quadratic order $\partial \bar{t}/\partial s_f = \partial \bar{t}_L/\partial s_f$ (Marko and Siggia, 1995), which yields a Gaussian approximation for the energy function (Kovac and Crabb, 1982),

$$E_{WLC} = k_B T \int_0^{L_c} \left[\frac{l_p}{2} \left(\frac{\partial \bar{t}_L}{\partial s_f} \right)^2 - f \bar{t}_L^2 \right] ds_f - k_B T f L_c. \quad (2.29)$$

Using the Fourier transform for the lateral tangent vector to decouple the energy into normal modes yields (Marko and Siggia, 1995),

$$\tilde{\bar{t}}_L(q) \equiv \int_0^{L_c} e^{iqs} \bar{t}_L(s_f) ds_f, \quad (2.30)$$

$$E_{WLC} = k_B T \left\{ \frac{1}{2} \int_0^{L_c} \frac{|\tilde{\bar{t}}_L^2|}{2\pi} [l_p q^2 + f] dq - f L_c \right\}. \quad (2.31)$$

Unlike biological and synthetic filaments with limited configurational space whose elasticity is governed by changes in internal energy (Castro et al., 2008a; Garikipati et al., 2008), semiflexible filaments' entropic fluctuations within their configurational space is

driven by thermal energy. The principle of equipartition of energy (Waterston, 1846; Boltzmann, 1871; Boltzmann, 1876) states that, once the system reaches thermal equilibrium, molecules equally share their averaged energy among the independent degrees of freedom of their motion. For a system in which the system's energy (E_{sys}) varies quadratically with a parameter (ξ), $E_{\text{sys}}=c \xi^2$ (where c is a constant), the average energy is (Howard, 2001),

$$\begin{aligned}
\langle E_{\text{sys}} \rangle &= \int_{-\infty}^{\infty} E_{\text{sys}}(\xi) p(\xi) d\xi = \frac{1}{Z} \int_{-\infty}^{\infty} E_{\text{sys}}(\xi) \exp[-E_{\text{sys}}(\xi)/k_B T] d\xi \\
&= \frac{\int_{-\infty}^{\infty} E_{\text{sys}}(\xi) \exp[-E_{\text{sys}}(\xi)/k_B T] d\xi}{\int_{-\infty}^{\infty} \exp[-E_{\text{sys}}(\xi)/k_B T] d\xi} = \frac{\int_{-\infty}^{\infty} c \xi^2 \exp[-c \xi^2/k_B T] d\xi}{\int_{-\infty}^{\infty} \exp[-c \xi^2/k_B T] d\xi} \\
&= \frac{1}{2} k_B T
\end{aligned} \tag{2.32}$$

Applying the equipartition of energy to the wormlike chain, we find that

$$\langle \bar{l}_L^2 \rangle = \int_0^{\infty} \frac{\langle \tilde{l}_L^2 \rangle}{2\pi} dq = 2 \int_0^{\infty} \frac{1}{2\pi(l_p q^2 + f)} dq = \frac{1}{\sqrt{l_p f}}. \tag{2.33}$$

where the factor of 2 has been included to capture both lateral components of \bar{l}_L (Marko and Siggia, 1995), and the extension of the WLC can now be given to quadratic order as (Marko and Siggia, 1995),

$$\frac{r}{L_c} = \bar{l} \cdot \hat{x} = 1 - \frac{\langle \bar{l}_L^2 \rangle}{2} = 1 - \frac{1}{2\sqrt{l_p f}}. \tag{2.34}$$

Solving in terms of the force yields,

$$f_{\text{WLC}} = \frac{kT}{16l_p} \left(1 - \frac{r}{L_c} \right)^{-2}, \tag{2.35}$$

which captures the WLC behavior in the inextensible limit for which $r/L_c \sim f^{-1/2}$. As the filament is stretched close to its contour length, the amplitude of the undulations decreases and the tangent vector fluctuates minimally about the x-axis (Kovac and Crabb, 1982). This decrease in thermal undulation amplitude results in a corresponding decrease in available filament conformations to sample, leading to an increase in the axial stiffness of the flexible filament.

The WLC model has been effective at describing the entropic elasticity of a number of single molecules when $L_c > l_p$, including DNA at low to moderate strains (Bustamante et al., 1994), single RNA molecules (Liphardt et al., 2001), and titin (Rief et al., 1997). Although its full force-extension relationship requires numerical evaluation of the path integral, interpolation approximations have been successfully used to simplify calculations. For example, the popular interpolation approximation from Marko and Siggia (Marko and Siggia, 1995) is

$$f_{WLC,M-S} = \frac{k_B T}{l_p} \left[\frac{r}{L_c} + \frac{1}{4(1-r/L_c)^2} - \frac{1}{4} \right]. \quad (2.36)$$

This approximation was created to encompass the small-force and high-force regimes, but it diverges from the exact WLC path integral solution in the cross-over region as seen in Figure 2-4.

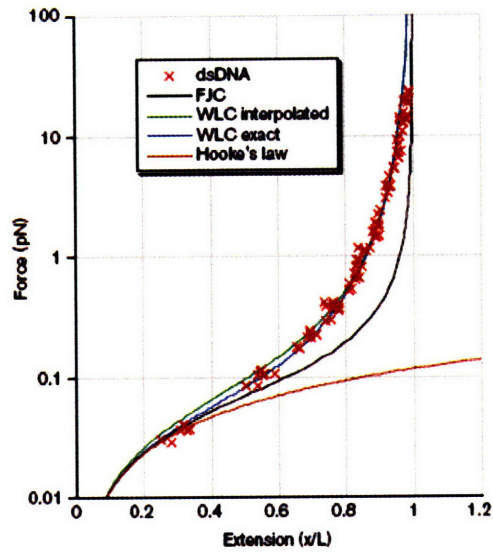


Figure 2–4. Comparison of WLC, FJC, and linear models for dsDNA data (Bustamante et al., 2000)

Figure 2–4 also demonstrates that the WLC provides a superior fit, for biopolymers such as dsDNA, compared to the FJC or a linear relationship (note that linear results are not straight due to the semi-log plot format). One should consider, however, that the Marko-Siggia approximation requires an end-to-end distance of zero for no applied force ($r_{F=0}=0$), and is only defined for $L_c \gg l_p$ (Marko and Siggia, 1995). The Marko-Siggia approximation also exhibits the non-intuitive behavior of requiring a decreasing extensional force with increasing filament bending stiffness with other quantities fixed (Figure 2–5).

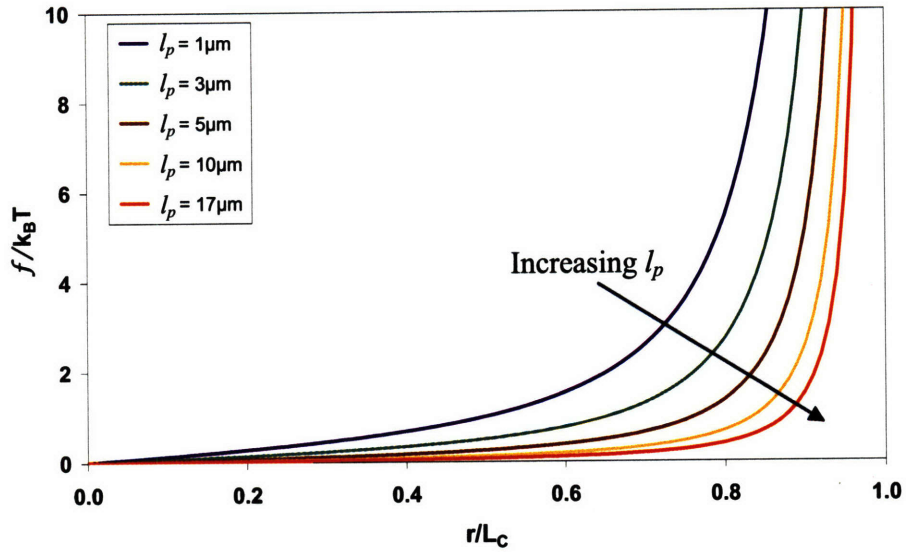


Figure 2–5. Normalized force-extension plot of WLC approximation for increasing persistence length, l_p

While these issues are not of concern with biopolymers such as dsDNA or titin (both with $L_c \gg l_p$), they become more significant for networks of semiflexible filaments.

Subsequent molecular theories (e.g. (MacKintosh et al., 1995)) have addressed the semiflexible regime for $L_c \sim l_p$ with energy functionals and force-deflection relationships that are still entropic in origin but allow for $r_{F=0} > 0$ as would be encountered in a cytoskeletal network. Still following the Kratky-Porod formulation, the MacKintosh model is derived in the following pages for bending deformations due to thermal fluctuations (MacKintosh et al., 1995; MacKintosh, 2006). The MacKintosh model describes a filament at a finite temperature, with transverse thermal fluctuations that result in a contraction, $(\Delta L)_{F=0}$ in Figure 2–3, causing the end-to-end distance, r , at an axial force, F , of zero to be less than the filament contour length, $r_{F=0} = L_c - (\Delta L)_{F=0}$. Letting the x-axis define the average orientation of the filament and u define one of the two transverse displacements, the incremental change along a filament segment (ds_j) is

$$ds_f \cong \sqrt{dx^2 + du^2} \cong dx\sqrt{1 + (du/dx)^2}. \quad (2.37)$$

The projected length for small transverse displacements, du , is the contour length to leading quadratic order:

$$L_c = \int ds_f = \int dx\sqrt{1 + (du/dx)^2}. \quad (2.38)$$

Newton's iteration for calculating a square root \sqrt{n} is given by

$$\sqrt{n} = x_{k+1} = 1/2(x_k + n/x_k). \quad (2.39)$$

with $x_0=1$ and which converges quadratically in the limit of $\lim_{k \rightarrow \infty} x_k$. Taking the second term of the iteration (x_1), the change in length (ΔL) takes the form:

$$\Delta L = L_c - r = \int \sqrt{1 + (du/dx)^2} dx - \int dx \cong 1/2 \int (du/dx)^2 dx. \quad (2.40)$$

The total energy associated with applying an extensional force to the filament is

$$E_{Total} = \frac{1}{2} \int_0^{L_c} \left[\kappa \left(\frac{\partial^2 u}{\partial x^2} \right)^2 + F \left(\frac{\partial u}{\partial x} \right)^2 \right] dx. \quad (2.41)$$

The change in length and energy expression can be simplified by representing $u(x)$ as a Fourier series with pinned boundary conditions.

$$u = \sum_q u_q \sin(qx) \quad \text{with } q = \text{wavenumber} = n\pi/L_c. \quad (2.42)$$

$$E_{Total} = \frac{L_c}{4} \sum_q (\kappa q^4 + F q^2) u_q^2. \quad (2.43)$$

$$\Delta L = 1/2 \int \sum_q u_q^2 q^2 \cos^2(qx) dx = \frac{L_c}{4} \sum_q u_q^2 q^2. \quad (2.44)$$

The ensemble average contraction length is amended by inserting a factor of two to include the contributions of both (orthogonal) transverse degrees of freedom of a filament in 3D fluctuation.

$$\langle \Delta L \rangle = \frac{L_c}{4} \sum_q q^2 [2 \langle u_q^2 \rangle]. \quad (2.45)$$

In solving for the average transverse displacement $\langle u_q \rangle$, we apply the principle of equipartition of energy to this case, as was done earlier for the general WLC,

$$\frac{1}{2} k_B T \approx \frac{L_c}{4} (\kappa q^4 + F q^2) \langle u_q^2 \rangle. \quad (2.46)$$

Solving for the average transverse displacement for the cases of $F \neq 0$,

$$\langle u_q^2 \rangle \approx \frac{2 k_B T}{q^2 L_c (\kappa q^2 + F)}. \quad (2.47)$$

Based on the equilibrium amplitudes, the contraction (for small transverse fluctuations) is found by converting the wave number back from Fourier space and combining Equation (2.45) and Equation (2.47).

$$\langle \Delta L \rangle = L_c - r = \frac{L_c^2}{l_p \pi^2} \sum_n \frac{1}{(n^2 + \phi)} \quad (2.48)$$

where the dimensionless force $\phi = FL_c^2 / \kappa \pi^2$ (MacKintosh, 2006). The contraction length at the zero force condition is

$$\langle \Delta L \rangle_{\phi=0} = L_c - r_{F=0} = \frac{k_B T}{\kappa} \frac{L_c^2}{\pi^2} \sum_n \frac{1}{n^2} = \frac{L_c^2}{6 l_p}, \quad (2.49)$$

where the Riemann zeta function, $\sum_n 1/n^2 = \pi^2/6$, is used to solve for the series. The

value of r at the zero force condition can then be shown to be

$$r_{F=0} = L_c \left(1 - \frac{L_c}{6 l_p} \right). \quad (2.50)$$

We simplify the series relation of Equation (2.48) through the use of the earlier defined Langevin function. The series for the average contractions converges to the following expression:

$$\langle \Delta L \rangle = L_c - r = \frac{L_c^2}{l_p \pi^2} \left(\frac{\pi \sqrt{\phi} \coth(\pi \sqrt{\phi}) - 1}{2\phi} \right) = \frac{L_c^2}{2l_p} \left[\frac{\mathcal{L}(\pi \sqrt{\phi})}{\pi \sqrt{\phi}} \right] \quad (2.51)$$

where $\pi \sqrt{\phi} = L_c \sqrt{F/\kappa}$.

Since the functional dependence of F on r is of more interest than r as a function of F , Cohen's Padé approximation for the inverse Langevin equation (Cohen, 1991),

$$\mathcal{L}^{-1}(x) = x \frac{3-x^2}{1-x^2} + O(x^6) \quad (2.52)$$

is used to create a more useful force-extension relationship,

$$F = \frac{k_B T}{l_p} \left(\frac{1}{4(1-r/L_c)^2} \right) \left(\frac{L_c/l_p - 6(1-r/L_c)}{L_c/l_p - 2(1-r/L_c)} \right) \quad (2.53)$$

which reduces to Equation (2.49) for the zero force condition. The corresponding strain energy function is

$$w = \frac{k_B T}{l_p} \left[\frac{L_c}{4(1-r/L_c)} - l_p \left[\ln(L_c^2 - 2l_p L_c + 2l_p r) - \ln(r - L_c) \right] - c \right] \quad (2.54)$$

where c is a constant equal to the initial strain energy of the filament.

This approximation is valid for $(1 - 0.3L_c/l_p) < r/L_c < 1$; noting that $r_{F=0}/L_c = 1 - 0.167L_c/l_p$, this approximation covers the range of filament extension of relevance for the semiflexible ($l_p \sim L_c$) network. In order to maintain a positive extension, $r/L_c > 0$, the approximation is therefore subject to the following limit for tensile loads: $L_c < 6.0 l_p$. Densely cross-linked networks can accommodate much lower ratios of L_c/l_p , with

a reasonable lower limit of $L_c=1/10 l_p$ giving a limit of $0.98 < r/L_c < 1$. For the case of $L_c= l_p$, the extension range is $0.83 < r/L_c < 1$. The approximation is also valid, to a lesser extent, for negative (compressive) forces by increasing the range of values for r/L_c via the following relation: $(1-0.3L_c/l_p) < r/L_c < 1$, so that the extension limit becomes $0.7 < r/L_c < 1$ for $L_c= l_p$. The corresponding practical upper limit is then $L_c < 3.3 l_p$ (again, to ensure $0 < r/L_c < 1$). A lower limit value of $L_c=1/10 l_p$ yields an extension limit of $0.97 < r/L_c < 1$. Note that since all of the in vitro networks evaluated in the paper were densely cross-linked ($L_c < l_p$), none of these limits precluded the use of the approximation. It is also unlikely that in vivo actin networks would exist with contour lengths 3-6 times greater than the filament persistence length. The Padé approximation-based force-extension expression, Equation (2.53), compares very favorably with the exact numerical expression, Equation (2.48), with the average error for each of the four cases in Figure 2–6a ($l_p=3, 5, 7.5, 10\mu\text{m}$) equal to 0.4%, 0.8%, 1.2%, and 1.5%, respectively.

Figure 2–6a shows the single filament response of the MacKintosh model using characteristic properties of F-actin filaments from a densely cross-linked network ($l_p=3\text{-}10\mu\text{m}$, $L_c=1\mu\text{m}$). The end-to-end distance at zero force, $r_{F=0}$, depends strongly on the combination of persistence length l_p and contour length L_c . Here, keeping L_c constant and varying l_p from 3-10 μm , we see the effect of l_p on $r_{F=0}$ in the different starting points of Figure 2–6a where $r_{F=0}$ is smaller for smaller l_p . This then results in the increased initial chain stiffness with increase in l_p as shown in Figure 2–6a. Note that a densely cross-linked network ($l_p > L_c$) operates in this highly nonlinear regime of the force-extension

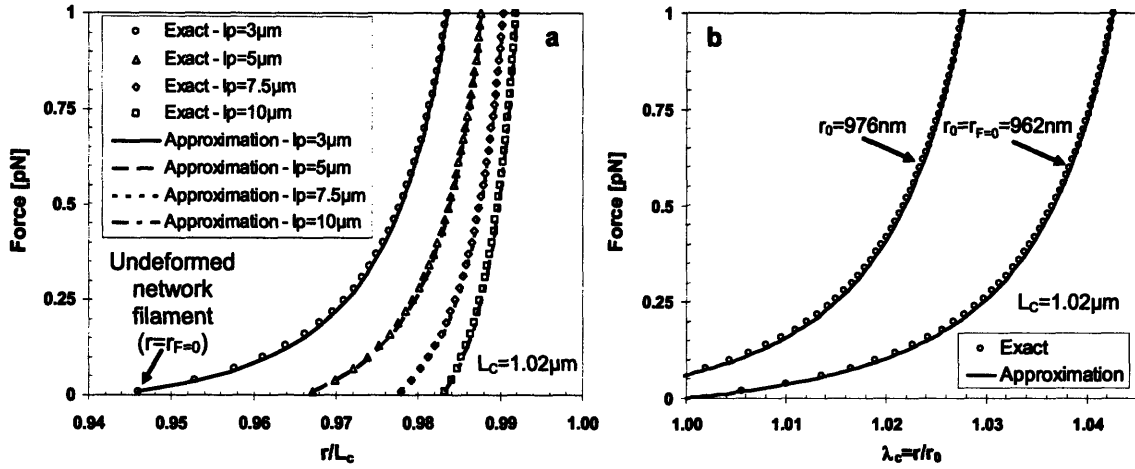


Figure 2–6. (a) The effect of persistence length on filament force-extension behavior as computed using MacKintosh model (fixing contour length to $L_c=1.02\mu\text{m}$); (b) the effect of pretension on filament force-stretch behavior as computed using MacKintosh model (for case of $L_c=1.02\mu\text{m}$; $l_p=3\mu\text{m}$). Both figures show exact results as well as results using the proposed approximation, Equation (2.53), illustrating the accuracy of the approximation.

curve (i.e. $r/L_c > 0.94$ in Figure 2–6a). Figure 2–6b shows the effect of a different initial end-to-end distance, r_0 , on the filament force-stretch ($\lambda_c = r/r_0$) behavior. Here, taking the case of $l_p=3\mu\text{m}$ and $L_c=1.0\mu\text{m}$ which has a zero force length of $r_{F=0}=0.962\mu\text{m}$, we compare the behavior when $r_0=r_{F=0}=0.962\mu\text{m}$ to that when $r_0=0.976\mu\text{m}$. The $r_0=0.976\mu\text{m}$ case begins with an initial tensile force on the filaments (i.e. chain pretension) of $F_0=0.07\text{pN}$. The pretension results in the observed increase in initial stiffness and decrease in limiting stretch as shown in Figure 2–6b. Conversely, a precompression condition will shift the curve to the right, resulting in a lower value on the ordinate axis, a reduced initial stiffness, and an increased limiting stretch.

The previous MacKintosh WLC derivation describes the limiting case of a filament with pinned-pinned boundary conditions. The other limiting case for a filament would be clamped-clamped boundary conditions. The expressions for length change (2.40) and energy (2.41) can therefore be simplified by representing $u(x)$ as a Fourier series with

clamped boundary conditions. In the clamped-clamped configuration, the length of the filament subject to significant thermal bending is reduced to $L_c/2$.

$$u = \sum_q u_q \sin(qx) \quad \text{with } q = \text{wavenumber} = 2n\pi/L_c. \quad (2.55)$$

$$E_{\text{Total}} = \frac{L_c}{8} \sum_q (\kappa q^4 + Fq^2) u_q^2. \quad (2.56)$$

$$\Delta L = 1/2 \int \sum_q u_q^2 q^2 \cos^2(qx) dx = \frac{L_c}{8} \sum_q u_q^2 q^2. \quad (2.57)$$

The ensemble average contraction length is amended by inserting a factor of two to include the contributions of both (orthogonal) transverse degrees of freedom of a filament in 3D fluctuation.

$$\langle \Delta L \rangle = \frac{L_c}{8} \sum_q q^2 [2 \langle u_q^2 \rangle]. \quad (2.58)$$

In solving for the average transverse displacement $\langle u_q \rangle$, we apply the principle of equipartition of energy to this case, as was done earlier for the general WLC and the pinned-pinned case,

$$\frac{1}{2} k_B T \approx \frac{L_c}{8} (\kappa q^4 + Fq^2) \langle u_q^2 \rangle. \quad (2.59)$$

Solving for the average transverse displacement for the cases of $F \neq 0$,

$$\langle u_q^2 \rangle \approx \frac{4k_B T}{q^2 L_c (\kappa q^2 + F)}. \quad (2.60)$$

Based on the equilibrium amplitudes, the contraction (for small transverse fluctuations) is found by converting the wave number back from Fourier space.

$$\langle \Delta L \rangle = L_c - r = \frac{L_c^2}{4l_p \pi^2} \sum_n \frac{1}{(n^2 + \phi_c)} \quad (2.61)$$

where the dimensionless force for the clamped filament is $\phi_c = FL_c^2/4\kappa\pi^2$. The contraction length at the zero force condition is

$$\langle \Delta L \rangle_{F=0} = L_c - r_{F=0} = \frac{k_B T}{4\kappa} \frac{L_c^2}{\pi^2} \sum_n \frac{1}{n^2} = \frac{L_c^2}{24l_p}, \quad (2.62)$$

where the Riemann zeta function, $\sum_n 1/n^2 = \pi^2/6$, is again used to solve for the series.

The value of r at the zero force condition for a clamped-clamped filament can then be shown to be

$$r_{F=0} = L_c \left(1 - \frac{L_c}{24l_p} \right), \quad (2.63)$$

which, as expected, give a larger value of $r_{F=0}$ than the pinned-pinned case. We can again simplify the series relation of Equation (2.61) through the use of the earlier defined Langevin function. The series for the average contractions converges to the following expression:

$$\langle \Delta L \rangle = L_c - r = \frac{L_c^2}{4l_p\pi^2} \left(\frac{\pi\sqrt{\phi_c} \coth(\pi\sqrt{\phi_c}) - 1}{2\phi_c} \right) = \frac{L_c^2}{8l_p} \left[\frac{\mathcal{L}(\pi\sqrt{\phi_c})}{\pi\sqrt{\phi_c}} \right] \quad (2.64)$$

where $\pi\sqrt{\phi_c} = L_c\sqrt{F/4\kappa}$.

Since the functional dependence of F on r is of more interest than r as a function of F , Cohen's Padé approximation for the inverse Langevin equation (Cohen, 1991),

$$\mathcal{L}^{-1}(x) = x \frac{3-x^2}{1-x^2} + \mathcal{O}(x^6) \quad (2.65)$$

is used again to create a more useful force-extension relationship for the clamped-clamped filament,

$$F_c = \frac{k_B T}{l_p} \left(\frac{1}{16(1-r/L_c)^2} \right) \left(\frac{L_c/l_p - 24(1-r/L_c)}{L_c/l_p - 8(1-r/L_c)} \right) \quad (2.66)$$

which reduces to Equation (2.63) for the zero force condition. The stiffer behavior of the WLC filament with clamped-clamped boundary conditions is shown in Figure 2–7.

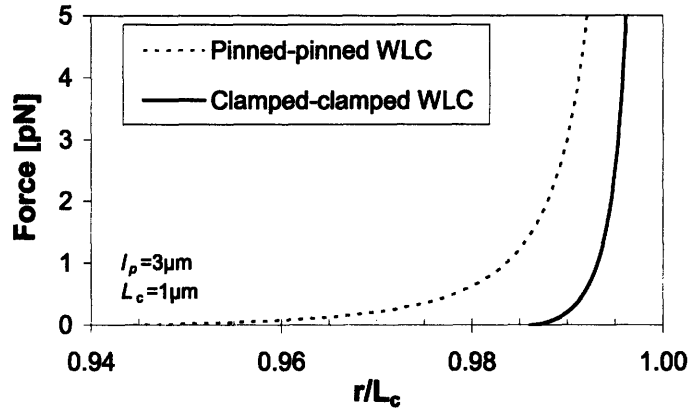


Figure 2–7. Force-extension behavior of WLC filaments subject to pinned-pinned or clamped-clamped boundary conditions ($L_c=1\mu\text{m}$; $l_p=3\mu\text{m}$)

An analytical extension-force relationship has also been recently obtained from the WLC energy functional, Equation (2.28), for a semiflexible filament with both pinned-pinned and clamped-clamped end conditions (Hori et al., 2007). Hori, et al. employ the small fluctuation approximation to create a Gaussian path integral for the energy function, which can in turn be given in terms of a Green’s function that gives the probability of the end-to-end distance, similar to previous treatments (Yamakawa, 1976; Spakowitz and Wang, 2005). In their “fluctuating rod” model of semiflexible filaments, Hori, et al. give the analytical extension- force relationship for the case of pinned-pinned boundaries as

$$\frac{r}{L_c} = 1 - \frac{d-1}{2} \left(\frac{\kappa_f L_c \cosh(\kappa_f L_c) - \sinh(\kappa_f L_c)}{2\kappa_f^2 L_c l_p \sinh(\kappa_f L_c)} \right) \quad (2.67)$$

where d is the number of dimensions and $\kappa_f L_c = L_c \sqrt{F/\kappa}$ (Hori et al., 2007). Note that this relationship gives the same response as the MacKintosh WLC, with $L_c \sqrt{F/\kappa} = \pi \sqrt{\phi}$ and with Equation (2.67) (for $d=3$) equivalent to our analytical expression of the MacKintosh WLC (Equation (2.51)). Indeed, both expressions reduce to $r_{F=0}/L_c = 1 - L_c/6l_p$ for the zero force condition. Hori, et al. also provide an analytical extension-force expression for a semiflexible filament with clamped ends (Hori et al., 2007),

$$\begin{aligned} \frac{r}{L_c} = & 1 - \frac{d-1}{2} \left(\frac{\kappa_f L_c \cosh(\kappa_f L_c) - \sinh(\kappa_f L_c)}{2\kappa_f^2 L_c l_p \sinh(\kappa_f L_c)} \right) \\ & + \frac{(d-1)(\kappa_f L_c \cosh(\kappa_f L_c) - 3\sinh(\kappa_f L_c) + 2\kappa_f L_c)}{2\kappa_f^3 L_c^2 l_p + 2\kappa_f^3 L_c^2 l_p \sinh(\kappa_f L_c) - 4\kappa_f^2 L_c l_p \sinh(\kappa_f L_c)} \end{aligned} \quad (2.68)$$

Although Equation (2.68) is not defined for $F=0$, Hori, et al. expanded it in the limit of small forces ($\kappa_f L_c \leq 1$) to yield the following approximation for the clamped case ($d = 3$) (Hori et al., 2007),

$$\frac{r}{L_c} \cong 1 - \frac{1}{30} \left(\frac{L_c}{l_p} \right) + \left(\frac{11F l_p}{25200 k_B T} \right) \left(\frac{L_c}{l_p} \right)^3, \quad (2.69)$$

which approaches $r_{F=0}/L_c = 1 - L_c/(30l_p)$, a larger value than the pinned case and very close to the value given in Equation (2.63) for the clamped MacKintosh WLC at the zero force limit.

2.3 Internal energy axial stretching model

Filament extensibility, for actin cytoskeletal filaments in particular, has been observed using multiple experimental techniques including optical traps (Dupuis et al., 1997; Adami et al., 1999), x-ray diffraction (Huxley et al., 1994; Wakabayashi et al., 1994; Bordas et al., 1999), light-scattering methods (Higuchi et al., 1995), or measurement of thermal fluctuations (Oosawa, 1977; Oosawa et al., 1977; Oosawa, 1980; Yanagida et al., 1984; Gittes et al., 1993; Ott et al., 1993; Kas et al., 1994; Kas et al., 1996). Due to their inextensible formulation, the previous entropic models diverge from a filament's true force-extension behavior as the filament approaches its extensional limit. Thus for extensions where the filament end-to-end distance approaches the contour length, the entropic-based force-deflection relationships for the flexible and semiflexible filaments have been expanded to include an additional term for the internal energy axial stretch contribution (Odijk, 1995; Smith et al., 1996; Wang et al., 1997; Storm et al., 2005). The model presented here will account for the internal energy contribution due to the stretching of inter-atomic bonds along the macromolecular backbone. The total extended length, L_T , for a straight filament is the sum of the initial contour length, L_c , and the additional extension in length due to axial stretching, L_s . Assuming small strain, linear elastic stretching, the force-extension and strain energy expressions are simply

$$f^s = \frac{EA}{L_c}(L_T - L_c) = \frac{K_s}{L_c}(L_s) \quad (2.70)$$

$$w^s = \frac{K_s}{2L_c}(L_T - L_c)^2 = \frac{K_s}{2L_c}(L_s)^2 \quad (2.71)$$

where A =cross-sectional area, $K_s=EA$ =linear stretching modulus with units of force. An attempt has been made in some previous studies (Grosberg and Khokhlov, 1994; Odijk,

1995; Storm et al., 2005) to define the linear stretching modulus in terms of the persistence length and filament radius, r_f , using the definitions: $l_p = EI/k_B T$, $K_s = EA$, $I = (\pi r_f^4)/4$, and $A = \pi r_f^2$,

$$K_s = \frac{4k_B T l_p}{r_f^2}. \quad (2.72)$$

While semiflexible filaments may be helical in nature (i.e. F-actin, vimentin), their cross-section is often taken to be equivalent to a homogeneous circular rod (e.g. $A_{AF} = \pi (3.5 \text{ nm})^2 = 38 \text{ nm}^2$). The noncircular cross-sectional area of an actin filament, however, has been estimated to be $A = 25 \text{ nm}^2$ based on its atomic model (Holmes et al., 1990; Kabsch et al., 1990), assuming that the area within the average contour of the filament cross-section is filled in homogeneously (Kojima et al., 1994). While this definition of stretching modulus relies on the assumption of a circular cross-section, we recognize that the area moment of inertia could be given more generally as $I = \xi A^2$ (where ξ is a filament-specific shape factor). This definition of stretching modulus also seeks to link the entropically-based bending stiffness, and therefore persistence length and thermal energy, with the internal energy-based axial stretching stiffness. The actin filament's helical structure and bonding that govern the bending stiffness is quite different from those which govern the axial stretching stiffness, while the relation given in Equation (2.72) assumes the same governing structural interaction. The resulting force and stretch behavior in bending and axial stretching will therefore differ significantly, and this difference is exemplified through an underprediction from Equation (2.72) when compared with empirically deduced values, as will be examined in Section 2.4.3 for comparisons with experimental data.

The next section will introduce an extensible WLC model that is not based on the Marko-Siggia approximation, and will thus be able to capture the extensible nature of filaments for $L_c < l_p$ (i.e. as found in densely cross-linked cytoskeletal networks). An overview of the single filament enthalpic (internal energy-based) and entropic models mentioned in the past three sections is included in Table 2-1.

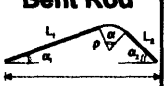
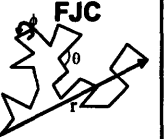
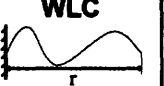

Model	Filament Type	$\langle r \rangle$	Force-Extension	Mechanisms
Rod	Stiff $L_c \ll l_p$	L_c	$F = (EA/L) \Delta r$	Internal energy stretching of bonds
Bent Rod 	Stiff $L_c \ll l_p$	$r_{F=0}$	$F = \frac{2EI}{\alpha_0 \rho_0} \frac{r_f^* (\alpha - \alpha_0)}{\sqrt{4L_c^2 (r_f^*)^2 - [(r_f^*)^2 + L_c^2 - L_1^2]^2}}$	Internal energy unbending
FJC 	Freely jointed rigid links $L_c \gg l_p$	0	$F = (k_b T / l_p) \mathcal{L}^{-1}(r/L_c)$ $\mathcal{L}(x) = \coth(x) - 1/x$	Entropic
WLC 	Bending $L_c \gg l_p$	0	$F \approx \frac{k_b T}{l_p} \left(\frac{r}{L_c} + \frac{1}{4(1-r/L_c)^2} - \frac{1}{4} \right)$	Entropic
	Bending $L_c \sim l_p$	$r_{F=0}$	$(r - r_0) = \frac{L_c}{l_p \pi^2} \sum_n \frac{\phi}{n^2(n^2 + \phi)}$ where $\phi = \frac{FL_c^2}{k\pi^2}$	Entropic

Table 2-1 Single filament force-extension models

2.4 Extensible model

This section introduces an extensible filament model that combines the MacKintosh entropic unbending model developed in Section 2.2 with the internal energy axial stretching model of Section 2.3. First we address two approaches to the kinematics

of the extensible filaments. The total fiber stretch is defined as $\lambda_f=r/r_0$ as shown in Figure 2–8.

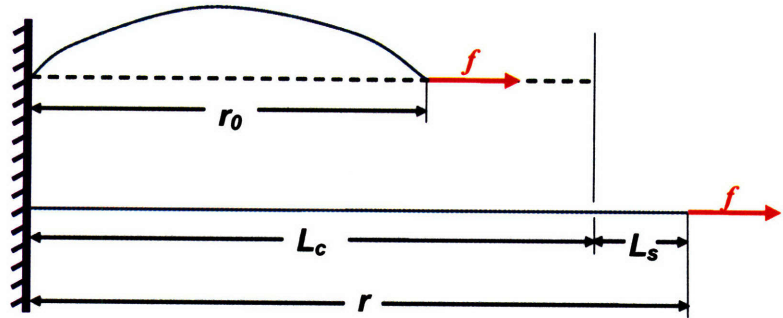


Figure 2–8. Extensible filament schematic including entropic unbending and internal energy stretching

2.4.1 Kinematics: multiplicative decomposition

The fiber stretch can be multiplicatively decomposed into stretches from entropic unbending (λ_f^u) and internal energy axial extension (λ_f^s) following a multiplicative decomposition (Kröner, 1959; Lee, 1969; Bertoldi and Boyce, 2007b)(see Figure 2–9).

$$\lambda_f = \lambda_f^s \lambda_f^u \tag{2.73}$$

Initial deformation of the filament will be accommodated by the entropic unbending stretch. As the filament approaches its extensibility limit ($r/L_c \rightarrow 1$), the fiber stiffens significantly, and the imposed end-to-end length must also be accommodated by axial internal energy stretching (see Figure 2–10). The additional extended length, L_s , beyond the filament’s contour length, L_c , due to axial stretching is

$$L_s = L_c(\lambda_f^s - 1). \tag{2.74}$$

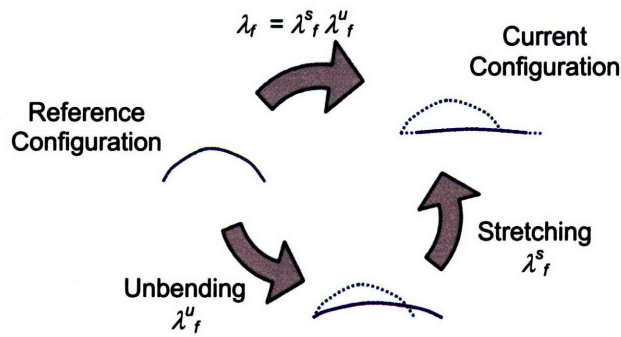


Figure 2–9. Multiplicative decomposition of λ_f into entropic unbending and internal energy stretching components. Adapted from (Bertoldi and Boyce, 2007b).

The relative stretch contributions of the unbending and stretching as a function of end-to-end distance can be seen in Figure 2–10, using the following filament properties: $l_p=3\mu\text{m}$, $\kappa=1.24\times 10^{-26}\text{Nm}^2$, $L_c=1\mu\text{m}$, $K_s=40\text{nN}$. There is no stretch contribution from internal energy axial extension below $r/L_c=0.98$, as the entropic unbending dominates the

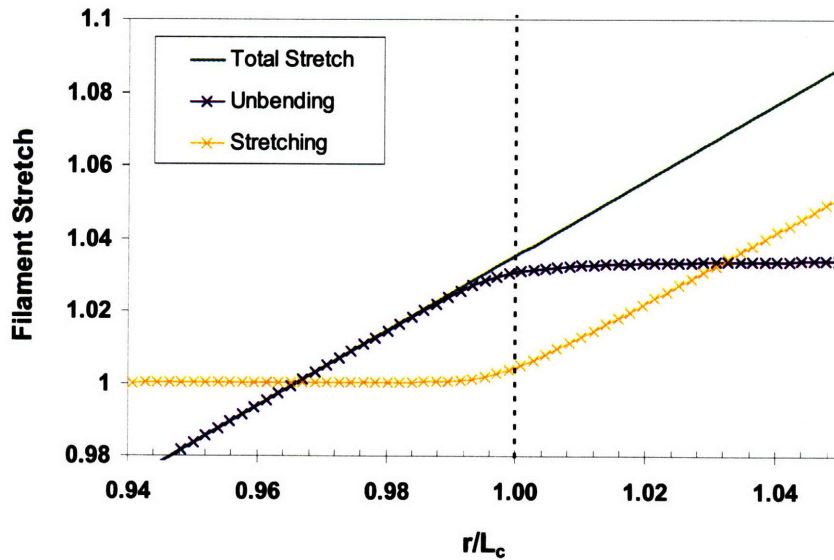


Figure 2–10. Stretch contributions from entropic unbending and internal energy stretching

filament's behavior. As $r/L_c \rightarrow 1$, however, the stretch contribution from entropic unbending diminishes and the internal energy axial stretching begins to increase. The axial stretch finally exceeds the stretch from unbending at $r/L_c=1.03$.

The force-stretch and strain energy expressions due to unbending are

$$f^u = \frac{k_B T}{l_p} \left(\frac{1}{4(1 - \lambda_f^u r_0 / L_c)^2} \right) \left(\frac{L_c / l_p - 6(1 - \lambda_f^u r_0 / L_c)}{L_c / l_p - 2(1 - \lambda_f^u r_0 / L_c)} \right) \quad (2.75)$$

$$w^u = \frac{kT}{l_p} \left[\frac{L_c}{4(1 - \lambda_f^u r_0 / L_c)} - l_p \left[\ln(L_c^2 - 2l_p L_c + 2l_p \lambda_f^u r_0) - \ln(\lambda_f^u r_0 - L_c) \right] - c \right] \quad (2.76)$$

where c is a constant equal to the initial strain energy of the filament. The resulting force-stretch and strain energy expressions for the internal energy axial stretching are

$$f^s = \frac{EA}{L_c} r_0 (\lambda_f^s - 1) = \frac{K_s}{L_c} r_0 (\lambda_f^s - 1) \quad (2.77)$$

$$w^s = \frac{K_s}{2L_c} r_0^2 (\lambda_f^s - 1)^2 \quad (2.78)$$

where A =cross-sectional area, $K_s=EA$ =linear stretching modulus. Fiber force equilibrium requires that

$$f = f^u = f^s. \quad (2.79)$$

Note that the stretches for entropic unbending and internal energy stretching are functions of

$$\begin{aligned} \lambda_f^s &= \hat{\lambda}_f^s(\lambda_f, K_s, l_p, L_c, \lambda_f^s) \\ \lambda_f^u &= \hat{\lambda}_f^u(\lambda_f, K_s, l_p, L_c, \lambda_f^u) \end{aligned} \quad (2.28)$$

which allows the force in the filament to be calculated by recursively solving for λ_f^u and λ_f^s , using Eqs. (2.73), (2.75), (2.77), and (2.79) via the bisection method. The extensible filament force is plotted as a function of r/L_c in Figure 2–11 and compared to the inextensible entropic unbending model. Consistent with Figure 2–10, the inextensible and extensible models begin to diverge as the stretch from internal energy axial extension begins to increase as $r/L_c \rightarrow 1$. For the given the filament properties $l_p=3\mu\text{m}$, $L_c=1\mu\text{m}$, there is less than 3% difference between the inextensible and extensible models for extensions below $r/L_c=0.99$. For extensions beyond $r/L_c=1$, the extensible model takes the slope of K_s/L_c . The strain energy of the unbending and stretching components is shown in Figure 2–12, with the internal energy stretching component dominating for $r/L_c > 1$, as expected.

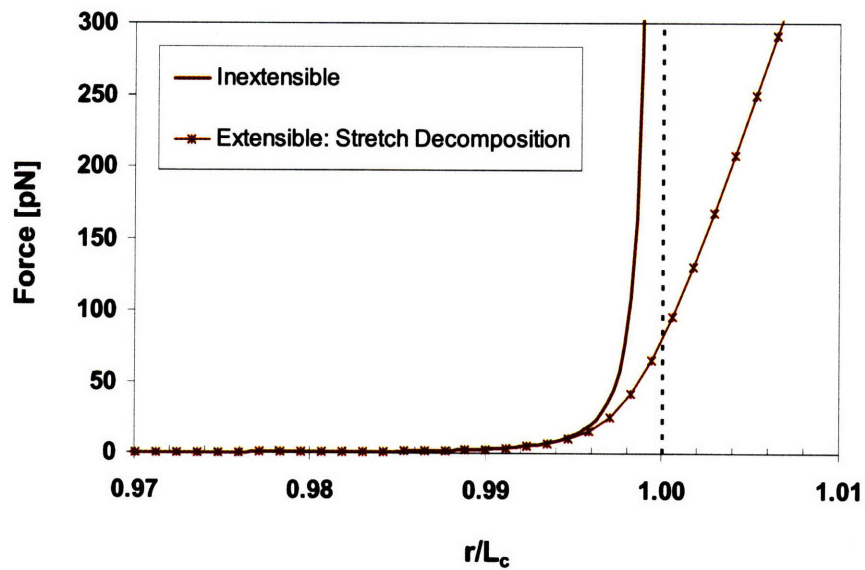


Figure 2–11. Force comparison of inextensible entropic unbending model and extensible model with stretch decomposition of entropic unbending and internal energy axial stretching

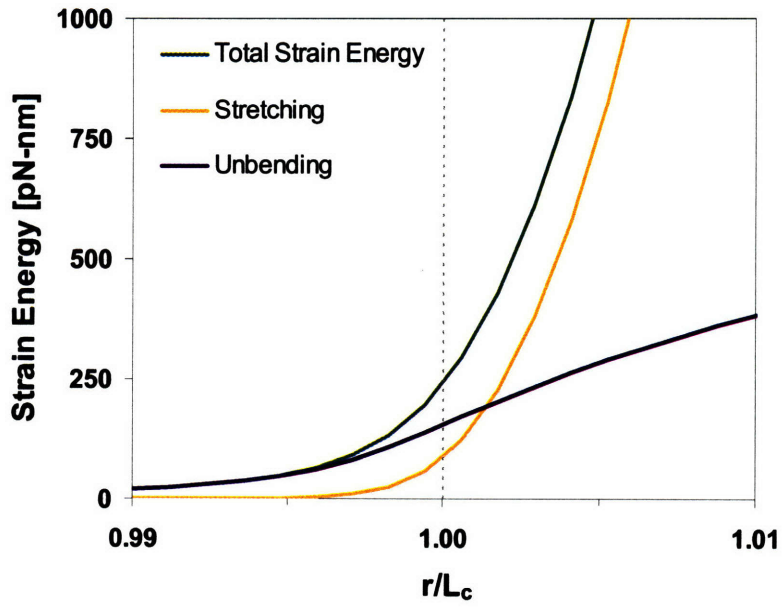


Figure 2-12. Strain energy contributions from entropic unbending and internal energy axial stretching

The extensible model's response for varying persistence lengths, but all other variables held constant, is included in Figure 2-13. The inextensible model's response for $l_p=3\mu\text{m}$

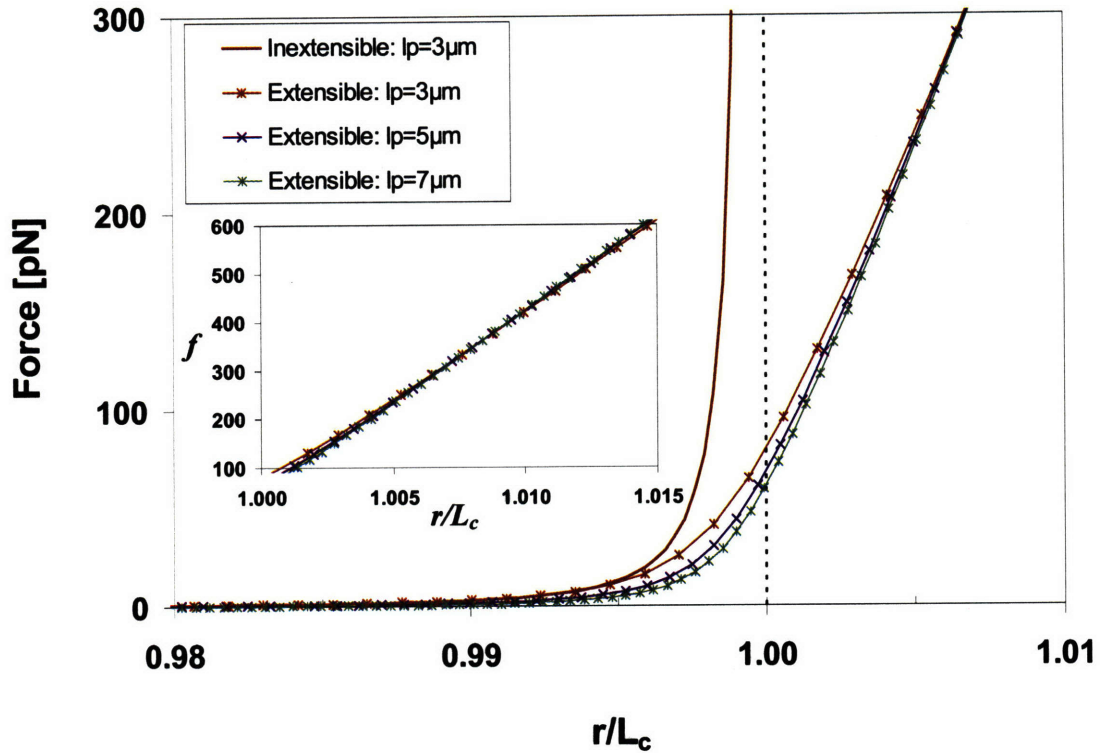


Figure 2–13. Force comparison of inextensible entropic unbending model and extensible model with varying persistence lengths

is also included for reference. The stretching modulus is held constant ($K_s=40\text{nN}$) for each extensible case. The impact of increasing l_p is seen in two regions of Figure 2–13. In the first region ($r/L_c < 1.$), the force response is initially lower for higher values of l_p due to an increase in $r_{F=0}$ which reduces the unbending strain energy (for $r/L_c < r_{F=0}/L_c$), but the response is stiffened as it extends into the extensible regime. Around $r/L_c=1.01$, the extensible curves then crossover and enter the second region in which larger values of l_p give a stiffer response (see inset of Figure 2–13). This crossover occurs in the region of actin filament rupture ($\sim 200\text{-}500\text{pN}$), depending on the amount of axial twisting due to thermal forces and/or mechanical loading as shown in the experimental data in Figure 2–14 (Tsuda et al., 1996).

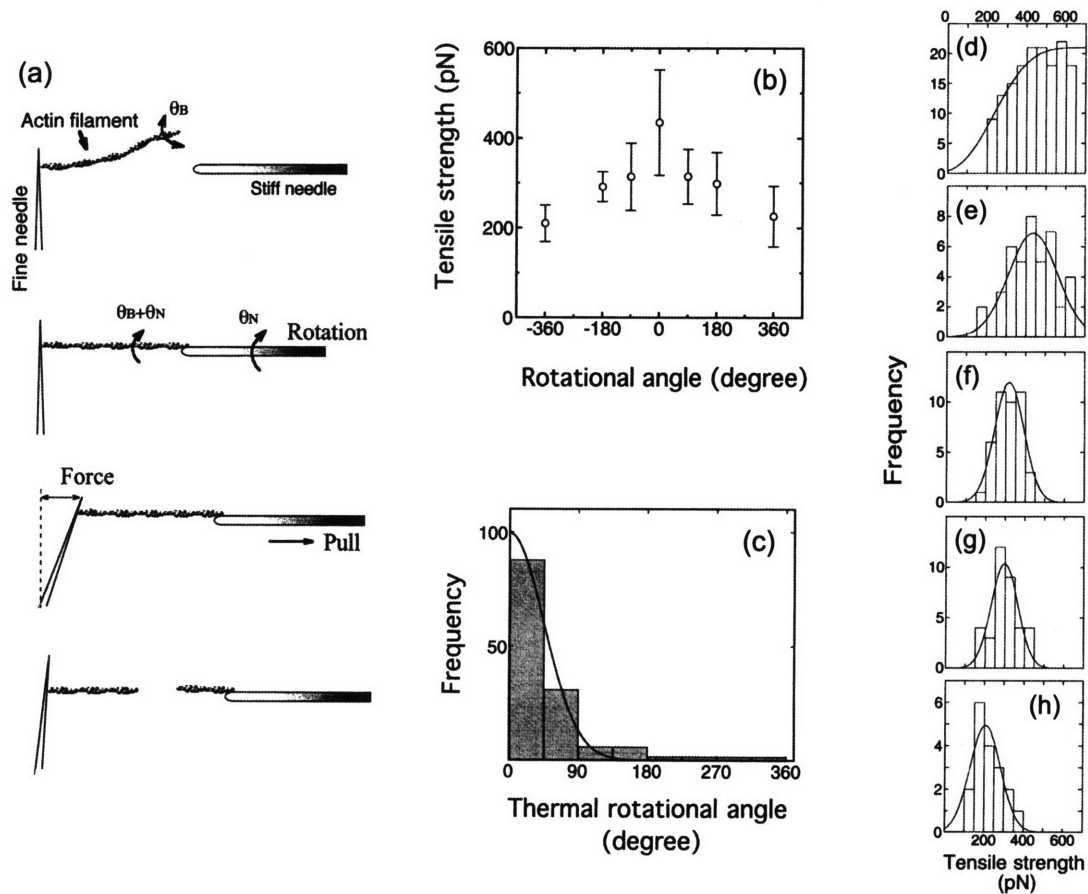


Figure 2–14. Tensile strength of actin filament as a function of rotational angle. (a) Schematic of experimental procedure using microneedles. θ_B is the rotational angle of the actin filament undergoing the rotation under no tension, and θ_N is the angle of the filament rotated by the needle. (b) Average tensile strengths of single actin filaments ($L_c=10\pm 2\mu\text{m}$). Temperature = $25\pm 2^\circ\text{C}$. Bars = SD for 20-150 filaments. (c) Distribution of thermal rotational angles ($\theta_N=0^\circ$). (d-h) Histograms of tensile strength of single actin filaments twisted by 0° (d), 45° (e), 90° (f), 180° (g), and 360° (h). Figures and experimental data from (Tsuda et al., 1996).

2.4.2 Kinematics: additive decomposition

An additive decomposition approach to the kinematics takes the unbending and stretching deformations as springs in series. The extension due to stretching is δ_s (or $\lambda_f^s r_0$), the

unbending extension is δ_u (or $\lambda_f^u r_0$), and the total extension is $\delta_T = \delta_s + \delta_u = r - r_0$. The stretching force-extension relationship is

$$f^s = \frac{K_s}{L_c} \delta_s \quad (2.80)$$

The unbending extension can therefore be solved as

$$\delta_u = r - f \frac{L_c}{K_s} \quad (2.81)$$

Employing Eqs. (2.75), (2.81), and (2.79), the force-extension expression can now be given as

$$f = f^u = \frac{k_B T}{l_p} \left(\frac{1}{4 \left(1 - \frac{r}{L_c} + \frac{f}{K_s} \right)^2} \right)^{\left(\frac{L_c/l_p - 6 \left(1 - \frac{r}{L_c} + \frac{f}{K_s} \right)}{L_c/l_p - 2 \left(1 - \frac{r}{L_c} + \frac{f}{K_s} \right)} \right)} \quad (2.82)$$

The results of using the multiplicative and additive decompositions are shown in Figure 2–15 using the following filament properties: $l_p = 3 \mu\text{m}$, $L_c = 1 \mu\text{m}$, $K_s = 40 \text{nN}$. The results of the two methods are in agreement within 3% or less for $r/L_c < 1$. The percent difference between the two methods increases for $r/L_c > 1$, with a difference of ~4% at $r/L_c = 1.01$.

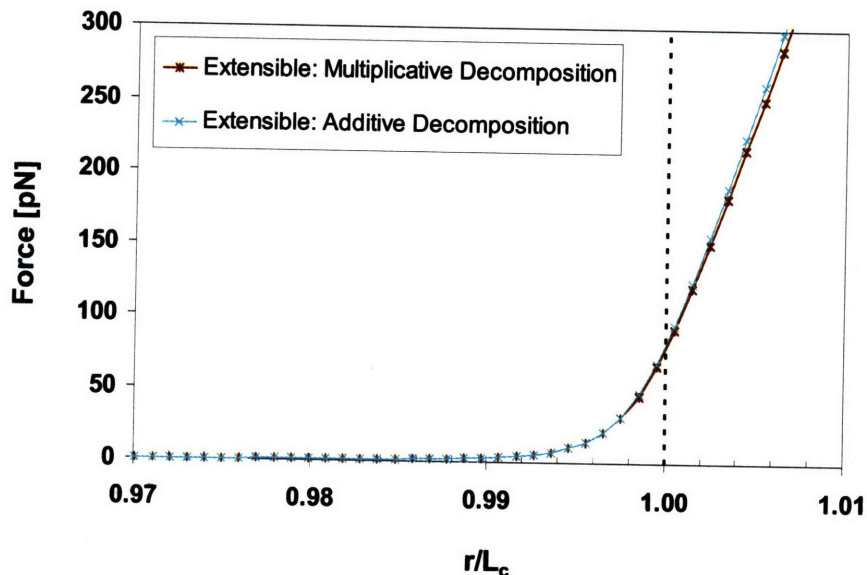


Figure 2–15. Comparison of kinematics methods in extensible model: additive and multiplicative decompositions

2.4.3 Comparison with F-actin stretching experiments

The extensible filament model is now used to compare to empirical data from F-actin stretching experiments conducted with nano-scale SiN_3 cantilevers and low pretension (Liu and Pollack, 2002). The experimental setup is shown in Figure 2–16. Liu and Pollack found best fit values of $K_s = 35.5 \pm 3.5 \text{ nN}$ and $l_p = 8.3 \mu\text{m}$ for actin filaments with contour lengths of $L_c = 19.1 \mu\text{m}$, as shown in Figure 2–17, with the curve fit using Odijk’s extensible WLC approximation (Odijk, 1995; Liu and Pollack, 2002). This value for K_s is approximately three times greater than what would be predicted using Equation (2.72), for $r_f = 3.5 \text{ nm}$, an underestimation described in Section 2.3 based on the assumption of a cylindrical cross-sectional area and linking filament structure and bonding that governs the entropically-based bending stiffness with the structural interactions governing the internal energy-based axial stretching stiffness. Odijk’s

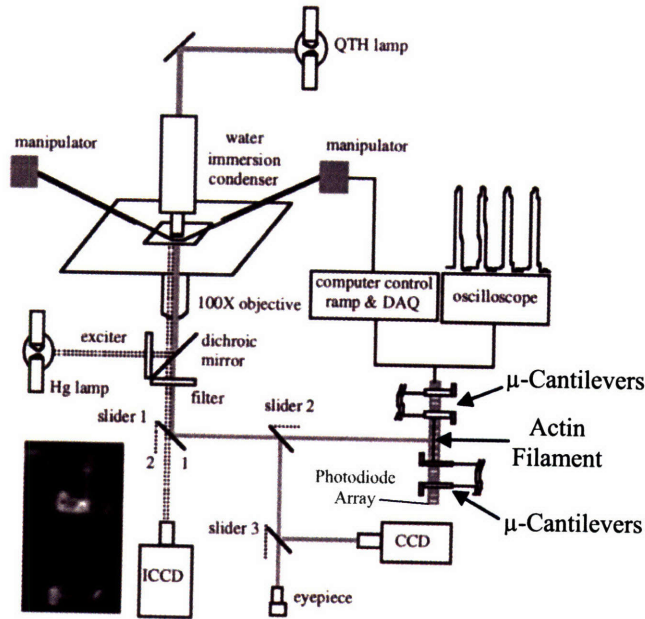


Figure 2–16. Experimental setup for F-actin stretching with micro-scale SiN_3 cantilevers. Inset fluorescence image shows a captured actin filament between two cantilevers (cantilever width $\sim 4\mu\text{m}$). Adapted from (Liu and Pollack, 2002).

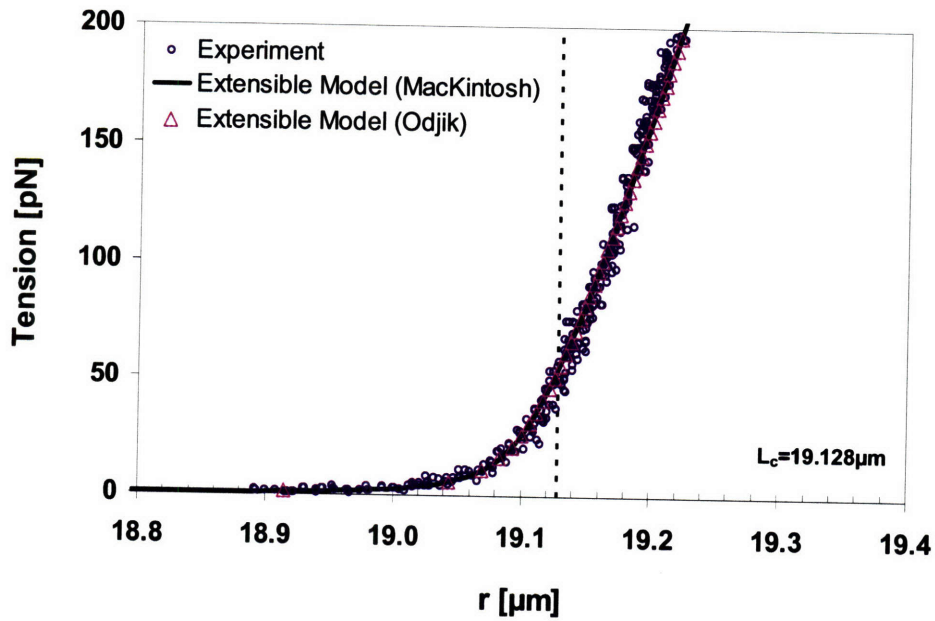


Figure 2–17. Experimental data using micro-scale cantilevers to stretch actin filaments ($L_c=19.128\mu\text{m}$). Best fits with extensible WLC models.(Liu and Pollack, 2002)

extensible WLC model is valid for the case of small elongations beyond the contour length ($|r-L_c| \ll r$) and weak undulations (Odijk, 1995),

$$\frac{r}{L_c} = 1 - \frac{1}{2} \left(\frac{k_B T}{f l_p} \right)^{1/2} + \frac{f}{K_s}, \quad (2.83)$$

which is not defined for $f=0$, and the first two terms provide the asymptotic response from Marko and Siggia's WLC approximation in Equation (2.36), while the third term provides for linear elastic stretching (Liu and Pollack, 2002). They were unable to fit the data with the extensible WLC approximation by Wang, et al. (Wang et al., 1997), which adds an extra term for axial stretching following the additive decomposition described earlier,

$$\frac{f l_p}{k_B T} = \frac{r}{L_c} + \frac{1}{4(1-r/L_c + f/K_s)^2} - \frac{1}{4} - \frac{f}{K_s}. \quad (2.84)$$

The experimental data in Figure 2-17 was taken with filaments that only had contour lengths greater than their persistence lengths, in order to utilize the Marko-Siggia WLC approximation. The extensible filament model developed in this section based on the MacKintosh WLC expression is also plotted in Figure 2-17 with the same values of $l_p=8.3\mu\text{m}$ and $L_c=19.128\mu\text{m}$ as used in the Odijk model fit, but with a stretching modulus of $K_s=56\text{nN}$. While this demonstrates that the Odijk extensible model produces a stiffer response within the axial stretching regime ($r/L_c > 1$), both models capture the extensible behavior of the actin filament using reasonable values for the stretching modulus. For example, the best fit values of K_s for both models are within 30% of values measured from similar experiments using microneedles (glass rods with 300 nm diameters) and high pretension that found a stretching modulus of $K_s=43.7 \pm 4.6\text{nN}$ for actin filaments with contour lengths of $L_c=1\mu\text{m}$ (Kojima et al., 1994).

It should also be noted that the Odijk WLC model, which becomes the limit of the Marko-Siggia WLC approximation for $r/L_c \sim 1$, exhibits similar behavior of decreasing stiffness for increasing persistence length (or bending stiffness), even in the extensible regime (see Figure 2–18), unlike the MacKintosh extensible model which exhibits a crossover once in the extensible region as shown in Figure 2–13.

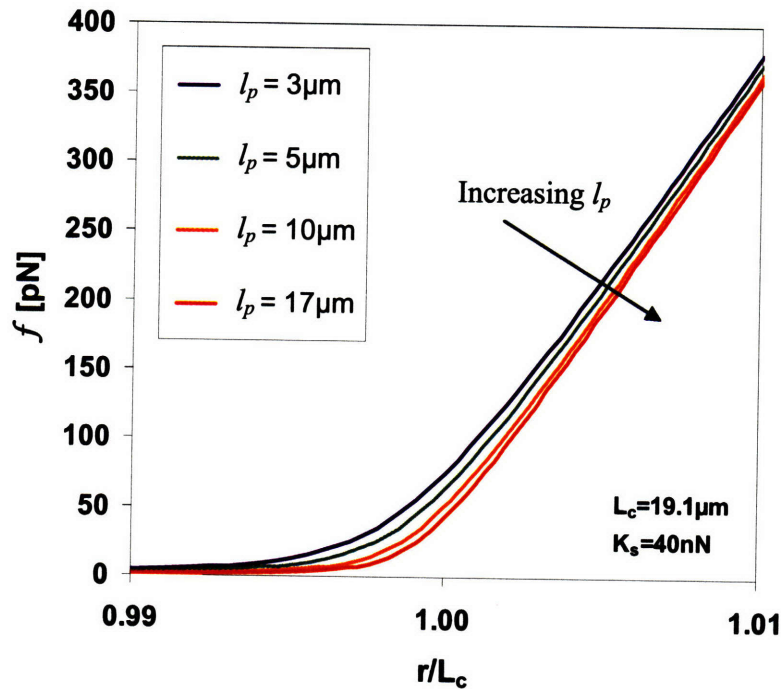


Figure 2–18. Force-extension plot of Odijk’s extensible WLC approximation for increasing persistence length, l_p ($L_c=19.1\mu\text{m}$, $K_s=34.5\text{nN}$)

CHAPTER 3 Network Model

3.1 Previous cell models and experimental techniques

There are an increasing number of experimental techniques using various bioassays to probe the mechanical response of cells. Several of these techniques are listed in Figure 3–1 along with a few examples of material models used to simulate the cellular mechanical response within the specific bioassay. The first three bioassays listed, atomic force microscope (AFM) indentation, cytoindentation, and magnetic twisting cytometry (MTC) are used to probe subcellular regions; shear flow and cell contraction via substrate deformation (SD) or microfabricated post array detector (mPAD) are used to measure adherence, deformation, and motility characteristics; and microplate compressors/stretchers (OS), micropipette aspiration (MA), and optical tweezers (OT) or magnetic tweezers (MT) are used to evaluate whole cell deformations (Suresh, 2007). The force scales and deformation length scales associated with these different biomechanical assays are listed in Figure 3–2 along with relevant cellular and subcellular processes and components. While these are relevant to the whole cellular response, other experimental techniques are used to explore the rheology of cytoskeletal systems (see Section 3.4).

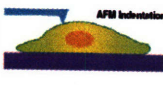
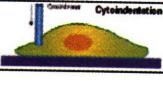
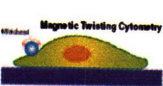
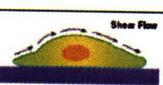


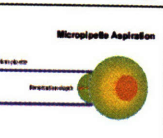
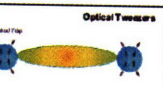
Experiment	Material model	References
 AFM Indentation	Linear elastic Nonlinear elastic	(Costa and Yin, 1999; Ohashi et al., 2002; Ng et al., 2007) (Costa and Yin, 1999; McElfresh et al., 2002)
 Cytoskeleton Cytoskeleton	Linear elastic Poroelectric	(Shin and Athanasiou, 1999)
 Magnetic Twisting Cytometry	Linear elastic Nonlinear elastic Maxwell viscoelastic Power law structural damping	(Charras and Horton, 2002; Mijailovich et al., 2002) (Ohayon et al., 2004) (Karcher et al., 2003) (Vaziri and Gopinath, 2008)
 Shear Flow	Linear elastic Nonlinear elastic	(Charras and Horton, 2002; Cao et al., 2007; Ferko et al., 2007) (Jadhav et al., 2005)
 Cell Contraction (Microarray/substrate)	Linear elastic Modified Maxwell viscoelastic Biochemomechanical	(Nelson et al., 2005) (McGarry et al., 2005) (Deshpande et al., 2006; Deshpande et al., 2007)
 Microplate Compression	Nonlinear elastic	(Caille et al., 2002)
 Microplate Aspiration	Linear elastic Nonlinear elastic Maxwell viscoelastic Modified Maxwell viscoelastic Poroelectric Poroviscoelastic	(Haider and Guilak, 2002) (Baaijens et al., 2005; Zhou et al., 2005) (Baaijens et al., 2005; Trickey et al., 2006) (Haider and Guilak, 2000) (Baaijens et al., 2005) (Baaijens et al., 2005; Trickey et al., 2006)
 Optical Tweezers	Nonlinear elastic Modified Maxwell viscoelastic	(Dao et al., 2003; Mills et al., 2004; Suresh et al., 2005) (Mills et al., 2004)

Figure 3–1. Biomechanical continuum models for whole cell deformation in common experimental techniques (adapted from (Vaziri et al., 2007)).

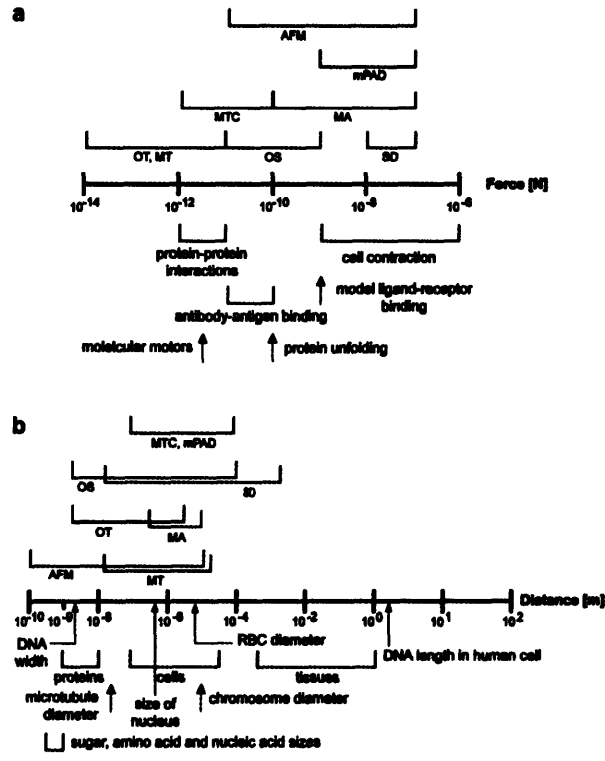


Figure 3–2. (a) Force scale and (b) deformation length scale associated with different biomechanical assays (Suresh, 2007)

There have been many approaches to modeling cells and their cytoskeletons. These methods can generally be grouped into four categories: cortical shell-liquid core and solid core continuum models, discrete member models, enthalpic cellular solid models, and biopolymer models.

Most of the material models listed in Figure 3–1 represent recent examples of the cortical shell-liquid core and solid core continuum models. Simple cortical shell-viscous fluid models have been used to simulate the response of entire cells during micropipette aspiration (Yeung and Evans, 1989; Tran-Son-Tay et al., 1998). A cortical shell along with hyperelastic neo-Hookean properties, describing the cytoplasm and nucleus, have been used to model lymphocytes deformed in cell poking experiments (Zahalak et al.,

1990). The red blood cell (RBC) membrane and cortical spectrin network have been modeled using hyperelastic models based on the first and second order terms of the first invariant of the Finger tensor (a 2-parameter Yeoh model (Yeoh, 1990)) to effectively predict RBC deformations from optical tweezers (Dao et al., 2003; Mills et al., 2004). Constitutive models of the stress-strain behavior for spectrin networks which capture the network stretch and chain force-extension behavior have also been developed (Arslan and Boyce, 2006; Arslan et al., 2008). Both the membrane/cortex and the cytoplasm/nucleus have been modeled as linear viscoelastic materials to predict the response of cell micromanipulation by magnetocytometry (Karcher et al., 2003) as well as cell recovery after expulsion from a micropipette (Chien et al., 1987; Tran-Son-Tay et al., 1991). The cytoplasm can alternatively be described by a poroelastic model in which the cytoskeleton is a porous, actively contractile, elastic network infiltrated with interstitial cytosolic fluid (Charras et al., 2005). The poroelastic components require the addition of a spatial diffusion term to the governing differential equation for viscoelastic behavior as originally presented by Biot for soil consolidation (Biot, 1941; Biot, 1956a; Biot, 1956b). Other biphasic poroviscoelastic models have been developed to model soft biological tissue, as pioneered by Mow for tissues (Mow et al., 1980) and recently applied to chondrocyte cells (Baaijens et al., 2005; Trickey et al., 2006). The poroelastic model, unlike viscoelastic models, accounts for spatio-temporally localized variations in hydrostatic pressure, and it is especially useful in simulating blebbing cells and other cases in which hydrostatic pressure can be used to power local cellular shape change (Charras et al., 2005). These models, however, do not account for either the

microstructural features of the cytoskeleton, their mechanobiological contribution, or their microstructural rearrangement.

The second type of cytoskeletal model is based on the interaction between discrete members (e.g. filaments) in a network. Many discrete member models assign discrete filaments randomly within a 2D (Head et al., 2003a; Head et al., 2003b; Wilhelm and Frey, 2003; Onck et al., 2005) or 3D (Huisman et al., 2007) network, allowing intersection points to become cross-links until a critical amount of network connectivity (or percolation threshold) is reached. When implemented in 3D, however, the analyst must include attractive force fields to initiate filament movement and create crosslinks between nearby filaments, that are not in contact, in order to create realistic network topologies (Huisman et al., 2007). The discrete filaments are modeled either as straight rods (i.e. pre-thermal undulations), or with a slightly curvature to simulate the geometry after thermal undulations. In either case, neither changes in filament curvature from thermal energy nor the entropic contribution to filament elasticity are considered. The percolation-based models identify the influence of node connectivity on the amount of non-affine behavior witnessed in biopolymer networks (Head et al., 2003a). Their models deformed in an affine behavior when dominated by filament stretching with no filament rotation, and they observed non-affine behavior with considerable filament rotation when filament bending dominated relative to axial filament stretching (Onck et al., 2005; Huisman et al., 2007). The observation that, in bending-dominated regimes, reorientation can play a much larger role than stretching in accommodating macroscopic deformation has also been seen in biopolymer models (Palmer and Boyce, 2008).

Tensegrity models also make use of discrete members by describing the actin microfilaments as the tensile elements and the microtubules as elements under compression (Ingber, 1993). The tensegrity approach is based on the principles of compression and tension elements in equilibrium as originally described by Buckminster Fuller (Fuller, 1975). Traction force microscopy experiments have been conducted to evaluate the tensegrity-related behavior of cells to explain combined cytoskeletal response during adhesion (Wang et al., 2001). Tensegrity principles allow for the scaling of shear modulus with solid fraction to the first power ($G \sim \phi$) (Stamenovic and Ingber, 2002). Although tensegrity networks have been defined as networks comprised of continuous tension and local compression in which local mechanical inputs produce distributed cytoskeletal responses (Ingber, 1993; Ingber, 1997; Pourati et al., 1998a), critical experiments have shown highly localized cytoskeletal responses to forces rather than integrated, spatially broad responses (Heidemann et al., 1999). Tensegrity models omit the influence of thermal fluctuations on elasticity, and also do not lend themselves to modeling polymerization of just one filament network that may occur in pseudopod growth.

A third approach to cytoskeletal modeling is the enthalpic cellular solid model originally developed by Gibson and Ashby (Gibson and Ashby, 1988) and extended to actin networks by Satcher and Dewey (Satcher and Dewey, 1996). It describes the cytoskeletal network using a cubical frame with an overall network modulus based on solid fraction and bending of the cell edges. If the relative solid fraction is very small, then the structural elastic modulus is proportional to either ϕ_s or ϕ_s^2 depending on whether enthalpic stretching or enthalpic bending and twisting of the edges, respectively, are

major modes of accommodating the imposed deformation (Warren and Kraynik, 1997). As with tensegrity networks, however, the cellular solid models do not account for the influence of thermal fluctuations on cytoskeletal elasticity (Kamm, 2006). They also do not account for nonaffine motion or the ability of networks to accommodate deformation through rotation of filaments.

The fourth class of cytoskeletal models extends polymer theory to biological macromolecules to create biopolymer network models. Some of the background details of biopolymer filament models from Chapter 2 are summarized here within the context of biopolymer network models. Polymers are traditionally categorized as flexible ($l_p \ll L_c$), rigid ($l_p \gg L_c$), or semiflexible ($l_p \sim L_c$). The worm-like chain model is a more appropriate representation of continuously flexible filaments rather than the traditional polymer theory of freely jointed chains of rigid rods. The entropically-based WLC model is derived from the total energy from sampling fewer configurations of unbent filaments as a filament, or network, is deformed. The WLC model has been effective at describing the entropic elasticity of very flexible biopolymers ($L_c \gg l_p$) including DNA at low to moderate strains (Bustamante et al., 1994). Other single filament behaviors, such as the “saw-tooth” pattern from the force-extension behavior of single biomacromolecules with folded domains, have also been modeled successfully with the WLC model for a variety of biological materials (Rief et al., 1997; Qi et al., 2006). The cortical spectrin cytoskeletal network of the red blood cell, has a well-defined triangulated geometry which has been successfully modeled based on a freely jointed chain (FJC) model (Arslan and Boyce, 2006; Arslan et al., 2008) as well as the WLC model (Li et al., 2005a; Dao et al., 2006; Li et al., 2007). Although its force-extension relationship requires

numerical evaluation of the path integral, interpolation formulas have been successfully used to simplify calculations in the small and large-force regimes (e.g. Marko and Siggia (Marko and Siggia, 1995)). The chain flexibility assumption ($L_c \gg l_p$) is considered for single, flexible polymers with random walk statistics such that the initial end-to-end distance, r_0 , is zero. While useful for analyzing single filaments, the WLC model must use a nonzero value of r_0 for analyzing dense, cross-linked networks. While WLC and FJC-based models have been evaluated with nonzero r_0 for spectrin networks with $L_c \gg l_p$ (Qi et al., 2006), they have not been applied to denser, stiffer cross-linked networks in which the effective contour lengths are lower than their persistence lengths ($L_c < l_p$).

Subsequent molecular theories (e.g. MacKintosh, et al. (MacKintosh et al., 1995)) have addressed the semiflexible regime for $L_c \sim l_p$ with similar energy functionals and force-deflection relationships that are still entropic in origin. At high strains, additional theories have expanded the force-deflection response of the semiflexible filaments to include terms for the enthalpic stretch contributions (once thermal fluctuations from bending are pulled out) in addition to the entropic elasticity due to thermal fluctuations (Storm et al., 2005).

The biopolymer network models calculate the bulk elastic properties of cytoskeletal networks by integrating the force-deflection behavior of individual elastic cytoskeletal filaments within network geometry models (MacKintosh et al., 1995; Isambert and Maggs, 1996; Storm et al., 2005). This also provides a framework for determining the impact of cross-linking proteins on the behavior of cytoskeletal filament networks. Empirically observed shear moduli for F-actin networks with permanent cross-

links (but the same concentration of F-actin) have been observed to vary over two orders of magnitude by varying the cross-link density (Gardel et al., 2004a).

In order to determine the bulk elastic network properties including cross-link effects, biopolymer models often employ a 3D volume averaged framework of the 1D filament force-extension response which is aligned in the primary load direction (see Figure 3–3) (MacKintosh et al., 1995; Isambert and Maggs, 1996). These models often assume affine network deformation, and can further be constructed to account for varying degrees of cross-link densities. For example, the amount of force required to extend a single F-actin filament a distance, δ , has been defined for the low force, linear regime by linearizing MacKintosh's equation from Chapter 2 about $r_{F=0}$ (Isambert and Maggs, 1996):

$$f \approx \frac{k_B T l_p^2}{L_c^4} \delta \approx \frac{\kappa l_p}{L_c^4} \delta \quad (3.1)$$

where δ = filament extension. Volume averaging is achieved starting with a given a mesh size of ξ for a cubical volume which gives $(1/\xi^2)$ chains per unit area. In shear, the chain extension (δ) is approximated by (γl_{CL}) where γ is the shear strain and l_{CL} is the end-to-end chain distance between cross-links (see Figure 3–3). For small transverse fluctuations, $l_{CL} \approx L_c$. Thus, the shear stress is approximated as (Kamm, 2006):

$$\tau \approx \frac{F}{\xi^2} \approx \frac{\kappa l_p}{\xi^2 l_{CL}^3} \gamma \quad (3.2)$$

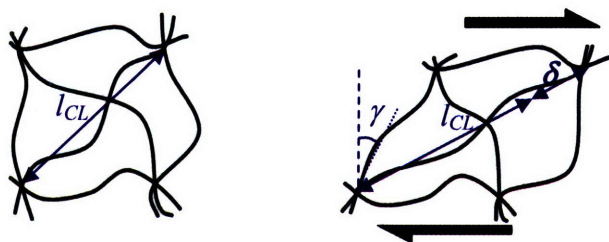


Figure 3-3. Single filament subjected to a shearing force [adapted from (MacKintosh, 2006)]

where the shear modulus is then defined as

$$G \approx \frac{\kappa l_p}{\xi^2 l_{CL}}. \quad (3.3)$$

Since the solid volume fraction is defined for a filament of diameter (a) as based on a

$$\phi_s \approx \frac{\xi a^2}{\xi^3} \approx \frac{a^2}{\xi^2} \quad (3.4)$$

Since the solid volume fraction is defined for a filament of diameter (a) as based on a mesh size of ξ , the volume-averaged network shear modulus scales linearly with solid fraction for low cross-link density ($G \sim \phi_s$). For the limit of maximum cross-link density (i.e. $l_{CL} \rightarrow \xi$) the shear modulus is related to the solid fraction as $G \sim \phi_s^{5/2}$. Biopolymer network models have shown promise for predicting the behavior of cross-linked filament networks. As an example, Figure 3-4 shows the theoretical predictions (based on both enthalpic stretching and entropic unbending contributions) for fibrin protofilament networks of varying concentration (Storm et al., 2005).

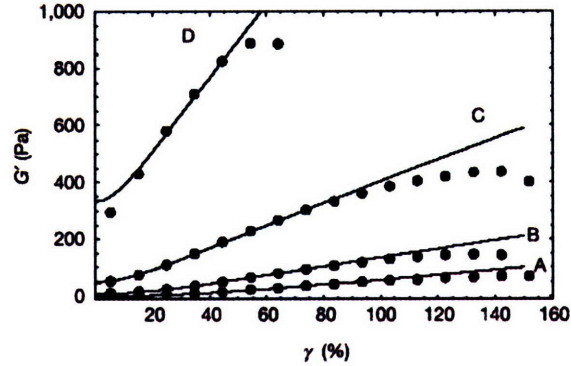


Figure 3-4. Experimental data for fibrin protofilaments (dots) at various concentrations, and corresponding theoretical curves (solid lines). Best-fit values were determined for A–D as follows: A, $c = 0.5$ mg/ml ($l_p = 0.39$ mm), $K_s = 67$ pN; B, $c = 1.0$ mg/ml ($l_p = 0.27$ mm), $K_s = 58$ pN; C, $c = 2.0$ mg/ml ($l_p = 0.19$ mm), $K_s = 73$ pN; D, $c = 4.5$ mg/ml ($l_p = 0.12$ mm), $K_s = 110$ pN (Storm et al., 2005)

Network models which essentially evaluate the volume averaged force extension of a single filament aligned with a primary load direction, however, do not properly account for how a network deforms to accommodate macroscopic deformations. Volume averaged networks based on the 1D models are limited by highly strained chains in primary load direction (Figure 3-5A), with the shear strain accommodated by extensive chain stretching and minor rotation of the chains.

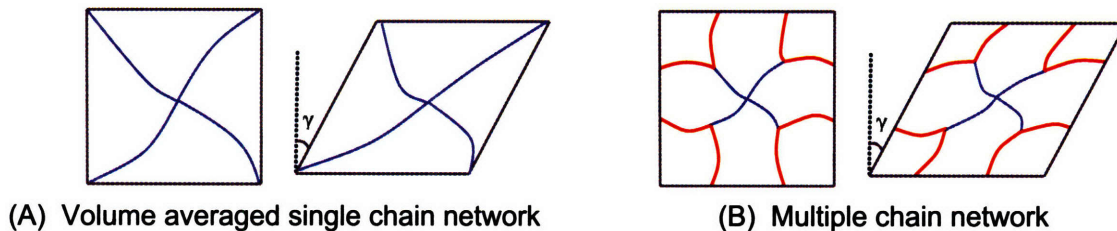


Figure 3-5. Chain stretch and rotation for 1D-based models in (A) volume averaged single chain network and (B) multiple chain networks

Real networks accommodate the macroscopic deformation with network constituent chains undergoing both rotation and stretch. Indeed, much of the imposed deformation will be accommodated by chain rotation with a small amount of chain stretch. For comparison purposes, the deformation of the network depicted in Figure 3–5A is contrasted to an alternative simple network shown in Figure 3–5B. For the network of Figure 3–5B, the imposed shear strain is primarily accommodated by the rotation of the constituent chains with relatively little chain stretch, especially as compared to the network deformation of Figure 3–5A. Hence, more realistic cytoskeletal network models must address the network’s ability to accommodate deformation by both rotation and stretching (where the minimum energy configuration that satisfies compatibility and equilibrium will be found by the network).

There have been many chain network models developed within the field of rubber elasticity over the past 65 years. Four models of note for chain networks (3-chain network, 4-chain network, full network, and 8-chain network) are briefly summarized here. Also see the review of rubber elasticity constitutive models by Boyce and Arruda (Boyce and Arruda, 2000). The 3-chain network model by Wang and Guth (Wang and Guth, 1952) is shown in Figure 3–6. The

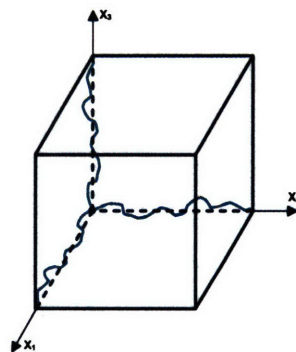


Figure 3–6. Geometry for 3-chain network model

3-chain model was created due to the inadequacy of Gaussian models to explain the well known stress-stretch behavior of rubber-like polymers at moderate and large strains (Wang and Guth, 1952). And while the Gaussian model is effective for uniaxial predictions at small strains, it is not able to accurately predict the corresponding shear and biaxial behavior.

To derive an expression for free energy Wang and Guth first obtained a statistical distribution function for the length of representative chains employing the inverse Langevin function (Wang and Guth, 1952). They then aligned these representative chains with the unit vectors of a cubic coordinate system defined by the directions of principle stretch (Wang and Guth, 1952).

Although the 3-chain model does not completely explain experimentally observed behavior, it does capture the main features of the stress-stretch response of rubber-like elasticity better than Gaussian treatments. The most significant reason that the model fails to predict the response accurately is the oversimplification of the network. The 3-chain model is limited to the response of a single chain during uniaxial deformation and therefore does not include any of the cooperative effects of other models.

The 4-chain model by Flory and Rehner (Flory and Rehner, 1943) accounts for the complex, and generally random, three dimensional network structure formed by the introduction of occasional cross-linkages between very long polymers. The four chains are cross-linked at a junction (point J) whose most probable location is at the center of the tetrahedral unit cell, point O in Figure 3–7. These cross-linkages are not fixed in space,

so they can move and diffuse within the confines of the tetrahedron. The end points of the chains attached to these cross-links define the four corners of an irregular tetrahedron

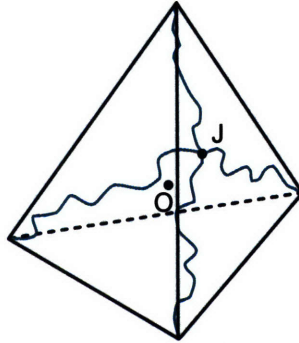


Figure 3-7. Geometry for 4-chain (tetrahedral) network model (adapted from (Treloar, 1958))

and, in turn, the center of neighboring tetrahedrons. Flory and Rehner make the following assumptions and approximations for a network comprised of these tetrahedrons (Flory and Rehner, 1943):

1. The actual random network of chains can be replaced by one in which each chain is the same contour length, forming an average cell.
2. The properties of the entire network can be computed based on those of the average cell.
3. The restraints imposed by the network on a given cross-linkage can be approximated by fixing the nearest neighbor cross-linkages at their most probable location.
4. The distribution function is applied to chains prior to vulcanization, fixing the lengths of chains and locations of the cross-links in the virgin material.

There cannot be affine motion of the center point since it would not satisfy force equilibrium. The outer nodes can move affinely, but the cells are not mutually exclusive and numerous tetrahedrons could partially occupy the same space. Also note that though

the cells can occupy the same space, each cell's volume is preserved due to incompressibility (Flory and Rehner, 1943).

The strain energy density functions are defined by the changes in entropy. It is assumed that the changes in entropy associated with displacements in directions perpendicular and parallel to tetrahedron faces are representative of a general deformation. Note that without the affine assumption the strain energy density for an entire macroscopic material must be calculated iteratively. Thus there is no constitutive law that can be easily derived and written in the form of a strain energy density function.

The first full network model by Treloar and Riding (Treloar and Riding, 1979) was derived and tested for biaxial extension along fixed axes under plane stress conditions, and later extended to a general formulation by Wu and van der Giessen (Wu and van der Giessen, 1993). The full network model does not assume a representative formation of the molecular chains within a network, but instead allows for all possible formations by assigning a probability distribution for any single cell to have its chains oriented in any direction. A central concept employed in the derivation of the full network model is the orientation distribution of individual molecules within the network. This Chain Orientation Distribution Function (CODF) is governed by balance equations and assumes the chains of all orientations deform affinely with the deformation of the continuum (Wu and van der Giessen, 1993). The affine assumption combined with the evaluation of chains in all directions causes the model's response to be overly influenced by the response of the chain oriented in the direction of the applied deformation. The concept of the CODF is used to derive a continuum model for rubber elasticity by summing the contribution of each chain to the free energy of individual chains to

determine total free energy over all chain orientations (Wu and van der Giessen, 1993).

Depending on the chosen chain model, solving the integral for the free energy of the network has no closed form solution and requires numerical integration, which makes it less feasible for inclusion with finite element analysis software.

3.2 8-chain Network Model

Here, a constitutive model is proposed for the stress-strain behavior of the cytoskeletal AF network. The force-extension behavior of the AF will be taken to follow a MacKintosh-type model. The AF network will be modeled as an effective 8-chain network to capture the molecular network structure.

A network structure can be described by four basic topological features (see Figure 3–8): (1) a distribution in the initial distance between network junctions which is called the junction-to-junction distance or initial filament length, r_0 ; (2) a distribution in the fully extended length (i.e. contour length) of a filament between network junctions, L_c ; (3) the network connectivity (functionality of network junctions); and (4) the orientation distribution of the filaments. In order to simplify the mathematical description of the network structure, these basic features of the network are represented in terms of average or idealized quantities: (1) an average initial filament length; (2) an average filament contour length; (3) an idealized network connectivity; and (4) the average orientation of the filaments. A further simplification takes the case of an initially isotropic network (no preferred orientation in the initial state).

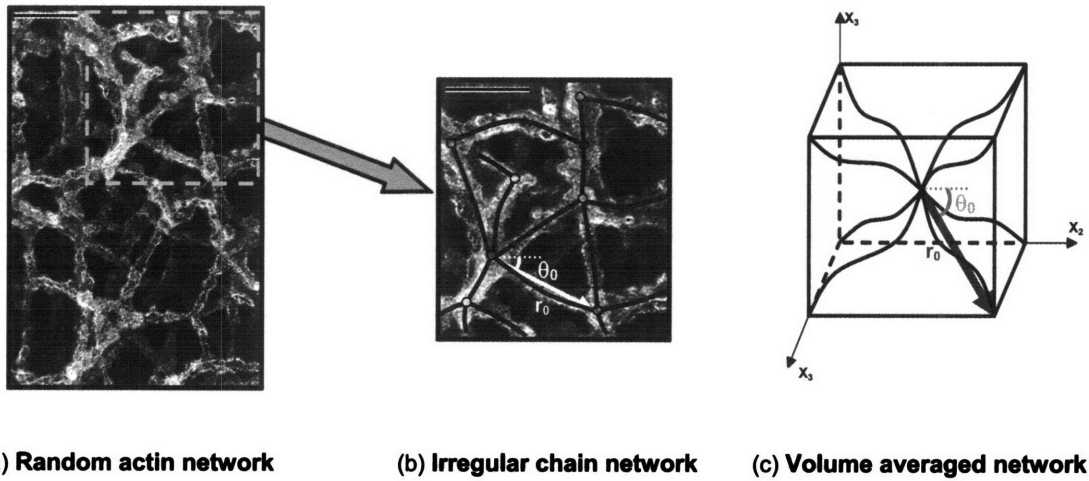


Figure 3–8. Random F-actin network and corresponding idealized eight-chain network model. The stereo micrograph of actin cortex reproduced from *The Journal of Cell Biology*, 1983, 96:1400-1413. Copyright 1983 The Rockefeller University Press (Niederman et al., 1983; Hartwig, 2004); bar in (a-b), 100 nm

The orientation of a filament can be defined by the angle between a reference axis and the junction-to-junction vector connecting the ends of the filament. For an initially isotropic network, filaments are randomly oriented in space. Thus, the average filament angle can be obtained by taking the volume average of all possible orientations and is given by $\langle \theta \rangle = \int_{\alpha_s=0}^{\pi/2} d\alpha_s \int_{\beta_s=0}^{\pi/2} d\beta_s \cos^{-1}[\cos \alpha_s \cos \beta_s] \cos \alpha_s = 57.3^\circ$ where α_s and β_s are the azimuthal and polar angles, respectively, in the spherical coordinate system (see Bergstrom and Boyce (Bergstrom and Boyce, 2001) for the analogous case of molecular orientation in polymeric networks). An alternative average can be obtained using Hermann's orientation function and gives 54.7° . Therefore, an idealized network topology should capture an initial average filament orientation close to that of 54° - 57° . The network features used in this model are represented in terms of average or idealized quantities to simplify the mathematical description. Distributions of model parameters

have been successfully incorporated within an 8-chain network model in, for example, Qi, et al. (Qi et al., 2006) who examine a distribution of initial contour lengths for different chains when examining protein unfolding. Qi, et al. found that the first protein unfolding event for distributed networks occurred at significantly lower values of stress and stretch when compared to the uniform network (Qi et al., 2006). They also noted that the stress-stretch curve of the distributed network exhibits a smoother character with smaller peak values and smaller force drops during unfolding compared to the uniform network. The approach of using distributions for network features is reserved for future work.

An idealized network structure that has been found to capture this initial orientation in an average sense is the eight-chain network model of Arruda-Boyce which was originally proposed to capture three-dimensional aspects of macromolecular network structure and its evolution with deformation in elastomeric (Arruda and Boyce, 1993b) and glassy thermoplastic (Arruda and Boyce, 1993a) materials. A combined WLC/8-chain model has also been extended to anisotropic biopolymer networks such as the collagen network in skin tissue by Bischoff, et al. (Bischoff et al., 2002b) and Kuhl, et al. (Kuhl et al., 2005), and an isotropic 8-chain network model of unfolding modular chains developed by Qi, et al. (Qi et al., 2006). Bertoldi and Boyce extended both of these models to capture the behavior of mussel byssus via an anisotropic 8-chain network model with a filament model that captures the straightening out of bends in byssus molecular chains using an elastica-type solution followed by axial stretching of the chains and subsequent force-induced unfolding of the modular domains (Bertoldi and Boyce, 2007a). Here, the 8-chain network approach is applied to densely cross-linked and

bundled cytoskeletal networks in which $L_c < l_p$. The eight-chain network considers an averaged or idealized structure of eight chains located along the diagonals of a cubic unit cell and connected by a centrally located junction (see Figure 3–9). For the isotropic network, the cell is taken to be aligned with and to deform with the macroscopic principal stretches. Therefore, taking

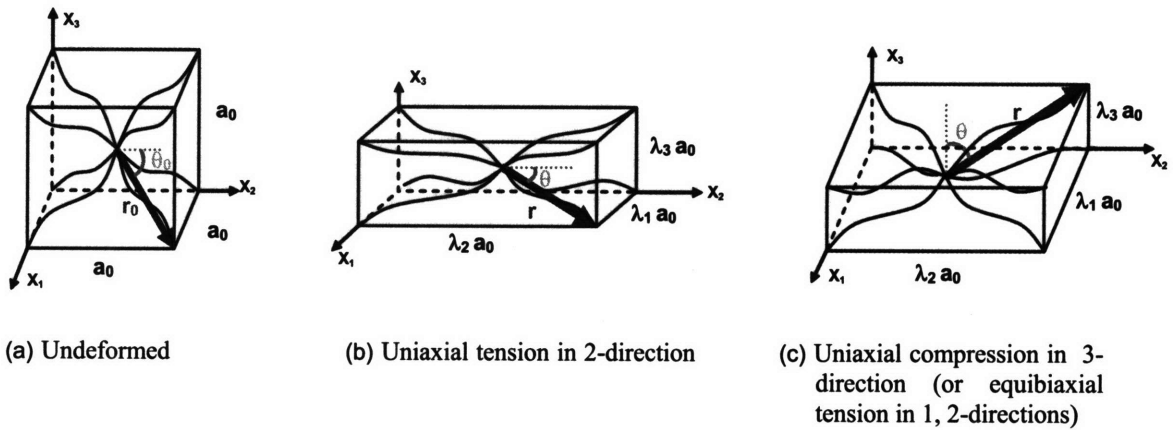


Figure 3–9. Eight-chain network model geometry and deformation (adapted from (Arruda and Boyce, 1993b))

the normal to any face of the cell as the reference axis, the average initial chain orientation of this network is simply the initial orientation of the eight chains or 54.7° , capturing the average orientation for a randomly oriented network. Since the cell deforms with the principal stretch state λ_i (where i represents the three principal directions), the stretch on any chain in this network, λ_c , is the root-mean square of the principal stretches and is always tensile for isochoric deformations, $\lambda_c = r/r_0 = \sqrt{(\lambda_1^2 + \lambda_2^2 + \lambda_3^2)/3} = \sqrt{I_1/3}$, where $I_1 = \lambda_1^2 + \lambda_2^2 + \lambda_3^2$ is the first invariant of the left or right Cauchy-Green tensor. In this thesis, chains and filaments are synonymous, so the chain stretch (λ_c) and filament stretch (λ_f) are equivalent. The initial end-to-end

distance is related to the network's actin concentration (c_{AF}) and filament properties (L_c , l_p). The chains are also found to rotate towards the maximum principal stretch direction(s). For example, in the case of uniaxial tension, the chains extend and rotate towards the tensile axis (Figure 3–9b); in the case of uniaxial compression (or equibiaxial tension), the chains extend and rotate away from the compression axis (Figure 3–9c). For the cases of uniaxial tension and uniaxial compression, the principal axes remain fixed throughout the deformation, and thus the chains in the unit cell rotate and stretch in an affine manner.

The “non-affine” mapping of macroscopic deformation to network chain deformation is more apparent when examining the case of simple shear (see Figure 3–10). The macroscopic basis is denoted as $[xyz]$ while the principal basis is shown as $[123]$. In the undeformed state, the principal basis is undefined and could be oriented in any direction (see Figure 3–10a). Upon application of simple shear, the principal axes of stretch are identified and will rotate with deformation and, furthermore, the chains will undergo additional rotation relative to the maximum principal stretch direction (θ_1 - Figure 3–10b).

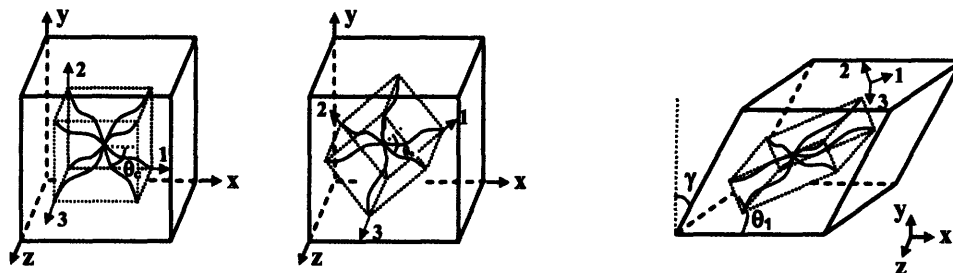


Figure 3–10. Simple shear deformation of eight-chain network model

Note that during simple shear deformation the principal stretch direction does not stay coincident with the diagonal of the unit cell. For example, if the unit cell was originally oriented along the 45° diagonal, at $\tan(\gamma)=0$, an affine motion would require the unit cell

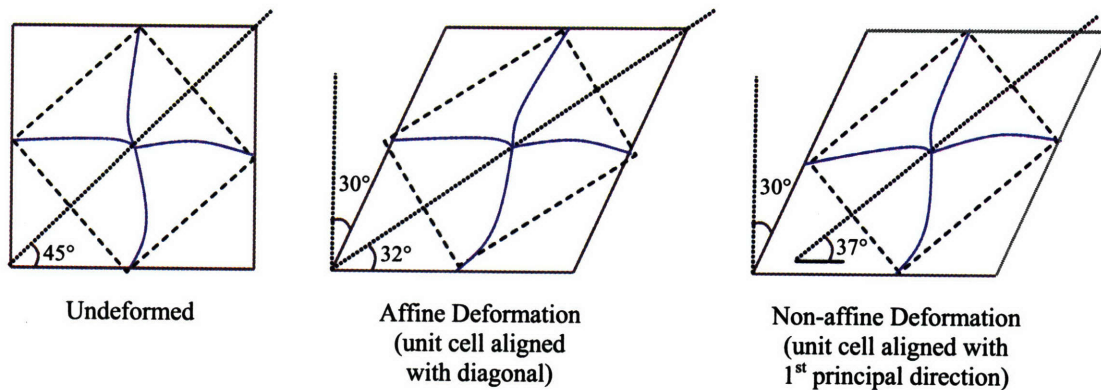


Figure 3–11. 2D illustration of affine and non-affine simple shear deformation

to remain oriented along the diagonal throughout the deformation (shown in 2D for clarity in Figure 3–11). The eight-chain network model allows the unit cell to rotate with the maximum principal direction, which does not stay coincident with the diagonal throughout the simple shear deformation (Figure 3–11).

This network representation is seen to accommodate the imposed shear by both non-affine rotation and non-affine stretching of the constituent chains, effectively sampling the non-affine nature of the network behavior in a simple but effective manner. The physical counterpart would be to view the rotated unit cell as a method of sampling the rotation and stretching of chains (in eight directions with respect to the maximum principal direction) such that the overall non-affine network response is captured in an averaged sense. The eight-chain network model formulation captures the basic features that Chandran, et al. (Chandran and Barocas, 2006) and Onck, et al. (Onck et al., 2005)

observe in their many membered discrete network modeling approaches, in particular, the significant reorientation of filaments that accommodates macroscopic deformation.

Due to the ability of the eight-chain network to effectively mimic the initial state of a randomly oriented network and to also capture the evolution in chain stretch and orientation with different deformation states, this simplified network topology will be utilized to represent the cytoskeletal network.

3.2.1 Stress-strain behavior

The three-dimensional stress-stretch behavior of the AF network can be determined using the eight-chain network topology and its evolution with stretch together with a representation of the axial force-stretch behavior of an AF where the initial length of the filament is the initial junction-to-junction distance, r_0 , and the limiting length is essentially the contour length, L_c , of the filament. Cytoskeletal filaments, especially AF, are observed to have only a slight curvature between junction points (Figure 3–8a). The force-extension relations govern the filament's response during axial stretching by displacing the two junction points and thus increasing the junction-to-junction distance from r_0 to r . The force-stretch behavior will consist of an initially linear elastic region; followed by a strain stiffening region as the junction-to-junction distance r approaches the filament contour length L_c (see Figure 2-5a). The limiting filament stretch is therefore defined as $\lambda_L=L_c/r_0$.

The work done by each chain can be found by integrating the filament force-extension expression [Equation (2.26)]: $\Delta W_c = \int f dr$, and is equal to the filament strain energy. The strain energy density of the network, W , is simply the product of the

filament density, n (number of filaments per unit volume), multiplied by the strain energy of a single filament, w_f , in the eight-filament network: $W = nw_f$ since all filaments in the 8-chain network experience the same stretch. The expression for the strain energy density of the eight-filament cytoskeletal network model is

$$W = \frac{nk_B T}{l_p} \left[\frac{L_c}{4(1-r/L_c)} - l_p [\ln(L_c^2 - 2l_p L_c + 2l_p r) - \ln(r - L_c)] - c \right] \quad (3.5)$$

where c is a constant equal to the initial strain energy density from the filaments. Since $r = \lambda_c r_0 = r_0 \sqrt{I_1/3}$, the strain energy density expression is a function of I_1 .

The actin cytoskeleton is embedded in a nearly incompressible fluid (cytosol) and hence is taken to deform at constant volume. Note that this network model will be incorporated into a poroelastic framework in Chapter 6 to capture fluid flow and, consequently, swelling/deswelling effects on the mechanical behavior. The Cauchy stress is found by differentiating the strain energy density:

$$\mathbf{T} = 2 \frac{\partial W}{\partial I_1} \mathbf{B} - p^* \mathbf{I} = \frac{nk_B T}{3l_p} \frac{r_0}{\lambda_c} \left(\frac{1}{4(1-\lambda_c r_0/L_c)^2} \right) \left(\frac{L_c/l_p - 6(1-\lambda_c r_0/L_c)}{L_c/l_p - 2(1-\lambda_c r_0/L_c)} \right) \mathbf{B} - p^* \mathbf{I}, \quad (3.6)$$

where $\mathbf{B} = \mathbf{F}\mathbf{F}^T$ is the left Cauchy-Green tensor (Finger tensor), $\lambda_c = \sqrt{\text{tr}(\mathbf{B})/3}$, \mathbf{F} is the deformation gradient, $\mathbf{F} = \partial \mathbf{x} / \partial \mathbf{X}$ where \mathbf{x} is the position vector of a material point in the current configuration and \mathbf{X} is the original position. Also in Equation (3.6), \mathbf{I} is the identity tensor and p^* is the additional pressure required due to the incompressibility constraint and obtained by satisfying equilibrium.

Alternatively, the effects of compressibility can be included in the constitutive relationship by adding a term to the strain energy function to account for the additional entropic contribution due to volume change as well as adding a term for the bulk response.

$$\begin{aligned}
W_{Comp} = & \frac{nk_B T}{l_p} \left[\frac{L_c}{4(1-r/L_c)} - l_p [\ln(L_c^2 - 2l_p L_c + 2l_p r) - \ln(r - L_c)] - c \right] \\
& - \frac{nk_B T}{l_p} \left\{ \left[\frac{L_c}{4(1-r_0/L_c)^2} - \frac{1}{(1-r_0/L_c)(L_c/l_p - 2(1-r_0/L_c))} \right] \frac{r_0}{3} \ln J \right\} \\
& + \frac{K_B}{2} (J-1)^2
\end{aligned} \quad (3.7)$$

where K_B is the bulk modulus. The compressible Cauchy stress can then be found as

$$\begin{aligned}
\mathbf{T} = & \frac{2}{J} \frac{\partial W}{\partial I_1} \mathbf{B} + \frac{\partial W}{\partial J} \mathbf{I} \\
= & \frac{nr_0 k_B T}{3l_p} \left\{ \begin{aligned} & \frac{1}{\lambda_c} \left[\left(\frac{1}{4(1-\lambda_c r_0/L_c)^2} \right) \left(\frac{L_c/l_p - 6(1-\lambda_c r_0/L_c)}{L_c/l_p - 2(1-\lambda_c r_0/L_c)} \right) \right] \mathbf{B} \\ & - \left[\left(\frac{1}{4(1-r_0/L_c)^2} \right) \left(\frac{L_c/l_p - 6(1-r_0/L_c)}{L_c/l_p - 2(1-r_0/L_c)} \right) \right] \mathbf{I} \end{aligned} \right\} + K_B (J-1) \mathbf{I}
\end{aligned} \quad (3.8)$$

The Cauchy shear stress-strain relationship becomes

$$\tau_{Mac} = \frac{nk_B T}{3l_p} \frac{r_0}{\lambda_c} \left(\frac{1}{4(1-\lambda_c r_0/L_c)^2} \right) \left(\frac{L_c/l_p - 6(1-\lambda_c r_0/L_c)}{L_c/l_p - 2(1-\lambda_c r_0/L_c)} \right) \tan \gamma. \quad (3.9)$$

The initial shear modulus is given by:

$$G_0 = \frac{nk_B T r_0}{3l_p} \left(\frac{1}{4(1-r_0/L_c)^2} \right) \left(\frac{L_c/l_p - 6(1-r_0/L_c)}{L_c/l_p - 2(1-r_0/L_c)} \right). \quad (3.10)$$

The constitutive model presented here is a function of the material properties n , l_p , L_c , and r_0 . The filament density, n (filaments/m³), is defined as $n = \rho_L/L_c$. The actin

length density, ρ_L ($\mu\text{m}/\text{m}^3$), is defined as $\rho_L = (c_{AF} \cdot M_{AM}) / \rho_{AF}$ where c_{AF} is the experimental actin monomer concentration, ρ_{AF} ($\text{Da}/\mu\text{m}$) is the linear actin density and M_{AM} ($\text{Da}/\text{monomer}$) is the molecular mass of each actin monomer. Both ρ_{AF} and M_{AM} are actin material properties, defined *a priori*. As defined earlier, the zero force junction-to-junction distance $r_{F=0}$ is a function of L_c , l_p , where a network initial junction-to-junction distance r_0 slightly larger than $r_{F=0}$ indicates a prestress in the network due to *in vitro* or *in vivo* environmental conditions (Zhu et al., 2000; Wang et al., 2002a; Kasza et al., 2007). Here, the percent increase (α) of r_0 beyond $r_{F=0}$ is defined as $r_0 = r_{F=0} (1+\alpha)$. In principle, r_0 and L_c are measurable from micrographs and l_p is measurable from single molecule bending, however they are operationally fit from empirical stress-strain data for each network.

3.2.2 Implementation in finite element analysis

The constitutive model is incorporated as a user-defined material within the ABAQUS finite element software (Simulia Dassault Systèmes, Providence, RI, USA). The ABAQUS user subroutine UMAT is used to define a material's mechanical behavior, and requires the calculation of the 4th order Jacobian tensor (\mathbf{C}) and 2nd order Cauchy (true) stress (\mathbf{T}) at the end of each increment. \mathbf{C} is taken to be an approximate value and need not be exact for convergence of the finite element model. The generalized derivation for the Jacobian tensor is given here following the approach given by Wilson (Wilson, 2005). The derivation of the Jacobian for the inextensible 8-chain MacKintosh network model follows the generalized derivation, while the Cauchy stress tensor was

given in Equation(3.6). The Jacobian (\mathbf{C}) is defined through the variation in Kirchoff stress as

$$\delta(J \mathbf{T}) = \mathbf{J} \mathbf{C} : \mathbf{D} \quad (3.11)$$

where $J = \det(\mathbf{F})$ and \mathbf{D} is the rate of stretch, defined as the symmetric part of the velocity gradient (\mathbf{L}):

$$\mathbf{D} = \text{Sym}(\mathbf{L}) = \frac{1}{2}(\mathbf{L} + \mathbf{L}^T) \quad (3.12)$$

$$\mathbf{L} = \frac{\partial \mathbf{v}}{\partial \mathbf{x}} = \frac{\partial \dot{\mathbf{x}}}{\partial \mathbf{x}} = \delta \mathbf{F} \mathbf{F}^{-1}. \quad (3.13)$$

The left hand side of Equation (3.11), $\delta(J \mathbf{T})$, can be equivalently taken to be

$$\delta(J \mathbf{T}) = \mathbf{T} \delta J + J \delta \mathbf{T} = \left(\mathbf{T} \otimes \frac{\delta J}{\delta \mathbf{F}} + J \frac{\delta \mathbf{T}}{\delta \mathbf{F}} \right) : \delta \mathbf{F} = \mathbf{A} : \delta \mathbf{F} \quad (3.14)$$

Substituting Equation (3.13) into Equation (3.14) gives

$$\delta(J \mathbf{T}) = \mathbf{A} : (\mathbf{L} \mathbf{F}) = \mathbf{A}^{RT} : (\mathbf{F}^T \mathbf{L}^T) = (\mathbf{A}^{RT} \mathbf{F}^T) : \mathbf{L}^T. \quad (3.15)$$

If $(\mathbf{A}^{RT} \mathbf{F}^T)$ is right symmetric, Equation (3.15) can be given as

$$\delta(J \mathbf{T}) = (\mathbf{A}^{RT} \mathbf{F}^T) : \mathbf{D}. \quad (3.16)$$

Note that if $(\mathbf{A}^{RT} \mathbf{F}^T)$ is not right symmetric, there will be a small error in \mathbf{C} . This should not, however, inhibit convergence of the finite element model since \mathbf{C} is only taken as an approximate value from the UMAT subroutine. The 4th order Jacobian tensor from Equation (3.11) can therefore be shown as

$$\mathbf{C} = \frac{1}{J} (\mathbf{A}^{RT} \mathbf{F}^T) = \frac{1}{J} \left(\mathbf{T} \otimes \frac{\delta J}{\delta \mathbf{F}} + J \frac{\delta \mathbf{T}}{\delta \mathbf{F}} \right)^{RT} \mathbf{F}^T \quad (3.17)$$

where $\delta J / \delta \mathbf{F}$ is defined as

$$\frac{\delta J}{\delta \mathbf{F}} = \frac{\delta \det(\mathbf{F})}{\delta \mathbf{F}} = J\mathbf{F}^{-T}. \quad (3.18)$$

Thus, given a material-specific expression for the Cauchy stress (\mathbf{T}), the Jacobian (\mathbf{C}) can be determined by solving for the derivative $\delta \mathbf{T} / \delta \mathbf{F}$.

The Jacobian may now be specialized to the constitutive model for the inextensible 8-chain MacKintosh network model. In order to simplify the expressions, the following abbreviations are used within Equation (3.8),

$$\zeta = \frac{1}{\lambda_c} \left[\left(\frac{1}{4(1 - \lambda_c r_0 / L_c)^2} \right) \left(\frac{L_c / l_p - 6(1 - \lambda_c r_0 / L_c)}{L_c / l_p - 2(1 - \lambda_c r_0 / L_c)} \right) \right] \quad (3.19)$$

$$\varsigma = \left(\frac{1}{4(1 - r_0 / L_c)^2} \right) \left(\frac{L_c / l_p - 6(1 - r_0 / L_c)}{L_c / l_p - 2(1 - r_0 / L_c)} \right), \quad (3.20)$$

noting that ς is a material-dependent constant and ζ is a function of λ_c . The expression for the Cauchy stress for a compressible material is now given by

$$\mathbf{T} = \frac{nr_0 k_B T}{3Jl_p} (\zeta \mathbf{B} - \varsigma \mathbf{I}) + K_B (J - 1) \mathbf{I} \quad (3.21)$$

The Jacobian (\mathbf{C}) is now found by solving for the derivative $\delta \mathbf{T} / \delta \mathbf{F}$,

$$\frac{\delta \mathbf{T}}{\delta \mathbf{F}} = \frac{nr_0 k_B T}{3Jl_p} \left\{ \frac{-1}{J^2} \frac{\delta J}{\delta \mathbf{F}} (\zeta \mathbf{B} - \varsigma \mathbf{I}) + \frac{1}{J} \left(\zeta \frac{\delta \mathbf{B}}{\delta \mathbf{F}} \right) + \frac{1}{J} \left(\frac{\delta \zeta}{\delta \mathbf{F}} \mathbf{B} \right) \right\} + K_B \frac{\delta J}{\delta \mathbf{F}} \mathbf{I} \quad (3.22)$$

where the terms within Equation (3.22) are defined as

$$\frac{\delta \mathbf{B}}{\delta \mathbf{F}} = 2(\mathbf{I}^s \mathbf{F})^{RT} = 2(\mathbf{I}_{ijkl}^s \mathbf{F})^{RT} = 2(\mathbf{I}_{ijkl}^s \mathbf{F})^{RT} \quad (3.23)$$

$$\mathbf{I}_{ijkl}^s = \frac{\delta_{ik} \delta_{jl} + \delta_{il} \delta_{jk}}{2} \quad (3.24)$$

$$\frac{\delta\zeta}{\delta\mathbf{F}} = \frac{1}{\lambda_c} \left[\begin{aligned} & \frac{r_0}{2L_c(1-\lambda_c r_0/L_c)^3} + \frac{2l_p^2 r_0}{L_c(1-\lambda_c r_0/L_c)(L_c - 2l_p(1-\lambda_c r_0/L_c))^2} \\ & - \frac{l_p r_0}{L_c(1-\lambda_c r_0/L_c)^2(L_c - 2l_p(1-\lambda_c r_0/L_c))} - \frac{1}{4\lambda_c(1-\lambda_c r_0/L_c)^2} \\ & + \frac{l_p}{\lambda_c(1-\lambda_c r_0/L_c)(L_c - 2l_p(1-\lambda_c r_0/L_c))} \end{aligned} \right] \frac{\delta\lambda_c}{\delta\mathbf{F}} \quad (3.25)$$

$$\frac{\delta\lambda_c}{\delta\mathbf{F}} = \frac{\delta\lambda_c}{\delta I_1} \frac{\delta I_1}{\delta\mathbf{F}} = \frac{1}{6\lambda_c} 2\mathbf{F} = \frac{1}{3\lambda_c} \mathbf{F}. \quad (3.26)$$

3.3 Isotropically prestressed Networks

Isotropic prestress (i.e. in the absence of an applied deformation) occurs in both *in vitro* or *in vivo* networks due to a variety of environmental conditions and is an important component in the cell stiffening response (Hubmayr et al., 1996; Cai et al., 1998; Pourati et al., 1998b; Zhu et al., 2000; Wang et al., 2001; Wang et al., 2002a; Kasza et al., 2007). Prestress in spectrin networks within red blood cells has been captured via continuum models and shown to increase the initial elastic modulus of the network and significantly decrease the stress and stretch levels required for subdomain unfolding (Arslan and Boyce, 2006; Arslan et al., 2008). *In vitro* or *in vivo* actin networks could experience the isotropic prestress from sources including osmotic/swelling pressures, external tractions due an adherent cell membrane's interactions with the ECM (or the *in vitro* gel's interactions with the substrate), and/or internal myosin-generated contractile forces. Stiffening of actin networks from myosin contractile tension has been attributed to the tension in the actin filaments and not the crosslinks (Mizuno et al., 2007). The proposed 8-chain MacKintosh network model can account for filament pretension and network

isotropic prestress, and hence can be used to parametrically explore the effect of isotropic prestress on the stress-strain behavior. The actin network isotropic prestress is accounted for directly through a percent increase (α) in r_0 beyond $r_{f=0}$. Figure 3–12 demonstrates the effect of an increase in network isotropic prestress on the overall network shear stress-strain behavior. The results show that increasing isotropic prestress results in an increase in the initial shear modulus of the network and a decrease in the network extensibility (as seen in the dramatic increase in tangent modulus (slope) of the stress-strain curve occurring at smaller strains when isotropic prestress is increased).

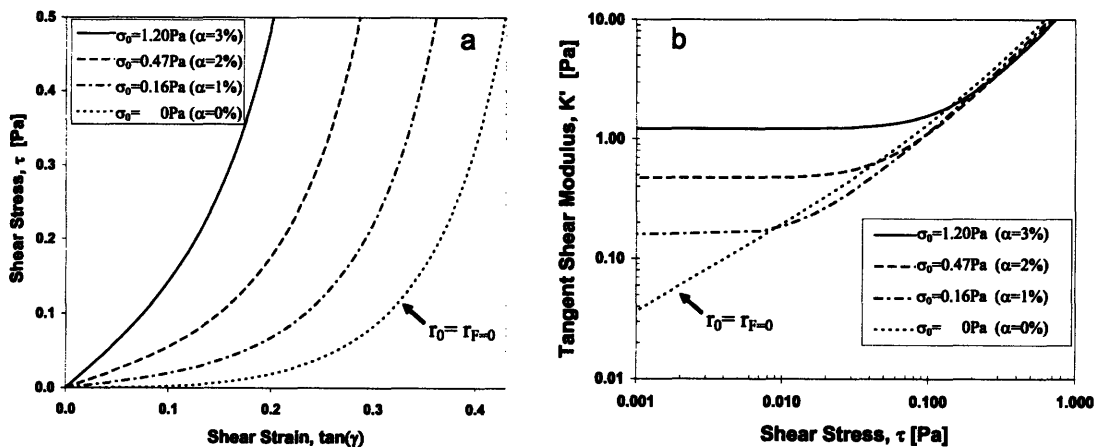


Figure 3–12. Effect of network isotropic prestress on the network shear stress-shear strain behavior (a) and the network tangent modulus-shear stress behavior (b), with the initial isotropic prestress (σ_0) based on $r_0 = r_{f=0}(1 + \alpha)$

3.4 Rheological experimental techniques

Although many variations exist to explore the rheology of cytoskeletal systems, the experimental techniques usually fall into one of two categories: bulk rheology or

microrheology. For microrheology, the mean squared displacements (MSD) of microscopic probe particles embedded within a cell are tracked via laser or optical tracking techniques while their displacement is either actively driven by external forces or passively driven by local thermal energy (i.e. Brownian motion) (Brau et al., 2007). Then a generalized Langevin equation of motion for a microsphere in a viscoelastic medium (Xu et al., 1998b) is used to transform the MSD into elastic and viscous moduli (Tseng et al., 2002a). Alternately, a viscoelastic memory function can be calculated using equipartition and a Laplace transformation, and then solving for the shear modulus with the generalized Stokes law (Mason et al., 1997; Janmey and Schmidt, 2006). Figure 3–13

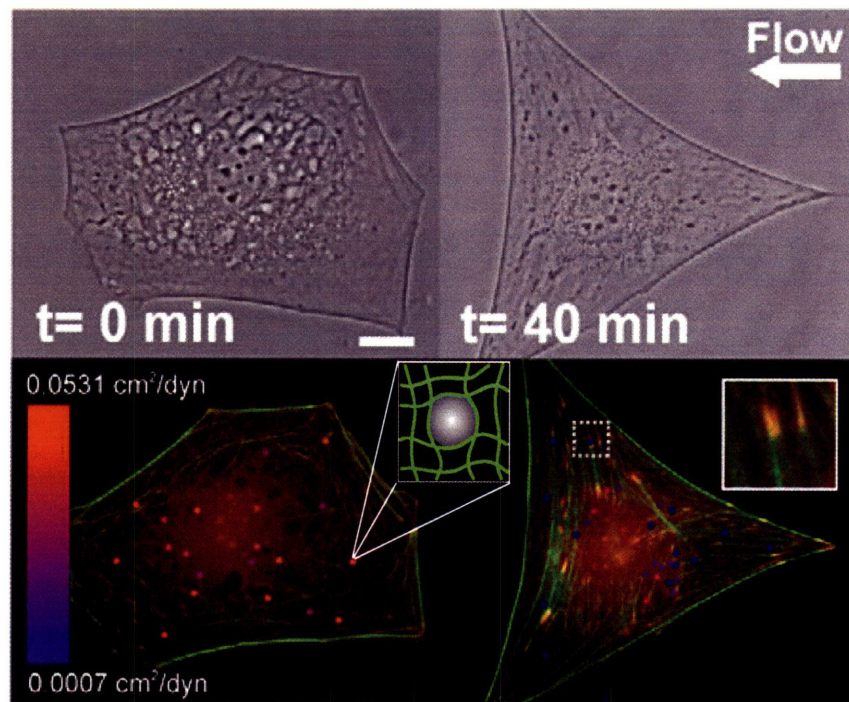


Figure 3–13. Phase contrast (top) and immunofluorescence (bottom) micrographs of 100nm fluorescent nanoparticles in Swiss 3T3 fibroblasts before (left) and after (right) shear flow. The inset is a magnified view of focal adhesions at the ends of actin stress fibers. Bar, $20\mu\text{m}$. Adapted from (Lee et al., 2006).

shows an example of multiple particle tracking to monitor the local changes in cell stiffness in a cell subjected to a shearing flow (Lee et al., 2006). The 100nm nanoparticles are enlarged and colored in the micrograph to show regions of the cytoskeletal networks (actin=green, vinculin=red) that were structurally altered to stiffen their response (blue) or regions retained their original level of elasticity (red) (Lee et al., 2006).

Active microrheology techniques generally employ one- or two-particle methods. Large discrepancies can occur between macroscopic viscoelastic moduli and moduli found by one-particle microrheology if any characteristic length scales (mesh size, persistence length) in the cytoskeletal network exceed the size of the particle size (i.e. application of the generalized Stokes law is not valid) (Janmey and Schmidt, 2006). Two-particle microrheology was developed (Crocker et al., 2000; Levine and Lubensky, 2000) to avoid these problems by cross-correlating the displacements of two particles separated at a given distance which then becomes the relevant length scale (i.e. influence of particle size/shape is reduced), see Figure 3–14 (Janmey and Schmidt, 2006).

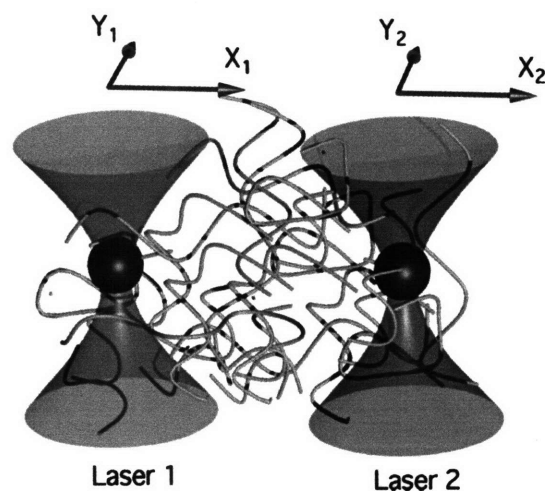


Figure 3–14. Sketch of 1-particle and 2-particle microrheology using lasers for trapping, displacing, detecting. (Janmey and Schmidt, 2006)

Bulk rheometers are usually categorized as rotational (“stress-strain”) rheometers, capillary rheometer, and extensional rheometer, with the rotational rheometers most commonly used to explore bulk behavior of reconstituted cytoskeletal networks. The rotational rheometers use different experimental geometries (cone and plate, parallel plates, or annular cylinders) to shear a material by applying an oscillatory force or displacement in order to measure the elastic (in-phase) or viscous (out-of-phase) response. The “cone and plate” and “parallel plate” rotational (torsional) rheometers hold one plate fixed while applying a torque to the other plate/cone (Figure 3–15). Both are useful for measuring gels with viscosities greater than 10mPa-s. The cone and plate

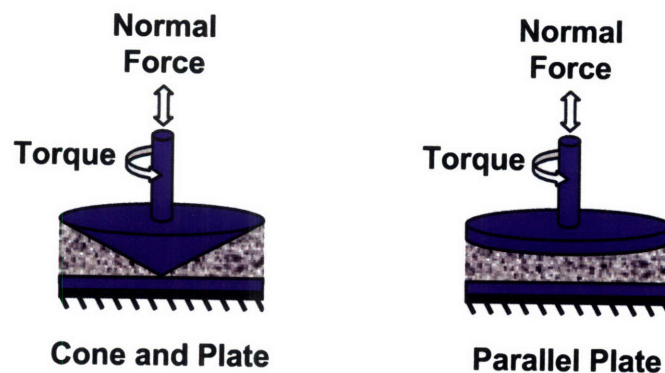


Figure 3–15. Torsional rheometer geometries

rheometer provides a uniform radial strain field due to its geometry. Many models of both torsional rheometers, however, use a load cell in the vertical direction to measure the normal force exerted by the material, often a positive force due to the Poynting effect (Poynting, 1909) although negative normal forces have been observed in some complex

fluids at high flow rates (Lin-Gibson et al., 2004; Montesi et al., 2004) and some semiflexible polymer gels (Janmey et al., 2007).

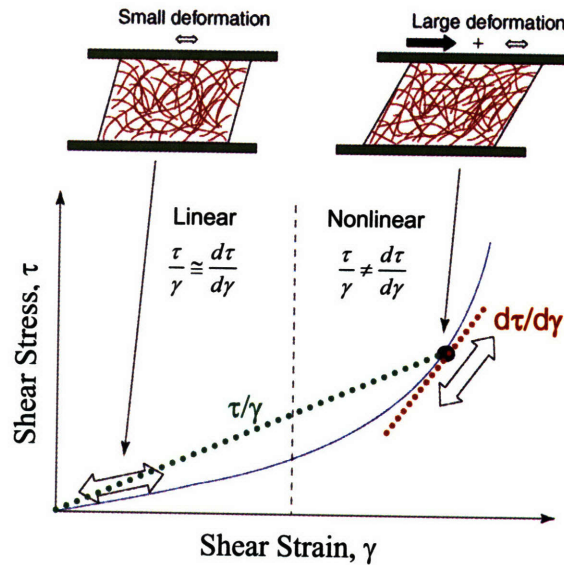


Figure 3–16. Linear and nonlinear rheology with stress stiffening from cross-linked gels (adapted from (Kasza et al., 2007))

The shear stress-strain behavior, like the force-extension response, of semiflexible biopolymers is characterized by a linear region followed by a nonlinear region of increasing tangent stiffness as the filament’s extensional limit is reached (Fernandez et al., 2006; Kasza et al., 2007). The linear response occurs for small deformations, and small oscillatory stresses or strains (white double-headed arrow in Figure 3–16) can be used to measure the elastic shear (storage) modulus, G' , and the viscous shear (loss) modulus, G'' . The differential change in shear stress-strain in the nonlinear region is characterized as a tangent shear modulus, $K=d\tau/d\gamma$, instead of a secant shear modulus, $G=\tau/\gamma$ (Figure 3–16). Thus, at larger strains an initial stress or strain is applied to the

material to place it in the nonlinear regime, followed by the oscillatory stress or strain to measure the differential elastic (K') and viscous (K'') response.

3.5 8-chain/MacKintosh Network Model Results

3.5.1 Experimental data used for comparison

The rheology of actin networks has been quantified in several studies (Janmey et al., 1991; Janmey et al., 1994; Isambert and Maggs, 1996; Gardel et al., 2004a; Gardel et al., 2004b). The model will be compared to the Gardel, et al. data (Gardel et al., 2004a), introduced in Chapter 1, which systematically varied the actin concentration, c_{AF} , while holding $R = c_{CL}/c_{AF}$ constant (where c_{CL} is the cross-link concentration). This data measured the shear rheology of F-actin cross-linked with scruin cross-linking proteins, and observed a network response for $R > 0.03$ in which the elastic behavior dominated the viscous behavior for the frequencies of interest (see Figure 3–17).

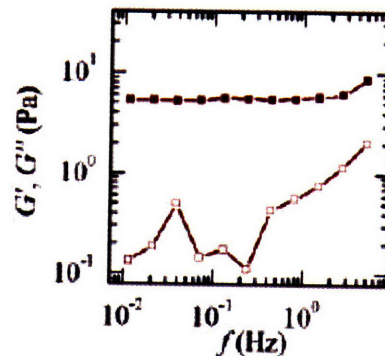


Figure 3–17. Storage modulus (G') and loss modulus (G'') over a range of frequencies for reconstituted actin-scrutin networks (adapted from (Gardel et al., 2004a))

3.5.2 Representative low concentration case

The model was evaluated by first fitting the model to the data with the lowest actin concentration found to exhibit entangled network behavior, $c_{AF} = 8\mu\text{M}$ and $R=0.03$. The contour length was calculated following the relation presented by Gardel, et al. (Gardel et al., 2004a) and the empirically derived exponent (0.2) given by Shin, et al. (Shin et al., 2004) for actin-scruin networks,

$$L_c = \frac{R^{0.2} d_{Actin}}{2} \sqrt{\frac{\pi}{c_{AF}}}, \quad (3.27)$$

with $d_{Actin}=7\text{nm}$, $R=0.03$, and $c_{AF}=8\mu\text{M}$, resulting in $L_c=1.1\mu\text{m}$. The chain density is determined to be $n=1.2\text{e}19$ filaments/ m^3 based on the values of $L_c = 1.1\mu\text{m}$, $c_{AF} = 8\mu\text{M}$, $\rho_{AF}= 16 \text{MDa}/\mu\text{m}$, and $M_{AM}=42 \text{kDa}/\text{monomer}$. The values of l_p and α are chosen to best fit the model to the $8\mu\text{M}$ experimental data, noting that the value of r_θ associated with α will be nearly equal to L_c based on the observed network topology of nearly straight filaments between junctions. The best fit of $l_p=3\mu\text{m}$ agrees with observed values of $l_p\sim 3\mu\text{m}$ for F-actin with $L_c\sim 1-3\mu\text{m}$ (Steinmetz et al., 1997a).

The shear stress-strain results are shown in Figure 3–18a, with the tangent modulus-shear stress results shown in Figure 3–18b. The network modeling parameters are $n=1.2\text{e}19$ filaments/ m^3 , $l_p=3.0\mu\text{m}$, $L_c=1.1\mu\text{m}$, and $r_\theta=1.0\mu\text{m}$. The network model captures the experimental data through the entire range of shear strain using physically realistic material properties. The network model also fits well with the experimental tangent modulus-shear stress behavior, including the low stress region of relatively stress-independent modulus and the nonlinear increase in tangent modulus at higher levels of shear stress.

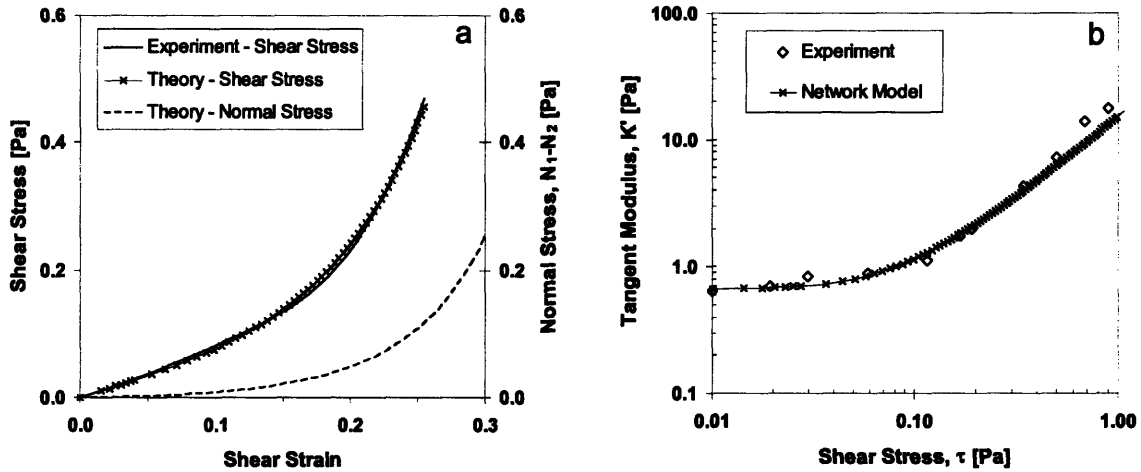


Figure 3–18. (a) Shear stress and normal stress difference ($N_1 - N_2$) vs. shear strain and (b) Tangent shear modulus vs. shear stress for *in vitro* F-actin networks ($c_{AF} = 8\mu\text{M}$, $R=0.03$). (experimental data adapted from (Gardel et al., 2004a))

The network model could alternatively use the WLC filament model with clamped-clamped boundary conditions (developed in Chapter 2) instead of the WLC model with pinned-pinned boundary conditions. The shear stress-shear strain behavior of both models is shown in Figure 3–19a, with the tangent modulus-shear stress results shown in Figure 3–19b. The network parameters for both models are $n=1.2e19$ filaments/ m^3 , $l_p=3.0\mu\text{m}$, $L_c=1.1\mu\text{m}$, and $\sigma_0=0.7\text{Pa}$. While the network model with the pinned WLC filaments captures the experimental data through the entire range of shear strain using physically realistic material properties, the network with the clamped WLC filaments quickly diverges due to its inherently stiffer response and would require an unrealistically small persistence length to fit the experimental data.

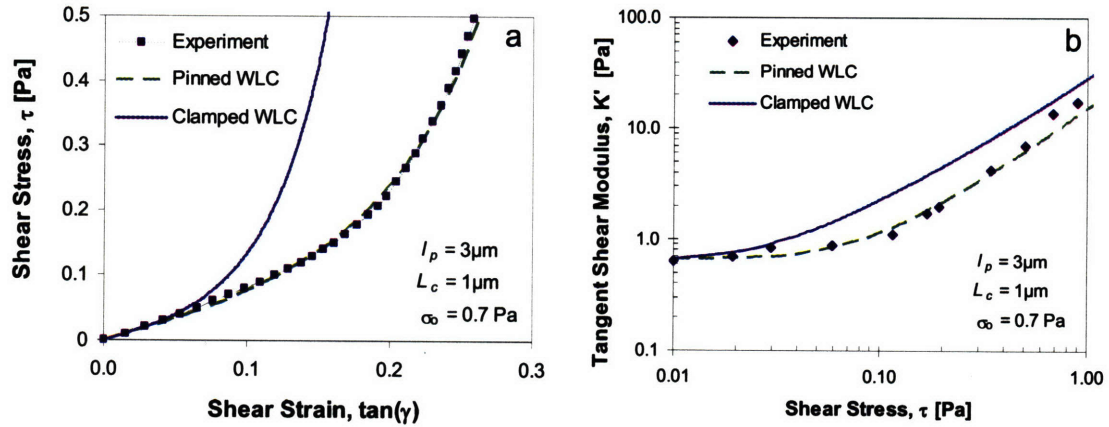


Figure 3–19. (a) Shear stress vs. shear strain and (b) Tangent shear modulus vs. shear stress for *in vitro* F-actin networks ($c_{AF} = 8\mu\text{M}$, $R=0.03$) using WLC filament model with pinned-pinned or clamped-clamped boundary conditions. Experimental data adapted from (Gardel et al., 2004a).

The AF network model also enables tracking of the evolution in filament orientation and stretch with macroscopic deformation. The average orientation of a filament is expressed as the azimuthal angle with respect to the direction of maximum principal stretch (θ_f), together with the direction of the maximum principal stretch defined by its angle (θ_1) with respect to the direction of imposed shear (see inset of Figure 3–20). The filament orientation evolution shows that the shear strain is accommodated by significant filament rotation and a small amount of filament stretch. The eight-filament network gives a filament stretch of $\lambda_f=1.0004$ for a shear strain of $\tan(\gamma)=0.05$ and $\lambda_f=1.01$ for $\tan(\gamma)=0.25$. In contrast, an affine network with a dominating diagonal filament (e.g. Figure 3–5a) subjected to shear strains of $\tan(\gamma)=0.05$ and 0.25 requires much larger filament stretches of $\lambda_f=1.03$ and 1.15 , respectively.

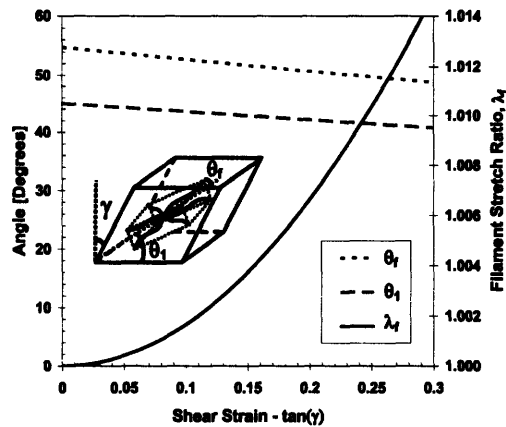


Figure 3–20. F-actin filament molecular orientation evolution

Figure 3–18a also shows the normal stress difference, $N_1 - N_2$ (where $N_1 = T_{11} - T_{22}$, $N_2 = T_{22} - T_{33}$) as a function of shear strain during the simple shear deformation. The normal stress difference is found to be negligible at small strains and to monotonically increase as a positive value, as expected, for an initially isotropic network based on the first invariant of strain. Gardel, et al. did not present results for the normal stress difference for their networks. However, recent work by Janmey, et al. (Janmey et al., 2007) has observed a negative normal stress difference during finite shear of much higher concentration, cross-linked actin networks. This suggests a possible initial anisotropy in the Janmey network configuration which could be modeled using an anisotropic formulation of the 8-chain network (e.g., Bischoff, et al. (Bischoff et al., 2002a)), or, alternatively suggests a cross-linking condition that favors direct axial stretching of the filament over filament rotation; this effect could be captured in future expansions of the strain energy function by including torsional potential contributions of the cross-linking junctions and the enthalpic contributions from direct axial stretching of the chains.

3.5.3 Effects of increasing actin concentration

Gardel, et al., have further explored the effects of varying actin concentration and cross-link concentration on the shear rheology of the network. Figure 3–21a shows the tangent modulus-stress behavior for four levels of c_{AF} at fixed $R=0.03$. Note in Figure 3–21a that the tangent shear modulus for the $c_{AF}=21\mu\text{M}$ case is constant up to a shear stress of $\tau=0.5\text{Pa}$, while the trend of nonlinear strain stiffening observed in the other three concentrations suggests that the $21\mu\text{M}$ network should begin strain stiffening at approximately $\tau=0.2\text{Pa}$. The shear stress-strain data were obtained by taking a curve fit of the raw tangent modulus-stress data to calculate the shear stress-strain behavior. The experimental data in Figure 3–21b show the resulting shear stress-strain behavior for varying c_{AF} at fixed $R=0.03$.

The focus is now turned to explore the ability of the proposed model to capture the effect of actin concentration on the stress-strain behavior by attributing the observed effects to changes in network structure (n , r_0 , etc.). Next, the model’s ability to capture network isotropic prestress and bundling effects by parametrically changing r_0 and l_p , respectively, is evaluated. This evaluation begins by determining l_p , L_c , and α (due to isotropic prestress) for the lowest concentration case ($8\mu\text{M}$) as shown previously. The persistence length is then held constant (indicating a “no bundling” assumption), while the contour length is taken to scale with concentration ($L_c \sim c_{AF}^{-1/2}$) following Equation (3.27). The percent increase (α) in r_0 beyond $r_{F=0}$ due to isotropic prestress for each concentration is then adjusted to provide a fit to the experimental results as shown in Figure 3–21. Table 3–1 contains the network parameters used for each concentration case, with the initial isotropic prestress (σ_0) based on $r_0 = r_{F=0} (1+\alpha)$. Note also that α

decreases monotonically with $c_{AF} = 8, 12, 29\mu\text{M}$ (ignoring the anomalous $21\mu\text{M}$ data) approximately following the relationship $\alpha = 6.2(c_{AF})^{-1/2}$.

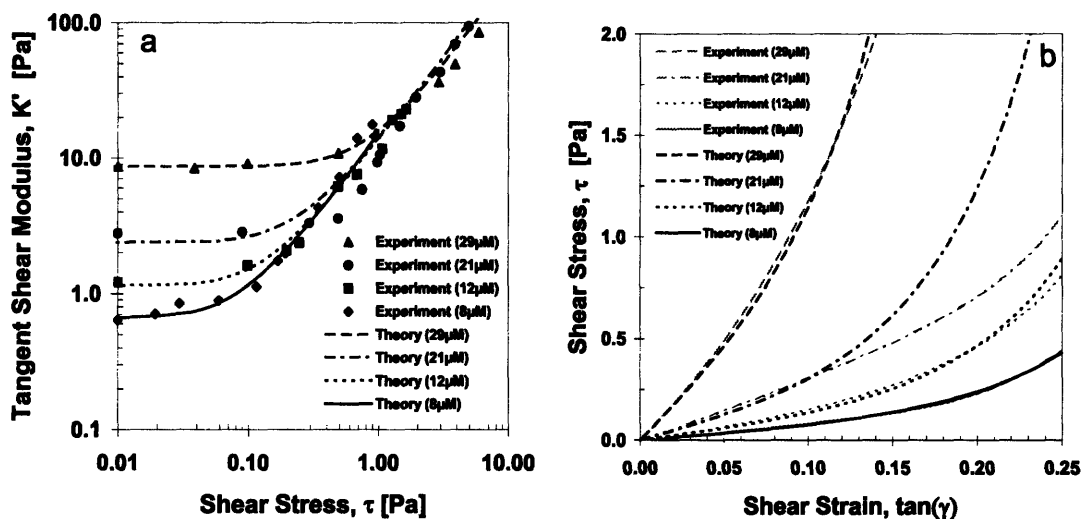


Figure 3–21. (a) Tangent shear modulus-shear stress theory and experimental data, (b) shear stress-shear strain theory and experimental curve fit data of actin networks with varying actin concentration ($c_{AF}=8, 12, 21, 29\mu\text{M}$, $R=0.03$), (experimental data adapted from (Gardel et al., 2004a))

CONCENTRATION	l_p [μm]	n [m^{-3}]	L_c [μm]	$r_{F=0}$ [μm]	r_0 [μm]	α [%]	σ_0 [Pa]
8 μM	3.0	1.2e19	1.07	1.00	1.03	2.7	0.66
12 μM	3.0	2.1e19	0.89	0.85	0.87	2.1	1.1
21 μM	3.0	5.1e19	0.67	0.64	0.65	1.2	2.4
29 μM	3.0	8.2e19	0.57	0.55	0.56	1.4	8.6

Table 3–1. Network parameters for different actin concentrations

The stress-strain results correlate well with both the $12\mu\text{M}$ and $29\mu\text{M}$ data as shown in Figure 3–21b. The model also captures the experimental behavior for the entire range of applied shear stress as shown in the originally published log-log plot of tangent modulus vs. shear stress shown in Figure 3–21a. The good agreement between the model result and the data also indicates that there is relatively little bundling in these cases, and that the increasing stiffness with increasing c_{AF} is due to the change in network topology. The

good agreement in the high stress region, where strain stiffening occurs, is a benefit of using a network model that accounts for the non-affine deformation of a network, accommodating macroscopic deformation by rotation of filaments and a small amount of filament stretch.

Note that the network model results for the 21 μM case in Figure 3–21 exhibits the transition to nonlinear strain stiffening behavior by $\tau=0.2\text{Pa}$, consistent with the empirical trend exhibited by the other concentrations. The network model results for the 21 μM case also exhibit good agreement with the experimental tangent modulus-shear stress data in Figure 3–21a in both the low and high stress regions. The 21 μM shear stress-strain predictions of Figure 9b are in good agreement with the data up to a strain of 0.10, but exhibit a much stiffer behavior at larger strains. This is likely a direct result of the ambiguity of the 21 μM tangent modulus data in the transition region which is key to reconstructing the stress-strain curves.

3.5.4 Parametric evaluation of bundling effects

The network will also become stiffer with increasing persistence length. Filament bundling increases the persistence length of the “effective” bundled filament. At large values of R ($R=1$), the actin network behavior is dominated by thick bundles in contrast to almost no bundling observed at $R=0.03$ (Gardel et al., 2004a). Here, the ability of the proposed model to capture the stiffening effects of bundling is explored.

The bending stiffness of the bundle, and hence l_p , can be determined from the number of filaments per bundle (m). Filament bundles might be unbonded, partially bonded along the length, or fully bonded along the entire axial length of the filaments.

Next is an examination of the two limiting cases of “unbonded bundles” and fully “bonded bundles”. The stiffness of unbonded bundles will scale linearly with the number of filaments in the bundle. The stiffness of bonded bundles will scale by the ratio of the effective moments of inertia of the bonded geometry with that of the single filament; this scaling is determined by estimating the effective bonded bundle radius (R_{eff}).

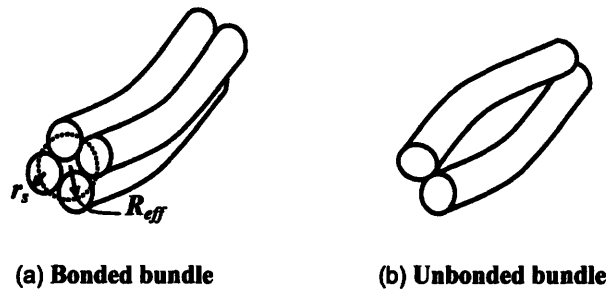


Figure 3–22. Filament bundling geometry with (a) bonded bundles and (b) unbonded bundles

For bundles with two adjacent filaments ($m=2$), the stiffness is simply twice the stiffness of an individual filament. For bundles with $m \geq 3$, the unbonded bundle stiffness will simply scale linearly with m . For bonded bundles with $m \geq 3$, the increase in R_{eff} , which leads to an increase in stiffness from bundling, is illustrated in Figure 3–22a (where r_s is the radius of a single fiber) and the effective radius required for an equivalent cross-sectional area is $R_{eff} = \sqrt{m} r_s$. Since the area moment of inertia of a solid cylinder is $I = (\pi R_{eff}^4)/4$, the ratio of increasing effective stiffness for bonded bundled filaments can be calculated as follows (with E as Young’s modulus):

$$\frac{l_{p,m}}{l_{p,s}} = \frac{\kappa_m}{\kappa_s} = \frac{(EI)_m}{(EI)_s} = \frac{(R_{eff})^4}{(r_s)^4} = m^2. \quad (3.28)$$

The results for scaling the persistence length of a single actin filament to obtain the effective persistence length, $l_{p,m}$, of a bonded bundle of m filaments are given in Figure 3–23. Table 3–2 contains the network parameters used for each case in Figure 3–23. Each actin network was taken to have an isotropic prestress set by assuming $\alpha=1\%$, but with the persistence length increasing for increasing numbers of bundled filaments. The contour length was calculated using Equation (3.27) with $d_{Actin}=7\text{nm}$ and $c_{AF}=7\mu\text{M}$, resulting in $L_c=2.04\mu\text{m}$.

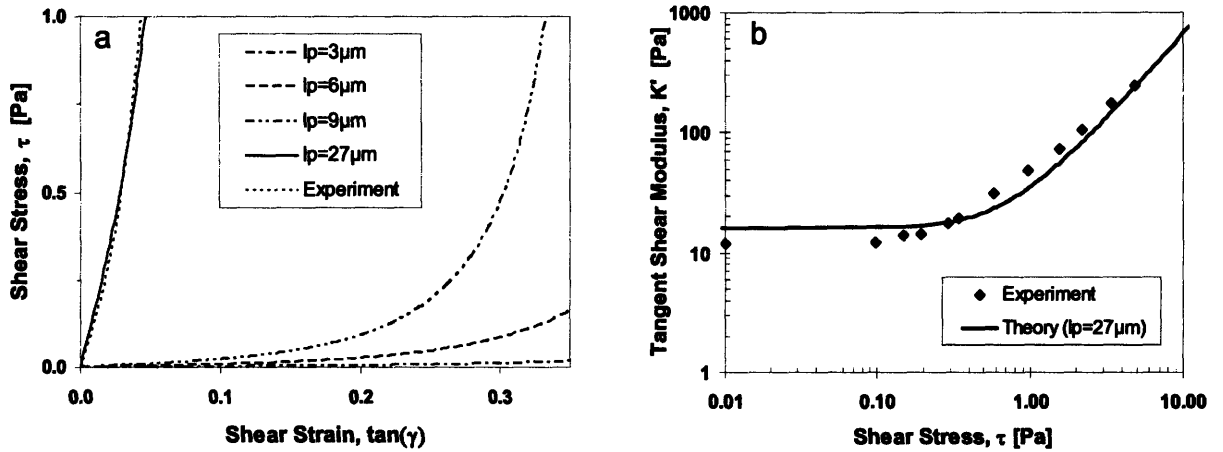


Figure 3–23. (a) Shear stress-shear strain response and (b) tangent shear modulus-shear stress response of bundled F-actin networks with varying persistence length ($R=0.5$, $c_{AF}=7\mu\text{M}$) (experimental data from (Gardel et al., 2004a))

m_{bonded} [#/bundle]	m_{unbonded} [#/bundle]	$l_{p,m}$ [μm]	$r_{F=0}$ [μm]	r_0 [μm]	α [%]	R	c_{AF} [μM]	L_c [μm]	n [m^{-3}]
1	1	3	1.81	1.83	1	0.5	7	2.04	$5.4\text{e}18$
2	2	6	1.92	1.94	1	0.5	7	2.04	$5.4\text{e}18$
--	3	9	1.96	1.98	1	0.5	7	2.04	$5.4\text{e}18$
3	9	27	2.01	2.03	1	0.5	7	2.04	$5.4\text{e}18$

Table 3–2. Network parameters for different amounts of filament bundling

The case of $l_p=6\mu\text{m}$ represents a bundle of two filaments while the case of $l_p=3^2 \times 3=27\mu\text{m}$ represents a bonded bundle of three filaments. The smallest stable

filament bonded bundle is assumed to consist of three filaments, and this case also exhibits excellent agreement with the experimental shear stress-strain data (Figure 3–23a) as well as the tangent shear modulus-stress data of Gardel, et al. (Figure 3–23b).

Alternatively, if the model assumes linear scaling of bending stiffness due to unbonded bundles (Figure 3–22b), then the same case ($R=0.5$, $c_{AF}=7\mu M$) with three filaments would exhibit reduced stiffness as shown by the $l_p=9\mu m$ curve in Figure 3–23a. Of course, the unbonded, bundled case matches the $R=0.5$ data equally as well if nine filaments are bundled instead of three ($l_p=9 \times 3=27\mu m$). This unbonded bundle of nine filaments would have an average diameter ($D_B \sim 30-40nm$ depending on spacing between filaments) on the order of the actin-scrutin bundle diameters observed by Shin, et al. (Shin et al., 2004) via confocal microscopy ($D_B \sim 20-65nm$ for $R=1$, with $D_B \sim R^{0.3}$). This would suggest that bundled actin fibers in the Gardel networks are only minimally bonded to each other for the case of $c_{AF}=7\mu M$, $R=0.5$.

3.5.5 Network stress-strain with linear filament force-extension

Here the network behavior obtained considering the constituent filaments to follow a linear force-extension behavior is compared with that obtained when the chains exhibit the nonlinear force-extension behavior as represented earlier with the MacKintosh model. This comparison will help highlight the source of nonlinearity in the network stress-strain behavior arising from the evolution in structure geometry due to chain rotation from that arising due to the nonlinearity of the filament behavior.

The force-extension relationship for the linear model is shown below, where k_{lin} is the linear stiffness of the filament.

$$F_{Linear} = k_{lin} \delta = k_{lin} (r - r_0) = k_{lin} r_0 (\lambda_c - 1) \quad (3.29)$$

Figure 3–24 compares the force—end-to-end distance and force—stretch behaviors of the MacKintosh and linear models using F-actin network properties (see Table 3–3 in the next section

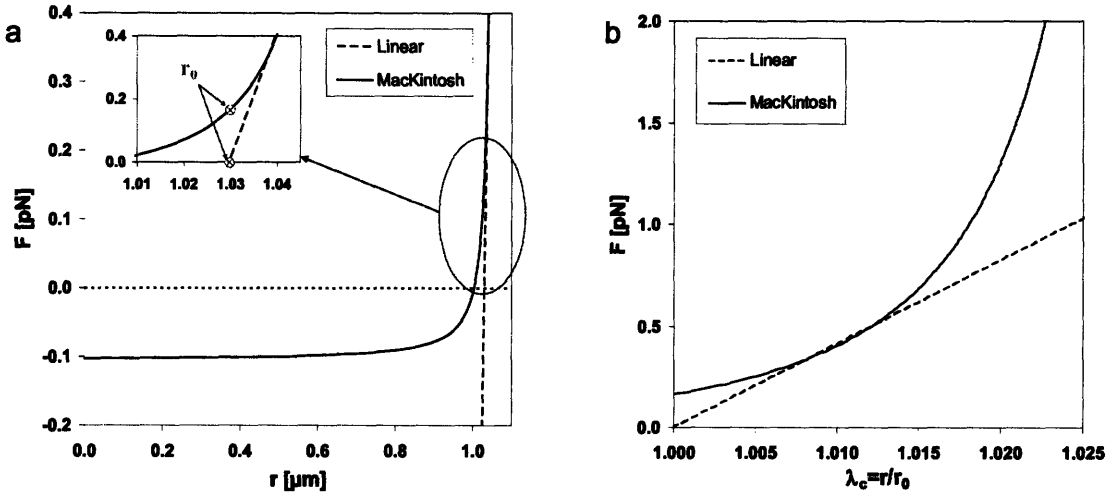


Figure 3–24. (a) Force vs. end-to-end distance and (b) force vs. chain stretch behavior of F-actin filaments using the linear and MacKintosh models

for values and discussion), with r_0 labeled for each model. Note in Figure 3–24b that MacKintosh response (with $r_0 > r_{F=0}$) leads to an automatic chain pretension at $r=r_0$ ($\lambda_c=1$).

The expressions for the strain energy density of the eight-filament cytoskeletal network models based on the linear and MacKintosh model are

$$U_{Linear} = nk_{lin} \left(\frac{r^2}{2} - rr_0 - c \right) \quad (3.30)$$

$$U_{Mac} = \frac{nk_B T}{l_p} \left[\frac{L_c}{4(1-r/L_c)} - l_p \left[\ln(L_c^2 - 2l_p L_c + 2l_p r) - \ln(r - L_c) \right] - c \right]$$

where c is a constant equal to the initial strain energy of the filament. Following the derivation of the Cauchy stress-strain relationship developed earlier for the MacKintosh model, the corresponding Cauchy shear stress-strain relationships for the three single filament models become

$$\tau_{Linear} = \frac{nk_{lin}r_0^2}{3} \left(1 - \frac{1}{\lambda_c}\right) \tan \gamma \quad (3.31)$$

$$\tau_{Mac}(r) = \frac{nk_B T}{3l_p} \frac{r_0}{\lambda_c} \left(\frac{1}{4(1-r/L_c)^2} \right) \left(\frac{L_c/l_p - 6(1-r/L_c)}{L_c/l_p - 2(1-r/L_c)} \right) \tan \gamma$$

3.5.5.1 Comparison with representative low concentration case

The models were evaluated by comparing to the data with the lowest actin concentration ($c_{AF} = 8\mu\text{M}$ and $R=0.03$) shown to exhibit network behavior (Gardel et al., 2004a). The parameters in Table 3–3 are used in the MacKintosh and linear network models.

	MACKINTOSH	LINEAR
n (filaments/ m^3)	1.2e19	1.2e19
Stiffness term	$l_p=3.0\mu\text{m}$	$k_{lin}=40\mu\text{N/m}$
L_c (μm)	1.07	1.07
r_0 (μm)	1.03	1.03
$r_{F=0}$ (μm)	1.00	1.03

Table 3–3. Network parameters and material properties MacKintosh, Linear models

The stiffness-related term (l_p or k_{lin}) and r_0 (via α) are chosen to best fit the models to the $8\mu\text{M}$ experimental data. The shear stress-strain results are shown in Figure 3–25a, with the tangent modulus-shear stress results shown in Figure 3–25b. If the linear stiffness is related to actin filament geometry as $k_{lin} = AE/L_c = (AEI)/(L_c I) = (16l_p k_B T)/(d_{AF}^2 L_c)$ with $d_{AF}=7\text{nm}$; then $l_p=0.03\mu\text{m}$ for the best overall fit shown in Figure 3–25a. This persistence

length value is two orders of magnitude lower than experimentally observed F-actin values ($l_p \sim 3\text{-}17\mu\text{m}$).

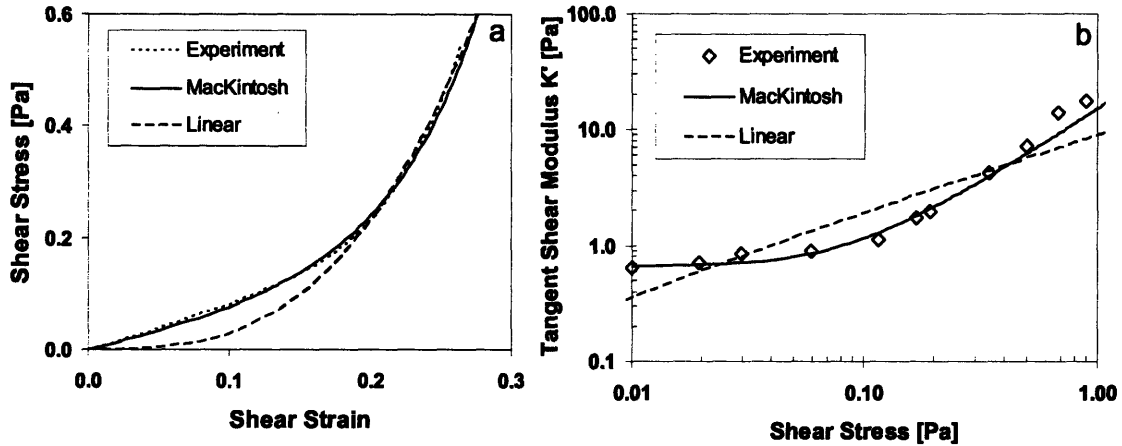


Figure 3–25. (a) Shear stress-strain and (b) tangent shear modulus-shear stress for *in vitro* F-actin networks ($c_{AF} = 8\mu\text{M}$, $R=0.03$). Experimental data from (Gardel et al., 2004a).

Note that the network with linear filaments exhibits a nonlinear network shear stress-shear strain behavior in Figure 3–25a due to the filament rotation effects (Arslan and Boyce, 2006). The linear model, however, captures neither the shear stress-strain nor the tangent modulus-stress behavior of the actin network, emphasizing the importance of using a nonlinear force-extension relationship for single F-actin filaments. The tangent modulus-stress response of the MacKintosh model, when used in an 8-chain network, closely matches the predictions given by Gardel, et al. (Gardel et al., 2004a), with a good fit at low stresses as well as in the strain stiffening region at higher stresses (Figure 3–25b). The 8-chain MacKintosh network model, because of its superior performance when compared to experimental data, was chosen for comparison with actin networks at varying concentrations.

3.5.6 Network model performance with varying persistence length

The network model's ability to fit experimental data over a range of persistence lengths is addressed in this section. There is a range of published values and testing methods for persistence lengths of *in vitro* actin filaments ($l_p \sim 3\text{--}17\mu\text{m}$). The model's behavior is compared for $l_p = 3, 10, 17\mu\text{m}$ ($c_{AF} = 8.33\mu\text{M}$, $R = 0.03$) by only varying L_c to obtain a best fit to the initial shear modulus (see Figure 3–26).

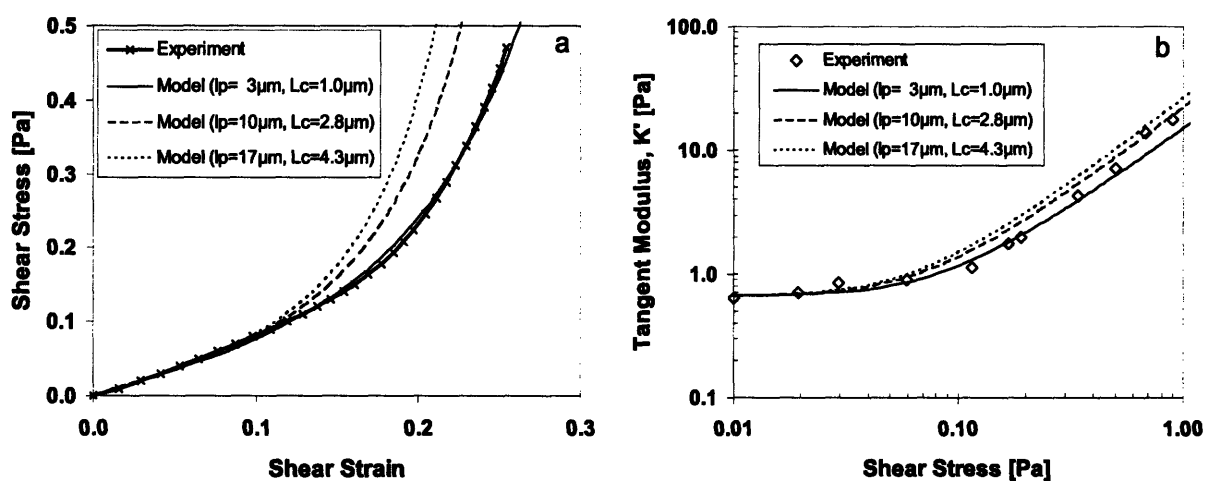


Figure 3–26. (a) Shear stress-shear strain and (b) tangent shear modulus-shear stress for *in vitro* F-actin networks over the range of published persistence lengths $l_p = 3, 10, 17\mu\text{m}$ ($c_{AF} = 8\mu\text{M}$, $R = 0.03$), vary L_c for best fit. Experimental data from (Gardel et al., 2004a).

In order to obtain a best fit to the data, an increase in the persistence length to $10\mu\text{m}$ or $17\mu\text{m}$ requires the contour length to be increased to $L_c = 2.8, 4.3\mu\text{m}$, respectively; both of which are beyond experimentally observed values (i.e. $L_c \sim 1\mu\text{m}$). Note that while the fit appears good in the tangent modulus-shear stress plot (with log-log axes) in Figure 3–26b, the shear stress-strain plot in Figure 3–26a reveals divergent behavior in the nonlinear strain stiffening region for larger persistence lengths. A better overall fit can be obtained by varying α as well as L_c as seen in Figure 3–27.

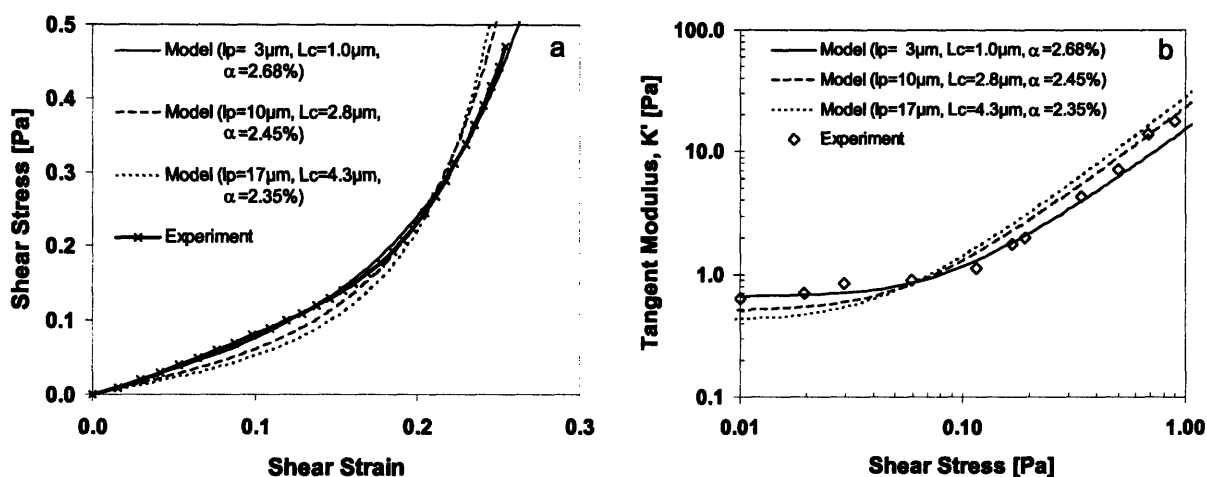


Figure 3–27. (a) Shear stress-shear strain and (b) tangent shear modulus-shear stress for *in vitro* F-actin networks over the range of published persistence lengths $l_p = 3, 10, 17\mu\text{m}$ ($c_{AF} = 8\mu\text{M}$, $R = 0.03$), vary L_c and α for best fit. Experimental data from (Gardel et al., 2004a).

Decreasing α while holding the contour lengths constant (from Figure 3–26) gives a better fit in the strain stiffening region at the expense of a poorer fit to the initial shear modulus. The model’s performance with higher persistence lengths, however, still does not achieve as good of a fit to the $8.33\mu\text{M}$ data as with the $l_p = 3\mu\text{m}$. The persistence length has a significant effect on the transition to the strain stiffening region as the bends in the filaments are straightened out, which enables a better fit of the more compliant actin-scrutin filaments with the lower value of l_p . Since the best fit was obtained with $l_p = 3\mu\text{m}$ and a realistic contour length of $L_c = 1.0\mu\text{m}$, these values were used for earlier comparisons.

3.6 Extensible 8-chain Network Model

The strain energy functions for entropic unbending and enthalpic stretching of a compressible material are given within the extensible model framework as

$$\begin{aligned}
 W_{comp}^u = & \frac{nk_B T}{l_p} \left[\frac{L_c}{4(1-r/L_c)} - l_p \left[\ln(L_c^2 - 2l_p L_c + 2l_p r) - \ln(r - L_c) \right] - c \right] \\
 & - \frac{nk_B T}{l_p} \left\{ \left[\frac{L_c}{4(1-r_0/L_c)^2} - \frac{1}{(1-r_0/L_c)(L_c/l_p - 2(1-r_0/L_c))} \right] \frac{r_0}{3} \ln J \right\} \\
 & + \frac{K_B}{2} (J-1)^2
 \end{aligned} \tag{3.32}$$

$$W_{comp}^s = \frac{nK_s}{2L_c} r_0^2 (\lambda_f^s - 1)^2 + \frac{K_B}{2} (J-1)^2. \tag{3.33}$$

Note that the right hand side of Equation (3.32) is equivalent to that of Equation (3.7).

The Cauchy stress for a compressible, extensible 8-chain MacKintosh network model is based on either of the strain energy density functions given in Equation (3.32) or Equation (3.33) due to force equilibrium between entropic unbending and enthalpic stretching. Choosing the enthalpic stretching strain energy density, and recalling that $f = \delta w / \delta r$, gives the Cauchy stress as

$$\begin{aligned}
 \mathbf{T} &= \frac{2}{J} \frac{\partial W}{\partial I_1} \mathbf{B} + \frac{\partial W}{\partial J} \mathbf{I} \\
 &= \frac{2}{J} \left(\frac{n \partial w}{\partial r} \frac{\partial r}{\partial \lambda_f} \frac{\partial \lambda_f}{\partial I_1} \right) \mathbf{B} + \frac{\partial W}{\partial J} \mathbf{I} = \frac{2}{J} \left((nf)(r_0) \left(\frac{1}{6\lambda_f} \right) \right) \mathbf{B} + \frac{\partial W}{\partial J} \mathbf{I} \\
 &= \frac{nr_0^2}{3\lambda_f J} \frac{K_s}{L_c} (\lambda_f^s - 1) \mathbf{B} + K_B (J-1) \mathbf{I}
 \end{aligned} \tag{3.34}$$

3.6.1 Implementation in finite element analysis

The Jacobian may now be specialized to the constitutive model for the extensible 8-chain MacKintosh network model. As before, the Jacobian (C) is found by solving for the derivative $\delta\mathbf{T}/\delta\mathbf{F}$,

$$\frac{\delta\mathbf{T}}{\delta\mathbf{F}} = \frac{nr_0^2 K_s}{3L_c} \left\{ \begin{array}{l} \frac{(\lambda_f^s - 1) \delta\lambda_f^{-1}}{J} \mathbf{B} + \frac{(\lambda_f^s - 1) \delta J^{-1}}{\lambda_f} \mathbf{B} \\ + \frac{1}{J\lambda_f} \frac{\delta\lambda_f^s}{\delta\mathbf{F}} \mathbf{B} + \frac{(\lambda_f^s - 1) \delta\mathbf{B}}{J\lambda_f} \end{array} \right\} + K_B \frac{\delta J}{\delta\mathbf{F}} \mathbf{I} \quad (3.35)$$

where the terms within Equation (3.35) are defined earlier except for

$$\frac{\delta\lambda_f^s}{\delta\mathbf{F}} = \frac{\delta(\lambda_f/\lambda_f^u)}{\delta\lambda_f} \frac{\delta\lambda_f}{\delta\mathbf{F}} = \frac{1}{\lambda_f^u} \frac{1}{3\lambda_f} \mathbf{F} = \frac{\lambda_f^s}{3\lambda_f^2} \mathbf{F}. \quad (3.36)$$

3.6.2 Evaluation of extensible network model behavior

The relative stretch contributions of the unbending and stretching in an extensible network subjected to simple shear deformation can be seen in Figure 3–28, using $K_s=40\text{nN}$ (used for other parametric comparisons in Chapter 2), and the following filament properties, $l_p=3.0\mu\text{m}$, $L_c=1.07\mu\text{m}$, that provided a best fit with the experimental data from Gardel, et al. (Gardel et al., 2004a).

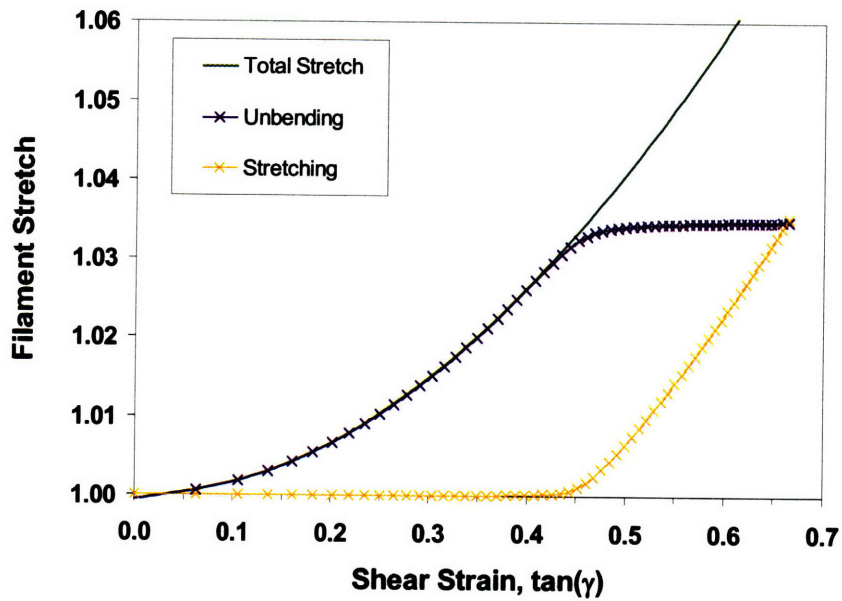


Figure 3–28. Stretch contributions from entropic unbending and enthalpic stretching in a network subjected to simple shear deformation

Note that the stretching energy does not contribute much to the overall filament stretch until a network shear strain of approximately $\tan(\gamma) \sim 0.4$, larger than the shear strain at failure for the actin-scrutin networks by Gardel, et al.. As before, the force in the filament, and now the shear stress in the network, can be calculated by recursively solving for λ_f^u and λ_f^s . The extensible network's shear stress-strain and shear stress-filament extension behaviors are shown in Figure 3–29 and compared to the inextensible entropic unbending model. Consistent with force comparisons, the inextensible and extensible models diverge as the average filament extension approaches the inextensible limit. At the inextensible limit ($r/L_c=1$) the inextensible model asymptotes to larger stress values as $r/L_c \rightarrow 1$, while beyond the limit the extensible model converges to a slope of K_s/L_c ,

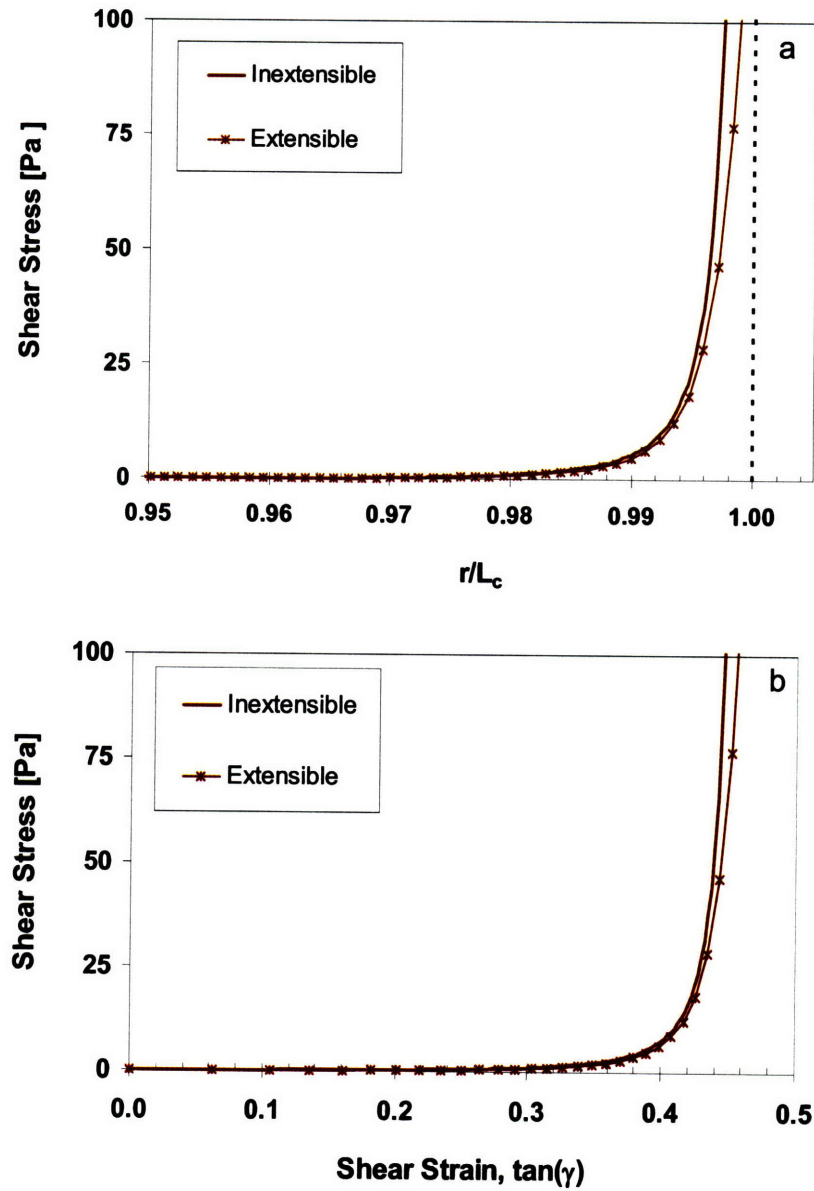


Figure 3–29. (a) Shear stress-strain and (b) shear stress-filament extension comparison of inextensible model and extensible model

The extensible model's response for varying persistence lengths (with a constant $K_s=40\text{nN}$) is included in Figure 3–30. The inextensible model's response for $l_p=3\mu\text{m}$ is also included for reference. As expected, the initial stiffness increases for both shear and normal behavior with larger values of l_p .

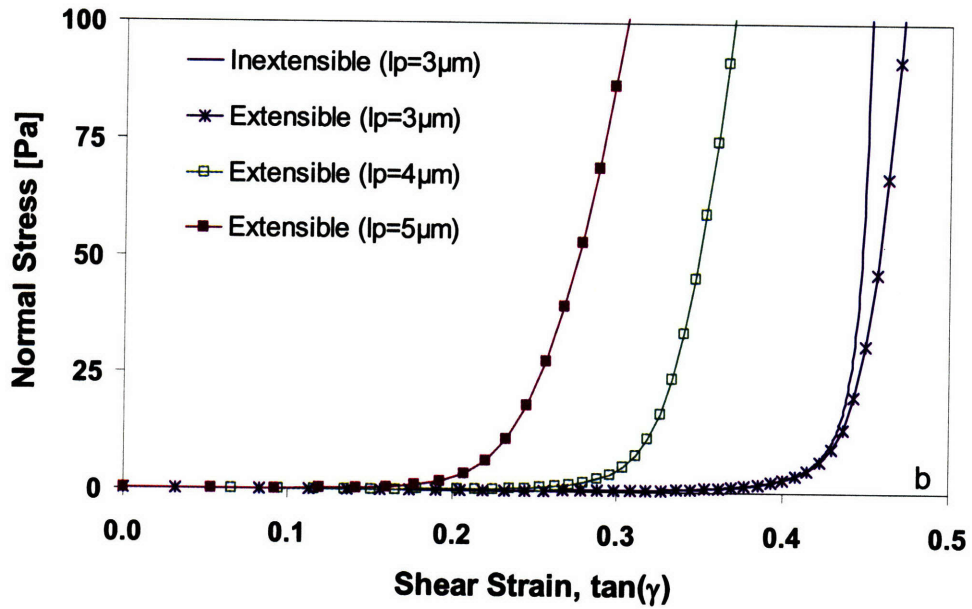
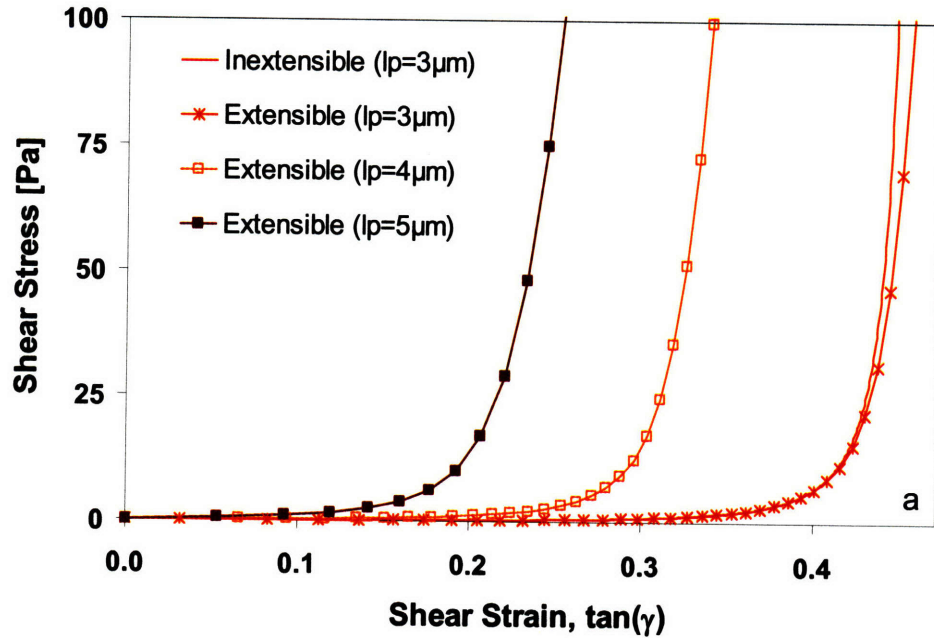


Figure 3–30. (a) Shear stress-shear strain and (b) Normal stress-shear strain comparison of inextensible model and extensible model with varying persistence lengths

3.7 Equilibrium swelling of cytoskeletal networks

Equilibrium swelling of elastomeric networks has been studied extensively within the rubber elasticity field (Flory and Rehner, 1943; Treloar, 1944; Flory, 1953; Treloar, 1975), and recently reviewed by Boyce and Arruda (Boyce and Arruda, 2001). A resurgence of interest in the thermodynamics and mechanics of swelling has been driven by investigations on the swelling of hydrogels (Horkay and McKenna, 1996; Dolbow et al., 2004; Dolbow et al., 2005; Hong et al., 2008), active polymers (Therkelsen, 2005), osmotic swelling of biological cells and tissues (Gu et al., 1997; Wilson et al., 2005b; Ateshian et al., 2006; Haider et al., 2006), and swelling as a contributor to cellular motility in lamellipodia (Oster et al., 1982; Oster and Odell, 1984; Oster and Perelson, 1985; Oster and Perelson., 1987) and amoeboid pseudopods (Dembo and Harlow, 1986; Zhu and Skalak, 1988; Herant et al., 2003; Herant and Dembo, 2006). This section will address the statistical mechanics model for equilibrium swelling following the approach of Boyce and Arruda (Boyce and Arruda, 2001) and Therkelsen (Therkelsen, 2005). This equilibrium model will be coupled with a kinetic law while addressing poroelastic behavior in networks. The poroviscoelastic and swelling models will establish the framework to capture part of the cytoplasm's dynamic response during migrational processes such as extension and translocation as well as during other amoeboid processes such as blebbing.

3.7.1 Kinematics of equilibrium swelling

Swelling in networks incorporates an internal balance of network tensile stress and osmotic/swelling pressure from an influx of solvent molecules. This balance of internal stress and isotropic pressure results in zero macroscopic stress for a traction-free network. The mechanical response of the cytoskeletal network due to the resultant localized swelling of the cytoplasm will be captured using a constitutive model employing multiplicative decomposition of mechanical and swelling stretches (see Figure 3–31).

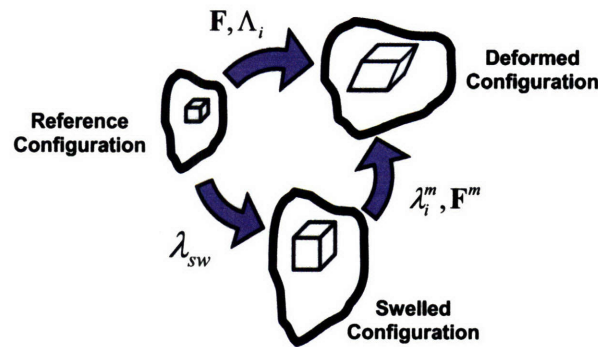


Figure 3–31. Swelling decomposition [adapted from (Therkelsen, 2005)]

In Figure 3–31, the principal values of total stretch (Λ_i) are defined as

$$\Lambda_i = \lambda_i^m \lambda_{sw} \quad (3.37)$$

where λ_i^m are principal values of the mechanical stretch and λ_{sw} is the isotropic swelling stretch. The deformation gradient (\mathbf{F}) can be multiplicatively decomposed into mechanical and swelling gradients,

$$\mathbf{F} = \mathbf{F}^m \mathbf{\Lambda}_{sw} \quad (3.38)$$

where the swelling stretch tensor is $\Lambda_{sw} = \lambda_{sw} \mathbf{I}$ and \mathbf{F}^m is the mechanical deformation gradient (Boyce and Arruda, 2001; Therkelsen, 2005). The swelling, mechanical, and total volume ratios are defined, respectively, as

$$J_{sw} = \frac{V_{sw}}{V_0} = \lambda_{sw}^3 \quad (3.39)$$

$$J_m = \frac{V}{V_{sw}} = \det(\mathbf{F}^m) = \lambda_1^m \lambda_2^m \lambda_3^m \quad (3.40)$$

$$J_T = \frac{V}{V_0} = \det(\mathbf{F}) = \Lambda_1 \Lambda_2 \Lambda_3 = \lambda_{sw}^3 \lambda_1^m \lambda_2^m \lambda_3^m = J_{sw} J_m. \quad (3.41)$$

The volume fraction of the polymer with respect to the dry state can then be defined

$$v_p = \frac{1}{\lambda_{sw}^3} = \frac{1}{J_{sw}} \quad (3.42)$$

or, alternatively, as $\lambda_{sw} = (v_p)^{-1/3}$. The mechanical left Cauchy-Green strain tensor is

$$\mathbf{B}^m = \mathbf{F}^m \mathbf{F}^{mT}. \quad (3.43)$$

The mechanical left Cauchy-Green tensor can be related to the total left Cauchy-Green tensor by

$$\begin{aligned} \mathbf{B}^m &= \mathbf{F}^m \mathbf{F}^{mT} = \mathbf{F} \Lambda_{sw}^{-1} (\mathbf{F} \Lambda_{sw}^{-1})^T = \mathbf{F} \Lambda_{sw}^{-1} \Lambda_{sw}^{-T} \mathbf{F}^T \\ &= \mathbf{F} \Lambda_{sw}^{-2} \mathbf{F}^T = \mathbf{F} (\lambda_{sw}^{-2} \mathbf{I}) \mathbf{F}^T = \lambda_{sw}^{-2} \mathbf{F} \mathbf{F}^T, \\ &= \lambda_{sw}^{-2} \mathbf{B} = v_p^{2/3} \mathbf{B} \end{aligned} \quad (3.44)$$

The total and mechanical stretch invariants are then given by

$$I_1 = \text{trace}(\mathbf{B}) = \Lambda_1^2 + \Lambda_2^2 + \Lambda_3^2, \quad (3.45)$$

$$I_2 = \frac{1}{2} \left((\text{trace}(\mathbf{B}))^2 - \text{trace}(\mathbf{B}^2) \right) = \Lambda_1^2 \Lambda_2^2 + \Lambda_2^2 \Lambda_3^2 + \Lambda_1^2 \Lambda_3^2, \quad (3.46)$$

$$I_3 = \det(\mathbf{B}) = \Lambda_1^2 \Lambda_2^2 \Lambda_3^2, \quad (3.47)$$

and

$$I_1^m = \text{trace}(\mathbf{B}^m) = \lambda_1^{m^2} + \lambda_2^{m^2} + \lambda_3^{m^2}, \quad (3.48)$$

$$I_2^m = \frac{1}{2} \left((\text{trace} \mathbf{B}^m)^2 - \text{trace}(\mathbf{B}^{m^2}) \right) = \lambda_1^{m^2} \lambda_2^{m^2} + \lambda_2^{m^2} \lambda_3^{m^2} + \lambda_1^{m^2} \lambda_3^{m^2}, \quad (3.49)$$

$$I_3^m = \det(\mathbf{B}^m) = \lambda_1^{m^2} \lambda_2^{m^2} \lambda_3^{m^2}, \quad (3.50)$$

3.7.2 Thermodynamics, constitutive equations for equilibrium swelling

Swelling phenomena on a microscopic scale are governed by the statistical thermodynamics of the constituents. For swelling of polymer networks, the driving force for the swelling is the entropy of mixing, where entropy is maximized through the creation of a uniform mixture (Therkelsen, 2005). If the two mixing constituents are gas particles, the total entropy change from an unmixed state to a completely mixed state is given by the entropy of mixing (Flory, 1953),

$$\Delta S_M = -k_B (n_1 \ln v_1 + n_2 \ln v_2), \quad (3.51)$$

where $v_i = n_i / (n_1 + n_2)$ is the number fraction of the i^{th} constituent (or volume fraction if the constituents are the same size). Unlike mixing gases, a polymer gel is constrained from freely interchanging particles during mixing. Using Flory's assumption of long chain molecules composed of "x" segments that are equal in size to the solvent molecules (Flory, 1969), we can consider the polymer-solvent mixture to be equivalent to the mixture of ideal gases. An increase in intermolecular forces between the polymer chains accompanies the influx of solvent molecules. In equilibrium, the increase in entropy from mixing is equal to the entropy lost from polymer chain stretch, thereby preventing further fluid intake (Therkelsen, 2005). Thus, the osmotic pressure of the solvent is

balanced by the tension within the stretching chains. The total change in entropy for the system is the sum of the entropy change from mixing ($\Delta S'_M$) and the configurational entropy lost from chain stretching during swelling ($\Delta S'_{sw}$)

$$\Delta S'_{total} = \Delta S'_{sw} + \Delta S'_M, \quad (3.52)$$

where the prime on $\Delta S'$ denotes that the entropy change is per unit unswollen volume.

The mixing entropy, per unit reference volume (V_2), is then

$$\Delta S'_M = \frac{-k_B(n_1 \ln v_1 + n_2 \ln v_2)}{V_2}, \quad (3.53)$$

where n_1 and v_1 are the number and volume fraction of solute molecules and n_2 and v_2 are the number and volume fraction of polymer segments (assuming each chain segment is equal in size to a solvent molecule). Assuming that the chain segments occupy the same volume as the unmixed solvent, there must be an equal number of solute molecules per unit reference volume (n_1/V_2) as there are chain segments per unit reference volume (n_2/V_2), which leads to the reduced form of the mixing entropy per unit unswollen volume,

$$\Delta S'_M = -k_B x N_c ((J-1) \ln(1-v_p) + \ln v_p), \quad (3.54)$$

where $v_1=1-v_p$, $n_2/V_2=xN_c$ and $n_1/V_2=xN_c(J-1)$ with x =number of solute sized chain segments, and N_c =number of chain molecules per unit reference volume (Therkelsen, 2005).

Assuming that the swelling process has occurred slowly enough to reach an equilibrium state, the next step is to apply a mechanical stretch to the swollen polymer. The entropy change due to mechanical stretching from the swollen state (*but with respect to the unswollen state*) is given by

$$\Delta S' = \Delta S'_{total} - \Delta S'_{sw}. \quad (3.55)$$

For the inextensible network model, $\Delta S'_{total}$ is given by

$$\Delta S'_{total} = \frac{nk_B}{l_p} \left[\frac{\frac{L_c}{4(1-\Lambda_c r_0/L_c)} - l_p [\ln(L_c^2 - 2l_p L_c + 2l_p \Lambda_c r_0) - \ln(\Lambda_c r_0 - L_c)]}{-\frac{r_0}{3} \left(\frac{1}{4(1-r_0/L_c)^2} - \frac{1}{(1-r_0/L_c)(L_c/l_p - 2(1-r_0/L_c))} \right)} \right] \ln J_T - c, \quad (3.56)$$

and $\Delta S'_{sw}$ is found by replacing the total stretch (Λ_c) with the swelling stretch (λ_{sw}),

$$\Delta S'_{sw} = \frac{nk_B}{l_p} \left[\frac{\frac{L_c}{4(1-\lambda_{sw} r_0/L_c)} - l_p [\ln(L_c^2 - 2l_p L_c + 2l_p \lambda_{sw} r_0) - \ln(\lambda_{sw} r_0 - L_c)]}{-\frac{r_0}{3} \left(\frac{1}{4(1-r_0/L_c)^2} - \frac{1}{(1-r_0/L_c)(L_c/l_p - 2(1-r_0/L_c))} \right)} \right] \ln J_{sw} - c. \quad (3.57)$$

The change in entropy due to mechanical stretching from the swollen state (per unit swollen volume) is calculated as

$$\Delta S = \Delta S' \frac{V_0}{V_{sw}} = \Delta S' v_p = \frac{\Delta S'}{\lambda_{sw}^3}. \quad (3.58)$$

The elastic stress of the polymer network must balance the osmotic pressure in the absence of surface tractions or body forces. Thus, there is no contribution to the strain energy density from volume change due to swelling (Therkelsen, 2005). The strain energy per unit swollen volume for a compressible network can therefore be given as

$$W = \frac{\nu_p n k_B T}{l_p} \left[\frac{\frac{L_c}{4 \left(1 - \frac{\Lambda_c r_0}{L_c}\right)} - l_p \left[\ln(L_c^2 - 2l_p L_c + 2l_p \Lambda_c r_0) - \ln(\Lambda_c r_0 - L_c) \right]}{\frac{L_c}{4 \left(1 - \frac{\lambda_{sw} r_0}{L_c}\right)} - l_p \left[\ln(L_c^2 - 2l_p L_c + 2l_p \lambda_{sw} r_0) - \ln(\lambda_{sw} r_0 - L_c) \right]} + K_B (J_m - 1)^2, \right. \\ \left. \frac{r_0}{3} \left(\frac{1}{4(1-r_0/L_c)^2} - \frac{1}{(1-r_0/L_c)(L_c/l_p - 2(1-r_0/L_c))} \right) \ln J_m \right] \quad (3.59)$$

noting that $\ln(J_T) - \ln(J_{sw}) = \ln(J_m)$. The network stress represents the network tension balanced by the osmotic pressure from swelling, combined with a mechanical deformation. The Cauchy stress is given by

$$\mathbf{T} = \frac{2}{J_T} \frac{\partial W}{\partial I_1} \mathbf{B} + \frac{\partial W}{\partial J_T} \mathbf{I} \\ = \frac{n r_0 k_B T}{3 \lambda_{sw}^3 J_T l_p} \left\{ \frac{1}{\Lambda_c} \left[\left(\frac{1}{4(1-\Lambda_c r_0/L_c)^2} \right) \left(\frac{L_c/l_p - 6(1-\Lambda_c r_0/L_c)}{L_c/l_p - 2(1-\Lambda_c r_0/L_c)} \right) \right] \mathbf{B} \right. \\ \left. - \left[\left(\frac{1}{4(1-r_0/L_c)^2} \right) \left(\frac{L_c/l_p - 6(1-r_0/L_c)}{L_c/l_p - 2(1-r_0/L_c)} \right) \right] \mathbf{I} \right\} + K_B (J_m - 1) \mathbf{I} \quad (3.60)$$

The compressible Cauchy stress for the extensible network model may similarly be given as

$$\mathbf{T} = \frac{n r_0^2}{3 \lambda_{sw}^3 \Lambda_c J_T L_c} K_s (\lambda_f^s - 1) \mathbf{B} + K_B (J_m - 1) \mathbf{I}. \quad (3.61)$$

3.7.3 Implementation in finite element analysis

The constitutive model is incorporated in the ABAQUS finite element software (Simulia Dassault Systèmes, Providence, RI, USA) using the previously defined user

subroutine (UMAT), which defines a material's mechanical behavior through the 4th order Jacobian tensor (C) and 2nd order Cauchy (true) stress (T) at the end of each increment. The user may wish to calculate the constitutive equations in terms of the mechanical deformation gradient (F^m). The total deformation gradient (F), however, is input into the UMAT subroutine, and may be transformed to F^m using the multiplicative swelling decomposition developed earlier,

$$\mathbf{F}^m = \mathbf{F}(\Lambda_{sw})^{-1}, \quad (3.62)$$

$$(\Lambda_{sw})^{-1} = (1/\lambda_{sw}) \mathbf{I}. \quad (3.63)$$

The compressible Cauchy stress for the extensible network model can be given in terms of F^m, λ_{sw}, and J_m=det(F^m),

$$\begin{aligned} \mathbf{T} &= \frac{nr_0^2}{3\lambda_{sw}^3 \Lambda_f J_T} \frac{K_s}{L_c} (\lambda_f^s - 1) \mathbf{B} + K_B (J_m - 1) \mathbf{I} \\ &= \frac{nr_0^2}{3\lambda_{sw}^3 (\lambda_{sw} \lambda_f^m) (\lambda_{sw}^3 J_m)} \frac{K_s}{L_c} (\lambda_f^s - 1) \lambda_{sw}^2 \mathbf{B}^m + K_B (J_m - 1) \mathbf{I}. \\ &= \frac{nr_0^2}{3\lambda_f^m \lambda_{sw}^5 J_m} \frac{K_s}{L_c} (\lambda_f^s - 1) \mathbf{B}^m + K_B (J_m - 1) \mathbf{I} \end{aligned} \quad (3.64)$$

The 4th order Jacobian tensor (C) is calculated as defined in Sections 3.2 and 3.6, while recognizing that the volume ratio and filament stretch are replaced with their swelling counterparts: J → J_T, λ_f → Λ_c. The Jacobian (C) is found for the inextensible model by

$$\frac{\delta \mathbf{T}}{\delta \mathbf{F}} = \frac{nr_0 k_B T}{3\lambda_{sw}^3 J_T l_p} \left\{ \frac{-1}{J_T^2} \frac{\delta J_T}{\delta \mathbf{F}} (\zeta \mathbf{B} - \zeta \mathbf{I}) + \frac{1}{J_T} \left(\zeta \frac{\delta \mathbf{B}}{\delta \mathbf{F}} \right) + \frac{1}{J_T} \left(\frac{\delta \zeta}{\delta \mathbf{F}} \mathbf{B} \right) \right\} + \frac{K_B}{\lambda_{sw}^3} \frac{\delta J_T}{\delta \mathbf{F}} \mathbf{I} \quad (3.65)$$

where the terms within Equation (3.65) are defined in Section 3.2. The Jacobian (C) is found for the extensible model using

$$\frac{\delta \Gamma}{\delta \mathbf{F}} = \frac{nr_0^2 K_s}{3\lambda_{sw}^3 L_c} \left\{ \begin{array}{l} \left(\frac{(\lambda_f^s - 1)}{J_T} \frac{\delta \lambda_f^{-1}}{\delta \mathbf{F}} \mathbf{B} + \frac{(\lambda_f^s - 1)}{\lambda_f} \frac{\delta J_T^{-1}}{\delta \mathbf{F}} \mathbf{B} \right) \\ + \frac{1}{J_T \lambda_f} \frac{\delta \lambda_f^s}{\delta \mathbf{F}} \mathbf{B} + \frac{(\lambda_f^s - 1)}{J_T \lambda_f} \frac{\delta \mathbf{B}}{\delta \mathbf{F}} \end{array} \right\} + \frac{K_B}{\lambda_{sw}^3} \frac{\delta J_T}{\delta \mathbf{F}} \mathbf{I} \quad (3.66)$$

where the terms within Equation(3.66) are defined in Section 3.6.

3.7.4 Swelling of actin networks in a spherical geometry

The 3D cytoskeletal network model with equilibrium swelling is now included within a spherical finite element model. The spherical model is first evaluated by observing the swelling experienced in the absence of viscoelastic or poroelastic effects. The spherical structure is evaluated with uniform properties throughout the volume (i.e. a 6 μm diameter sphere composed only of an actin gel with a concentration of $c_{AF} = 170\mu\text{M}$). The axisymmetric model is fixed at its center and is not subject to external tractions or body forces, allowing stress-free swelling to occur in the radial direction. Figure 3–32 shows the boundary conditions for uniform, spherical actin gel as well as the radial displacement from a swelling stretch of $\lambda_{sw}=1.1$.

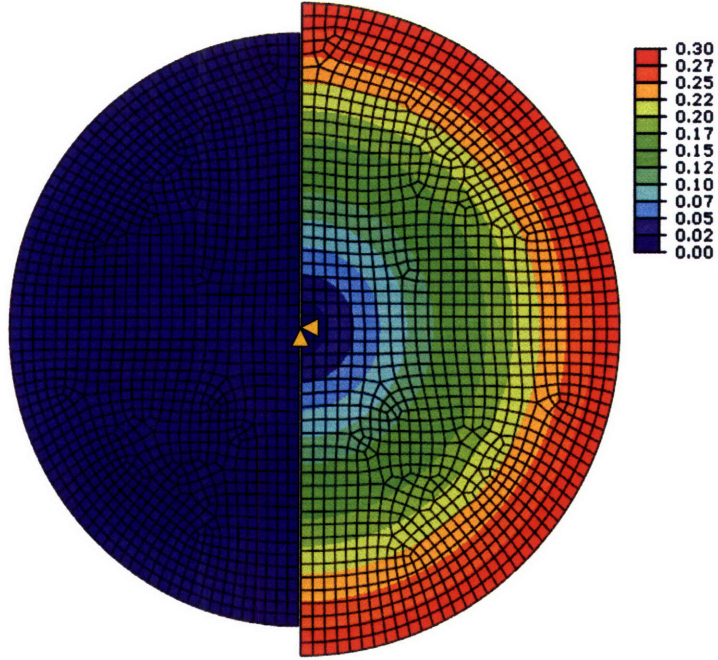


Figure 3–32. (a) Undeformed axisymmetric mesh and (b) Radial expansion in a swelled sphere ($\lambda_{sw}=1.1$) held fixed at its center. $6\mu\text{m}$ diameter sphere consists of an actin network ($c_{AF}=170\mu\text{M}$, $L_c=0.9\mu\text{m}$, $l_p=3\mu\text{m}$, $\alpha=1.1\%$).

After the first step of swelling, the spherical actin gel is now subjected to a second step in which the cell is compressed between two plates. The final vertical distance between the two plates is equal to the original, unswelled, diameter of the actin sphere. The increasing reaction forces on the plates for increasing swelling stretch ratios of $\lambda_{sw}=1.02, 1.03, 1.04,$ and 1.05 are shown in Figure 3–33a. Figure 3–33b also shows the contour plot of normal strain in the vertical, 2-direction after the sphere is compressed back to its original diameter. The corresponding normal stresses in the 2-direction for the four swelling cases are shown in the contour plots of Figure 3–34. Note that while the spatial distribution of stresses is essentially equivalent for all four swelling cases, the

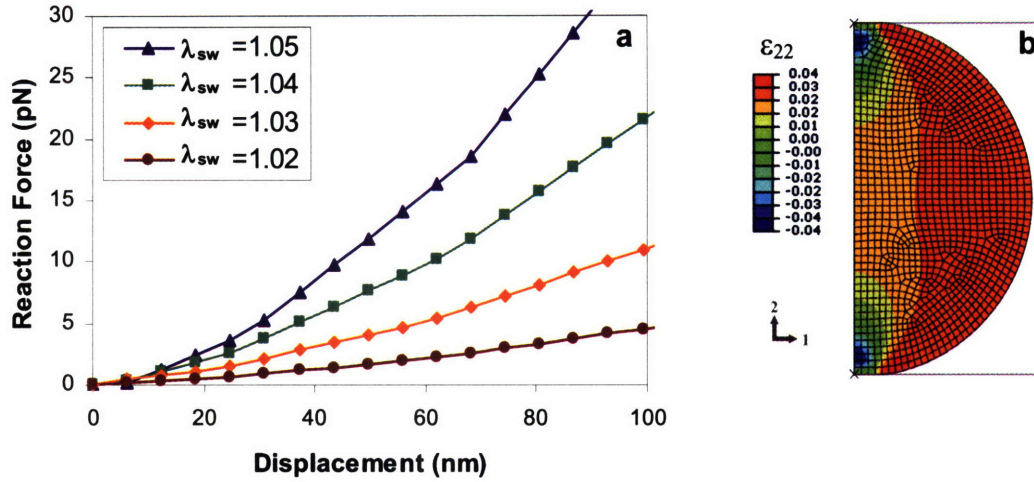


Figure 3–33. (a) Reaction forces on plates compressing a swelled sphere ($\lambda_{sw} = 1.02, 1.03, 1.04, 1.05$). The $6\mu\text{m}$ diameter sphere consists of an actin network ($c_{AF}=170\mu\text{M}, L_c=0.9\mu\text{m}, l_p=3\mu\text{m}, \alpha=1.1\%$). (b) Contour plot of normal strain in 2-direction.

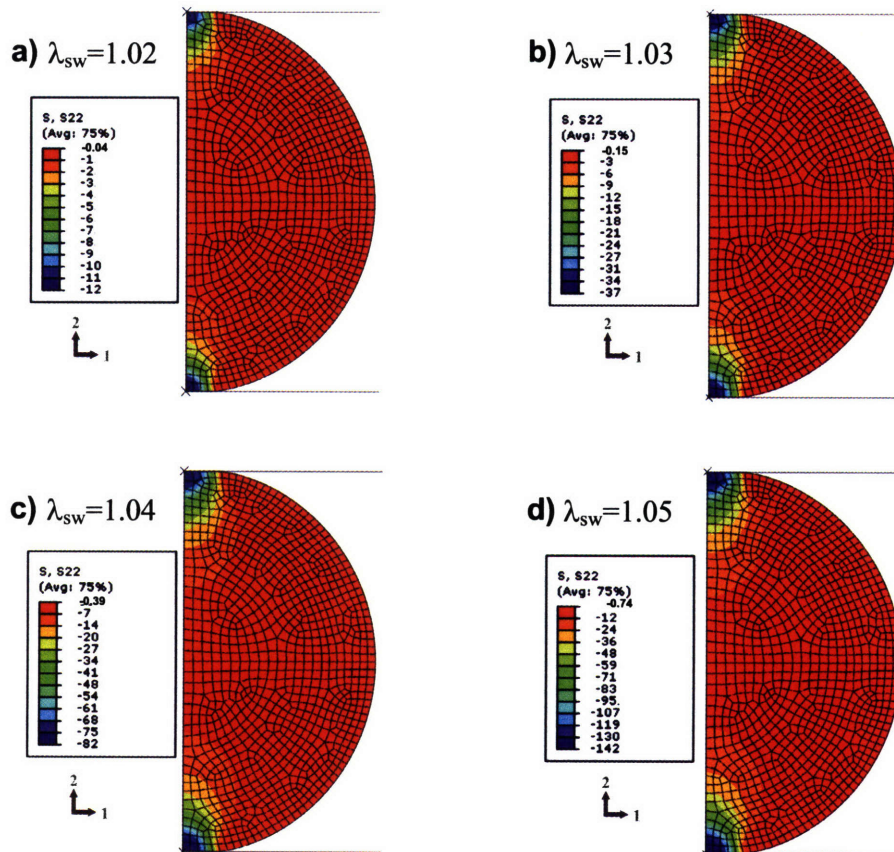


Figure 3–34. Contour plots of normal stress in 2-direction from plates compressing a swelled sphere: (a) $\lambda_{sw}=1.02$, (b) $\lambda_{sw}=1.03$, (c) $\lambda_{sw}=1.04$, (d) $\lambda_{sw}=1.05$. The $6\mu\text{m}$ diameter sphere consists of an actin network ($c_{AF}=170\mu\text{M}, L_c=0.9\mu\text{m}, l_p=3\mu\text{m}, \alpha=1.1\%$). Stress units are Pascals.

magnitude of the compressive normal stresses varies significantly. For example, the maximum compressive stress for $\lambda_{sw}=1.02$ ($\sigma_{22}=-12\text{Pa}$ in Figure 3–34a) is more than an order of magnitude smaller than the maximum compressive stress for $\lambda_{sw}=1.05$ ($\sigma_{22}=-142\text{Pa}$ in Figure 3–34d).

The same simulation is now conducted with a swollen, spherical neo-Hookean solid compressed between two plates. The final vertical distance between the two plates is once again equal to the original, unswollen, diameter of the neo-Hookean sphere. The constant shear modulus for the nearly incompressible neo-Hookean material was chosen to match the initial shear modulus of the actin gel ($G=13.5\text{Pa}$). Of course, the neo-Hookean solid does not exhibit the nonlinear strain stiffening behavior exhibited by the actin gel, and the resulting reaction forces on the plates for the neo-Hookean solid decrease with increasing swelling stretch ratios as shown in Figure 3–35a. Figure 3–35b also shows the contour plot of normal strain in the vertical, 2-direction after the sphere is compressed back to its original diameter. The corresponding normal stresses in the 2-direction for the four swelling cases are shown in the contour plots of Figure 3–36. The spatial distributions of stresses are very similar for all four swelling cases, and the magnitude of the compressive normal stresses, like the reaction forces, is much lower than those for the actin gel and do not exhibit a large difference across the range of swelling stretches. The maximum compressive stress for $\lambda_{sw}=1.02$ ($\sigma_{22}=-4.2\text{Pa}$ in Figure 3–36a), for example, is only 40% less than the maximum compressive stress for $\lambda_{sw}=1.05$ ($\sigma_{22}=-6.8\text{Pa}$ in Figure 3–36d).

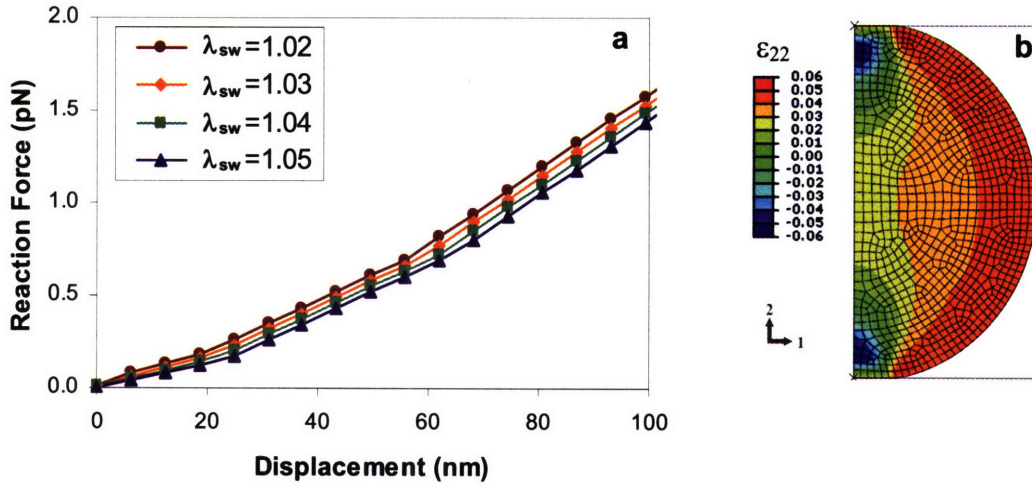


Figure 3–35. (a) Reaction forces on plates compressing a swelled sphere ($\lambda_{sw} = 1.02, 1.03, 1.04, 1.05$). The $6\mu\text{m}$ diameter sphere consists of a nearly incompressible neo-Hookean solid ($G=13.5\text{Pa}$). (b) Contour plot of normal strain in 2-direction.

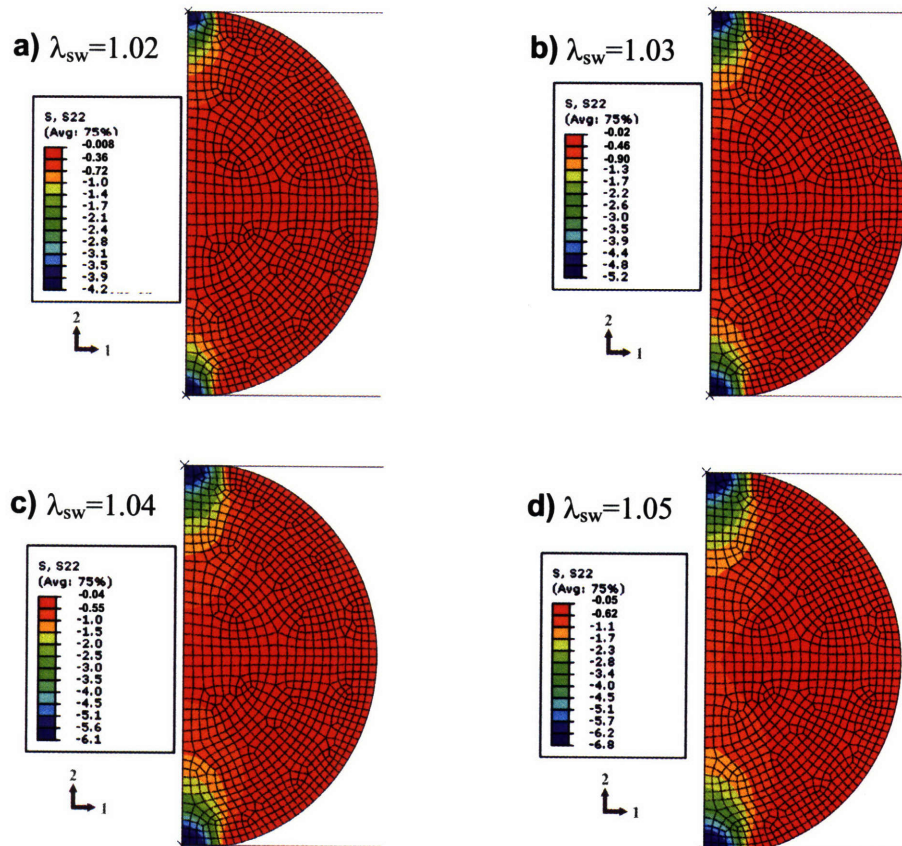


Figure 3–36. Contour plots of normal stress in 2-direction from plates compressing a swelled sphere: (a) $\lambda_{sw}=1.02$, (b) $\lambda_{sw}=1.03$, (c) $\lambda_{sw}=1.04$, (d) $\lambda_{sw}=1.05$. The $6\mu\text{m}$ diameter sphere consists of a nearly incompressible neo-Hookean solid ($G=13.5\text{Pa}$). Stress units are Pascals.

Although the previous swelling simulation of actin networks was not intended as an example of cell propulsion, it is interesting to note that swelling of cortical actin networks ($c_{AF} = 100\text{-}200\mu\text{M}$) can produce forces of the same order of magnitude as the viscous drag forces which oppose cellular motion [e.g. $f_D \sim 20$ pN for *Listeria* at a velocity of 100 nm/s (Mogilner and Oster, 1996), which is also roughly equivalent to actin polymerization velocity (Theriot et al., 1992)]. This suggests that localized swelling of actin networks is capable of providing the forces required to contribute to cellular processes involved with cell motility. The network swelling model will be coupled with the poroelastic network model in Chapter 6 in order to begin to evaluate their combined contribution to cellular motility.

CHAPTER 4 Influence of network cross-links

4.1 Cross-link types, roles, and geometries

The different types of cross-linking proteins were introduced in Chapter 1 as the mechanical link to enable naturally occurring bundled and cross-linked network morphologies that are necessary for normal cellular functions (structural stability, mechanotransduction, etc.) as well as providing the ability to actively rearrange the cytoskeletal microstructure in response to mechanical stimuli. Intra-network cross-links (e.g. actin binding proteins/ABPs) and inter-network cross-linking proteins (e.g. MACF) bind to the network filaments at different angles and with varying stiffness depending on their structural role. For example, fimbrin is a monomer that binds actin in a tight parallel bundle (14 nm diameter), while α -actinin is a dimer that binds actin looser than fimbrin (Lodish et al., 2004). Spectrin is a tetramer that binds actin in a loose parallel arrangement in the cortex; and filamin-a (FLNa) is a dimer that crosslinks actin filaments at almost right angles to each other (Lodish et al., 2004). Table 4–1 contains a sampling of the structural binding proteins of actin and some key properties.

<i>Name</i>	<i>Shape</i>	<i>Molecular Weight</i>	<i>Common Location</i>	<i>Comments</i>
α -actinin	30 nm anti-parallel overlapping dimeric rod	100 kDa	Loose bundles in cells	
Arp2/3	10 × 15 nm ellipsoid	225 kDa	Cell cortex branches, bacterial “comet tails”	
Dystrophin	150 nm rod	430 kDa	Near muscle cell membranes	
Fascin	5 nm globular monomer	55 kDa	Tight bundles within membrane protrusions	
Filamin	160 nm V-shaped dimer	560 kDa (dimer)	3-D large-angle junctions throughout cells	
Fimbrin	14 nm rod	20 kDa	Tight bundles in cells	
Fodrin	200 nm anti-parallel overlapping tetrameric rod	240 kDa	(monomer)	2-D large-angle junctions near membrane
Scruin	10 nm rod	120 kDa	Tight bundles in sperm acrosomes	Coats actin in perpendicular fashion; scruin cross-links by binding to each other, not multiple F-actin
Spectrin	200 nm anti-parallel overlapping tetrameric rod	930 kDa (tetramer)	2-D large-angle junctions near membranes	In erythrocytes
Titin	1000 nm rod	3000 kDa	Muscle sarcomeres	Largest known protein
Villin	10 nm rod	95 kDa	Tight bundles in microvilli	Related to gelsolin

Table 4–1. Structural binding proteins of actin and their properties (Hartemink, 2005)

Figure 4–1 shows the different actin network morphologies possible with different ABP (FLNa, α -actinin) under identical preparation conditions. Although the geometrical (and some mechanical properties) of the cross-linking proteins are generally known, their impact on the coupled response of filament networks under different loading conditions is not as well understood. Recent work by Bathe, et al. has evaluated the stretching, bending, and inter-filament shearing of actin bundles through simulation of the ABP using internal energy-based linear elastic springs (Bathe et al., 2008). Exploring and quantifying these effects is a key component in understanding the overall cytoskeletal

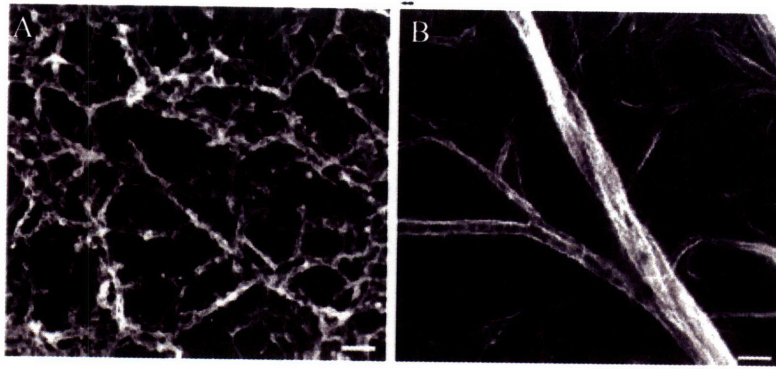


Figure 4–1. (A) Orthogonal actin network polymerized in presence of FLNa (B) Identically prepared actin network/bundles except polymerized with α -actinin. Bars, 100 nm. (Stossel et al., 2001)

behavior. The work in this chapter focuses on role of cross-linking proteins in isotropic actin networks. The effects of bundling proteins were addressed in Chapter 3 for actin-scrutin networks.

This section will expand the constitutive model for cytoskeletal networks through torsional potentials to include the strain energy for compliant intra-network cross-links (e.g. ABPs such as FLNa and avidin). Filamin, the most common ABP within actin networks, is critical to cellular functions such as motility and membrane morphology (Cunningham et al., 1992; Cunningham, 1995) as well as human embryo development (Fox et al., 1998). A schematic of an actin-FLNa network is shown in Figure 4–2a. The

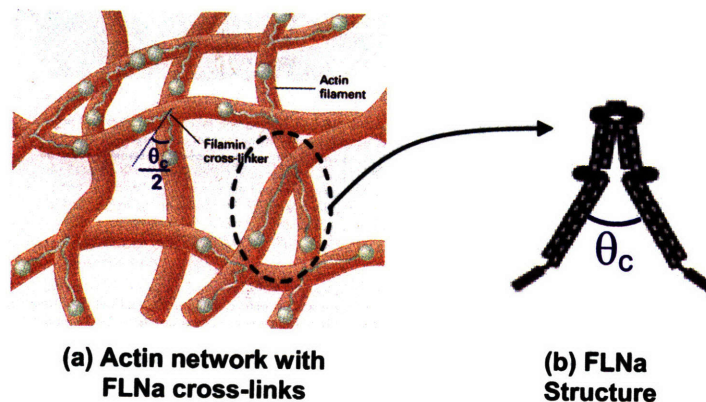


Figure 4–2. Schematics of (a) actin network with FLNa cross-links (adapted from (Lodish, 2000)), (b) FLNa structure (adapted from (Gardel et al., 2006b)).

schematic is intended to convey the 3D nature of the network since the FLNa cross-links maintain a relatively constant chain angle, θ_c , of 72° . The structure of FLNa is shown in Figure 4–2b, with two arm-like subunits of length 80 nm and 3–5nm diameter (Hartwig and Stossel, 1981). Each subunit of the V-shaped dimer is interrupted by irregularities in the primary sequence of Ig repeats: between repeats 15/16 midway along the subunit and 23/24 at the vertex of the dimer (Gardel et al., 2006b). These gaps are considered to serve as hinges between the rod-like components of the subunits (Gorlin et al., 1990).

Streptavidin (or avidin) and biotin form a stiff, commonly used cross-link. The interaction between avidin and biotin exhibits the highest known affinity between a protein and a ligand (Bayer et al., 1975). The structure of the avidin-biotin composite cross-link is shown in Figure 4–3.

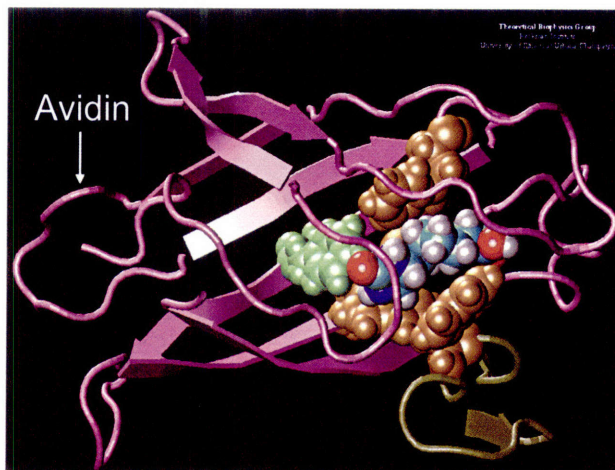


Figure 4–3. Schematics of avidin-biotin cross-link structure (Theoretical Biophysics Group, 2007).

Cross-linking proteins play a large role in modulating the geometry, elasticity, and durability of actin networks. Considerable in vitro rheological experiments with reconstituted actin gel-like networks have been conducted with varying levels of actin and cross-link concentrations (Janmey et al., 1988; MacKintosh et al., 1995; Gisler and

Weitz, 1999; Shin et al., 2004; Storm et al., 2005; Gardel et al., 2006b). Empirically observed shear moduli for F-actin networks with permanent cross-links (but the same concentration of F-actin) have been observed to vary over two orders of magnitude by varying the cross-link density (Gardel et al., 2004a). Examples of the rheological behavior of FLNa and avidin within actin networks is shown in Figure 4–4 and Figure 4–5, respectively.

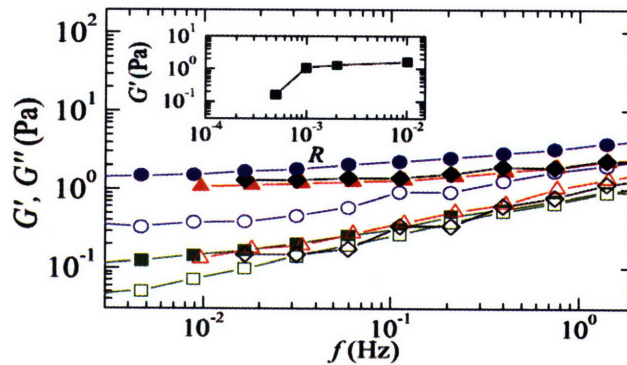


Figure 4–4. Storage (G' , closed symbols) and loss (G'' , open symbols) moduli of $12\mu\text{M}$ actin-FLNa. R is varied from $1/2000$ (squares), $1/1000$ (triangles), $1/500$ (diamonds), and $1/100$ (circles). Inset: G' at 0.01 Hz as a function of R (Gardel et al., 2006a).

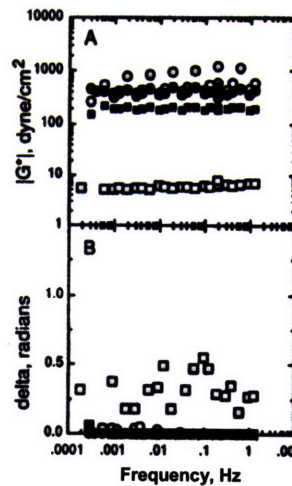


Figure 4–5. Frequency dependence of the complex modulus and phase shift for $15\mu\text{M}$ actin-avidin networks with 2% biotinylated actin alone (\square), $0.03\mu\text{M}$ avidin (\blacksquare), $0.1\mu\text{M}$ avidin (\circ), or $0.3\mu\text{M}$ avidin (\bullet) (Wachsstock et al., 1994).

Figure 4–4 demonstrates that the viscoelastic behavior of actin-FLN networks is highly dependent on the frequency and value of R. For example, the elastic and viscous response is essentially equivalent for $R=1/2000$, especially at higher frequencies; while the elastic response dominates the viscous response for $R=1/1000$ at lower frequencies. For Figure 4–5, the magnitude of the complex modulus, G^* , is $|G^*| = \sqrt{G'^2 + G''^2}$ and the phase lag, δ , between the elastic and viscous response is given by $\tan(\delta) = G''/G'$. Thus, the elastic response dominates the behavior of actin-avidin networks for different values of R.

This framework for cross-link torsion assumes that the cross-links remain completely bonded to the chains during deformation. Once cross-links such as filamin detach from the chain they can accommodate further deformation through unbending and unfolding of Ig domains. Below the force threshold for unfolding, the extension of unbonded filamin cross-links can be modeled as entropic unbending, behaving as a wormlike chain (DiDonna and Levine, 2006). Above the force threshold for unfolding, Ig domains are ruptured and unfolded as shown in the sawtooth pattern in Figure 4–6a. The Ig domain unfolding has been modeled using the worm-like chain approximation (Marko and Siggia, 1995) (see example in Figure 4–6b), with $L_c=150\text{nm}$, $l_p=13.8\text{nm}$ for folded filamin and $L_c=10\text{nm}$, $l_p=0.33\text{nm}$ for the unfolded filamin domains (Furuike et al., 2001; Hartemink, 2005; Ferrer et al., 2008). At larger extensions, however, enthalpic stretching of the cross-link will occur prior to rupture.

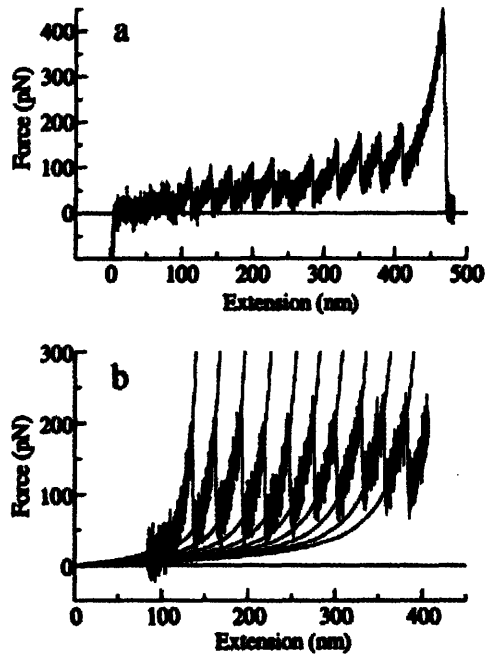


Figure 4–6. (a) A force-extension curve of Filamin A molecule in aqueous solution measured by AFM at room temperature. Filamin A was stretched at a pulling speed of $0.37 \mu\text{m/s}$. (b) The fit between the WLC model and the sawtooth pattern of the force-extension curve where the force gradually increased after the abrupt decrease in force. Filamin A was stretched at a pulling speed of $0.37 \mu\text{m/s}$ (Furuike et al., 2001).

4.2 Cross-link stiffness and torsion properties

The cross-link torsional stiffness has been calculated for some ABPs, including FLN and Arp2/3. The torsional stiffness is based on the standard deviation of junction angle between subunits. Based on the work by Hartemink (Hartemink, 2005) that showed the FLN subunits to be bonded along their entire length to the actin filaments, the FLN junction angle is also taken to be the previously defined chain angle, θ_c , between actin filaments. From the equipartition theorem, the thermal energy, $k_B T$, is related to the

cross-link torsional stiffness, k_{CL} , and the variance of the junction (or chain) angle, and can be rewritten as

$$\langle \theta_c^2 \rangle = \frac{k_B T}{k_{CL}}. \quad (4.1)$$

Hartemink measured the average chain angle of filamin molecules bound to single actin filaments in a dilute solution and found $\langle \theta_{c,FLN} \rangle = 71.8^\circ \pm 15.5^\circ$ (Hartemink, 2005). This gives a torsional stiffness of

$$k_{CL} = \frac{k_B T}{\langle \theta_c^2 \rangle} = \frac{(1.38e-23 J/K)(300 K)}{(0.27 \text{ rad})^2} = 56 \frac{\text{pN} \cdot \text{nm}}{\text{rad}^2}. \quad (4.2)$$

Blanchoin, et al. performed a similar high speed imaging experiment with Arp2/3 cross-links in a $4 \mu\text{M}$ actin solution (see) (Blanchoin et al., 2000). The mean angle for bovine Arp2/3 complex was found to be $\langle \theta_{Arp2/3} \rangle = 77^\circ \pm (13^\circ)$, yielding a torsional stiffness of $k_{CL,Arp2/3} = 76 \text{ pN} \cdot \text{nm} / \text{rad}^2$.

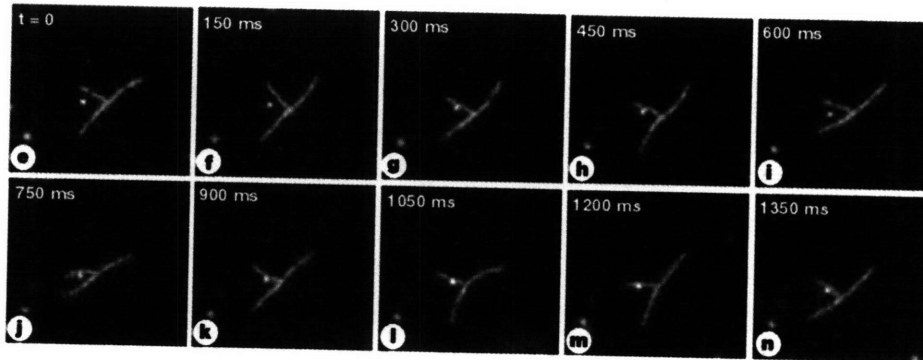


Figure 4-7. Thermal fluctuations of branched actin filaments formed from $4 \mu\text{M}$ muscle actin and 15 nM Arp2/3 complex. Every frame illustrates the stiffness of the branch point relative to the flexibility of the filament. Branch length = $2 \mu\text{m}$. (Blanchoin et al., 2000)

4.3 Cross-link torsional potential model

A torsional potential is shown schematically in Figure 4–8 within the context of the 8-chain network. The junctions within the 8-chain network are taken as pinned connections (see Chapter 3), with torsional resistance about the junction governed by the mechanical properties of the cross-link. The limiting case of a filament with clamped boundary conditions, equivalent to an infinite torsional stiffness, is included in Section 4.4 for the discussion on the effects of cross-link stiffness on the filament entropic configuration space. The FLN cross-link torsional stiffness was measured by thermal fluctuations, indicating their importance for FLN molecules bound to single actin filaments in a dilute solution. Since both of the FLN subunits completely bond to actin filaments in a network structure, however, we will assume a limited entropic configurational space, with their elasticity governed by changes in internal energy, and use the measured torsional stiffness as an initial estimate for the enthalpic torsional stiffness. Further evaluation of entropically-based torsional elasticity in cross-links is left to future work. Proceeding with the internal energy-based torsional elasticity, the cross-links exert a torque due to enthalpic unbending which is measured by the network chain

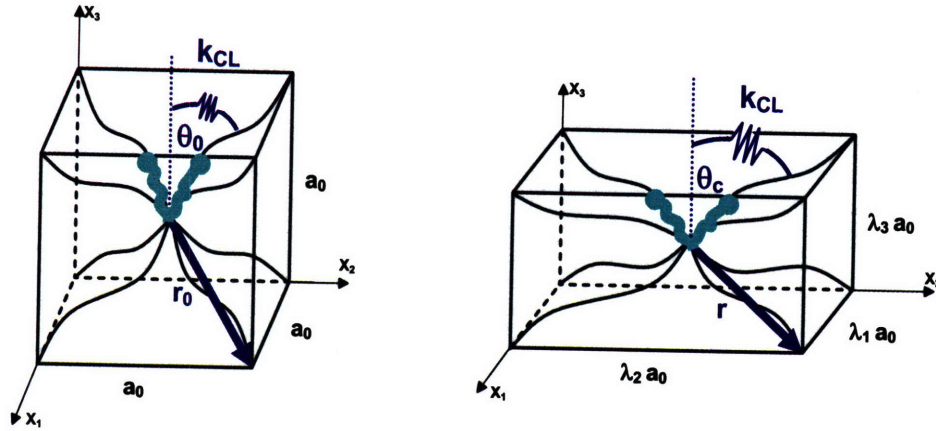


Figure 4-8. Schematics of torsion potential to simulate cross-link stiffness in 8-chain unit cell.

angle (θ_c). The initial focus of this model is below the force threshold required to detach the cross-link subunits from the chain. Within this regime, the cross-link imparts some structural stiffness to the network chain while deforming solely through enthalpic torsion at its hinge. Note that the 8-chain framework provides the forces exerted by the chains at the cross-link junctions. Given the average debonding and/or failure forces for a cross-link, the model can be adjusted to allow for junction stretching and/or failure. For a completely bonded cross-link, however, the torque due to a change in chain angle from an initial angle (θ_0) is

$$t_{CL} = -k_{CL}(\theta_c - \theta_0) \quad (4.3)$$

where the initial chain angle is defined for an 8-chain unit cell (with sides of initial length a_0) as $\theta_0=54.7^\circ$ and the chain angle, θ_c , is defined in terms of the principal stretches,

$$\begin{aligned}\theta_c &= \cos^{-1}\left(\frac{\lambda_1 A}{r}\right) = \cos^{-1}\left(\frac{\lambda_1 (a_0/2)}{\lambda_c r_0}\right) = \cos^{-1}\left(\frac{\lambda_1 (a_0/2)}{\left(\sqrt{I_1/3}\right)\left(\sqrt{3(a_0/2)^2}\right)}\right) \\ &= \cos^{-1}\left(\frac{\lambda_1}{\sqrt{I_1}}\right) = \cos^{-1}\left(\frac{\lambda_1}{\sqrt{\lambda_1^2 + \lambda_2^2 + \lambda_3^2}}\right).\end{aligned}\quad (4.4)$$

The strain energy density function can now be given as

$$W_{CL} = n_{CL} \int_{\theta_0}^{\theta_c} t_{CL} d\theta_c' = n_{CL} \int_{\theta_0}^{\theta_c} -k_{CL} (\theta_c' - \theta_0) d\theta_c' = \frac{n_{CL} k_{CL}}{2} (\theta_c - \theta_0)^2 \quad (4.5)$$

where n_{CL} is the cross-link density within the network. Note that the strain energy density expression can be written as a function of the principal stretches.

$$W_{CL} = \hat{W}_{CL}(\lambda_1, \lambda_2, \lambda_3) = \frac{n_{CL} k_{CL}}{2} \left[\cos^{-1}\left(\frac{\lambda_1}{\sqrt{\lambda_1^2 + \lambda_2^2 + \lambda_3^2}}\right) - \theta_0 \right]^2 \quad (4.6)$$

The principal stresses are given by

$$\begin{aligned}T_i &= \frac{\lambda_i}{J} \frac{\partial W}{\partial \lambda_i} + \frac{\partial W}{\partial J} \\ &= \frac{\lambda_i}{J} n_{CL} k_{CL} (\theta_c - \theta_0) \frac{\partial \theta_c}{\partial \lambda_i}\end{aligned}\quad \text{(no sum on } i), \quad (4.7)$$

and the derivatives of the chain angle with respect to the principal stretches are

$$\frac{\partial \theta_c}{\partial \lambda_1} = \frac{\partial \cos^{-1}\left(\frac{\lambda_1}{\sqrt{\lambda_1^2 + \lambda_2^2 + \lambda_3^2}}\right)}{\partial \lambda_1} = \frac{-\sqrt{I_1 - \lambda_1^2}}{I_1} \quad (4.8)$$

$$\frac{\partial \theta_c}{\partial \lambda_2} = \frac{\partial \cos^{-1}\left(\frac{\lambda_1}{\sqrt{\lambda_1^2 + \lambda_2^2 + \lambda_3^2}}\right)}{\partial \lambda_2} = \frac{\lambda_1 \lambda_2}{I_1 \sqrt{I_1 - \lambda_1^2}} \quad (4.9)$$

$$\frac{\partial \theta_c}{\partial \lambda_3} = \frac{\partial \cos^{-1}\left(\frac{\lambda_1}{\sqrt{\lambda_1^2 + \lambda_2^2 + \lambda_3^2}}\right)}{\partial \lambda_3} = \frac{\lambda_1 \lambda_3}{I_1 \sqrt{I_1 - \lambda_1^2}}. \quad (4.10)$$

The principal stress tensor is given as

$$\mathbf{T}^p = \sum_i^3 T_i (\mathbf{e}_i \otimes \mathbf{e}_i) \quad (4.11)$$

The Cauchy stress is computed through a simple transformation from principal space (\mathbf{T}^p) to the current space (\mathbf{T})

$$\mathbf{T} = \mathbf{Q} \mathbf{T}^p \mathbf{Q}^T \quad (4.12)$$

where \mathbf{Q} is a proper orthogonal rotation tensor and has the following property

$$\mathbf{Q}^T \mathbf{Q} = \mathbf{I}. \quad (4.13)$$

The three columns of the rotation tensor \mathbf{Q} are composed of the three eigenvectors from the spectral decomposition of the left Cauchy-Green tensor (\mathbf{B}), since the eigenvectors for stress and strain are equivalent for isotropic materials.

$$\mathbf{B} = \sum_i^3 \lambda_i^2 (\tilde{\mathbf{n}}_i \otimes \tilde{\mathbf{n}}_i) \quad (4.14)$$

where $\tilde{\mathbf{n}}$ is the eigenvector in the current configuration. The derivative of a principal stretch with respect to \mathbf{B} will be important in determining the Jacobian, and is shown below (Holzapfel, 2000).

$$d\mathbf{B} = \sum_i^3 2\lambda_i d\lambda_i (\tilde{\mathbf{n}}_i \otimes \tilde{\mathbf{n}}_i) + \lambda_i^2 (d\tilde{\mathbf{n}}_i \otimes \tilde{\mathbf{n}}_i + \tilde{\mathbf{n}}_i \otimes d\tilde{\mathbf{n}}_i) \quad (4.15)$$

Since $\tilde{\mathbf{n}}_i$ constitute an orthonormal basis ($\tilde{\mathbf{n}}_i \cdot \tilde{\mathbf{n}}_j = \delta_{ij}$), the change of a vector with constant length is always orthogonal to the vector ($\tilde{\mathbf{n}}_i \cdot d\tilde{\mathbf{n}}_i = 0$). Therefore, pre- and post-multiplying Equation (4.15) by $\tilde{\mathbf{n}}_i$ yields

$$\tilde{\mathbf{n}}_i \cdot d\mathbf{B}\tilde{\mathbf{n}}_i = 2\lambda_i d\lambda_i \quad (i=1,2,3) \quad (4.16)$$

Using the identity $\mathbf{u} \cdot \mathbf{A}\mathbf{v} = \mathbf{A} : (\mathbf{u} \otimes \mathbf{v})$, Equation (4.16) becomes

$$d\mathbf{B} : (\tilde{\mathbf{n}}_i \otimes \tilde{\mathbf{n}}_i) = 2\lambda_i d\lambda_i \quad (i=1,2,3). \quad (4.17)$$

This can be rewritten recognizing that $d\mathbf{B} = (\partial\mathbf{B}/\partial\lambda_i)d\lambda_i$,

$$\frac{1}{2\lambda_i} \left(\frac{\partial\mathbf{B}}{\partial\lambda_i} \right) : (\tilde{\mathbf{n}}_i \otimes \tilde{\mathbf{n}}_i) = 1 \quad (i=1,2,3), \quad (4.18)$$

or, equivalently,

$$\frac{1}{2\lambda_i} \left(\frac{\partial\mathbf{B}}{\partial\lambda_i} \right) : (\tilde{\mathbf{n}}_i \otimes \tilde{\mathbf{n}}_i) = \left(\frac{\partial\mathbf{B}}{\partial\lambda_i} \right) : \left(\frac{\partial\lambda_i}{\partial\mathbf{B}} \right) \quad (i=1,2,3). \quad (4.19)$$

From Equation (4.19) we can determine the relation for the derivative of a principal stretch with respect to \mathbf{B} .

$$\frac{\partial\lambda_i}{\partial\mathbf{B}} = \tilde{\mathbf{n}}_i \otimes \tilde{\mathbf{n}}_i \quad (i=1,2,3). \quad (4.20)$$

4.3.1 Implementation in finite element analysis

Since the stress is given in principal space, the Jacobian is also computed in principal space (C^p), then rotated into the current space by the following relation

$$\mathbf{C} = \mathbf{Q}\mathbf{Q}C^p\mathbf{Q}^T\mathbf{Q}^T. \quad (4.21)$$

The principal Jacobian (C^p) is found by solving for the derivative $\delta\mathbf{I}^p/\delta\mathbf{F}^p$, which has three components along its diagonal

$$\frac{\partial T_1}{\partial \mathbf{F}^p} = n_{CL} k_{CL} \left\{ \begin{array}{l} \frac{\lambda_1(\theta_c - \theta_0) \sqrt{I_1 - \lambda_1^2}}{J^2 I_1} \frac{\partial J}{\partial \mathbf{F}^p} + \frac{(\theta_c - \theta_0) \sqrt{I_1 - \lambda_1^2}}{J I_1} \frac{\partial \lambda_1}{\partial \mathbf{F}^p} \\ \frac{\lambda_1(\theta_c - \theta_0) \sqrt{I_1 - \lambda_1^2}}{J I_1^2} \frac{\partial I_1}{\partial \mathbf{F}^p} + \frac{\lambda_1(\theta_c - \theta_0)}{2 J I_1 \sqrt{I_1 - \lambda_1^2}} \left(\frac{\partial I_1}{\partial \mathbf{F}^p} - 2 \lambda_1 \frac{\partial \lambda_1}{\partial \mathbf{F}^p} \right) \\ \frac{\lambda_1 \sqrt{I_1 - \lambda_1^2}}{J I_1} \frac{\partial \theta_c}{\partial \mathbf{F}^p} \end{array} \right\} \quad (4.22)$$

$$\frac{\partial T_2}{\partial \mathbf{F}^p} = n_{CL} k_{CL} \left\{ \begin{array}{l} \frac{\lambda_1 \lambda_2^2 (\theta_c - \theta_0)}{J^2 I_1 \sqrt{I_1 - \lambda_1^2}} \frac{\partial J}{\partial \mathbf{F}^p} + \frac{\lambda_2^2 (\theta_c - \theta_0)}{J I_1 \sqrt{I_1 - \lambda_1^2}} \frac{\partial \lambda_1}{\partial \mathbf{F}^p} + \frac{2 \lambda_1 \lambda_2 (\theta_c - \theta_0)}{J I_1 \sqrt{I_1 - \lambda_1^2}} \frac{\partial \lambda_2}{\partial \mathbf{F}^p} \\ \frac{\lambda_1 \lambda_2^2 (\theta_c - \theta_0)}{J I_1^2 \sqrt{I_1 - \lambda_1^2}} \frac{\partial I_1}{\partial \mathbf{F}^p} - \frac{\lambda_1 \lambda_2^2 (\theta_c - \theta_0)}{2 J I_1 (I_1 - \lambda_1^2)^{3/2}} \left(\frac{\partial I_1}{\partial \mathbf{F}^p} - 2 \lambda_1 \frac{\partial \lambda_1}{\partial \mathbf{F}^p} \right) \\ + \frac{\lambda_1 \lambda_2^2}{J I_1 \sqrt{I_1 - \lambda_1^2}} \frac{\partial \theta_c}{\partial \mathbf{F}^p} \end{array} \right\} \quad (4.23)$$

$$\frac{\partial T_3}{\partial \mathbf{F}^p} = n_{CL} k_{CL} \left\{ \begin{array}{l} \frac{\lambda_1 \lambda_3^2 (\theta_c - \theta_0)}{J^2 I_1 \sqrt{I_1 - \lambda_1^2}} \frac{\partial J}{\partial \mathbf{F}^p} + \frac{\lambda_3^2 (\theta_c - \theta_0)}{J I_1 \sqrt{I_1 - \lambda_1^2}} \frac{\partial \lambda_1}{\partial \mathbf{F}^p} + \frac{2 \lambda_1 \lambda_3 (\theta_c - \theta_0)}{J I_1 \sqrt{I_1 - \lambda_1^2}} \frac{\partial \lambda_3}{\partial \mathbf{F}^p} \\ \frac{\lambda_1 \lambda_3^2 (\theta_c - \theta_0)}{J I_1^2 \sqrt{I_1 - \lambda_1^2}} \frac{\partial I_1}{\partial \mathbf{F}^p} - \frac{\lambda_1 \lambda_3^2 (\theta_c - \theta_0)}{2 J I_1 (I_1 - \lambda_1^2)^{3/2}} \left(\frac{\partial I_1}{\partial \mathbf{F}^p} - 2 \lambda_1 \frac{\partial \lambda_1}{\partial \mathbf{F}^p} \right) \\ + \frac{\lambda_1 \lambda_3^2}{J I_1 \sqrt{I_1 - \lambda_1^2}} \frac{\partial \theta_c}{\partial \mathbf{F}^p} \end{array} \right\}, \quad (4.24)$$

where the terms within Eqs. (3.35), (4.23), and (4.24) are defined earlier except for

$$\mathbf{F}^p = \mathbf{Q}^T \mathbf{F} \mathbf{Q} \quad (4.25)$$

$$\frac{\partial J}{\partial \mathbf{F}^p} = \mathbf{J} \mathbf{F}^{p-T} \quad (4.26)$$

$$\frac{\partial I_1}{\partial \mathbf{F}^p} = 2 \mathbf{F}^p \quad (4.27)$$

$$\frac{\partial \mathbf{B}^p}{\partial \mathbf{F}^p} = (2 \mathbf{I}^s \mathbf{F}^p)^{RT} \quad (4.28)$$

$$\frac{\partial \lambda_i}{\partial \mathbf{B}^p} = \tilde{n}_i^p \otimes \tilde{n}_i^p \quad (i=1,2,3) \quad (4.29)$$

$$\frac{\partial \lambda_i}{\partial \mathbf{F}^p} = \left(\frac{\partial \lambda_i}{\partial \mathbf{B}^p} \right) \left(\frac{\partial \mathbf{B}^p}{\partial \mathbf{F}^p} \right) = (\tilde{n}_i^p \otimes \tilde{n}_i^p) (2\mathbf{I}^s \mathbf{F}^p)^{RT} \quad (i=1,2,3) \quad (4.30)$$

$$\frac{\partial \theta_c}{\partial \mathbf{F}^p} = \left(\frac{\partial \theta_c}{\partial \lambda_1} \right) \left(\frac{\partial \lambda_1}{\partial \mathbf{F}^p} \right) = -\frac{\sqrt{I_1 - \lambda_1^2}}{I_1} (\tilde{n}_i^p \otimes \tilde{n}_i^p) (2\mathbf{I}^s \mathbf{F}^p)^{RT} \quad (4.31)$$

4.3.2 Parametric evaluation of cross-link torsion model

The contribution of the shear and normal stress difference from the cross-links are shown in Figure 4–9, using filamin properties with $k_{CL}=56\text{pN}\cdot\text{nm}$, $n_{CL}=1.2\text{e}20\text{m}^{-3}$ for a network under simple shear. Figure 4–9 also shows the relative impact of doubling or halving the torsional stiffness of the cross-link. The contribution of the cross-link torsion to network elasticity of an actin network is shown in Figure 4–10. Figure 4–10a contains the separate shear stress-shear strain responses for the filamin cross-links ($k_{CL}=56\text{pN}\cdot\text{nm}$) and an extensible actin network ($l_p=3\mu\text{m}$, $L_c=1\mu\text{m}$, $c_{AF}=20\mu\text{M}$, $\alpha=1.1\%$) in addition to

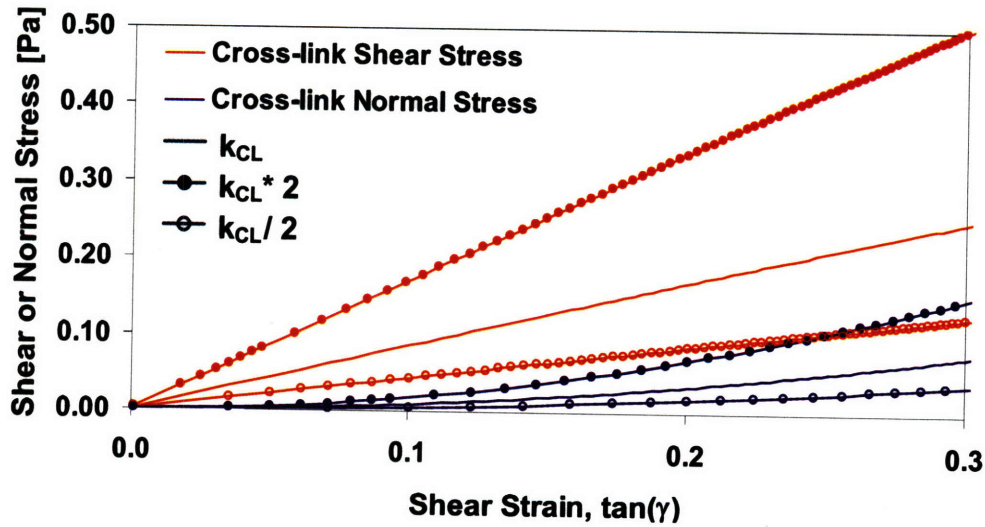


Figure 4–9. Shear stress and normal stress contributions from cross-link torsion

their combined response. It also shows the combined response of the actin network with cross-links that are five times stiffer ($k_{CL}=280\text{pN}\cdot\text{nm}$), representing the effect of using a more rigid actin binding protein.

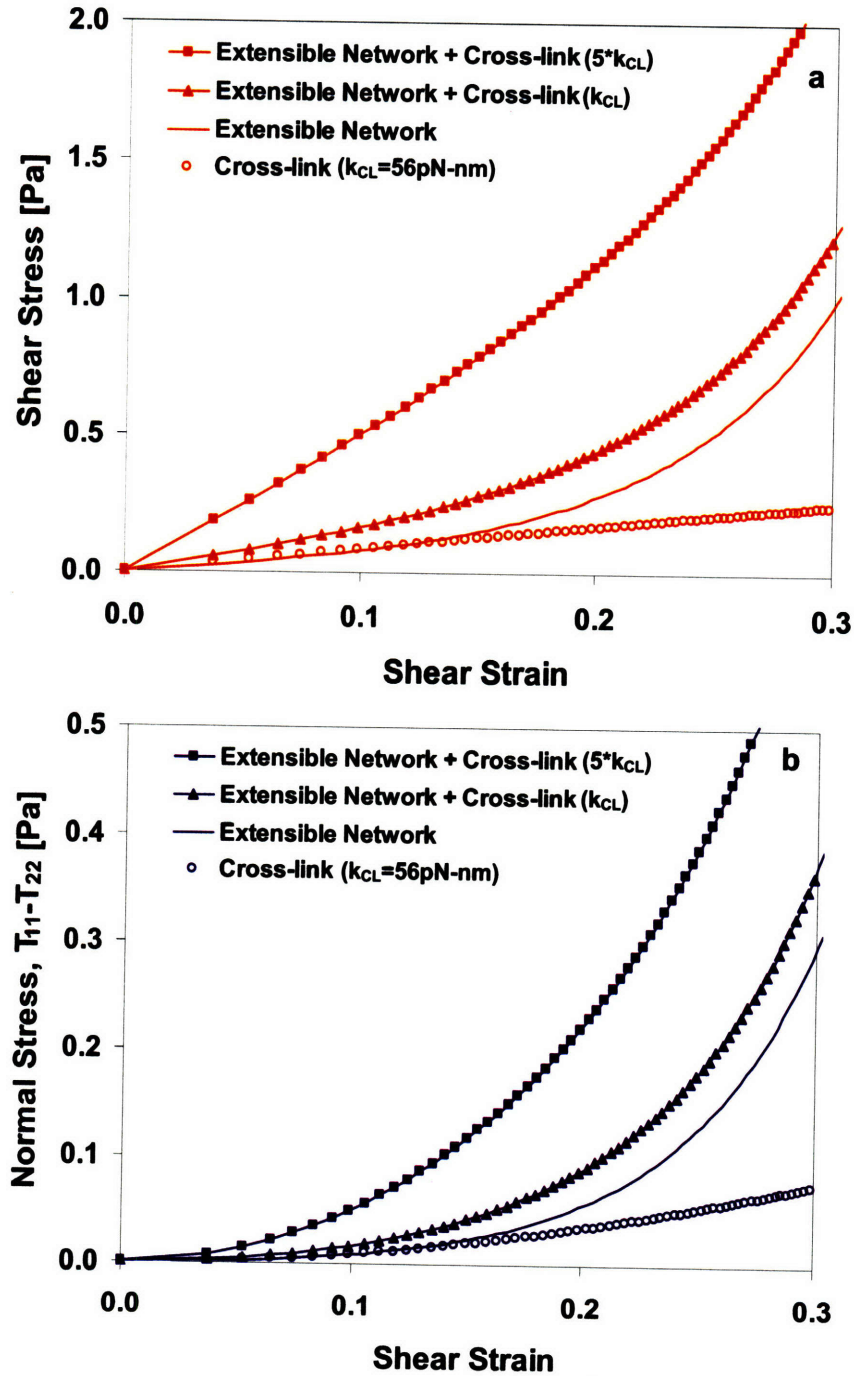


Figure 4-10. Cross-link torsion contribution to network elasticity: (a) Shear stress and (b) normal stress difference

4.3.3 Comparison with experimental data of actin-FLNa networks

The rheology of actin networks has been quantified with several different actin binding proteins as cross-links, including scruin (Janmey et al., 1991; Janmey et al., 1994; Isambert and Maggs, 1996; Gardel et al., 2004a; Gardel et al., 2004b), filamin (Gardel et al., 2006b; Lee and Kamm, 2008), and streptavidin-biotin (Wachsstock et al., 1994; Lee and Kamm, 2008), among others. The model will be compared to unpublished data by Lee and Kamm (Lee and Kamm, 2008), who evaluated the rheology of F-actin networks with FLNa and streptavidin cross-links. Filamin cross-links are very compliant, contributing relatively little to the initial response of the network, but contributing more to the nonlinear strain stiffening of the networks. The biotin/streptavidin cross-links create an irreversible bond with a dissociation equilibrium constant near that of a covalent bond (Wachsstock et al., 1994). This behavior, along with their relative ease of use when compared with scruin, makes them a preferred cross-link substitute for scruin.

The first comparison was with actin-FLNa networks at actin concentrations of $c_{AF}=20\mu\text{M}$, $R=c_{CL}/c_{AF}=0.02$, and $\omega=0.05\text{Hz}$ (where c_{CL} is the cross-link concentration). At this frequency and R value, they found G' to be approximately 2-4 times greater than

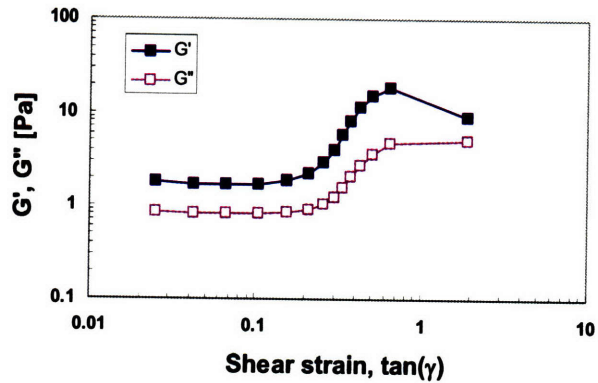


Figure 4–11. Experimental storage modulus (G') and loss modulus (G'') of actin-FLNa networks ($c_{AF} = 20\mu\text{M}$, $R=0.02$, and $\omega=0.05\text{Hz}$) (Lee and Kamm, 2008)

G'' for shear strains up to $\tan(\gamma)=0.5$ (Figure 4–11). So while the network behavior is primarily elastic, the viscous response is not negligible. Accordingly, this viscoelastic behavior of this network will also be taken into account models developed in Chapter 5 (Viscoelastic network model). The modeling results, considering hyperelastic contributions only, are shown in Figure 4–12, with the modeling parameters in Table 3–1. The actin concentration, chain density, and contour length were based on experimental conditions or observations, while the persistence length used in the actin-scrutin networks is also used here. The isotropic network prestress was fit to the data by adjusting the percent increase in r_0 ($\alpha=1.1\%$), which was approximately equal to the value ($\alpha=1.2\%$) used for the $21\mu\text{M}$ actin-scrutin data in Chapter 3. There is excellent agreement between the model and the data for shear strains less than 35%, which corresponds to a shear

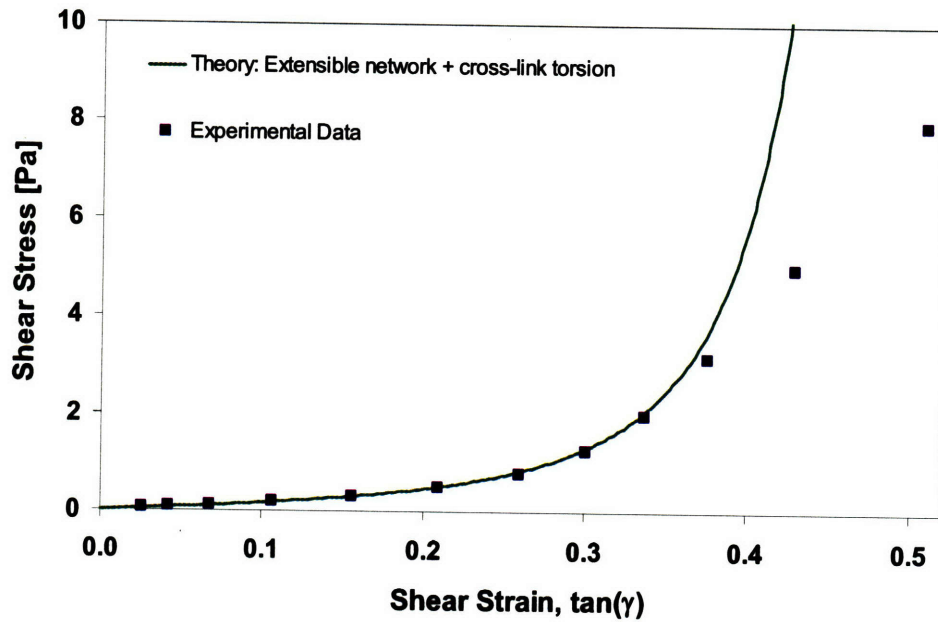


Figure 4-12. Shear stress-shear strain comparison of extensible network model with cross-link torsion with experimental data of actin-FLNa networks ($c_{AF}=20\mu\text{M}$, $R=0.02$, and $\omega=0.05\text{Hz}$) (Lee and Kamm, 2008)

c_{AF}	l_p [μm]	n_{AF} [m^{-3}]	L_c [μm]	$r_{F=0}$ [μm]	r_0 [μm]	α [%]	σ_0 [Pa]	k_{CL} [pN-nm]
20 μM	3.0	3.2e19	0.9	0.85	0.86	1.1	0.6	56

Table 4-2. Network parameters for actin-FLNa model

stress of roughly 3Pa. The significance of the divergence becomes more apparent after examining the differential (tangent) shear modulus in Figure 4-13. The experimental actin-FLNa network leaves the strain stiffening regime at a shear stress of approximately $\tau \sim 2\text{-}3\text{Pa}$, as seen by the change in slope of the tangent

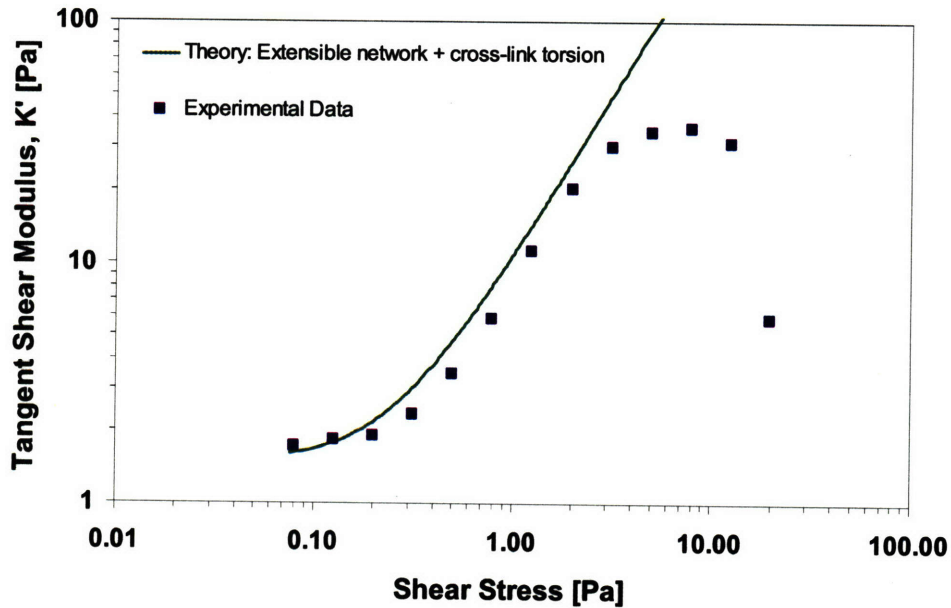


Figure 4–13. Tangent shear modulus-shear stress comparison of extensible network model with cross-link torsion with experimental data of actin-FLNa networks ($c_{AF}=20\mu\text{M}$, $R=0.02$, and $\omega=0.05\text{Hz}$) (Lee and Kamm, 2008)

modulus in Figure 4–13. At this point, the actin filaments have undergone end-to-end extension primarily via entropic unbending ($\lambda_f^u \sim 1.02$) and a very small magnitude of enthalpic stretching ($\lambda_f^s \sim 1.0002$), but the network is beginning to fail likely due to cross-link deformation. The FLNa cross-links continue to deform through unbending and/or stretching until a shear stress of approximately $\tau \sim 10\text{Pa}$ at which point the cross-links (and network) fail. Two regimes of cross-link behavior emerge based on the network response. The first regime ($\tau < 3\text{Pa}$) consists of standard strain stiffening network behavior, which is accurately captured using an extensible network model and cross-links in torsion. The network model gives us insight into the second regime ($3\text{Pa} < \tau < 10\text{Pa}$) by showing that while the network elasticity is deteriorating, the actin filaments are not at their extensible limit, which suggests that the FLNa cross-links are deforming (via

entropic unbending, enthalpic stretching, and/or Ig domain unfolding). This is confirmed by the experimental data in Figure 4–13 with the rapid decrease in strain stiffening after $\tau < 3\text{Pa}$, followed by network failure.

4.3.4 Comparison with experimental data of actin-avidin networks

The second comparison considers actin-streptavidin networks at $c_{AF} = 20\mu\text{M}$, $R=0.01$, and $\omega=0.05\text{Hz}$. At this frequency and R value, G' was approximately 10 times greater than G'' for shear strains up to $\tan(\gamma)=0.2$ and stresses up to $\tau=1\text{Pa}$ (Figure 4–14). A comparison between the theory and the experimental data is only examined within the linear regime since the experiment produced constant values of G' , G'' until the network detached from the rheometer plates at a shear strain of $\tan(\gamma)\sim 0.2$ ($\tau\sim 1\text{Pa}$).

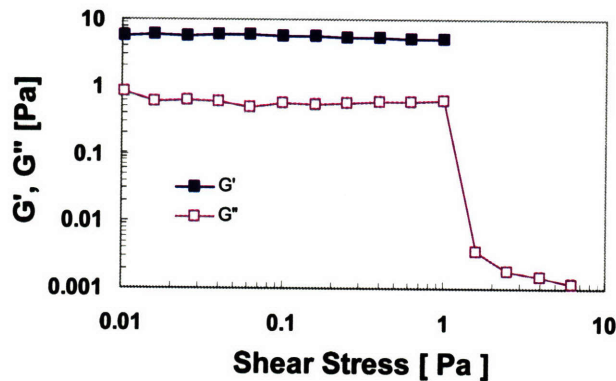


Figure 4–14. Experimental storage modulus (G') and loss modulus (G'') as a function of shear stress (τ) for actin-avidin networks ($c_{AF}=20\mu\text{M}$, $R=0.01$, and $\omega=0.05\text{Hz}$) (Lee and Kamm, 2008)

Unlike the actin-FLNa network, the elastic response of the actin-avidin network dominates the viscous response. The modeling results are shown in Figure 4–15, with the modeling parameters in Table 4–3. All actin modeling parameters (c_{AF} , n_{AF} , L_c , l_p , α)

were kept fixed to the values used for the actin-FLNa network comparison (with l_p and α approximately equal to the values used for the 21 μ M actin data from Gardel, et al. (Gardel et al., 2004a) in Chapter 3). Since avidin is a much stiffer cross-link, but of unknown torsional stiffness, the torsional stiffness was fit to the data using a value of $k_{CL}=560$ pN-nm.

c_{AF}	l_p [μ m]	n_{AF} [m^{-3}]	L_c [μ m]	$r_{F=0}$ [μ m]	r_0 [μ m]	α [%]	σ_0 [Pa]	k_{CL} [pN-nm]
20 μ M	3.0	3.2e19	0.9	0.85	0.86	1.1	0.6	560

Table 4-3. Network parameters for actin-avidin model

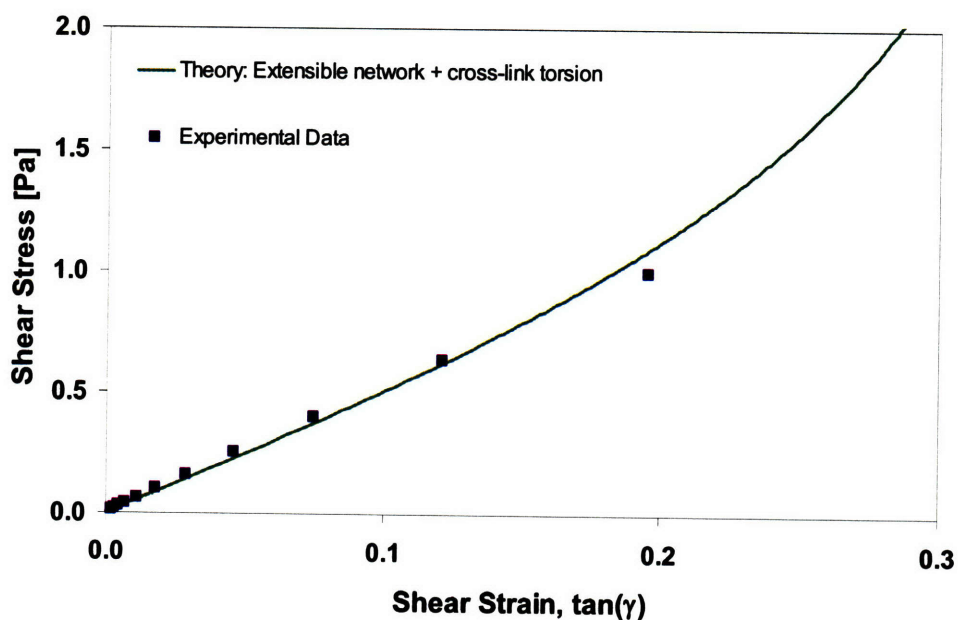


Figure 4-15. Shear stress-shear strain comparison of extensible network model with cross-link torsion with experimental data of actin-FLNa networks ($c_{AF}=20\mu$ M, $R=0.01$, and $\omega=0.05$ Hz) (Lee and Kamm, 2008)

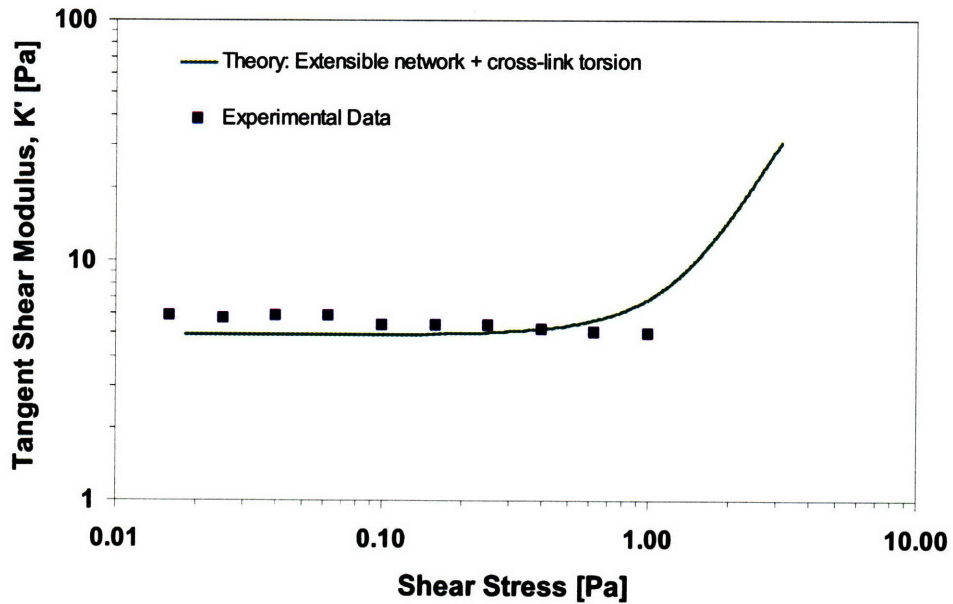


Figure 4–16. Tangent shear modulus-shear stress comparison of extensible network model with cross-link torsion with experimental data of actin-avidin networks ($c_{AF}=20\mu\text{M}$, $R=0.01$, and $\omega=0.05\text{Hz}$) (Lee and Kamm, 2008)

There is excellent agreement between the model and the data for shear strains in the linear regime (before strain stiffening), measured before the plate slipped in the torsional rheometer. There is also good agreement between the model and the data in linear region of the differential (tangent) shear modulus in Figure 4–16. While the comparison within the nonlinear strain stiffening regime awaits future experimental data, the model seem to fit the initial response of the actin-avidin networks using the same actin parameters except for an increase in the cross-link torsional stiffness.

4.4 Evaluation of cross-link coupling with entropic configuration space

The torsional stiffness of cross-links does more, however, than just contribute to the strain energy of the network. By resisting the rotation of filaments about their cross-linked junctions, the cross-link has an influence on the entropic bending configuration space of the filaments. The hypothesis is that increasing cross-link torsional stiffness (k_{CL}) reduces the number of bending configurations available to an actin filament, thereby leading to a stiffer mechanical response by the filament. This hypothesis is examined with two simulations: a finite element beam model and a hybrid of the extensible filament model. The first simulation uses a finite element beam model of actin filament with torsional springs on ends representing the FLNa cross-link (see Figure 4–17 with model parameters in Table 4–4).

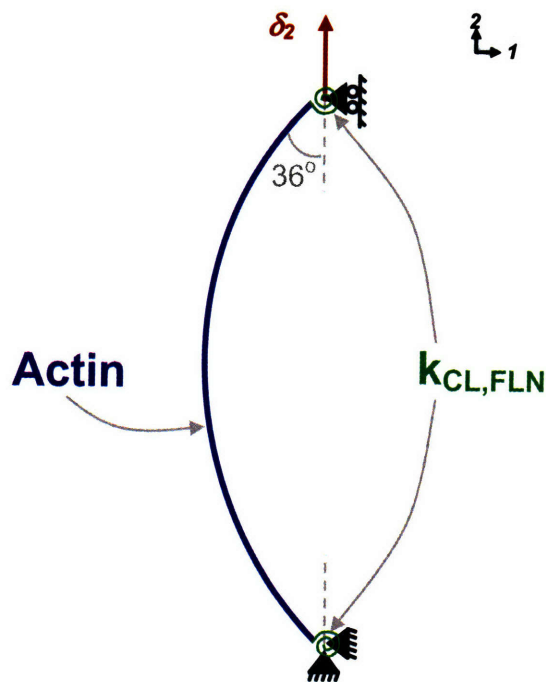


Figure 4–17. Schematic of finite element model of actin filament cross-linked by FLNa

d_{AF} [nm]	$l_{p,AF}$ [μm]	EI_{AF} [Nm ²]	L_c [nm]	r_0 [nm]	$l_{p,CL}$ [nm]	EI_{CL} [Nm ²]	k_{CL} [pN-nm]
7	3	1.2e-26	1000	936	20	8.3e-29	0
7	3	1.2e-26	1000	936	20	8.3e-29	56
7	3	1.2e-26	1000	936	20	8.3e-29	112
7	3	1.2e-26	1000	936	20	8.3e-29	280
7	3	1.2e-26	1000	936	20	8.3e-29	560

Table 4–4. Network parameters for finite element actin-FLN model with varying filament stiffness

The actin filament and torsional springs are given an initial, relaxed position with an angle of 36° ($\theta_c/2$) between the filament and the axis of extension. The F-actin beam is then extended to $r/L_c=1$ while tracking the change in angle and beam shape. This simulation is evaluated within the parametric space of increasing torsional stiffness by factors of 2, 5, and 10 to give the following cases $k_{CL}=0, 56, 112, 280, 560$ pN-nm. Figure 4–18 shows the force-extension results for increasing torsional stiffness, including the stiffest response from the limiting case of a filament with clamped ends which represents an infinite torsional stiffness, $k_{CL}\rightarrow\infty$. Figure 4–19 shows the associated changes in curvature with increasing torsional stiffness at extensions from undeformed to $r/L_c=1$. The results of the first model show that increasing k_{CL} leads to stiffer bending response of actin filament and a smaller beam mid-section that is available for sampling entropic unbending (in the extensible model). With a shorter length of filament in the middle of the beam, there are fewer available entropic

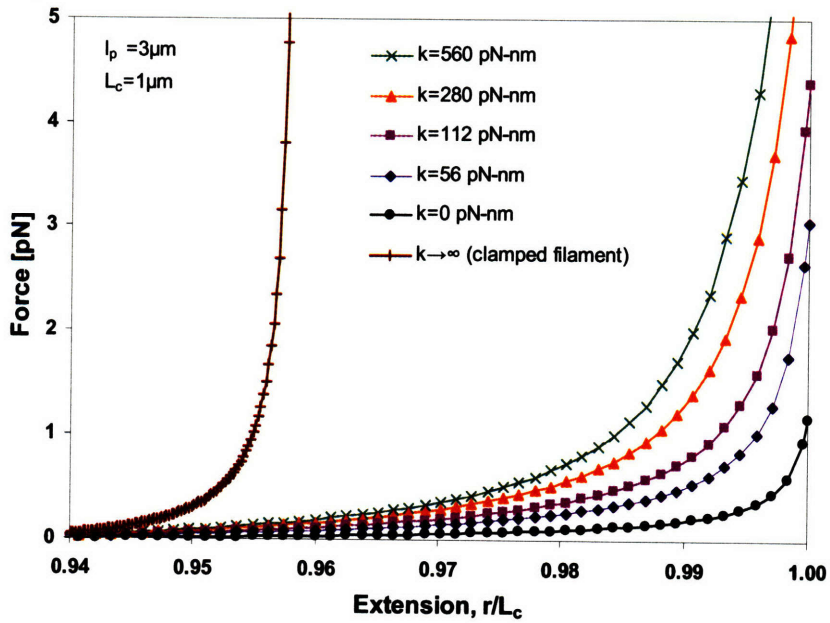


Figure 4-18. Force-extension response of actin-FLN finite element model

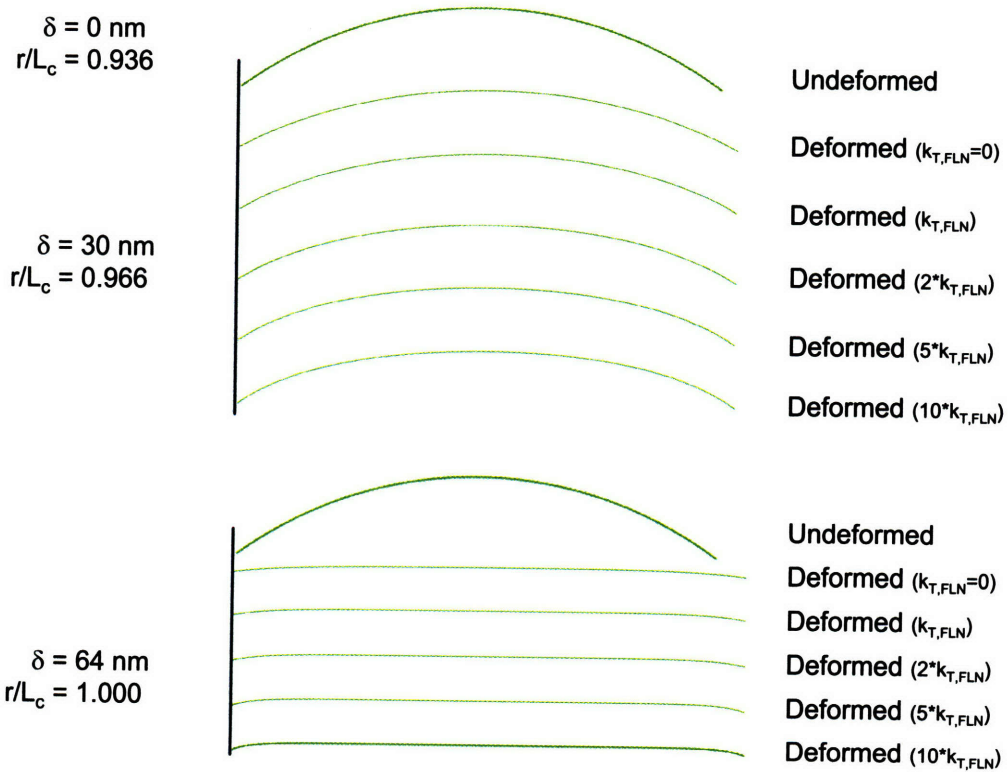


Figure 4-19. Curvature evolution with extension of actin-FLN finite element model for varying torsional stiffness

bending configurations which leads to an increase in the overall axial stiffness of the filament (i.e. stiffness relating axial forces to end-to-end displacement). The results from the first simulation support the hypothesis qualitatively, but the second simulation will require some quantitative results to determine the impact of the cross-links on the overall axial stiffness of the filament. Therefore, Figure 4–20 gives the chain angle evolution as a function of extension for increasing torsional stiffness. The limiting case of a filament with clamped boundary conditions ($k_{CL} \rightarrow \infty$) maintains a constant angle during extension, while a filament with pinned boundary conditions ($k_{CL} = 0$), but with the same initial curvature and flexural rigidity, will see a steady decrease in chain angle followed by a rapid decrease in angle as $r/L_c \rightarrow 1$ as shown in Figure 4–20.

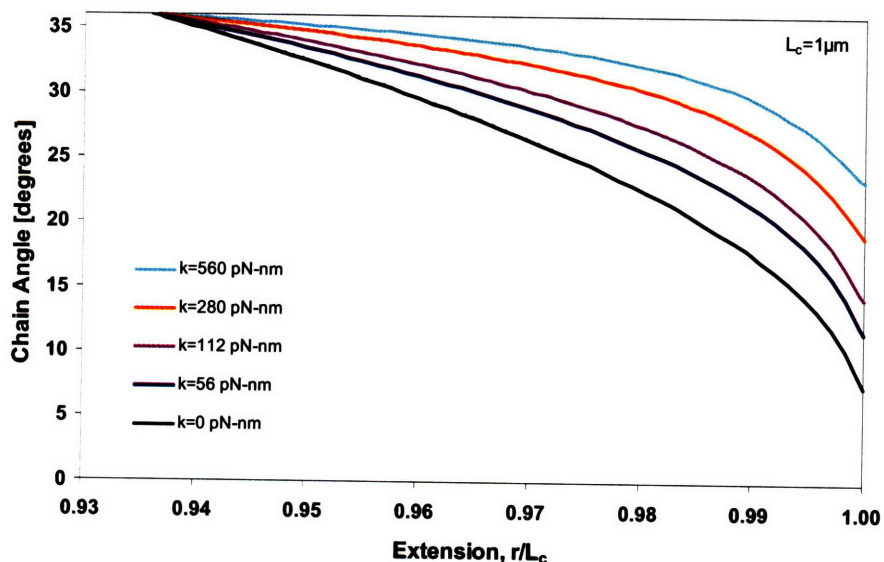


Figure 4–20. Chain angle evolution with extension of actin-FLN finite element model for varying torsional stiffness

As the torsional stiffness increases, this initial decrease in chain angle becomes more moderate and persists to larger extensions (Figure 4–20). Although the beam bending in the finite element model is enthalpic, it gives insight into the coupling between the torsional resistance and the reduced entropic unbending configuration space. The second simulation will connect the chain angle with this reduced entropic unbending configuration space.

The second simulation is a hybrid extensible filament model with rigid ends and a middle section that deforms elastically via entropic unbending and enthalpic stretching. The model geometry for the second simulation must be recalculated for each increment in extension since a change to the entropic configuration space is realized through changes to r_0 , and to a lesser extent L_c . The kinematical framework for the hybrid model is based on separating the filament into three regions: the two ends and the center section (Figure 2–3).

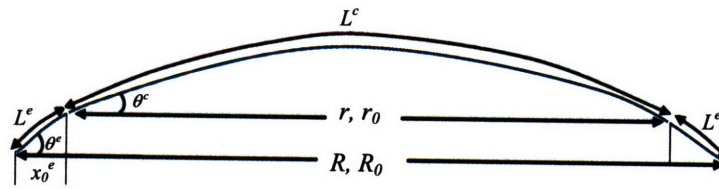


Figure 4–21. Geometry for hybrid model with three sections: two ends and center

The total extension for the filament, R , and the total stretch, λ^T , are given as

$$R = 2x^e + r \quad (4.32)$$

$$\lambda^T = \frac{R}{R_0} = \frac{2x^e + r}{2x_0^e + r_0} \quad (4.33)$$

The center section is composed of an extensible filament, with the same multiplicative decomposition of stretch into the entropic unbending and enthalpic extension stretches:

$$\lambda^c = \frac{r}{r_0} = \lambda_s^c \lambda_u^c \quad (4.34)$$

where r_0 and r are now defined as

$$r_0 = R_0 - 2x_0^e = R_0 - 2L_0^e \cos(\theta_0^e) \quad (4.35)$$

$$r = R - 2x^e = R - 2L^e \cos(\theta^e). \quad (4.36)$$

The end sections are only subject to enthalpic stretching and rotation. The kinematics may be simplified by assuming that the end sections are straightened out and/or are rigid. One could alternatively note that the enthalpic stretch from the center section will be much larger than the enthalpic stretch for the end section ($\lambda_s^c \gg \lambda_s^e$) leading to the recognition that $\lambda_s^e = L^e/L_0^e \approx 1$ may be neglected without introducing much error. Therefore, $L^e = L_0^e$, and the end stretch is given by the following multiplicative decomposition between end stretch from enthalpic extension, λ_s^e , and end stretch from a rotation of the chain angle, λ_θ^e ,

$$\lambda^e = \frac{x^e}{x_0^e} = \lambda_s^e \lambda_\theta^e \approx \lambda_\theta^e \quad (4.37)$$

where

$$\lambda_\theta^e = \frac{L^e \cos(\theta)}{L_0^e \cos(\theta_0)} \approx \frac{\cos(\theta^e)}{\cos(\theta_0^e)}. \quad (4.38)$$

The initial conditions are given at $R=R_0$, $\theta^e = \theta_0^e = 36^\circ$. And since the sections are in series, the force equilibrium gives

$$f^T = f^e = f^c \quad (4.39)$$

We begin to parametrically evaluate the behavior of the hybrid model by retaining the assumption that the contour lengths of the rigid ends remain constant. We also choose the chain angle evolution from the first simulation associated with a five fold increase in torsion stiffness ($k_{CL}=280$). A close look at Figure 4–19, however, shows that the rigid ends can have different lengths. Figure 4–22 shows the force-extension behavior for the hybrid model with different rigid end lengths that remain constant throughout the deformation. Increasing the rigid end length decreases the contour length available to the center section, leading to a decrease in available configurations and an increase in axial filament stiffness.

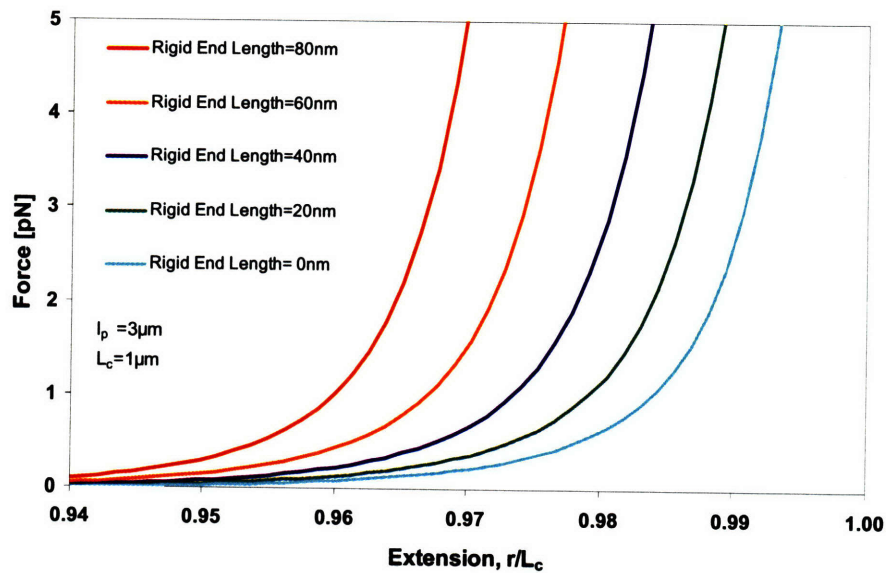


Figure 4–22. Force-extension of hybrid model with constant rigid end length

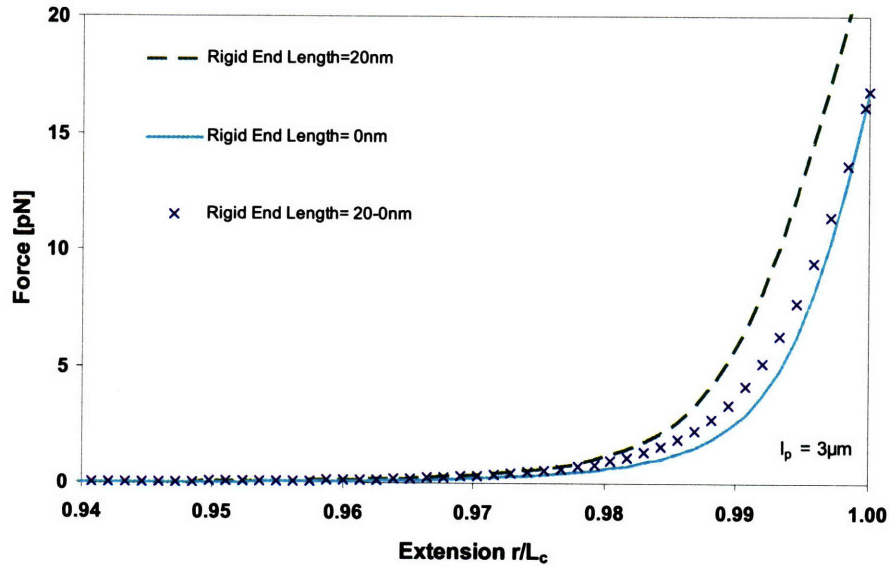


Figure 4–23. Force-extension of hybrid model with varying rigid end length

Figure 4–23 shows the force-extension behavior for the hybrid model with two constant rigid end lengths and a third case in which the rigid end length decreases proportionally to the decreasing chain angle, following the trends seen in Figure 4–19. The decrease in rigid end length mitigates some of the strain stiffening effects at higher extensions as the variable end length curve crosses over between the $L^e=20\text{nm}$ and $L^e=0\text{nm}$ cases.

In concert, the two simulations demonstrate the coupling between cross-links and the entropic unbending response of the extensible filament. The influence of this coupling is greater for cross-links with larger torsional stiffnesses. The influence is mitigated somewhat by the observed decrease in lengths of the rigid ends (which serves to increase the entropic unbending configuration space).

CHAPTER 5 Viscoelastic network model

5.1 Previous viscoelastic modeling work

The importance of understanding the viscoelastic behavior of cells is evident by observing the significant difference in viscoelastic properties between healthy and diseased cells. For example, a decrease in cell modulus and apparent viscosity has been linked with transformations of cells into chondrosarcomas, providing insight into how the viscoelastic properties reflect the metastatic potential and invasiveness of these cells (Darling et al., 2007). Cytoskeletal filament networks can exhibit significant viscoelastic effects independent of fluid flow, as summarized in Chapter 1 for AF, IF, and MT. There have been multiple viscoelastic continuum modeling approaches for the time-dependent response of cells and/or their cytoskeletal networks.

5.1.1 Maxwell model

In addition to the cortical shell-liquid/solid core models referenced in Chapter 3, linear Maxwell viscoelastic models have been used to predict the response of the membrane/cortex during deformation by microcantilevers (Hwang and Waugh, 1997), micropipette aspiration (Evans, 1989; Zhelev et al., 1994), falling ball viscosimetry (Dimova et al., 1999), optical traps (Dao et al., 2003; Mills et al., 2004). The cytoskeleton has similarly been modeled as a linear Maxwell viscoelastic solid during deformations from laser tracking microscopy (Yamada et al., 2000), magnetocytometry (Karcher et al., 2003), AFM (Wu et al., 1998; Darling et al., 2006), and micropipette

aspiration (Schmid-Schonbein et al., 1981; Theret et al., 1988). The Maxwell leg within a rheological model is depicted in Figure 5–1, consisting

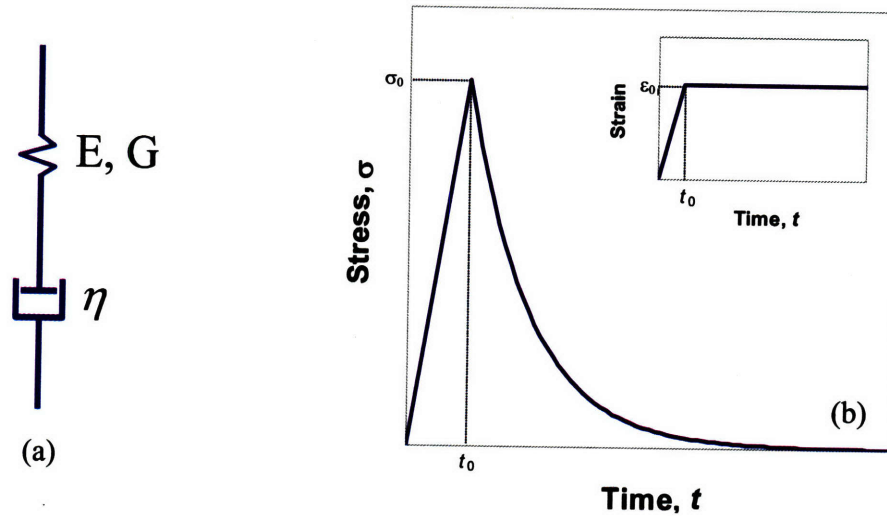


Figure 5–1. (a) Maxwell viscoelastic rheological model and (b) corresponding stress relaxation response from constant strain input (inset).

of a linear elastic spring characterized by either its Young's modulus (E) or shear modulus (G), and a viscous dashpot characterized by its viscosity (η). For a constant strain input, ϵ_0 , the Maxwell model captures the viscoelastic stress relaxation response (to a final stress of zero) from an initial stress of σ_0 for $t > t_0$, as illustrated in Figure 5–1 and given by

$$\sigma_{Maxwell} = \sigma_0 \exp\left(-\frac{E}{\eta}(t-t_0)\right), \quad (5.1)$$

where σ is the stress, and t is time. Based on Equation (5.1), the characteristic relaxation time is given by $t_r = \eta/E$.

5.1.2 Kelvin-voigt model

The Maxwell model is often combined with the Kelvin-Voigt model (Figure 5–2) which captures the creep response of materials subjected to a constant stress.

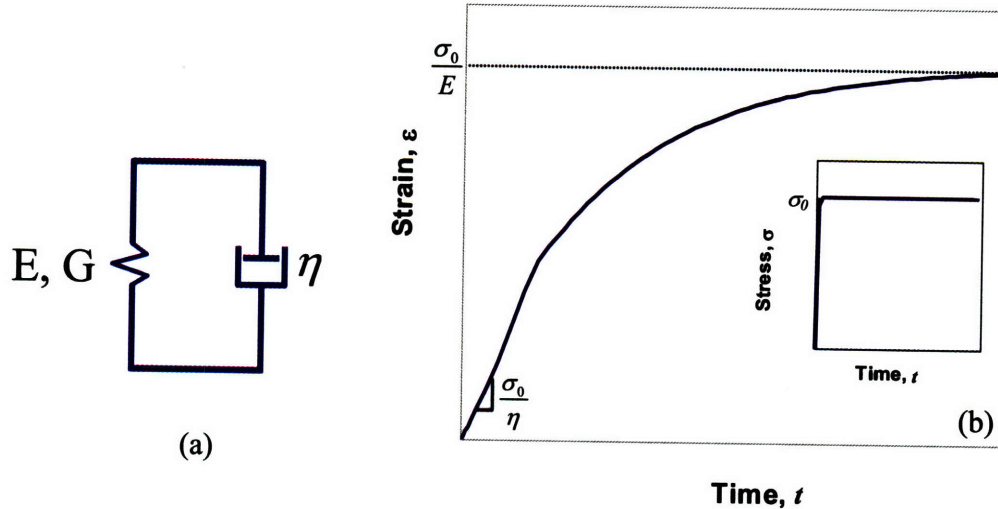


Figure 5–2. (a) Kelvin-Voigt viscoelastic rheological model and (b) corresponding creep response from constant stress input (inset).

For a constant input stress, σ_0 , the Kelvin-Voigt model captures the viscoelastic creep response for $t > t_0$, as illustrated in Figure 5–2b and given by

$$\varepsilon_{KV} = \varepsilon_0 \exp\left(-\frac{E}{\eta}(t-t_0)\right). \quad (5.2)$$

The initial response is dominated by the dashpot, with the initial slope (σ_0/η) in Figure 5–2b solely a function of the initial stress and the dashpot’s viscosity. After the dashpot begins to strain, compatibility constraints dictate that the spring strains an equal amount, and stress gets transferred to the spring. Finally, at long times the spring dominates the response and gives the equilibrium strain (σ_0/E) based on its linear constitutive law.

Maxwell models are widely used as elements in rheological models to simulate cytoskeletal behavior, including recent magnetocytometry experiments on NIH 3T3 fibroblasts (Karcher et al., 2003). Karcher, et al. simulated the vertical displacement of the magnetic bead into a fibroblast cell monolayer using Maxwell (and also Voigt) viscoelastic properties within a finite element model (Karcher et al., 2003). They found for a time constant of 1 sec, the best fit Maxwell shear modulus was approximately 600Pa, while the best fit Voigt shear modulus was about 100Pa, with the Maxwell model slightly more consistent with experimental observations as shown in Figure 5–3 (Karcher et al., 2003).

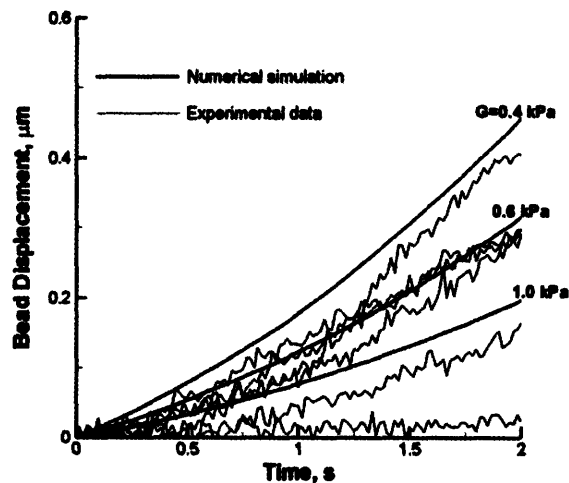


Figure 5–3. Vertical displacement of magnetic bead center as a function of time for three cytoskeletal shear moduli ($G=0.4, 0.6, 1.0\text{kPa}$) using a Maxwell model. Experimental data performed on NIH 3T3 fibroblasts. (Karcher et al., 2003)

5.1.3 Standard linear solid model

The Maxwell model in parallel with a spring element forms a standard linear solid model (SLS) shown in Figure 5–4, which is therefore able to capture both the stress

relaxation and creep responses of a material. For example, the time-dependent stress relaxation

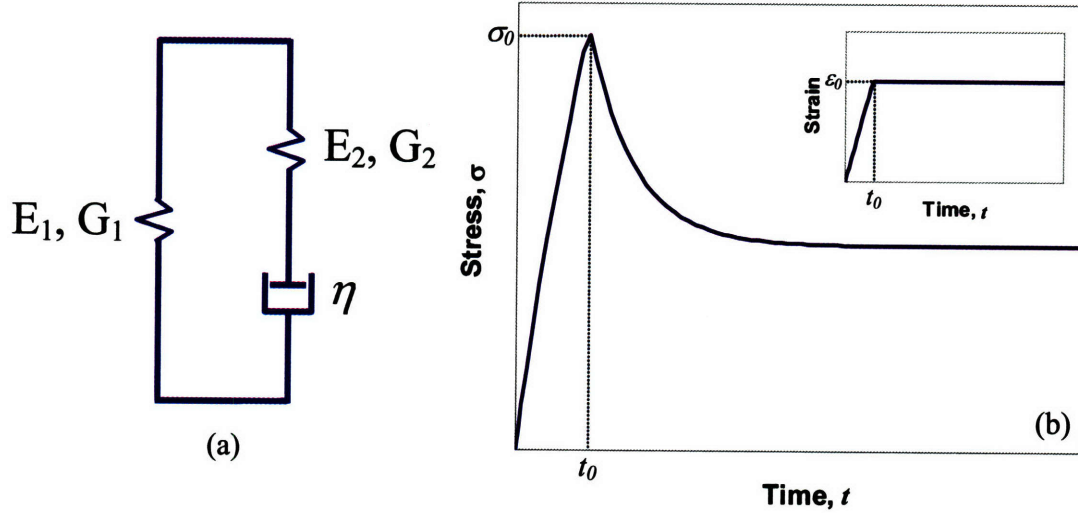


Figure 5–4. Standard linear solid rheological model, and (b) corresponding stress relaxation response from constant strain input (inset).

response for the SLS model (Figure 5–4) subjected to a constant strain, ϵ_0 is

$$\sigma(t) = \left[E_1 + E_2 \exp\left(-\frac{E_2}{\eta} t\right) \right] \epsilon_0 h(t), \quad (5.3)$$

where $h(t)$ is the Heaviside step function defined as

$$h(t) = \begin{cases} 0 & t < 0 \\ 1 & t \geq 0 \end{cases}. \quad (5.4)$$

The relaxation modulus is identified as

$$E_r(t) = E_1 + E_2 \exp\left(-\frac{E_2}{\eta} t\right). \quad (5.5)$$

Thus, the initial, short-term glassy relaxation modulus (E_{rg}) and long-term, equilibrium relaxation modulus (E_{re}), and relaxation time constant (t_r) are found to be

$$E_{rg}(t) = E_r(t = 0^+) = E_1 + E_2 \quad (5.6)$$

$$E_{re}(t) = E_r(t \rightarrow \infty) = E_1 \quad (5.7)$$

$$t_r = \frac{\eta}{E_2}. \quad (5.8)$$

Additional dashpots have also been added to the SLS model to capture the additional creep response of cells probed via magnetic bead microrheology. Figure 5–5

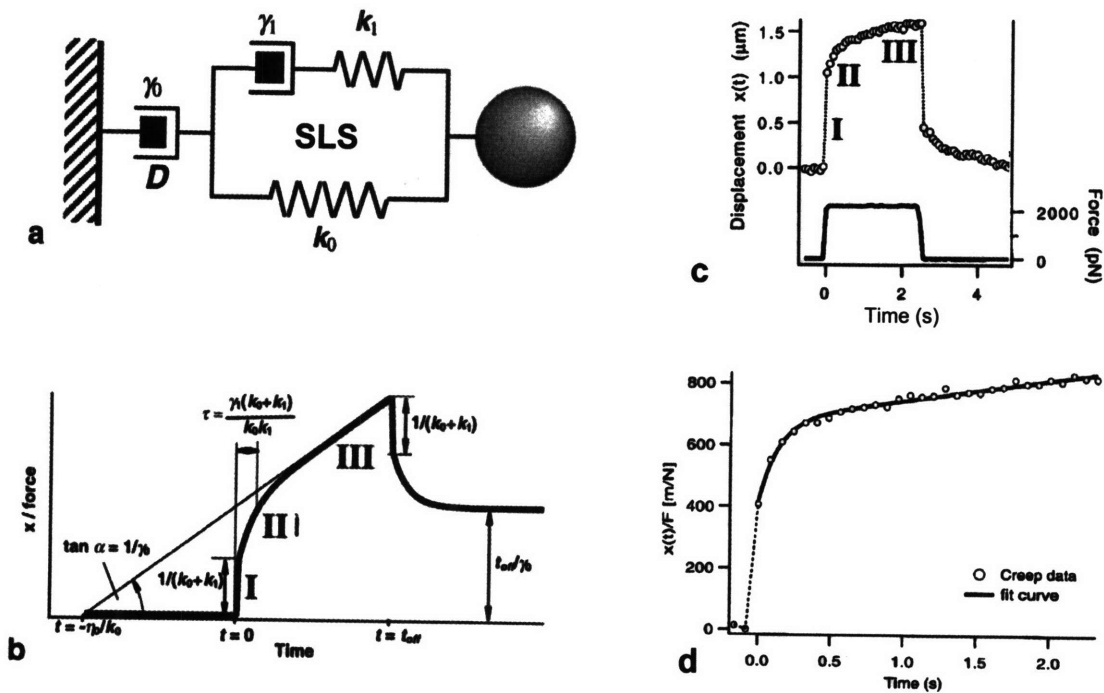


Figure 5–5. (a) Rheological model consisting of a SLS model in series with an extra dashpot (D), (b) Creep response and relaxation curve for rheological model with three response regions (I-III), (c) Experimental force input and displacement response with corresponding response regions (I-III), (d) Curve fit for creep data for $F=1.1\text{ nN}$ on a cell probed via magnetic bead microrheology. Adapted from (Bausch et al., 1998).

shows the rheological model and experimental data for a 4.5- μm bead bound to the membrane of a 3T3 fibroblast through a presumed fibronectin-integrin linkage (Bausch et al., 1998). They experimentally observed three regimes of creep response (Figure 5–5c). The SLS model, however, was only capable of explaining the behavior in regions I and II (Figure 5–5b). The total rheological model therefore consists of a SLS model in series with an extra dashpot (Figure 5–5a) to capture the end slope observed in region III, as demonstrated through the curve fit in Figure 5–5d. There is considerable variability in the viscoelastic response between cells of the *same* cell type, with viscoelastic parameters differing by up to an order of magnitude, while noting that that the values obtained for each individual cell differ by much less (Bausch et al., 1998).

The basic SLS model, however, has been used to capture the viscoelastic behavior of many biomaterials, including the stress-relaxation response for superficial and deep articular chondrocytes. The test consisted of rapid indentation via an AFM of the cell using closed-loop control to hold the displacement constant, followed by a 60 second stress relaxation phase as shown in Figure 5–6 (Darling et al., 2006). The cantilever compressed the cell until a force of 2.5 nN was reached, then the AFM's displacement was held to observe the stress-relaxation of the cell, indenting the cell approximately 1.3-

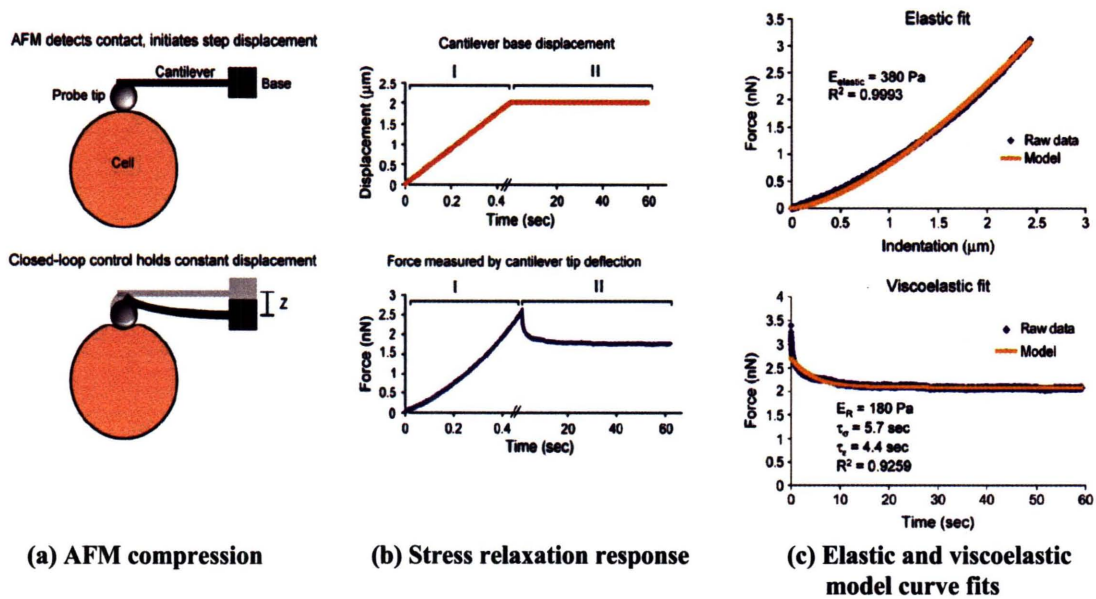


Figure 5–6. (a) Closed-loop control during stress-relaxation tests of an articular chondrocyte using a spherical AFM probe tip, (b) corresponding AFM probe displacement input and stress relaxation response of chondrocytes, and (c) example data sets shown with elastic and viscoelastic curve fits. Adapted from (Darling et al., 2006).

2.1 μm (Darling et al., 2006). Note that the schematic of the AFM probe tip in Figure 5–6a is not to scale since the probe tip diameter was 5 μm and the cell diameters ranged from 7-15 μm (Darling et al., 2006). The elastic modulus of the deep chondrocytes cells was calculated from the initial indentation ($E_{\text{elastic}} = 610 \pm 340 \text{ Pa}$) and after relaxation ($E_{\text{equil}} = 240 \pm 130 \text{ Pa}$) using a modified Hertz equation (Harding and Sneddon, 1945),

$$F = \frac{4Er^{1/2}}{3(1-\nu^2)} \delta_z^{3/2} \quad (5.9)$$

where F is the applied force via the AFM cantilever, E is Young's modulus, r is the relative radius ($r = (1/r_{\text{tip}} + 1/r_{\text{cell}})^{-1}$), ν is the Poisson ratio, and δ_z is the vertical indentation distance (Darling et al., 2006). Both types of cells exhibited stress relaxation behavior that was captured with a SLS model, reaching an equilibrium reaction force in approximately 30 s (Darling et al., 2006). The viscoelastic moduli for deep chondrocytes

($E_{rg}=290\pm 140\text{Pa}$, $E_{re}=170\pm 90\text{Pa}$, $t_r=5.2\pm 3.5$ sec) found by fitting the relaxation data, agreed with the indentation-derived elastic moduli within 50% for initial values and 30% for equilibrium values (Darling et al., 2006). Significant differences in mechanical properties were observed between the two types of chondrocytes, with measured values for the superficial cells exceeding those of the middle/deep cells by 90% on average (Darling et al., 2006).

The time-dependent shear stress-strain response of a linear viscoelastic material subject to an arbitrary strain history may be defined in terms of the shear relaxation modulus, $G(t-t')$, and the strain history using the superposition principle of linear viscoelasticity,

$$\tau(t-t') = \int_{-\infty}^t G(t-t') \frac{d\gamma}{dt'} dt' \quad (5.10)$$

where $d\gamma/dt'$ is the rate of shear strain. Note that the shear relaxation modulus can be related to the axial relaxation modulus $E_r(t)$ and Poisson ratio $\nu(t)$. The frequency dependence of the elastic response, rather than the time dependence, is often used to measure the viscoelastic behavior. Thus we introduce an oscillating shear strain and shear strain rate of

$$\begin{aligned} \gamma(t) &= \gamma_0 \sin(\omega t) \\ \frac{d\gamma(t)}{dt} &= \omega \gamma_0 \cos(\omega t) \end{aligned} \quad (5.11)$$

where ω is the frequency in radians/sec, γ_0 is the initial amplitude and $\gamma(t=0)=0$ for convenience. Substituting Eqs (5.11) into (5.10) and employing a new integration variable, $t''=t-t'$ and the trigonometric identity $\cos(\alpha-\beta)=\sin\alpha \sin\beta + \cos\alpha \cos\beta$, yields a new expression for the shear stress with a frequency dependence,

$$\tau = \left[\omega \int_0^{\infty} \sin(\omega t'') dt'' \right] \gamma_0 \sin(\omega t) + \left[\omega \int_0^{\infty} \cos(\omega t'') dt'' \right] \gamma_0 \cos(\omega t). \quad (5.12)$$

This can be simplified with Eqs (5.11) and introducing a frequency-dependent storage modulus, $G'(\omega)$, and loss modulus, $G''(\omega)$,

$$\tau = G'(\omega)\gamma(t) + \frac{G''(\omega)}{\omega} \frac{d\gamma(t)}{dt}. \quad (5.13)$$

Note that $G'(\omega)$ and $G''(\omega)$ are 90° out of phase. If $G''(\omega)=0$, $G'(\omega)$ becomes a frequency-dependent version of the elastic shear modulus and elastic energy is stored and retrieved within the system. Conversely, if $G'(\omega)=0$, then the viscous response dominates and $G''(\omega)/\omega$ becomes a frequency-dependent dynamic viscosity within Newton's law for a viscous fluid. The complex shear modulus which incorporates both the storage and loss moduli, and their phase separation is defined

$$G^* = G'(\omega) + iG''(\omega) \quad (5.14)$$

$$\tan \delta = \frac{G''(\omega)}{G'(\omega)}, \quad (5.15)$$

where δ is the phase angle in radians. The storage and loss moduli are then obtained in terms of the phase angle and amplitudes of the shear stress (τ_0) and shear strain (γ_0) in forced oscillation.

$$G'(\omega) = \frac{\tau_0}{\gamma_0} \cos \delta \quad (5.16)$$

$$G''(\omega) = \frac{\tau_0}{\gamma_0} \sin \delta \quad (5.17)$$

The absolute magnitude of the complex shear modulus is then given by

$$|G^*| = \frac{\tau_0}{\gamma_0} = \sqrt{[G'(\omega)]^2 + [G''(\omega)]^2}. \quad (5.18)$$

Note that the same approach can be used for axial loading conditions to obtain E' , E'' , and E^* .

5.1.4 Quasilinear viscoelastic model

Another phenomenological viscoelastic model often used to model connective tissues (e.g., articular cartilage, ligament, tendon) is the quasilinear viscoelastic (QLV) model developed by Fung (Fung, 1980). The soft tissue is often taken to be incompressible (Giles et al., 2007). The QLV model is similarly defined through a convolution integral of the stress relaxation function which is now separated into a time-dependent reduced relaxation function, $\Xi(t)$, and the time derivative of the instantaneous elastic stress function, σ_e , which is a function of the strain,

$$\sigma(t) = \int_{-\infty}^t \Xi(t-t') \frac{d\sigma_e(\epsilon(t'))}{dt'} dt' = \int_{-\infty}^t \Xi(t-t') \frac{d\sigma_e(\epsilon(t'))}{d\epsilon} \frac{d\epsilon}{dt'} dt' \quad (5.19)$$

where the reduced relaxation function $\Xi(t)$ is given by

$$\Xi(t) = \frac{1 + c \left[\int_{t/\tau_2}^{\infty} \frac{e^{-t}}{t} dt - \int_{t/\tau_1}^{\infty} \frac{e^{-t}}{t} dt \right]}{1 + c \ln \left(\frac{\tau_2}{\tau_1} \right)}, \quad (5.20)$$

and where c is the relaxation index ($c > 0$), τ_1 is the short relaxation time constant, and τ_2 is the long relaxation time constant (Fung, 1980). As $t \rightarrow \infty$, $\Xi(\infty)$ reduces to

$$\Xi(\infty) = \left[1 + c \ln \left(\frac{\tau_2}{\tau_1} \right) \right]^{-1}. \quad (5.21)$$

Note that $\Xi(t)$ is taken to be a scalar here, but could be given as a fourth order tensor in a more general formulation. The QLV model is therefore linear with respect to the relaxation response while still including the dependence on large nonlinear deformation. The nonlinear deformation within the model comes from the elastic tangent stiffness term, $d\sigma_e(\epsilon)/d\epsilon$, with σ_e defined for many soft tissues such as tendon (Woo et al., 1981; Woo et al., 1993; Hewitt et al., 2001; Sverdluk and Lanir, 2002), cartilage (Woo et al., 1976; Roth and Mow, 1980; Elliott et al., 2002), ligament (Kwan et al., 1993; Puso and Weiss, 1998; Weiss and Gardiner, 2001; Abramowitch and Woo, 2004), aortic valves (Doehring et al., 2004), bladder tissue (Nagatomi et al., 2004), and meniscus (Fithian et al., 1989; Fithian et al., 1990). The general form is given by

$$\sigma_e = A(\exp(B\epsilon) - 1) \quad (5.22)$$

where the material-specific constants A and B ($A > 0$, units of Pa; B is unitless) (Sarver et al., 2003). Approximations for simplifying the process for fitting QLV constants have been recently proposed (Toms et al., 2002; Abramowitch and Woo, 2004).

The QLV viscoelastic (c , τ_1 , τ_2) and elastic (A , B) parameters are traditionally fit to the stress relaxation data after normalizing the data by the peak stress (Kwan et al., 1993; Yang et al., 2006). This approach (denoted as the “G” method in Figure 5–7a) uses a single strain step and exhibits a strain-dependence (Sarver et al., 2003). While the QLV theory is able to fit the data using the standard G-method, a strain-independent approach developed by Sarver, et al. to evaluate the QLV theory (which also assumes strain-independent relaxation). The strain-independent normalization (denoted as the “Q_n”

method in Figure 5–7b) also accounts for the relaxation as the load is applied, and is defined as (Sarver et al., 2003)

$$\frac{\sigma(t) - \sigma_f^i}{\sigma_p^i - \sigma_f^i} = \frac{Q^i(t)}{Q^i(t_p^i)} = Q_n^i(t), \quad (5.23)$$

where σ_f is the final stress, σ_p is the peak stress, t_p is the peak time, Q is the relaxation factor, and Q_n is the normalized relaxation factor.

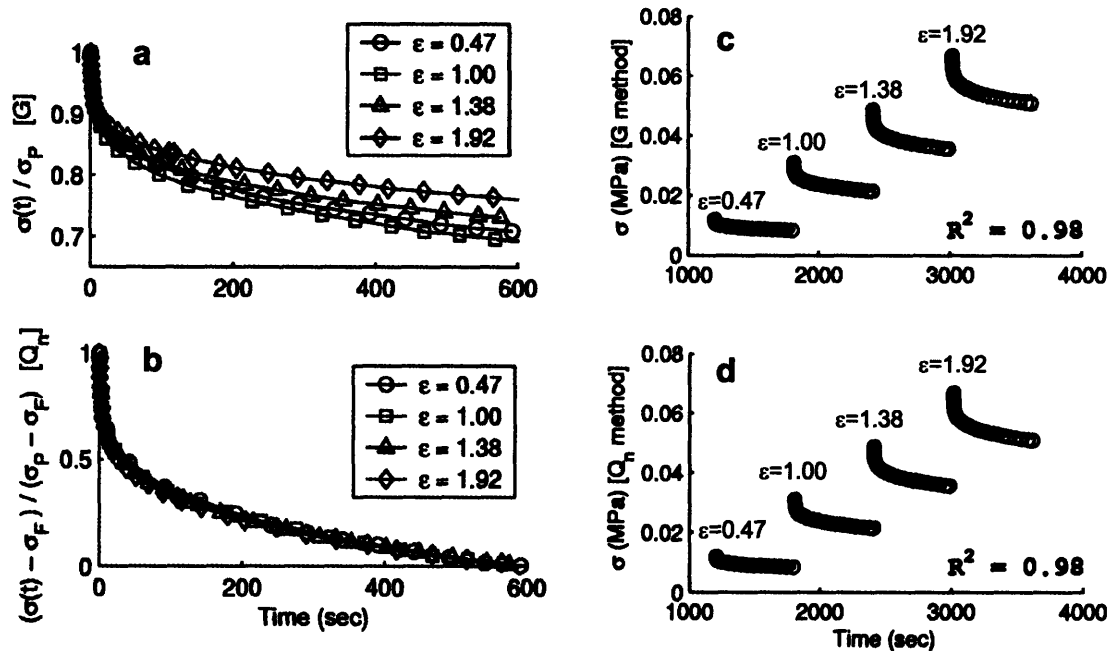


Figure 5–7. Normalized (a,b) and nonnormalized (c,d) stress relaxation of flexor tendon at different strains using the G-method (a,c) and Q_n -method (b,d). Adapted from (Sarver et al., 2003).

Note that the final relaxation stress at $t=600$ sec is not at equilibrium, but Sarver, et al. project that equilibrium relaxation would occur at $t=2000$ sec, and their sensitivity analysis indicated that the additional decrease in stress required to reach equilibrium would be unlikely to affect the calculated parameters (Sarver et al., 2003). The

viscoelastic and elastic QLV parameters used to fit the data in Figure 5–7 are shown in Table 5–1.

Parameter	G-method	Q _n -method
C	0.90±1.16	2.01±3.22
τ ₁ (sec)	1.56±1.07	1.07±0.57
τ ₂ (sec)	1478±634	1159±179
A (MPa)	1.87±2.32	1.65±2.19
B	9.87±0.31	29.3±37.4

Table 5–1 QLV viscoelastic (C , τ_1 , τ_2) and elastic (A , B) parameters used to fit stress relaxation data of flexor tendon at four strain increments using the G-method and the Q_n-method. Adapted from (Sarver et al., 2003).

The viscoelastic parameters (C , τ_1 , τ_2) were similar for both methods, with smaller standard deviations for the time constants via the Q_n-method. While the methods also had similar values for A , they differed in their estimation of B , with high standard deviations in the Q_n-method. Sarver, et al. used a sensitivity analysis to note that there is poor confidence in both methods for estimating B , but that estimating B by fitting to the nonlinear equilibrium stress-strain function, Equation (5.22), provides a better estimate by decoupling estimation of elastic and viscoelastic parameters of the QLV model (Sarver et al., 2003). Their sensitivity analysis also indicated greater confidence in the two relaxation time constants via the Q_n-method (Sarver et al., 2003). While the Q_n-method was seen to be preferable for stress relaxation studies with incremental strains, the overall validity of the QLV assumption of strain-independent relaxation remains an open question.

QLV has also been used successfully to model other soft tissues which respond on different time-scales, such as esophageal tissue which had relaxation time constants of

approximately $\tau_1 \sim 3\text{sec}$ $\tau_2 \sim 90\text{sec}$ for strains of $\epsilon \sim 0.4-0.8$ with a maximum fitting error of $<4\%$ (Yang et al., 2006). The stress relaxation time constants for the esophageal tissue did not significantly vary with increasing strain, supporting the QLV assumption of strain-independent relaxation (Yang et al., 2006).

There has been some recent work which suggests that the QLV model is insufficient to simulate interrelated creep and stress relaxation in soft biological tissues such as tendon. Since QLV assumes a separable relation as a product of functions of time and strain, it does not allow interrelations between creep and relaxation since a separable form for creep becomes a nonseparable form for relaxation (Lakes and Vanderby, 1999; Oza et al., 2006). QLV has also been unable to capture low load regions where creep rate is a strong function of stress level (Provenzano et al., 2001). Lakes, et al. have utilized modified, nonlinear, superposition instead of QLV to model the strain-dependent stress-relaxation and creep behavior of ligaments (Provenzano et al., 2002; Oza et al., 2006). The modified superposition approach allows the relaxation function to depend on strain, as well as time, through a nonseparable strain-dependent power law, $\Xi(\gamma, t) = A(\gamma) t^{B(\gamma)}$, where $A(\gamma)$ represents the initial modulus, $\Xi(t=0)$, and $B(\gamma)$ characterizes the strain-dependent rate of stress relaxation and can take the form $B(\gamma) = g(\gamma)n_0$, where n_0 is an initial relaxation rate and $g(\gamma)$ accounts for strain-dependent nonlinearity in the relaxation rate (Provenzano et al., 2002). Thornton, et al. have showed that the experimental creep response of ligaments is not captured by the time domain function for creep predicted from the experimental QLV stress relaxation function (Thornton et al., 1997). They note that Fung (Fung, 1993) also speculated that creep is more nonlinear than relaxation, and that creep-related microstructural processes

could be very different from relaxation-related processes, perhaps related to the crimp pattern in the collagen fiber structure of ligaments (Thornton et al., 1997; Thornton et al., 2001). Instead, they model fiber creep with the inverse stress relaxation function and use a microstructural model that include linear variations in crimp pattern to simulate collagen fiber recruitment to capture the experimental creep behavior of ligaments (Thornton et al., 2001).

The QLV model has recently been used, however, to describe the experimentally observed phenomenon in which myocardium and skin tissues exhibit a decrease in nonlinear stiffness with an increase in loading rate during cyclic, load-controlled tests as shown in Figure 5–8a (Giles et al., 2007). This is counter-intuitive based on the increased stiffness that accompanies increased loading rates in cyclic, strain-controlled experiments (Haut and Little, 1972; Demer and Yin, 1983; Pioletti et al., 1999; Pioletti and Rakotomanana, 2000). Giles, et al. found that this behavior is not restricted to cyclic load-controlled experiments and is based on the nonlinear effects and creep behavior

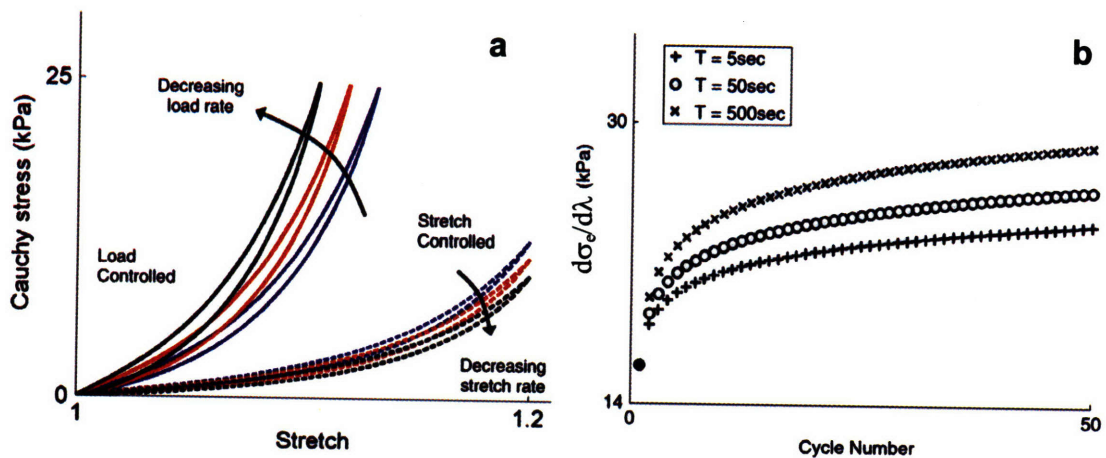


Figure 5–8. (a) Fully preconditioned stress -stretch response for uniaxial tension of porcine skin and myocardium with varying stretch or load rates (cyclic deformation periods of $t=5, 50, 500$ sec), and (b) elastic tangent stiffness ($d\sigma_e/d\lambda$) at the start of each loading cycle as a function of cycle number with the same deformation periods. Adapted from (Giles et al., 2007).

within the context of cyclic load controlled deformations during preconditioning of tissues (Giles et al., 2007). Substantial creep occurs during preconditioning, with subsequent loading cycles beginning at larger prestretches, and therefore well into the nonlinear regime of the elastic stress response (Giles et al., 2007). Figure 5–8b shows the elastic tangent stiffness term, $d\sigma_e(\epsilon)/d\lambda$, as a function of the number of uniaxial load cycles for the same deformation periods shown in Figure 5–8a, ($t=5, 50, 500\text{sec}$), with increasing period (slower loading rate) leading to an increase in material creep and therefore a stiffer response (Giles et al., 2007).

The QLV theory has also been used to model the frequency-dependent response of soft tissues under oscillatory loading conditions. The complex shear modulus may be applied to the QLV model to yield frequency-dependent storage and loss moduli (Chan and Titze, 2000),

$$G'(\omega) = \frac{1 + \frac{c}{2} [\ln(1 + \omega^2 \tau_2^2) - \ln(1 + \omega^2 \tau_1^2)]}{1 + c \ln(\tau_2/\tau_1)} \quad (5.24)$$

$$G''(\omega) = \frac{c [\tan^{-1}(\omega \tau_2) - \tan^{-1}(\omega \tau_1)]}{1 + c \ln(\tau_2/\tau_1)}. \quad (5.25)$$

In general, larger values of the viscoelastic parameter c correspond to a higher damping ratio across a wide range of frequency (10^{-3} - 10^3 Hz), an increase in frequency sensitivity, and an increase in stress relaxation magnitude and rate (Sauren and Rousseau, 1983). The time constants (τ_1, τ_2) define the range of the stress relaxation spectrum and thus the frequency-insensitive range of the damping curve, with τ_1 governing the fast viscous phenomenon (high-frequency limit of the damping curve) and τ_2 governing the low viscous phenomenon (low-frequency limit of the damping curve) (Sauren and

Rousseau, 1983; Chan and Titze, 2000). Therefore a reduction in τ_1 or an increase in τ_2 increases the bandwidth of the damping curve and in turn makes the model more frequency-insensitive (Chan and Titze, 2000).

Frequency-dependent analyses using the QLV with some modifications have also been made for plantar soft tissue (Ledoux et al., 2004), lumbar nucleus pulposus (spinal disk) (Iatridis et al., 1997). The results of a frequency-dependent analysis of canine vocal fold mucosa (“vocal chords”) using the QLV model are shown in Figure 5–9. Chan used

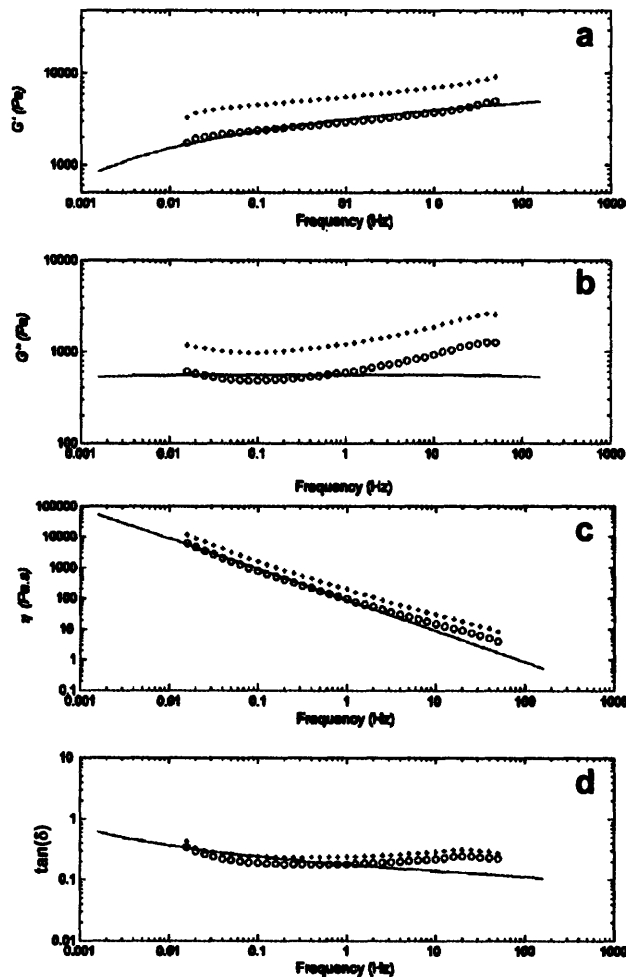


Figure 5–9. (a) Storage modulus (G'), (b) loss modulus (G''), (c) dynamic viscosity (η), and (d) damping ratio ($\tan(\delta)$) for canine vocal fold mucosa based on the QLV model (o=mean value, +=standard deviation). Adapted from(Chan, 2004).

a controlled strain torsional rheometer to obtain higher frequency (up to 50 Hz) measurements compared with previous stress controlled rheometric experiments. The best fit QLV viscoelastic properties were $c=10$, $\tau_1=0.1\text{msec}$, and $\tau_2=1000\text{sec}$, with reasonably accurate descriptions of G' and η (Figure 5–9a,c) and poor performance for G'' and $\tan(\delta)$ (Figure 5–9b,d) (Chan, 2004). The QLV model could not capture the gradual increase in G'' , and the corresponding increase in $\tan(\delta)$, from 1-50Hz with the greatest error at the relatively higher frequencies (15-50Hz) (Chan, 2004).

5.1.5 Power law model

Absolute values of the complex shear modulus, G^* , and relaxation time spectra have been measured using AFM and then fit to an empirical power-law structural damping model (Alcaraz et al., 2003; Smith et al., 2005), given as

$$G^*(\omega) = \bar{G}_0(1 + i\bar{\eta}) \left(\frac{\omega}{\omega_0} \right)^{\alpha'} \Gamma(1 - \alpha') \cos\left(\frac{\pi\alpha'}{2}\right) + i\omega\mu, \quad (5.26)$$

where $\bar{\eta} = \tan(\alpha'\pi/2)$ is the structural damping coefficient, α' is the power-law exponent, \bar{G}_0 is a scale factor for the storage and loss moduli, μ is viscosity, Γ is the gamma function, and ω_0 is a scale factor for the frequency. The factor $\Gamma(1-\alpha')\cos(\pi\alpha'/2)$ is close to unity for small values of α' (Smith et al., 2005). The structural (or hysteretic) damping power-law relationship was developed in part by (Weber, 1841; Kohlrausch, 1866; Crandall, 1970) and applied to biological structures by (Hildebrandt, 1969; Fredberg and Stamenovic, 1989; Fabry et al., 2001). The power-law model and the spring/dashpot

rheological models, however, do not include microstructural details of the cytoskeleton, their mechanobiological contribution, or the ability to account for their microstructural rearrangement.

Most viscoelastic cytoskeletal models also assume the cytoplasm to be a homogeneous, continuous medium that does not include spatial variation within the cell (Hochmuth and Waugh, 1987; Sato et al., 1990; Schmid-Schonbein et al., 1995; Satcher and Dewey, 1996; Thoumine and Ott, 1997b; Thoumine and Ott, 1997a). The tensegrity model has been adapted for viscoelastic behavior (Canadas et al., 2002), and compared with the viscoelastic response of the cellular solid model to determine the influence of spatial rearrangement and bending of filaments (Canadas et al., 2003), which emphasized the coupling between the cellular viscoelastic response and the underlying cytoskeletal architecture. As seen before with tensegrity models and cellular solid models, however, they omit the influence of thermal fluctuations on elasticity, do not lend themselves to modeling polymerization of just one filament network, and also do not account for either the nonaffine motion or the ability of networks to accommodate deformation through rotation of filaments. Therefore, we need a cytoskeletal network model that captures the viscoelastic behavior within a microstructurally-informed framework.

5.2 Linear rheological model

The viscoelastic response is captured in this model by adding a linear viscoelastic Maxwell leg to the network model to account for intermolecular shear viscosity (see Figure 5–10), since the Maxwell model has been shown to be somewhat more consistent

with experimental observations of cytoskeletal contributions to cellular mechanical behavior (Karcher et al., 2003).

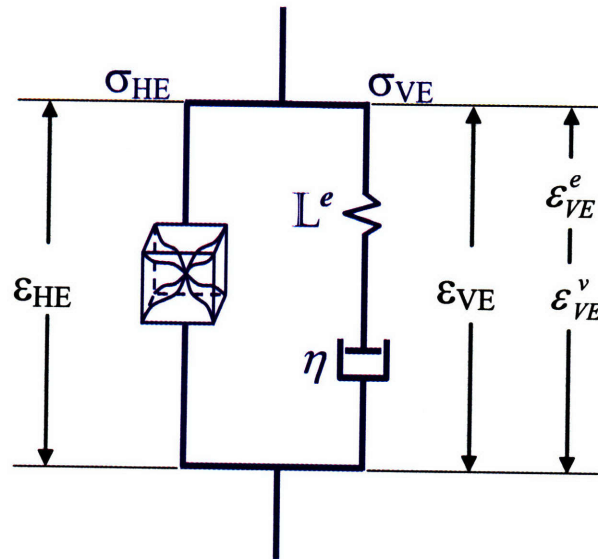


Figure 5–10. Viscoelastic rheological model for cytoskeletal network with intermolecular shear viscosity.

The rheological model shown in Figure 5–10 is the standard linear solid model commonly used to simulate viscoelastic behavior in cells (Schmid-Schonbein et al., 1981; Sung et al., 1988; Lipowsky et al., 1991), but adapted here with a nonlinear hyperelastic leg and a linear viscoelastic Maxwell leg (with η = viscosity and L^e = the 4th order elastic modulus tensor). The hyperelastic leg contains the extensible network model with its contributions from entropic filament unbending, enthalpic filament stretching, cross-link torsion, and bulk compressibility.

5.2.1 Continuum mechanics derivation

The inclusion of the SLS rheological model for intermolecular shear viscoelasticity within the 3D network framework, for finite deformation, is detailed in this section. The Cauchy stress in the hyperelastic leg in Figure 5–10 is defined as

$$\mathbf{T}_{HE} = \mathbf{T}_{Network} + \mathbf{T}_{Cross-link} + K_B (J - 1) \mathbf{I} \quad (5.27)$$

where $\mathbf{T}_{Network}$ was defined by Eqs. (2.31), (2.33), (2.35), (2.37), (3.34) and $\mathbf{T}_{Cross-link}$ was defined by Eqs. (4.7)-(4.12). The Cauchy stress in the viscoelastic leg is defined by

$$\mathbf{T}_{VE} = (1/J) L^e \ln(\mathbf{V}_{VE}^e) \quad (5.28)$$

where $\ln(\mathbf{V}_{VE}^e)$ is the Hencky strain tensor defined by (Anand, 1979)

$$\ln(\mathbf{V}_{VE}^e) = \frac{1}{2} \ln[\mathbf{F}_{VE}^e (\mathbf{F}_{VE}^e)^T]. \quad (5.29)$$

Since the legs are in parallel, stress equilibrium requires that the total stress be the sum of the stress in the two legs.

$$\mathbf{T} = \mathbf{T}_{HE} + \mathbf{T}_{VE} \quad (5.30)$$

Conversely, the deformation gradients of the two parallel legs are equivalent.

$$\mathbf{F} = \mathbf{F}_{HE} = \mathbf{F}_{VE} \quad (5.31)$$

The deformation gradient, \mathbf{F} , can be multiplicatively decomposed into elastic (\mathbf{F}^e) and viscous (\mathbf{F}^v) components following a Kröner-Lee decomposition (Kröner, 1959; Lee, 1969) for viscoelastic materials (Boyce et al., 1988; Bergstrom and Boyce, 2000; Qi and Boyce, 2005; Mulliken and Boyce, 2006) (Figure 2–9).

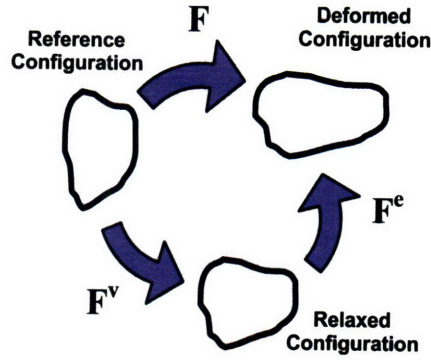


Figure 5–11. Multiplicative decomposition of the deformation gradient into viscous and elastic components

This decomposition can be related in terms of the rheological model in Figure 5–10 as

$$\mathbf{F} = \mathbf{F}_{HE} = \mathbf{F}_{VE} = \mathbf{F}^e \mathbf{F}^v, \quad (5.32)$$

which can be rearranged to define the elastic deformation gradient as

$$\mathbf{F}^e = \mathbf{F} (\mathbf{F}^v)^{-1}, \quad (5.33)$$

The initial conditions for the viscous deformation gradient and its rate of change are

$$\mathbf{F}^v = \mathbf{1}, \quad \dot{\mathbf{F}}^v = \mathbf{0} \quad (t = 0). \quad (5.34)$$

For times greater than zero, the viscous deformation gradient is updated using a simple forward Euler integration according to

$$\mathbf{F}_{t+\Delta t}^v = \mathbf{F}_t^v + \dot{\mathbf{F}}_t^v \Delta t \quad (t > 0). \quad (5.35)$$

We now need to find $\dot{\mathbf{F}}^v$ at each time step in order to solve for \mathbf{F}^v . We start with the viscous velocity gradient (\mathbf{L}^v) of the relaxed configuration, defined as

$$\mathbf{L}^v = \dot{\mathbf{F}}^v \mathbf{F}^{v-1} = \mathbf{D}^v + \mathbf{W}^v, \quad (5.36)$$

or in the current, loaded configuration,

$$\tilde{\mathbf{L}}^v = \tilde{\mathbf{D}}^v + \tilde{\mathbf{W}}^v, \quad (5.37)$$

where $\tilde{\mathbf{D}}^v$ is the (symmetric) rate of viscous stretch tensor in the loaded configuration defined as

$$\tilde{\mathbf{D}}^v = \frac{1}{2} [\tilde{\mathbf{L}}^v + (\tilde{\mathbf{L}}^v)^T], \quad (5.38)$$

and $\tilde{\mathbf{W}}^v$ is the (skew) rate of viscous spin tensor in the loaded configuration defined as

$$\tilde{\mathbf{W}}^v = \frac{1}{2} [\tilde{\mathbf{L}}^v - (\tilde{\mathbf{L}}^v)^T] = 0, \quad (5.39)$$

and taken to be zero with no loss in generality (Boyce et al., 1988). The total velocity gradient can be given in terms of its elastic and viscous components,

$$\begin{aligned} \mathbf{L} &= \dot{\mathbf{F}}\mathbf{F}^{-1} = \dot{\mathbf{F}}^e\mathbf{F}^{e-1} + \mathbf{F}^e\dot{\mathbf{F}}^v\mathbf{F}^{v-1}\mathbf{F}^{e-1} = \mathbf{L}^e + \mathbf{F}^e\tilde{\mathbf{L}}^v\mathbf{F}^{e-1}, \\ &= \mathbf{L}^e + \tilde{\mathbf{L}}^v \end{aligned}, \quad (5.40)$$

where \mathbf{L}^e is the elastic velocity gradient in the relaxed configuration and $\tilde{\mathbf{L}}^v$ is the viscous velocity gradient in the loaded, current configuration. Here we employ a linear viscoelastic constitutive relationship to define the rate of stretch in the loaded configuration, $\tilde{\mathbf{D}}^v$, although nonlinear relationships could easily be substituted (Bergstrom and Boyce, 2000; Qi and Boyce, 2005; Mulliken and Boyce, 2006),

$$\tilde{\mathbf{D}}^v = \dot{\gamma} \mathbf{N}^v \quad (5.41)$$

where the magnitude is given by $\dot{\gamma}$, the effective shear strain rate, and the direction is given by the tensor \mathbf{N}^v (in the loaded configuration). The viscous direction tensor, \mathbf{N}^v , is taken to be in the same direction as the deviatoric Cauchy stress acting on the viscoelastic component and therefore given by

$$\mathbf{N}^v = \frac{\mathbf{T}'_{VE}}{|\mathbf{T}'_{VE}|} = \frac{\mathbf{T}'_{VE}}{\sqrt{2}\tau^v}, \quad (5.42)$$

where \mathbf{T}'_{VE} is deviatoric Cauchy stress of the viscoelastic component (in the loaded configuration),

$$\mathbf{T}'_{VE} = \mathbf{T}_{VE} - \frac{1}{3} \text{tr}(\mathbf{T}_{VE}) \mathbf{I} = \mathbf{T}_{VE} - \frac{1}{3} \text{tr}(T_{VE,11} + T_{VE,22} + T_{VE,33}) \mathbf{I}, \quad (5.43)$$

and τ^v is the equivalent shear stress,

$$\tau^v = \sqrt{\frac{1}{2} \mathbf{T}'_{VE} \cdot \mathbf{T}'_{VE}}. \quad (5.44)$$

Finally, the effective shear strain rate, $\dot{\gamma}$, is given in terms of the linear viscosity, η , previously defined in the rheological model,

$$\dot{\gamma} = \frac{\tau^v}{\eta}. \quad (5.45)$$

Note that in the loaded configuration, the rate of viscous stretch can also be given as

$$\tilde{\mathbf{D}}^v = \tilde{\mathbf{L}}^v = \mathbf{F}^e \mathbf{L}^v \mathbf{F}^{e-1} = \mathbf{F}^e \dot{\mathbf{F}}^v \mathbf{F}^{v-1} \mathbf{F}^{e-1}. \quad (5.46)$$

Rearranging this equation to solve for $\dot{\mathbf{F}}^v$ yields

$$\dot{\mathbf{F}}^v = \mathbf{F}^{e-1} \tilde{\mathbf{D}}^v \mathbf{F}^e \mathbf{F}^v, \quad (5.47)$$

which we can simplify using Eqs. (5.32),(5.41)-(5.45) to give

$$\dot{\mathbf{F}}^v = \frac{1}{\sqrt{2}\eta} \mathbf{F}^{e-1} \mathbf{T}'_{VE} \mathbf{F}. \quad (5.48)$$

5.2.2 Comparison with actin-FLNa experimental data

The viscoelastic network model is now compared to the unpublished data by Lee and Kamm (Lee and Kamm, 2008) introduced in Chapter 4, which evaluated the rheology of F-actin networks with FLNa and streptavidin cross-links using a Texas

Instruments AR-2000 torsional rheometer. The AR-2000 software has four options for reducing the viscoelastic parameters from the data (Texas Instruments: Thermal Analysis & Rheology, 2008):

1. Maxwell model: 4 spring/dashpot elements
2. Spriggs model: Infinite number of Maxwell elements (each with the same value of G), with relaxation times related by an inverse power series
3. Oldroyd (Jeffreys) model: Maxwell element and dashpot in parallel
4. Power Law model: $G' = k\omega^n$, $G'' = k \cot(n\pi/2) \omega^n$

The four element Maxwell model was chosen for its accuracy with polymer solutions, with the storage and loss moduli defined as

$$G'(\omega) = \sum_{n=1}^4 \frac{\eta_n t_{R,n} \omega^2}{1 + \omega^2 t_{R,n}^2} \quad (5.49)$$

$$G''(\omega) = \sum_{n=1}^4 \frac{\eta_n \omega}{1 + \omega^2 t_{R,n}^2} \quad (5.50)$$

where the relaxation times, $t_{R,n}$ (sec), and the viscosities, η_n (Pa-s), are chosen through a fitting algorithm to best match the data.

The first comparison was with actin-FLNa networks at $c_{AF} = 20\mu\text{M}$, $R=0.02$, and $\omega=0.05\text{Hz}$. At this frequency and R value, they found G' to be approximately 2-4 times greater than G'' for shear strains up to $\tan(\gamma)=0.5$ (Figure 4-11), thus the viscous response is not dominated by the elastic response. We use the same network parameters given in Table 4-2 to define the actin network represented by the hyperelastic leg in the rheological model. Within the viscoelastic leg, the best fit values for the elastic shear modulus is $G=1.74\text{Pa}$ (or $E=5.2\text{ Pa}$ for $\nu=0.49$) and the viscosity is $\eta=8.9\text{ Pa-s}$.

Following the experimental procedure, the viscoelastic response was then quantified by deforming the network with an oscillatory shear strain of $\tan(\gamma)=\pm(0.01-0.45)$ to determine the storage and loss moduli. An example of the input strain time history, and the leading stress time history, is shown in Figure 5–12. The resulting storage and loss shear moduli are shown in Figure 4–11 for increasing network strain.

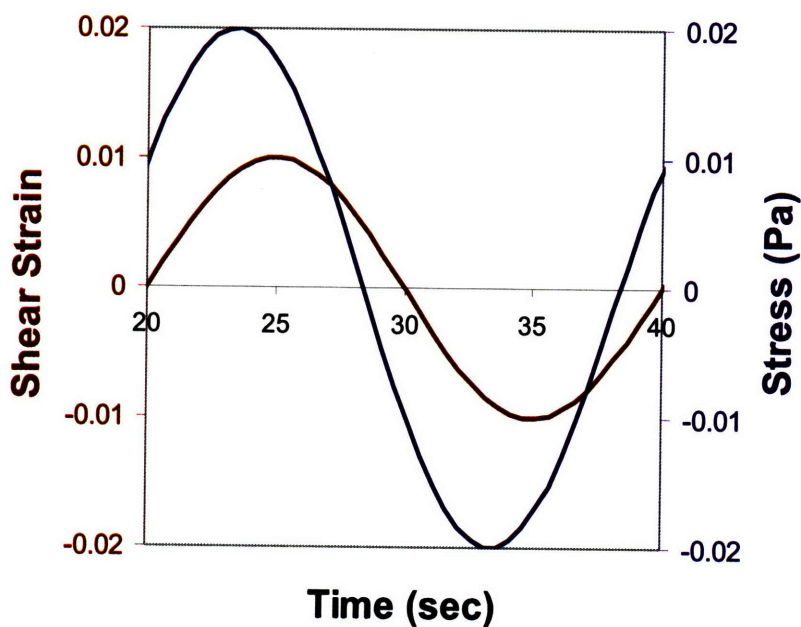


Figure 5–12. Simulated time histories of shear strain and shear stress for actin-FLNa networks ($c_{AF}=20\mu\text{M}$, $R=0.02$, and $\omega=0.05\text{Hz}$)

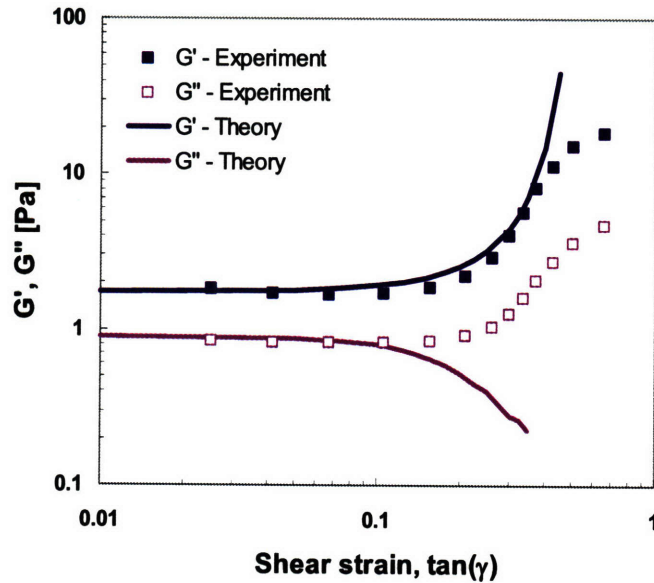


Figure 5–13. Theoretical and experimental storage modulus (G') and loss modulus (G'') of actin-FLNa networks ($c_{AF}=20\mu\text{M}$, $R=0.02$, and $\omega=0.05\text{Hz}$) (Lee and Kamm, 2008)

The linear viscoelastic model captures the storage modulus behavior well through the strain stiffening region, up to $\tan(\gamma)\sim 0.35$ where network behavior was found to deteriorate, possibly due to cross-link deformations (Figure 4–11). The theoretical linear viscoelastic response also agrees with the experimentally measured loss modulus for small shear strains ($\tan(\gamma)<0.1$).

The nonlinear behavior of the loss modulus beyond $\tan(\gamma)=0.1$, however, illustrates the need for incorporating nonlinear viscoelastic terms within the model. Since the experimental network gel is experiencing an oscillation of $\tan(\gamma)=\pm(0.01-0.45)$, the response of the actin network goes well into the nonlinear strain stiffening regime. Within this range, the highly nonlinear stress from the network dominates the stress contribution from the linear viscoelastic Maxwell leg (see Figure 5–12b for the shear stress response to an oscillating shear strain of $\tan(\gamma)=\pm 0.4$). The shear strain contributions for the three components of the rheological model (8-chain network, linear

elastic spring, viscous dashpot) can also be seen in the simulated time histories of Figure 5–12a for an oscillating shear strain of $\tan(\gamma)=\pm 0.4$. Note that the strain in the 8-chain network is equal to the total strain. A quick evaluation of the maxima of the total stress and total strain in Figure 5–12 reveals that the lack of contribution from the viscoelastic leg fails to create a significant lag in the shear strain, leading to a small phase angle and the low values for G'' seen in Figure 4–11 at high shear strains.

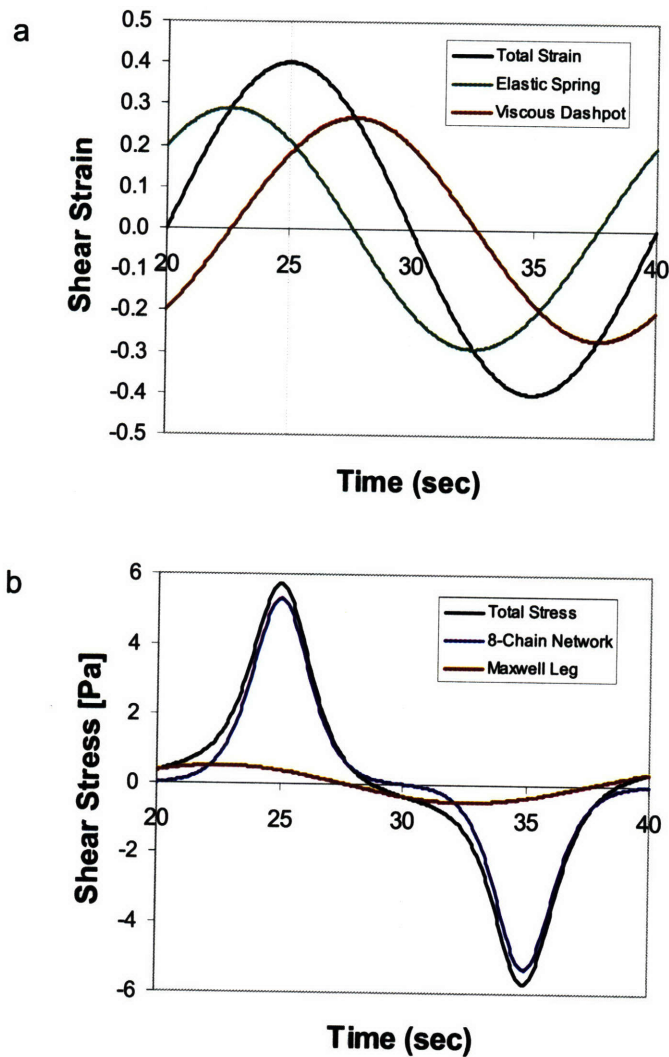


Figure 5–14. (a) Simulated time history of an oscillating shear strain ($\tan(\gamma)=\pm 0.4$) for the three components of the rheological model (8-chain network, linear elastic spring, viscous dashpot), with the strain in the 8-chain network equal to the total strain. (b) Time history for shear stress in linear elastic Maxwell leg, 8-chain network, and total stress.

5.3 Nonlinear rheological model

The rheological model presented in this section incorporates nonlinear, microstructurally-motivated elements in the Maxwell leg in order to capture the nonlinear behavior at large strains. The nonlinear viscoelastic behavior at large strains is due in part to intermolecular steric interactions and intramolecular network effects (e.g. cross-link deformation and/or unfolding/refolding of cross-link subdomains). These interactions increase nonlinearly as the molecular network deforms through significant chain rotation combined with some chain stretching (see Chapter 3). The hyperelastic response of the network is therefore modeled by separating the network into the two, parallel rheological springs (see Figure 5–15). The two hyperelastic network elements are scaled using a volume fraction approach, following the Bergström-Boyce method (Bergstrom and Boyce, 2000), where a percentage (ν_f) of the network remains fixed and does not relax while the remaining volume fraction of the network ($\nu_r=1-\nu_f$) relaxes. The stresses due to cross-links are also included within the relaxing network in the Maxwell leg, and thus the model considers a corresponding percentage of the cross-links to be located within the region of the network undergoing relaxation, implicitly including the viscoelastic response due to intramolecular network effects. The Cauchy stress in the viscoelastic leg (without including volume fraction scaling) is now defined by

$$\mathbf{T}_{VE} = \frac{nr_0 k_B T}{3Jl_p} \left\{ \frac{1}{\lambda_c} \left[\left(\frac{1}{4(1-\lambda_c r_0/L_c)^2} \right) \left(\frac{L_c/l_p - 6(1-\lambda_c r_0/L_c)}{L_c/l_p - 2(1-\lambda_c r_0/L_c)} \right) \right] \mathbf{B}_{VE}^e \right. \\ \left. - \left[\left(\frac{1}{4(1-r_0/L_c)^2} \right) \left(\frac{L_c/l_p - 6(1-r_0/L_c)}{L_c/l_p - 2(1-r_0/L_c)} \right) \right] \mathbf{I} \right\} + K_B (J-1) \mathbf{I} \quad (5.51)$$

where \mathbf{B}_{VE}^e is the left Cauchy-Green strain tensor for the viscoelastic Maxwell leg defined using the elastic component of the viscoelastic deformation gradient,

$$\mathbf{B}_{VE}^e = \mathbf{F}_{VE}^e (\mathbf{F}_{VE}^e)^T. \quad (5.52)$$

Since the legs are in parallel, stress equilibrium requires that the total stress be the sum of the stress in the two legs, in this case with both components functions of the cross-linked hyperelastic network.

$$\mathbf{T} = v_f \mathbf{T}_{HE} + v_r \mathbf{T}_{VE} = v_f \mathbf{T}_{HE} + (1-v_f) \mathbf{T}_{VE} \quad (5.53)$$

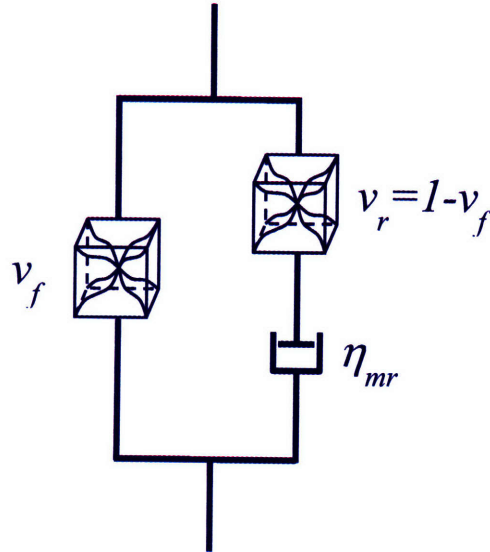


Figure 5–15. Nonlinear viscoelastic rheological model for cytoskeletal network with the hyperelastic network response separated into fixed regions with volume fraction v_f , and relaxing regions with volume fraction $v_r=1-v_f$; the nonlinear viscosity due to molecular relaxation is η_{mr} .

The material properties for the hyperelastic network remain the same as those used in Chapter 4 to capture the actin-FLN experimental data. The effective shear strain rate, $\dot{\gamma}$, is given in terms of a nonlinear viscosity, η_{mr} , to capture the network's molecular relaxation at large strains, adapted from the approach by Adams, et al. (Adams et al., 2000) and Dupaix and Boyce (Dupaix and Boyce, 2007) for cessation of molecular relaxation,

$$\dot{\gamma} = \frac{\tau^v}{\eta_{mr}} = \frac{\tau^v}{\left[\frac{\left(\frac{\theta_0}{\theta_r} - 1 \right)}{\left(\frac{\theta}{\theta_r} - 1 \right) C \theta} \right]} = \frac{\left(\frac{\theta}{\theta_r} - 1 \right) C \theta \tau^v}{\left(\frac{\theta_0}{\theta_r} - 1 \right)}, \quad (5.54)$$

where C is a constant, θ is the average chain angle of the network, θ_0 is the initial average chain angle, θ_r is the average chain angle for relaxation cutoff. The nonlinear viscosity is shown in Figure 5–16 as a function of increasing shear strain using the best fit values $C=0.15 \text{ (Pa-s)}^{-1}$ and $\theta_r=47^\circ$ for the actin-FLN networks ($c_{AF}=20\mu\text{M}$, $R=0.02$) evaluated in Chapter 4. The viscosity increases significantly from $\tan(\gamma)>0.1$, which represents the onset of strain stiffening, through $\tan(\gamma)=0.35$, after which the actin-FLN network begins to undergo strain softening behavior. The average network chain angle, also shown in Figure 5–16, is based on the network parameters ($l_p=3\mu\text{m}$, $L_c=0.89\mu\text{m}$, $\alpha=1.08\%$) used to capture the actin-FLN hyperelastic behavior in Chapter 4. Note that since the average network chain angle does not reach $\theta_r=47^\circ$ until $\tan(\gamma)>0.35$, the network continues to relax until the network transitions into the strain softening regime.

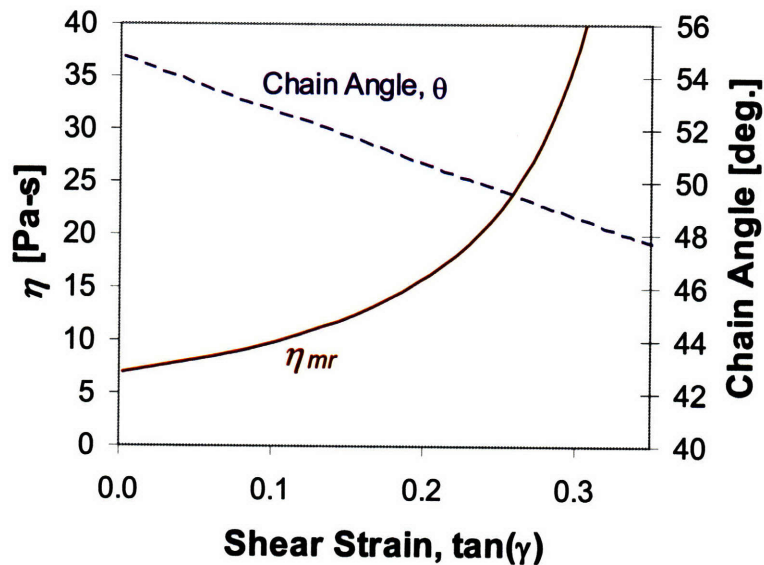


Figure 5-16. Nonlinear viscosity ($C=0.15$, $\theta_r = 47^\circ$) and average network chain angle as a function of shear strain

The stress from the relaxing network ($\nu_r=0.66$) in the nonlinear viscoelastic Maxwell leg is now no longer dominated by the nonlinear stress from the fixed network ($\nu_r=0.34$) as shown in Figure 5-17b for the shear stress response to an oscillating shear strain of $\tan(\gamma)=\pm 0.3$. The shear strain contributions for the three components of the rheological model (hyperelastic spring for fixed cross-linked network, hyperelastic spring for relaxing cross-linked network, nonlinear dashpot) can also be seen in the simulated time histories of Figure 5-17a for an oscillating shear strain of $\tan(\gamma)=\pm 0.3$. As noted earlier, the strain in the fixed 8-chain network is equal to the total strain.

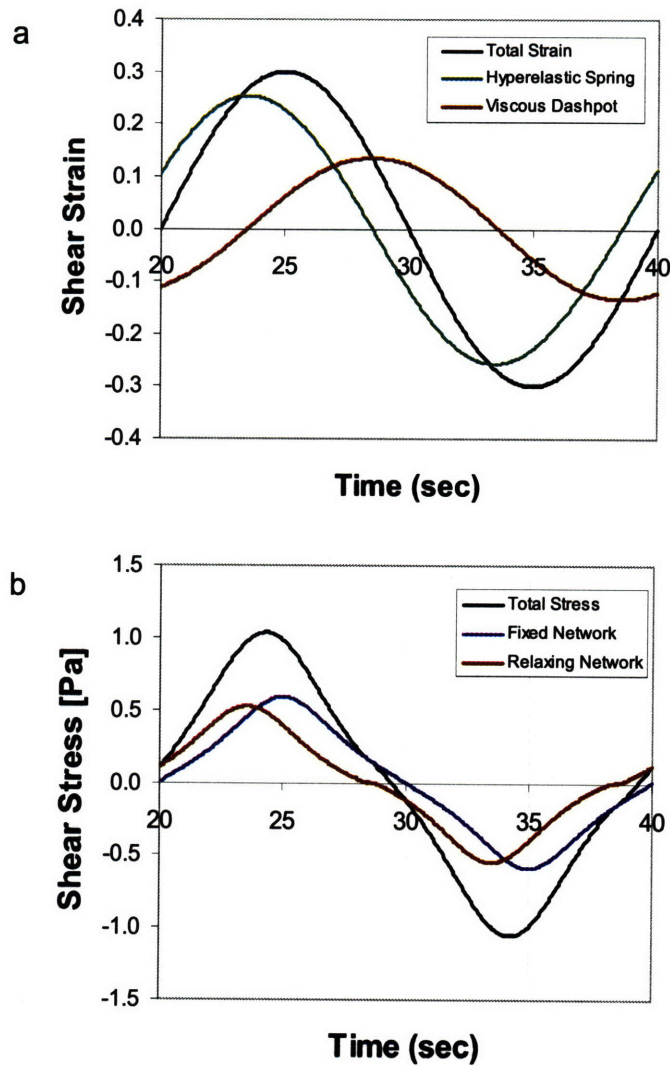


Figure 5–17. (a) Nonlinear viscoelastic elements included in the simulated time history of an oscillating shear strain ($\tan(\gamma)=\pm 0.3$) for the three components of the rheological model (Fixed hyperelastic network spring, Relaxing hyperelastic network spring, nonlinear dashpot), with the strain in the 8-chain network equal to the total strain. (b) Time history for shear stress in relaxing 8-chain network, fixed 8-chain network, and total stress.

The phase lag between the strain input and stress response can also be seen qualitatively in Figure 5–17, but is shown explicitly in Figure 5–18. The linear viscoelastic model declines significantly beyond $\tan(\gamma)=0.1$, corresponding to the decrease in G'' seen in Figure 4–11, while the nonlinear viscoelastic model gives a constant phase angle across the strain range with a larger discrepancy for smaller strains.

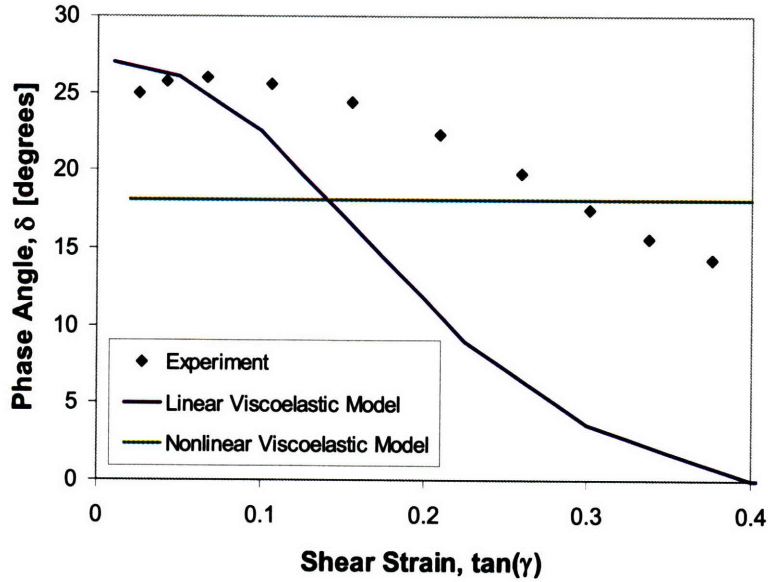


Figure 5–18. Phase angle for linear viscoelastic model, nonlinear viscoelastic model, and experiments of actin-FLNa networks ($c_{AF}=20\mu\text{M}$, $R=0.02$, and $\omega=0.05\text{Hz}$) (Lee and Kamm, 2008)

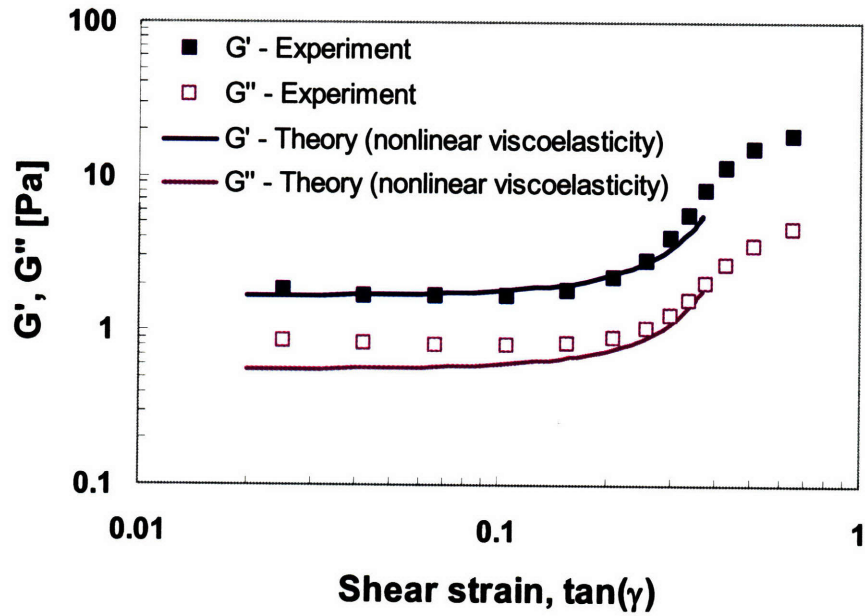


Figure 5–19. Theoretical (with nonlinear viscoelasticity) and experimental storage modulus (G') and loss modulus (G'') of actin-FLNa networks ($c_{AF}=20\mu\text{M}$, $R=0.02$, and $\omega=0.05\text{Hz}$) (Lee and Kamm, 2008)

The resulting storage and loss shear moduli are shown in Figure 5–19 for increasing network strain. The nonlinear viscoelastic model also captures the storage modulus behavior well through the strain stiffening region, up to $\tan(\gamma) \sim 0.4$. The nonlinear viscoelastic response now also agrees, however, with the experimentally measured loss modulus for shear strains through the strain stiffening region (and prior to the strain softening response for $\tan(\gamma) > 0.35$). This reversal of behavior for the loss modulus, from monotonically decreasing to monotonically increasing with shear strain, emphasizes the importance of including nonlinear effects to capture the true viscoelastic response of cross-linked actin cytoskeletal networks.

The nonlinear viscoelastic response also varies with frequency. These responses are shown in Figure 5–20 for the nonlinear viscoelastic network model in terms of their shear stress-strain behavior. The values are calculated by evaluating the shear stress response for an shear strain input of $\tan(\gamma) = \pm 0.01$ (see Figure 5–20 inset) oscillating at varying frequencies, and taking $\tau = (G^*)\tan(\gamma)$. Note that the stress-strain behavior shown in Figure 5–20 is limited to the linear response due to the small shear strain oscillation.

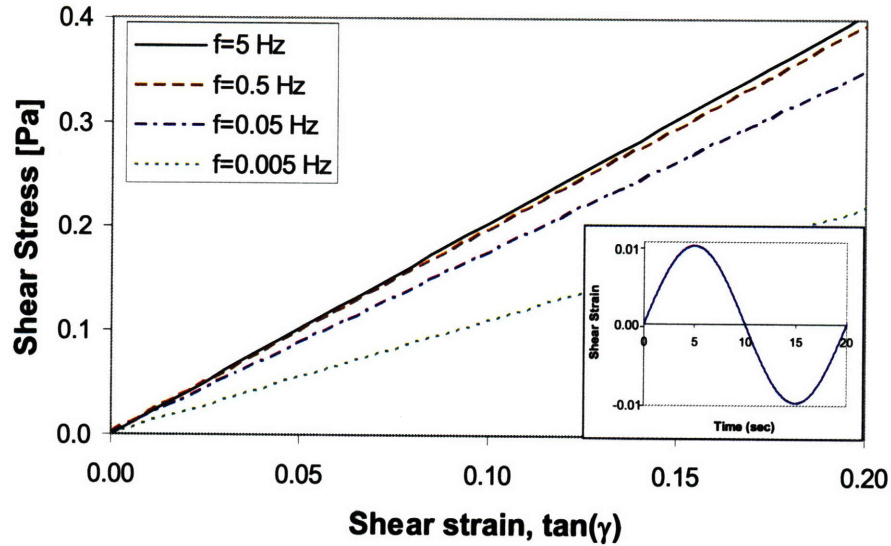


Figure 5–20. Shear stress-strain response for nonlinear viscoelastic model of actin-FLN at multiple frequencies ($\omega=0.005, 0.05, 0.5, 5$ Hz) taking $\tau=G^* \tan(\gamma)$

At the lowest frequency (0.005 Hz), the viscoelastic network approaches its relaxed, equilibrium state. At the highest frequency (5 Hz), the network responds with a short-term behavior. The storage and loss moduli also vary with frequency (see Figure 5–21). The storage modulus increases with frequency to a plateau value, as seen in experimental actin-FLN networks in Figure 4-4 (Gardel et al., 2006b) of Section 4.1. The loss modulus, based on a single relaxation time constant, increases for low frequencies but decreases for frequencies greater than 0.03 Hz, suggesting that the viscoelastic behavior of actin-FLN networks consists of a distribution of relaxation times, as is seen in many macromolecular networks. Since the model assumes a single Maxwell leg to capture the average

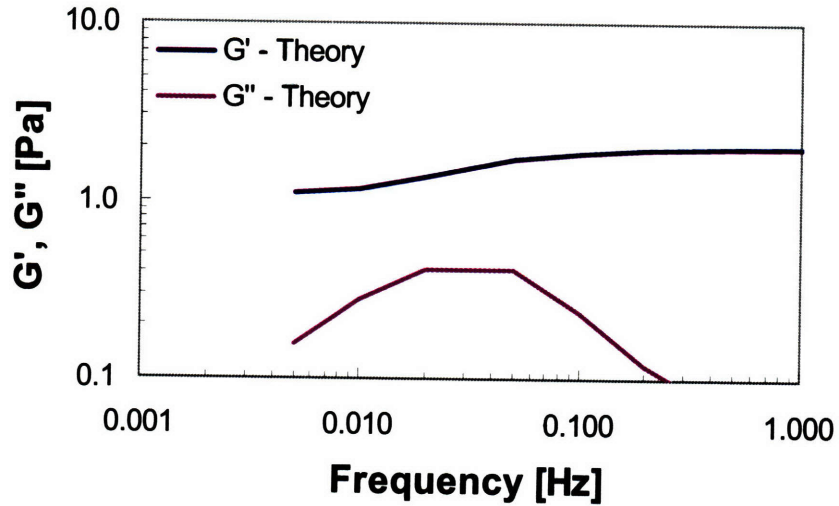


Figure 5-21. Shear storage modulus (G') and loss modulus (G'') for nonlinear viscoelastic model at multiple frequencies ($\omega=0.005-0.5$ Hz)

relaxation time due to intermolecular shear between filaments of an averaged length, more Maxwell legs can be incorporated into the rheological model to approximate the relaxation times of shorter filaments that relax more quickly (i.e. at observable at higher frequencies). The distribution of relaxation times can be accommodated through adding more nonlinear network spring-dashpot elements as done in a classic Wiechert model as illustrated in Figure 5-22, though evaluating the required number of elements and magnitudes of the viscoelastic parameters is saved for future work.

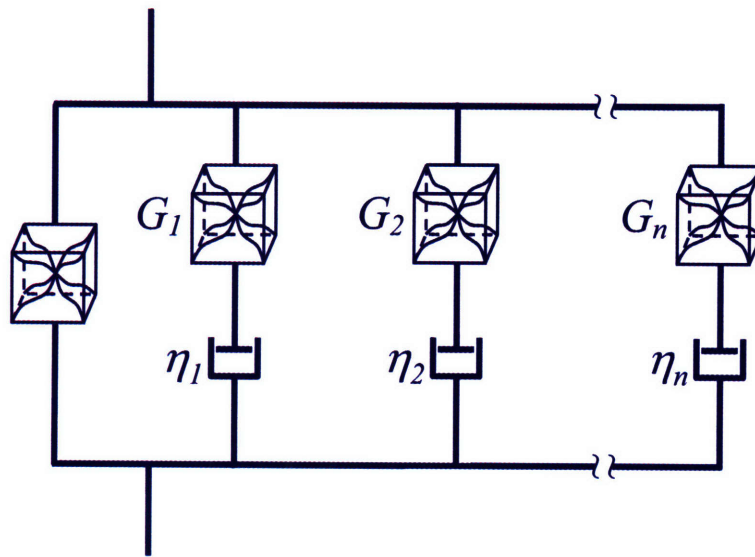


Figure 5–22. Wiechert rheological model with n Maxwell elements for cytoskeletal network to capture distribution of relaxation times for intermolecular shear viscosity.

The SLS rheological model shown in Figure 5–10 can be used to model the viscoelastic stress relaxation and creep responses of the network as well, with the same values used previously to match the storage and loss moduli for the actin-FLN network. The stress relaxation of the network is shown in Figure 5–23 for three shear strains that linearly ramp from $\tan(\gamma)=0$ to $\tan(\gamma)=5\%$, 10% , 15% over $t=0.01\text{sec}$ and then are held constant for $t \geq 0.01\text{sec}$. The response of the G'' as a function of frequency exhibits the peak at $\omega \sim 0.05\text{Hz}$, which corresponds to a relaxation time of $t_R=1/(2\pi\omega)=3.2\text{sec}$. This peak in G'' and δ is consistent with the characteristic shear relaxation time based on the rheological properties, which is $t_R=\eta/G=3.8\text{sec}$, which is also on the same order of viscoelastic timescales observed experimentally for fibroblasts ($t_R \sim 1\text{sec}$) (Karcher et al., 2003) and actin networks in phagocytotic neutrophils ($t_R \sim 2\text{sec}$) (Herant et al., 2006). The short-term response at $\tan(\gamma)=0.10$ gives a short-term relaxation modulus of $G_{rg}=2.0\text{Pa}$ and a long-term equilibrium relaxation modulus of $G_{re}=1.1\text{Pa}$ (Figure 5–24).

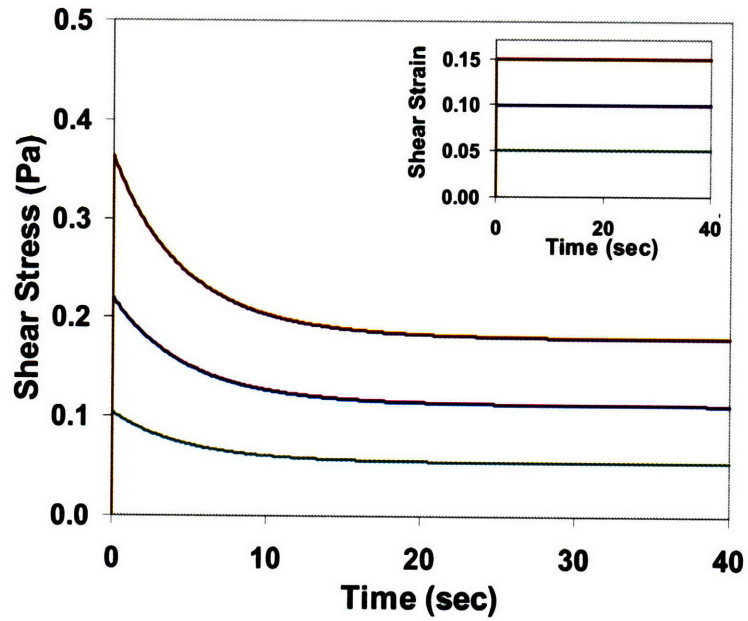


Figure 5-23. Simulated stress relaxation of an actin-FLNa network ($c_{AF}=20\mu\text{M}$, $R=0.02$) with constant shear strains of $\tan(\gamma)=0.05, 0.1, 0.15$ (inset).

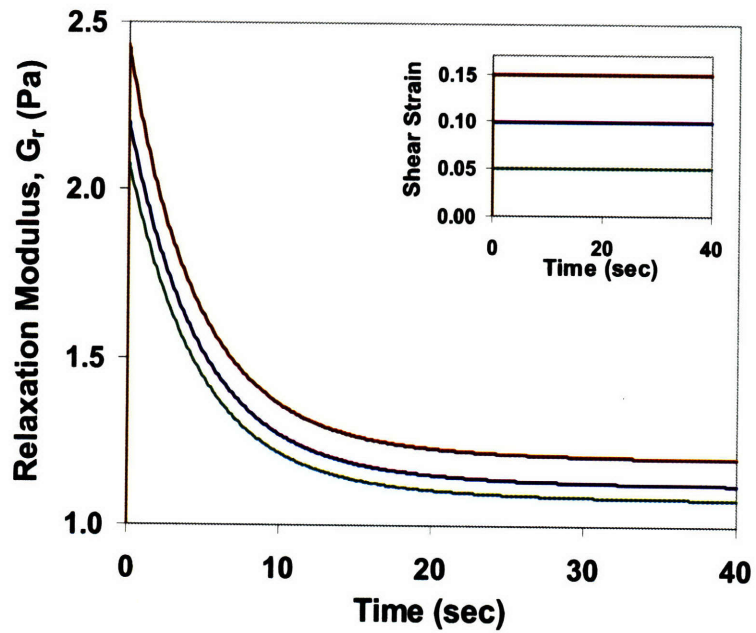


Figure 5-24. Simulated stress relaxation modulus of an actin-FLNa network ($c_{AF}=20\mu\text{M}$, $R=0.02$) with constant shear strains of $\tan(\gamma)=0.05, 0.1, 0.15$ (inset).

The creep response is given in Figure 5–25 for three shear stresses that linearly ramp from $\tau=0$ to $\tau=0.02, 0.04, 0.06\text{Pa}$ over $t=0.01\text{sec}$ and then are held constant for $t \geq 0.01$ seconds. The short-term response at $\tau=0.04\text{Pa}$ gives a short-term creep function of $J_{cg}=0.50\text{Pa}^{-1}$ and a long-term equilibrium creep function of $J_{ce}=0.92\text{Pa}^{-1}$ (see Figure 5–26).

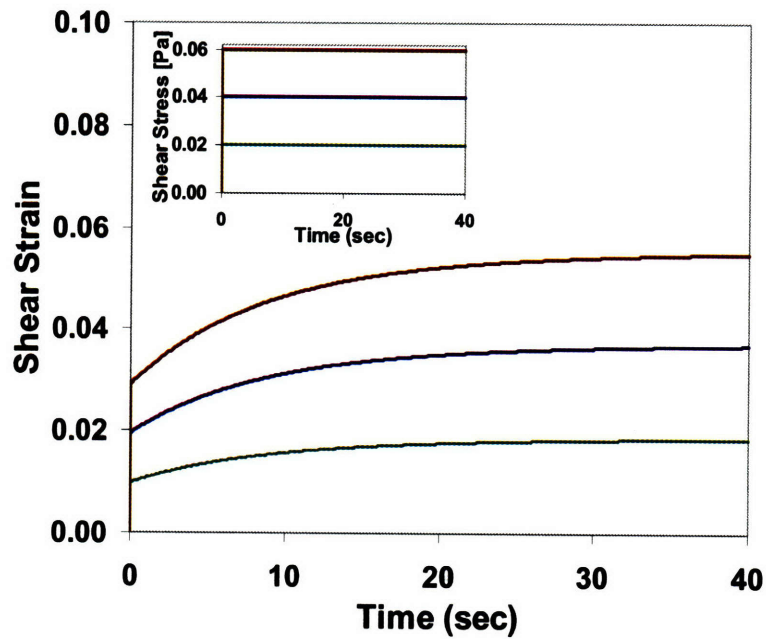


Figure 5–25. Simulated creep response of an actin-FLNa network ($c_{AF}=20\mu\text{M}$, $R=0.02$) with a constant shear stress of $\tau=0.02, 0.04, 0.06\text{ Pa}$ (inset).

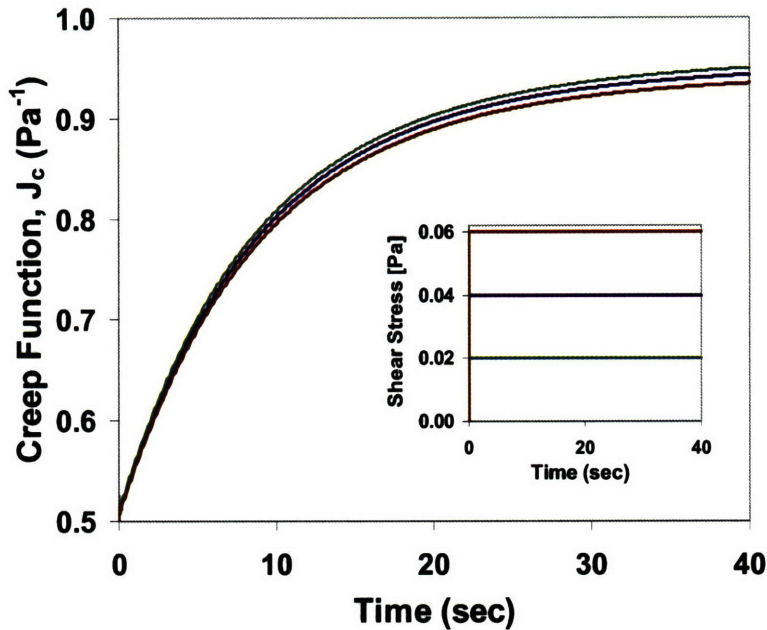


Figure 5–26. Simulated creep function of an actin-FLNa network ($c_{AF}=20\mu\text{M}$, $R=0.02$) with a constant shear stress of $\tau=0.02, 0.04, 0.06$ Pa (inset).

5.3.1 Actin-avidin networks

The second comparison was with actin-streptavidin networks at $c_{AF}=20\mu\text{M}$, $R=0.01$, and $\omega=0.05\text{Hz}$. At this frequency and R value, G' was approximately 10 times greater than G'' for shear strains up to $\tan(\gamma)=0.2$ and stresses up to $\tau=1\text{Pa}$ (Figure 4-14), thus the viscous response is dominated by the elastic response. We use the same network parameters as for the actin-FLN network, and originally given in Table 4-2, to define the actin networks in the rheological model as used with the actin-FLN network. The resulting best fit values are $C=0.38 (\text{Pa}\cdot\text{s})^{-1}$, $\theta_r=47^\circ$, and network volume fractions for the fixed network ($v_f=0.8$) and the relaxing network ($v_r=0.2$). Following the same experimental procedure used for the actin-FLN networks, the viscoelastic response was quantified by deforming the network with an oscillatory shear strain of $\tan(\gamma)=\pm(0.01-$

0.35) to determine the storage and loss moduli. An example of the input strain time history, and the leading stress time history, is shown in Figure 5–27. The resulting storage and loss shear moduli are shown in Figure 5–28 for increasing network strain. A comparison between the theory and the experimental data is only examined within the linear viscoelastic regime since the experiment produced constant values of G' , G'' until it experienced plate slippage at a shear strain of $\tan(\gamma) \sim 0.2$. The nonlinear viscoelastic response again shows the storage and loss moduli monotonically increasing with shear strain.

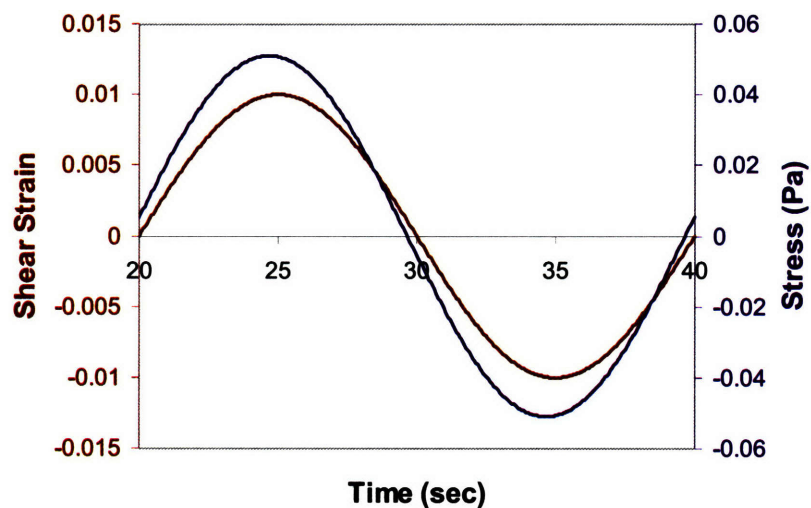


Figure 5–27. Simulated time histories of shear strain and shear stress for actin-avidin networks ($C_{AF} = 20\mu\text{M}$, $R=0.01$, and $\omega=0.05\text{Hz}$)

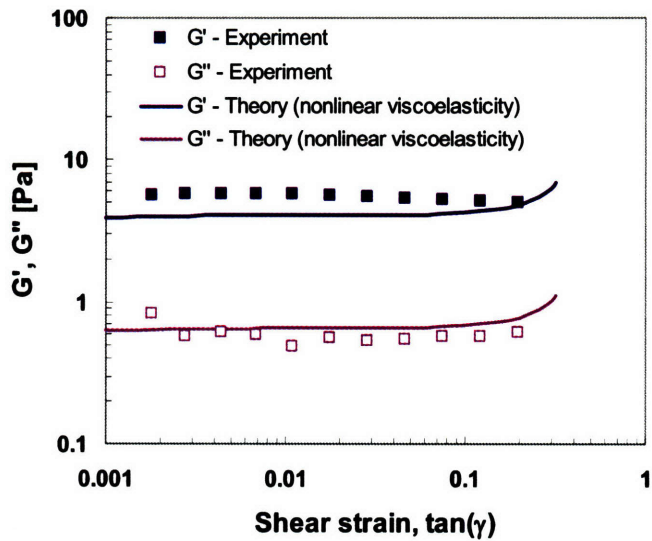


Figure 5–28. Theoretical (with nonlinear viscoelasticity) and experimental storage modulus (G') and loss modulus (G'') of actin-avidin networks ($c_{AF}=20\mu\text{M}$, $R=0.01$, and $\omega=0.05\text{Hz}$). Experimental data from (Lee and Kamm, 2008).

The nonlinear viscoelastic network model captures the storage and loss moduli behavior well in the linear viscoelastic region up to $\tan(\gamma)\sim 0.2$. The nonlinear model also gives some insight into a possible contributor to the plate slippage, since it predicts a transition into the strain stiffening region at $\tan(\gamma)\sim 0.2$ – precisely when the network detached from the rheometer plates. This prediction of the onset of strain stiffening at $\tan(\gamma)\sim 0.2$ is also significant for future work since the strain stiffening behavior (and the regime’s strain threshold) has not been demonstrated in the technical literature.

The shear strain contributions for the three components of the rheological model (fixed network/hyperelastic spring, relaxing network/hyperelastic spring, nonlinear dashpot) are shown again in the simulated time histories of Figure 5–29a for an

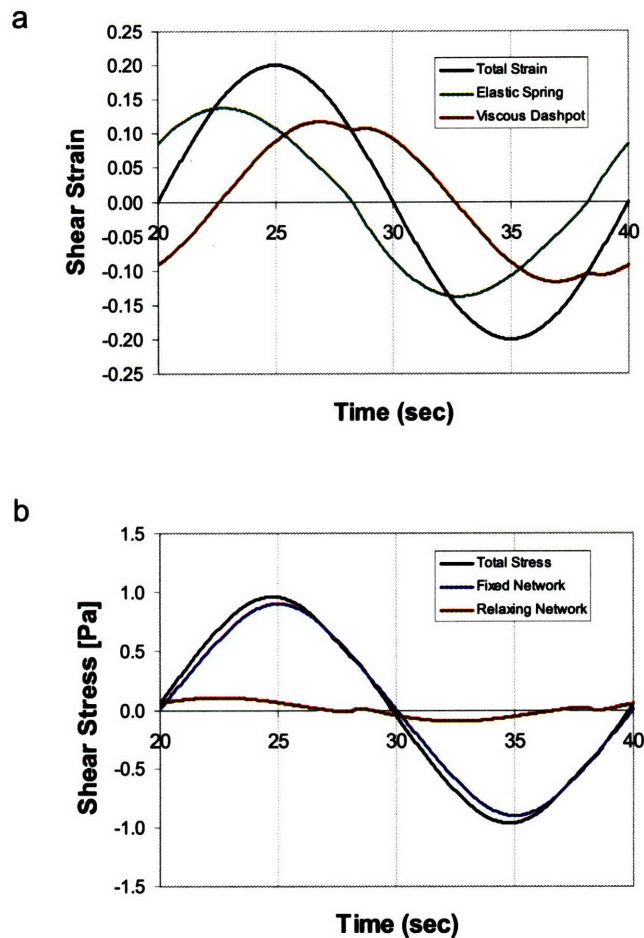


Figure 5–29. (a) Nonlinear scaling included in the simulated time history of an oscillating shear strain ($\tan(\gamma)=\pm 0.2$) for the three components of the rheological model (Fixed hyperelastic network spring, Relaxing hyperelastic network spring, nonlinear dashpot), with the strain in the 8-chain network equal to the total strain. (b) Time history for shear stress in relaxing 8-chain network, fixed 8-chain network, and total stress.

oscillating shear strain of $\tan(\gamma)=\pm 0.2$. As noted earlier, the strain in the fixed 8-chain network is equal to the total strain. The network shear stress is now dominated by the response of the much stiffer avidin-biotin cross-linkers (Figure 5–29b). The phase lag between the strain input and stress response is relatively small as shown qualitatively in Figure 5–29, and explicitly in Figure 5–30. Other than some early fluctuations in the experimental data, the phase angle is relatively constant with a mild increase by

$\tan(\gamma)=0.2$, mirroring the G'' behavior in Figure 5–28. While the viscoelastic network model also gives a constant response in Figure 5–30, it overestimates the phase lag (although the difference would be reduced through a better fit with the G' values over the strain range in Figure 5–28).

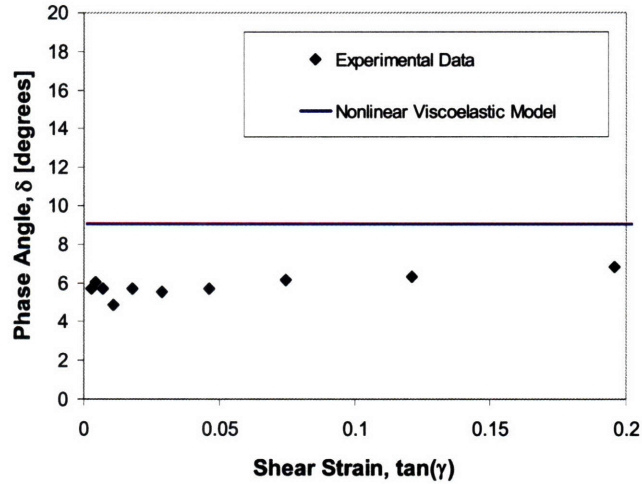


Figure 5–30. Phase angle for nonlinear viscoelastic network model and experiments of actin-avidin networks ($c_{AF}=20\mu\text{M}$, $R=0.01$, and $\omega=0.05\text{Hz}$) (Lee and Kamm, 2008)

The nonlinear viscoelastic response also varies with frequency. These responses are shown in Figure 5–31 for the nonlinear viscoelastic network model in terms of their shear stress-strain behavior. The values are calculated by evaluating the shear stress response for an shear strain input of $\tan(\gamma)=\pm 0.05$ (see Figure 5–31 inset) oscillating at varying frequencies, and taking $\tau=(G^*)\tan(\gamma)$. Note that the stress-strain behavior shown in Figure 5–31 is limited to the linear response due to the small shear strain oscillation.

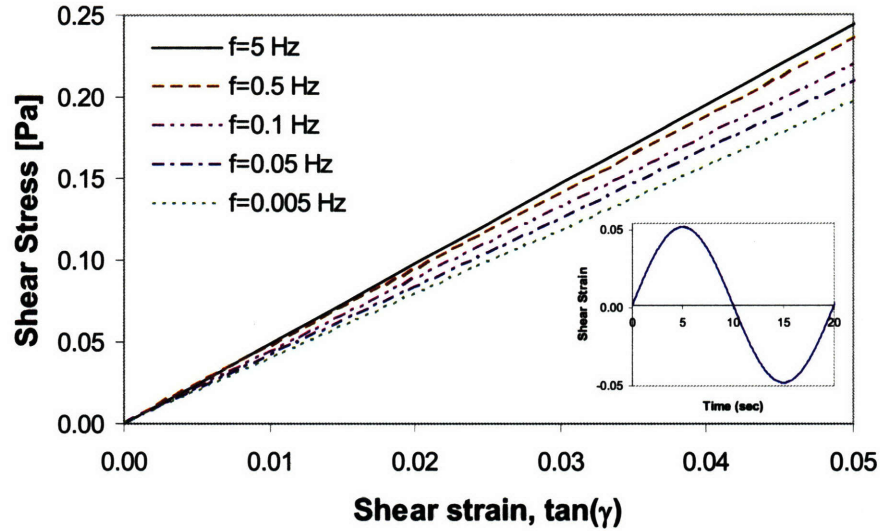


Figure 5–31. Shear stress-strain response for nonlinear viscoelastic model of actin-avidin at multiple frequencies ($\omega=0.005, 0.05, 0.5, 5$ Hz) taking $\tau=(G^*)\tan(\gamma)$

At the lowest frequency (0.005 Hz), the viscoelastic network approaches its relaxed, equilibrium modulus. At the highest frequency (5 Hz), the network responds with the short-term modulus. The complex, storage and loss moduli also vary with frequency (see Figure 5–32). The storage modulus dominates the loss modulus by an order of magnitude at almost all frequencies. Therefore the G' , and consequently G^* , are relatively constant throughout the range of frequencies, which is consistent with experimental actin-avidin networks, e.g. (Wachsstock et al., 1994) as shown in Figure 4-5 of Section 4.1, and reproduced here in Figure 5–33. The loss modulus increases for low frequencies, but decreases for frequencies greater than 0.05-0.06 Hz. Note that the low values of loss modulus correspond with low values of phase angle (i.e. $\delta < 9^\circ, 0.16$ rad.)

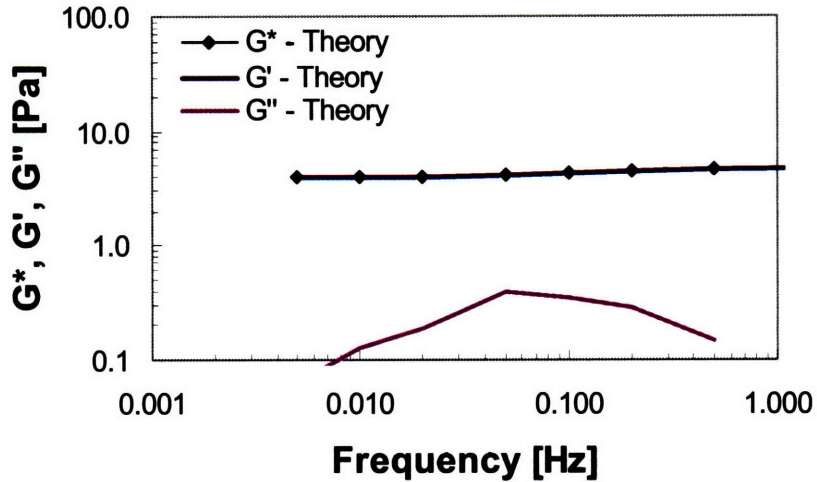


Figure 5–32. Shear storage modulus (G') and loss modulus (G'') for nonlinear viscoelastic model as a function of frequency

for the range of frequencies, which is also consistent with experimental actin-avidin networks, e.g. $c_{AF}=15\mu\text{M}$ and $R=c_{CL}/c_{AF}=0.02$ from (Wachsstock et al., 1994). Figure 5–33 shows the data by Wachsstock, et al. compared to the current viscoelastic model that was fit to the data at a single frequency by Kamm and Lee ($\omega=0.05\text{hz}$, $c_{AF}=20\mu\text{M}$ and $R=0.02$). The magnitudes of the complex modulus are relatively constant across the frequency range, although at different magnitudes, with the Wachsstock magnitudes of G^* higher due to higher concentrations of the stiff cross-linker avidin. Although the two experimental data sets were of actin-avidin networks at different c_{AF} and R values, the trends of G^* and δ are very consistent over the range of frequencies.

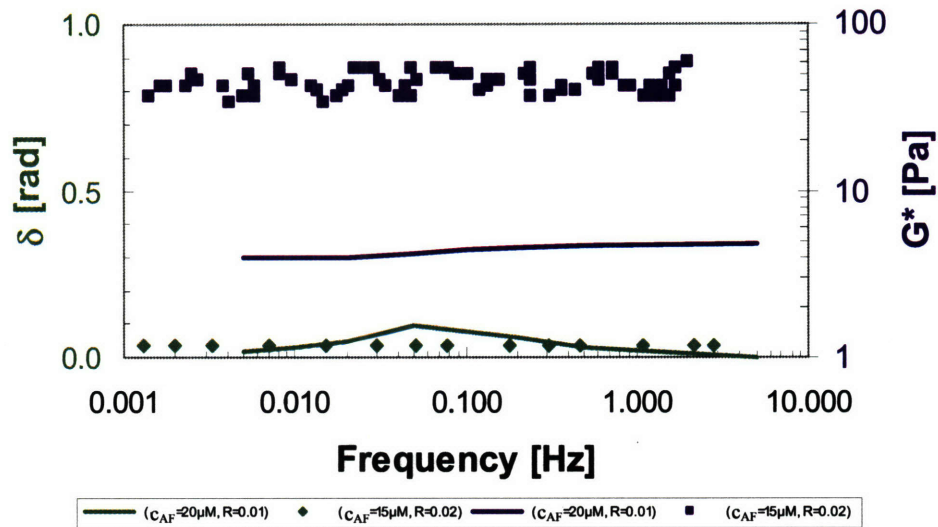


Figure 5–33. Complex shear modulus, G^* , and phase shift, δ , as a function of frequency for theory (fit to $c_{AF}=20\mu\text{M}$, $R=0.01$) and experimental ($c_{AF}=15\mu\text{M}$, $R=0.02$) (Wachsstock et al., 1994) actin-avidin networks

The SLS rheological model shown in Figure 5–15 can be used again to model the viscoelastic stress relaxation and creep responses of the actin-avidin network as well. The stress relaxation of the network is shown in Figure 5–34 for three shear strains that linearly ramp from $\tan(\gamma)=0.0-0.05, 0.1, 0.15$ over $t=0.01$ seconds and then are held constant for $t \geq 0.01$ seconds. The response of the G'' and δ as a function of frequency exhibit the peak at $\omega=0.06\text{Hz}$, which corresponds to a relaxation time of $t_R=1/(2\pi\omega)=2.7\text{sec}$. This peak in G'' and δ is consistent with the characteristic shear relaxation time based on the rheological properties, which is $t_R=\eta/G=3.2\text{ sec}$. The response at $\tan(\gamma)=0.1$ gives a short-term relaxation modulus of $G_{rg}=4.8\text{ Pa}$ and a long-term equilibrium relaxation modulus of $G_{re}=4.0\text{ Pa}$ (see Figure 5–35).

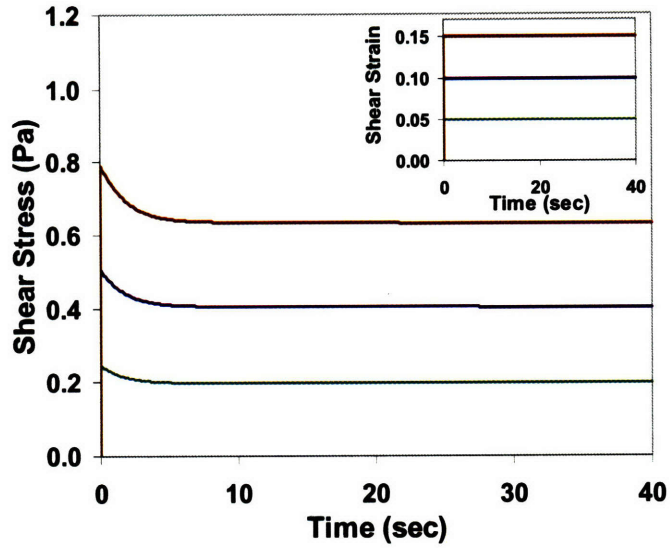


Figure 5–34. Simulated stress relaxation of an actin-avidin network ($c_{AF}=20\mu\text{M}$, $R=0.01$) with constant shear strains of $\tan(\gamma)=0.05, 0.1, 0.15$ (inset).

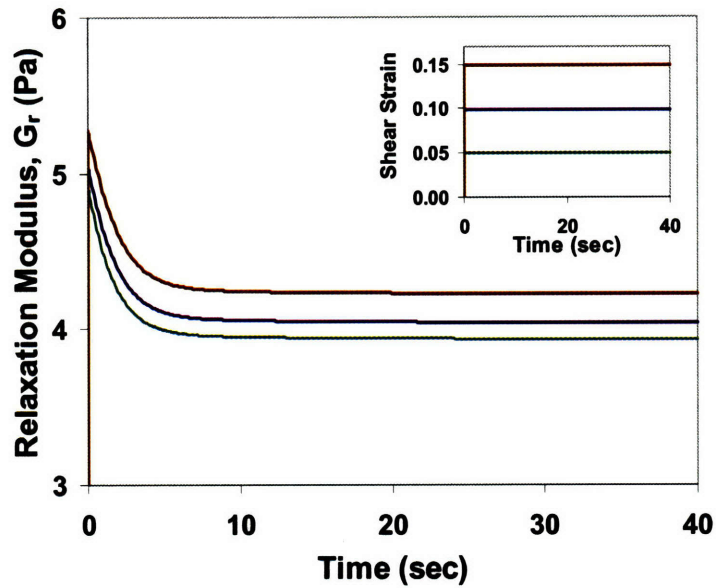


Figure 5–35. Simulated stress relaxation modulus of an actin-avidin network ($c_{AF}=20\mu\text{M}$, $R=0.01$) with constant shear strains of $\tan(\gamma)=0.05, 0.1, 0.15$ (inset).

The creep response is given in Figure 5–36 for three shear stresses that linearly ramp from $\tau=0$ to $\tau=0.02, 0.04, 0.06\text{Pa}$ over $t=0.01$ seconds and then are held constant for

$t \geq 0.01$. The short-term response at $\tau=0.04$ gives a creep function of $J_{cg}=0.23 \text{ Pa}^{-1}$ and a long-term equilibrium creep function of $J_{cc}=0.28 \text{ Pa}^{-1}$ (see Figure 5–37).

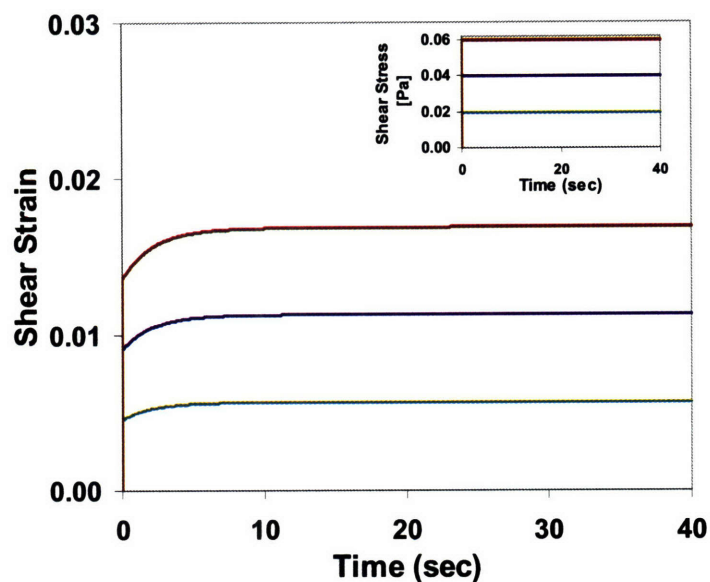


Figure 5–36. Simulated creep response of an actin-avidin network ($c_{AF}=20\mu\text{M}$, $R=0.01$) with constant shear stresses of $\tau=0.02, 0.04, 0.06\text{Pa}$ (inset).

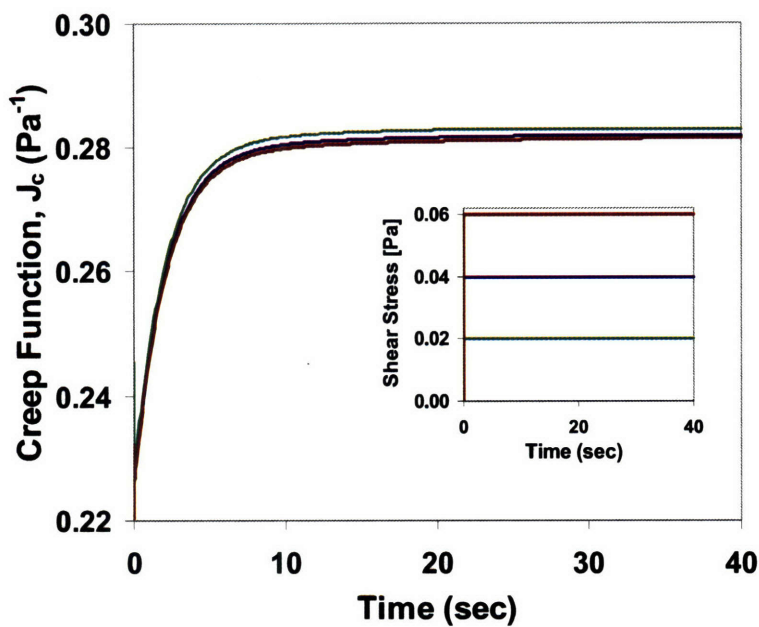


Figure 5–37. Simulated creep function of an actin-avidin network ($c_{AF}=20\mu\text{M}$, $R=0.01$) with constant shear stresses of $\tau=0.02, 0.04, 0.06\text{Pa}$ (inset).

5.4 Stress relaxation of actin networks in a cell

geometry

The 3D viscoelastic cytoskeletal network model is now integrated with membrane and nucleus models in a finite element-based micromechanical model of the cell which provides the ability to assign and evolve mechanical properties and filament concentrations as a function of location within the cell. The composite cellular viscoelastic model is evaluated by observing the stress relaxation experienced by a cell under compression. The $6\mu\text{m}$ diameter cell (Figure 5–38) includes a nucleus ($1\mu\text{m}$ diameter) which will be modeled as a neo-Hookean material as a simplifying assumption,

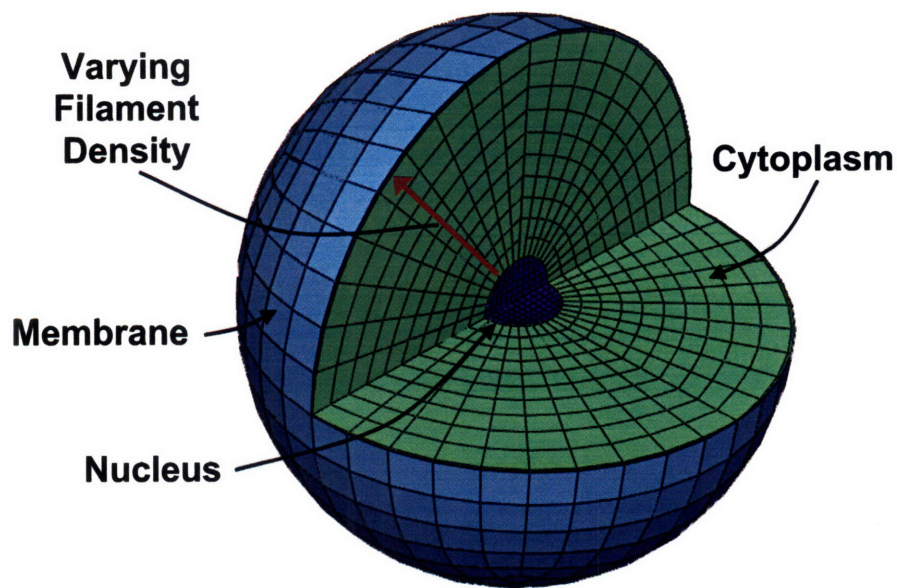


Figure 5–38. 3D whole cell geometry

and a membrane (10nm thickness), which will be modeled as an orthotropic, incompressible linear elastic material. The 3D finite element illustration in Figure 5–38 also notes that the cytoskeletal filament density can be varied as a function of radial position. The viscoelastic actin-FLN network developed in the previous sections will be employed as the load bearing cytoskeletal network within the cytoplasm. The actin concentration will initially be held constant at $c_{AF} = 20\mu\text{M}$ across the cytoplasm. This will be followed by an analysis of the cell model with the actin concentration varying over three equally spaced regions of the cytoplasm: $c_{AF,inner} = 10\mu\text{M}$, $c_{AF,middle} = 30\mu\text{M}$, $c_{AF,outer} = 170\mu\text{M}$ to simulate in vivo actin gradients.

5.4.1 Mechanical properties of the nucleus and membrane

The elastic modulus for nuclei have varied considerably, e.g. 18 Pa - 10kPa (Tseng et al., 2004; Dahl et al., 2005; Mofrad et al., 2006). Nuclei are typically stiffer and more viscous than the surrounding cytoplasm, as demonstrated by chondrocytes nuclei which are three to four times stiffer and roughly twice as viscous as the cytoplasm, as measured via micropipette aspiration (Guilak and Mow, 2000). The relaxation time constant reported for mechanically and chemically isolated nuclei of chondrocytes is $t_R = 20, 25\text{sec}$, respectively (Guilak et al., 2000), which is almost an order of magnitude larger than the relaxation times for the actin-FLN and actin-avidin networks. The viscoelastic timescale of the cytoplasm has been observed experimentally for fibroblasts ($t_R \sim 1\text{sec}$) (Karcher et al., 2003) and actin networks in phagocytotic neutrophils ($t_R \sim 2\text{sec}$) (Herant et al., 2006). The nuclei within viscoelastic cells are therefore often considered to behave elastically due to their higher viscosity and the resulting slower response time

with respect to the surrounding cytoplasm (Mofrad et al., 2006). The contribution of the nucleus to cellular mechanical properties has been measured through uniaxial compression of the cell as well as isolated nuclei, with average properties for the nuclei of endothelial cells found to be $E=1000$ Pa, $K_B=5000$ Pa, and $G=340$ Pa (Caille et al., 2002).

The lipid bilayer membrane behaves more fluid-like (Evans and Yeung, 1989; Evans, 1989) with viscoelastic time constants on the order of 10s of μ s (Mofrad et al., 2006) that would allow a minimal mechanical contribution during cellular deformations such as axial compression or magnetocytometry (Karcher et al., 2003). The membrane, in conjunction with the underlying cytoskeletal cortex, can undergo three basic modes of deformation (Figure 5–39).

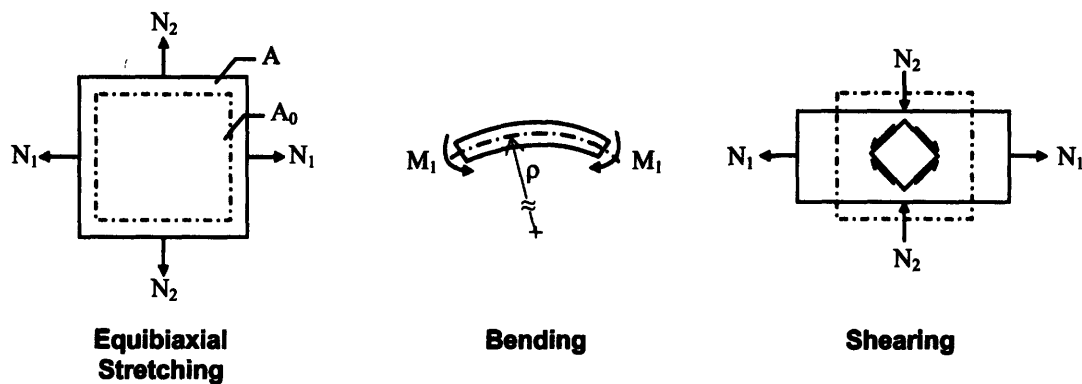


Figure 5–39. Membrane deformation modes

The membrane stretching and membrane bending are subject to the following constitutive relations, respectively.

$$\begin{Bmatrix} N_1 \\ N_2 \end{Bmatrix} = \frac{E_m \cdot d_m}{1-\nu^2} \begin{bmatrix} 1 & \nu \\ \nu & 1 \end{bmatrix} \begin{Bmatrix} \varepsilon_{m1} \\ \varepsilon_{m2} \end{Bmatrix}, \quad (5.55)$$

$$\begin{Bmatrix} M_1 \\ M_2 \end{Bmatrix} = \frac{E_m \cdot d_m^3}{12(1-\nu^2)} \begin{bmatrix} 1 & \nu \\ \nu & 1 \end{bmatrix} \begin{Bmatrix} \kappa_{m1} \\ \kappa_{m2} \end{Bmatrix}, \quad (5.56)$$

where N_i are the normal stresses, M_i are the moments, ε_{mi} are the membrane strains, $\kappa_{mi} = 1/\rho_i$ are the membrane curvatures (for $i = 1, 2$), d_m is the membrane thickness and ν is the Poisson ratio. Noting that $\varepsilon_{11} = \varepsilon_{22}$ for equibiaxial stretching, and using the definition of the area modulus, k_A , we can extract a relation for k_A from Equation (5.55),

$$N_1 = \frac{E_m \cdot d_m}{1-\nu^2} (1+\nu) \varepsilon_{11}, \quad (5.57)$$

$$N = k_A \cdot \varepsilon, \quad (5.58)$$

$$k_A = \frac{E_m \cdot d_m}{1-\nu}. \quad (5.59)$$

We can similarly note that $\varepsilon_{11} = -\varepsilon_{22}$ for shear, and using the definition of the shear modulus, k_S , we can extract a relation for k_S from Equation (5.55),

$$N_1 = \frac{E_m \cdot d_m}{1-\nu^2} (1-\nu) \varepsilon_{11}, \quad (5.60)$$

$$N = k_S \cdot \varepsilon, \quad (5.61)$$

$$k_S = \frac{E_m \cdot d_m}{1+\nu}. \quad (5.62)$$

Finally, we recognize that $\kappa_{m1} = \kappa_{m2}$ for bending, and using the definition of the bending modulus, κ_B , we can extract a relation for κ_B from Equation(5.56),

$$M_1 = \frac{E_m \cdot d_m^3}{12(1-\nu^2)} (1+\nu) \kappa_{m1}, \quad (5.63)$$

$$M = \kappa_B \cdot \kappa_m, \quad (5.64)$$

$$\kappa_B = \frac{E_m \cdot d_m^3}{12(1-\nu)}. \quad (5.65)$$

These equations can be rearranged to solve for the elastic modulus of the membrane, E_m , in terms of the area modulus, shear modulus, and membrane thickness,

$$E_m = \frac{2k_A k_S}{d_m (k_A + k_S)}. \quad (5.66)$$

The Poisson ratio can similarly be given in terms of the area modulus, shear modulus,

$$\nu = \frac{k_A - k_S}{k_A + k_S}. \quad (5.67)$$

The lipid bilayer membrane has an area expansion modulus of 0.1-1.0 J/m², and 0.45 J/m² for red blood cells (Waugh and Evans, 1979). The area modulus for undulating, wavy membranes, such as those found in B lymphocytes, have been found to be on the order of ten times smaller than area moduli for the smooth membranes of red blood cells (Castro et al., 2008b), so we will assume $k_A=0.045$ J/m². Pure lipid bilayers have a negligible shear modulus, while red blood cells have a membrane shear modulus of $k_S \sim 10^{-6}$ J/m² (Evans and Rawicz, 1990). The membrane is modeled in the finite element model with shell elements as an orthotropic linear elastic material under plane stress conditions, defined by the in-plane properties $E_1, E_2, G_{12}, \nu_{12}$, and the transverse shear moduli G_{13}, G_{23} (and $E_1, E_2, G_{12}, G_{13}, G_{23} > 0$ and $|\nu_{12}| < (E_1/E_2)^{1/2}$ for a positive-definite stiffness matrix and material stability) (Lempriere, 1968). Assuming a 2D emulation of an undulating, wavy membrane with a thickness of approximately $d_m=10$ nm, the in-plane elastic modulus of the membrane is $E_1=E_2= E_m=200$ Pa, and the in-plane Poisson ratio is $\nu_{12} = 0.6$, with little contribution from in-plane or transverse shearing ($G_{12}=G_{13}=G_{23}= G_m=E_m/10=20$ Pa).

5.4.2 Axisymmetric cell model

During the axisymmetric simulations the cell is compressed by applying an axial normal strain ($\epsilon_{2,\text{total}}=-5\%$, -10% , -15%) on the top plate according to a linear ramp for $t=0.01$ second, followed by a hold time of 20 seconds (see Figure 5–40b). Figure 5–40a shows the undeformed axisymmetric mesh next to the deformed mesh (with axial normal displacement contours at $t=0.01$ seconds, $U_2=-0.9\mu\text{m}$ or $\epsilon_{2,\text{total}}=-15\%$ for a $6\mu\text{m}$ diameter cell).

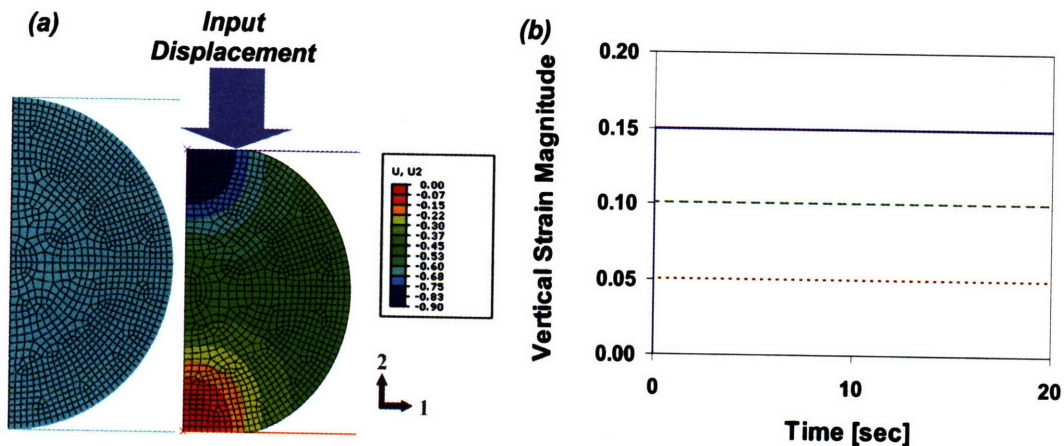


Figure 5–40. (a) Axisymmetric mesh schematic with axial normal strain contours in deformed mesh, and (b) Input (total) strain time history for compression of a viscoelastic cell with loading ramp time of 0.01 second and a hold time of 20 seconds.

The axial normal strain (ϵ_{22}) of the elements within the compressed cell is shown in Figure 5–46 for $t=0.01$ and $t=20$ seconds. There is very little change in the axial normal strain between the initially compressed state (Figure 5–41a) and the relaxed state (Figure 5–41b). But both plots help to identify the regions of largest compressive axial normal

strain (blue) directly under the load along the center axis of the cell, as well as the regions of little or no compressive axial normal strain (tan-orange), including the stiffer nucleus.

The contour plots

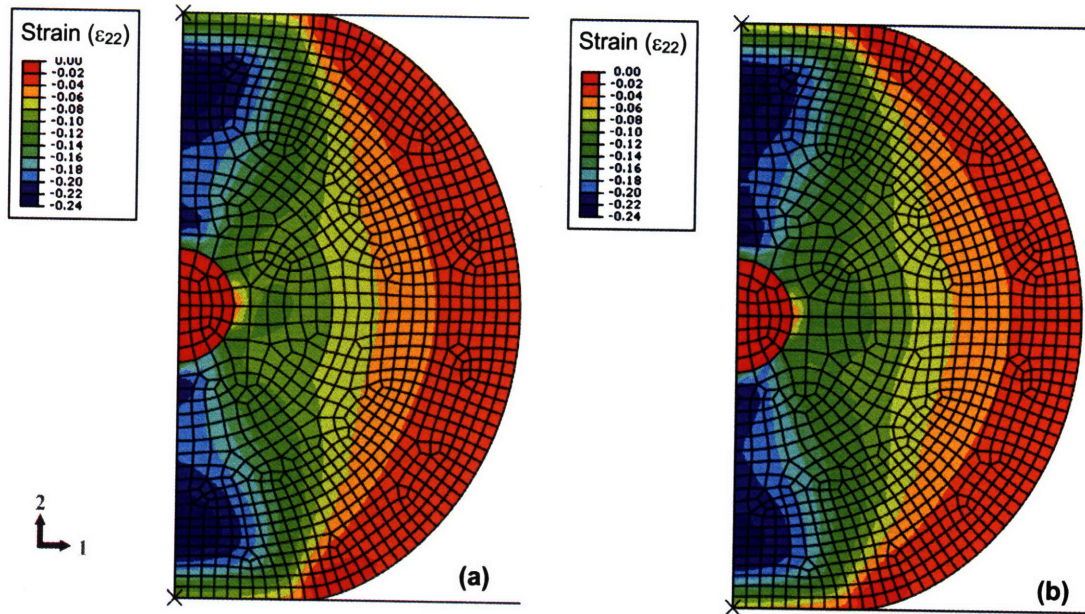


Figure 5–41. Element strain in the 2-direction (ϵ_{22}) within actin networks in a compressed cell ($\epsilon_{2,\text{total}} = -15\%$) at two different times, (a) $t=0.01$ sec, immediately after compression and (b) $t=20$ sec, in the compressed but relaxed state.

of the axial normal stress (σ_{22}) of the elements within the compressed cell is shown in Figure 5–42 for $t=0.01$ and $t=20$ seconds, illustrating the relaxation of compressive axial normal stresses, especially in the regions with the highest compressive stresses that are adjacent to the plates.

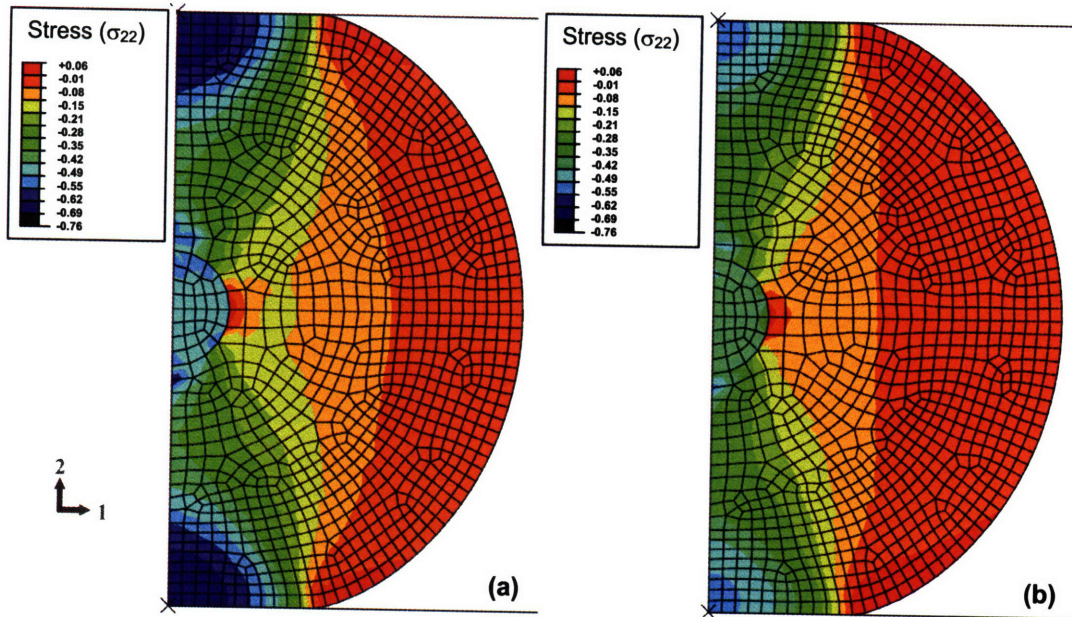


Figure 5–42. Element stress in the 2-direction (σ_{22}) within actin networks in a compressed cell ($\epsilon_{2,\text{total}} = -15\%$) at two different times, (a) $t=0.01$ sec, immediately after compression and (b) $t=20$ sec, in the compressed but relaxed state. Units are Pa.

The reaction force time history is shown in Figure 5–43 for an actin network ($c_{AF}=20\mu\text{M}$, $L_c=0.89\mu\text{m}$, $l_p=3\mu\text{m}$, $\alpha=1.08\%$) with the same nonlinear scaling for the viscoelastic Maxwell leg developed in Section 5.4, and subject to the three compressive strain cases ($\epsilon_{2,\text{total}}=-5\%$, -10% , -15%). The relaxation time constant is $t_R = 3.8$ seconds.

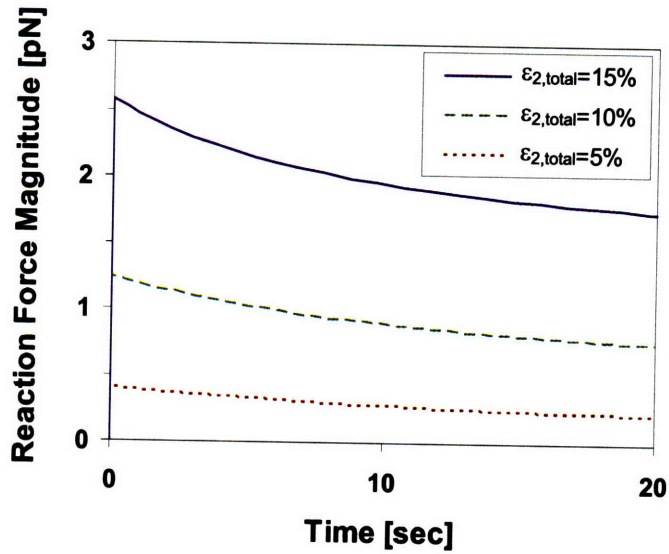


Figure 5-43. Relaxation of reaction force on a solid plate compressing a cell ($\epsilon_{2,\text{total}}=-5\%$, -10% , and -15%). Cell consists of a neo-Hookean nucleus, orthotropic membrane, and a cytoplasm consisting of an actin network ($c_{AF}=20\mu\text{M}$, $L_c=0.9\mu\text{m}$, $l_p=3\mu\text{m}$, $\alpha=1.1\%$).

Figure 5-43 shows the change in peak reaction forces with increasing strain loads, with the cell fully relaxed by $t=20$ seconds. The relative amount of relaxation for each case of compressive strain loading is shown in Figure 5-44 by normalizing the reaction forces

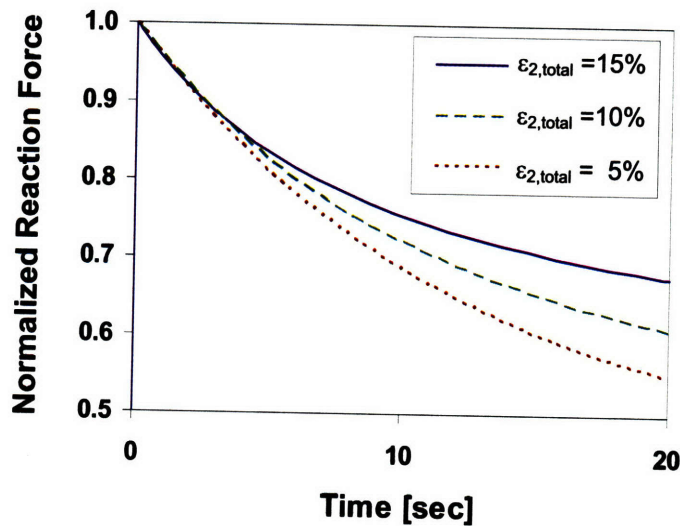


Figure 5-44. Relaxation of reaction force on a solid plate compressing a cell ($\epsilon_{2,\text{total}}=-5\%$, -10% , and -15%). Cell consists of a neo-Hookean nucleus, orthotropic membrane, and a cytoplasm consisting of an actin network ($c_{AF}=20\mu\text{M}$, $L_c=0.9\mu\text{m}$, $l_p=3\mu\text{m}$, $\alpha=1.1\%$).

for each case, $\varepsilon_{2,\text{total}} = -5\%$, -10% , -15% , by their peak reaction force at $t = 0.01$ sec, $f_R = -0.4$, -1.2 , -2.6 pN respectively. The results show that increasing compressive strain on uniform actin networks in a cellular geometry results in more total reaction force relaxation, but slightly less relaxation relative to the peak reaction force for each case. These results will be compared to the poroelastic response of actin networks in a cellular geometry in the following chapter.

5.4.3 Axisymmetric cell model with varying actin concentration

The actin concentration is now varied over three equally spaced regions of the cytoplasm: $c_{AF,inner} = 10\mu\text{M}$, $c_{AF,middle} = 30\mu\text{M}$, $c_{AF,outer} = 170\mu\text{M}$ to approximately simulate *in vivo* actin gradients. The thickness of the region nearest the membrane (800 nm) is an upper bound for observed thickness of the actin cortex, $\leq 1\mu\text{m}$ (Hartwig and Shevlin, 1986; Nakata and Hirokawa, 1992; Keller and Eggli, 1998; Lang et al., 2000). Note that this concentration gradient creates intracellular regions with sharp transitions in material properties. The change, and evolution, of the material response within a cell is much smoother due to the diverse, and dynamic, nature of the different cytoskeletal networks. Thus, while the concentration and mechanical contribution from actin networks decrease from the cell membrane toward the nucleus, the structural role of intermediate filaments increases due to their higher concentrations near the middle and inner regions of the cytoplasm. The microtubules will likewise make a separate contribution as their long, stiff structures extend from the centrosome toward the

membrane, often while cross-linking with other cytoskeletal networks. These additional networks will need to be modeled to capture the total micromechanical behavior of the cell. The following analysis serves to show the mechanical contributions from actin networks when evaluated with concentration gradients and boundary conditions (i.e. membrane and nucleus) that are more representative of a cellular environment.

The axisymmetric simulations again compress the cell by applying a axial normal strain ($\epsilon_{2,\text{total}}=-5\%$, -10% , -15%) on the top plate according to a linear ramp for $t=0.01$ second, followed by a hold time of 20 seconds (see Figure 5–45b). Figure 5–45a shows the undeformed axisymmetric mesh next to the deformed mesh (with axial normal displacement contours at $t=0.01$ seconds, $U_2=-0.9\mu\text{m}$ or $\epsilon_{2,\text{total}}=-15\%$ for a $6\mu\text{m}$ diameter

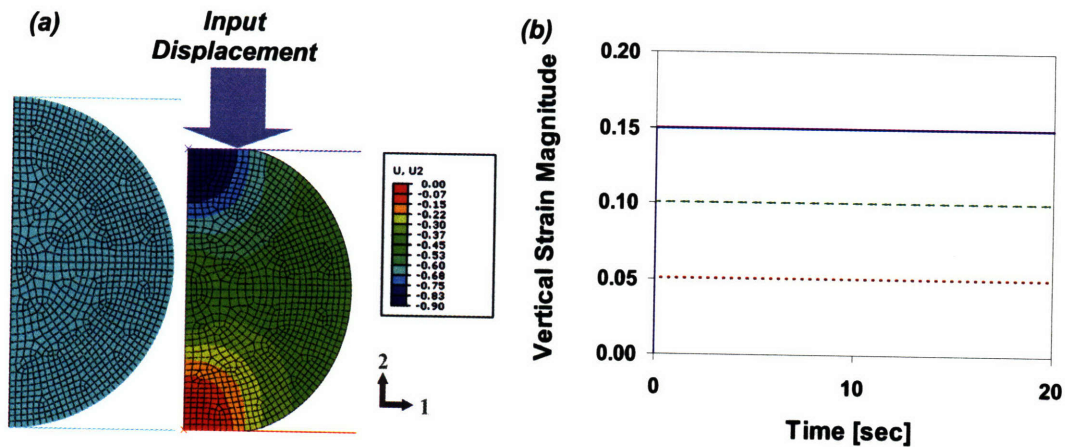


Figure 5–45. (a) Axisymmetric mesh schematic with axial normal strain contours in deformed mesh, and (b) Input (total) strain time history for compression of a viscoelastic cell with loading ramp time of 0.01 second and a hold time of 20 seconds.

cell). The axial normal strain (ϵ_{22}) of the elements within the compressed cell is shown in Figure 5–46 for $t=0.01$ and $t=20$ seconds. There is again very little change in the axial normal strain between the initially compressed state (Figure 5–46a) and the relaxed state

(Figure 5–46b), but now with a sharper transition in strain between the outer and middle regions and a larger maximum compressive strain. Both plots still help to identify the regions of largest compressive axial normal strain (blue) directly under the load along the center axis of the cell, as well as the regions of little or no compressive axial normal strain (tan-orange),

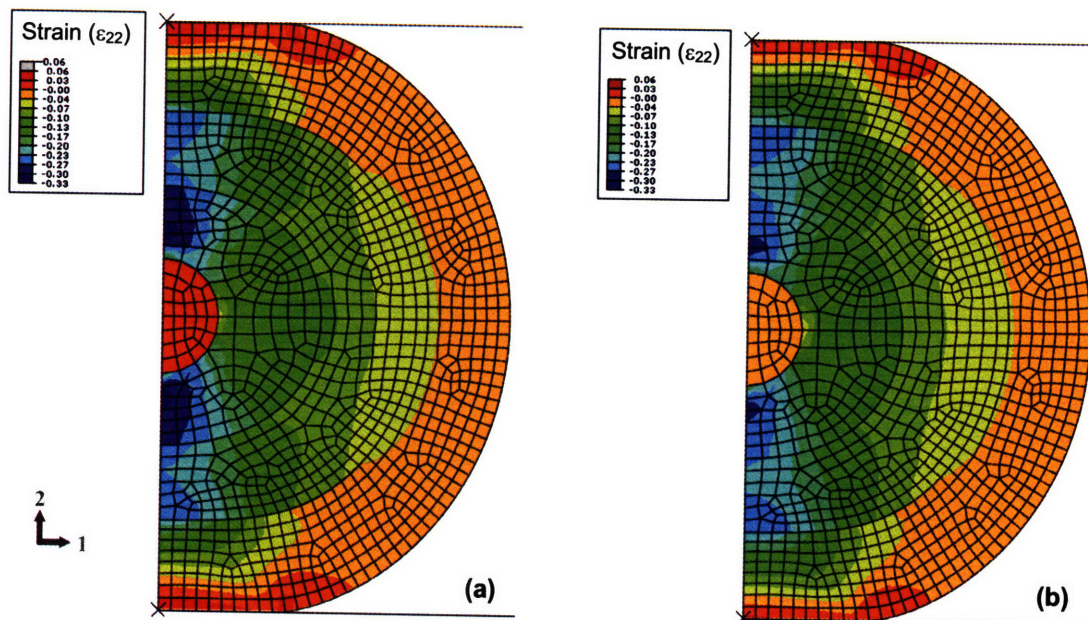


Figure 5–46. Element strain in the 2-direction (ϵ_{22}) within actin networks in a compressed cell ($\epsilon_{2,\text{total}} = -15\%$) at two different times, (a) $t=0.01$ sec, immediately after compression and (b) $t=20$ sec, in the compressed but relaxed state.

including the stiffer nucleus. The contour plots of the axial normal stress (σ_{22}) of the elements within the compressed cell is shown in Figure 5–47 for $t=0.01$ and $t=20$ seconds, illustrating the relaxation of compressive axial normal stresses, especially in the regions with the highest compressive stresses that are adjacent to the plates.

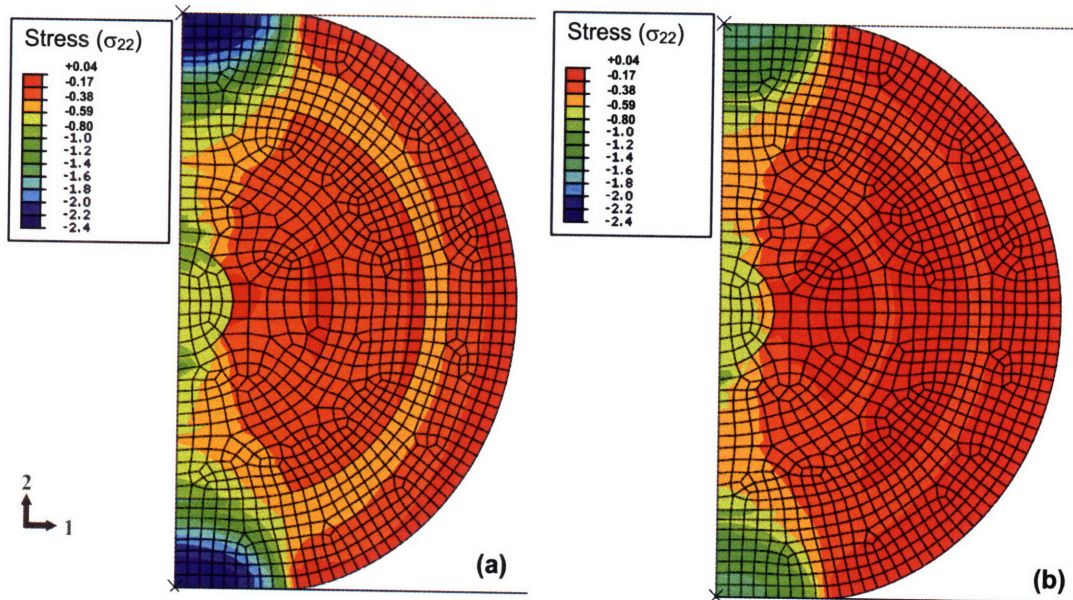


Figure 5-47. Element stress in the 2-direction (σ_{22}) within actin networks in a compressed cell ($\epsilon_{2,\text{total}} = -15\%$) at two different times, (a) $t=0.01$ sec, immediately after compression and (b) $t=20$ sec, in the compressed but relaxed state. Units are Pa.

The reaction force time history is shown in Figure 5-48 for an actin network ($c_{AF}=10\text{-}170\mu\text{M}$, $L_c=0.89\mu\text{m}$, $l_p=3\mu\text{m}$, $\alpha=1.08\%$) with the same nonlinear scaling for the viscoelastic Maxwell leg developed in Section 5.4, and subject to the three compressive strain cases ($\epsilon_{2,\text{total}}=-5\%$, -10% , -15%). The relaxation time constant remains at $t_R = 3.8$ seconds.

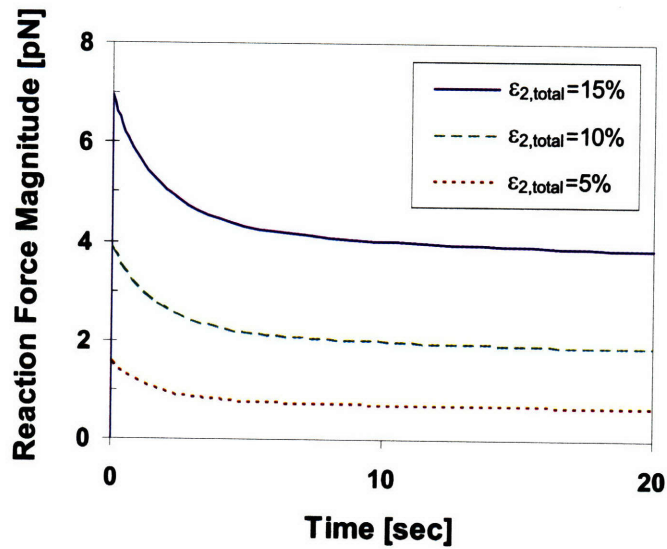


Figure 5–48. Relaxation of reaction force on a solid plate compressing a cell ($\epsilon_{2,\text{total}} = -5\%$, -10% , and -15%). Cell consists of a neo-Hookean membrane and nucleus, and a cytoplasm consisting of three regions of actin networks ($c_{AF} = 10\text{--}170\mu\text{M}$, $L_c = 0.9\mu\text{m}$, $l_p = 3\mu\text{m}$, $\alpha = 1.1\%$).

Figure 5–48 shows the change in peak reaction forces with increasing strain loads, with the cell fully relaxed by $t = 10\text{--}15$ seconds. The relative amount of relaxation for each case of compressive strain loading is shown in Figure 5–49 by normalizing the reaction forces

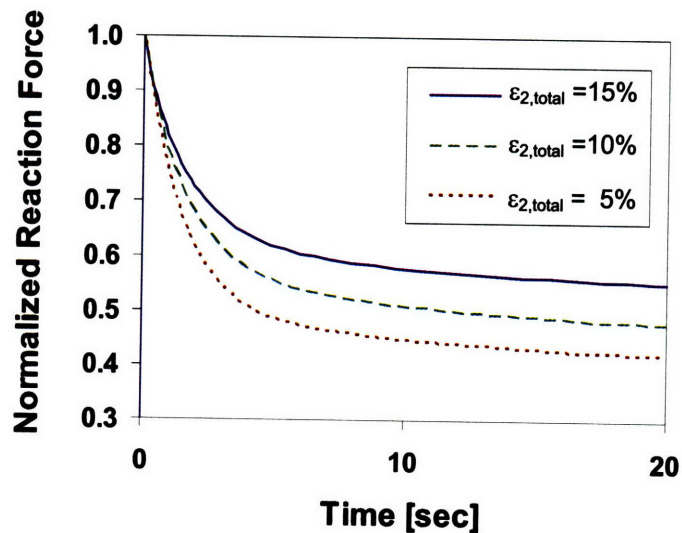


Figure 5–49. Relaxation of reaction force on a solid plate compressing a cell ($\epsilon_{2,\text{total}} = -5\%$, -10% , and -15%). Cell consists of a neo-Hookean membrane and nucleus, and a cytoplasm consisting of three regions of actin networks ($c_{AF} = 10\text{--}170\mu\text{M}$, $L_c = 0.9\mu\text{m}$, $l_p = 3\mu\text{m}$, $\alpha = 1.1\%$).

for each case, $\epsilon_{2,\text{total}} = -5\%$, -10% , -15% , by their peak reaction force at $t = 0.01$ sec, $f_R = 1.5$, -3.9 , -7.0 pN respectively. The model with three regions of actin concentration exhibits a stiffer overall response, and the results still show that increasing compressive strain on actin networks in a cellular geometry results in more total reaction force relaxation but less relaxation relative to the peak reaction force.

CHAPTER 6 Poroelastic network models

6.1 Background

Many previous approaches to modeling the biomechanical response of cells have tried to capture either the cell's solid-like or fluid-like behavior. Viscoelastic continuum models have followed this trend (Evans and Yeung, 1989; Needham and Hochmuth, 1992; Karcher et al., 2003), in some cases using a rheological model that includes both fluid and solid behaviors (Bausch et al., 1998). Structural-based cytoskeletal models such as tensegrity (Ingber, 1993) or cellular solids (Satcher and Dewey, 1996) simulate the elastic response through the cooperative deformation of solid elements. Recent work, however, has used a multiphasic approach (solid, liquid, and sometime ionic) to simulate the interactions between the phases as observed experimentally in volumetric changes of cells subjected to mechanical loads and/or osmotic pressures as well as a possible source of time-dependent effects normally attributed to viscoelasticity (Guilak et al., 2006). Biphasic interactions also occur during the creation of migratory protrusions necessary for cell migration (Pollard and Borisy, 2003). The cylindrical-like protrusions, or pseudopods, extend into the 3D ECM via a polymerization/depolymerization cycle of cytoskeletal filaments at the inner surface of the membrane (Mahadevan and Matsudaira, 2000; Mogilner and Oster, 2003; Rafelski and Theriot, 2004) in conjunction with localized cytosolic swelling and poroviscoelastic effects (Herant and Dembo, 2006). A combination of polymerization and poroelastic effects have also been identified as possible contributors to the acrosomal extension (Tilney and Inoue, 1985; Condeelis,

1993). The polymerization process at the leading edge may also be bolstered by delivery of actin monomers into protrusions via cytosolic fluid flow at rates not achievable by diffusion alone, as measured in fibroblasts using the FLAP (fluorescence localization after photobleaching) method (Zicha et al., 2003). Simulation of these types of effects requires a modeling framework that captures the biphasic interactions of cytosolic fluid flow with the cytoskeletal microstructure.

This chapter will simulate the time-dependent behavior of the cytoplasm through a biphasic, poroviscoelastic approach that accounts for the spatial diffusion of the cytosol within the porous, viscohyperelastic filament network. Flow-dependent viscoelastic effects are due to cytosolic flow (with mass balance governing the pressure gradient), and flow-independent (time-dependent) effects are due to the material shear viscoelasticity. Both effects manifest themselves in an apparent viscoelastic behavior (e.g. stress relaxation and creep) but for different underlying reasons. As a first approximation, the material shear viscoelasticity for the modeled F-actin networks is neglected due to the low loss modulus observed for *in vitro* gels at the frequencies of interest (Janmey et al., 1991; Gardel et al., 2004a). This approximation will be re-evaluated at the end of the chapter to compare the relative time-dependent contributions from poroelasticity and material shear viscoelasticity .

6.1.1 Biphasic, poroelastic models: Terzaghi model

Although recent work has employed a poroelastic approach to cell and tissue mechanics, the origins of poroelasticity date back much farther to applications of soil

consolidation in geomechanics. The origins of equilibrium thermodynamics of fluid transport in elastic solids can be traced back as far as Gibbs (Gibbs, 1878). Karl von Terzaghi initiated the field of Erdbaumechanik, or soil mechanics, in 1925 when he accepted an appointment at MIT and introduced a 1D model to describe the consolidation of a column of soil subject to a constant vertical load and laterally constrained on its sides (Terzaghi, 1925). This new soil mechanics approach considered the soil particles bound together by molecular forces to form a porous, elastic material (see Figure 6–1).

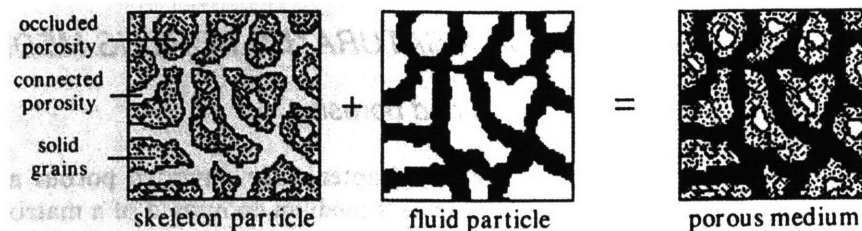


Figure 6–1. Biphasic porous media in soil mechanics from the superposition of two continuous media [adapted from (Mokdad et al., 2004)]

Terzaghi’s 1D consolidation framework relies on the following assumptions:

1. Fully saturated soil
2. Incompressible water and soil particles
3. Permeability-based kinetic law (Darcy's law)
4. Compression load and fluid flow are one-dimensional
5. Linear elastic solid “skeleton” phase
6. External loading is applied suddenly and remains constant
7. Homogenous soil layer
8. Strains are small

The “effective” stresses within the elastic solid skeleton, σ_{eff} , is then the pore pressure of the interstitial fluid, p_f , subtracted from the total stress, σ_{total} , for the porous medium,

$$\sigma_{eff} = \sigma_{total} - p_f \quad (6.1)$$

Since the solid phase is considered to be linearly elastic, Terzaghi used the following relationship

$$\sigma_{eff} = \frac{1}{m_v} \varepsilon_z, \quad (6.2)$$

where m_v is a soil constant that acts as a measure of compliance. Terzaghi employs Darcy’s law, originally developed to evaluate the flow of water through sand bed filters for the municipal water supply in Dijon, France (Darcy, 1856), in one dimension as a mass balance for fluid flow at the boundary,

$$v_{f,z} = \frac{-k_D}{\mu} \frac{\partial p_f}{\partial z} \quad (6.3)$$

where $v_{f,z}$ is the velocity (flow rate), z is the distance measured downward from the top surface of the consolidating mass, k_D is the Darcy or intrinsic permeability [m^2], and μ is the dynamic viscosity [Pa-s]. The Darcy (intrinsic) permeability for soils is strongly dependent on the fluid fraction, ϕ_f , or porosity, (i.e. $k_D \sim \phi_f^m$ with $m > 3$) (Detournay and Cheng, 1993). There are many power law relationships for k_D (see, for example, (Torquato, 1991)), including the Carman-Kozeny law (Scheidegger, 1974) which gives a power law relation of $k_D \sim \phi_f^3 / (1 - \phi_f)^2$ based on a conceptual model of packing of spheres. Darcy’s law can also be considered to be a linearized version of a quadratic relation given later by (Forchheimer, 1901),

$$\alpha v_{f,z} + \beta v_{f,z}^2 = \frac{\partial p_f}{\partial z} \quad (6.4)$$

where $\alpha v_{f,z}$ and $\beta v_{f,z}^2$ vary with viscous and inertial effects, respectively (Rahli et al., 1996). Assuming that the total stress is constant, the governing equation of the time evolution of the interstitial fluid pressure is a homogeneous diffusion equation,

$$\frac{\partial p_f}{\partial t} - c_v \frac{\partial^2 p_f}{\partial z^2} = 0 \quad (6.5)$$

where c_v is the coefficient of consolidation [m^2/sec] given by

$$c_v = \frac{k_H}{m_v \gamma_w} \quad (6.6)$$

where k_H is the hydraulic permeability ($k_H = k_D / \mu$) and γ_w is the specific weight of the fluid (water in this case). And since the soil properties are considered to be homogeneous and constant, c_v and m_v do not vary with depth, z , or time. Thus, soil with a high permeability will consolidate more quickly, while a soil with a more compliant solid matrix will consolidate more slowly. Results for the consolidation of a column of soil using Terzaghi's model is shown in Figure 6–2 and Figure 6–3. The model has an initial step in which a vertical pressure load is applied suddenly with the porous platen closed, and then held constant. The material then consolidates during the following step with the porous platen open, as shown through the decreasing normalized vertical displacement in Figure 6–2. The open porous platen condition gives a zero pressure boundary condition and allows fluid to flow out of the bottom surface. The normalized fluid pore pressure evolution with time during the second step is shown in Figure 6–3. The normalized pore pressure is shown for the material point just below the solid platen that is compressing the sample. Both plots are given in normalized values to qualitatively illustrate general 1D poroelastic behavior rather than to quantify the response of a particular soil. The color contours (inset in Figure 6–2 and Figure 6–3) represent the gradient in vertical

stress (σ_{22}) and pore pressure, respectively, after the porous platen has been opened, and they are shown to illustrate the non-uniform response of poroelastic state variables.

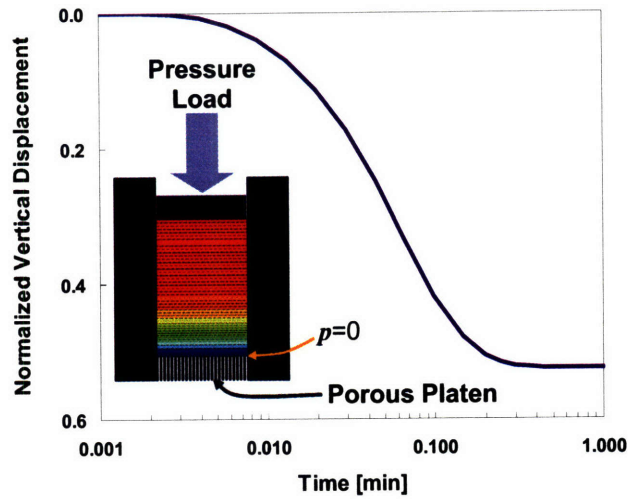


Figure 6–2. Normalized vertical displacement evolution of a soil in confined compression with a porous platen boundary ($p=0$) and subject to a sudden vertical pressure load. Qualitative contour plot of vertical stress (σ_{22}) shown in inset at $t=0.01\text{min}$.

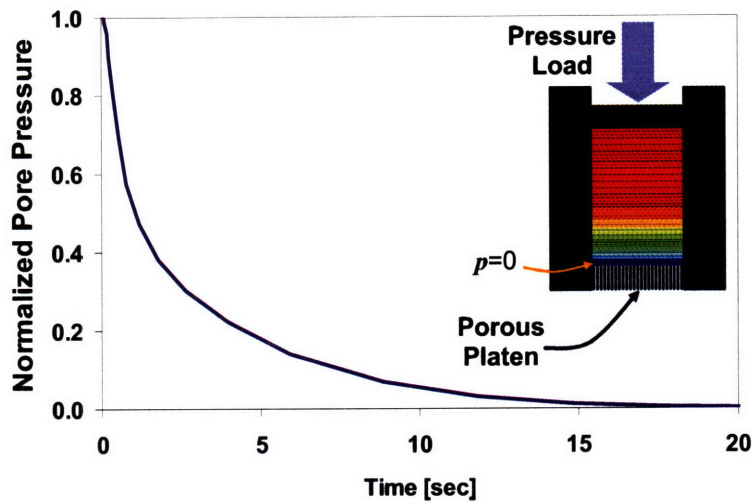


Figure 6–3. Normalized pore pressure evolution of a soil in confined compression with a porous platen boundary ($p=0$) and subject to a sudden vertical pressure load. Qualitative contour plot of pore pressure shown in inset at $t=0.01\text{min}$ (0.9sec).

6.1.2 Biphasic, poroelastic models: Biot model

In 1941, Maurice Biot presented a more rigorous and complete treatment of Terzaghi's soil consolidation theory that extended it to three-dimensions and generalized it to include an arbitrary load that could vary with time, a compressible solid phase, and a partially saturated porous medium (Biot, 1941). Other than those enhancements, Biot made similar assumptions as Terzaghi (Biot, 1941):

1. Isotropic materials
2. Linear elastic solid
3. Water is incompressible
4. Permeability-based kinetic law (Darcy's law)
5. Strains are small
6. Constant reservoir temperature
7. No mass exchange between solid and fluid phases
8. Neglect inertial and body forces

The poroelastic constitutive relationship can be given by the stress-strain equation

$$\boldsymbol{\sigma}_{eff} = \boldsymbol{\sigma} + \alpha p_f \mathbf{I} = 2G\boldsymbol{\varepsilon} + \frac{2G\nu_u}{1-2\nu_u} \varepsilon_v \mathbf{I}, \quad (6.7)$$

where ν_u is the undrained Poisson ratio, $\boldsymbol{\varepsilon}$ is the small strain tensor, ε_v is the volumetric strain, and α is the ratio of the fluid volume gained (or lost) in a material element to the volume change of that element, when the pore pressure is allowed to return to its initial state (Detournay and Cheng, 1993). The last term in Equation (6.7) captures both the fluid pore pressure response and the volumetric response of the solid phase. Note that

Equation (6.7) reduces to the familiar constitutive relationship for drained linear elastic material (i.e. for $p_f = 0$). These parameters are defined to be

$$\varepsilon_v = \text{tr}(\boldsymbol{\varepsilon}), \quad (6.8)$$

$$p_{total} = -\frac{1}{3} \text{tr}(\boldsymbol{\sigma}), \quad (6.9)$$

$$\alpha = \frac{p_{total} + K\varepsilon_v}{p_f}, \quad (6.10)$$

$$\boldsymbol{\varepsilon} = \frac{1}{2}(\nabla \mathbf{u} + \nabla \mathbf{u}^T) = \varepsilon_{ij} = \frac{1}{2} \left(\frac{\partial u_i}{\partial x_j} + \frac{\partial u_j}{\partial x_i} \right), \quad (6.11)$$

$$\nu_u = \frac{3K_u - 2G}{2(3K_u + G)}, \quad (6.12)$$

where K and K_u are the drained and undrained bulk moduli, respectively, u_i is the solid displacement vector of the porous solid with respect to the reference configuration, p_{total} is the total pressure. The variation of α is $[0, 1]$, ν_u is $[\nu, 0.5]$, and K_u is $[K, \infty]$.

Biot's poroelastic framework also uses Darcy's law in 3D as the governing kinetic law (neglecting body forces),

$$\frac{\mathbf{Q}}{A} = \mathbf{v}_f = -\frac{k_D}{\mu} \nabla p_f \quad (6.13)$$

where \mathbf{Q} is the volumetric flow rate vector, A is the cross-sectional area, \mathbf{v}_f is the fluid velocity vector. Darcy's law is an empirical relation that can also be derived through the Navier-Stokes equation by neglecting the inertial terms (Bear, 1972). The standard stress equilibrium expression apply (neglecting body forces)

$$\nabla \cdot \boldsymbol{\sigma} = \mathbf{0}. \quad (6.14)$$

The continuity equation for the mixture is given by

$$\nabla \cdot (\phi_f \mathbf{v}_f + \phi_s \mathbf{v}_s) = 0. \quad (6.15)$$

where \mathbf{v}_s is the velocity vector of the solid and $\phi_s = (1 - \phi_f)$ is the solid volume ratio. This theory was later expanded by Biot to include flow of a compressible, viscous fluid through a porous solid (Biot, 1956a; Biot, 1956b). Biot's formulation led to the evaluation of many different poroelastic materials subjected to experimental conditions beyond the constant load dictated by Terzaghi's model.

6.1.3 Biphasic, poroelastic models: Mow model

Following Biot's poroelastic framework, Van Mow developed a successful biphasic theory to describe the time-dependent mechanical behavior of articular cartilage and other hydrated soft tissues (Mow et al., 1980). As with Terzaghi's formulation, the tissue was initially modeled as a linear elastic isotropic solid and an inviscid fluid that are both homogeneous, immiscible, and incompressible, with the same continuity equation as given in Equation (6.15) (Cohen et al., 1998).

$$\boldsymbol{\sigma}_s = \boldsymbol{\sigma}_E - \phi_s p_f \mathbf{I} \quad (6.16)$$

$$\boldsymbol{\sigma}_f = -\phi_f p_f \mathbf{I} \quad (6.17)$$

$$\boldsymbol{\sigma}_{total} = \boldsymbol{\sigma}_s + \boldsymbol{\sigma}_f = \boldsymbol{\sigma}_E - p_f \mathbf{I} \quad (6.18)$$

where $\boldsymbol{\sigma}_s$ is the stress tensor of the solid phase, $\boldsymbol{\sigma}_f$ is the stress tensor of the fluid phase, $\boldsymbol{\sigma}_s$ is the total stress tensor, and $\boldsymbol{\sigma}_E$ is the elastic stress tensor of the solid phase which was initially assumed to be isotropic and linear elastic according to

$$\boldsymbol{\sigma}_E = 2G_s \boldsymbol{\varepsilon} + \lambda_s \boldsymbol{\varepsilon}_v \mathbf{I} \quad (6.19)$$

where G_s , λ_s are the Lamé constants. It should be noted that the aggregate modulus, $H_a=2G_s + \lambda_s$, is a commonly used term in the description of the equilibrium behavior of connective tissues (e.g. a larger water content leads to a smaller value of H_a , which in turn permits a larger equilibrium deformation) (Woo et al., 1987). The equilibrium equations for the total stress, σ_{total} , are the standard ones also used by Biot,

$$\nabla \cdot \sigma_{total} = \mathbf{0}. \quad (6.20)$$

And the coupled momentum balance equations for the individual fluid and solid phases are

$$\nabla \cdot \sigma_E - \phi_s \nabla p_f + K_D (\mathbf{v}_f - \mathbf{v}_s) = \mathbf{0} \quad (6.21)$$

$$-\phi_f \nabla p_f + K_D (\mathbf{v}_f - \mathbf{v}_s) = \mathbf{0} \quad (6.22)$$

where K_D is the diffusive drag coefficient defined by (Lai and Mow, 1980)

$$K_D = \frac{\phi_f^2}{k_H}. \quad (6.23)$$

Here the hydraulic permeability, k_H , of cartilage was taken to be isotropic and constant throughout the material although it has been shown to be strain-dependent in cartilage (Mansour and Mow, 1976; Lai and Mow, 1980) as shown in Figure 6-4.

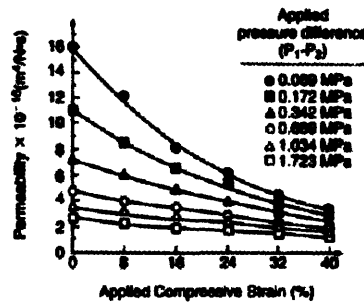


Figure 6-4. Articular cartilage permeability for varying compressive strain and applied pressure (Lai and Mow, 1980)

6.1.4 Poroelastic testing procedures

Permeability and other intrinsic biphasic material properties are determined by standard experimental procedures such as uniaxial confined compression, unconfined compression and indentation (Mow et al., 1980; Armstrong et al., 1984; Mak, 1986; Cohen et al., 1998). The schematic for a confined compression experiment is shown in Figure 6–5 along with the displacement profile, stress relaxation response, and calculated permeability variation with compressive strain.

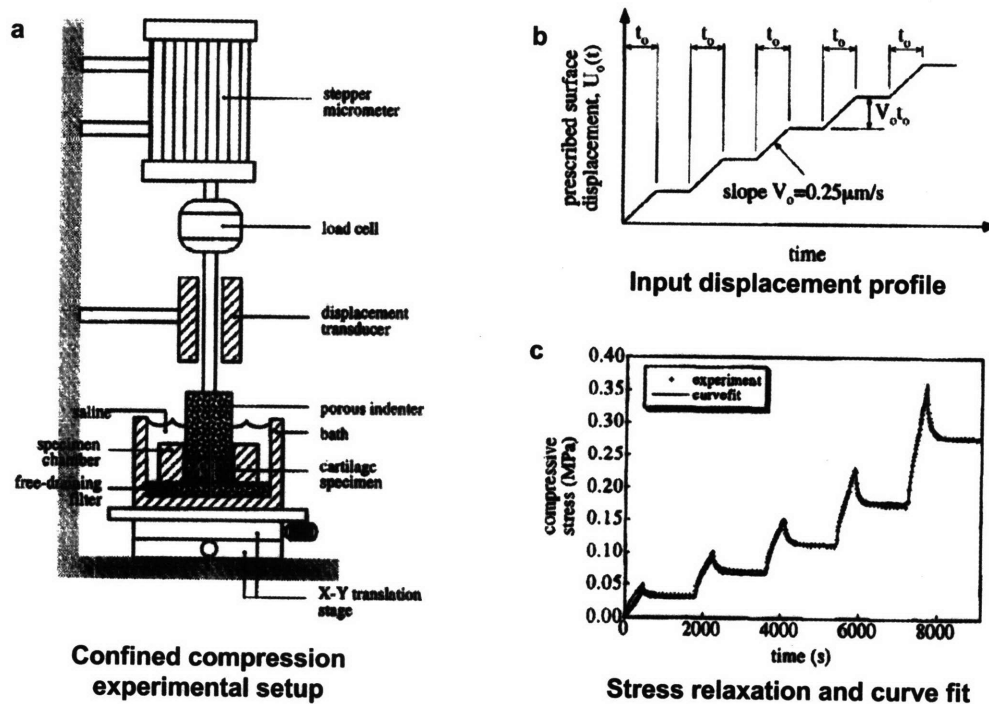


Figure 6–5. (a) Schematic for confined compression test, (b) Input displacement profile with ramp time (t_0), and (c) Stress relaxation time history and curve fit of bovine cartilage (adapted from (Ateshian et al., 1997)).

The experimental stress relaxation and equilibrium data was used to calculate average material constants (i.e. k_H , H_a) of the poroelastic theory using a nonlinear regression

analysis (Ateshian et al., 1997). An example of the results from an unconfined compression experiment with a varying compressive loading rate is shown in Figure 6-6.

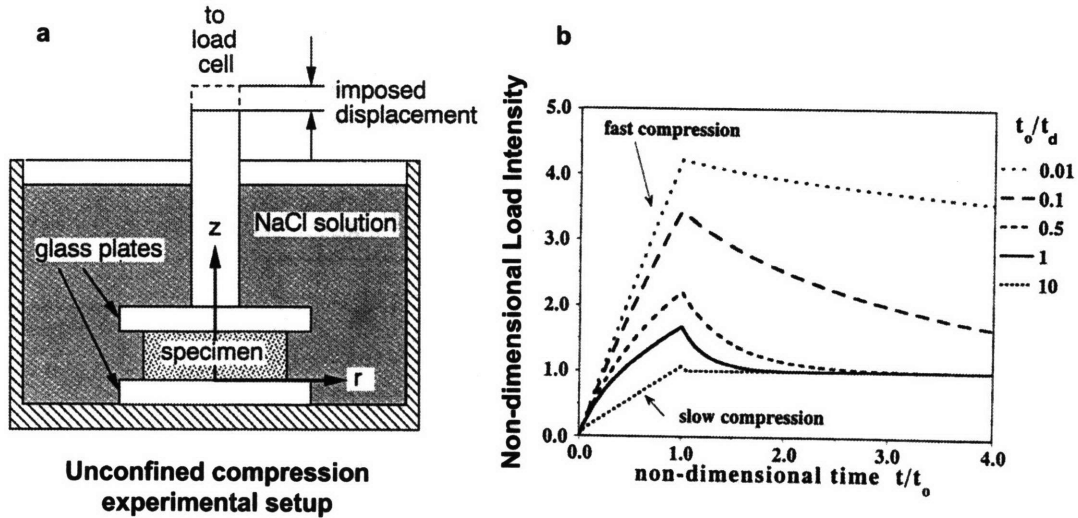


Figure 6-6. (a) Schematic for unconfined compression test and (b) Stress relaxation time history for a ramped displacement with ramp time (t_0) and an internal material diffusion time (t_d) of bovine cartilage (adapted from (Cohen et al., 1998)).

Evaluation of the unconfined axisymmetric material behavior under a compressive loading rate (Figure 6-6) would not have been achievable using Terzaghi's model. Although Mow's governing equations were essentially the same as Biot's, Mow and others changed the constitutive relations appropriately for application to biomaterials (e.g. altering the stiffness tensor for transversely anisotropic cartilage (Cohen et al., 1998) and also including a viscoelastic solid phase (Mak, 1986; Setton et al., 1993; Suh and DiSilvestro, 1999) to account for observed fluid flow-independent viscoelasticity in articular cartilage (Hayes and Mockros, 1971; Hayes and Bodine, 1978)).

6.1.5 Biphasic poroviscoelastic theory

The popular biphasic poroviscoelastic theory (BPVE) employs such a viscoelastic solid phase to capture flow-independent viscoelasticity in addition to the poroelastic behavior. Using the quasilinear viscoelasticity (QLV) theory of Fung (Fung, 1980) to describe the solid phase (see Chapter 5 for details on QLV), Mak developed an isotropic biphasic model of cartilage (Mak, 1986). The BPVE often modifies the QLV relaxation function, $G(t)$,

$$\begin{aligned} G(0) &= 1 + c \ln\left(\frac{\tau_2}{\tau_1}\right), \\ G(\infty) &= 1 \end{aligned} \quad (6.24)$$

in order for the viscoelastic stress to reduce to the elastic stress at equilibrium (Huang et al., 2001). As before, the model considers a biphasic mixture of an incompressible solid phase (composed of collagen fibers, proteoglycans, and chondrocytes), and an incompressible fluid (i.e. the interstitial water) (Mow et al., 1980). The governing equations for the BPVE are the same as for the poroelastic model, but with the elastic stress term replaced with a viscoelastic stress based on the modified QLV.

$$\nabla \cdot \boldsymbol{\sigma} = \nabla \cdot \boldsymbol{\sigma}_{VE} - \phi_s \nabla p_f = \mathbf{0} \quad (6.25)$$

The inclusion of intrinsic viscoelasticity into porous media models has enabled them to better capture the empirical behavior of connective tissues (i.e. compared with poroelastic models) (DiSilvestro et al., 1999; Suh and Bai, 1997), with some exceptions (Soltz and Ateshian, 2000). Other constitutive models have also been included within the biphasic model framework that are specifically suited to connective tissues (e.g. conewise linear elasticity (currier) for the bimodular stress-strain response of cartilage), but often only for infinitesimal strains (Huang et al., 2001).

The BPVE model has also been applied at the cellular level to chondrocytes in cartilage. Guilak, et al. have employed the biphasic theory with established linear elastic, hyperelastic, and bimodal compressible viscoelastic constitutive models for the solid phase to evaluate the mechanical properties of chondrocytes during micropipette aspiration (Trickey et al., 2000; Baaijens et al., 2005; Trickey et al., 2006). In these studies, the chondrocyte is taken to be a homogeneous material with poroviscoelastic properties, but without differentiation between the membrane, cytoplasm/cytoskeleton, or nucleus. Mechanical properties such as the Poisson ratio, aggregate modulus, and hydraulic permeability are determined by fitting the BPVE model to the experimentally observed cellular creep and relaxation behavior (Trickey et al., 2000; Baaijens et al., 2005; Trickey et al., 2006). A comparison between the ability of the biphasic elastic model and BPVE model to fit the creep response of the chondrocytes after micropipette aspiration resulted in a better fit for the BPVE model, suggesting that the creep response was due to the intrinsic viscoelasticity of the solid phase (Baaijens et al., 2005). BPVE models have also been used to evaluate the biphasic behavior and interactions between chondrocytes cells and the surrounding extracellular matrix, (Guilak and Mow, 2000), while linear biphasic models have been used for chondrocyte-pericellular matrix interactions (Alexopoulos et al., 2005).

These poroelastic and poroviscoelastic models generally restrict their focus to infinitesimal strains defined in Equation (6.11) (Hayes et al., 1972; Hori and Mockros, 1976; Armstrong and Mow, 1982; Holmes et al., 1985; Jurvelin et al., 1987; Mow et al., 1989; Athanasiou et al., 1991). The biphasic model has been extended to finite deformation (Holmes, 1986; Holmes and Mow, 1990; Kwan et al., 1990; Cohen et al.,

1998) while capturing kinetic (creep, stress relaxation) behavior in addition to the equilibrium behavior (Ateshian et al., 1997).

The contribution of flow-independent viscoelasticity in biphasic tissues has been examined (Huang et al., 2001). A viscoelastic response in torsional shear depends on intrinsic, flow-independent, viscoelasticity of the solid phase (Hayes and Mockros, 1971; Zhu et al., 1993) since an isotropic poroelastic model subject to infinitesimal torsional shearing gives an isochoric deformation, precluding interstitial fluid pressurization and flow (Huang et al., 2001). However, anisotropy and higher order changes in compressive strain (neglected by the assumption of infinitesimal strains) can produce significant interstitial fluid pressurization and flow typified by porous media models (Mow et al., 1980; Frank and Grodzinsky, 1987; Lai et al., 1991; Huang et al., 2001).

Attributing experimentally observed time-dependent effects solely to intrinsic shear viscoelasticity of the solid phase has also been questioned. Triphasic models (solid, fluid, ions) have been employed to evaluate tissue electromechanics, including the role of

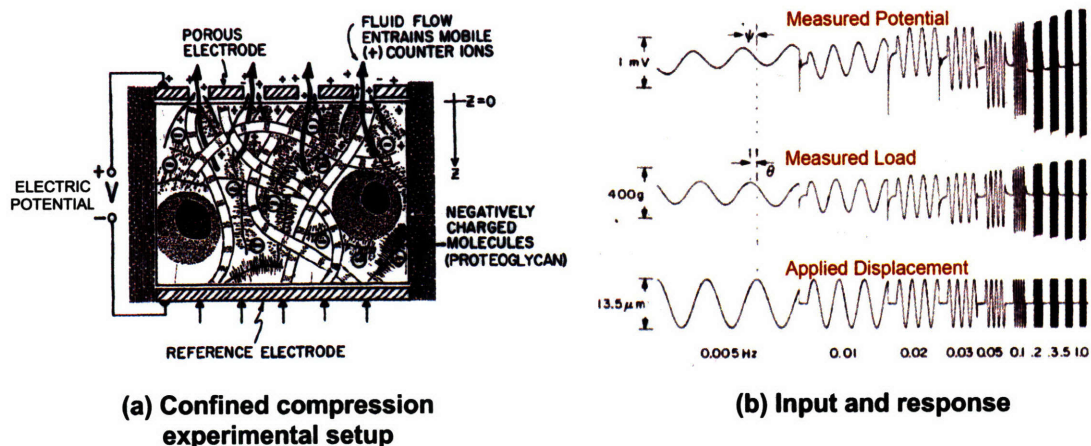


Figure 6–7. (a) Electrokinetic transduction in cartilage via confined compression setup with a streaming potential, and (b) Oscillatory input displacement with measured load and streaming potential response (adapted from (Frank and Grodzinsky, 1987))

flow-dependent viscoelasticity (Frank and Grodzinsky, 1987; Lai et al., 1991; Huyghe et al., 1997; Wilson et al., 2005a). Figure 6–7a shows the confined compression setup that uses a streaming potential connected to a porous electrode to measure electrokinetic transduction in cartilage. The streaming potential is a surrogate marker for the fluid velocity as the fluid flow from the applied compression entrains mobile ions that pass through the porous electrode, and the oscillatory response shown in Figure 6–7b cannot be predicted from a flow-independent viscoelastic model (Frank and Grodzinsky, 1987).

Heterogeneous pressure gradients possible on length-, time-scales associated with cell motility (Charras et al., 2005). The poroelastic model, unlike viscoelastic models, accounts for transient, localized hydrostatic pressure gradients, and it is especially useful in simulating blebbing cells and other cases in which hydrostatic pressure can be used to power local cellular shape change (Charras et al., 2005). Cellular blebbing occurs during apoptosis (Mills et al., 1998), cytokinesis (Fishkind et al., 1991; Burton and Taylor, 1997), and cell motility (Trinkaus, 1973; Friedl and Wolf, 2003) through a detachment of the cell membrane from the actin cytoskeletal cortex followed by an inflation of the detached membrane from cytosolic fluid flow (Charras et al., 2005). Charras, et al. used a one-dimensional version of Mow’s biphasic model (including Darcy’s law) with a linear elastic solid phase to estimate the diffusion distance of the pressure gradient for observed blebbing timescales, concluding that poroelastic effects in the cytoplasm make a key contribution to cell motility (Charras et al., 2005). Charras, et al. also experimentally measured the drained bulk modulus of the network to be $K_s \sim 2$ kPa (Charras et al., 2005).

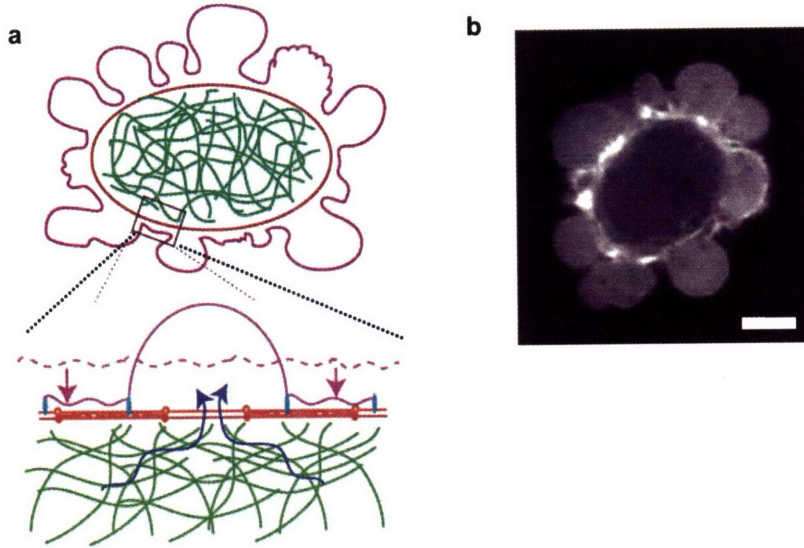


Figure 6–8. (a) Schematic of isochoric blebbing based on poroelastic fluid flow. (b) Confocal micrograph of a GFP–actin-transfected cell during bleb expansion. Scale bar, 5 μm (adapted from (Charras et al., 2005))

While previous poroviscoelastic models (Mow et al., 1980; DiSilvestro et al., 2001; Wilson et al., 2005b) did not include microstructural details, work on cervical tissue by Febvay and Socrate (Febvay, 2003) includes fluid flow through filaments modeled using 3D microstructurally-based constitutive models. Febvay and Socrate use a numerical treatment of the interstitial fluid flow by considering the interstitial mass diffusion physics analogous to heat diffusion physics, with the pore fluid pressure equivalent to the temperature. The governing equation for the time evolution of the interstitial fluid pressure, based on Darcy’s law , is

$$\chi_f \partial p_f / \partial t = k_H \nabla^2 p_f - \text{tr} \mathbf{D} \quad (6.26)$$

where $\chi_f = \phi_f / K_f$, ϕ_f is the fluid volume fraction, K_f is fluid bulk modulus, k_H is the hydraulic permeability, p_f is the dynamic interstitial fluid pressure, and $\mathbf{D} = \frac{1}{2}(\mathbf{L} + \mathbf{L}^T)$ is the global rate of stretch (with velocity gradient \mathbf{L} as defined earlier) (Febvay, 2003). This method is integrated into a finite element model via a coupled thermal-mechanical

analysis in which the coupling occurs through the “heat source” term, which in this case is the macroscopic rate of volume change, $\text{tr}(\mathbf{D})$.

Although Febvay and Socrate have included microstructurally-based constitutive models for tissues, the simulation of biphasic behavior at the cellular level requires a modeling framework that captures the biphasic interactions of cytosolic fluid flow with the cytoskeletal microstructure. These poroelastic and poroviscoelastic models presented, however, do not account for either the microstructural features of the cytoskeleton, their mechanobiological contribution, or their microstructural rearrangement.

6.2 Poroelastic governing equations

This section gives the governing equations for the 3D partially saturated poroelastic model which includes the 3D cytoskeletal network model developed in Chapter 3. As mentioned previously, the material shear viscoelasticity for the modeled F-actin networks is initially neglected due to the low loss modulus observed for *in vitro* gels at the frequencies of interest (Janmey et al., 1991; Gardel et al., 2004a), and also to allow for independent evaluation of fluid flow effects on material behavior. The poroelastic framework is implemented using the Soils analysis and pore pressure elements within the ABAQUS finite element software (Simulia Dassault Systèmes, Providence, RI, USA). The porous media is considered to consist of three possible phases: a compressible wetting cytosolic fluid, trapped interstitial gas (compressible), and an incompressible, hyperelastic cytoskeletal solid. The total Cauchy stress for the

$$\mathbf{T}_{Total} = \mathbf{T}_{s,CSK} + \mathbf{T}_{s,CL} + K_f(J-1)\mathbf{I} - \chi p_f \mathbf{I} \quad (6.27)$$

multiphase system where $\mathbf{T}_{s,CSK}$ is the Cauchy stress tensor of the solid cytoskeleton (Chapter 3), $\mathbf{T}_{s,CL}$ is the Cauchy stress from the cytoskeletal cross-links (Chapter 4), K_f is the bulk modulus of the fluid, J is the volume ratio, χ is the saturation factor (1.0 for a fully saturated medium, 0.0 for unsaturated), and p_f is the cytosolic fluid pore pressure. Note that the saturation factor can also be varied as a function of time or as a function of another state variable (e.g. stress, stretch, etc.). This framework also allows the flexibility to distinguish between trapped fluid and fluid that is free to flow through the cytoskeletal network. A cellular biomechanical analog to the trapped fluid would be fluid trapped within organelles. Although trapped fluid is relevant to geophysical applications, it is of less importance in evaluation of poroelastic fluid flow at the cell periphery (i.e. through the actin cortex), and will be neglected. Equilibrium is satisfied in the weak form through the principle of virtual work, and includes surface traction forces (\mathbf{t}_{surf}) and body forces per unit volume ($\hat{\mathbf{f}}$),

$$\int_V (\mathbf{T}_{total} : \delta \mathbf{D}) dV = \int_S (\mathbf{t}_{surf} : \delta \mathbf{v}) dS + \int_V (\hat{\mathbf{f}} : \delta \mathbf{v}) dV, \quad (6.28)$$

where $\delta \mathbf{D}$ is the virtual rate of deformation, and $\delta \mathbf{v}$ is the virtual velocity field. Ignoring trapped fluid, the continuity equation follows the familiar form

$$\nabla \cdot (\phi_f \mathbf{v}_f + \phi_s \mathbf{v}_s) = 0, \quad (6.29)$$

where \mathbf{v}_f and \mathbf{v}_s are the velocity vectors of the fluid and solid, respectively, ϕ_f is the fluid volume ratio and $\phi_s = (1 - \phi_f)$ is the solid volume ratio. The void ratio is defined

$$e = \frac{\phi_f}{1 - \phi_f}. \quad (6.30)$$

Darcy's law is once again employed as the kinetic law, in terms of the hydraulic permeability, $\hat{\mathbf{k}}_H$, neglecting body forces (e.g. gravity),

$$\mathbf{v}_f = -\hat{\mathbf{k}}_H \cdot \frac{\partial p_f}{\partial \mathbf{x}}, \quad (6.31)$$

where \mathbf{x} is the position vector of a material point in the current configuration and $\hat{\mathbf{k}}_H$ can be anisotropic and is a function of the saturation, χ , and the porosity, ϕ_f , (or void ratio, e) of the material. Darcy's law is applicable for the low Reynolds number ($Re \ll 1$) environment of cytosolic fluid flow within cytoskeletal networks (Scheidegger, 1974; Zhu and Skalak, 1988). We take these dependencies to be separable according to

$$\hat{\mathbf{k}}_H = k_\chi \mathbf{k}_{\phi_f}, \quad (6.32)$$

where $k_\chi(\mathbf{x}, \chi)$ depends on the saturation with $k_\chi(\mathbf{x}, 1) = 1.0$ and $\mathbf{k}_{\phi_f}(\mathbf{x}, \phi_f)$ is the permeability of the fully saturated medium. Nguyen and Durso observed that for steady flow through a partially saturated medium, the permeability varies with χ^3 (Nguyen and Durso, 1983), therefore k_χ is taken to vary with χ^3 ,

$$k_\chi(\mathbf{x}, \chi) \approx \chi^3, \quad (6.33)$$

noting that the permeability may also be defined (and updated) in terms of location and stress, stretch, or another state variable.

The fluid flow throughout the network alters the volume of local regions within the network. At each increment in time, the updated total volume ratio is the product of the mechanical and swelling volume ratios ($J_T = J_m J_{sw}$), as described in Section 3.7 on network swelling. For nearly incompressible materials, $J_m \rightarrow 1$, thus the swelling stretch

can be given in terms of the total volume ratio which includes the effects of local volume change due to fluid flow,

$$\lambda_{sw} = \sqrt[3]{J_T} . \quad (6.34)$$

Local volume changes in the ensuing poroelastic analyses can be tracked through the fluid volume ratio or the total volume ratio, and will therefore enable the poroelastic analyses to account for the contribution from network swelling.

6.3 Actin permeability

Poroelastic effects driven by heterogeneous pressure gradients are possible on length-scales and time-scales associated with cell motility, pseudopod growth, and blebbing (Charras et al., 2005; Herant and Dembo, 2006). Unfortunately, there is a dearth of experimental data regarding the permeability of the actin cytoskeletal networks that play such a key role in these cellular processes.

In support of their 1D poroelastic model for cell blebbing, Charras, et al. have given an estimate for the hydraulic permeability of actin networks following the relation

$$k_H \approx \frac{\xi^2}{\mu\phi_f^{1/3}}, \quad (6.35)$$

where ξ is the pore size (units of nm), and μ the viscosity of the cytosol. They used an effective cytoplasmic viscosity $\mu \sim 0.05$ Pa-s based on the diffusion of molecules up to 100\AA , a pore size $\xi \sim 10$ nm derived from examination of electron micrographs of the cell line and size-exclusion experiments, and a very low fluid fraction, $\phi_f \sim 0.2$, to give a Darcy permeability of $k_D \sim 1.7 \times 10^{-4} \mu\text{m}^2$ and a hydraulic permeability of $k_H \sim 3.4 \times 10^{-15}$

$\text{m}^4/(\text{N}\cdot\text{s})$ (Charras et al., 2005). This permeability value for F-actin networks is on the higher end of measured hydraulic permeabilities of networks within cartilage, $k_H \sim 10^{-15}$ - 10^{-16} (McCutchen, 1962; Lai and Mow, 1980; Trickey et al., 2000) which has porous gaps between GAG chains on the order of single nanometers.

Diffusion-based effective cytoplasmic viscosities, however, can overestimate the viscous nature of the cytosolic fluid by including all impediments to the diffusive motion: binding and collision effects in addition to the fluid-phase viscosity (Kao et al., 1993). This overestimation of viscosity would result in a smaller permeability estimate. The fluid-phase cytoplasmic viscosity has been measured by picosecond polarization microfluorimetry and found to be 28% greater than the viscosity of water, i.e. $\mu_f = 1.28 \times 10^{-3}$ Pa-s (Fushimi and Verkman, 1991). The fluid-phase cytoplasmic viscosity is ~ 40 x smaller than the effective cytoplasmic viscosity used by Charras, et al., which will now lead to a higher value for the network's permeability. While the permeability for F-actin networks has not been measured, it can be calculated using the Kozeny-Carman theory (Scheidegger, 1974; Ethier, 1983; Curry, 1986) as a function of ϕ_f and the F-actin diameter, d_{AF} :

$$K = \frac{d_{AF}^2 \phi_f^3}{80(1 - \phi_f)^2}, \quad (6.36)$$

$$k_H = \frac{K}{\phi_f \mu_f}, \quad (6.37)$$

which have been used to estimate k_D (i.e. $k_D = K/\phi_f$) for actin networks within leukocyte pseudopods (Zhu and Skalak, 1988) and keratocyte lamellipodia (Rubinstein et al., 2005). Equation (6.36) follows the familiar form, $k_D = r^2 f(\phi_f)$, of many empirical relationships developed to calculate the Darcy permeability of monodisperse fibrous porous media

with high porosities (Jackson and James, 1986; Ethier, 1991; Rahli et al., 1996), where r is the filament radius and not the pore size (ξ). Before calculating the permeability of an F-actin network, however, we need to establish the fluid volume ratio, or porosity, for the region of interest within the network. Based on an average F-actin diameter of 7 nm ($d_{AF}=6-8\text{nm}$, (Pryzwansky et al., 1983)) and an average filament spacing of $h=50$ nm, with measured values from $h=20$ nm (Luby-Phelps et al., 1986) to $h=100$ nm (Hartwig and Shevlin, 1986), the porosity of the F-actin network within a pseudopod is $\phi_f=0.954$ (Zhu and Skalak, 1988). The Darcy permeability is then $k_D=2.6 \times 10^{-4} \mu\text{m}^2$, on the same order as estimated by (Leshansky, 2006) for actin tails in *Listeria.*, who also estimates the tail porosity at $\phi_f=0.982-0.995$. Note that the estimate for k_D is also roughly equivalent to that of (Charras et al., 2005), although they use a different approach and a much lower porosity of $\phi_f = 0.2$. The hydraulic permeability within the F-actin network in a pseudopod is found from Eqs. (6.36) and (6.37) to be $k_H=2 \times 10^{-13} \text{m}^4/(\text{N}\cdot\text{s})$.

$$k_{H,pseudopod} = 2 \times 10^{-13} \frac{\text{m}^4}{\text{N}\cdot\text{s}}, \quad (6.38)$$

The porosity of a more dense F-actin network within a sperm cell during the acrosomal process is $\phi_f=0.82$ (Zhu and Skalak, 1988), resulting in a smaller permeabilities of $k_D=0.1 \times 10^{-4} \mu\text{m}^2$ and $k_H=0.1 \times 10^{-13} \text{m}^4/(\text{N}\cdot\text{s})$.

Existing experimental equipment for measuring poroelastic behavior (e.g. in confined/unconfined compression conditions) of biological tissues are ill-suited for measuring permeability of actin networks. Even highly concentrated actin networks, with elastic moduli on the order of 1-10 Pa, are not stiff enough to be used in unconfined compression setups. The abundance of small diameter ($\sim 7\text{nm}$) filaments with lengths of

1-20 μm can additionally present clogging problems for the porous platens utilized in confined compression setups. A MEMS-based assay might be able to overcome these challenges to provide actin permeability measurements that would be eagerly welcomed by scientists and engineers evaluating actin networks within in vivo, in vitro, and in silico environments.

6.4 Confined and unconfined compression simulations

Here we apply the poroelastic model described in Section 6.2 with the new estimates for actin permeability (Section 6.3) in confined and unconfined compression simulations. The confined compression simulation applies a sudden vertical pressure load ($p_{\text{input}}=10$ Pa), then opens the porous platen. The material consolidates with the porous platen open, as shown through the decreasing normalized vertical displacement in Figure 6–9. The open porous platen gives a zero pressure boundary condition and allows fluid to flow out of the bottom surface. The normalized fluid pore pressure evolution with time during the second step is shown in Figure 6–10. Although the pore pressure will vary by position, the normalized pore pressure is shown for the material point just below the solid platen that is compressing the sample. The two F-actin networks shown in Figure 6–9 and Figure 6–10 represent the two types of cortical actin regions (in an acrosome or pseudopod) whose permeability was calculated in the previous section. Here, they share common F-actin network properties (e.g. $c_{AF}=170\mu\text{M}$, $L_c=1\mu\text{m}$, $l_p=3\mu\text{m}$, $\alpha=1\%$, $L_c=1\mu\text{m}$), but different permeability values in order to see the impact of permeability in confined compression. The color contours (inset in Figure 6–9 and

Figure 6–10) again represent the gradient in vertical stress (σ_{22}) and pore pressure, respectively, after the porous platen has been opened, and they are shown to illustrate the non-uniform response of poroelastic state variables. Figure 6–10 shows the transient

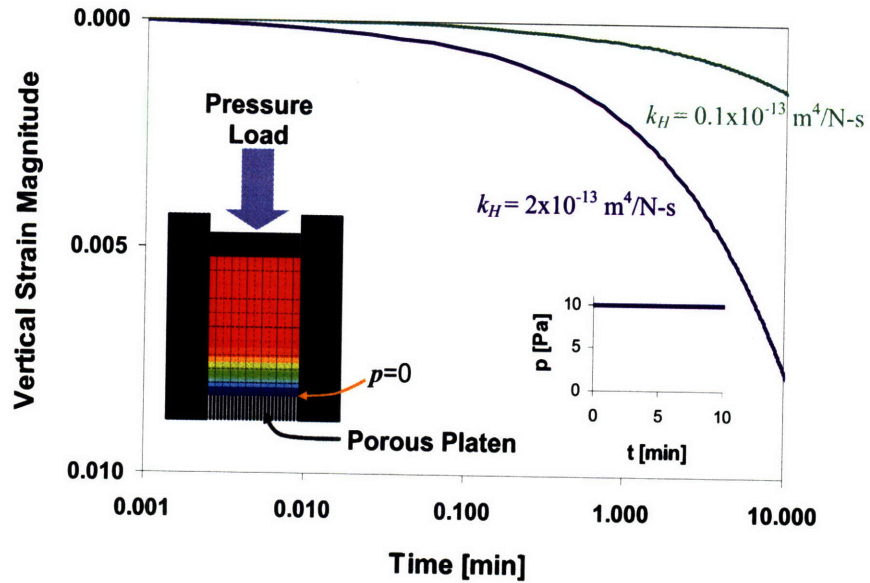


Figure 6–9. Vertical strain magnitude of F-actin networks ($k_H=0.1 \times 10^{-13}$, $2 \times 10^{-13} \text{ m}^4/\text{N-s}$) in confined compression with a porous platen boundary ($p=0$) and subject to a sudden vertical pressure load of $p=10 \text{ Pa}$. Inset: Time history of applied pressure load, and qualitative contour plot of vertical stress (σ_{22}) shown in inset at $t=10 \text{ min}$.

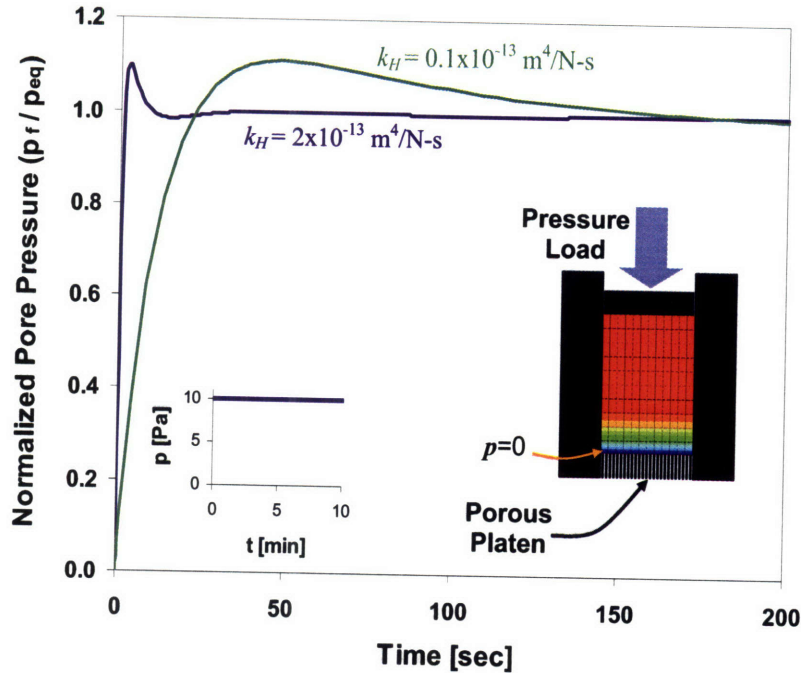


Figure 6–10. Time evolution of fluid pore pressure of top nodes below solid platen, normalized by equilibrium pore pressure in confined compression with a porous platen boundary ($p=0$) and subject to a sudden vertical pressure load of $p=10\text{Pa}$. F-actin network ($k_H=0.1 \times 10^{-13}$, $2 \times 10^{-13} \text{ m}^4/\text{N}\cdot\text{s}$). Inset: Time history of applied pressure load, and qualitative contour plot of pore pressure shown in inset at $t=10\text{min}$.

nature of the poroelastic network, as fluid pore pressure (of the point just below the solid platen) peaks several seconds after the input pressure load, then begins to relax to an equilibrium value. The pore pressure overshoot ($p_f > p_{input}$) in Figure 6–10 experiences a delayed response for the smaller value of permeability, along with a more gradual relaxation to the equilibrium value. This behavior emphasizes the role of permeability on the transient response of the material, even though it was already defined in relation to the fluid velocity.

A similar simulation, unconfined compression, can be performed to evaluate the transient, poroelastic response of F-actin networks in more than one dimension. The unconfined compression simulation linearly ramps to a constant vertical displacement on the top surface ($\epsilon_{2,\text{total}}=-15\%$) with the ramp occurring from $t=0-0.1$ seconds (see Figure

5–45), with zero pressure boundary conditions on the side surfaces. The top and bottom surfaces of the sample are restrained by solid (nonporous) platens. After the vertical, compressive

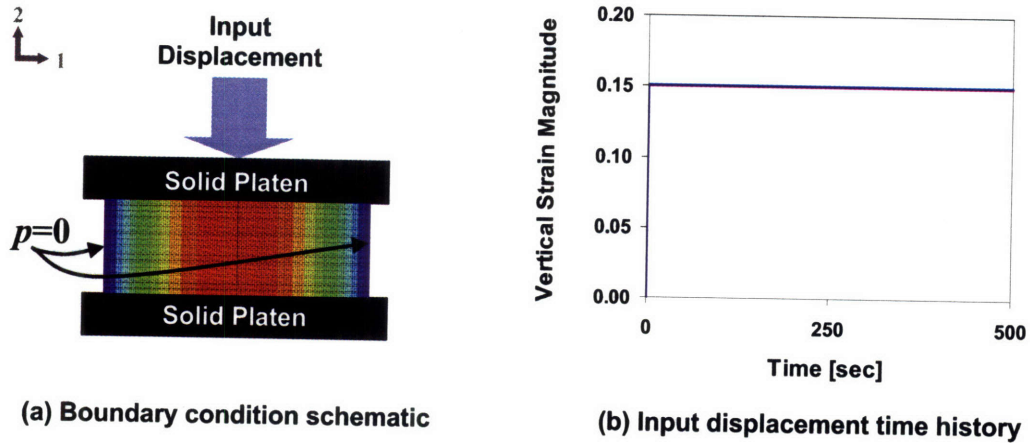


Figure 6–11. (a) Boundary conditions and (b) Input displacement time history for unconfined compression simulation

displacement is applied, the network initially expands in the lateral direction (1-direction in Figure 5–45). Then as the fluid begins to flow radially out of the specimen's periphery, the reaction force on the solid platen begins to relax and the side surfaces begin to contract inward. The lateral strain contraction and the force relaxation time histories are shown in Figure 6–12 for an actin network ($c_{AF}=170\mu\text{M}$, $L_c=1\mu\text{m}$, $l_p=3\mu\text{m}$, $\alpha=1\%$) at two different hydraulic permeabilities, $k_H=0.1\times 10^{-13}\text{ m}^4/\text{N}\cdot\text{s}$, $2\times 10^{-13}\text{ m}^4/\text{N}\cdot\text{s}$, in order to see the impact of permeability in unconfined compression.

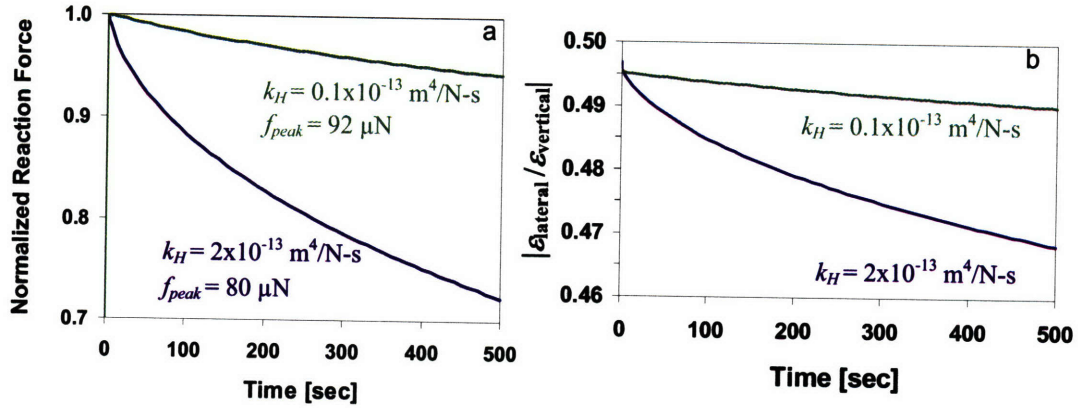


Figure 6–12. (a) Reaction force normalized by the peak reaction force, and (b) Lateral strain/vertical strain of F-actin networks ($k_H=0.1 \times 10^{-13}$, $2 \times 10^{-13} \text{ m}^4/\text{N-s}$) in unconfined compression with porous side boundaries ($p=0$) and $\epsilon_2=-15\%$ compressive vertical strain with a peak lateral strain of $\epsilon_1=-8.4\%$ for both cases

The reaction forces for the cases of $k_H=0.1 \times 10^{-13} \text{ m}^4/\text{N-s}$, $2 \times 10^{-13} \text{ m}^4/\text{N-s}$ in Figure 6–12a are normalized by their peak reaction forces at $t=0.1$ sec, $f_R=92.3$, $80.0 \text{ } \mu\text{N}$. The corresponding reaction forces at $t=500$ sec are $f_R=87.1$, $57.8 \text{ } \mu\text{N}$. The ratios of lateral strain to vertical strain for the cases of small and large permeability are shown in Figure 6–12b as a poroelastic analog to a “Poisson ratio”, with a common peak lateral strain at $t=0.1$ sec, $\epsilon_{l,peak}=-8.4\%$. Figure 6–12b illustrates that while the sides of the specimen do expand and contract, the lateral strains are roughly one-half of the imposed vertical strain. The corresponding lateral strains for the small and large permeability cases at $t=500$ sec are $\epsilon_l=-8.3\%$, -7.9% , respectively. The denser actin network, with a lower porosity and permeability ($k_H=0.1 \times 10^{-13} \text{ m}^4/\text{N-s}$), experiences much less relaxation (both in reaction force and contraction of the lateral sides) due to the reduced fluid flow out of the network.

The relaxation of actin networks in unconfined compression also varies as a function of the applied compressive strain. The actin network representative of the

pseudopod ($c_{AF}=170\mu\text{M}$, $L_c=1\mu\text{m}$, $l_p=3\mu\text{m}$, $\alpha=1\%$, $k_H=2\times 10^{-13}\text{ m}^4/\text{N}\cdot\text{s}$) is evaluated in Figure 6–13 to see the impact of varying the compressive strains on the reaction forces.

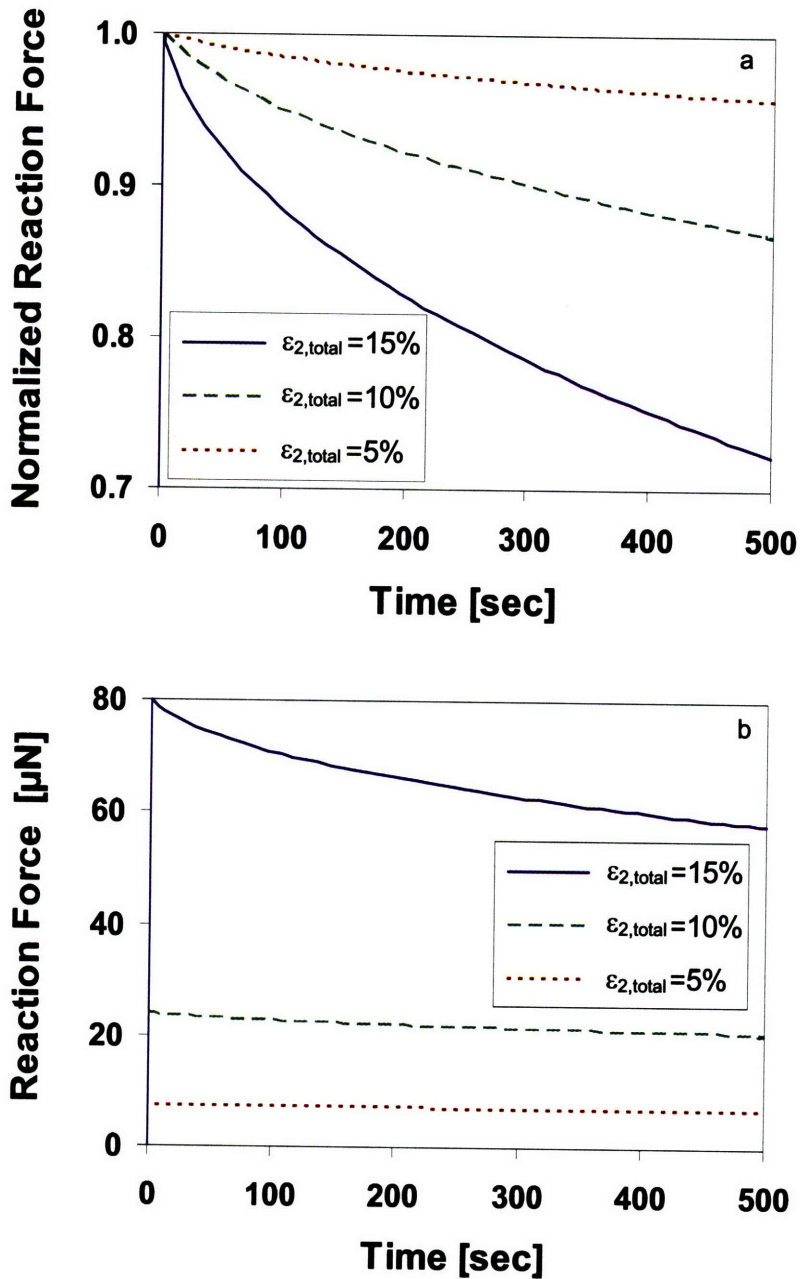


Figure 6–13. (a) Reaction force normalized by peak reaction forces and (b) Reaction force magnitudes of an F-actin network ($k_H = 2 \times 10^{-13}\text{ m}^4/\text{N}\cdot\text{s}$) in unconfined compression with porous side boundaries ($p=0$) and 5%, 10%, and 15% total compressive vertical strain

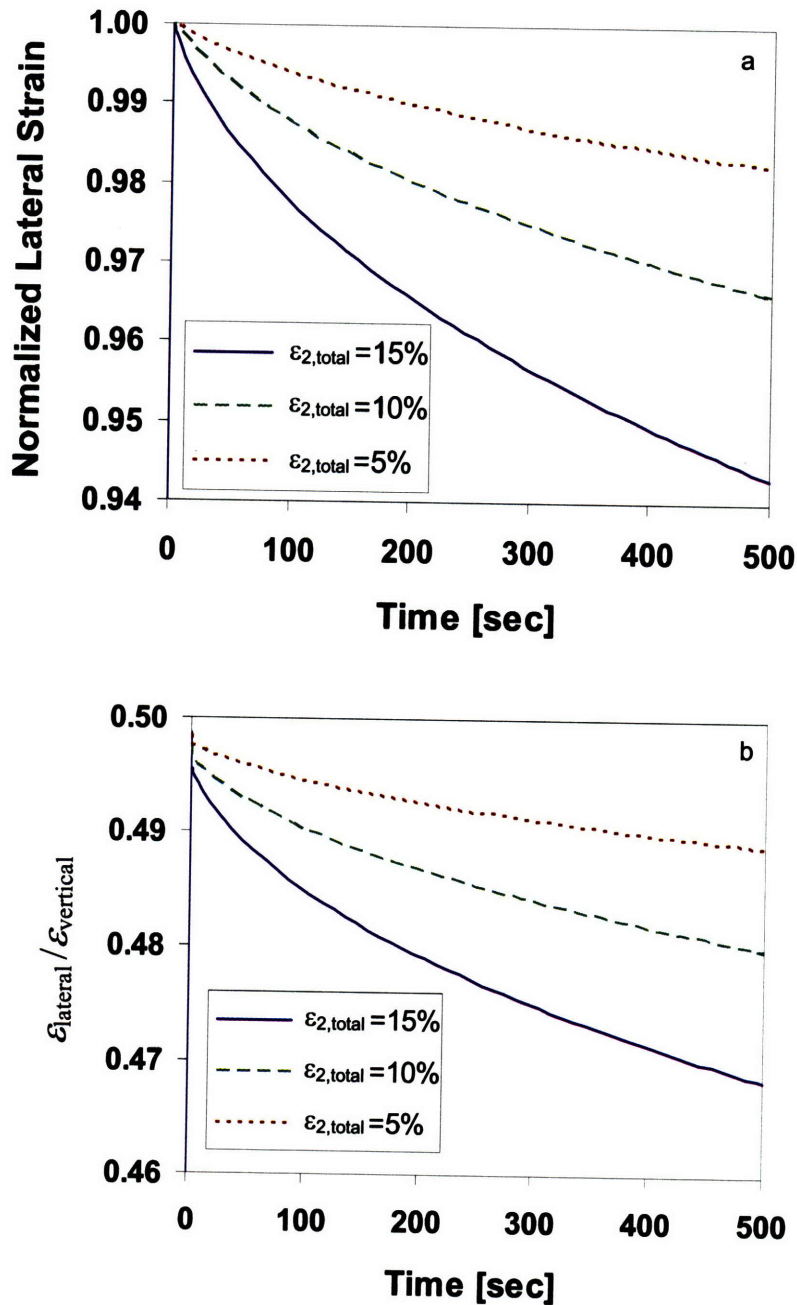


Figure 6-14. (a) Lateral strain normalized by peak lateral strain and (b) Lateral strain/vertical strain of an F-actin network ($k_H = 2 \times 10^{-13} \text{ m}^4/\text{N-s}$) in unconfined compression with porous side boundaries ($p=0$) and 5%, 10%, and 15% total compressive vertical strain

The vertical displacements are applied on the top surface ($\epsilon_{2,total} = -5\%$, -10% , -15%) following a linear ramp from $t=0-0.1$ seconds, then held constant for 500 seconds. The

reaction forces in Figure 6–13a for the cases of $\varepsilon_{2,total} = -5\%$, -10% , -15% are normalized by their reaction forces at $t=0.1$ sec, $f_R = 7.1, 23.8, 80.0$ μN respectively (seen in Figure 6–13b). The corresponding reaction forces at $t=500$ sec are $f_R = 6.8, 20.7, 57.8$ μN . The lateral strains in Figure 6–14a for the cases of $\varepsilon_{2,total} = -5\%$, -10% , -15% are normalized by their lateral strains at $t=0.1$ sec, $\varepsilon_{1,peak} = 2.6\%$, 5.4% , 8.4% respectively. The ratios of lateral strain to vertical strain for the three vertical strain cases are shown again in Figure 6–14b as a poroelastic analog to a Poisson ratio. Figure 6–14b illustrates that while the sides of the specimen do expand and contract, the lateral strains are still just less than one-half of the imposed vertical strain. The corresponding lateral strains at $t=500$ sec are $\varepsilon_1 = 2.5\%$, 5.2% , 7.9% . The results show that increasing compressive strain on actin networks results in more relaxation (both in reaction force and contraction of the lateral sides) due to the increased fluid loss from the network.

The transient response of actin networks under unconfined compression also varies as a function of lateral location. The fluid pore pressures will be highest at the center of the network (Figure 5–45), decreasing to zero at the side boundary of the network, with the pressure gradient relatively flat toward the center. This pore pressure gradient will also evolve over time, as shown in Figure 6–15.

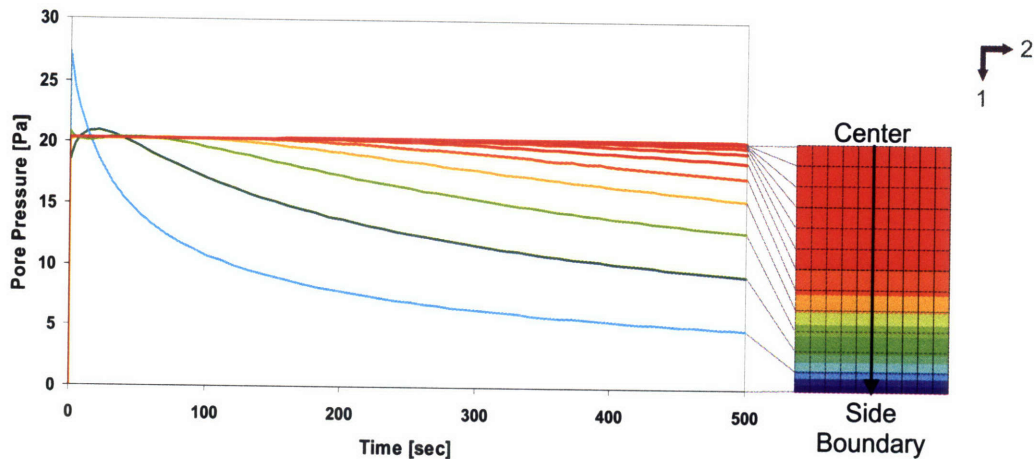


Figure 6–15. Pore pressure time history for an F-actin network ($k_H=2 \times 10^{-13} \text{ m}^4/\text{N}\cdot\text{s}$) in unconfined compression with porous side boundaries ($p=0$) and 15% compressive strain with a ramp time of 0.1 second. Pore pressure data are from nodes equidistantly spaced from the specimen’s center to just inside the outer boundary as shown in the pore pressure contour plot on the right.

The pore pressure response in Figure 6–15 represents the time history of several nodes (equidistantly spaced, see pore pressure contour plot in Figure 6–15) following the radius from the specimen’s center to just inside the outer boundary surface. The pore pressure on the outer surface is set to $p=0$. Note that the nodes just inside the outer boundary experience an initial spike in pore pressure that decreases for nodes located toward the center. The pore pressure of all nodes decreases with time, with the largest decrease occurring for nodes located near the side boundary as they experience more fluid loss. Increasing the ramp time for the applied compressive displacement will eliminate the pore pressure spike in the nodes near the boundary (Figure 6–16). While this is a method to avoid the initial pore pressure spike, it can obscure the initial poroelastic response of the network since considerable fluid flow (and therefore stress relaxation) occurs during the increased ramp time.

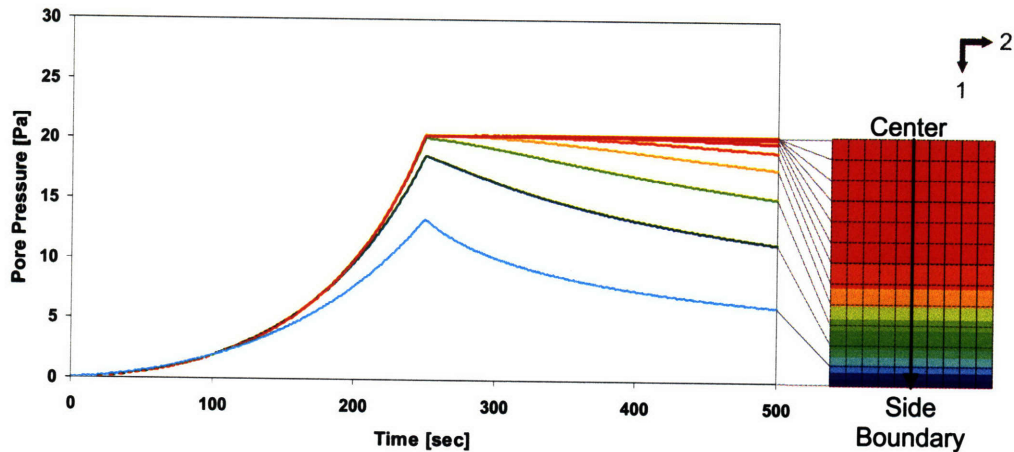


Figure 6–16. Pore pressure time history for an F-actin network ($k_H=2 \times 10^{-13} \text{ m}^4/\text{N}\cdot\text{s}$) in unconfined compression with porous side boundaries ($p=0$) and 15% compressive strain with a ramp time of 250 seconds. Pore pressure data are from nodes equidistantly spaced from the specimen’s center to just inside the outer boundary as shown in the pore pressure contour plot on the right.

The filament swelling stretch evolution in time is shown in Figure 6–17. As was the case for the pore pressure time history plots, the swelling stretch response represents the time history of several nodes (equidistantly spaced, see λ_{sw} contour plot in Figure 6–17) following the radius from the specimen’s center to just inside the outer boundary surface. The swelling stretch on the side boundary surface experiences an initial increase as fluid flows into nodes on the side boundary after the specimen is initially compressed. This initial increase is reduced almost immediately as the zero pressure boundary condition is applied and then continues to relax as fluid continues to flow out of the side boundary at a steadily decreasing rate. The node just inside the outer boundary experiences a similar initial spike which decreases for nodes located toward the center that experience less initial influx of fluid. The swelling stretch of all nodes decreases with time, with the largest decrease occurring for nodes located near the side boundary as they experience more net fluid loss from their original state.

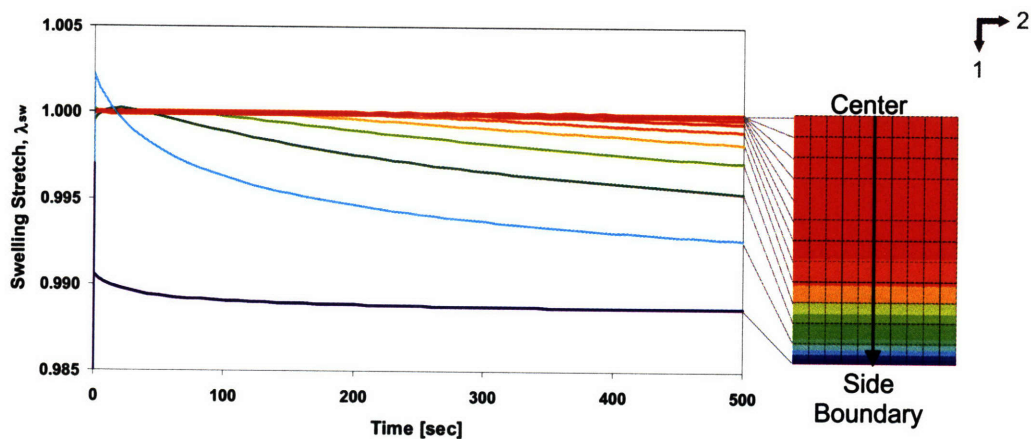


Figure 6–17. Swelling stretch time history for an F-actin network ($k_H=2 \times 10^{-13} \text{ m}^4/\text{N}\cdot\text{s}$) in unconfined compression with porous side boundaries ($p=0$) and 15% compressive strain with a ramp time of 0.1 second. Swelling stretch data are from nodes equidistantly spaced from the specimen’s center to just inside the outer boundary as shown in the swelling stretch contour plot on the right.

6.5 Compressed cell simulation

6.5.1 Poroelastic cell compression

The 3D poroelastic cytoskeletal network model is now integrated with membrane and nucleus models in a finite element-based micromechanical model of the cell, as was done with the viscoelastic network model in the previous chapter. The composite cellular poroelastic model is evaluated by observing the relaxation experienced by a cell under compression in the *absence* of any viscoelastic properties. The geometry and properties of the $6\mu\text{m}$ diameter cell, and its nucleus and membrane, remain the same as described in Section 5.5, and are summarized in Table 3–1. The nucleus is modeled as nonporous, neo-Hookean material with the membrane modeled as a nonporous, orthotropic linear elastic material.

NUCLEUS	CYTOPLASM	MEMBRANE
Radius = 0.5 μ m	Radius = 0.5-3.0 μ m	Radius = 3.00-3.01 μ m
$E = 1000$ Pa	$c_{AF} = 20\mu$ M	$E_m = 200$ Pa
$K_B = 5000$ Pa	$L_c = 0.9\mu$ m	$G_m = 20$ Pa
$G = 340$ Pa	$l_p = 3.0\mu$ m	$\nu_m = 0.6$
	$\alpha = 1.1\%$	
	$k_H = 2 \times 10^{-13}$ m ⁴ /N-s	

Table 6-1. Summary of geometry and key mechanical properties for cellular model

The poroelastic actin network developed in the previous section will be employed as the load bearing cytoskeletal network within the cytoplasm. The actin concentration will remain constant across the cytoplasm: $c_{AF} = 20\mu$ M.

6.5.2 Axisymmetric poroelastic cell model and results

During the axisymmetric simulations the cell is compressed by applying a axial normal strain ($\epsilon_{2,total} = -5\%$, -10% , -15%) on the top plate according to a linear ramp for $t = 0.01$ second, followed by a hold time of 1.0 second (see Figure 6-18b). Figure 6-18a shows the undeformed axisymmetric mesh next to the deformed mesh (with axial normal displacement contours at $t = 0.01$ seconds, $U_2 = -0.9\mu$ m or $\epsilon_{2,total} = -15\%$ for a 6μ m diameter cell). The time-scale of relevance for the poroelastic response is a function of the permeability and porosity of the biphasic network. The following section will show that the previously determined permeability and porosity of the actin networks will drive the compressed networks to fully relax within 1.0 second under different axial normal strains.

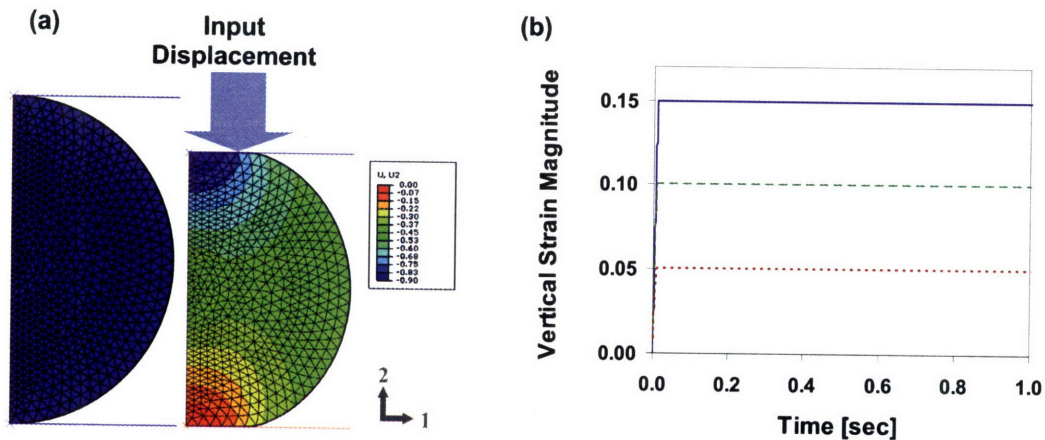


Figure 6–18. (a) Axisymmetric mesh schematic with axial normal displacement contours in deformed mesh at $t=0.01$ sec for $\epsilon_{2,\text{total}}=15\%$, and (b) Input (total) strain time history for compression of a poroelastic cell with loading ramp time of $t=0.01$ sec and a hold time of $t=1.0$ sec.

The axial normal strain (ϵ_{22}) of the elements within the compressed cell is shown in Figure 5–46 for $t=0.01$ and $t=1.0$ seconds. There is little change in the axial normal strain between the initially compressed state (Figure 5–46a) and the relaxed state (Figure 5–46b). But both plots help to identify the regions of largest compressive axial normal strain (blue) directly under the load along the center axis of the cell, as well as the regions of little or no compressive axial normal strain (tan-orange), including the stiffer, nonporous nucleus. Note that there is a small region near the points where the cell membrane diverges from loading plates in Figure 5–46 where there is a positive axial normal strain. This positive axial normal strain is due to the shearing region between the compressed center and the less deformed outer region of the cell (see shear contour plots in Figure 6–20).

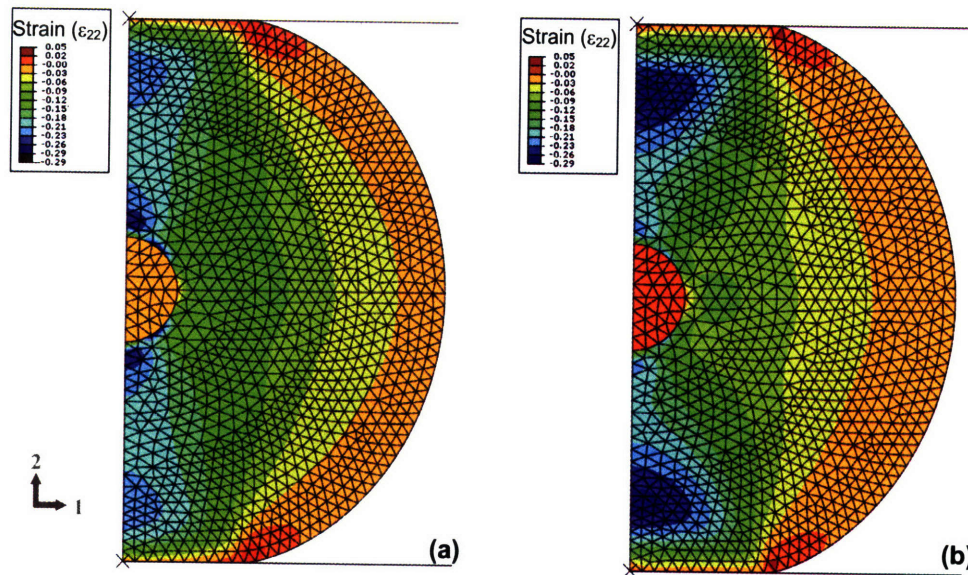


Figure 6-19. Element strain in the 2-direction (ϵ_{22}) within actin networks in a compressed cell ($\epsilon_{2,\text{total}} = -15\%$) at two different times, (a) $t=0.01$ sec, immediately after compression and (b) $t=1.0$ sec, in the compressed but relaxed state.

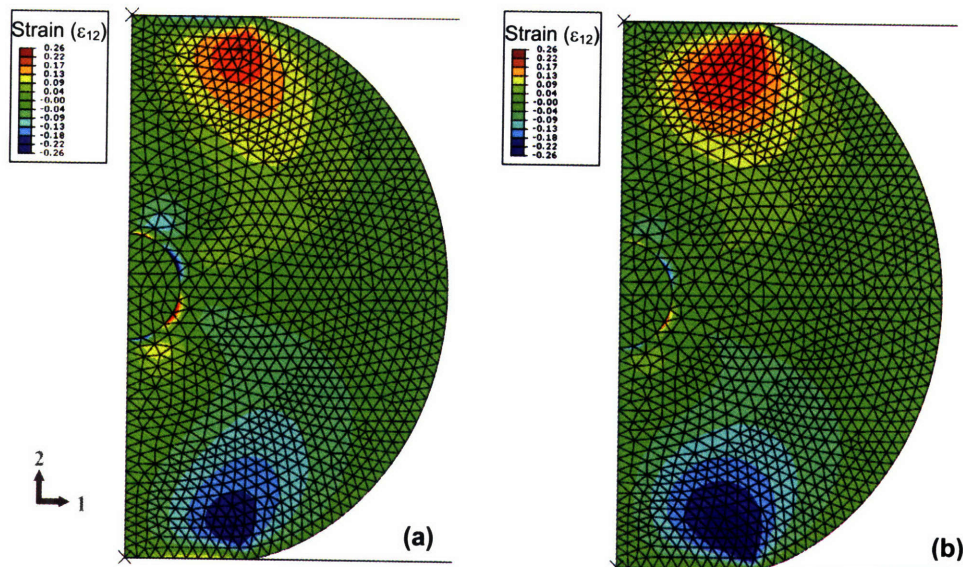


Figure 6-20. Element shear strain (ϵ_{12}) within actin networks in a compressed cell ($\epsilon_{2,\text{total}} = -15\%$) at two different times, (a) $t=0.01$ sec, immediately after compression and (b) $t=1.0$ sec, in the compressed but relaxed state.

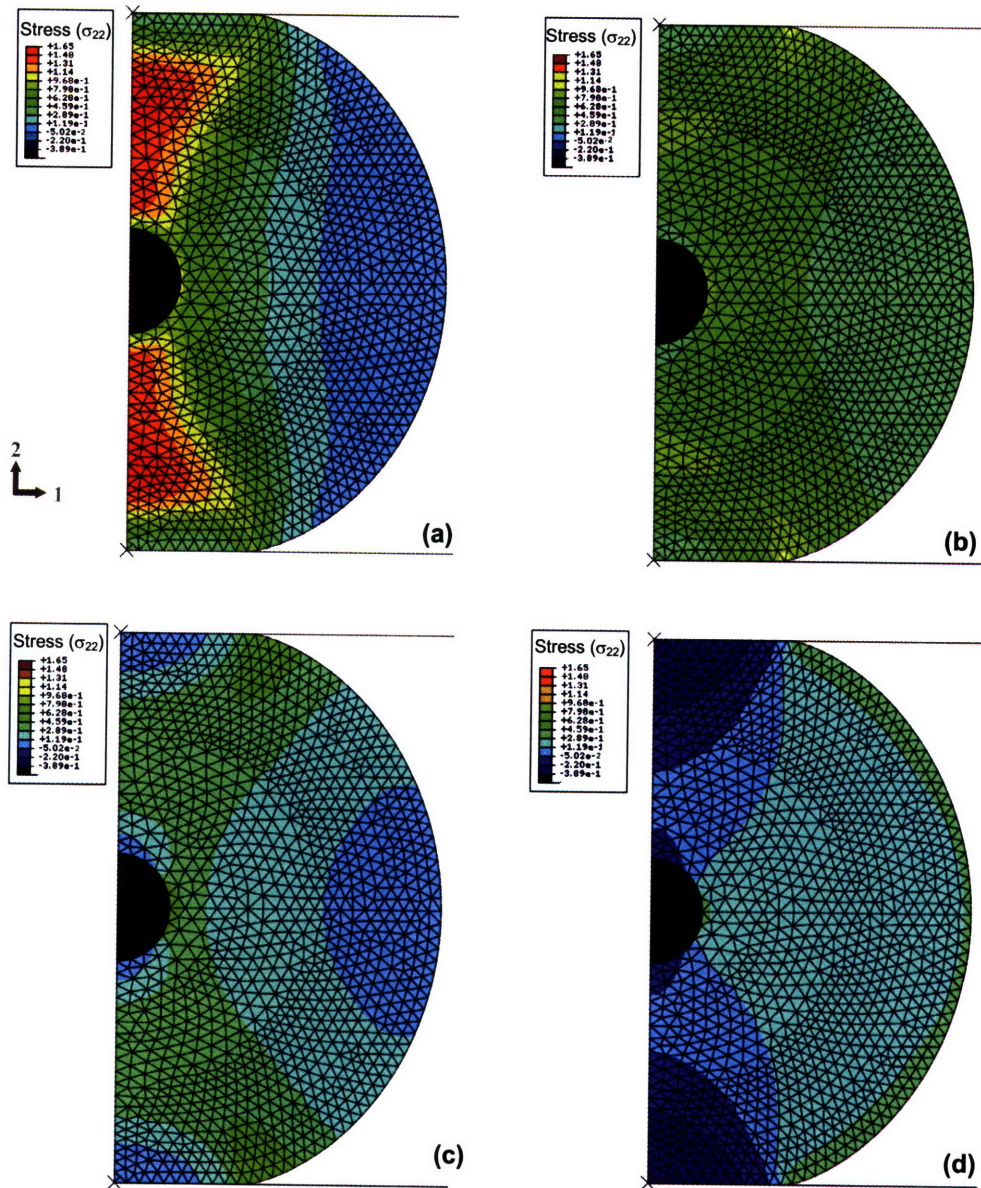


Figure 6–21. Element axial normal stress (σ_{22}) in a compressed cell ($\epsilon_{2,\text{total}} = -15\%$) at four different times, (a) $t=0.01\text{sec}$, immediately after compression, (b) $t=0.02\text{sec}$, (c) $t=0.05\text{sec}$, (d) $t=1.0\text{ sec}$, in the compressed but relaxed state. Cell consists of a neo-Hookean nucleus, orthotropic membrane, and a poroelastic cytoplasm consisting of an actin network ($c_{AF}=20\mu\text{M}$, $L_c=0.9\mu\text{m}$, $l_p=3\mu\text{m}$, $\alpha=1.1\%$, $k_H = 2 \times 10^{-13} \text{ m}^4/\text{N-s}$), Units in Pa.

The axial normal stress (σ_{22}) of the elements within the compressed cell is shown in Figure 6–21 for $t=0.01$ through $t=1.0$ seconds. These contour plots show the progression from the initially compressed state (Figure 6–21a), in which high pore pressures along the

center axial normal axis leads to higher stresses, to the relaxed state (Figure 5–46b) in which the pore pressure has become homogenous across the cell, and with lower, compressive stresses now shown along the center axial normal axis.

The relative amount of relaxation for each case of compressive strain loading is shown in Figure 5–48 by normalizing the reaction forces for each case, $\epsilon_{2,\text{total}}=-5\%$, -10% ,

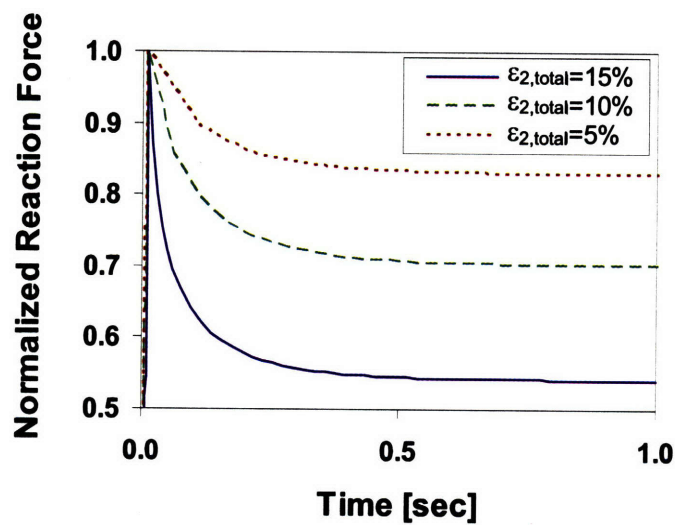


Figure 6–22. Relaxation of reaction force normalized by peak reaction force on a solid plate compressing a cell ($\epsilon_{2,\text{total}}=-5\%$, -10% , and -15%). Cell consists of a neo-Hookean nucleus, orthotropic membrane, and a poroelastic cytoplasm consisting of an actin network ($c_{AF}=20\mu\text{M}$, $L_c=0.9\mu\text{m}$, $l_p=3\mu\text{m}$, $\alpha=1.1\%$, $k_H=2\times 10^{-13}\text{ m}^4/\text{N}\cdot\text{s}$).

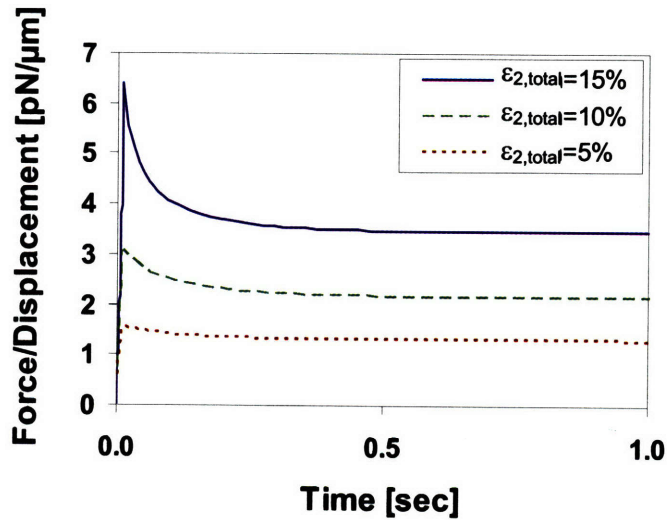


Figure 6–23. Reaction force/displacement relaxation for a solid plate compressing a cell ($\epsilon_{2,\text{total}}=-5\%$, -10% , and -15%). Cell consists of a neo-Hookean nucleus, orthotropic membrane, and a poroelastic cytoplasm consisting of an actin network ($c_{AF}=20\mu\text{M}$, $L_c=0.9\mu\text{m}$, $l_p=3\mu\text{m}$, $\alpha=1.1\%$, $k_H=2\times 10^{-13}\text{ m}^4/\text{N-s}$).

-15% , by their peak reaction force at $t=0.01$ sec, $f_R=-0.5$, -1.8 , -5.7 pN respectively. Figure 6–23 contains the relaxation of the reaction force normalized by the axial normal displacement, as a function of time, illustrating greater relaxation in the overall stiffness of the cell with greater amounts of axial normal compression. Figure 5–49 shows the reaction force time histories and the change in peak reaction forces with increasing strain loads, with the cell fully relaxed by $t=1.0$ second. The results show that increasing compressive strain on actin networks in a cellular geometry results in more total reaction force relaxation and more relaxation relative to the peak reaction force for each case. Note that the reaction force magnitudes in Figure 5–49 scale nonlinearly with strain due to the nonlinear network elasticity.

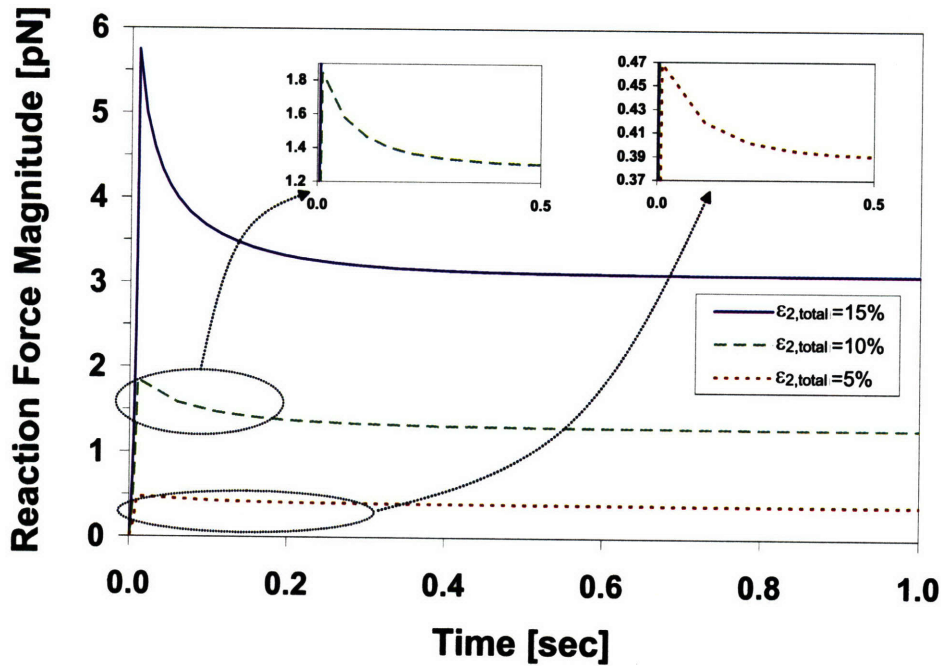


Figure 6–24. Relaxation of reaction force on a solid plate compressing a cell ($\epsilon_{2,\text{total}}=-5\%$, -10% , and -15%). Cell consists of a neo-Hookean nucleus, orthotropic membrane, and a poroelastic cytoplasm consisting of an actin network ($c_{AF}=20\mu\text{M}$, $L_c=0.9\mu\text{m}$, $l_p=3\mu\text{m}$, $\alpha=1.1\%$, $k_H=2\times 10^{-13}\text{ m}^4/\text{N}\cdot\text{s}$).

The relaxation of the reaction force for the poroelastic cell is due to the reduction in pore pressure gradients throughout the cell. Recall that this simulation does not permit fluid flow across the membrane or into the nucleus. The compression of the cell therefore creates pore pressure gradients throughout the cytoplasm (Figure 6–25a). Figure 6–25b illustrates the uniform pore pressure field when the cell is in the relaxed state. The poroelastic network model also gives insight into the average mechanical response of the microstructural features of the cytoskeleton. The swelling stretches are shown in Figure 6–26, illustrating the localized flow away from the regions of highest compressive stresses. The undeformed cell starts with a filament stretch of one ($\lambda_f=1$), but Figure 6–27a shows the average filament stretch increases within the actin networks

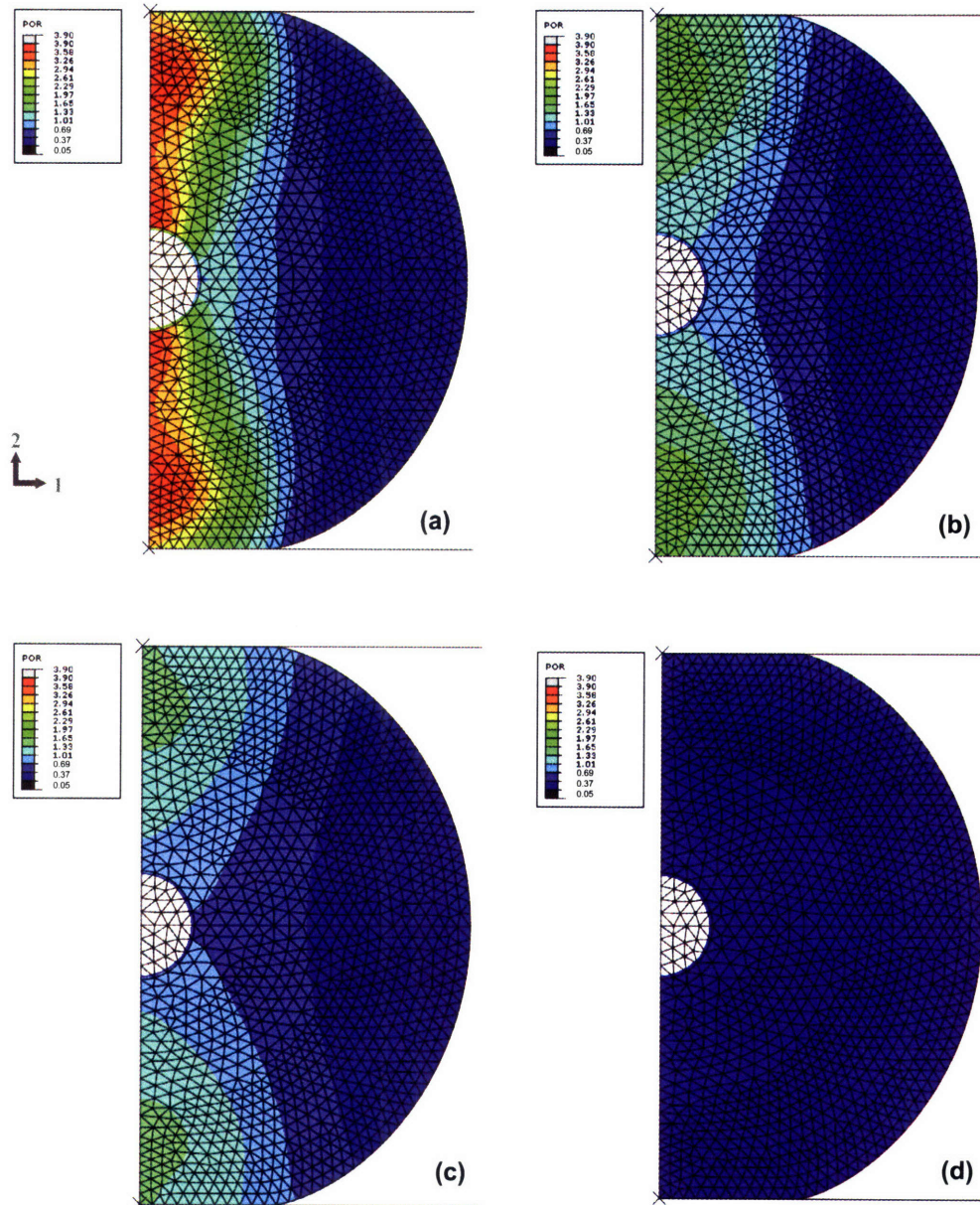


Figure 6-25. Pore pressure in a compressed cell ($\epsilon_{2,\text{total}} = -15\%$) at four different times, (a) $t=0.01\text{sec}$, immediately after compression, (b) $t=0.02\text{sec}$, (c) $t=0.05\text{sec}$, (d) $t=1.0\text{ sec}$, in the compressed but relaxed state. Cell consists of a neo-Hookean nucleus, orthotropic membrane, and a poroelastic cytoplasm consisting of an actin network ($c_{AF}=20\mu\text{M}$, $L_c=0.9\mu\text{m}$, $l_p=3\mu\text{m}$, $\alpha=1.1\%$, $k_H = 2 \times 10^{-13} \text{ m}^4/\text{N}\cdot\text{s}$), pore pressure units in Pa.

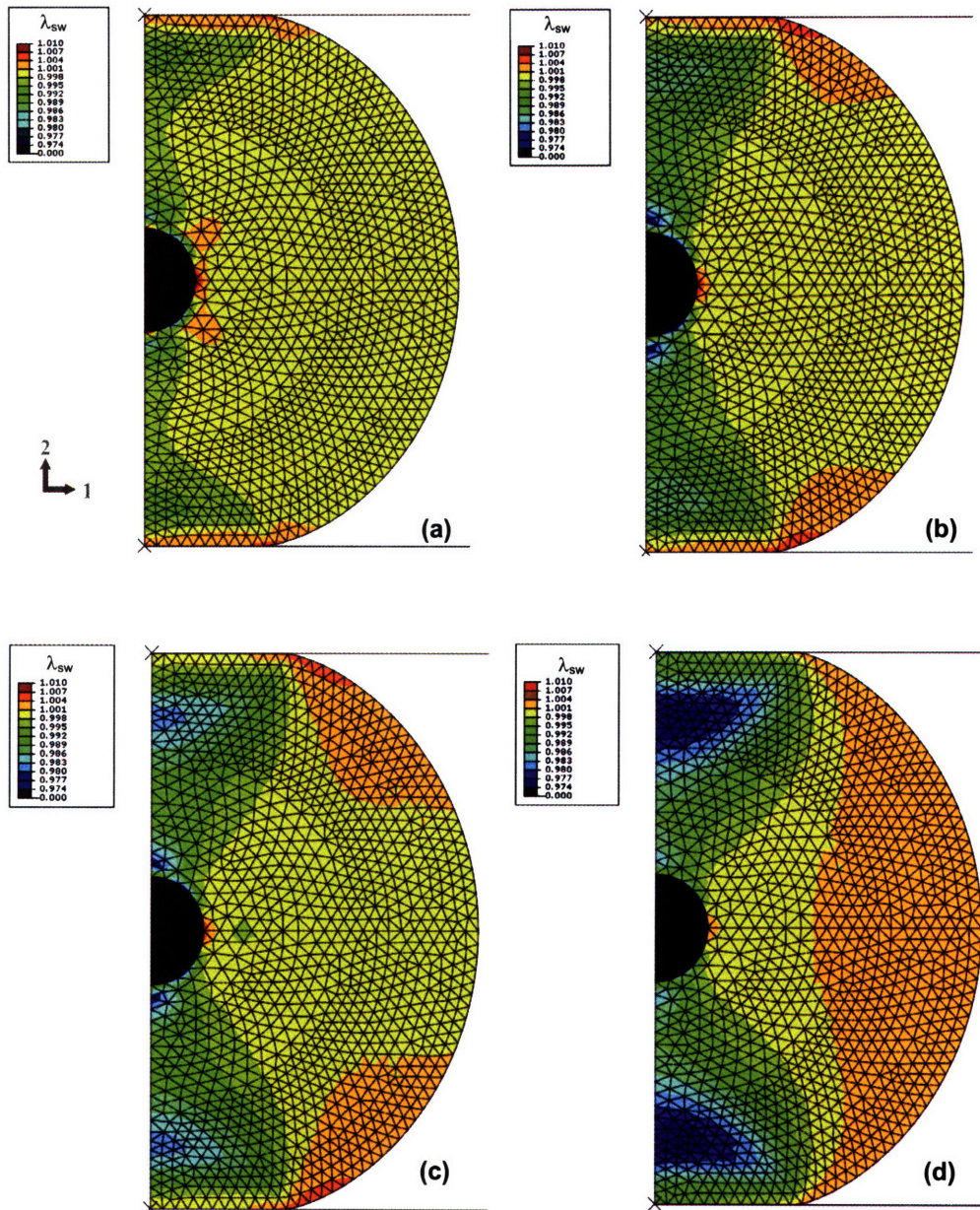


Figure 6-26. Swelling stretch within actin networks in a compressed cell ($\epsilon_{2,\text{total}} = -15\%$) at four different times, (a) $t=0.01$ sec, immediately after compression, (b) $t=0.02$ sec, (c) $t=0.05$ sec, (d) $t=1.0$ sec, in the compressed but relaxed state.

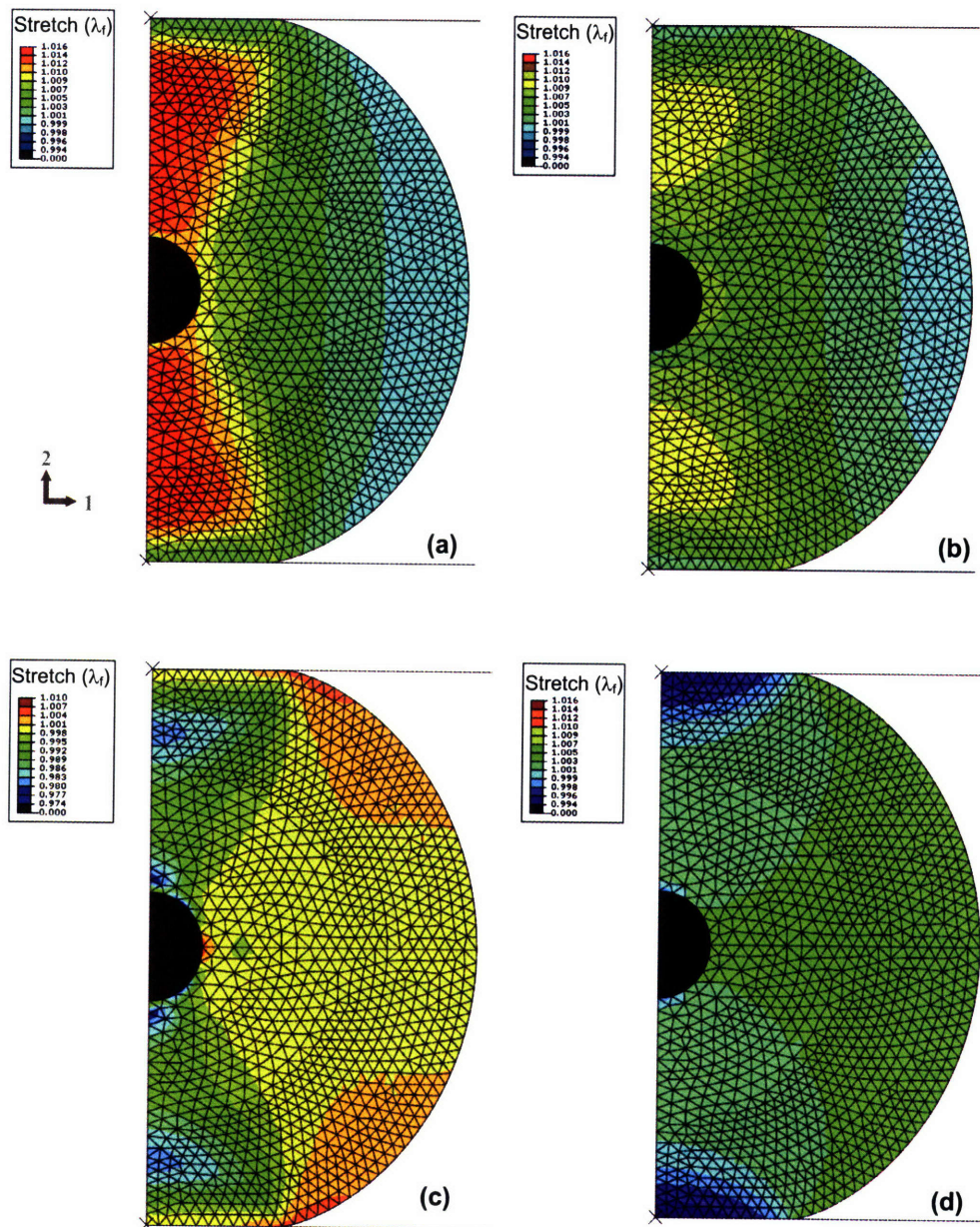


Figure 6–27. Filament stretch within actin networks in a compressed cell ($\epsilon_{2,\text{total}} = -15\%$) at four different times, (a) $t=0.01$ sec, immediately after compression, (b) $t=0.02$ sec, (c) $t=0.05$ sec, (d) $t=1.0$ sec, in the compressed but relaxed state.

just after the cell has been compressed ($t=0.01$ sec), especially near the center axis of the cell where the macroscopic deformation and pore pressures are the highest. The contours of highest filament stretch in Figure 6–27a correlate closely to the contours of highest

pore pressures in Figure 6–25a, demonstrating the microstructural effects of cytosolic fluid flow through actin networks. Just as Figure 6–25b shows a uniform pressure field throughout the cell, Figure 6–27b also shows a more uniform, relaxed stretch field ($\lambda_f \sim 1$), with some slightly compressed filaments in small regions near the plates with $\lambda_f < 1$ due to decreased fluid volume ratios (with respect to the initial state). Note that there is still some positive filament stretch in the uniform green region in Figure 6–27b due to the deformed state of the cell, however it is now reduced to less than $\lambda_f < 1.003$ (compared to peak values of $\lambda_f < 1.015$ in Figure 6–27a).

The average initial angle of the filaments within the network model is $\theta_{f,0} = 54.7^\circ$, as discussed in Chapter 3. This filament angle is taken with respect to the maximum principal stretch direction of the 8-chain network unit cell. Figure 6–28 shows that the average filament angle within undeformed areas (i.e. away from the center axis of the cell where the macroscopic deformation is the highest) remains approximately $\theta_f = \theta_{f,0} = 54.7^\circ$ (with θ_f relative to the maximum principal stretch direction for each element). While the filament stretch in the relaxed state (Figure 6–27b) correlate well with the relaxed pressure field in Figure 6–25b, the filament angle contours in Figure 6–28 correlate well to the axial normal strain (ε_{22}) contours in Figure 5–46 for both the peak and relaxed states, reinforcing the observation that macroscopic network deformations are primarily accommodated through rotation of the network filaments, with significantly less filament stretch. A connection between the filament angle and the absolute orientation is found through the corresponding angle between the maximum principal stretch direction and the horizontal (2-direction), given in Figure 6–29 and which only exhibit subtle changes from the peak state to the relaxed state.

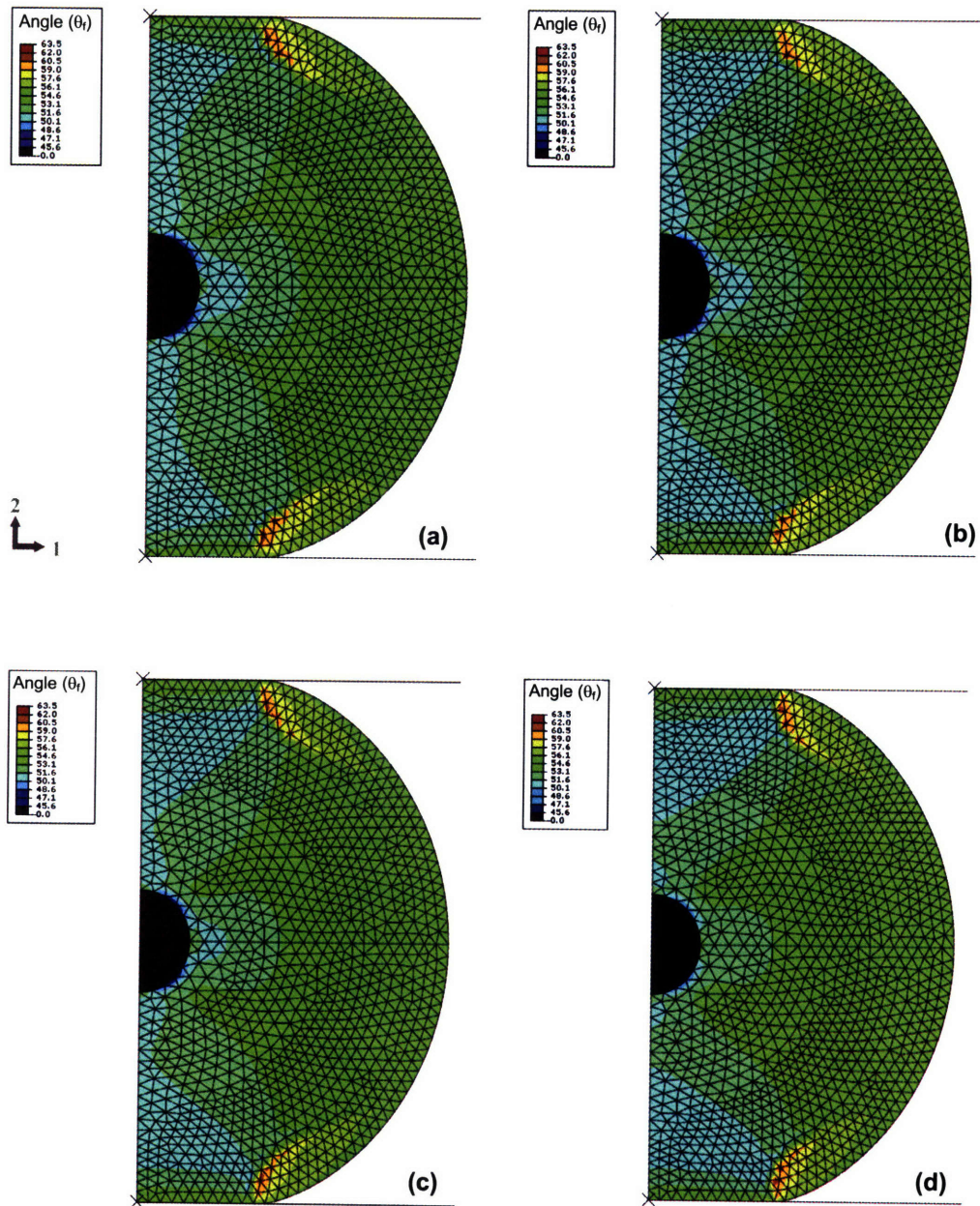


Figure 6–28. Angle between filaments and the maximum principal stretch direction of the 8-chain network unit cell for actin networks in a compressed cell ($\epsilon_{2,\text{total}} = -15\%$) at four different times, (a) $t=0.01$ sec, immediately after compression, (b) $t=0.02$ sec, (c) $t=0.05$ sec, (d) $t=1.0$ sec, in the compressed but relaxed state. Angles shown in degrees.

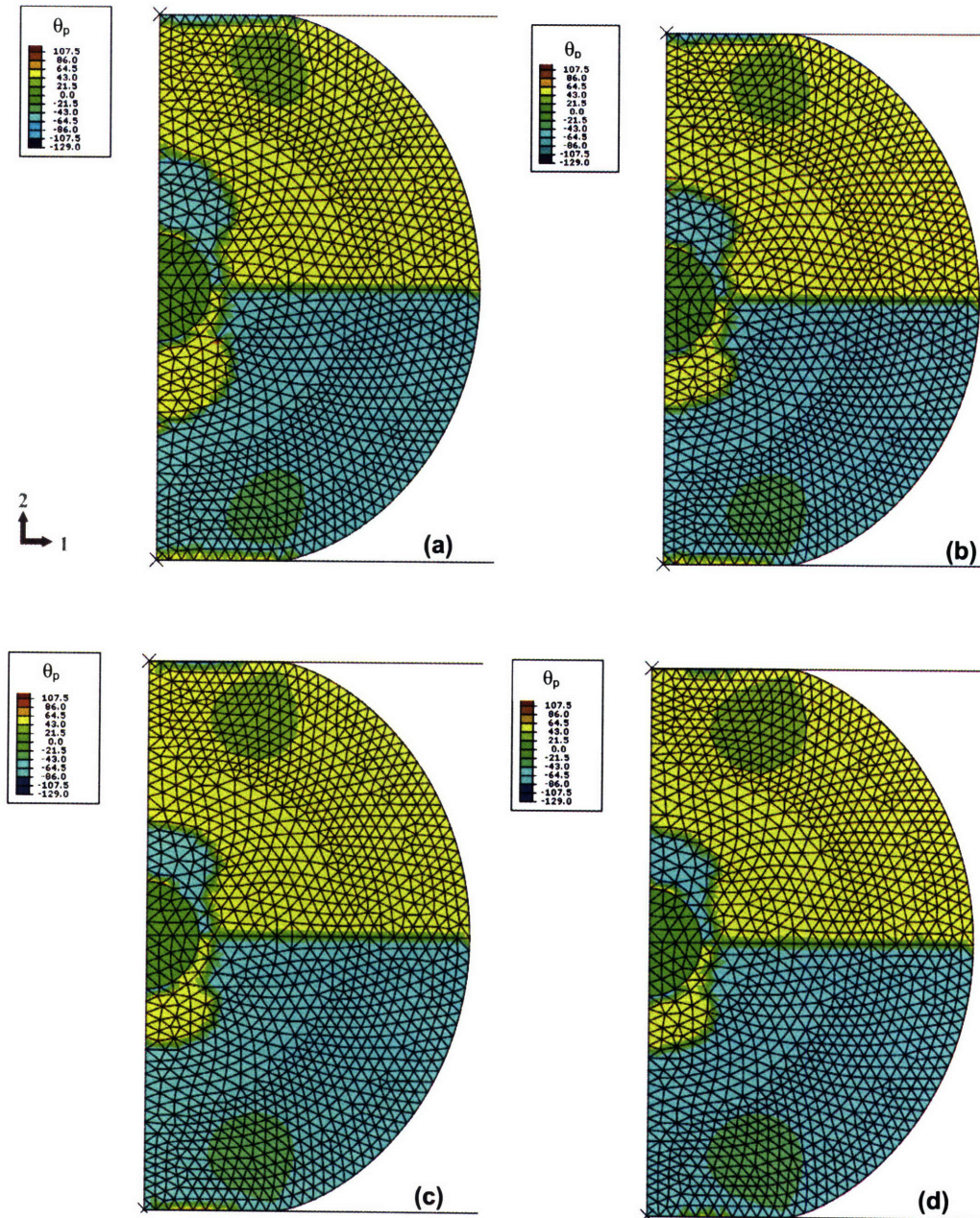


Figure 6–29. Angle between maximum principal stretch direction and horizontal, 2-direction for actin networks in a compressed cell ($\epsilon_{2,\text{total}} = -15\%$) at four different times, (a) $t=0.01$ sec, immediately after compression, (b) $t=0.02$ sec, (c) $t=0.05$ sec, (d) $t=1.0$ sec, in the compressed but relaxed state. Angles shown in degrees.

6.5.3 Poroviscoelastic cell compression

The 3D poroelastic and viscoelastic cytoskeletal network models are now combined with the membrane and nucleus models in a finite element-based micromechanical model of the cell. The composite cellular poroviscoelastic model is also evaluated by observing the relaxation experienced by a cell under compression. The geometry and properties of the 6 μ m diameter cell, and its nucleus and membrane, remain the same as before. In the first simulation, the reaction force time histories are compared between the viscoelastic, poroelastic, and poroviscoelastic cytoskeletal network models within a cell compressed by applying a axial normal strain ($\epsilon_{2,\text{total}}=-10\%$) on the top plate according to a linear ramp for $t=0.01$ second, followed by a hold time of 20 seconds. Figure 6–30 shows the reaction force time histories and the change in peak reaction forces, with the cell fully relaxed by $t=20$ seconds. The poroelastic response provides a minimal contribution to the poroviscoelastic response for $t > 1$ second since the pressure field within the cell has equilibrated.

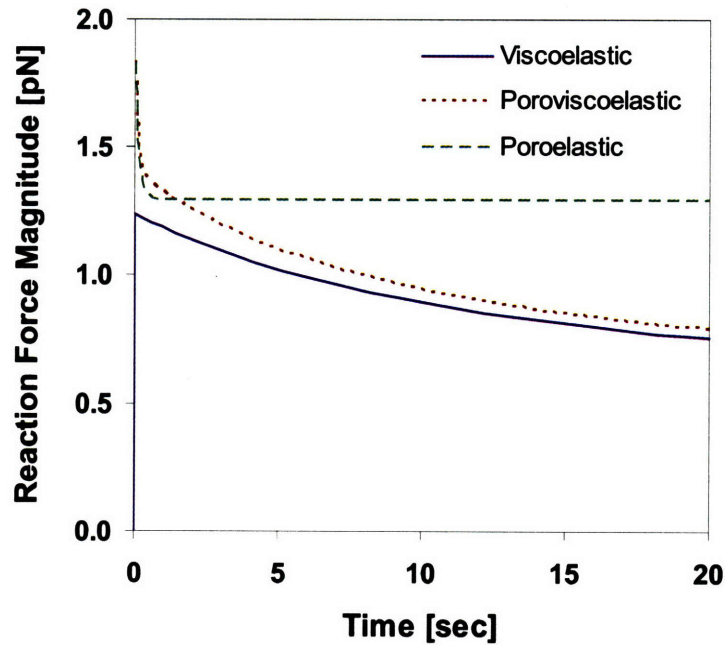


Figure 6–30. Relaxation of reaction force on a solid plate compressing a cell ($\epsilon_{2,\text{total}}=-10\%$). Cell consists of a neo-Hookean nucleus, orthotropic membrane and either a poroelastic, viscoelastic, or poroviscoelastic cytoplasm consisting of an actin network ($c_{AF}=20\mu\text{M}$, $L_c=0.9\mu\text{m}$, $l_p=3\mu\text{m}$, $\alpha=1.1\%$, $k_H=2\times 10^{-13}\text{ m}^4/\text{N}\cdot\text{s}$).

The relative amount of relaxation for each case is shown in Figure 6–31 by normalizing the reaction forces for each case (viscoelastic, poroelastic, poroviscoelastic) by their peak reaction force at $t=0.01$ sec, $f_R=-1.2$, -1.8 , -1.9 pN respectively. The viscoelastic response relaxes at a much larger time-scale, as expected, while the short-term response for $t < 1$ second (inset of Figure 6–31) shows a larger impact of poroelastic effects on the poroviscoelastic relaxation response.

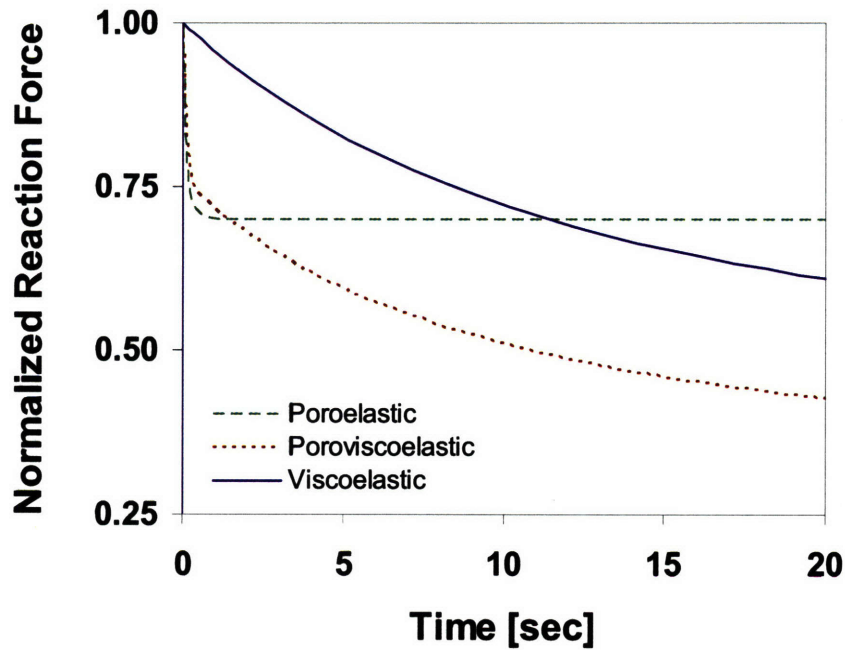


Figure 6–31. Relaxation of reaction force normalized by peak reaction force on a solid plate compressing a cell ($\varepsilon_{2,\text{total}}=-10\%$). Cell consists of a neo-Hookean nucleus, orthotropic membrane and either a poroelastic, viscoelastic, or poroviscoelastic cytoplasm consisting of an actin network ($c_{AF}=20\mu\text{M}$, $L_c=0.9\mu\text{m}$, $l_p=3\mu\text{m}$, $\alpha=1.1\%$, $k_H=2\times 10^{-13}\text{ m}^4/\text{N}\cdot\text{s}$).

The time-scale of relevance for the poroelastic response is a function of the permeability and porosity of the biphasic network. A second set of actin properties for a denser network ($\phi_f=0.82$) and smaller permeability ($k_H=0.1\times 10^{-13}\text{ m}^4/(\text{N}\cdot\text{s})$) during the acrosomal process in sperm cells was given in Section 6.3. This denser, less permeable network will now be used to compare the poroviscoelastic response of networks with different porosities and permeabilities in the same cell geometry and boundary conditions as previously used. Figure 6–32 shows the reaction force time histories for the poroelastic and poroviscoelastic response of the two networks. The poroelastic response from the denser network, inset (b) of Figure 6–32, exhibits much less relaxation due to restricted fluid flow and consequently leads to less initial relaxation in the poroviscoelastic response (inset (a) of Figure 6–32). Conversely, the pressure gradients within the denser

actin network take longer to dissipate, thereby increasing the relevant time-scale for the poroelastic effects compared to the more porous network.

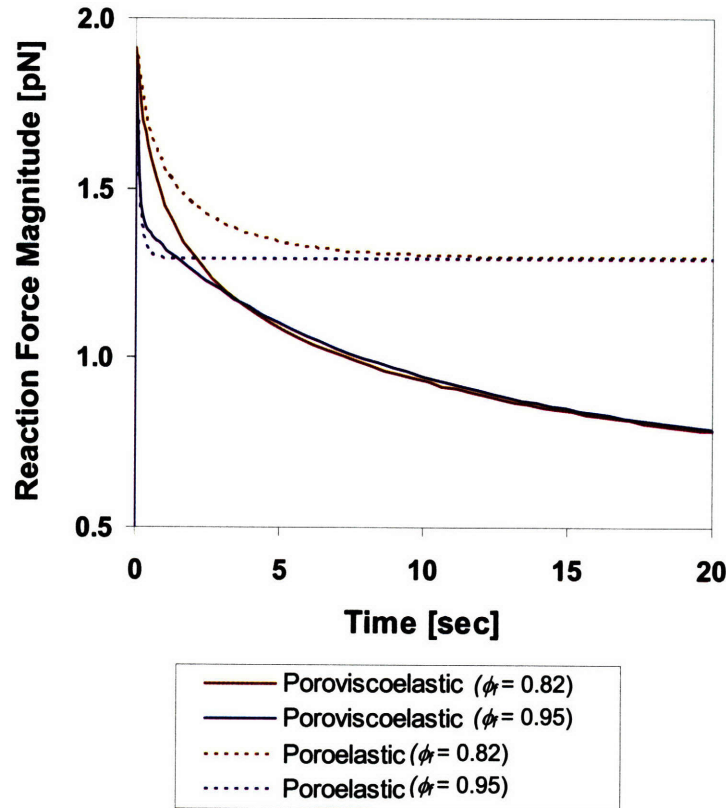


Figure 6–32. Relaxation of reaction force on a solid plate compressing a cell ($\epsilon_{2,\text{total}}=-10\%$). Cell consists of a neo-Hookean nucleus, orthotropic membrane, and either a poroelastic or poro-viscoelastic cytoplasm consisting an actin network ($c_{AF}=20\mu\text{M}$, $L_c=0.9\mu\text{m}$, $l_p=3\mu\text{m}$, $\alpha=1.1\%$) with either $\phi_f=0.95$, $k_H=2\times 10^{-13}\text{ m}^4/\text{N}\cdot\text{s}$ or $\phi_f=0.82$, $k_H=0.1\times 10^{-13}\text{ m}^4/\text{N}\cdot\text{s}$.

The relative amount of relaxation for each case is shown in Figure 6–33 by again normalizing the reaction forces for each poro-viscoelastic case ($\phi_f=0.82$, $k_H=0.1\times 10^{-13}\text{ m}^4/(\text{N}\cdot\text{s})$; and $\phi_f=0.95$, $k_H=2.0\times 10^{-13}\text{ m}^4/(\text{N}\cdot\text{s})$) by their peak reaction force at $t=0.01\text{ sec}$, $f_R=-1.91, -1.85\text{ pN}$ respectively. While the denser network has a significant impact on the short-term poroelastic response (for $t < 4$ seconds), the impact is reduced for the poro-viscoelastic response to times $t < 1$ second (Figure 6–33).

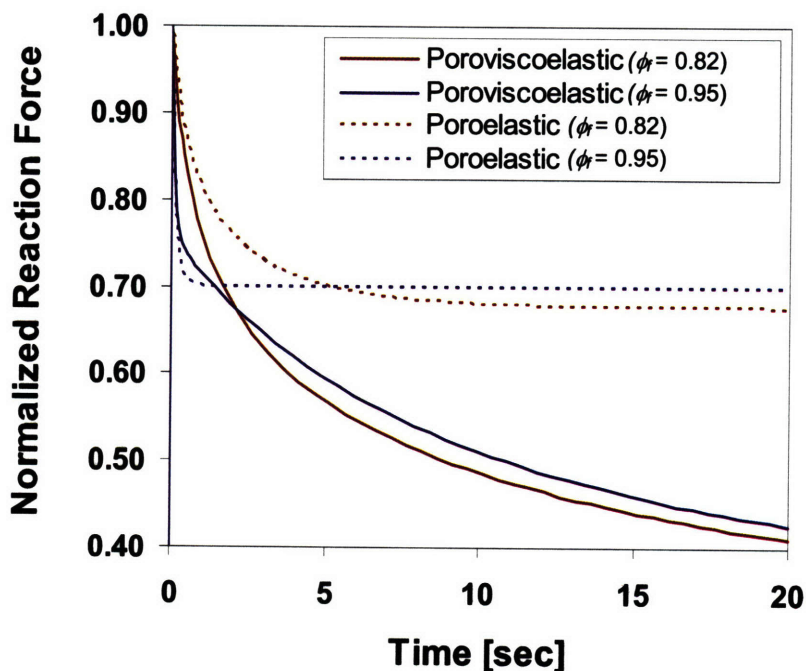


Figure 6–33. Relaxation of reaction force normalized by peak reaction force on a solid plate compressing a cell ($\epsilon_{2,\text{total}}=-10\%$). Cell consists of a neo-Hookean membrane and nucleus, and either a poroelastic or poroviscoelastic cytoplasm consisting of three regions of actin networks ($c_{Af}=10\text{-}170\mu\text{M}$, $L_c=0.9\mu\text{m}$, $l_p=3\mu\text{m}$, $\alpha=1.1\%$) with either $\phi=0.95$, $k_H=2\times 10^{-13}\text{ m}^4/\text{N}\cdot\text{s}$ or $\phi=0.82$, $k_H=0.1\times 10^{-13}\text{ m}^4/\text{N}\cdot\text{s}$.

The behavior of both networks show that while viscoelastic effects may dominate the long-term response of cytoskeletal networks, poroelastic effects cannot be neglected for shorter time-scales in which pressure fields within the cell are not uniform. Both time-scales have biological importance with regard to cytoskeletal mechanics. The overall network turnover and decay time for motile neutrophils is approximately 20 seconds (Herant et al., 2003). However, localized flow/turnover of actin crosslinkers, e.g. a-actinin (Kuhlman et al., 1994; Wachsstock et al., 1994), and actin monomers in neutrophils (Cassimeris et al., 1990; Cano et al., 1991) and other amoeboid cells (Sund and Axelrod, 2000) has been observed to occur on a time-scale of less than 1 second during cell motility. The combined poroviscoelastic network model captures transient

mechanical effects on both of these time-scales, and it provides the framework for further evaluation of the relevance and influence of pressure gradient-driven poroelastic effects at locations throughout the cell which have different porosities and permeabilities, including fluid flow into pseudopods as a partial contributor to amoeboid cell motility.

CHAPTER 7 Summary and Future

Applications

7.1 Summary discussion

The central role of the cytoskeleton in cellular biomechanical processes makes it a compelling subject for detailed 3D numerical modeling. The focus of this doctoral research has been the development of a microstructurally-motivated model of the 3D biomechanical response of cross-linked, semiflexible cytoskeletal networks during elastic and viscoelastic deformations, with a specific emphasis on actin networks. These models have been integrated into a 3D finite element cell model (along with membrane and nucleus models) with the capability to vary material properties spatially within the cell.

7.1.1 Inextensible filament and network models

Constitutive models for F-actin microstructural network behavior have been created using single molecule models for individual filament force-extension behavior in conjunction with an eight-chain network model to capture the non-affine 3D molecular network behavior. The single filament force-extension constitutive model was based on the MacKintosh derivation of the Kratky-Porod energy functional for semiflexible filaments ($l_p \sim L_c$). In further developing this model, we developed an accurate approximation for the MacKintosh force-extension expression of the form $F_{Mac} = \hat{F}_{Mac}(r)$ using a Padé approximation. When combined with the eight-chain network model, the

MacKintosh model was able to accurately capture the initial stiffness and nonlinear strain stiffening behavior observed in shear rheology experiments. The 3D cytoskeletal network constitutive model presented provides the ability to track microstructural stretch and orientation states under macroscopic stretching conditions in an averaged manner, and also enables variation of the filament mechanical properties and concentrations. An 8-chain network model considering a linear constitutive model of the filament force-extension behavior was presented and compared to the nonlinear MacKintosh model. The linear force-extension relationship was found to result in strain stiffening of the network, a consequence of filament rotation during network deformation. However, the evolution in stiffness with strain differed from the behavior seen in experiments, underscoring the need to also include nonlinear force-extension relationships for actin filaments.

Using the 8-chain MacKintosh network constitutive model, we examined the experimentally observed effects on the network stress-strain behavior that occur from increasing the actin concentration. The model's shear stress-shear strain response compares favorably with rheological data at low ($8,12\mu\text{M}$) and high ($29\mu\text{M}$) actin concentrations. The network model also exhibited good agreement with the experimental tangent modulus-shear stress data for $c_{AF}=21\mu\text{M}$ in both the low and high stress regions, but not in the intermediate transition region. The experimental $21\mu\text{M}$ data was shown to exhibit an anomalous, delayed transition to strain stiffening behavior in comparison to the other experimental concentration cases, which explained its diverging behavior from the theoretical prediction. The network model's prediction for the transition to strain stiffening behavior for the $21\mu\text{M}$ case, however, did coincide with the trend exhibited by

the other experimental concentration cases. The tangent shear moduli in the nonlinear strain stiffening region, often difficult to model, also correlate well with the data for all concentrations. This suggests that the network model is effectively simulating the cooperative network behavior and the accommodation of the shear strain through chain rotation and a small amount of end-to-end chain extension.

The relationship between filament pretension and isotropic network prestress is also examined within the framework of the network model. We parametrically varied the filament pretension to quantify its influence on network stress-strain behavior. Small increases in filament pretension (α) leads to an isotropic network prestress and produces large increases in initial network stiffness (G_0), with a constant relation between tangent shear modulus and shear stress for high stresses. Changes to filament geometries from bundling also influence the network behavior. We found an increase in network stiffness by increasing $l_{p,m}$, with excellent agreement between experimentally bundled actin networks ($R=0.5$, $c_{AF}=7\mu\text{M}$) and the corresponding modeled networks composed of three-filament bundles. The overall constitutive framework enables predictions of large-strain multi-axial deformation of 3D isotropic F-actin filament networks, and can be extended to model *in vivo* F-actin networks or *in vitro* networks of other filaments once updated with the proper material properties.

7.1.2 Extensible filament and network models

The behavior of single cytoskeletal filaments has been extended beyond entropic unbending to include enthalpic axial stretching of inter-atomic bonds along the

macromolecular backbone. These two behaviors are combined through a multiplicative decomposition of their mechanical stretch ratios to form an extensible model that is in turn integrated into eight-chain cytoskeletal network model. The single filament extensible model is compared with experimental data of single actin filament stretching, and found to capture the behavior through the full range of extension. The single filament and network extensible models are parametrically evaluated to show the increasing mechanical contribution of axial filament stretching as the inextensible limit is approached ($r/L_c \rightarrow 1$).

7.1.3 Equilibrium network swelling model

The mechanical response of the cytoskeletal network due to the resultant localized equilibrium swelling of the cytoplasm was captured using a constitutive model employing multiplicative decomposition of mechanical and swelling stretches. The reaction force of a swelled actin gel in a simplified spherical geometry is parametrically evaluated by imposing a uniform swelling stretch on the actin network, then compressing the sphere back to its original diameter. This equilibrium swelling model is later coupled with Darcy's law, enabling the contributions of network swelling to be included in the ensuing poroelastic fluid flow.

7.1.4 Cross-link effects

The constitutive model for cytoskeletal networks was expanded through torsional potentials to include the strain energy for compliant intra-network cross-links (e.g. ABPs such as FLNa and avidin). The mechanical contribution of network cross-links (through

torsional potentials) is also examined, as well as the cross-links' influence on the entropic configuration space. The initial focus of this model was below the force threshold required to detach the cross-link subunits from the chain. Within this regime, the cross-link imparts some structural stiffness to the network chain while deforming solely through enthalpic torsion at its hinge. The influence of cross-link torsional stiffness on network elasticity was parametrically evaluated for varying torsional stiffnesses. The network model with cross-link torsion was compared to experimental actin networks with filamin (FLN) and avidin cross-linkers. Two regimes of cross-link behavior emerge based on the actin-FLN network response. The first regime ($\tau < 3\text{Pa}$) consists of standard strain stiffening network behavior, which is accurately captured using an extensible network model and cross-links in torsion. The network model gives us insight into the second regime ($3\text{Pa} < \tau < 10\text{Pa}$) by showing that while the network elasticity is deteriorating, the actin filaments are not at their extensible limit, which suggests that the FLN cross-links are deforming (via entropic unbending, enthalpic stretching, and/or Ig domain unfolding). This is confirmed by the experimental data with the rapid decrease in strain stiffening after $\tau < 3\text{Pa}$, followed by network failure. The model was then compared to the stiffer actin-avidin networks (although the torsional stiffness of the individual avidin-biotin cross-links has not been measured). The model also showed excellent agreement with the measured initial response of the experimental actin-avidin networks using the same actin parameters and by increasing the cross-link torsional stiffness by an order of magnitude.

The torsional stiffness of cross-links does more, however, than just contribute to the strain energy of the network. By resisting the rotation of filaments about their cross-

linked junctions, the cross-link has an influence on the entropic bending configuration space of the filaments. A finite element simulation and a new hybrid extensible filament model were used to evaluate the extent to which increasing cross-link torsional stiffness (k_{CL}) reduces the number of bending configurations available to an actin filament, thereby leading to a stiffer mechanical response by the filament. The hybrid extensible filament model contains rigid ends and a middle section that deforms elastically via entropic unbending and enthalpic stretching. In concert, the two simulations demonstrate the coupling between cross-links and the entropic unbending response of the extensible filament. The influence of this coupling is greater for cross-links with larger torsional stiffnesses. The influence is mitigated, however, by the observed decrease in lengths of the rigid ends (which serves to increase the entropic unbending configuration space). These models can be enhanced by adding a time-dependent stretching for the actin-FLN bonds, as well as incorporating different deformation modes for the cross-links including internal energy-based axial stretching, entropic unbending, and possibly unfolding of cross-link subdomains.

7.1.5 Viscoelastic network models

The effects of interfilament shear viscoelasticity were added to the network model and compared with rheological experimental data of actin-FLN and actin-avidin networks. The viscoelastic response is captured by adding a nonlinear viscoelastic Maxwell leg to the network model to account for molecular shear viscosity by incorporating a hyperelastic spring based on the volume fraction of the relaxing portion of the cytoskeletal network and a nonlinear dashpot based on the changing orientation of

the network filaments. The relaxation in the Maxwell leg is included via a multiplicative decomposition of the deformation gradient (\mathbf{F}) into elastic (\mathbf{F}^e) and viscous (\mathbf{F}^v) components. The nonlinear viscoelastic model captures the storage modulus behavior well through the strain stiffening region, up to $\tan(\gamma) \sim 0.3$ for the actin-FLN networks. The nonlinear viscoelastic response agrees with the experimentally measured loss modulus for shear strains through the strain stiffening region. The model also captures the measured small strain linear viscoelastic response of the actin-avidin network. The nonlinear viscoelastic model is evaluated at different frequencies as well as for creep and stress relaxation conditions. The viscoelastic cytoskeletal model was also incorporated within a larger finite element model of the cell that includes a neo-Hookean membrane and nucleus. The stress relaxation of the combined cell was observed after subjecting it to different amounts of compressive displacements. The results show that increasing compressive strain on actin networks in a cellular geometry results in more total reaction force relaxation, but less relaxation relative to the peak reaction force for each case.

7.1.6 Poroviscoelastic network models

The mechanical effect of cytosolic fluid flowing through the cytoskeletal network via a poroelastic network model was demonstrated in confined compression, unconfined compression, and compression of a cell with a membrane and nucleus. The time-dependent behavior of the cytoplasm was integrated into the cytoskeletal model in a poroviscoelastic manner that accounts for the spatial diffusion of the cytosol within the porous, viscohyperelastic filament network. Flow-dependent viscoelastic effects are due to cytosolic flow (with mass balance governed the pressure gradient), as compared with

the flow-independent (time-dependent) effects due to the material shear viscoelasticity. The 3D partially saturated poroviscoelastic model expanded on previous work (e.g. biphasic theory for soil consolidation and connective tissues) by including microstructural details for cellular applications. The saturation factor can also be varied as a function of time or as a function of another state variable (e.g. stress, stretch, etc.). This framework also allows the flexibility to distinguish between trapped fluid and fluid that is free to flow through the cytoskeletal network. The local fluid volume changes are tracked through the fluid volume ratio, enabling the poroelastic analyses to account for the contribution from network swelling. Although not measured empirically, the hydraulic permeability for actin networks is estimated via the Kozeny-Carman theory at high porosities.

The poroelastic behavior of actin networks are parametrically evaluated with varying permeabilities and compressive strains under confined compression and unconfined compression conditions. Spatial variation in pressure gradients in unconfined compression is also shown. The unconfined compression results show that increasing compressive strain on actin networks results in more relaxation (both in reaction force and contraction of the lateral sides) due to the increased fluid loss from the network. Axisymmetric poroelastic and poroviscoelastic cell models are also parametrically evaluated to observe the reaction force relaxation after an applied compressive strain. The simulation does not permit fluid flow across the membrane or into the nucleus, although the model could easily be adapted to allow fluid flow into the nucleus as well as out of the cell.

The results show that increasing compressive strain on actin networks in a cellular geometry results in more total reaction force relaxation and more relaxation relative to the peak reaction force for each case. The relaxation of the reaction force for the poroelastic cell is due to the reduction in pore pressure gradients throughout the cell. In the absence of fluid flow at the boundaries (i.e. such as in unconfined compression), the compression of the cell creates pore pressure gradients throughout the cytoplasm. The pore pressure field becomes uniform over time, allowing the cell to be in a relaxed state. The poroelastic network model also gives insight into the average mechanical response of the microstructural features of the cytoskeleton. The undeformed cell starts with a filament stretch of one ($\lambda_f = 1$), but the average filament stretch increases within the actin networks just after the cell has been compressed, especially near the center axis of the cell where the macroscopic deformation and pore pressures are the highest. The contours of highest filament stretch correlate closely to the contours of highest pore pressures, demonstrating the microstructural effects of cytosolic fluid flow through actin networks. The average filament angle within undeformed areas (i.e. away from the center axis of the cell where the macroscopic deformation is the highest) remains approximately equal to the initial filament angle. While the filament stretch in the relaxed state has largely returned to $\lambda_f = 1$, the filament angle contours correlate well to the vertical strain (ϵ_{22}) contours for both the peak and relaxed states, reinforcing the observation that macroscopic network deformations are primarily accommodated through rotation of the network filaments, with significantly less filament stretch.

The poroelastic response has a minimal contribution to the poroviscoelastic response of actin networks for $t > 1$ second since the pressure field within the cell has

equilibrated. The time-scale of relevance for the poroelastic response is a function of the permeability and porosity of the biphasic network. The poroelastic responses from denser networks exhibit much less relaxation due to restricted fluid flow, and consequently lead to less initial relaxation in the poroviscoelastic response. Conversely, the pressure gradients within denser actin networks take longer to dissipate, thereby increasing the relevant time-scale for the poroelastic effects compared to the more porous networks. The behavior of both networks show that while viscoelastic effects may dominate the long-term response of cytoskeletal networks, poroelastic effects cannot be neglected for shorter time-scales in which pressure fields within the cell are not uniform, since both time-scales have biological importance with regard to cytoskeletal mechanics. The poroviscoelastic and swelling models can be used in the future to capture part of the cytoplasm's dynamic response during migrational processes like extension and translocation as well as during other amoeboid processes like blebbing.

The poroviscoelastic model also has applications with cancer cells and their surrounding tissue. Empirical and theoretical investigations (Netti et al., 1995) of the time constants of transvascular and interstitial fluid exchange in tumors have been used to improve oncologic drug delivery (Netti et al., 1999). The interstitial transport in cancerous tumors has been found, via two-photon correlation microscopy technique, to be biphasic in nature (Alexandrakis et al., 2004). Although biphasic theory has been applied to interstitial lymphatic transport (Swartz et al., 1999), microstructurally-motivated 3D poroviscoelastic models could yield new insights into methods for altering solid tumor pressure, which has been used as diagnostic and prognostic value in the management of cancer (Sahani et al., 2005; Kremser et al., 2006).

The models developed through this doctoral research provide a beginning framework for including active remodeling of cytoskeletal networks, such as the actin network's reformulation in response to mechanical and chemical stimuli. A fully coupled 3D cytoskeletal network model could be integrated with membrane and nucleus models in the finite element-based micromechanical model of the cell which already provides the ability to assign and evolve mechanical properties and filament concentrations as a function of location within the cell. Enhancements such as these, and others detailed below, could eventually lead to a composite cellular microstructural model that would enable detailed mechanical modeling of eukaryotic cells under a wide variety of loading conditions encountered during both healthy and diseased cellular functions.

7.2 Future applications in cell motility

7.2.1 Dynamic nature of cytoskeleton for cell motility

Biological cells respond to mechanical as well as chemical stimuli. Mechanical stimuli from its external environment, e.g. extracellular matrix (ECM), can lead to microstructural changes in the cell membrane, the nucleus, and the cytoskeleton, and even biochemical changes via mechanotransduction (Huang et al., 2004; Ingber, 2006). The cell membrane can gather/concentrate focal adhesion complexes (FAC) (Davies et al., 1994; Hu et al., 2003; Chen et al., 2004; Hu et al., 2004), while the nucleus can experience changes in conformation of chromatin (Ingber, 1997; Maniotis et al., 1997; Jean et al., 2005) in response to mechanical forces. The cytoskeletal filaments can

actively rearrange their microstructure in response to mechanical stimuli. The morphology of endothelial cells, for example, is changed dramatically from shear loads from blood flow which cause elongation of the cells in the direction of shear stress. The change in morphology is achieved by a reorientation and assembly of F-actin stress fibers at the basal cell surface that ultimately protrudes the upstream and downstream limits of the plasma membrane (McCue et al., 2004). Mechanical deformation of neutrophils flowing in pulmonary capillaries can cause cytoskeletal disruption, pseudopod projections, and a resulting decrease in shear modulus of more than 60% (Yap and Kamm, 2005).

Cytoskeletal reorganization, extension, and contraction are critical to cell migration, especially the mesenchymal migration of leukocytes and some metastatic cancer cells. Cell migration has been studied for many biological processes such as embryogenesis (Duncan and Tin Su, 2004), leukocyte extravasation and invasion (Barreiro et al., 2004; Britta Engelhardt, 2004; Vicente-Manzanares and Sanchez-Madrid, 2004), cancer metastasis (Yamazaki et al., 2005), and migration of fibroblasts and vascular endothelial cells during wound healing (Martin, 1997). Cell migration involves multiple processes that are regulated by various signaling molecules (Ridley et al., 2003). The actin cytoskeleton plays a critical role in many parts of cell motility and migration. During cell migration, the actin cytoskeleton is dynamically remodeled via polymerization, and this reorganization produces the force necessary for cell migration (Pollard and Borisy, 2003). Regulating or inhibiting actin polymerization decreases cell motility. An increased understanding of the mechanics of the cellular protrusions and contractions can therefore augment understanding of critical immunological responses

(i.e. extravasation, migration) as well as actin polymerization regulation therapies for treating cancer (Zigmond, 2004; Quinlan et al., 2005; Walker and Olson, 2005).

Leukocytes in particular experience many deformation states to successfully complete critical immune system processes. When unstressed, passive leukocytes present a spherical morphology with numerous membrane folds (Schmid-Schonbein, 1990). Passive leukocytes exhibit viscoelastic behavior with the stress shared by the cytoplasm, nucleus, and the compliant, folded membrane. Activated leukocytes exhibit many complex biomechanical behaviors (cytoplasmic poroviscoelasticity, cytoskeletal network behavior and remodeling, membrane unfolding, etc.) during active processes such as cell spreading, adhering to endothelial walls, cell rolling under high hemodynamic shear loads, and migration through 3D extracellular matrix (ECM). Leukocytes, such as T and B lymphocytes (T and B cells) and neutrophils, are highly migratory cells that exhibit a variety of versatile migration modalities to enter and transmigrate through various tissues and organs during critical immune system processes (Friedl et al., 2001). These modalities are typically categorized as either mesenchymal or amoeboid migration.

Leukocyte movement on 2D substrates follow a mesenchymal pattern consisting of four ordered processes: membrane protrusion at the leading edge, adhesion of the protrusions to the substrate, translocation of the cell body via contraction, and finally retraction of the trailing edge (Lauffenburger, 1996). Mesenchymal migration in 3D extracellular matrix (ECM), e.g. for fibroblasts (Langholz et al., 1995) and tumor cells (Friedl and Wolf, 2003), is typically accompanied by proteolytic matrix degradation enzymes that slowly accumulate in an integrin-dependent manner at the leading edge of migrating cells (Wolf et al., 2003a), leaving a trail of damaged ECM in its wake.

Mesenchymal cell migration in 3D matrices has been simulated with force-based computational models (Zaman et al., 2005).

Amoeboid migration, however, is typified by faster, low-affinity movement of a rounded yet flexible cell morphology and dynamic pseudopod protrusions/retractions which are independent of integrin-mediated focal adhesions (Devreotes and Zigmond, 1988). Lymphocytes move in this integrin-independent manner by changing shape and squeezing through gaps in the 3D ECM both *in vitro* (Friedl et al., 1998) and *in vivo* (Brakebusch et al., 2002) without degradation of the ECM. Since they are not dependent on focal adhesions during amoeboid movement, T cells use stiff lateral pseudopod protrusions as “footholds” that remain stationary and locked between fibers while the cell mass flows forward (Friedl et al., 2001). The lymphocyte then squeezes through narrow gaps (if greater than 1-2 μm in diameter) or changes migration direction to circumnavigate around less porous obstacles with near-undiminished velocity (Wolf et al., 2003b). As T cells squeeze through narrow regions, constriction points or rings act as anchors for anterograde flow of the cytoplasm and forward propulsion of the cell (Friedl et al., 2001). Finally, the cell contracts the lateral pseudopods and/or trailing edge uropod. B cells (Carrasco et al., 2004) and neutrophils (Mandeville et al., 1997) can also exhibit amoeboid migration behavior in 3D ECM. The cylindrical-like protrusions, or pseudopods, are thicker than filopodia and extend/contract into the 3D ECM via polymerization/depolymerization and thermal ratcheting at the inner surface of the membrane. The pseudopods are termed invadopodium when proteolytic matrix degradation enzymes, e.g. matrix metalloproteinases (MMPs), accumulate in an integrin-dependent manner at the leading edge of migrating cells (Wolf et al., 2003a).

Amoeboid migration, shown in Figure 7–1, is seen both in non-neoplastic (i.e. non-tumorous) cells such as lymphocytes and neutrophils as well as in neoplastic cells like lymphoma and small-cell lung carcinoma (Friedl et al., 2001; Francis et al., 2002; Wang et al., 2002b). While understanding the complex biomechanics of leukocyte deformation for passive and active states (e.g. amoeboid motility) yields insight into essential processes of immune function, there is added value to this pursuit since some tumor cells, (e.g. some fibrosarcomas) have been shown to undergo conversion from a mesenchymal cell type towards an amoeboid cell type, which is termed a mesenchymal-amoeboid transition (MAT) (Wolf et al., 2003a).

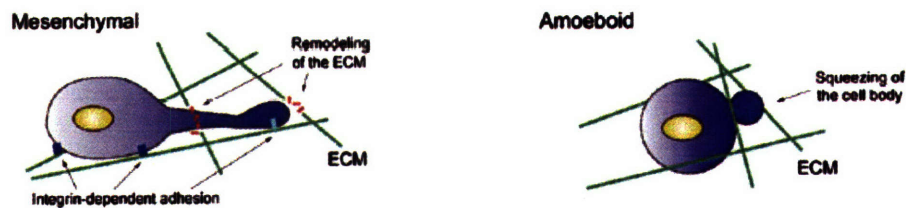


Figure 7–1. Mesenchymal and amoeboid migration in ECM (Yamazaki et al., 2005)

Pseudopod growth and contraction presents a unique, dynamic intracellular mechanobiochemical state that plays a key role in mesenchymal migration (Figure 7–1). The unique intracellular mechanical state is further confounded through interactions of the actin microfilament and microtubule networks (Pantaloni et al., 2001). For instance, the elongation of actin filaments may facilitate polarized microtubule instability, and microtubules can modulate the actin cytoskeleton to control the direction of cell migration through specific signaling pathways (Li et al., 2005b). Pseudopods and lamellipodia dynamics have been examined for keratins (Pollard and Borisy, 2003),

listeria (Cameron et al., 1999), and neutrophils (Chodniewicz et al., 2004; Zhelev et al., 2004), among other cells, yet are still not completely understood.

The 3D cytoskeletal network models developed in this thesis provide the framework to model the dynamic, mechanical response of pseudopods and motility-enabling contractions. These models will require anisotropic microstructural detail to capture filament behavior at the leading/trailing edges of polymerization. In addition, the cytoskeletal network models developed in this thesis will need to extend beyond the cross-linking proteins that mediate the response within individual networks (e.g. isotropic cross-linking, bundling) to include interactions between different networks (e.g. AF-MT cross-linking). Further evaluation can also be made of the different types of cross-link extension and failure, including entropic unbending, enthalpic stretching, and subdomain unfolding. Empirically obtained failure and deformation thresholds can be implemented in the network model by monitoring the average chain force and adjusting local network properties accordingly.

7.2.2 Cell motility modalities and modeling needs

Modeling the migrational capabilities of highly motile cells such as leukocytes will require multiple models in order to simulate the different biological functions involved (see Figure 7-2).

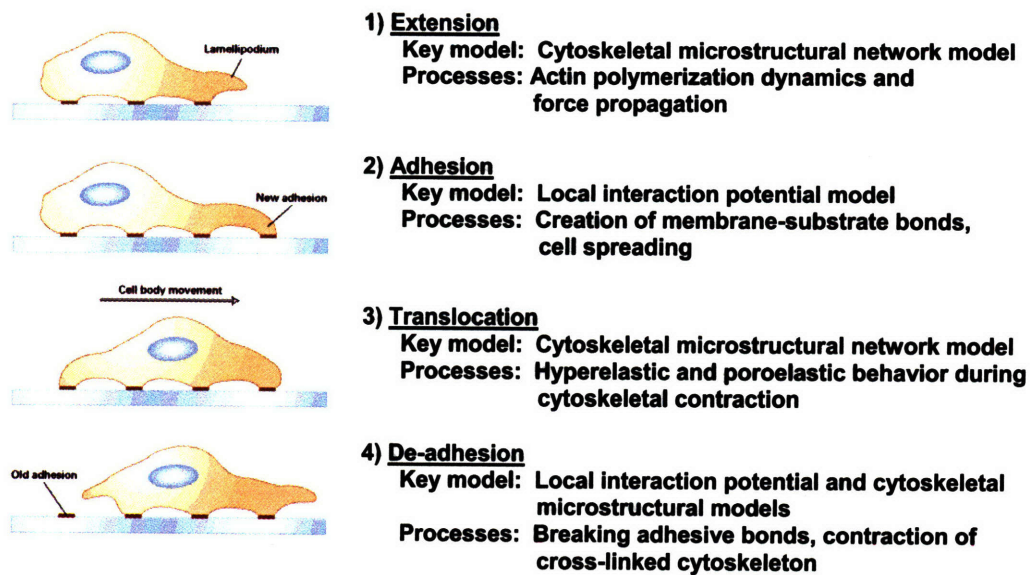


Figure 7-2. Summary of cell motility and modeling needs [illustration from (Lodish, 2000)]

The steps shown in Figure 7-2 will require biomechanical models simulating the dynamic behavior of cross-linked cytoskeletal filament networks and membrane-substrate adhesion in addition to the basic membrane and nucleus models. During cell extension (1), the baseline cytoskeletal model of cross-linked filament networks developed here will require an additional actin polymerization submodel to simulate the leading edge of the cell as it expands due to actin polymerization force propagation. For the cell adhesion step (2) during migration (or any adhesive process), a local interaction potential submodel will be needed in conjunction with the cytoskeletal model to simulate cell spreading and FAC-substrate bond creation. The translocation force (3), generated from cellular contraction through cytoplasmic actin-myosin generated tensile forces, is simulated through loads applied to the hyperelastic- and poroelastic-based cytoskeletal model also developed in this thesis. Finally, during cell detachment (4), a combination of

all models is required for the final cytoplasmic contraction in addition to the detachment of FAC at trailing edge of cell.

7.2.3 Modeling of anisotropic migrational cellular structures

Amoeboid cellular motility in the 3D ECM is driven at least in part by polymerization of F-actin filaments to create both lateral and axial pseudopods, followed by localized cytoskeletal contractions. Modeling pseudopod growth will require evaluation of the forces driving the mechanical behavior in addition to quantifying monomer concentration levels for polymerization in migrating cells. To capture the creation of a pseudopod during amoeboid migration one can use the poroviscohyperelastic cytoskeletal network model developed here along with a polymerization submodel. The cytoskeletal network model allows us to monitor cytoskeletal microstructural chain orientation, stretch, and force during deformation. This structural information can be utilized to appropriately develop polymerization models to actively reconfigure and evolve the network during protrusion growth as well as other loading conditions. The ability of the model to monitor the force at the cross-link junctions can also be utilized to explore effects of the rupture of cross-links at larger strains.

The preferential polymerization of F-actin filaments in the direction of protrusion necessitates the use of an anisotropic strain energy function in the cytoskeletal network model. The strain energy density of an isotropic material reinforced by a single group of fibers, with direction \mathbf{v}_0 in the reference configuration, depends on the first five strain invariants $U = \hat{U}(I_1, I_2, I_3, I_4, I_5)$ (Spencer, 1984). While the strain energy density of

materials that include n groups of reinforcing fibers, in directions $\mathbf{v}_0^{(i)}$, additionally depend on higher order invariants to capture interaction effects between the fiber groups (Spencer, 1984); the dependence of the material response on $I_2, I_5^{(i)}$ and the higher order invariants is generally weak (Humphrey et al., 1990). This allows the use of a simplified strain energy density function with both isotropic and anisotropic terms (Bischoff et al., 2002a; Bertoldi and Boyce, 2007c; Cantournet et al., 2007), $U = \hat{U}_{iso}(I_1, I_3) + \hat{U}_{ani}(I_4^{(i)})$, where $I_3 = \det(\mathbf{B})$ and $I_4^{(i)} = \mathbf{v}_0 \cdot \mathbf{B}\mathbf{v}_0$ is a measure of the fiber stretch of the preferentially aligned F-actin filaments. The polymerization submodel will simulate the dynamic remodeling of the actin network in the preferential direction by adjusting chain and network properties (local concentrations, cross-link densities, contour lengths, and orientations) at the critical polymerization thresholds. The area of F-actin polymerization in free protrusions contains higher actin monomer densities. The resulting repulsive self-interaction (due to either electrostatic interactions or thermal agitation) between actin monomers in the high density region can expand the cytoskeleton and draw in cytosol which provides volume flow that can also contribute to pseudopod growth (Herant et al., 2003). The expansion into the cell is balanced by the viscous resistance of the cytoplasm (Herant and Dembo, 2006). The existing poroviscoelastic submodel will capture this additional method of pseudopod growth, while the anisotropic polymerization model provides the ability to capture the structural behavior of preferentially oriented cytoskeletal networks (e.g. Arp2/3 branching in lamellipodia).

7.2.4 Membrane-substrate interactions

The cell's interaction with the three-dimensional ECM and its biomechanical features (e.g. stiffness, ligand density) will also affect *in vivo* cell deformation. The detailed adhesive behavior of the membrane and the receptor binding affinities of the ECM's ligands are not dominant influences on amoeboid migration. Therefore a basic adhesion model could be included in the 3D finite element model to capture the short-lived membrane-substrate interactions that occur in a diffusely distributed manner on contact areas. A local interaction potential model could be used to simulate the proximity-dependent force of the weaker membrane-substrate bonds. The local interaction potential model can be implemented via a user subroutine with an interaction potential based on empirically measured adhesion properties (Lauffenburger, 1991; N'Dri et al., 2003). Many aspects of the mechanics of substrate interactions have been evaluated, including the stability of the circular front of advancing focal adhesion complexes under sinusoidal perturbations (Shenoy and Freund, 2005), size effects on receptor-mediated endocytosis of viruses (Gao et al., 2005), experimental and finite element analysis of bacterial adhesion strength (Tsang et al., 2006), and constitutive modeling of the entropic energy associated with binder distribution and migration within a focal adhesion zone (Freund and Lin, 2004).

Membrane tension is regulated by cytoskeletal forces, pressures and the membrane reservoir. Extra membrane surface from the membrane reservoir will affect the deformation behavior of leukocytes (e.g. B lymphocytes). The current membrane model, based on basic membrane (tensile) and bending behavior, can also be enhanced to include undulations/bends to account for the reservoir material.

7.2.5 Model validation

Validation studies can be conducted by comparing model predictions to empirical data from published results in the technical literature as was done in this thesis using rheological experiments involving cross-linked *in vitro* filament networks. The forces, monomer flows, and concentrations associated with actin polymerization can be obtained from published data (Cassimeris et al., 1990; Cassimeris et al., 1992; Coates et al., 1992; Westlin et al., 1992; Entschladen et al., 1997; Zigmond, 1998; Zigmond et al., 1998; Friedl et al., 2001) including flow visualization (Danuser and Oldenbourg, 2000) and microsphere-based motility (Cameron et al., 1999) assays. Further predictions of overall cellular elastic and viscoelastic cell behavior can be compared to results from whole cell rheology studies using micropipette aspiration (Schmid-Schonbein et al., 1981; Dong et al., 1991; Tran-Son-Tay et al., 1991; Herant et al., 2003), microchannels (Yap and Kamm, 2005), as well as cell poking (Elson, 1988; Zahalak et al., 1990). Comparison to experiments involving more complex leukocyte deformation states such as cell spreading (Bunnell et al., 2001; Coughlin and Schmid-Schonbein, 2004; Sumoza-Toledo and Santos-Argumedo, 2004; Herant et al., 2006) and 3D migration in natural tissues and synthetic gels (Haston et al., 1982; Parkhurst and Saltzman, 1992; Kuntz and Saltzman, 1997; Friedl and Brocker, 2000; Tan et al., 2001; Miller et al., 2002; Stoll et al., 2002; Wolf et al., 2003a; Wolf et al., 2003b) can also be examined. A validated model will also enable new insights into the efficacy of cytoskeletal inhibitors that can regulate polymerization, which would impact diseased cell motility based on cytoskeletal reorganization.

References

- Abramowitch, S.D., and S.L. Woo. 2004. An improved method to analyze the stress relaxation of ligaments following a finite ramp time based on the quasi-linear viscoelastic theory. *J Biomech Eng.* 126:92-7.
- Adami, R., D. Choquet, and E. Grazi. 1999. Rhodamine phalloidin F-actin. Critical concentration versus tensile strength. *European Journal of Biochemistry.* 263:270-275.
- Adams, A.M., C.P. Buckley, and D.P. Jones. 2000. Biaxial hot drawing of poly(ethylene terephthalate): measurements and modelling of strain-stiffening. *Polymer.* 41:771-786.
- Alberts, B. 1996. The art of MBoC³ the complete set of figures from Molecular biology of the cell. Garland Pub., New York. 1 computer optical disc ; 4 3/4 in. + Includes: 1 user's guide (16 p.).
- Alberts, B. 2002. Molecular biology of the cell. Garland Science.
- Alcaraz, J., L. Buscemi, M. Grabulosa, X. Trepas, B. Fabry, R. Farre, and D. Navajas. 2003. Microrheology of human lung epithelial cells measured by atomic force microscopy. *Biophys J.* 84:2071-9.
- Alexandrakis, G., E.B. Brown, R.T. Tong, T.D. McKee, R.B. Campbell, Y. Boucher, and R.K. Jain. 2004. Two-photon fluorescence correlation microscopy reveals the two-phase nature of transport in tumors. *Nat Med.* 10:203-207.
- Alexopoulos, L.G., G.M. Williams, M.L. Upton, L.A. Setton, and F. Guilak. 2005. Osteoarthritic changes in the biphasic mechanical properties of the chondrocyte pericellular matrix in articular cartilage. *J Biomech.* 38:509-17.
- Alieva, I.B., and I.A. Vorobev. 1992. [A stereoscopic analysis of centrosome structure in the cells of a tissue culture under the action of energy metabolism inhibitors. I. 2,4-Dinitrophenol, deoxyglucose, sodium azide and the calcium ionophore A23187]. *Tsitologiya.* 34:65-75.
- Allen, P.G., C.B. Shuster, J. Kas, C. Chaponnier, P.A. Janmey, and I.M. Herman. 1996. Phalloidin Binding and Rheological Differences among Actin Isoforms. *Biochemistry.* 35:14062-14069.
- Amos, L.A., and T.S. Baker. 1979. The three-dimensional structure of tubulin protofilaments. *Nature.* 279:607-12.

- Anand, L. 1979. On H. Hencky's Approximate Strain-Energy Function for Moderate Deformations. *Journal of Applied Mechanics-Transactions of the Asme*. 46:78-82.
- Armstrong, C.G., W.M. Lai, and V.C. Mow. 1984. An Analysis of the Unconfined Compression of Articular-Cartilage. *Journal of Biomechanical Engineering-Transactions of the Asme*. 106:165-173.
- Armstrong, C.G., and V.C. Mow. 1982. Variations in the intrinsic mechanical properties of human articular cartilage with age, degeneration, and water content. *J Bone Joint Surg Am*. 64:88-94.
- Arruda, E.M., and M.C. Boyce. 1993a. Evolution of Plastic Anisotropy in Amorphous Polymers during Finite Straining. *International Journal of Plasticity*. 9:697-720.
- Arruda, E.M., and M.C. Boyce. 1993b. A three-dimensional constitutive model for the large stretch behavior of rubber elastic materials. *Journal of the Mechanics and Physics of Solids*. 41:389-412.
- Arslan, M., and M.C. Boyce. 2006. Constitutive Modeling of the Finite Deformation Behavior of Membranes Possessing a Triangulated Network Microstructure. *Journal of Applied Mechanics*. 73:536-543.
- Arslan, M., M.C. Boyce, H.J. Qi, and C. Ortiz. 2008. Constitutive Modeling of the Stress-Stretch Behavior of Two-Dimensional Triangulated Macromolecular Networks Containing Folded Domains *Journal of Applied Mechanics*. 75:011020.
- Ateshian, G.A., M. Likhitpanichikul, and C.T. Hung. 2006. A mixture theory analysis for passive transport in osmotic loading of cells. *Journal of Biomechanics*. 39:464-475.
- Ateshian, G.A., W.H. Warden, J.J. Kim, R.P. Grelsamer, and V.C. Mow. 1997. Finite deformation biphasic material properties of bovine articular cartilage from confined compression experiments. *J Biomech*. 30:1157-64.
- Athanasίου, K.A., M.P. Rosenwasser, J.A. Buckwalter, T.I. Malinin, and V.C. Mow. 1991. Interspecies comparisons of in situ intrinsic mechanical properties of distal femoral cartilage. *J Orthop Res*. 9:330-40.
- Baaijens, F.P., W.R. Trickey, T.A. Laursen, and F. Guilak. 2005. Large deformation finite element analysis of micropipette aspiration to determine the mechanical properties of the chondrocyte. *Ann Biomed Eng*. 33:494-501.
- Barreiro, O., M. Vicente-Manzanares, A. Urzainqui, M. Yanez-Mo, and F. Sanchez-Madrid. 2004. Interactive protrusive structures during leukocyte adhesion and transendothelial migration. *Front Biosci*. 9:1849-63.
- Bathe, M., C. Heussinger, M.M.A.E. Claessens, A.R. Bausch, and E. Frey. 2008. Cytoskeletal Bundle Mechanics. *Biophys. J*. 94:2955-2964.

- Bausch, A.R., W. Moller, and E. Sackmann. 1999. Measurement of local viscoelasticity and forces in living cells by magnetic tweezers. *Biophys J.* 76:573-9.
- Bausch, A.R., F. Ziemann, A.A. Boulbitch, K. Jacobson, and E. Sackmann. 1998. Local Measurements of Viscoelastic Parameters of Adherent Cell Surfaces by Magnetic Bead Microrheometry. *Biophys. J.* 75:2038-2049.
- Bayer, E.A., T. Viswanatha, and M. Wilchek. 1975. The use of a homologous series of affinity labeling reagents in the study of the biotin transport system in yeast cells. *FEBS Lett.* 60:309-12.
- Bear, J. 1972. Dynamics of fluids in porous media. American Elsevier Pub. Co., New York.
- Bergstrom, J.S., and M.C. Boyce. 2000. Large strain time-dependent behavior of filled elastomers. *Mechanics of Materials.* 32:627-644.
- Bergstrom, J.S., and M.C. Boyce. 2001. Deformation of elastomeric networks: Relation between molecular level deformation and classical statistical mechanics models of rubber elasticity. *Macromolecules.* 34:614-626.
- Bertoldi, K., and M. Boyce. 2007a. Mechanics of the hysteretic large strain behavior of mussel byssus threads. *Journal of Materials Science.*
- Bertoldi, K., and M.C. Boyce. 2007b. Mechanics of the hysteretic large strain behavior of mussel byssus threads. *Journal of Materials Science.* 42:8943-8956.
- Bertoldi, K., and M.C. Boyce. 2007c. Mechanics of the hysteretic large strain behavior of mussel byssus threads. *Accepted for publication.*
- Biot, M.A. 1941. General Theory of Three-Dimensional Consolidation. *Journal of Applied Physics.* 12:155-164.
- Biot, M.A. 1956a. Theory of Propagation of Elastic Waves in a Fluid-Saturated Porous Solid. I. Low-Frequency Range. *The Journal of the Acoustical Society of America.* 28:168-178.
- Biot, M.A. 1956b. Theory of Propagation of Elastic Waves in a Fluid-Saturated Porous Solid. II. Higher Frequency Range. *The Journal of the Acoustical Society of America.* 28:179-191.
- Bischoff, J.E., E.A. Arruda, and K. Grosh. 2002a. A Microstructurally Based Orthotropic Hyperelastic Constitutive Law. *Journal of Applied Mechanics.* 69:570-579.
- Bischoff, J.E., E.M. Arruda, and K. Grosh. 2002b. Orthotropic Hyperelasticity in Terms of an Arbitrary Molecular Chain Model. *Journal of Applied Mechanics.* 69:198-201.

- Blanchoin, L., K.J. Amann, H.N. Higgs, J.B. Marchand, D.A. Kaiser, and T.D. Pollard. 2000. Direct observation of dendritic actin filament networks nucleated by Arp2/3 complex and WASP/Scar proteins. *Nature*. 404:1007-11.
- Boal, D.H. 2002. *Mechanics of the cell*. Cambridge University Press, Cambridge, UK ; New York. xiv, 406 p. pp.
- Boltzmann, L. 1871. Einige allgemeine Sätze über Wärmegleichgewicht (Some general statements on thermal equilibrium). *Wiener Berichte*. 63:679-711.
- Boltzmann, L. 1876. Über die Natur der Gasmoleküle (On the nature of gas molecules). *Wiener Berichte*. 74:553-560.
- Bordas, J., E.M. Mandelkow, and E. Mandelkow. 1983. Stages of tubulin assembly and disassembly studied by time-resolved synchrotron X-ray scattering. *J Mol Biol*. 164:89-135.
- Bordas, J., A. Svensson, M. Rothery, J. Lowy, G.P. Diakun, and P. Boesecke. 1999. Extensibility and Symmetry of Actin Filaments in Contracting Muscles. *Biophys. J*. 77:3197-3207.
- Boyce, M.C., and E.A. Arruda. In preparation. *Mechanics of Polymer Networks*.
- Boyce, M.C., and E.M. Arruda. 2000. Constitutive models of rubber elasticity: A review. *Rubber Chemistry and Technology*. 73:504-523.
- Boyce, M.C., and E.M. Arruda. 2001. Swelling and mechanical stretching of elastomeric materials. *Mathematics and Mechanics of Solids*. 6:641-659.
- Boyce, M.C., D.M. Parks, and A.S. Argon. 1988. Large Inelastic Deformation of Glassy-Polymers .1. Rate Dependent Constitutive Model. *Mechanics of Materials*. 7:15-33.
- Brakebusch, C., S. Fillatreau, A.J. Potocnik, G. Bungartz, P. Wilhelm, M. Svensson, P. Kearney, H. Korner, D. Gray, and R. Fassler. 2002. Beta1 integrin is not essential for hematopoiesis but is necessary for the T cell-dependent IgM antibody response. *Immunity*. 16:465-77.
- Brangwynne, C.P., F.C. MacKintosh, S. Kumar, N.A. Geisse, J. Talbot, L. Mahadevan, K.K. Parker, D.E. Ingber, and D.A. Weitz. 2006. Microtubules can bear enhanced compressive loads in living cells because of lateral reinforcement. *J. Cell Biol*. 173:733-741.
- Brau, R.R., J.M. Ferrer, H. Lee, C.E. Castro, B.K. Tam, P.B. Tarsa, P. Matsudaira, M.C. Boyce, R.D. Kamm, and M.J. Lang. 2007. Passive and active microrheology with optical tweezers. *Journal of Optics a-Pure and Applied Optics*. 9:S103-S112.

- Bray, D. 2001. Cell movements : from molecules to motility. Garland Pub., New York. xiv, 372 p. pp.
- Britta Engelhardt, H.W. 2004. Mini-review: Transendothelial migration of leukocytes: through the front door or around the side of the house? *European Journal of Immunology*. 34:2955-2963.
- Bunnell, S.C., V. Kapoor, R.P. Tribble, W. Zhang, and L.E. Samelson. 2001. Dynamic Actin Polymerization Drives T Cell Receptor-Induced Spreading: A Role for the Signal Transduction Adaptor LAT. *Immunity*. 14:315-329.
- Burton, K., and D.L. Taylor. 1997. Traction forces of cytokinesis measured with optically modified elastic substrata. *Nature*. 385:450-4.
- Bustamante, C., J.F. Marko, E.D. Siggia, and S. Smith. 1994. Entropic elasticity of lambda-phage DNA. *Science*. 265:1599-600.
- Bustamante, C., S.B. Smith, J. Liphardt, and D. Smith. 2000. Single-molecule studies of DNA mechanics. *Curr Opin Struct Biol*. 10:279-85.
- Cai, S., L. Pestic-Dragovich, M.E. O'Donnell, N. Wang, D. Ingber, E. Elson, and P. De Lanerolle. 1998. Regulation of cytoskeletal mechanics and cell growth by myosin light chain phosphorylation. *American Journal of Physiology-Cell Physiology*. 44:C1349-C1356.
- Caille, N., O. Thoumine, Y. Tardy, and J.J. Meister. 2002. Contribution of the nucleus to the mechanical properties of endothelial cells. *Journal of Biomechanics*. 35:177-187.
- Cameron, L.A., M.J. Footer, A. van Oudenaarden, and J.A. Theriot. 1999. Motility of ActA protein-coated microspheres driven by actin polymerization. *Proc Natl Acad Sci U S A*. 96:4908-13.
- Campbell, N.A., J.B. Reece, and L.G. Mitchell. 1999. Biology. Benjamin Cummings, Menlo Park, Calif. IF figure reprinted at <http://academic.brooklyn.cuny.edu/biology/bio4fv/page/intermediate-fil.html> pp.
- Canadas, P., V.M. Laurent, P. Chabrand, D. Isabey, and S. Wendling-Mansuy. 2003. Mechanisms governing the visco-elastic responses of living cells assessed by foam and tensegrity models. *Med Biol Eng Comput*. 41:733-9.
- Canadas, P., V.M. Laurent, C. Oddou, D. Isabey, and S. Wendling. 2002. A cellular tensegrity model to analyse the structural viscoelasticity of the cytoskeleton. *J Theor Biol*. 218:155-73.
- Cano, M.L., D.A. Lauffenburger, and S.H. Zigmond. 1991. Kinetic analysis of F-actin depolymerization in polymorphonuclear leukocyte lysates indicates that

- chemoattractant stimulation increases actin filament number without altering the filament length distribution. *J Cell Biol.* 115:677-87.
- Cantournet, S., M.C. Boyce, and A.H. Tsou. 2007. Micromechanics and macromechanics of carbon nano tube-enhanced elastomers. *Journal of the Mechanics and Physics of Solids.* 55:1321-1339.
- Cao, Y.F., R. Bly, W. Moore, Z. Gao, A.M. Cuitino, and W. Soboyejo. 2007. On the measurement of human osteosarcoma cell elastic modulus using shear assay experiments. *Journal of Materials Science-Materials in Medicine.* 18:103-109.
- Carrasco, Y.R., S.J. Fleire, T. Cameron, M.L. Dustin, and F.D. Batista. 2004. LFA-1/ICAM-1 Interaction Lowers the Threshold of B Cell Activation by Facilitating B Cell Adhesion and Synapse Formation. *Immunity.* 20:589-599.
- Cassimeris, L., H. McNeill, and S.H. Zigmond. 1990. Chemoattractant-stimulated polymorphonuclear leukocytes contain two populations of actin filaments that differ in their spatial distributions and relative stabilities. *J Cell Biol.* 110:1067-75.
- Cassimeris, L., D. Safer, V.T. Nachmias, and S.H. Zigmond. 1992. Thymosin beta 4 sequesters the majority of G-actin in resting human polymorphonuclear leukocytes. *J Cell Biol.* 119:1261-70.
- Castro, C.E., M.J. Lang, and M.C. Boyce. 2008a. An Elastica Approximate for Fibers and Fibrous Networks. *Submitted for publication.*
- Castro, C.E., M.J. Lang, and M.C. Boyce. 2008b. Physiological Role of B Lymphocyte Membrane Mechanics, Unpublished work. MIT.
- Chan, R.W. 2004. Measurements of vocal fold tissue viscoelasticity: Approaching the male phonatory frequency range. *The Journal of the Acoustical Society of America.* 115:3161-3170.
- Chan, R.W., and I.R. Titze. 2000. Viscoelastic shear properties of human vocal fold mucosa: Theoretical characterization based on constitutive modeling. *The Journal of the Acoustical Society of America.* 107:565-580.
- Chandran, P.L., and V.H. Barocas. 2006. Affine versus non-affine fibril kinematics in collagen networks: theoretical studies of network behavior. *J Biomech Eng.* 128:259-70.
- Charras, G.T., and M.A. Horton. 2002. Determination of cellular strains by combined atomic force microscopy and finite element modeling. *Biophysical Journal.* 83:858-879.
- Charras, G.T., J.C. Yarrow, M.A. Horton, L. Mahadevan, and T.J. Mitchison. 2005. Non-equilibration of hydrostatic pressure in blebbing cells. *Nature.* 435:365-369.

- Chen, C.S., J. Tan, and J. Tien. 2004. Mechanotransduction at cell-matrix and cell-cell contacts. *Annu Rev Biomed Eng.* 6:275-302.
- Chien, S., K.L. Sung, G.W. Schmid-Schonbein, R. Skalak, E.A. Schmalzer, and S. Usami. 1987. Rheology of leukocytes. *Ann NY Acad Sci.* 516:333-347.
- Chodniewicz, D., A.M. Alteraifi, and D.V. Zhelev. 2004. Experimental Evidence for the Limiting Role of Enzymatic Reactions in Chemoattractant-induced Pseudopod Extension in Human Neutrophils. *J. Biol. Chem.* 279:24460-24466.
- Coates, T.D., R.G. Watts, R. Hartman, and T.H. Howard. 1992. Relationship of F-actin distribution to development of polar shape in human polymorphonuclear neutrophils. *J Cell Biol.* 117:765-74.
- Cohen, A. 1991. A Pade Approximant to the Inverse Langevin Function. *Rheologica Acta.* 30:270-273.
- Cohen, B., W.M. Lai, and V.C. Mow. 1998. A Transversely Isotropic Biphasic Model for Unconfined Compression of Growth Plate and Chondroepiphysis. *Journal of Biomechanical Engineering.* 120:491-496.
- Condeelis, J. 1993. Life at the leading edge: the formation of cell protrusions. *Annu Rev Cell Biol.* 9:411-44.
- Costa, K.D., and F.C.P. Yin. 1999. Analysis of indentation: Implications for measuring mechanical properties with atomic force microscopy. *Journal of Biomechanical Engineering-Transactions of the Asme.* 121:462-471.
- Coughlin, M.F., and G.W. Schmid-Schonbein. 2004. Pseudopod Projection and Cell Spreading of Passive Leukocytes in Response to Fluid Shear Stress. *Biophys. J.* 87:2035-2042.
- Coulombe, P.A., and P. Wong. 2004. Cytoplasmic intermediate filaments revealed as dynamic and multipurpose scaffolds. *Nat Cell Biol.* 6:699-706.
- Crandall, S.H. 1970. The role of damping in vibration theory. *J Sound Vib.* 13: 3-18.
- Crocker, J.C., M.T. Valentine, E.R. Weeks, T. Gisler, P.D. Kaplan, A.G. Yodh, and D.A. Weitz. 2000. Two-point microrheology of inhomogeneous soft materials. *Physical Review Letters.* 85:888-891.
- Cummings, B. 2001. Schematic of cytoskeletal filaments in endothelial cell. Addison Wesley Longman, Inc.
- Cunningham, C.C. 1995. Actin polymerization and intracellular solvent flow in cell surface blebbing. *J Cell Biol.* 129:1589-99.

- Cunningham, C.C., J.B. Gorlin, D.J. Kwiatkowski, J.H. Hartwig, P.A. Janmey, H.R. Byers, and T.P. Stossel. 1992. Actin-binding protein requirement for cortical stability and efficient locomotion. *Science*. 255:325-7.
- Curry, F.E. 1986. Determinants of capillary permeability: a review of mechanisms based on single capillary studies in the frog. *Circ Res*. 59:367-80.
- Dahl, K.N., A.J. Engler, J.D. Pajerowski, and D.E. Discher. 2005. Power-law rheology of isolated nuclei with deformation mapping of nuclear substructures. *Biophys J*. 89:2855-64.
- Daniels, B.R., B.C. Masi, and D. Wirtz. 2006. Probing Single-Cell Micromechanics In Vivo: The Microrheology of *C. elegans* Developing Embryos. *Biophys. J*. 90:4712-4719.
- Danuser, G., and R. Oldenbourg. 2000. Probing f-actin flow by tracking shape fluctuations of radial bundles in lamellipodia of motile cells. *Biophys J*. 79:191-201.
- Dao, M., J. Li, and S. Suresh. 2006. Molecularly based analysis of deformation of spectrin network and human erythrocyte. *Materials Science and Engineering: C*. 26:1232-1244.
- Dao, M., C.T. Lim, and S. Suresh. 2003. Mechanics of the human red blood cell deformed by optical tweezers. *Journal of the Mechanics and Physics of Solids*. 51:2259-2280.
- Darcy, H. 1856. Les fontaines publiques de la ville de Dijon : Exposition et application des principes a suivre et des formules a employer dans les questions de distribution d'eau; ouvrage terminé par un appendice relatif aux fournitures d'eau de plusieurs villes au filtrage des eaux et a la fabrication des tuyaux de fonte, de plomb, de tole et de bitume. Victor Dalmont, Libraire des Corps imperiaux des ponts et chaussées et des mines, Paris. 647 pp.
- Darling, E.M., S. Zauscher, J.A. Block, and F. Guilak. 2007. A thin-layer model for viscoelastic, stress-relaxation testing of cells using atomic force microscopy: do cell properties reflect metastatic potential? *Biophys J*. 92:1784-91.
- Darling, E.M., S. Zauscher, and F. Guilak. 2006. Viscoelastic properties of zonal articular chondrocytes measured by atomic force microscopy. *Osteoarthritis Cartilage*. 14:571-9.
- Davies, P.F., A. Robotewskyj, and M.L. Griem. 1994. Quantitative studies of endothelial cell adhesion. Directional remodeling of focal adhesion sites in response to flow forces. *J Clin Invest*. 93:2031-8.
- Deguchi, S., T. Ohashi, and M. Sato. 2005. Newly designed tensile test system for in vitro measurement of mechanical properties of cytoskeletal filaments. *Jsm*

International Journal Series C-Mechanical Systems Machine Elements and Manufacturing. 48:396-402.

- Dembo, M., and F. Harlow. 1986. Cell motion, contractile networks, and the physics of interpenetrating reactive flow. *Biophys J.* 50:109-21.
- Demer, L.L., and F.C.P. Yin. 1983. Passive biaxial mechanical properties of isolated canine myocardium. *Journal of Physiology.* Vol. 339:615-630.
- Deshpande, V.S., R.M. McMeeking, and A.G. Evans. 2006. A bio-chemo-mechanical model for cell contractility. *Proceedings of the National Academy of Sciences of the United States of America.* 103:14015-14020.
- Deshpande, V.S., R.M. McMeeking, and A.G. Evans. 2007. A model for the contractility of the cytoskeleton including the effects of stress-fibre formation and dissociation. *Proceedings of the Royal Society a-Mathematical Physical and Engineering Sciences.* 463:787-815.
- Detournay, E., and A.H.-D. Cheng. 1993. Fundamentals of poroelasticity. *In Comprehensive Rock Engineering: Principles, Practice and Projects, Vol. II, Analysis and Design Method.* C. Fairhurst, editor. Pergamon Press, Oxford. pp. 113-171.
- Devreotes, P.N., and S.H. Zigmond. 1988. Chemotaxis in eukaryotic cells: a focus on leukocytes and Dictyostelium. *Annu Rev Cell Biol.* 4:649-86.
- DiDonna, B.A., and A.J. Levine. 2006. Filamin cross-linked semiflexible networks: fragility under strain. *Phys Rev Lett.* 97:068104.
- Dimova, R., C. Dietrich, A. Hadjiisky, K. Danov, and B. Pouligny. 1999. Falling ball viscosimetry of giant vesicle membranes: Finite-size effects. *European Physical Journal B.* 12:589-598.
- DiSilvestro, M.R., Q. Zhu, and J.-K. Suh. 1999. Biphasic Poroviscoelastic Theory Predicts the Strain Rate Dependent Viscoelastic Behavior of Articular Cartilage. *In Proc. 1999 Bioeng. Conf., ASME BED.* Vol. 42. pp. 105-106.
- DiSilvestro, M.R., Q. Zhu, M. Wong, J.S. Jurvelin, and J.K. Suh. 2001. Biphasic poroviscoelastic simulation of the unconfined compression of articular cartilage: I--Simultaneous prediction of reaction force and lateral displacement. *J Biomech Eng.* 123:191-7.
- Doehring, T.C., E.O. Carew, and I. Vesely. 2004. The Effect of Strain Rate on the Viscoelastic Response of Aortic Valve Tissue: A Direct-Fit Approach. *Annals of Biomedical Engineering.* 32:223-232.
- Dogterom, M., J.W.J. Kerssemakers, G. Romet-Lemonne, and M.E. Janson. 2005. Force generation by dynamic microtubules. *Current Opinion in Cell Biology.* 17:67-74.

- Doi, M., and N.Y. Kuzuu. 1980. Rheology of star polymers in concentrated solutions and melts. *Journal of Polymer Science: Polymer Letters Edition*. 18:775-780.
- Dolbow, J., E. Fried, and H. Ji. 2004. Chemically induced swelling of hydrogels. *Journal of the Mechanics and Physics of Solids*. 52:51-84.
- Dolbow, J., E. Fried, and H. Ji. 2005. A numerical strategy for investigating the kinetic response of stimulus-responsive hydrogels. *Computer Methods in Applied Mechanics and Engineering*. 194:4447-4480.
- Dong, C., R. Skalak, and K.L.P. Sung. 1991. Cytoplasmic Rheology of Passive Neutrophils. *Biorheology*. 28:557-567.
- Duncan, T., and T. Tin Su. 2004. Embryogenesis: Coordinating Cell Division with Gastrulation. *Current Biology*. 14:R305-R307.
- Dupaix, R.B., and M.C. Boyce. 2007. Constitutive modeling of the finite strain behavior of amorphous polymers in and above the glass transition. *Mechanics of Materials*. 39:39-52.
- Dupuis, D., W. Guilford, J. Wu, and D. Warshaw. 1997. Actin filament mechanics in the laser trap. *Journal of Muscle Research and Cell Motility*. 18:17-30.
- Egelman, E.H., and R. Padron. 1984. X-ray diffraction evidence that actin is a 100 [angst] filament. *Nature*. 307:56-58.
- Elliott, D.M., D.A. Narmoneva, and L.A. Setton. 2002. Direct measurement of the Poisson's ratio of human patella cartilage in tension. *Journal of Biomechanical Engineering-Transactions of the Asme*. 124:223-228.
- Elson, E.L. 1988. Cellular mechanics as an indicator of cytoskeletal structure and function. *Annu Rev Biophys Biophys Chem*. 17:397-430.
- Entschladen, F., B. Niggemann, K.S. Zanker, and P. Friedl. 1997. Differential requirement of protein tyrosine kinases and protein kinase C in the regulation of T cell locomotion in three-dimensional collagen matrices. *J Immunol*. 159:3203-10.
- Ethier, C.R. 1983. Hydrodynamics of Flow Through Gels with Applications to the Eye. *In Mechanical Engineering*. Vol. S.M. Thesis. Massachusetts Institute of Technology, Cambridge.
- Ethier, C.R. 1991. Flow through Mixed Fibrous Porous Materials. *Aiche Journal*. 37:1227-1236.
- Evans, E., and W. Rawicz. 1990. Entropy-driven tension and bending elasticity in condensed-fluid membranes. *Phys Rev Lett*. 64:2094-2097.

- Evans, E., and A. Yeung. 1989. Apparent viscosity and cortical tension of blood granulocytes determined by micropipet aspiration. *Biophys J.* 56:151-60.
- Evans, E.A. 1989. Structure and deformation properties of red blood cells: Concepts and quantitative methods. *In Methods in Enzymology.* Vol. Volume 173. Academic Press. 3-35.
- Fabry, B., G.N. Maksym, J.P. Butler, M. Glogauer, D. Navajas, and J.J. Fredberg. 2001. Scaling the microrheology of living cells. *Phys Rev Lett.* 87:148102.
- Febvay, S. 2003. A three-dimensional constitutive model for the mechanical behavior of cervical tissue *In Mechanical Engineering.* Vol. S.M. Massachusetts Institute of Technology, Cambridge, MA. 159.
- Felgner, H., R. Frank, J. Biernat, E.M. Mandelkow, E. Mandelkow, B. Ludin, A. Matus, and M. Schliwa. 1997. Domains of neuronal microtubule-associated proteins and flexural rigidity of microtubules. *Journal of Cell Biology.* 138:1067-1075.
- Felgner, H., R. Frank, and M. Schliwa. 1996. Flexural rigidity of microtubules measured with the use of optical tweezers. *Journal of Cell Science.* 109:509-516.
- Ferko, M.C., A. Bhatnagar, M.B. Garcia, and P.J. Butler. 2007. Finite-element stress analysis of a multicomponent model of sheared and focally-adhered endothelial cells. *Annals of Biomedical Engineering.* 35:208-223.
- Fernandez, P., P.A. Pullarkat, and A. Ott. 2006. A master relation defines the nonlinear viscoelasticity of single fibroblasts. *Biophys J.* 90:3796-805.
- Ferrer, J.M., H. Lee, F. Nakamura, R.D. Kamm, and M.J. Lang. 2008. Measuring Molecular Interaction Between Single Actin Filament And Actin Binding Proteins Using Optical Tweezers. *Biophys. J.* 94:142-.
- Fishkind, D.J., L.G. Cao, and Y.L. Wang. 1991. Microinjection of the catalytic fragment of myosin light chain kinase into dividing cells: effects on mitosis and cytokinesis. *J Cell Biol.* 114:967-75.
- Fithian, D.C., M.A. Kelly, and V.C. Mow. 1990. Material Properties and Structure-Function-Relationships in the Menisci. *Clinical Orthopaedics and Related Research:*19-31.
- Fithian, D.C., W.B. Zhu, A. Ratcliffe, M.A. Kelly, B.C. Mow, and T.I. Malinin. 1989. Exponential Law Representation of Tensile Properties of Human Mensicus. *In Inst. Mech. Eng.* 85-90.
- Fixman, M., and J. Kovac. 1973. Polymer Conformational Statistics .3. Modified Gaussian Models of Stiff Chains. *Journal of Chemical Physics.* 58:1564-1568.

- Flory, P.J. 1953. Principles of polymer chemistry. Cornell University Press, Ithaca. 672 pp.
- Flory, P.J. 1969. Statistical mechanics of chain molecules. Interscience Publishers, New York, xix, 432 p. pp.
- Flory, P.J., and J.J. Rehner. 1943. Statistical Mechanics of Cross-Linked Polymer Networks I. Rubberlike Elasticity. *The Journal of Chemical Physics*. 11:512-520.
- Forchheimer, P.H. 1901. Wasserbewegung Durch Boden. *Zeitschrift des Vereines Deutscher Ingenieure*. 49-50:1736.
- Fox, J.W., E.D. Lamperti, Y.Z. Eksioglu, S.E. Hong, Y. Feng, D.A. Graham, I.E. Scheffer, W.B. Dobyns, B.A. Hirsch, R.A. Radtke, S.F. Berkovic, P.R. Huttenlocher, and C.A. Walsh. 1998. Mutations in filamin 1 prevent migration of cerebral cortical neurons in human periventricular heterotopia. *Neuron*. 21:1315-25.
- Francis, K., B. Palsson, J. Donahue, S. Fong, and E. Carrier. 2002. Murine Sca-1(+)/Lin(-) cells and human KG1a cells exhibit multiple pseudopod morphologies during migration. *Exp Hematol*. 30:460-3.
- Frank, E.H., and A.J. Grodzinsky. 1987. Cartilage electromechanics--II. A continuum model of cartilage electrokinetics and correlation with experiments. *J Biomech*. 20:629-39.
- Fredberg, J.J., and D. Stamenovic. 1989. On the imperfect elasticity of lung tissue. *J Appl Physiol*. 67:2408-19.
- Freund, L.B., and Y. Lin. 2004. The role of binder mobility in spontaneous adhesive contact and implications for cell adhesion. *Journal of the Mechanics and Physics of Solids*. 52:2455-2472.
- Friedl, P., S. Borgmann, and E.B. Brocker. 2001. Amoeboid leukocyte crawling through extracellular matrix: lessons from the Dictyostelium paradigm of cell movement. *Journal of Leukocyte Biology*. 70:491-509.
- Friedl, P., and E.B. Brocker. 2000. The biology of cell locomotion within three-dimensional extracellular matrix. *Cell Mol Life Sci*. 57:41-64.
- Friedl, P., F. Entschladen, C. Conrad, B. Niggemann, and K.S. Zanker. 1998. CD4+ T lymphocytes migrating in three-dimensional collagen lattices lack focal adhesions and utilize beta1 integrin-independent strategies for polarization, interaction with collagen fibers and locomotion. *Eur J Immunol*. 28:2331-43.
- Friedl, P., and K. Wolf. 2003. Tumour-cell invasion and migration: Diversity and escape mechanisms. *Nature Reviews Cancer*. 3:362-374.

- Fuchs, E., and D.W. Cleveland. 1998. A structural scaffolding of intermediate filaments in health and disease. *Science*. 279:514-9.
- Fudge, D.S., K.H. Gardner, V.T. Forsyth, C. Riekel, and J.M. Gosline. 2003. The mechanical properties of hydrated intermediate filaments: insights from hagfish slime threads. *Biophys J*. 85:2015-27.
- Fuller, R. 1975. *Synergetics*. Macmillan, New York. 372-434 pp.
- Fung, Y.C. 1980. *Biomechanics : Mechanical properties of Living Tissues*. Springer-Verlag.
- Fung, Y.C. 1993. *Biomechanics : mechanical properties of living tissues*. Springer-Verlag, New York.
- Furuike, S., T. Ito, and M. Yamazaki. 2001. Mechanical unfolding of single filamin A (ABP-280) molecules detected by atomic force microscopy. *FEBS Letters*. 498:72-75.
- Fushimi, K., and A.S. Verkman. 1991. Low viscosity in the aqueous domain of cell cytoplasm measured by picosecond polarization microfluorimetry. *J Cell Biol*. 112:719-25.
- Gao, H., W. Shi, and L.B. Freund. 2005. From The Cover: Mechanics of receptor-mediated endocytosis. *Proceedings of the National Academy of Sciences*. 102:9469-9474.
- Gardel, M.L., F. Nakamura, J. Hartwig, J.C. Crocker, T.P. Stossel, and D.A. Weitz. 2006a. Stress-Dependent Elasticity of Composite Actin Networks as a Model for Cell Behavior. *Physical Review Letters*. 96:088102-4.
- Gardel, M.L., F. Nakamura, J.H. Hartwig, J.C. Crocker, T.P. Stossel, and D.A. Weitz. 2006b. Prestressed F-actin networks cross-linked by hinged filamins replicate mechanical properties of cells. *Proceedings of the National Academy of Sciences of the United States of America*. 103:1762-1767.
- Gardel, M.L., J.H. Shin, F.C. MacKintosh, L. Mahadevan, P. Matsudaira, and D.A. Weitz. 2004a. Elastic behavior of cross-linked and bundled actin networks. *Science*. 304:1301-5.
- Gardel, M.L., J.H. Shin, F.C. MacKintosh, L. Mahadevan, P.A. Matsudaira, and D.A. Weitz. 2004b. Scaling of F-actin network rheology to probe single filament elasticity and dynamics. *Phys Rev Lett*. 93:188102.
- Garikipati, K., S. Göktepe, and C. Miehe. 2008. Elastica-based strain energy functions for soft biological tissue. *Journal of the Mechanics and Physics of Solids*. 56:1693-1713.

- Gibbs, J.W. 1878. The Scientific Papers of J. Willard Gibbs. pp. 184, 201, 215.
- Gibson, L.J., and M.F. Ashby. 1988. Cellular solids : structure & properties. Pergamon Press, Oxford [Oxfordshire] ; New York. ix, 357 p. pp.
- Giles, J.M., A.E. Black, and J.E. Bischoff. 2007. Anomalous rate dependence of the preconditioned response of soft tissue during load controlled deformation. *Journal of Biomechanics*. 40:777-785.
- Gisler, T., and D.A. Weitz. 1999. Scaling of the Microrheology of Semidilute F-Actin Solutions. *Physical Review Letters*. 82:1606.
- Gittes, F., and F.C. MacKintosh. 1998. Dynamic shear modulus of a semiflexible polymer network. *Physical Review E*. 58:R1241.
- Gittes, F., B. Mickey, J. Nettleton, and J. Howard. 1993. Flexural rigidity of microtubules and actin filaments measured from thermal fluctuations in shape. *J Cell Biol*. 120:923-34.
- Gorlin, J.B., R. Yamin, S. Egan, M. Stewart, T.P. Stossel, D.J. Kwiatkowski, and J.H. Hartwig. 1990. Human endothelial actin-binding protein (ABP-280, nonmuscle filamin): a molecular leaf spring. *J Cell Biol*. 111:1089-105.
- Grazi, E. 1997. What is the diameter of the actin filament? *FEBS Letters*. 405:249-252.
- Grosberg, A.I., and A.R. Khokhlov. 1994. Statistical physics of macromolecules. AIP Press, New York.
- Gu, W.Y., W. M. Lai, C. T. Hung, Z. P. Liu, and V.C. Mow. 1997. Analysis of transient swelling and electrical responses of an isolated cell to sudden osmotic loading. *Adv. Bioeng. BED*. 36:189-190.
- Guilak, F., M.A. Haider, L.A. Setton, T.A. Laursen, and F.P.T. Baaijens. 2006. Multiphasic models of cell mechanics. *In Cytoskeletal mechanics : models and measurements*. M.K. Mofrad and R.D. Kamm, editors. Cambridge University Press, Cambridge.
- Guilak, F., and V.C. Mow. 2000. The mechanical environment of the chondrocyte: a biphasic finite element model of cell-matrix interactions in articular cartilage. *J Biomech*. 33:1663-73.
- Guilak, F., J.R. Tedrow, and R. Burgkart. 2000. Viscoelastic properties of the cell nucleus. *Biochem Biophys Res Commun*. 269:781-6.
- Haider, M., R. Schugart, L. Setton, and F. Guilak. 2006. A Mechano-chemical Model for the Passive Swelling Response of an Isolated Chondron under Osmotic Loading. *Biomechanics and Modeling in Mechanobiology*. 5:160-171.

- Haider, M.A., and F. Guilak. 2000. An axisymmetric boundary integral model for incompressible linear viscoelasticity: Application to the micropipette aspiration contact problem. *Journal of Biomechanical Engineering-Transactions of the Asme*. 122:236-244.
- Haider, M.A., and F. Guilak. 2002. An axisymmetric boundary integral model for assessing elastic cell properties in the micropipette aspiration contact problem. *Journal of Biomechanical Engineering-Transactions of the Asme*. 124:586-595.
- Harding, J.W., and I.N. Sneddon. 1945. The elastic stresses produced by the indentation of the plane surface of a semi-infinite elastic solid by a rigid punch. *Proc Cambridge Philos Soc*. 41:16-26.
- Hartemink, C.A. 2005. The Cross-linking Mechanism of Filamin A in the Actin Cytoskeleton. In Harvard-MIT Division of Health Sciences and Technology. Vol. Ph.D. MIT, Cambridge, MA. 144.
- Hartwig, J. 2004. Fig. 19-5b. In *Molecular cell biology*. H.F. Lodish, P.T. Matsudaira, C. Kaiser, and M. Krieger, editors. W.H. Freeman and Company, New York.
- Hartwig, J.H., and P. Shevlin. 1986. The architecture of actin filaments and the ultrastructural location of actin-binding protein in the periphery of lung macrophages. *J Cell Biol*. 103:1007-20.
- Hartwig, J.H., and T.P. Stossel. 1981. Structure of macrophage actin-binding protein molecules in solution and interacting with actin filaments. *J Mol Biol*. 145:563-81.
- Haston, W.S., J.M. Shields, and P.C. Wilkinson. 1982. Lymphocyte locomotion and attachment on two-dimensional surfaces and in three-dimensional matrices. *J Cell Biol*. 92:747-52.
- Haut, R.C., and R.W. Little. 1972. CONSTITUTIVE EQUATION FOR COLLAGEN FIBERS. *Journal of Biomechanics*. 5:423-430.
- Hayes, W.C., and A.J. Bodine. 1978. Flow-Independent Viscoelastic Properties of Articular Cartilage Matrix. *J. Biomech*. 11:407-419.
- Hayes, W.C., L.M. Keer, G. Herrmann, and L.F. Mockros. 1972. A mathematical analysis for indentation tests of articular cartilage. *J Biomech*. 5:541-51.
- Hayes, W.C., and L.F. Mockros. 1971. Viscoelastic Properties of Human Articular Cartilage. *J. Appl. Physiol*. 31:562-568.
- Head, D.A., A.J. Levine, and F.C. MacKintosh. 2003a. Deformation of cross-linked semiflexible polymer networks. *Phys Rev Lett*. 91:108102.

- Head, D.A., F.C. MacKintosh, and A.J. Levine. 2003b. Nonuniversality of elastic exponents in random bond-bending networks. *Physical Review E*. 68:-.
- Heidemann, S.R., S. Kaech, R.E. Buxbaum, and A. Matus. 1999. Direct observations of the mechanical behaviors of the cytoskeleton in living fibroblasts. *J Cell Biol*. 145:109-22.
- Hein, S., S. Kostin, A. Heling, Y. Maeno, and J. Schaper. 2000. The role of the cytoskeleton in heart failure. *Cardiovascular Research*. 45:273-278.
- Herant, M., and M. Dembo. 2006. Active cellular protrusion: continuum theories and models. In *Cytoskeletal mechanics: models and measurements*. M.K. Mofrad and R.D. Kamm, editors. Cambridge University Press, Cambridge; New York. 204-224.
- Herant, M., V. Heinrich, and M. Dembo. 2006. Mechanics of neutrophil phagocytosis: experiments and quantitative models. *J Cell Sci*. 119:1903-1913.
- Herant, M., W.A. Marganski, and M. Dembo. 2003. The Mechanics of Neutrophils: Synthetic Modeling of Three Experiments. *Biophys. J*. 84:3389-3413.
- Herrmann, H., and U. Aebi. 2004. Intermediate Filaments: Molecular Structure, Assembly Mechanism, and Integration Into Functionally Distinct Intracellular Scaffolds. *Annual Review of Biochemistry*. 73:749-789.
- Hewitt, J., F. Guilak, R. Glisson, and T.P. Vail. 2001. Regional material properties of the human hip joint capsule ligaments. *Journal of Orthopaedic Research*. 19:359-364.
- Higgs, H. 2001. Getting down to basics with actin. *Nat Cell Biol*. 3:E189-E189.
- Higuchi, H., T. Yanagida, and Y.E. Goldman. 1995. Compliance of thin filaments in skinned fibers of rabbit skeletal muscle. *Biophys. J*. 69:1000-1010.
- Hildebrandt, J. 1969. Comparison of mathematical models for cat lung and viscoelastic balloon derived by Laplace transform methods from pressure-volume data. *Bull Math Biophys*. 31:651-67.
- Hinner, B., M. Tempel, E. Sackmann, K. Kroy, and E. Frey. 1998. Entanglement, elasticity, and viscous relaxation of actin solutions. *Physical Review Letters*. 81:2614-2617.
- Hochmuth, R.M., and R.E. Waugh. 1987. Erythrocyte membrane elasticity and viscosity. *Annu Rev Physiol*. 49:209-19.
- Hohenadl, M., T. Storz, H. Kirpal, K. Kroy, and R. Merkel. 1999. Desmin Filaments Studied by Quasi-Elastic Light Scattering. *Biophys. J*. 77:2199-2209.

- Holmes, K.C., D. Popp, W. Gebhard, and W. Kabsch. 1990. Atomic model of the actin filament. *Nature*. 347:44-49.
- Holmes, M.H. 1986. Finite deformation of soft tissue: analysis of a mixture model in uniaxial compression. *J Biomech Eng*. 108:372-81.
- Holmes, M.H., W.M. Lai, and V.C. Mow. 1985. Singular perturbation analysis of the nonlinear, flow-dependent compressive stress relaxation behavior of articular cartilage. *J Biomech Eng*. 107:206-18.
- Holmes, M.H., and V.C. Mow. 1990. The nonlinear characteristics of soft gels and hydrated connective tissues in ultrafiltration. *J Biomech*. 23:1145-56.
- Holzappel, G.A. 2000. Nonlinear solid mechanics : a continuum approach for engineering. Wiley. xiv, 455 p. : ill. ; 25 cm.
- Hong, W., X. Zhao, J. Zhou, and Z. Suo. 2008. A theory of coupled diffusion and large deformation in polymeric gels. *Journal of the Mechanics and Physics of Solids*. In Press.
- Hori, R.Y., and L.F. Mockros. 1976. Indentation tests of human articular cartilage. *J Biomech*. 9:259-68.
- Hori, Y., A. Prasad, and J. Kondev. 2007. Stretching short biopolymers by fields and forces. *Physical Review E (Statistical, Nonlinear, and Soft Matter Physics)*. 75:041904-10.
- Horkay, F., and G.B. McKenna. 1996. Gels. In *Physical Properties of Polymers Handbook*. J.E. Mark, editor. American Institute of Physics Press, Woodbury, NY.
- Hoshijima, M. 2006. Mechanical stress-strain sensors embedded in cardiac cytoskeleton: Z disk, titin, and associated structures. *Am J Physiol Heart Circ Physiol*. 290:H1313-1325.
- Howard, J. 2001. *Mechanics of motor proteins and the cytoskeleton*. Sinauer Associates, Publishers, Sunderland, Mass. xvi, 367 p. pp.
- Hu, S., J. Chen, B. Fabry, Y. Numaguchi, A. Gouldstone, D.E. Ingber, J.J. Fredberg, J.P. Butler, and N. Wang. 2003. Intracellular stress tomography reveals stress focusing and structural anisotropy in cytoskeleton of living cells. *Am J Physiol Cell Physiol*. 285:C1082-90.
- Hu, S., L. Eberhard, J. Chen, J.C. Love, J.P. Butler, J.J. Fredberg, G.M. Whitesides, and N. Wang. 2004. Mechanical anisotropy of adherent cells probed by a three-dimensional magnetic twisting device. *Am J Physiol Cell Physiol*. 287:C1184-91.

- Huang, C.Y., V.C. Mow, and G.A. Ateshian. 2001. The role of flow-independent viscoelasticity in the biphasic tensile and compressive responses of articular cartilage. *J Biomech Eng.* 123:410-7.
- Huang, H., R.D. Kamm, and R.T. Lee. 2004. Cell mechanics and mechanotransduction: pathways, probes, and physiology. *Am J Physiol Cell Physiol.* 287:C1-11.
- Hubmayr, R.D., S.A. Shore, J.J. Fredberg, E. Planus, R.A. Panettieri, W. Moller, J. Heyder, and N. Wang. 1996. Pharmacological activation changes stiffness of cultured human airway smooth muscle cells. *American Journal of Physiology-Cell Physiology.* 40:C1660-C1668.
- Huisman, E.M., T. van Dillen, P.R. Onck, and E. Van der Giessen. 2007. Three-dimensional cross-linked F-actin networks: Relation between network architecture and mechanical behavior. *Physical Review Letters.* 99:-.
- Humphrey, J.D., R.K. Strumpf, and F.C.P. Yin. 1990. Determination of a Constitutive Relation for Passive Myocardium .1. a New Functional Form. *Journal of Biomechanical Engineering-Transactions of the Asme.* 112:333-339.
- Huxley, H.E., A. Stewart, H. Sosa, and T. Irving. 1994. X-ray diffraction measurements of the extensibility of actin and myosin filaments in contracting muscle. *Biophys. J.* 67:2411-2421.
- Huyghe, J.M., A.J.H. Frijns, and J.D. Janssen. 1997. Quadriphasic mechanics of swelling materials. *Computational Plasticity: Fundamentals and Applications, Pts 1 and 2:*1012-1017.
- Hwang, W.C., and R.E. Waugh. 1997. Energy of dissociation of lipid bilayer from the membrane skeleton of red blood cells. *Biophysical Journal.* 72:2669-2678.
- Iatridis, J.C., L.A. Setton, M. Weidenbaum, and V.C. Mow. 1997. The viscoelastic behavior of the non-degenerate human lumbar nucleus pulposus in shear. *Journal of Biomechanics.* 30:1005-1013.
- Inagaki, M., Y. Gonda, S. Ando, S. Kitamura, Y. Nishi, and C. Sato. 1989. Regulation of assembly-disassembly of intermediate filaments in vitro. *Cell Struct Funct.* 14:279-86.
- Ingber, D.E. 1993. Cellular tensegrity: defining new rules of biological design that govern the cytoskeleton. *J Cell Sci.* 104 (Pt 3):613-27.
- Ingber, D.E. 1997. Tensegrity: the architectural basis of cellular mechanotransduction. *Annu Rev Physiol.* 59:575-99.
- Ingber, D.E. 2005. Mechanical control of tissue growth: function follows form. *Proc Natl Acad Sci U S A.* 102:11571-2.

- Ingber, D.E. 2006. Cellular mechanotransduction: putting all the pieces together again. *Faseb J.* 20:811-27.
- Isambert, H., and A.C. Maggs. 1996. Dynamics and Rheology of Actin Solutions. *Macromolecules.* 29:1036-1040.
- Isambert, H., P. Venier, A.C. Maggs, A. Fattoum, R. Kassab, D. Pantaloni, and M.F. Carlier. 1995. Flexibility of actin filaments derived from thermal fluctuations. Effect of bound nucleotide, phalloidin, and muscle regulatory proteins. *J Biol Chem.* 270:11437-44.
- Itano, N., S. Okamoto, D. Zhang, S.A. Lipton, and E. Ruoslahti. 2003. Cell spreading controls endoplasmic and nuclear calcium: a physical gene regulation pathway from the cell surface to the nucleus. *Proc Natl Acad Sci U S A.* 100:5181-6.
- Jackson, G.W., and D.F. James. 1986. The Permeability of Fibrous Porous-Media. *Canadian Journal of Chemical Engineering.* 64:364-374.
- Jadhav, S., C.D. Eggleton, and K. Konstantopoulos. 2005. A 3-D computational model predicts that cell deformation affects selectin-mediated leukocyte rolling. *Biophysical Journal.* 88:96-104.
- Janmey, P.A. 2000. Actin Filaments. In *Biophysics Textbook On-Line.* Biophysical Society.
- Janmey, P.A., E.J. Amis, and J.D. Ferry. 1983. Rheology of Fibrin Clots. VI. Stress Relaxation, Creep, and Differential Dynamic Modulus of Fine Clots in Large Shearing Deformations. *Journal of Rheology.* 27:135-153.
- Janmey, P.A., U. Euteneuer, P. Traub, and M. Schliwa. 1991. Viscoelastic properties of vimentin compared with other filamentous biopolymer networks. *J Cell Biol.* 113:155-60.
- Janmey, P.A., S. Hvidt, J. Kas, D. Lerche, A. Maggs, E. Sackmann, M. Schliwa, and T.P. Stossel. 1994. The mechanical properties of actin gels. Elastic modulus and filament motions. *J Biol Chem.* 269:32503-13.
- Janmey, P.A., S. Hvidt, J. Peetermans, J. Lamb, J.D. Ferry, and T.P. Stossel. 1988. Viscoelasticity of F-Actin and F-Actin Gelsolin Complexes. *Biochemistry.* 27:8218-8227.
- Janmey, P.A., M.E. McCormick, S. Rammensee, J.L. Leight, P.C. Georges, and F.C. Mackintosh. 2007. Negative normal stress in semiflexible biopolymer gels. *Nature Materials.* 6:48-51.
- Janmey, P.A., and C.F. Schmidt. 2006. Experimental measurements of intracellular mechanics. In *Cytoskeletal mechanics : models and measurements.* M.K. Mofrad and R.D. Kamm, editors. Cambridge University Press, Cambridge.

- Janson, M.E., and M. Dogterom. 2004. A bending mode analysis for growing microtubules: Evidence for a velocity-dependent rigidity. *Biophysical Journal*. 87:2723-2736.
- Jean, R.P., C.S. Chen, and A.A. Spector. 2005. Finite-element analysis of the adhesion-cytoskeleton-nucleus mechanotransduction pathway during endothelial cell rounding: Axisymmetric model. *Journal of Biomechanical Engineering-Transactions of the Asme*. 127:594-600.
- Jurvelin, J., I. Kiviranta, J. Arokoski, M. Tammi, and H.J. Helminen. 1987. Indentation study of the biochemical properties of articular cartilage in the canine knee. *Eng Med*. 16:15-22.
- Kabsch, W., H.G. Mannherz, D. Suck, E.F. Pai, and K.C. Holmes. 1990. Atomic structure of the actin: DNase I complex. *Nature*. 347:37-44.
- Kamm, R.D. 2006. *Mechanics of the Cytoskeleton*. Massachusetts Institute of Technology, Cambridge, MA.
- Kao, H.P., J.R. Abney, and A.S. Verkman. 1993. Determinants of the translational mobility of a small solute in cell cytoplasm. *J Cell Biol*. 120:175-84.
- Karakesisoglou, I., Y. Yang, and E. Fuchs. 2000. An epidermal plakin that integrates actin and microtubule networks at cellular junctions. *J Cell Biol*. 149:195-208.
- Karcher, H., J. Lammerding, H. Huang, R.T. Lee, R.D. Kamm, and M.R. Kaazempur-Mofrad. 2003. A three-dimensional viscoelastic model for cell deformation with experimental verification. *Biophys J*. 85:3336-49.
- Kas, J., H. Strey, and E. Sackmann. 1994. Direct imaging of reptation for semiflexible actin filaments. *Nature*. 368:226-229.
- Kas, J., H. Strey, J.X. Tang, D. Finger, R. Ezzell, E. Sackmann, and P.A. Janmey. 1996. F-actin, a model polymer for semiflexible chains in dilute, semidilute, and liquid crystalline solutions. *Biophysical Journal*. 70:609-625.
- Kasas, S., A. Kis, B.M. Riederer, L. Forro, G. Dietler, and S. Catsicas. 2004. Mechanical properties of microtubules explored using the finite elements method. *ChemPhysChem*. 5:252-7.
- Kasza, K.E., A.C. Rowat, J. Liu, T.E. Angelini, C.P. Brangwynne, G.H. Koenderink, and D.A. Weitz. 2007. The cell as a material. *Curr Opin Cell Biol*. 19:101-7.
- Keller, H., and P. Eggli. 1998. Actin accumulation in pseudopods or in the tail of polarized Walker carcinosarcoma cells quantitatively correlates with local folding of the cell surface membrane. *Cell Motility and the Cytoskeleton*. 40:342-353.

- Kikumoto, M., M. Kurachi, V. Tosa, and H. Tashiro. 2006. Flexural rigidity of individual microtubules measured by a buckling force with optical traps. *Biophys J.* 90:1687-96.
- Kis, A., S. Kasas, B. Babic, A.J. Kulik, W. Benoit, G.A. Briggs, C. Schonenberger, S. Catsicas, and L. Forro. 2002. Nanomechanics of microtubules. *Phys Rev Lett.* 89:248101.
- Koenderink, G.H., M. Atakhorrami, F.C. MacKintosh, and C.F. Schmidt. 2006. High-Frequency Stress Relaxation in Semiflexible Polymer Solutions and Networks. *Physical Review Letters.* 96:138307-4.
- Kohlrausch, F.W. 1866. Beiträge zur Kenntnis der elastischen Nachwirkung 419. *Pogg. Ann. Phys.* 128:1-19, 207-227, 399-419.
- Kojima, H., A. Ishijima, and T. Yanagida. 1994. Direct Measurement of Stiffness of Single Actin-Filaments with and without Tropomyosin by in-Vitro Nanomanipulation. *Proceedings of the National Academy of Sciences of the United States of America.* 91:12962-12966.
- Kovac, J., and C.C. Crabb. 1982. Modified Gaussian Model for Rubber Elasticity .2. The Wormlike Chain. *Macromolecules.* 15:537-541.
- Kratky, O., and G. Porod. 1949. Röntgenuntersuchung gelöster Fadenmoleküle. *Rec. Trav. Chim. Pays-Bas.* 68:1106-1123.
- Kremser, C., T.R. Trieb, W. Judmaier, A.F. DeVries, D. Sahani, S. Kalva, and P.F. Hahn. 2006. Assessing Tumor Perfusion and Treatment Response in Rectal Cancer. *Radiology.* 238:756-757.
- Kröner, E. 1959. Allgemeine Kontinuumstheorie der Versetzungen und Eigenspannungen. *Archive for Rational Mechanics and Analysis.* 4:273-334.
- Kroy, K., and E. Frey. 1996. Force-Extension Relation and Plateau Modulus for Wormlike Chains. *Physical Review Letters.* 77:306-309.
- Kuchnir Fygenon, D., M. Elbaum, B. Shraiman, and A. Libchaber. 1997. Microtubules and vesicles under controlled tension. *Physical Review E.* 55:850.
- Kuhl, E., K. Garikipati, E.M. Arruda, and K. Gosh. 2005. Remodeling of biological tissue: Mechanically induced reorientation of a transversely isotropic chain network. *Journal of the Mechanics and Physics of Solids.* 53:1552-1573.
- Kuhlman, P.A., J. Ellis, D.R. Critchley, and C.R. Bagshaw. 1994. The kinetics of the interaction between the actin-binding domain of alpha-actinin and F-actin. *FEBS Lett.* 339:297-301.

- Kuhn, W., and F. Grün. 1942. Beziehungen zwischen elastischen Konstanten und Dehnungsdoppelbrechung hochelastischer Stoffe. *Colloid & Polymer Science*. 101:248-271.
- Kuntz, R.M., and W.M. Saltzman. 1997. Neutrophil motility in extracellular matrix gels: mesh size and adhesion affect speed of migration. *Biophys. J.* 72:1472-1480.
- Kurachi, M., M. Hoshi, and H. Tashiro. 1995. Buckling of a single microtubule by optical trapping forces: direct measurement of microtubule rigidity. *Cell Motil Cytoskeleton*. 30:221-8.
- Kurz, J.C., and R.C. Williams. 1995. Microtubule-Associated Proteins and the Flexibility of Microtubules. *Biochemistry*. 34:13374-13380.
- Kwan, M.K., W.M. Lai, and V.C. Mow. 1990. A finite deformation theory for cartilage and other soft hydrated connective tissues--I. Equilibrium results. *J Biomech*. 23:145-55.
- Kwan, M.K., T.H. Lin, and S.L. Woo. 1993. On the viscoelastic properties of the anteromedial bundle of the anterior cruciate ligament. *J Biomech*. 26:447-52.
- Lai, W.M., J.S. Hou, and V.C. Mow. 1991. A triphasic theory for the swelling and deformation behaviors of articular cartilage. *J Biomech Eng*. 113:245-58.
- Lai, W.M., and V.C. Mow. 1980. Drag-Induced Compression of Articular-Cartilage during a Permeation Experiment. *Biorheology*. 17:111-123.
- Lakes, R.S., and R. Vanderby. 1999. Interrelation of Creep and Relaxation: A Modeling Approach for Ligaments. *Journal of Biomechanical Engineering*. 121:612-615.
- Landau, L.D., and E.M. Lifshitz. 1951. Course of theoretical physics. Volume 5, Statistical physics, Part I. Addison-Wesley Pub. Co., Reading, Mass. (1974 reprint). xii, 484 pp.
- Lang, T., I. Wacker, I. Wunderlich, A. Rohrbach, G. Giese, T. Soldati, and W. Almers. 2000. Role of Actin Cortex in the Subplasmalemmal Transport of Secretory Granules in PC-12 Cells. *Biophys. J.* 78:2863-2877.
- Langholz, O., D. Rockel, C. Mauch, E. Kozłowska, I. Bank, T. Krieg, and B. Eckes. 1995. Collagen and collagenase gene expression in three-dimensional collagen lattices are differentially regulated by alpha 1 beta 1 and alpha 2 beta 1 integrins. *J Cell Biol*. 131:1903-15.
- Lauffenburger, D.A. 1991. Models for Receptor-Mediated Cell Phenomena: Adhesion and Migration. *Annual Review of Biophysics and Biophysical Chemistry*. 20:387-414.
- Lauffenburger, D.A. 1996. Cell motility. Making connections count. *Nature*. 383:390-1.

- Ledoux, W.R., D.F. Meaney, and H.J. Hillstrom. 2004. A Quasi-Linear, Viscoelastic, Structural Model of the Plantar Soft Tissue With Frequency-Sensitive Damping Properties. *Journal of Biomechanical Engineering*. 126:831-837.
- Lee, E.H. 1969. Elastic plastic deformation at finite strain. *ASME Journal of Applied Mechanics*. 36:1-6.
- Lee, H., and R.D. Kamm. 2008. Rheology of F-actin networks with filamin and streptavidin cross-links, Unpublished work. MIT.
- Lee, J.S.H., P. Panorchan, C.M. Hale, S.B. Khatau, T.P. Kole, Y. Tseng, and D. Wirtz. 2006. Ballistic intracellular nanorheology reveals ROCK-hard cytoplasmic stiffening response to fluid flow. *Journal of Cell Science*. 119:1760-1768.
- Lee, V.M.Y. 1995. Disruption of the cytoskeleton in Alzheimer's disease. *Current Opinion in Neurobiology*. 5:663-668.
- Lemler, M.S., R.D. Bies, M.G. Frid, A. Sastravaha, L.S. Zisman, T. Bohlmeier, A.M. Gerdes, J.T. Reeves, and K.R. Stenmark. 2000. Myocyte cytoskeletal disorganization and right heart failure in hypoxia-induced neonatal pulmonary hypertension. *Am J Physiol Heart Circ Physiol*. 279:H1365-1376.
- Lempriere, B.M. 1968. Poisson's ratio in orthotropic materials. *AIAA Journal*. 6:2226-2227.
- Leshansky, A.M. 2006. Actin-based propulsion of a microswimmer. *Phys Rev E Stat Nonlin Soft Matter Phys*. 74:012901.
- Leung, C.L., D. Sun, M. Zheng, D.R. Knowles, and R.K. Liem. 1999. Microtubule actin cross-linking factor (MACF): a hybrid of dystonin and dystrophin that can interact with the actin and microtubule cytoskeletons. *J Cell Biol*. 147:1275-86.
- Levine, A.J., and T.C. Lubensky. 2000. One- and two-particle microrheology. *Physical Review Letters*. 85:1774-1777.
- Li, J., M. Dao, C.T. Lim, and S. Suresh. 2005a. Spectrin-Level Modeling of the Cytoskeleton and Optical Tweezers Stretching of the Erythrocyte. *Biophys. J*. 88:3707-3719.
- Li, J., G. Lykotrafitis, M. Dao, and S. Suresh. 2007. Cytoskeletal dynamics of human erythrocyte. *PNAS*. 104:4937-4942.
- Li, S., J.L. Guan, and S. Chien. 2005b. Biochemistry and biomechanics of cell motility. *Annual Review of Biomedical Engineering*. 7:105-150.
- Li, S., N.F. Huang, and S. Hsu. 2005c. Mechanotransduction in endothelial cell migration. *Journal of Cellular Biochemistry*. 96:1110-1126.

- Lim, C.T., E.H. Zhou, and S.T. Quek. 2006. Mechanical models for living cells--a review. *Journal of Biomechanics*. 39:195-216.
- Lin-Gibson, S., J.A. Pathak, E.A. Grulke, H. Wang, and E.K. Hobbie. 2004. Elastic Flow Instability in Nanotube Suspensions. *Physical Review Letters*. 92:048302.
- Liphardt, J., B. Onoa, S.B. Smith, I.J. Tinoco, and C. Bustamante. 2001. Reversible unfolding of single RNA molecules by mechanical force. *Science*. 292:733-7.
- Lipowsky, H.H., D. Riedel, and G.S. Shi. 1991. In vivo mechanical properties of leukocytes during adhesion to venular endothelium. *Biorheology*. 28:53-64.
- Liu, J., M.L. Gardel, K. Kroy, E. Frey, B.D. Hoffman, J.C. Crocker, A.R. Bausch, and D.A. Weitz. 2006. Microrheology probes length scale dependent rheology. *Phys Rev Lett*. 96:118104.
- Liu, X.M., and G.H. Pollack. 2002. Mechanics of F-actin characterized with microfabricated cantilevers. *Biophysical Journal*. 83:2705-2715.
- Lodish, H.F. 2000. Molecular cell biology. W.H. Freeman. xxxvi, 1084, G-17, I-36 p. : ill. (some col.); cm. 1 computer laser optical disc (4 3/4 in.).
- Lodish, H.F., P.T. Matsudaira, C. Kaiser, and M. Krieger. 2004. Molecular cell biology. W.H. Freeman and Company, New York. 1 v. (various pagings) pp.
- Luby-Phelps, K., D.L. Taylor, and F. Lanni. 1986. Probing the structure of cytoplasm. *J Cell Biol*. 102:2015-22.
- Lyass, L.A., A.D. Bershadsky, J.M. Vasiliev, and I.M. Gelfand. 1988. Microtubule-dependent effect of phorbol ester on the contractility of cytoskeleton of cultured fibroblasts. *Proc Natl Acad Sci U S A*. 85:9538-41.
- MacKintosh, F.C. 2006. Polymer-based models of cytoskeletal networks. *In Cytoskeletal mechanics : models and measurements*. M.K. Mofrad and R.D. Kamm, editors. Cambridge University Press, Cambridge.
- MacKintosh, F.C., J. Kas, and P.A. Janmey. 1995. Elasticity of semiflexible biopolymer networks. *Physical Review Letters*. 75:4425-4428.
- Mahadevan, L., and P. Matsudaira. 2000. Motility powered by supramolecular springs and ratchets. *Science*. 288:95-100.
- Mak, A.F. 1986. The Apparent Viscoelastic Behavior of Articular-Cartilage - the Contributions from the Intrinsic Matrix Viscoelasticity and Interstitial Fluid-Flows. *Journal of Biomechanical Engineering-Transactions of the Asme*. 108:123-130.

- Mandeville, J.T., M.A. Lawson, and F.R. Maxfield. 1997. Dynamic imaging of neutrophil migration in three dimensions: mechanical interactions between cells and matrix. *J Leukoc Biol.* 61:188-200.
- Maniotis, A.J., C.S. Chen, and D.E. Ingber. 1997. Demonstration of mechanical connections between integrins, cytoskeletal filaments, and nucleoplasm that stabilize nuclear structure. *Proc Natl Acad Sci U S A.* 94:849-54.
- Mansour, J.M., and V.C. Mow. 1976. The permeability of articular cartilage under compressive strain and at high pressures. *J Bone Joint Surg Am.* 58:509-16.
- Marko, J.F., and E.D. Siggia. 1995. Stretching DNA. *Macromolecules.* 28:209-212.
- Martin, P. 1997. Wound Healing--Aiming for Perfect Skin Regeneration. *Science.* 276:75-81.
- Mason, T.G., H. Gang, and D.A. Weitz. 1997. Diffusing-wave-spectroscopy measurements of viscoelasticity of complex fluids. *Journal of the Optical Society of America a-Optics Image Science and Vision.* 14:139-149.
- McCue, S., S. Noria, and B.L. Langille. 2004. Shear-Induced Reorganization of Endothelial Cell Cytoskeleton and Adhesion Complexes. *Trends in Cardiovascular Medicine.* 14:143-151.
- McCutchen, C.W. 1962. The frictional properties of animal joints. *Wear.* 5(1):1-17.
- McElfresh, M., E. Baesu, R. Balhorn, J. Belak, M.J. Allen, and R.E. Rudd. 2002. Combining constitutive materials modeling with atomic force microscopy to understand the mechanical properties of living cells. *Proceedings of the National Academy of Sciences of the United States of America.* 99:6493-6497.
- McGarry, J.P., B.P. Murphy, and P.E. McHugh. 2005. Computational mechanics modelling of cell-substrate contact during cyclic substrate deformation. *Journal of the Mechanics and Physics of Solids.* 53:2597-2637.
- McMurray, C.T. 2000. Neurodegeneration: diseases of the cytoskeleton? *Cell Death Differ.* 7:861-5.
- Medalia, O., I. Weber, A.S. Frangakis, D. Nicastro, G. Gerisch, and W. Baumeister. 2002. Macromolecular architecture in eukaryotic cells visualized by cryoelectron tomography. *Science.* 298:1209-13.
- Mickey, B., and J. Howard. 1995. Rigidity of Microtubules Is Increased by Stabilizing Agents. *Journal of Cell Biology.* 130:909-917.
- Mijailovich, S.M., M. Kojic, M. Zivkovic, B. Fabry, and J.J. Fredberg. 2002. A finite element model of cell deformation during magnetic bead twisting. *Journal of Applied Physiology.* 93:1429-1436.

- Miller, M.J., S.H. Wei, I. Parker, and M.D. Cahalan. 2002. Two-Photon Imaging of Lymphocyte Motility and Antigen Response in Intact Lymph Node. *Science*. 296:1869-1873.
- Mills, J.C., N.L. Stone, J. Erhardt, and R.N. Pittman. 1998. Apoptotic membrane blebbing is regulated by myosin light chain phosphorylation. *J Cell Biol*. 140:627-36.
- Mills, J.P., L. Qie, M. Dao, C.T. Lim, and S. Suresh. 2004. Nonlinear Elastic and Viscoelastic Deformation of the Human Red Blood Cell with Optical Tweezers. *Molecular & Cellular Biomechanics*. 1:169-180.
- Mizuno, D., C. Tardin, C.F. Schmidt, and F.C. MacKintosh. 2007. Nonequilibrium mechanics of active cytoskeletal networks. *Science*. 315:370-373.
- Mizushima-Sugano, J., T. Maeda, and T. Miki-Noumura. 1983. Flexural rigidity of singlet microtubules estimated from statistical analysis of their contour lengths and end-to-end distances. *Biochim Biophys Acta*. 755:257-62.
- Mofrad, M.R.K., H. Karcher, and R. Kamm. 2006. Continuum elastic or viscoelastic models for the cell. In *Cytoskeletal mechanics : models and measurements*. M.K. Mofrad and R.D. Kamm, editors. Cambridge University Press, Cambridge.
- Mogilner, A., and G. Oster. 1996. Cell motility driven by actin polymerization. *Biophys. J*. 71:3030-3045.
- Mogilner, A., and G. Oster. 2003. Polymer motors: pushing out the front and pulling up the back. *Curr Biol*. 13:R721-33.
- Mokdad, M., A. Courtois, J.F. Georjgin, I. Petre-Lazar, and D. Dauffer. 2004. Effect of the casting defects on the ageing of the natural draught cooling towers. In *Natural Draught Cooling Towers*. Routledge. 355 - 362.
- Montesi, A., A.A. Peña, and M. Pasquali. 2004. Vorticity Alignment and Negative Normal Stresses in Sheared Attractive Emulsions. *Physical Review Letters*. 92:058303.
- Mow, V.C., M.C. Gibbs, W.M. Lai, W.B. Zhu, and K.A. Athanasiou. 1989. Biphasic indentation of articular cartilage--II. A numerical algorithm and an experimental study. *J Biomech*. 22:853-61.
- Mow, V.C., S.C. Kuei, W.M. Lai, and C.G. Armstrong. 1980. Biphasic Creep and Stress-Relaxation of Articular-Cartilage in Compression - Theory and Experiments. *Journal of Biomechanical Engineering-Transactions of the Asme*. 102:73-84.
- Mucke, N., L. Kreplak, R. Kirmse, T. Wedig, H. Herrmann, U. Aebi, and J. Langowski. 2004. Assessing the flexibility of intermediate filaments by atomic force microscopy. *J Mol Biol*. 335:1241-50.

- Mulliken, A.D., and M.C. Boyce. 2006. Mechanics of the rate-dependent elastic-plastic deformation of glassy polymers from low to high strain rates. *International Journal of Solids and Structures*. 43:1331-1356.
- N'Dri, N.A., W. Shyy, and R. Tran-Son-Tay. 2003. Computational Modeling of Cell Adhesion and Movement Using a Continuum-Kinetics Approach. *Biophys. J.* 85:2273-2286.
- Nagatomi, J., D.C. Gloeckner, M.B. Chancellor, W.C. deGroat, and M.S. Sacks. 2004. Changes in the Biaxial Viscoelastic Response of the Urinary Bladder Following Spinal Cord Injury. *Annals of Biomedical Engineering*. 32:1409-1419.
- Nakata, T., and N. Hirokawa. 1992. Organization of cortical cytoskeleton of cultured chromaffin cells and involvement in secretion as revealed by quick-freeze, deep-etching, and double-label immunoelectron microscopy. *J. Neurosci.* 12:2186-2197.
- Needham, D., and R.M. Hochmuth. 1992. A Sensitive Measure of Surface Stress in the Resting Neutrophil. *Biophysical Journal*. 61:1664-1670.
- Nelson, C.M., R.P. Jean, J.L. Tan, W.F. Liu, N.J. Sniadecki, A.A. Spector, and C.S. Chen. 2005. Emergent patterns of growth controlled by multicellular form and mechanics. *Proceedings of the National Academy of Sciences of the United States of America*. 102:11594-11599.
- Netti, P.A., L.T. Baxter, Y. Boucher, R. Skalak, and R.K. Jain. 1995. Time-dependent Behavior of Interstitial Fluid Pressure in Solid Tumors: Implications for Drug Delivery. *Cancer Res.* 55:5451-5458.
- Netti, P.A., L.M. Hamberg, J.W. Babich, D. Kierstead, W. Graham, G.J. Hunter, G.L. Wolf, A. Fischman, Y. Boucher, and R.K. Jain. 1999. Enhancement of fluid filtration across tumor vessels: Implication for delivery of macromolecules. *Proceedings of the National Academy of Sciences*. 96:3137-3142.
- Ng, L., H.H. Hung, A. Sprunt, S. Chubinskaya, C. Ortiz, and A. Grodzinsky. 2007. Nanomechanical properties of individual chondrocytes and their developing growth factor-stimulated pericellular matrix. *Journal of Biomechanics*. 40:1011-1023.
- Nguyen, H.V., and D.F. Durso. 1983. Absorption of Water by Fiber Webs - an Illustration of Diffusion Transport. *Tappi Journal*. 66:76-79.
- Niederman, R., P.C. Amrein, and J. Hartwig. 1983. Three-dimensional structure of actin filaments and of an actin gel made with actin-binding protein. *J Cell Biol.* 96:1400-13.
- Nigel J Cairns, V.M.Y.L.J.Q.T. 2004. The cytoskeleton in neurodegenerative diseases. *The Journal of Pathology*. 204:438-449.

- O'Brien, F.J., E. Farrell, M.A. Waller, I. Connell, D. O'Mahoney, J.P. McGarry, B.P. Murphy, P.E. McHugh, V.A. Campbell, and P.J. Prendergast. 2004. Scaffolds and cells: preliminary biomechanical analysis and results for the use of a collagen-GAG scaffold for bone tissue engineering. *In Topics in bio-mechanical engineering : proceedings of the 1st symposium on biomechanical engineering held between the Trinity Centre for Bioengineering and the National Centre for Biomedical Engineering Science under the Programme for Research in Third Level Institutions.* P.J. Prendergast and P.E. McHugh, editors. Galway, Dublin. 167-183.
- Oda, T., K. Makino, I. Yamashita, K. Namba, and Y. Maeda. 1998. Effect of the Length and Effective Diameter of F-Actin on the Filament Orientation in Liquid Crystalline Sols Measured by X-Ray Fiber Diffraction. *Biophys. J.* 75:2672-2681.
- Odijk, T. 1995. Stiff Chains and Filaments under Tension. *Macromolecules.* 28:7016-7018.
- Ohashi, T., Y. Ishii, Y. Ishikawa, T. Matsumoto, and M. Sato. 2002. Experimental and numerical analyses of local mechanical properties measured by atomic force microscopy for sheared endothelial cells. *Bio-Medical Materials and Engineering.* 12:319-327.
- Ohayon, J., P. Tracqui, R. Fodil, S. Fereol, V.M. Laurent, E. Planus, and D. Isabey. 2004. Analysis of nonlinear responses of adherent epithelial cells probed by magnetic bead twisting: A finite element model based on a homogenization approach. *Journal of Biomechanical Engineering-Transactions of the Asme.* 126:685-698.
- Onck, P.R., T. Koeman, T. van Dillen, and E. van der Giessen. 2005. Alternative explanation of stiffening in cross-linked semiflexible networks. *Phys Rev Lett.* 95:178102.
- Oosawa, F. 1977. Actin-Actin Bond Strength and Conformational Change of F-Actin. *Biorheology.* 14:11-19.
- Oosawa, F. 1980. The flexibility of F-actin. *Biophysical Chemistry.* 11:443-446.
- Oosawa, F., Y. Maeda, S. Fujime, S. Ishiwata, T. Yanagida, and M. Taniguchi. 1977. Dynamic characteristics of F-actin and thin filaments in vivo and in vitro. *J Mechanochem Cell Motil.* 4:63-78.
- Oster, G.F., and G.M. Odell. 1984. The Mechanochemistry of Cytogels. *Physica D.* 12:333-350.
- Oster, G.F., and A.S. Perelson. 1985. Cell Spreading and Motility - a Model Lamellipod. *Journal of Mathematical Biology.* 21:383-388.

- Oster, G.F., A.S. Perelson, and L.G. Tilney. 1982. A Mechanical Model for Elongation of the Acrosomal Process in Thyone Sperm. *Journal of Mathematical Biology*. 15:259-265.
- Oster, G.F., and A.S. Perelson. 1987. The physics of cell motility. *J. Cell Sci.* . 8:35-54.
- Ott, A., M. Magnasco, A. Simon, and A. Libchaber. 1993. Measurement of the persistence length of polymerized actin using fluorescence microscopy. *Phys Rev E Stat Phys Plasmas Fluids Relat Interdiscip Topics*. 48:R1642-R1645.
- Oza, A., J.R. Vanderby, and R.S. Lakes. 2006. Generalized solution for predicting relaxation from creep in soft tissue: Application to ligament. *International Journal of Mechanical Sciences*. 48:662-673.
- Palmer, J.S., and M.C. Boyce. 2008. Constitutive modeling of the stress-strain behavior of F-actin filament networks. *Acta Biomaterialia*. 4:597-612.
- Pampaloni, F., G. Lattanzi, A. Jonas, T. Surrey, E. Frey, and E.-L. Florin. 2005. Elastic properties of grafted microtubules.
- Pampaloni, F., G. Lattanzi, A. Jonas, T. Surrey, E. Frey, and E.L. Florin. 2006. Thermal fluctuations of grafted microtubules provide evidence of a length-dependent persistence length. *Proc Natl Acad Sci U S A*.
- Pantaloni, D., C. Le Clairche, and M.F. Carrier. 2001. Mechanism of actin-based motility. *Science*. 292:1502-6.
- Parkhurst, M.R., and W.M. Saltzman. 1992. Quantification of human neutrophil motility in three-dimensional collagen gels. Effect of collagen concentration. *Biophys. J*. 61:306-315.
- Paszek, M.J., and V.M. Weaver. 2004. The tension mounts: Mechanics meets morphogenesis and malignancy. *Journal of Mammary Gland Biology and Neoplasia*. 9:325-342.
- Perrault, C.M., E.J. Bray, N. Didier, C.K. Ozaki, and R. Tran-Son-Tay. 2004. Altered rheology of lymphocytes in the diabetic mouse. *Diabetologia*. 47:1722-6.
- Piekenbrock, T., and E. Sackmann. 1992. Quasielastic light scattering study of thermal excitations of F-actin solutions and of growth kinetics of actin filaments. *Biopolymers*. 32:1471-1489.
- Pioletti, D.P., and L.R. Rakotomanana. 2000. Non-linear viscoelastic laws for soft biological tissues. *European Journal of Mechanics - A/Solids*. 19:749-759.
- Pioletti, D.P., L.R. Rakotomanana, and P.F. Leyvraz. 1999. Strain rate effect on the mechanical behavior of the anterior cruciate ligament-bone complex. *Medical Engineering & Physics*. 21:95-100.

- Podolski, J.L., and T.L. Steck. 1990. Length distribution of F-actin in Dictyostelium discoideum. *J Biol Chem.* 265:1312-8.
- Pollard, T.D., and G.G. Borisy. 2003. Cellular motility driven by assembly and disassembly of actin filaments. *Cell.* 112:453-65.
- Portet, S., J. Vassy, C.W. Hogue, J. Arino, and O. Arino. 2004. Intermediate filament networks: in vitro and in vivo assembly models. *C R Biol.* 327:970-6.
- Pourati, J., A. Maniotis, D. Spiegel, J.L. Schaffer, J.P. Butler, J.J. Fredberg, D.E. Ingber, D. Stamenovic, and N. Wang. 1998a. Is cytoskeletal tension a major determinant of cell deformability in adherent endothelial cells? *Am J Physiol.* 274:C1283-9.
- Pourati, J., A. Maniotis, D. Spiegel, J.L. Schaffer, J.P. Butler, J.J. Fredberg, D.E. Ingber, D. Stamenovic, and N. Wang. 1998b. Is cytoskeletal tension a major determinant of cell deformability in adherent endothelial cells? *American Journal of Physiology-Cell Physiology.* 43:C1283-C1289.
- Poynting, J.H. 1909. On Pressure Perpendicular to the Shear Planes in Finite Pure Shears, and on the Lengthening of Loaded Wires When Twisted. *Proceedings of the Royal Society of London. Series A, Containing Papers of a Mathematical and Physical Character.* 82:546-559.
- Provenzano, P., R. Lakes, T. Keenan, and R. vanderby. 2001. Nonlinear Ligament Viscoelasticity. *Annals of Biomedical Engineering.* 29:908-914.
- Provenzano, P.P., R.S. Lakes, D.T. Corr, and R. Vanderby. 2002. Application of nonlinear viscoelastic models to describe ligament behavior. *Biomechanics and Modeling in Mechanobiology.* 1:45-57.
- Pryzwansky, K.B., M. Schliwa, and K.R. Porter. 1983. Comparison of the three-dimensional organization of unextracted and Triton-extracted human neutrophilic polymorphonuclear leukocytes. *Eur J Cell Biol.* 30:112-25.
- Puso, M.A., and J.A. Weiss. 1998. Finite Element Implementation of Anisotropic Quasi-Linear Viscoelasticity Using a Discrete Spectrum Approximation. *Journal of Biomechanical Engineering.* 120:62-70.
- Qi, H.J., and M.C. Boyce. 2005. Stress-strain behavior of thermoplastic polyurethanes. *Mechanics of Materials.* 37:817-839.
- Qi, H.J., C. Ortiz, and M.C. Boyce. 2006. Mechanics of biomacromolecular networks containing folded domains. *Journal of Engineering Materials and Technology-Transactions of the Asme.* 128:509-518.
- Quinlan, M.E., J.E. Heuser, E. Kerkhoff, and R.D. Mullins. 2005. Drosophila Spire is an actin nucleation factor. *Nature.* 433:382-8.

- Rafelski, S.M., and J.A. Theriot. 2004. Crawling toward a unified model of cell mobility: spatial and temporal regulation of actin dynamics. *Annu Rev Biochem.* 73:209-39.
- Rahli, O., L. Tadrist, and M. Miscevic. 1996. Experimental analysis of fibrous porous media permeability. *Aiche Journal.* 42:3547-3549.
- Ridley, A.J., M.A. Schwartz, K. Burridge, R.A. Firtel, M.H. Ginsberg, G. Borisy, J.T. Parsons, and A.R. Horwitz. 2003. Cell migration: Integrating signals from front to back. *Science.* 302:1704-1709.
- Rief, M., M. Gautel, F. Oesterhelt, J.M. Fernandez, and H.E. Gaub. 1997. Reversible Unfolding of Individual Titin Immunoglobulin Domains by AFM. *Science.* 276:1109-1112.
- Riveline, D., C.H. Wiggins, R.E. Goldstein, and A. Ott. 1997. Elastohydrodynamic study of actin filaments using fluorescence microscopy. *Physical Review E.* 56:R1330-R1333.
- Rosenbluth, M.J., W.A. Lam, and D.A. Fletcher. 2006. Force microscopy of nonadherent cells: a comparison of leukemia cell deformability. *Biophys J.* 90:2994-3003.
- Roth, V., and V.C. Mow. 1980. The Intrinsic Tensile Behavior of the Matrix of Bovine Articular-Cartilage and Its Variation with Age. *Journal of Bone and Joint Surgery-American Volume.* 62:1102-1117.
- Rubinstein, B., K. Jacobson, and A. Mogilner. 2005. Multiscale Two-Dimensional Modeling of a Motile Simple-Shaped Cell. *Multiscale Modeling & Simulation.* 3:413-439.
- Sahani, D.V., S.P. Kalva, L.M. Hamberg, P.F. Hahn, C.G. Willett, S. Saini, P.R. Mueller, and T.-Y. Lee. 2005. Assessing Tumor Perfusion and Treatment Response in Rectal Cancer with Multisection CT: Initial Observations. *Radiology.* 234:785-792.
- Sarver, J.J., P.S. Robinson, and D.M. Elliott. 2003. Methods for Quasi-Linear Viscoelastic Modeling of Soft Tissue: Application to Incremental Stress-Relaxation Experiments. *Journal of Biomechanical Engineering.* 125:754-758.
- Satcher, R.L., Jr., and C.F. Dewey, Jr. 1996. Theoretical estimates of mechanical properties of the endothelial cell cytoskeleton. *Biophys. J.* 71:109-118.
- Sato, M., K. Nagayama, N. Kataoka, M. Sasaki, and K. Hane. 2000. Local mechanical properties measured by atomic force microscopy for cultured bovine endothelial cells exposed to shear stress. *J Biomech.* 33:127-35.
- Sato, M., D.P. Theret, L.T. Wheeler, N. Ohshima, and R.M. Nerem. 1990. Application of the micropipette technique to the measurement of cultured porcine aortic endothelial cell viscoelastic properties. *J Biomech Eng.* 112:263-8.

- Sauren, A.A., and E.P. Rousseau. 1983. A concise sensitivity analysis of the quasi-linear viscoelastic model proposed by Fung. *J Biomech Eng.* 105:92-5.
- Schaap, I.A.T., C. Carrasco, P.J. de Pablo, F.C. MacKintosh, and C.F. Schmidt. 2006. Elastic Response, Buckling, and Instability of Microtubules under Radial Indentation. *Biophys. J.* 91:1521-1531.
- Scheidegger, A.E. 1974. *The Physics of Flow Through Porous Media.* University of Toronto Press, Toronto.
- Schliwa, M. 1986. *The cytoskeleton : an introductory survey.* New York : Springer-Verlag, Wien. xi, 326 p. pp.
- Schliwa, M., K.B. Pryzwansky, and J. van Blerkom. 1982. Implications of cytoskeletal interactions for cellular architecture and behavior. *Philos Trans R Soc Lond B Biol Sci.* 299:199-205.
- Schmid-Schonbein, G.W. 1990. Leukocyte Biophysics - an Invited Review. *Cell Biophysics.* 17:107-135.
- Schmid-Schonbein, G.W., T. Kosawada, R. Skalak, and S. Chien. 1995. Membrane model of endothelial cells and leukocytes. A proposal for the origin of a cortical stress. *J Biomech Eng.* 117:171-8.
- Schmid-Schonbein, G.W., K.L. Sung, H. Tozeren, R. Skalak, and S. Chien. 1981. Passive mechanical properties of human leukocytes. *Biophys. J.* 36:243-256.
- Setton, L.A., W. Zhu, and V.C. Mow. 1993. The Biphasic Poroviscoelastic Behavior of Articular Cartilage: Role of the Surface Zone in Governing the Compressive Behavior. *J. Biomech.* 26:581-592.
- Shenoy, V.B., and L.B. Freund. 2005. Growth and shape stability of a biological membrane adhesion complex in the diffusion-mediated regime. *Proceedings of the National Academy of Sciences.* 102:3213-3218.
- Shin, D., and K. Athanasiou. 1999. Cytoindentation for obtaining cell biomechanical properties. *Journal of Orthopaedic Research.* 17:880-890.
- Shin, J.H., M.L. Gardel, L. Mahadevan, P. Matsudaira, and D.A. Weitz. 2004. Relating microstructure to rheology of a bundled and cross-linked F-actin network in vitro. *Proc Natl Acad Sci U S A.* 101:9636-41.
- Smith, B.A., B. Tolloczko, J.G. Martin, and P. Grutter. 2005. Probing the Viscoelastic Behavior of Cultured Airway Smooth Muscle Cells with Atomic Force Microscopy: Stiffening Induced by Contractile Agonist. *Biophys. J.* 88:2994-3007.

- Smith, S.B., Y. Cui, and C. Bustamante. 1996. Overstretching B-DNA: the elastic response of individual double-stranded and single-stranded DNA molecules. *Science*. 271:795-9.
- Soltz, M.A., and G.A. Ateshian. 2000. Interstitial fluid pressurization during confined compression cyclical loading of articular cartilage. *Ann Biomed Eng*. 28:150-9.
- Spakowitz, A.J., and Z.-G. Wang. 2005. End-to-end distance vector distribution with fixed end orientations for the wormlike chain model. *Physical Review E (Statistical, Nonlinear, and Soft Matter Physics)*. 72:041802-13.
- Spencer, A.J.M. 1984. Constitutive theory for strongly anisotropic solids. In *Continuum theory of the mechanics of fibre-reinforced composites*. A.J.M. Spencer, editor. Springer-Verlag, Wien. 1-32.
- Stamenovic, D., and D.E. Ingber. 2002. Models of cytoskeletal mechanics of adherent cells. *Biomech Model Mechanobiol*. 1:95-108.
- Stamenovic, D., and N. Wang. 2000. Invited review: Engineering approaches to cytoskeletal mechanics. *Journal of Applied Physiology*. 89:2085-2090.
- Steinmetz, M.O., K.N. Goldie, and U. Aebi. 1997a. A correlative analysis of actin filament assembly, structure, and dynamics. *J Cell Biol*. 138:559-74.
- Steinmetz, M.O., A. Hoenger, D. Stoffler, A.A. Noegel, U. Aebi, and C.-A. Schoenenberger. 2000. Polymerization, three-dimensional structure and mechanical properties of Dictyostelium versus rabbit muscle actin filaments. *Journal of Molecular Biology*. 303:171-184.
- Steinmetz, M.O., D. Stoffler, A. Hoenger, A. Bremer, and U. Aebi. 1997b. Actin: from cell biology to atomic detail. *J Struct Biol*. 119:295-320.
- Stoll, S., J. Delon, T.M. Brotz, and R.N. Germain. 2002. Dynamic Imaging of T Cell-Dendritic Cell Interactions in Lymph Nodes. *Science*. 296:1873-1876.
- Storm, C., J.J. Pastore, F.C. MacKintosh, T.C. Lubensky, and P.A. Janmey. 2005. Nonlinear elasticity in biological gels. *Nature*. 435:191-194.
- Stossel, T.P., J. Condeelis, L. Cooley, J.H. Hartwig, A. Noegel, M. Schleicher, and S.S. Shapiro. 2001. Filamins as integrators of cell mechanics and signalling. *Nat Rev Mol Cell Biol*. 2:138-45.
- Straub, F.B. 1942. Actin. *Stud Inst Med Chem Univ Szeged* II: 1-15.
- Suh, J.-K., and M.R. DiSilvestro. 1999. Biphasic Poroviscoelastic Behavior of Hydrated Biological Soft Tissue. *ASME J. Appl. Mech*. 66:528-535.

- Suh, J.K., and S. Bai. 1997. Biphasic poroviscoelastic behavior of articular cartilage in creep indentation test. *In Proc. 43rd Annual Meeting of the Orthopaedic Research Society*. Vol. 22. p. 823.
- Sumoza-Toledo, A., and L. Santos-Argumedo. 2004. The spreading of B lymphocytes induced by CD44 cross-linking requires actin, tubulin, and vimentin rearrangements. *J Leukoc Biol.* 75:233-239.
- Sund, S.E., and D. Axelrod. 2000. Actin Dynamics at the Living Cell Submembrane Imaged by Total Internal Reflection Fluorescence Photobleaching. *Biophys. J.* 79:1655-1669.
- Sung, K.L., C. Dong, G.W. Schmid-Schonbein, S. Chien, and R. Skalak. 1988. Leukocyte relaxation properties. *Biophys J.* 54:331-6.
- Suresh, S. 2007. Biomechanics and biophysics of cancer cells. *Acta Biomaterialia.* 3:413-438.
- Suresh, S., J. Spatz, J.P. Mills, A. Micoulet, M. Dao, C.T. Lim, M. Beil, and T. Seufferlein. 2005. Connections between single-cell biomechanics and human disease states: gastrointestinal cancer and malaria. *Acta Biomaterialia.* 1:15-30.
- Sverdlik, A., and Y. Lanir. 2002. Time-Dependent Mechanical Behavior of Sheep Digital Tendons, Including the Effects of Preconditioning. *Journal of Biomechanical Engineering.* 124:78-84.
- Svitkina, T.M., A.B. Verkhovsky, and G.G. Borisy. 1996. Plectin sidearms mediate interaction of intermediate filaments with microtubules and other components of the cytoskeleton. *J Cell Biol.* 135:991-1007.
- Swartz, M.A., A. Kaipainen, P.A. Netti, C. Brekken, Y. Boucher, A.J. Grodzinsky, and R.K. Jain. 1999. Mechanics of interstitial-lymphatic fluid transport: theoretical foundation and experimental validation. *Journal of biomechanics.* 32:1297-1307.
- Takebayashi, T., Y. Morita, and F. Oosawa. 1977. Electronmicroscopic investigation of the flexibility of F-actin. *Biochim Biophys Acta.* 492:357-63.
- Tan, J., H. Shen, and W.M. Saltzman. 2001. Micron-scale positioning of features influences the rate of polymorphonuclear leukocyte migration. *Biophys J.* 81:2569-79.
- Terzaghi, K. 1925. *Erdbaumechanik auf Bodenphysikalischer Grundlage*. Franz Deuticke, Vienna.
- Texas Instruments: Thermal Analysis & Rheology. 2008. Rheology Software Models (Oscillation) - RH064, <http://www.tainst.com>.

- Thamilselvan, V., A. Patel, J.V. van Zyp, and M.D. Basson. 2004. Colon cancer cell adhesion in response to Src kinase activation and actin-cytoskeleton by non-laminar shear stress. *Journal of Cellular Biochemistry*. 92:361-371.
- Theoretical Biophysics Group. 2007. Actin-biotin structure. In <http://www.ks.uiuc.edu/Research/vmd/gallery/big.gifs/70.gif>. Beckman Institute, UIUC.
- Theret, D.P., M.J. Levesque, M. Sato, R.M. Nerem, and L.T. Wheeler. 1988. The Application of a Homogeneous Half-Space Model in the Analysis of Endothelial-Cell Micropipette Measurements. *Journal of Biomechanical Engineering-Transactions of the Asme*. 110:190-199.
- Theriot, J.A., T.J. Mitchison, L.G. Tilney, and D.A. Portnoy. 1992. The rate of actin-based motility of intracellular *Listeria monocytogenes* equals the rate of actin polymerization. *Nature*. 357:257-260.
- Therkelsen, S.V. 2005. Constitutive modeling of active polymers In Dept. of Mechanical Engineering. Vol. S.M. Thesis. Massachusetts Institute of Technology, Cambridge, MA. 96.
- Thornton, G.M., C.B. Frank, and N.G. Shrive. 2001. Ligament creep behavior can be predicted from stress relaxation by incorporating fiber recruitment. *Journal of Rheology*. 45:493-507.
- Thornton, G.M., A. Oliynyk, C.B. Frank, and N.G. Shrive. 1997. Ligament creep cannot be predicted from stress relaxation at low stress: A biomechanical study of the rabbit medial collateral ligament. *Journal of Orthopaedic Research*. 15:652-656.
- Thoumine, O., and A. Ott. 1997a. Comparison of the mechanical properties of normal and transformed fibroblasts. *Biorheology*. 34:309-26.
- Thoumine, O., and A. Ott. 1997b. Time scale dependent viscoelastic and contractile regimes in fibroblasts probed by microplate manipulation. *J Cell Sci*. 110 (Pt 17):2109-16.
- Tilney, L.G., and S. Inoue. 1985. Acrosomal reaction of the Thyone sperm. III. The relationship between actin assembly and water influx during the extension of the acrosomal process. *J Cell Biol*. 100:1273-83.
- Toms, S.R., G.J. Dakin, J.E. Lemons, and A.W. Eberhardt. 2002. Quasi-linear viscoelastic behavior of the human periodontal ligament. *J Biomech*. 35:1411-5.
- Torquato, S. 1991. Random heterogeneous media: Microstructure and improved bounds on effective properties. *Appl. Mech. Rev*. 44:37-76.
- Tran-Son-Tay, R., H.C. Kan, H.S. Udaykumar, E. Damay, and W. Shyy. 1998. Rheological modelling of leukocytes. *Med Biol Eng Comput*. 36:246-50.

- Tran-Son-Tay, R., D. Needham, A. Yeung, and R.M. Hochmuth. 1991. Time-dependent recovery of passive neutrophils after large deformation. *Biophys. J.* 60:856-866.
- Tran, P.T., S.F. Parsons, R. Sterba, Z. Wang, M.P. Sheetz, and E.D. Salmon. 1995. Direct Measurement of Microtubule Flexural Rigidity with the Laser Trap. *Molecular Biology of the Cell.* 6:1509-1509.
- Treloar, L.R.G. 1944. Stress-strain data for vulcanized rubber under various types of deformation. *Trans. Faraday Soc.* 40:59-70.
- Treloar, L.R.G. 1958. The physics of rubber elasticity. Clarendon Press, Oxford., 342 pp.
- Treloar, L.R.G. 1975. The physics of rubber elasticity. Clarendon Press, Oxford., xii, 310 p. pp.
- Treloar, L.R.G., and G. Riding. 1979. A Non-Gaussian Theory for Rubber in Biaxial Strain. I. Mechanical Properties. *Proceedings of the Royal Society of London. Series A, Mathematical and Physical Sciences.* 369:261-280.
- Trickey, W.R., F.P. Baaijens, T.A. Laursen, L.G. Alexopoulos, and F. Guilak. 2006. Determination of the Poisson's ratio of the cell: recovery properties of chondrocytes after release from complete micropipette aspiration. *J Biomech.* 39:78-87.
- Trickey, W.R., G.M. Lee, and F. Guilak. 2000. Viscoelastic properties of chondrocytes from normal and osteoarthritic human cartilage. *J Orthop Res.* 18:891-8.
- Trinkaus, J.P. 1973. Surface activity and locomotion of *Fundulus* deep cells during blastula and gastrula stages. *Dev Biol.* 30:69-103.
- Tsang, P.H., G. Li, Y.V. Brun, L.B. Freund, and J.X. Tang. 2006. Adhesion of single bacterial cells in the micronewton range. *Proceedings of the National Academy of Sciences.* 103:5764-5768.
- Tseng, Y., T.P. Kole, and D. Wirtz. 2002a. Micromechanical Mapping of Live Cells by Multiple-Particle-Tracking Microrheology. *Biophys. J.* 83:3162-3176.
- Tseng, Y., J.S. Lee, T.P. Kole, I. Jiang, and D. Wirtz. 2004. Micro-organization and visco-elasticity of the interphase nucleus revealed by particle nanotracking. *J Cell Sci.* 117:2159-67.
- Tseng, Y., B.W. Schafer, S.C. Almo, and D. Wirtz. 2002b. Functional synergy of actin filament cross-linking proteins. *J Biol Chem.* 277:25609-16.
- Tsuda, Y., H. Yasutake, A. Ishijima, and T. Yanagida. 1996. Torsional rigidity of single actin filaments and actin-actin bond breaking force under torsion measured directly by in vitro micromanipulation. *Proceedings of the National Academy of Sciences.* 93:12937-12942.

- Vaziri, A., and A. Gopinath. 2008. Cell and biomolecular mechanics in silico. *Nature Materials*. 7:15-23.
- Vaziri, A., A. Gopinath, and V.S. Deshpande. 2007. Continuum-based computational models for cell and nuclear mechanics. *Journal of Mechanics of Materials and Structures*. 2:1169-1192.
- Venier, P., A.C. Maggs, M.F. Carrier, and D. Pantaloni. 1994. Analysis of microtubule rigidity using hydrodynamic flow and thermal fluctuations. *J Biol Chem*. 269:13353-60.
- Vicente-Manzanares, M., and F. Sanchez-Madrid. 2004. Role of the cytoskeleton during leukocyte responses. *Nature Reviews Immunology*. 4:110-122.
- Vinckier, A., C. Dumortier, Y. Engelborghs, and L. Hellemans. 1996. Dynamical and mechanical study of immobilized microtubules with atomic force microscopy. *Journal of Vacuum Science & Technology B*. 14:1427-1431.
- Wachsstock, D.H., W.H. Schwarz, and T.D. Pollard. 1994. Cross-linker dynamics determine the mechanical properties of actin gels. *Biophys J*. 66:801-9.
- Wagner, O.I., S. Rammensee, N. Korde, Q. Wen, J.F. Leterrier, and P.A. Janmey. 2007. Softness, strength and self-repair in intermediate filament networks. *Exp Cell Res*. 313:2228-35.
- Wakabayashi, K., Y. Sugimoto, H. Tanaka, Y. Ueno, Y. Takezawa, and Y. Amemiya. 1994. X-ray diffraction evidence for the extensibility of actin and myosin filaments during muscle contraction. *Biophys. J*. 67:2422-2435.
- Walker, K., and M.F. Olson. 2005. Targeting Ras and Rho GTPases as opportunities for cancer therapeutics. *Current Opinion in Genetics & Development*. 15:62-68.
- Wang, M.C., and E. Guth. 1952. Statistical theory of networks on non-Gaussian flexible chains. *J. Chem. Phys*. 20:1144-1157.
- Wang, M.D., H. Yin, R. Landick, J. Gelles, and S.M. Block. 1997. Stretching DNA with optical tweezers. *Biophysical Journal*. 72:1335-1346.
- Wang, N., K. Naruse, D. Stamenovic, J.J. Fredberg, S.M. Mijailovich, I.M. Toric-Norrelykke, T. Polte, R. Mannix, and D.E. Ingber. 2001. Mechanical behavior in living cells consistent with the tensegrity model. *Proceedings of the National Academy of Sciences of the United States of America*. 98:7765-7770.
- Wang, N., and D. Stamenovic. 2000. Contribution of intermediate filaments to cell stiffness, stiffening, and growth. *Am J Physiol Cell Physiol*. 279:C188-94.

- Wang, N., I.M. Tolic-Norrelykke, J. Chen, S.M. Mijailovich, J.P. Butler, J.J. Fredberg, and D. Stamenovic. 2002a. Cell prestress. I. Stiffness and prestress are closely associated in adherent contractile cells. *Am J Physiol Cell Physiol*. 282:C606-16.
- Wang, W., J.B. Wyckoff, V.C. Frohlich, Y. Oleynikov, S. Huttelmaier, J. Zavadil, L. Cermak, E.P. Bottinger, R.H. Singer, J.G. White, J.E. Segall, and J.S. Condeelis. 2002b. Single cell behavior in metastatic primary mammary tumors correlated with gene expression patterns revealed by molecular profiling. *Cancer Res*. 62:6278-88.
- Warren, W.E., and A.M. Kraynik. 1997. Linear elastic behavior of a low-density Kelvin foam with open cells. *Journal of Applied Mechanics-Transactions of the Asme*. 64:787-794.
- Waterston, J.J. 1846. On the physics of media that are composed of free and elastic molecules in a state of motion. *Roy. Soc. Proc.* . 5:604.
- Waugh, R., and E.A. Evans. 1979. Thermoelasticity of red blood cell membrane. *Biophys J*. 26:115-31.
- Weber, W. 1841. Ueber die Elasticität fester Körper. *Ann. Phys. Chem*. 54:1.
- Weiss, J.A., and J.C. Gardiner. 2001. Computational modeling of ligament mechanics. *Crit Rev Biomed Eng*. 29:303-71.
- Westlin, W.F., J.M. Kiely, and M.A. Gimbrone, Jr. 1992. Interleukin-8 induces changes in human neutrophil actin conformation and distribution: relationship to inhibition of adhesion to cytokine-activated endothelium. *J Leukoc Biol*. 52:43-51.
- Wiggins, C.H., D. Riveline, A. Ott, and R.E. Goldstein. 1998. Trapping and wiggling: Elastohydrodynamics of driven microfilaments. *Biophysical Journal*. 74:1043-1060.
- Wilhelm, J., and E. Frey. 2003. Elasticity of stiff polymer networks. *Physical Review Letters*. 91:-.
- Wilson, W. 2005. An Explanation for the Onset of Mechanically Induced Cartilage Damage. In *Biomedical Engineering*. Vol. Ph.D. Technische Universiteit Eindhoven, Eindhoven, The Netherlands. 161.
- Wilson, W., C.C. van Donkelaar, and J.M. Huyghe. 2005a. A comparison between mechano-electrochemical and biphasic swelling theories for soft hydrated tissues. *Journal of Biomechanical Engineering-Transactions of the Asme*. 127:158-165.
- Wilson, W., C.C. van Donkelaar, B. van Rietbergen, and R. Huiskes. 2005b. A fibril-reinforced poroviscoelastic swelling model for articular cartilage. *Journal of Biomechanics*. 38:1195-1204.

- Wolf, K., I. Mazo, H. Leung, K. Engelke, U.H. von Andrian, E.I. Deryugina, A.Y. Strongin, E.B. Brocker, and P. Friedl. 2003a. Compensation mechanism in tumor cell migration: mesenchymal-amoeboid transition after blocking of pericellular proteolysis. *Journal of Cell Biology*. 160:267-277.
- Wolf, K., R. Muller, S. Borgmann, E.B. Brocker, and P. Friedl. 2003b. Amoeboid shape change and contact guidance: T-lymphocyte crawling through fibrillar collagen is independent of matrix remodeling by MMPs and other proteases. *Blood*. 102:3262-9.
- Woo, S.L., G.A. Johnson, and B.A. Smith. 1993. Mathematical modeling of ligaments and tendons. *J Biomech Eng*. 115:468-73.
- Woo, S.L., V.C. Mow, and W.M. Lai. 1987. Biomechanical properties of articular cartilage. In *Handbook of Bioengineering*. R. Skalak and C.S. Chen, editors. McGraw-Hill Book Company, New York.
- Woo, S.L.Y., W.H. Akeson, and G.F. Jemmott. 1976. Measurements of Nonhomogeneous, Directional Mechanical-Properties of Articular-Cartilage in Tension. *Journal of Biomechanics*. 9:785-791.
- Woo, S.L.Y., M.A. Gomez, and W.H. Akeson. 1981. The Time and History-Dependent Viscoelastic Properties of the Canine Medial Collateral Ligament. *Journal of Biomechanical Engineering-Transactions of the Asme*. 103:293-298.
- Wu, H.W., T. Kuhn, and V.T. Moy. 1998. Mechanical properties of 1929 cells measured by atomic force microscopy: Effects of anticytoskeletal drugs and membrane crosslinking. *Scanning*. 20:389-397.
- Wu, P.D., and E. van der Giessen. 1993. On Improved Network Models for Rubber Elasticity and Their Applications to Orientation Hardening in Glassy-Polymers. *Journal of the Mechanics and Physics of Solids*. 41:427-456.
- Xu, J.Y., W.H. Schwarz, J.A. Kas, T.P. Stossel, P.A. Janmey, and T.D. Pollard. 1998a. Mechanical properties of actin filament networks depend on preparation, polymerization conditions, and storage of actin monomers. *Biophysical Journal*. 74:2731-2740.
- Xu, J.Y., V. Viasnoff, and D. Wirtz. 1998b. Compliance of actin filament networks measured by particle-tracking microrheology and diffusing wave spectroscopy. *Rheologica Acta*. 37:387-398.
- Yamada, S., D. Wirtz, and S.C. Kuo. 2000. Mechanics of living cells measured by laser tracking microrheology. *Biophysical Journal*. 78:1736-1747.
- Yamakawa, H. 1976. Statistical-Mechanics of Wormlike Chains. *Pure and Applied Chemistry*. 46:135-141.

- Yamazaki, D., S. Kurisu, and T. Takenawa. 2005. Regulation of cancer cell motility through actin reorganization. *Cancer Sci.* 96:379-86.
- Yanagida, T., M. Nakase, K. Nishiyama, and F. Oosawa. 1984. Direct Observation of Motion of Single F-Actin Filaments in the Presence of Myosin. *Nature.* 307:58-60.
- Yang, W., T.C. Fung, K.S. Chian, and C.K. Chong. 2006. Viscoelasticity of Esophageal Tissue and Application of a QLV Model. *Journal of Biomechanical Engineering.* 128:909-916.
- Yap, B., and R.D. Kamm. 2005. Mechanical deformation of neutrophils into narrow channels induces pseudopod projection and changes in biomechanical properties. *J Appl Physiol.* 98:1930-1939.
- Yeoh, O.H. 1990. Characterization of elastic properties of carbon-black-filled rubber vulcanizates. *Rubber Chemistry and Technology.* 63:792-805.
- Yeung, A., and E. Evans. 1989. Cortical shell-liquid core model for passive flow of liquid-like spherical cells into micropipets. *Biophys J.* 56:139-49.
- Zahalak, G.I., W.B. McConnaughey, and E.L. Elson. 1990. Determination of cellular mechanical properties by cell poking, with an application to leukocytes. *J Biomech Eng.* 112:283-94.
- Zaman, M.H., R.D. Kamm, P. Matsudaira, and D.A. Lauffenburger. 2005. Computational model for cell migration in three-dimensional matrices. *Biophys J.* 89:1389-97.
- Zhelev, D.V., A.M. Alteraifi, and D. Chodniewicz. 2004. Controlled Pseudopod Extension of Human Neutrophils Stimulated with Different Chemoattractants. *Biophys. J.* 87:688-695.
- Zhelev, D.V., D. Needham, and R.M. Hochmuth. 1994. A Novel Micropipet Method for Measuring the Bending Modulus of Vesicle Membranes. *Biophysical Journal.* 67:720-727.
- Zhou, E.H., C.T. Lim, and S.T. Quek. 2005. Finite element simulation of the micropipette aspiration of a living cell undergoing large viscoelastic deformation. *Mechanics of Advanced Materials and Structures.* 12:501-512.
- Zhu, C., G. Bao, and N. Wang. 2000. Cell mechanics: mechanical response, cell adhesion, and molecular deformation. *Annu Rev Biomed Eng.* 2:189-226.
- Zhu, C., and R. Skalak. 1988. A continuum model of protrusion of pseudopod in leukocytes. *Biophys J.* 54:1115-37.

- Zhu, W., V.C. Mow, T.J. Koob, and D.R. Eyre. 1993. Viscoelastic shear properties of articular cartilage and the effects of glycosidase treatments. *J Orthop Res.* 11:771-81.
- Zicha, D., I.M. Dobbie, M.R. Holt, J. Monypenny, D.Y. Soong, C. Gray, and G.A. Dunn. 2003. Rapid actin transport during cell protrusion. *Science.* 300:142-5.
- Zigmond, S.H. 1998. Actin cytoskeleton: the Arp2/3 complex gets to the point. *Curr Biol.* 8:R654-7.
- Zigmond, S.H. 2004. Formin-induced nucleation of actin filaments. *Current Opinion in Cell Biology.* 16:99-105.
- Zigmond, S.H., M. Joyce, C. Yang, K. Brown, M. Huang, and M. Pring. 1998. Mechanism of Cdc42-induced actin polymerization in neutrophil extracts. *J Cell Biol.* 142:1001-12.